OBSERVATIONS, INTERACTIONS, AND IMPLICATIONS OF INCREASINGLY DYNAMIC PERMAFROST COASTAL SYSTEMS

EDITED BY: Benjamin M. Jones, Louise Farquharson, Anna M. Irrgang, Nataliya G. Belova and Scott Raymond Dallimore

PUBLISHED IN: Frontiers in Earth Science and Frontiers in Environmental Science

frontiers Research Topics

frontiers

ISSN 1664-8714
ISBN 978-2-88976-024-4
DOI 10.3389/978-2-88976-024-4

About Frontiers

Frontiers is more than just an open-access publisher of scholarly articles: it is a pioneering approach to the world of academia, radically improving the way scholarly research is managed. The grand vision of Frontiers is a world where all people have an equal opportunity to seek, share and generate knowledge. Frontiers provides immediate and permanent online open access to all its publications, but this alone is not enough to realize our grand goals.

Frontiers Journal Series

The Frontiers Journal Series is a multi-tier and interdisciplinary set of open-access, online journals, promising a paradigm shift from the current review, selection and dissemination processes in academic publishing. All Frontiers journals are driven by researchers for researchers; therefore, they constitute a service to the scholarly community. At the same time, the Frontiers Journal Series operates on a revolutionary invention, the tiered publishing system, initially addressing specific communities of scholars, and gradually climbing up to broader public understanding, thus serving the interests of the lay society, too.

Dedication to Quality

Each Frontiers article is a landmark of the highest quality, thanks to genuinely collaborative interactions between authors and review editors, who include some of the world's best academicians. Research must be certified by peers before entering a stream of knowledge that may eventually reach the public - and shape society; therefore, Frontiers only applies the most rigorous and unbiased reviews.
Frontiers revolutionizes research publishing by freely delivering the most outstanding research, evaluated with no bias from both the academic and social point of view. By applying the most advanced information technologies, Frontiers is catapulting scholarly publishing into a new generation.

What are Frontiers Research Topics?

Frontiers Research Topics are very popular trademarks of the Frontiers Journals Series: they are collections of at least ten articles, all centered on a particular subject. With their unique mix of varied contributions from Original Research to Review Articles, Frontiers Research Topics unify the most influential researchers, the latest key findings and historical advances in a hot research area! Find out more on how to host your own Frontiers Research Topic or contribute to one as an author by contacting the Frontiers Editorial Office: frontiersin.org/about/contact

OBSERVATIONS, INTERACTIONS, AND IMPLICATIONS OF INCREASINGLY DYNAMIC PERMAFROST COASTAL SYSTEMS

Topic Editors:
Benjamin M. Jones, University of Alaska Fairbanks, United States
Louise Farquharson, University of Alaska Fairbanks, United States
Anna M. Irrgang, Alfred Wegener Institute Helmholtz Centre for Polar and Marine Research (AWI), Germany
Nataliya G. Belova, Lomonosov Moscow State University, Russia
Scott Raymond Dallimore, Geological Survey of Canada, Canada

Citation: Jones, B. M., Farquharson, L., Irrgang, A. M., Belova, N. G., Dallimore, S. R., eds. (2022). Observations, Interactions, and Implications of Increasingly Dynamic Permafrost Coastal Systems. Lausanne: Frontiers Media SA.
doi: 10.3389/978-2-88976-024-4

Table of Contents

frontiers in Earth Science

ORIGINAL RESEARCH
published: 12 May 2020
doi: 10.3389/feart.2020.00143

Geometric and Material Variability Influences Stress States Relevant to Coastal Permafrost Bluff Failure

Matthew A. Thomas[1†], Alejandro Mota[2], Benjamin M. Jones[3], R. Charles Choens[2], Jennifer M. Frederick[2] and Diana L. Bull[2]*

[1] U.S. Geological Survey, Geologic Hazards Science Center, Golden, CO, United States, [2] Sandia National Laboratories, Albuquerque, NM, United States, [3] Institute of Northern Engineering, College of Engineering and Mines, University of Alaska Fairbanks, Fairbanks, AK, United States

Scientific knowledge and engineering tools for predicting coastal erosion are largely confined to temperate climate zones that are dominated by non-cohesive sediments. The pattern of erosion exhibited by the ice-bonded permafrost bluffs in Arctic Alaska, however, is not well-explained by these tools. Investigation of the oceanographic, thermal, and mechanical processes that are relevant to permafrost bluff failure along Arctic coastlines is needed. We conducted physics-based numerical simulations of mechanical response that focus on the impact of geometric and material variability on permafrost bluff stress states for a coastal setting in Arctic Alaska that is prone to toppling mode block failure. Our three-dimensional geomechanical boundary-value problems output static realizations of compressive and tensile stresses. We use these results to quantify variability in the loci of potential instability. We observe that niche dimension affects the location and magnitude of the simulated maximum tensile stress more strongly than the bluff height, ice wedge polygon size, ice wedge geometry, bulk density, Young's Modulus, and Poisson's Ratio. Our simulations indicate that variations in niche dimension can produce radically different potential failure areas and that even relatively shallow vertical cracks can concentrate displacement within ice-bonded permafrost bluffs. These findings suggest that stability assessment approaches, for which the geometry of the failure plane is delineated *a priori*, may not be ideal for coastlines similar to our study area and could hamper predictions of erosion rates and nearshore sediment/biogeochemical loading.

Keywords: Arctic Alaska, coastal erosion, permafrost, bluff failure, numerical modeling, mechanics

OPEN ACCESS

Edited by:
Felix Ng,
University of Sheffield,
United Kingdom

Reviewed by:
Sebastian Westermann,
University of Oslo, Norway
Irina Overeem,
University of Colorado Boulder,
United States

****Correspondence:***
Matthew A. Thomas
matthewthomas@usgs.gov

†ORCID:
Matthew A. Thomas
orcid.org/0000-0002-9828-5539

Specialty section:
This article was submitted to Cryospheric Sciences, a section of the journal Frontiers in Earth Science

Received: *29 October 2019*
Accepted: *17 April 2020*
Published: *12 May 2020*

Citation:
Thomas MA, Mota A, Jones BM, Choens RC, Frederick JM and Bull DL (2020) Geometric and Material Variability Influences Stress States Relevant to Coastal Permafrost Bluff Failure. Front. Earth Sci. 8:143. doi: 10.3389/feart.2020.00143

INTRODUCTION

Permafrost coastlines account for one-third of the global coastline (Lantuit et al., 2012). Declining sea ice in the Arctic Ocean has increased the length of the open-water season, exposing permafrost coastlines to more frequent and intense forms of wave energy and storm surge (Maslanik et al., 2007; Serreze et al., 2007; Overeem et al., 2011; Simmonds and Rudeva, 2012; Stammerjohn et al., 2012; Vermaire et al., 2013; Barnhart et al., 2014a). Annual rates of erosion along ice-rich portions of the Arctic Alaska coast have doubled since the middle of the twentieth century (Jorgenson and Brown, 2005; Mars and Houseknecht, 2007; Jones et al., 2009, 2018; Ping et al., 2011; Gibbs and Richmond, 2015; Gibbs et al., 2017) and are accelerating to values that are among the highest

in the world (up to 20–30 m yr^{-1}; Reimnitz et al., 1988; Wobus et al., 2011; Barnhart et al., 2014b). Elevated erosion rates in the Arctic are projected to have significant environmental impacts on global carbon fluxes and marine food webs (Vonk et al., 2012; Fritz et al., 2017).

Much of Arctic Alaska is inaccessible by all-season roads; therefore, people and infrastructure are concentrated near the coastline. Native coastal villages in Alaska are now more frequently affected by erosion, with more than 30 facing relocation (U.S. Government Accountability Office, 2004, 2009). Active U.S. Department of Defense long-range Arctic coastal radars, which are dedicated to maintaining national sovereignty in the air, are experiencing higher-than-expected rates of bluff retreat (Hughes, 2016). Coastal erosion in Arctic Alaska is projected to increase the cost of maintaining infrastructure (e.g., roads and pipelines) by billions of dollars in the coming decades (Larsen et al., 2008). The financial impact of enhanced coastal erosion will likely be further exacerbated by emerging geopolitical pressures, including the discovery of natural resources (e.g., hydrocarbons and minerals) and the opening of new shipping routes and the construction of support facilities in the Arctic (Clement et al., 2013).

Thermo-denudation and thermo-abrasion are two thermal-mechanical processes that dominate the Arctic coastal erosion problem (Aré, 1988a,b; Günther et al., 2013). Thermo-denudation refers to the subaerial degradation of permafrost, which triggers ground failure that proceeds under the influence of gravity, typically in the form of subsidence or slumping. Thermo-abrasion refers to the combined effect of thermal and mechanical erosion of ice-rich permafrost bluffs due to wave action. Here, the parent material at the base of the bluff is warmed by the ocean and removed by the mechanical action of waves. A recess at the base of the bluff, commonly referred to as a "thermo-erosional niche," progresses landward until the overhanging material fails via translational or toppling mode block failure (Hoque and Pollard, 2009).

Pioneering studies that focused on simulating niche formation in frozen coastal bluffs developed an analytical solution for one-dimensional heat transfer that predicts niche depth as a function of nearshore oceanographic conditions including water temperature, water level, and storm duration (Kobayashi, 1985; Kobayashi and Aktan, 1986). Due to the high ice content of many permafrost bluffs, more recent studies that have focused on simulating niche formation (e.g., Wobus et al., 2011) have adopted empirical equations that were originally designed to predict the melting rate of free-drifting icebergs (e.g., Russell-Head, 1980; White et al., 1980). These computationally efficient, rule-based niche advancement models have been paired with geometric criteria, such a critical niche depth (Ravens et al., 2012), or limit-equilibrium expressions to develop stability nomograms (Hoque and Pollard, 2009, 2016) and quantify bluff retreat rates (e.g., Barnhart et al., 2014b). An important theme that has emerged from these scientific contributions is the episodic nature of block failure in coastal permafrost systems, a key factor in estimating coastal erosion rates meant to guide land-use decisions (Thomas and Loague, 2016).

A less-studied component of permafrost bluff erosion is the mechanical behavior of the bluff leading up to failure. Stress is an important mechanical factor because it is the physical state variable that responds to the oceanographic forcings that affect the spatiotemporal characteristics of niche development and subsequent bluff failure (Frederick et al., 2016). Herein, we employ physics-based geomechanical simulation, in a concept-development mode (Loague et al., 2010), to quantify the impact of bluff geometry and material variability on stress states for coastal permafrost coastlines that are susceptible to toppling mode block failure. Our numerical simulation approach is advantageous in that it is based on measurable physical properties (as opposed to indirect analytical or empirical proxies). Furthermore, the potential failure does not need to be defined *a priori*, but rather, can be interpreted from the multidimensional patterns of stress produced by the model. The value of the work we present here lies in its ability to (1) improve process-based understanding of coastal permafrost bluff failure characteristics and (2) provide a foundation for more complex simulation scenarios geared toward resolving long-term erosion rates from an event-based perspective.

DREW POINT, ALASKA

The geomechanical simulation scenarios that we formulated are informed by observations from Drew Point, Alaska. Located ∼100 km east of Utqiagvik (formerly known as Barrow; **Figure 1A**), the 9-km stretch of coastline at Drew Point consists of low-lying (∼5 m average height; Jones et al., 2018) bluffs that are set amid a broad coastal plain (**Figure 1B**). The bluffs host a network of ice wedges (1–3 m wide, 3–5 m deep; Jones et al., 2018) and ice wedge polygons (15 m average width; Jones et al., 2018) with fine-grained, ice-bonded marine sediments (∼40–90% ice by volume; Ping et al., 2011; Wobus et al., 2011; Kanevskiy et al., 2013; Barnhart et al., 2014b; **Figure 1C**) that were deposited in the late Quaternary (Jones et al., 2018). These bluff height and ice-content characteristics are typical for ∼25% of the Beaufort Sea coast (Barnhart et al., 2014b). The bluff stratigraphy at Drew Point includes vegetative matting, an active (seasonably unfrozen) surficial layer, and a complex sequence of terrestrial- and marine-derived sediments. Nearshore water depths at Drew Point are shallow (<2 m within 0.5 km of the shoreline; Jones et al., 2018) and exhibit microtidal (∼15 cm, daily to monthly; Barnhart et al., 2014b) fluctuations. During the sea ice-free summer/fall season, storms raise nearshore water levels and undercut the bluffs via thermo-abrasion (**Figures 2A,B**) until a toppling mode block failure occurs (**Figure 2C**). Although small-scale shear modes may exist, toppling appears to be the dominant failure mechanism at Drew Point. Typically, the failed blocks disintegrate in the nearshore environment (**Figure 2D**) over the course of days to weeks, providing only short-term armoring against further retreat (Barnhart et al., 2014b; Jones et al., 2018).

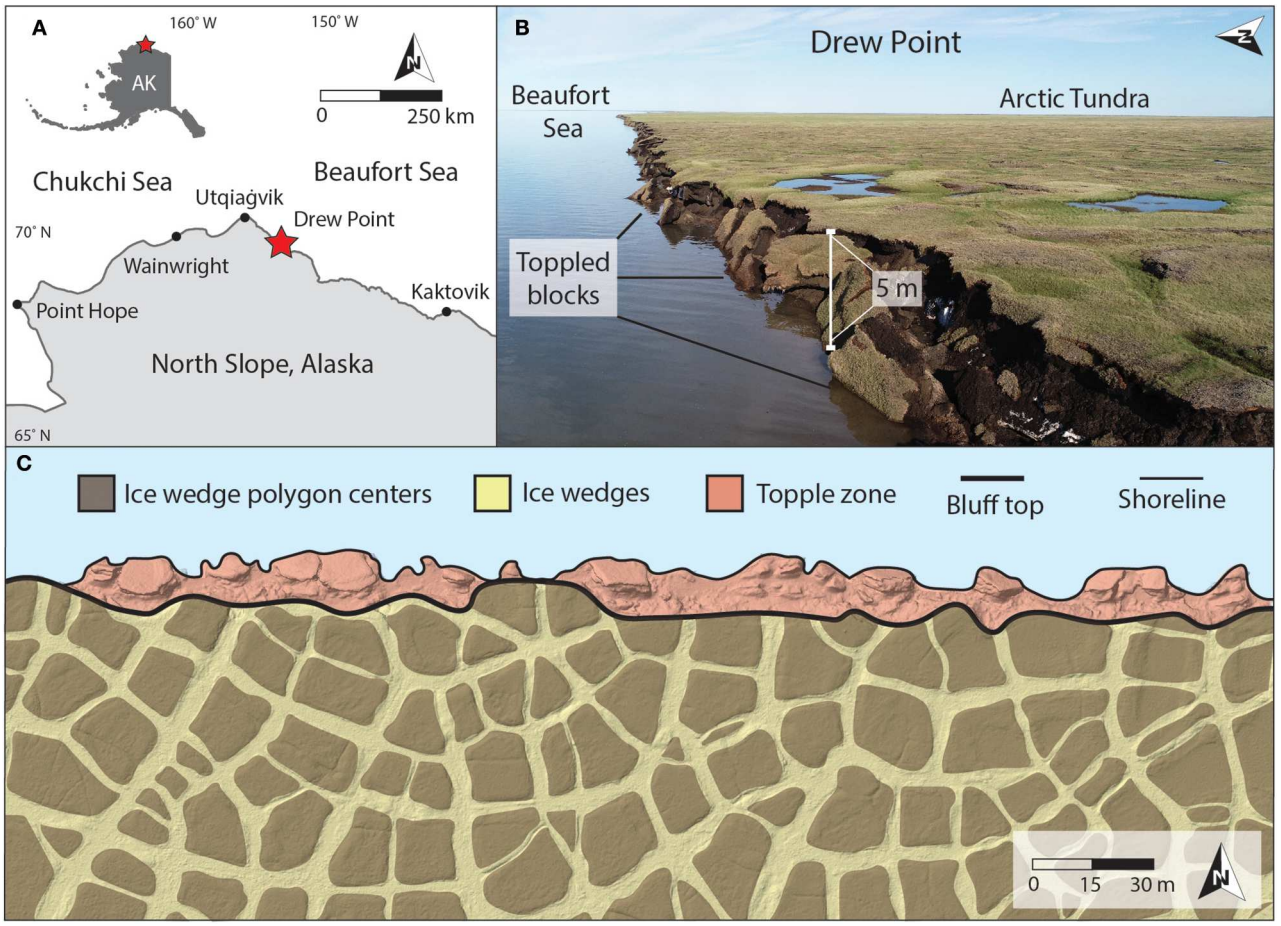

FIGURE 1 | (A) Location of the Drew Point study area (red star) along the north coast of Alaska, USA. **(B)** Oblique aerial view acquired by unmanned aerial vehicle (UAV) showing toppling mode block failure that is typical along the coastline at Drew Point. **(C)** UAV orthophoto mosaic showing the permafrost terrain configuration at Drew Point consisting of ice wedges, ice wedge polygon networks, and the topple zone. Roughly 75% of the block failures in this example occurred along an ice wedge, whereas 25% occurred in an ice wedge polygon center.

METHODS

We applied continuum mechanics theory with static simulations of three-dimensional (3D) heterogeneous elastic finite deformation to assess the impacts of bluff geometry and material variability on stress states leading up to permafrost bluff failure. We present the modeled state of stress here with the linear elastic equation, as the extent of deformation prior to the toppling block failure of the rigid, ice-rich permafrost bluff materials in our study area is relatively small over short (i.e., daily to weekly) timescales and well-approximates elastic finite deformation theory. Linear elastic theory has been used to examine stresses for vertical bluff geometries in a number of lower latitude, non-permafrost settings (e.g., Young and Ashford, 2008; Collins and Sitar, 2011; Lu et al., 2012). Static 3D linear elastic stress with a gravitational body force can be expressed (see Rao, 2007) as:

$$\frac{\partial \sigma_{xx}}{\partial \mathrm{x}} + \frac{\partial \sigma_{xy}}{\partial \mathrm{y}} + \frac{\partial \sigma_{zx}}{\partial \mathrm{z}} = 0 \quad (1)$$

$$\frac{\partial \sigma_{xy}}{\partial \mathrm{x}} + \frac{\partial \sigma_{yy}}{\partial \mathrm{y}} + \frac{\partial \sigma_{yz}}{\partial \mathrm{z}} = 0 \quad (2)$$

$$\frac{\partial \sigma_{zx}}{\partial \mathrm{x}} + \frac{\partial \sigma_{yz}}{\partial \mathrm{y}} + \frac{\partial \sigma_{zz}}{\partial \mathrm{z}} + \rho_b g = 0 \quad (3)$$

where σ is the stress [M/LT^2], ρ_b is the (permafrost or ice wedge) bulk density [M/L^3], g is the acceleration due to gravity [L/T^2], and x-y-z are the map-view and vertical coordinates [L]. The nine components of stress within the equilibrium equations are defined by:

$$\sigma_{xx} = \lambda \Delta + 2\mu \varepsilon_{xx} \quad (4)$$

$$\sigma_{yy} = \lambda \Delta + 2\mu \varepsilon_{yy} \quad (5)$$

$$\sigma_{zz} = \lambda \Delta + 2\mu \varepsilon_{zz} \quad (6)$$

$$\sigma_{xy} = \sigma_{yx} = \mu \varepsilon_{xy} \quad (7)$$

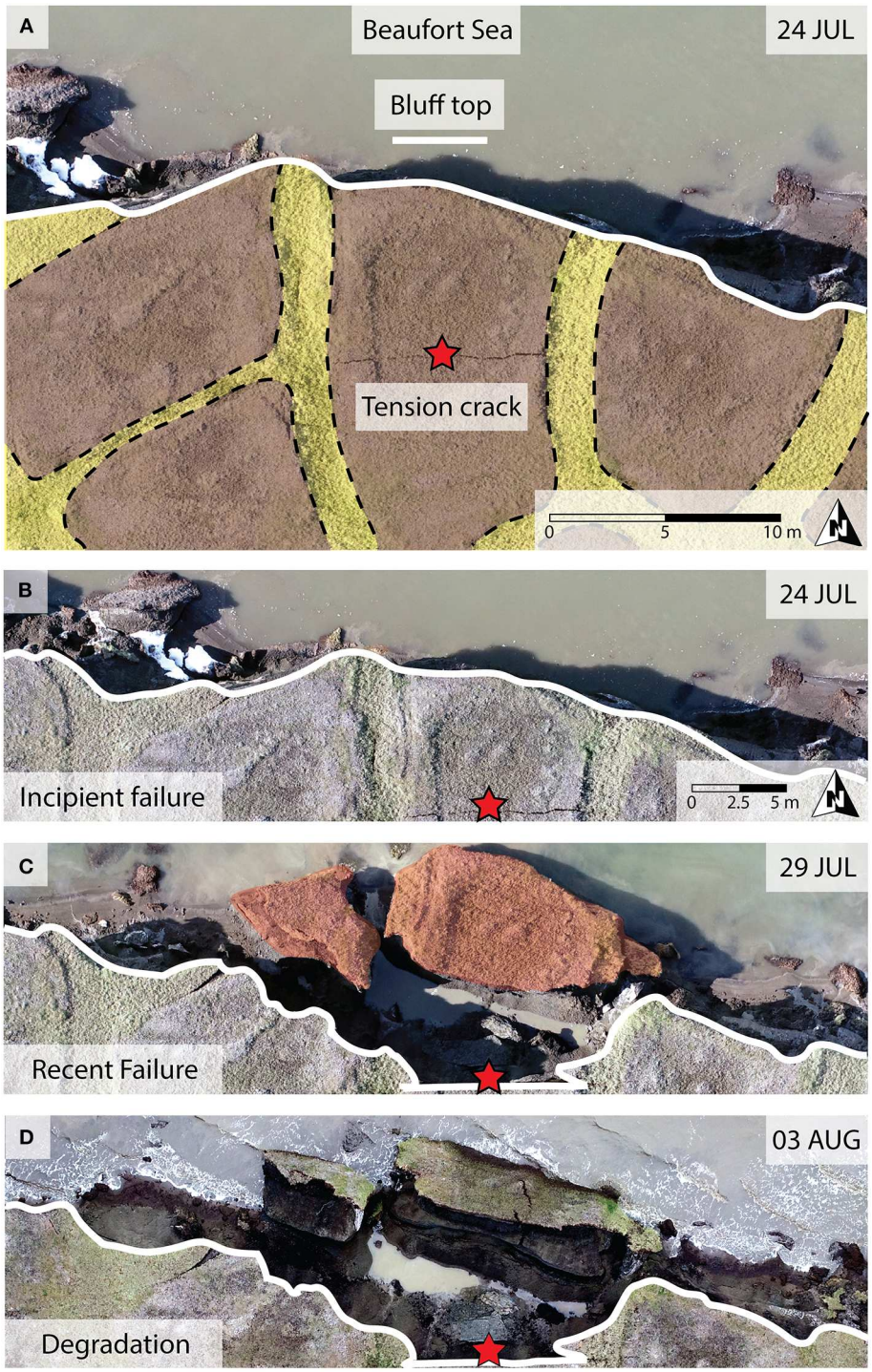

FIGURE 2 | (A) Unmanned aerial vehicle (UAV)-based orthophoto mosaic of a tension crack (red star) visible on 24 July 2018. The local bluff height, niche height, and niche depth are approximately 4.9, 1.9, and 4.5 m, respectively. Yellow and brown shaded areas highlight ice wedges and polygon centers, respectively. Sequence of repeat UAV-based orthophoto mosaics showing **(B)** incipient failure (24 July), **(C)** recent failure (29 July), and **(D)** degradation of the permafrost block in the nearshore environment (03 August).

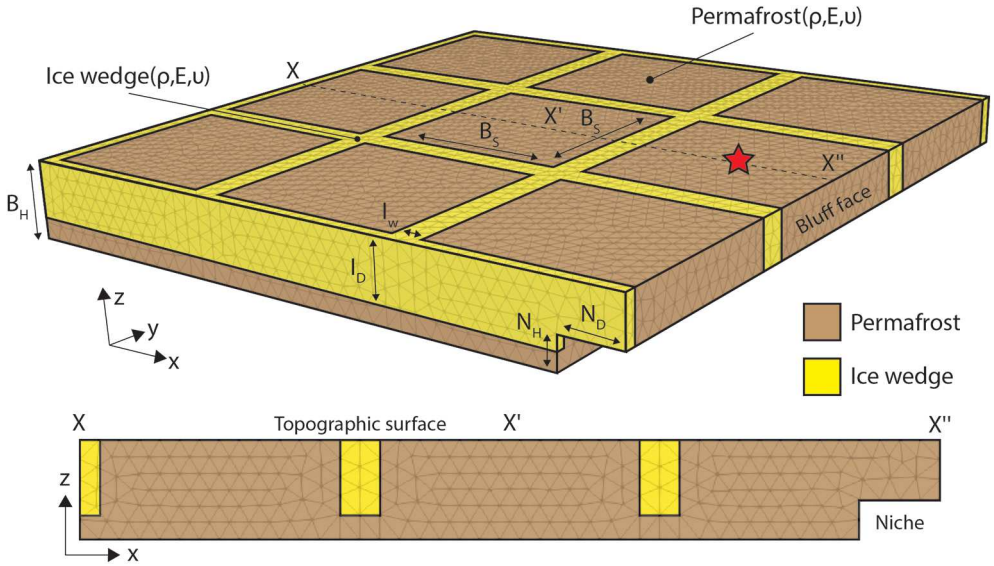

FIGURE 3 | Schematic of the base case three-dimensional geomechanical boundary-value problem (BVP). Geometric properties include the niche height (N_H), niche depth (N_D), ice wedge depth (I_D), ice wedge width (I_W), permafrost block size (B_S), and bluff height (B_H). Material properties include the bulk density (ρ), Young's Modulus (*E*), and Poisson's Ratio (υ) for ice wedges (yellow) and permafrost (brown). The red star corresponds to the approximate location of the tension crack that is visible in **Figure 2**.

$$\sigma_{yz} = \sigma_{zy} = \mu\varepsilon_{yz} \tag{8}$$

$$\sigma_{zx} = \sigma_{xz} = \mu\varepsilon_{zx} \tag{9}$$

where ε is the strain [dimensionless], λ and μ are Lamé parameters [M/LT^2], and $\Delta = \varepsilon_{xx} + \varepsilon_{yy} + \varepsilon_{zz}$. The nine components of strain are given as:

$$\varepsilon_{xx} = \frac{\partial \mathrm{u}}{\partial \mathrm{x}} \tag{10}$$

$$\varepsilon_{yy} = \frac{\partial \mathrm{v}}{\partial \mathrm{y}} \tag{11}$$

$$\varepsilon_{zz} = \frac{\partial \mathrm{w}}{\partial \mathrm{z}} \tag{12}$$

$$\varepsilon_{xy} = \varepsilon_{yx} = \frac{\partial \mathrm{u}}{\partial \mathrm{y}} + \frac{\partial \mathrm{v}}{\partial \mathrm{x}} \tag{13}$$

$$\varepsilon_{yz} = \varepsilon_{zy} = \frac{\partial \mathrm{w}}{\partial \mathrm{y}} + \frac{\partial \mathrm{v}}{\partial \mathrm{z}} \tag{14}$$

$$\varepsilon_{zx} = \varepsilon_{xz} = \frac{\partial \mathrm{u}}{\partial \mathrm{z}} + \frac{\partial \mathrm{w}}{\partial \mathrm{x}} \tag{15}$$

where u, v, and w are displacement components [L] parallel to the x, y, z axes. The Lamé parameters are:

$$\lambda = \frac{\upsilon E}{(1+\upsilon)(1-2\upsilon)} \tag{16}$$

and

$$\mu = \frac{E}{2(1+\upsilon)} \tag{17}$$

where *E* is the Young's modulus [M/LT^2] and υ is Poisson's Ratio [dimensionless] for permafrost or ice wedge.

The numerical code that we used is Albany, an open-source implicit unstructured finite-element application (Salinger et al., 2016; Sandia National Laboratories, 2017). The simulation domain is made up of square permafrost blocks intersected by a regular network of ice wedges (simplified as rectangular prisms) and is discretized with ∼2 × 10^4 nodes at 1-m average grid spacing (**Figure 3**). We did not include the active layer in our simulation framework for this study because its vertical extent is minimal (∼25 cm depth compared to the 5 m average bluff height) and its mechanical properties are poorly constrained for our study region. The lateral and rear surfaces, which include half ice wedge thicknesses, are symmetry-type displacement boundary conditions which mirror stress across the boundary. The basal surface is a fixed boundary with zero displacement, while the topographic surface and bluff face are free surfaces subject to displacement. The central portion of the bluff face is laterally separated by at least one permafrost block to reduce the impact of the displacement-type boundary conditions on the area of interest (i.e., cross section X-X″ in **Figure 3**). The geomechanical boundary-value problem produces steady-state snapshots of stress and displacement (**Figure 4**). These simulations facilitated examination of stress patterns within the bluff and identification of the location and magnitude of the maximum tensile stress (σ_{Tmax}) that forms along the topographic surface. The σ_{Tmax}, created by a bending moment along the bluff

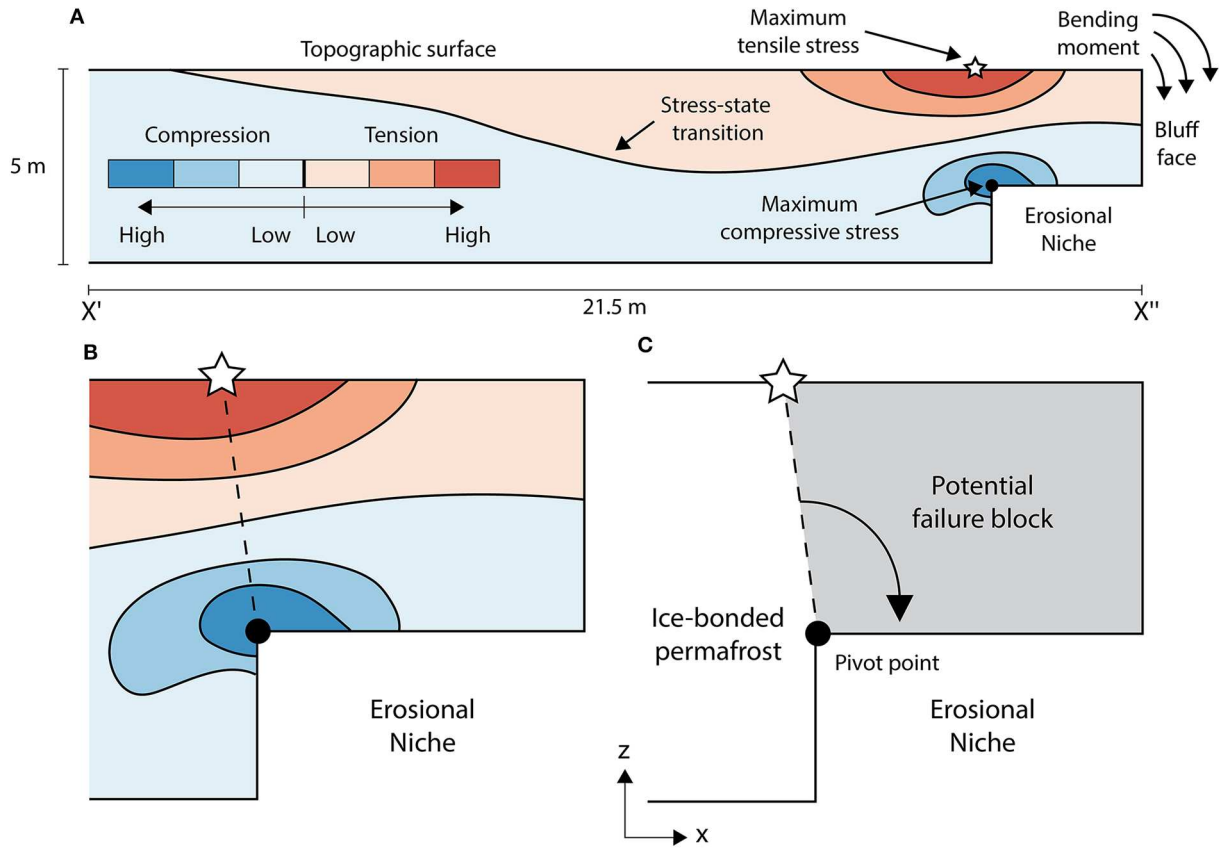

FIGURE 4 | (A) Conceptual cross section (X′-X″ in **Figure 3**) of patterns of stress based on elastic geomechanical simulation. **(B)** Enlargement of stress field in the vicinity of the bluff face and erosional niche. Dashed black line connects the points of maximum tensile and compressive stress. **(C)** Diagram of potential toppling mode block failure (gray area) about a pivot point (black circle).

face (**Figure 4A**), is an important metric because it reflects a likely initiation location for toppling mode block failure.

The modeling strategy that we adopted for this study was not an event-based reconstruction of stress encompassing bluff failure, but rather an evaluation of how the σ_{Tmax} is influenced by plausible variations in bluff geometry and the material properties. These variations are not meant to serve as validation cases for Drew Point or encompass all possibilities, but rather, serve as a set of plausible, internally consistent numerical experiments to quantify the relative impact of geometric and material variability on the bluff's stress state. The geometric characteristics that we considered (**Figure 3**) are niche height (N_H), niche depth (N_D), bluff height (B_H), permafrost block size (B_S), ice wedge thickness (I_W), and ice wedge depth (I_D). These characteristics were informed by field observations (e.g., hand survey methods such as a tape measure) and visual inspection of UAV-based aerial photography, as opposed to a formal statistical analysis. A series of UAV-derived orthophoto mosaics were created with Pix4D Mapper version 4.3.31 using ∼750 images in each survey acquired on 24 July 2018, 29 July 2018, and 03 August 2018, from a DJI Phantom 4 Pro V2 UAV for a 0.3 km^2 area located at Drew Point (**Figure 2**). We used the photos to examine ice wedge geometries, ice wedge polygon dimensions, niche dimensions, block failure locations relative to ice wedges, and block failure sizes. The ice wedge and permafrost mechanical properties that we considered (**Figure 3**) are bulk density (ρ_b), Young's Modulus (E), and Poisson's Ratio (υ). The base case geometric and material parameter values (**Table 1**) represent the median of the bounding values that we observe in the field and laboratory, respectively. The base case geometric parameter values also approximate geometric conditions that we have observed just prior to bluff failure (**Figure 2**). The mechanical property values (**Table 2**) are based on unconfined compressive strength and direct tension tests that were conducted on intact permafrost core from the study region or literature-based values for pure crystalline ice (i.e., Schulson, 1999; Randhawa, 2018). While not comprehensive, the experimentally obtained mechanical and material properties are illustrative of a potential range of values. We provide a description of the permafrost mechanical tests in the **Supplementary Material**.

Our initial simulation ensemble targeted variability in geometric characteristics. Here, we constrained our analysis to variability within bounding-type parameter pairs (i.e., niche height vs. niche depth, bluff height vs. permafrost block size,

TABLE 1 | Parameter values used to evaluate the impact of variability in geometric and material properties on the magnitude and location of the simulated maximum tensile stress.

Property	Parameter	Units	Values			Source
			Lower	Base Case	Higher	
G	B_S	m	10	15	20	Jones et al., 2018; UAV-based photography
G	B_H	m	2.5	5	7.5	Jones et al., 2018; UAV-based photography
G	I_D	m	50% B_H	75% B_H	100% B_H	Jones et al., 2018; field observations
G	I_W	m	1	2	3	Jones et al., 2018; field observations
G	N_H	m	1	2	3	Field observations
G	N_D	m	2	4	6	Field observations
M	E_{pf}	Pa	1.E+08	5.E+08	1.E+09	**Table 2**
M	υ_{pf}	Dimensionless	0.1	0.25	0.4	**Table 2**
M	$\rho_{b,pf}$	kg m^{-3}	1000	1,250	1,500	**Table 2**
M	E_i	Pa	5.E+08	7.5E+08	1.E+09	Schulson, 1999; Randhawa, 2018
M	υ_i	Dimensionless	0.1	0.25	0.4	Schulson, 1999; Randhawa, 2018
M	$\rho_{b,i}$	kg m^{-3}	871	917	963	Schulson, 1999; Randhawa, 2018

G, geometric; M, material; B_S, block size; B_H, bluff height; I_D, ice wedge depth; I_W, ice wedge width; N_H, niche height; N_D, niche depth; E, Young's modulus; υ, Poisson's Ratio; ρ_b, bulk density; $_{pf}$, permafrost; $_i$, ice.

TABLE 2 | Observed permafrost material property values used to inform the parameter ranges in **Table 1**.

ID*	Depth [cm]	Test	Temp [C]	E [Pa]	υ [dimensionless]	Failure stress [Pa]	ρ_b [kg m^{-3}]
1	189	C	−1	–	–	1.2E+06	1,066
2	230	C	−6	1.4E+08	0.33	2.9E+06	1,166
3	307	C	−3	1.1E+08	0.12	1.4E+06	1,054
4	349	C	−6	–	–	1.9E+06	1,465
5	349	C	−3	1.1E+08	0.26	2.1E+06	1,484
6	101	T	−1	–	–	4.5E+05	1,070
7	213	T	−3	–	–	8.2E+05	1,070
8	481	T	−6	3.3E+08	0.16	8.7E+05	–
9	500	T	−1	2.6E+08	0.12	4.3E+05	1,260
10	550	T	−6	–	–	1.1E+05	1,552
11	168	T	−3	–	–	1.0E+06	1,090
12	326	T	−6	7.9E+08	0.25	5.2E+05	1,180

** See **Supplementary Material** for a description of the geotechnical laboratory testing.*
C, unconfined compressive strength test; T, direct tension test; ρ_b, bulk density; E, Young's modulus; υ, Poisson's Ratio; ρ_b, bulk density.

and ice wedge thickness vs. ice wedge depth) to elucidate first-order impacts on the σ_{Tmax}. Specifically, we simulated all combinations of the low, base case, and high values for each geometric pair to evaluate how the location and magnitude of the σ_{Tmax} changes across the solution space. We simulated a similar ensemble for the material property pairs (i.e., ice wedge vs. permafrost ρ_b, *E*, and υ), and if we did not vary a physical parameter as part of the given pair, we applied the base case values.

After evaluating bulk sensitivities of tensile stress to variability in geometric and material properties, we focused on how niche formation affects the potential failure geometry. We manually advanced (via remeshing) the inland extent of the niche (at 0.5 m increments) for six erosional niche heights ranging from

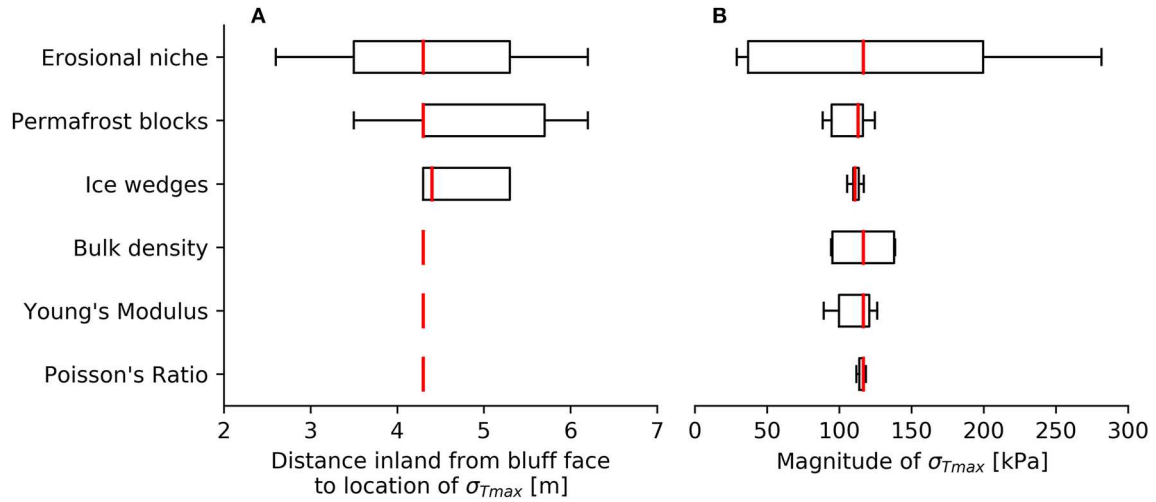

FIGURE 5 | Boxplots showing the impact of variability in geometric (i.e., erosional niche, permafrost block, and ice wedge) characteristics and ice/permafrost material properties (i.e., bulk density, Young's Modulus, and Poisson's Ratio) on the **(A)** location and **(B)** magnitude of the simulated maximum tensile stress (σ_{Tmax}). Geometric and material parameter values are reported in **Table 1**.

0.1 to 3 m, tracking the σ_{Tmax}, as well as the overall shape of the tensile vs. compressive stress fields. At each stage of niche advancement for the simulations, we noted whether or not the σ_{Tmax} exceeded the lower bound (∼100 kPa) tensile strength that was measured in the laboratory (**Table 2**). Our field observations suggest that once a tension crack forms at the surface, the permafrost bluff material on the ocean-facing side of the crack will eventually topple (**Figure 2**). Therefore, to compare the potential failure geometry for two end-member scenarios of niche height (i.e., 0.5 and 3 m) for cases where the tensile strength had been met (or exceeded), we drew a line from the point of σ_{Tmax} to the apex of the niche (**Figure 4C**) and used this geometry to estimate potential failure areas. This simple failure geometry, which assumes that the failure blocks are rigid, is a reasonable approximation based on our field observations (**Figure 2**).

To assess how a vertical crack could alter displacement within the vicinity of the potential failure block, we imposed a void in our finite-element mesh that originates at the point of σ_{Tmax} for the base case simulation scenario and extended it vertically downward. Our hypothetical fracture scenarios include voids that extend laterally in a straight line across a single permafrost block (parallel to the coast) and terminate at the bordering ice wedges, with a constant width (5 cm) and variable fracture depth (0–125 cm; F_D). The plan-view geometry of the simulated tension crack approximates conditions that we have observed in the field (**Figure 2A**). The depths represent 0–25% of the base case B_H (5 m). Because our simulations are governed by elastic principles that do not encompass permanent deformation, we focus on how patterns (as opposed to absolute values) of displacement are manifested in the vicinity of the potential failure block in the presence of a fracture.

RESULTS

Our geometric and material property simulation ensembles (**Figure 5**) indicate that niche characteristics exert the largest impact on the location and magnitude of the σ_{Tmax}, with the strongest gradient in simulated σ_{Tmax} following variability in niche depth (N_D). The σ_{Tmax} for our niche pairs ranges from 2.6 to 6.2 m (Δ 3.6 m) inland of the bluff face (**Figure 5A**) and 29–281 kPa (Δ 252 kPa; **Figure 5B**). The block size (B_S) vs. bluff height (B_H) geometric characteristics impose the second greatest impact to the σ_{Tmax}, which ranges from 3.5 to 6.2 m (Δ 2.7 m) inland of the bluff face (**Figure 5A**) and 88 to 125 kPa (Δ 37 kPa; **Figure 5B**). Whereas, B_S and B_H influence the location of the σ_{Tmax}, B_H dominates the overall impact to the magnitude of the σ_{Tmax}. Variability in the ice wedge width (I_W) and depth (I_D) impose ≤1 m and ≤15 kPa of change for the location and magnitude of the σ_{Tmax}, respectively (**Figure 5**). The reduction in σ_{Tmax} for cases of increasing I_W and I_D reflects an overall stiffening of the bluff in the presence of more massive ice wedge networks. For our simulation scenarios, variability in material properties influences the magnitude of the σ_{Tmax}. The σ_{Tmax} ranges from 94 to 139 kPa (Δ 45 kPa), 89 to 126 kPa (Δ 37 kPa), and 112 to 118 kPa (Δ 6 kPa) for the ice wedge vs. permafrost bulk density (ρ_b), Young's modulus (E), and Poisson's ratio (υ) material pairs (**Figure 5B**), with sensitivity gradients that are more strongly tied to the permafrost characteristics. The 89–139 kPa (Δ 50 kPa) σ_{Tmax} range for ρ_b and E, as opposed to the 112–118 kPa (Δ 6 kPa) σ_{Tmax} range for υ, highlights the

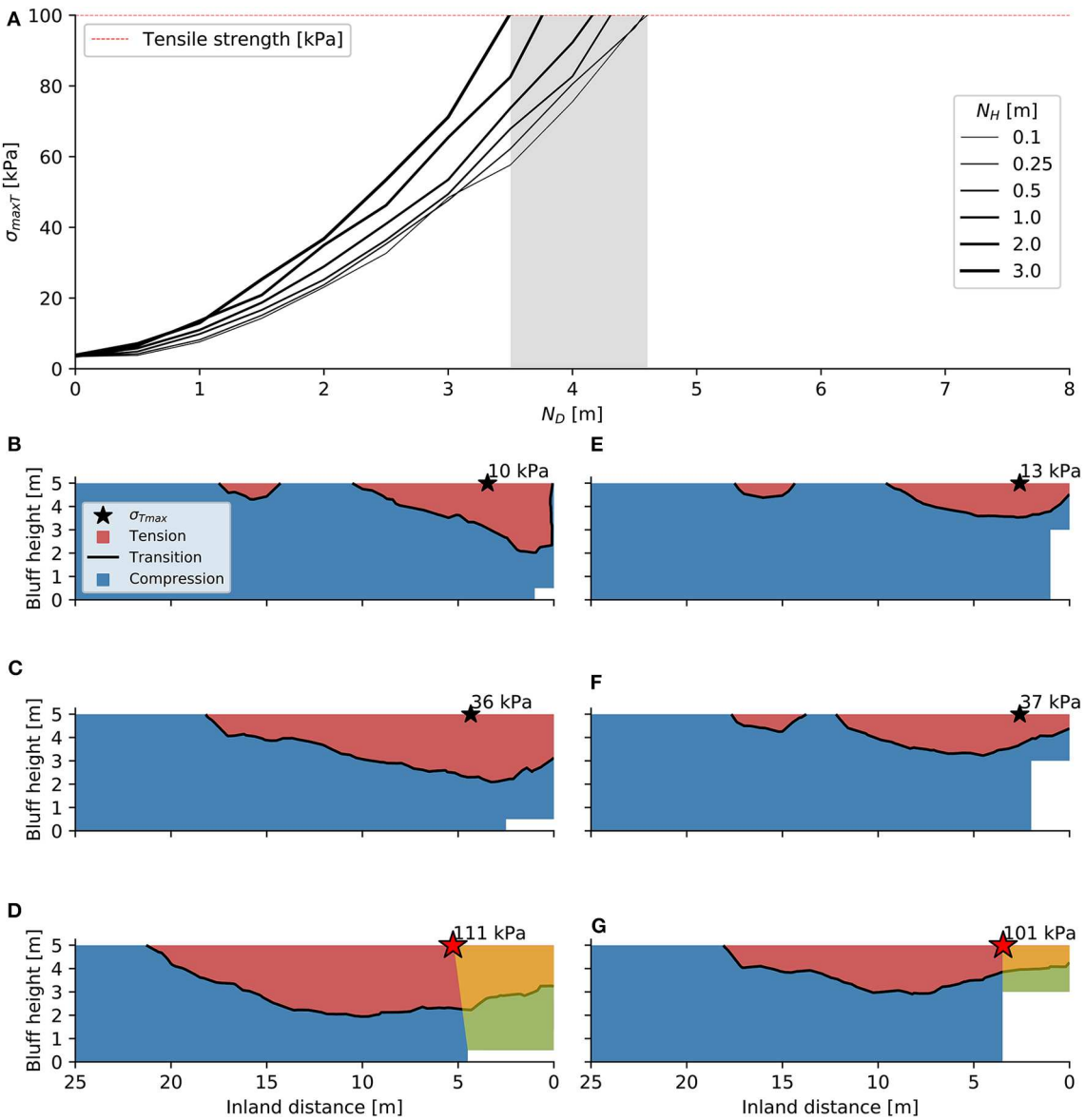

FIGURE 6 | (A) Simulated maximum tensile stress (σ_{Tmax}) for six niche height (N_H) scenarios throughout incremental stages of niche depth (N_D) advancement. Snapshots of compressive/tensile stress fields along cross section X-X″ (**Figure 3**) during niche advancement for the **(B–D)** short and **(E–G)** tall niche cases. The stars in **(B–G)** are the σ_{Tmax} location, with a red star indicating a value that the σ_{Tmax} met or exceeded the tensile strength. Yellow shading in **(D,G)** highlights potential failure areas.

importance of body forces and stiffness (as opposed to differences in lateral vs. axial strain characteristics) for our cantilever-type bluff conditions.

Based on the strong relationship between niche characteristics and σ_{Tmax}, we conducted geometric simulations with more incremental, quasi-temporal increases in N_D (0–10 m) for a wider range of N_H values (0.1–3 m; **Figure 6**). The σ_{Tmax} for the suite of niche advancement scenarios remain within ∼10 kPa of each other up until the N_D reaches ∼1.5 m (**Figure 6A**). The tallest and shortest niches (N_H = 3 and 0.1 m) exceed our lower bound tensile strength estimate when the N_D reaches 3.5 and 4.6 m, respectively (shaded area in **Figure 6A**). Niche advancement for end-member scenarios of N_H reveal systematic differences in the patterns of tensile/compressive stress, as well as the variability in the simulated σ_{Tmax}. During the advancement of a short (N_H = 0.5 m) niche (**Figures 6B–D**), the σ_{Tmax} consistently remains inland of the niche and results in a 21.8 m^2 potential failure area (**Figure 6D**). The advancement of the tall (N_H = 3 m) niche (**Figures 6E–G**) results in a considerably smaller, 8.7 m^2 potential failure area (**Figure 6G**). Throughout niche advancement, the shorter niche imparts a deeper and wider zone of tension, reflective of the greater extent of unsupported

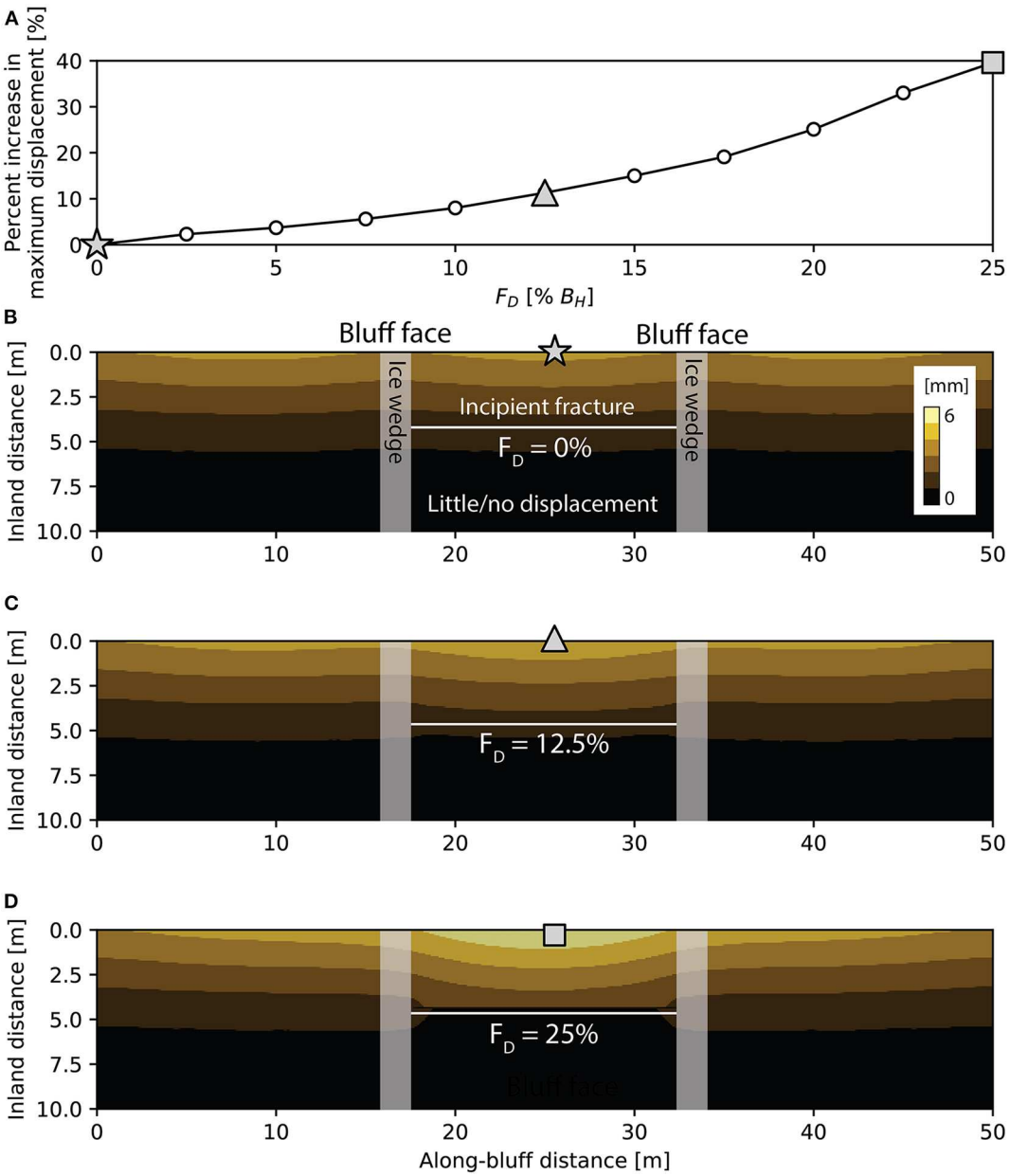

FIGURE 7 | (A) Percent increase in maximum simulated displacement for fracture depth (F_D) scenarios ranging from 0 to 25% of the total (5 m) bluff height. The light gray star, triangle, and square symbols correspond to locations in **(B–D)**, respectively. Plan-view perspective of displacement within the vicinity of a fracture with a F_D of **(B)** 0%, **(C)** 12.5%, and **(D)** 25%.

material. The highest compressive stresses generally coincide with the niche apex (**Figure 4**), although for the taller (≥3 m) and deeper niches (≥6 m), the maximum compressive stress moved slightly oceanward (up to ∼1 m).

We introduced vertical fractures (F_D ranging from 0 to 25% B_H) that extend downward from location of the σ_{Tmax} for our base case scenario (**Table 1**) to consider the impact of fracture geometries on displacement patterns for our geomechanical simulation framework (**Figure 7**). We tracked the percent increase in maximum displacement for each F_D (**Figure 7A**). As F_D increases, tension is focused near the tip of the fracture and the displacement field transitions from a relatively uniform (along-bluff) pattern to a more concentrated pattern with the maximum displacement located in the section of the bluff face that is directly seaward of the plan-view fracture midpoint (**Figures 7B–D**). The highest F_D (25% B_H) produces ∼40% more displacement than the lowest F_D (0% B_H), suggesting that the presence of a tension crack prior to failure can induce localized displacement.

DISCUSSION

Cross-Sectional Niche Characteristics

Among the geometric cases that we considered, the σ_{Tmax} is most sensitive to the cross-sectional niche characteristics (**Figure 5**). This result is physically consistent, as the niche geometry controls the degree to which the coastal bluff face acts as a cantilever with a bending moment that facilitates toppling mode block failure (**Figure 4A**). Based on our simulations, which include systematic variations of niche dimension (**Figure 6**), we found that bluffs with taller and narrower niches should fail in smaller masses compared to those with shorter and deeper niches (**Figures 6D,G**). Exposure of the bluff face to varying degrees of wave action and surge height is hypothesized to influence niche development (Kobayashi, 1985; Wobus et al., 2011; Ravens et al., 2012; Barnhart et al., 2014b; Hoque and Pollard, 2016). High-intensity, short-duration storm energy may create tall and narrow niches, whereas low-intensity, long-duration storm energy may create short and deep niches. Therefore, an important implication of our work is that the location and shape of the potential failure plane could be modulated by the transient characteristics of the oceanographic forcings (e.g., wave power, water depth, and water temperature) that are delivered to a coastline. This suggests that a stability assessment approach, for which the failure plane is assumed to coincide with a constant geometric feature (e.g., a geologic discontinuity such as an ice wedge) or a particular niche depth, may not be ideal for coastlines similar to our study area. The impact of storm-based metrics (e.g., surge height, dwell time, and water temperature) on niche morphology could be examined with a physics-based modeling approach that expands upon ours to include transient simulations of oceanographic conditions.

Vertical Tension Cracks

A vertical tension crack in a bluff can increase the likelihood of failure because the extent of material available to resist the bending moment prior to toppling has decreased. Whereas ice wedges have been invoked as preferential failure planes for toppling mode block failure (e.g., Hoque and Pollard, 2009, 2016; Barnhart et al., 2014b; Jones et al., 2018), we have observed that failure also occurs along tension cracks in ice wedge polygon centers (**Figure 2A**). Given laboratory-based estimates of permafrost tensile strength (**Table 2**), our simulations suggest that tension cracks can form within the range of N_D vs. N_H that we considered for this study (i.e., 2–6 m and 1–3 m, respectively). For example, the σ_{Tmax} for a simulation scenario with a 2 m N_H and 3.75 m N_D exceeds 100 kPa (**Figure 6A**) within 0.75 m of our field case, which shows a tension crack present for a bluff with a ∼1.9 m N_H and ∼4.5 m N_D (**Figure 2A**). Although the formation and propagation of tension cracks in coastal permafrost bluffs is currently not well-constrained, their presence is important because it signals that some amount of permanent deformation occurs prior to a topple. Neglecting this effect as part of a transient stability assessment approach could result in an underestimate of bluff failure potential.

Thermo-Mechanical Coupling

The numerical experiments that we present here do not include calculations of the thermodynamic state of the permafrost and ice wedge materials. However, the thermodynamic state of permafrost material is important because it determines the amount of frozen and unfrozen water content within the pore space, which has been shown to directly affect bulk mechanical properties (Arenson et al., 2007). In general, unfrozen water content weakens a partially frozen soil, resulting in a strength decrease and the possibility of larger deformations, because the presence of water reduces ice cementation. Fine-grained sediments, such as clays, tend to have the highest unfrozen water content even at temperatures well below the freezing point (Kruse and Darrow, 2017). The thermodynamic state of the permafrost material likely plays a role in niche development via the thermo-abrasion process and, therefore, the bluff geometry, which we have shown to have the largest impact on the location and magnitude of the σ_{Tmax}. We hypothesize that the time-varying temperature/ice content of the permafrost markedly influences the timing of block failure. Future studies which include tightly coupled thermo-mechanical simulations could improve our ability to resolve the transient nature of the niche formation and quantify the impact of more realistic niche geometries (e.g., tapered wedges) on the stress field. This transient framework could also be used to explore how niche development occurs in the presence of multiple soil types (e.g., coarse- and fine-grained material), internal structures (e.g., sediment warping in the vicinity of ice wedges), and more realistic ice wedge geometries.

CONCLUSION

We simulated the impacts of variability in coastal permafrost bluff geometry and material properties on stress states leading up to block failure using continuum mechanics theory with static simulations of 3D elastic finite deformation. Our simulation framework tracked the maximum simulated tensile stress (σ_{Tmax}) that forms along the topographic surface of a permafrost coastal bluff because it is a metric that reflects a likely initiation location for toppling mode block failure. We found that the geometric characteristics of the erosional niche exert the largest impact on the location and magnitude of the σ_{Tmax}, whereas material properties only influenced the magnitude of the σ_{Tmax}. Taller and narrower erosional niches promote smaller failure masses compared to those with shorter and deeper niches, suggesting that block failure characteristics could be tied to variations in the intensity and duration of storm energy that interacts with the coastline. We also observe that even relatively shallow vertical cracks can concentrate displacement within ice-bonded permafrost coastal bluffs, highlighting how deformation processes that create non-uniform patterns of displacement may play a role in localizing block failure. Taken together, our geomechanical simulations facilitate new hypothesis-testing regarding the prediction of decadal-scale erosion rates for increasingly dynamic coastal permafrost systems. We propose that developing a tightly coupled thermo-mechanical

model to solve heat transfer and finite deformation over the elastic-plastic regime for observed atmospheric/oceanographic conditions is a logical next step to (1) explore more complex geometric characteristics of the basal erosional niche and (2) track the development of tension cracks for coastal permafrost bluffs that are prone to toppling mode block failure. Comprehensive simulations of transient thermal-mechanical response could enable an investigation of stress states that encompass bluff failure.

DATA AVAILABILITY STATEMENT

All datasets generated for this study are included in the article/**Supplementary Material**.

AUTHOR CONTRIBUTIONS

The idea for this manuscript arose from discussions between all of the coauthors. MT conducted the simulations and drafted the manuscript. AM developed the mechanical simulation framework. BJ constrained the geometric model inputs with field observations and core sampling. RC constrained the material property model inputs with geotechnical laboratory testing. JF and DB provided valuable input on simulation ensemble design.

FUNDING

This project was supported by the Laboratory Directed Research and Development program at Sandia National Laboratories and National Science Foundation grants OISE-1927553 and OPP-1745369. Sandia National Laboratories is a multimission laboratory managed and operated by National Technology and Engineering Solutions of Sandia, LLC, a wholly owned subsidiary of Honeywell International Inc., for the U.S. Department of Energy's National Nuclear Security Administration under contract DE-NA0003525.

ACKNOWLEDGMENTS

Rex Baum, Li Erikson, and two reviewers provided constructive comments on an earlier version of this work. We appreciate thoughtful conversations with Ben Leshchinsky, Sam Johnstone, and Katy Barnhart during the course of this study. Any use of trade, firm, or product names is for descriptive purposes only and does not imply endorsement by the U.S. Government.

SUPPLEMENTARY MATERIAL

The Supplementary Material for this article can be found online at: https://www.frontiersin.org/articles/10.3389/feart.2020.00143/full#supplementary-material

REFERENCES

Aré, F. E. (1988a). Thermal abrasion of sea coasts (part I). *Polar Geol. Geol.* 12:1. doi: 10.1080/10889378809377343

Aré, F. E. (1988b). Thermal abrasion of sea coasts (part II). *Polar Geol. Geol.* 12:2. doi: 10.1080/10889378809377352

Arenson, L. U., Springman, S. M., and Sego, D. C. (2007). The rheology of frozen soils. *Appl. Rheol.* 17, 1–14. doi: 10.1515/arh-2007-0003

Barnhart, K. R., Anderson, R. S., Overeem, I., Wobus, C., Clow, G. D., and Urban, F. E. (2014b). Modeling erosion of ice-rich permafrost bluffs along the Alaskan Beaufort Sea coast. *J. Geophys. Res. Earth Surface* 119, 1155–1179. doi: 10.1002/2013JF002845

Barnhart, K. R., Overeem, I., and Anderson, R. S. (2014a). The effect of changing sea ice on the physical vulnerability of Arctic coasts. *Cryosphere* 8, 1777–1799. doi: 10.5194/tc-8-1777-2014

Clement, J. P., Bengtson, J. L., and Kelly, B. P. (2013). *Managing for the Future in a Rapidly Changing Arctic*. A Report to the President. Washington, DC: Interagency Working Grouping on Coordination of Domestic Energy Development and Permitting in Alaska, 59.

Collins, B. D., and Sitar, N. (2011). Stability of steep slopes in cemented sands. *J. Geotech. Geoenviron. Eng.* 137, 43–51. doi: 10.1061/(ASCE)GT.1943-5606.0000396

Frederick, J. M., Thomas, M. A., Bull, D. L., Jones, C. A., and Roberts, J. D. (2016). *The Arctic Coastal Erosion Problem.* Albuquerque, NM: Sandia National Laboratories SAND2016-9762, 122. doi: 10.2172/1431492

Fritz, M., Vonk, J. E., and Lantuit, H. (2017). Collapsing Arctic coastlines. *Nat. Clim. Change* 7, 6–7. doi: 10.1038/nclimate3188

Gibbs, A. E., Ohman, K. A., Coppersmith, R., and Richmond, B. M. (2017). *National Assessment of Shoreline Change: A GIS Compilation of Updated Vector Shorelines and Associated Shoreline Change Data for the North Coast of Alaska, U.S. Canadian Border to Icy Cape*. Reston, VA: U.S. Geological Survey. doi: 10.5066/F72Z13N1

Gibbs, A. E., and Richmond, B. M. (2015). *National Assessment of Shoreline Change-Historical Shoreline Change Along the North Coast of Alaska, U.S.-Canadian Border to Icy Cape*. Reston, VA: U.S. Geological Survey, Open-File Report 2015-1048, 96. doi: 10.3133/ofr20151048

Günther, F., Overduin, P. P., Sandakov, A. V., Grosse, G., and Grigoriev, M. N. (2013). Short- and long-term thermo-erosion of ice-rich permafrost coasts in the Laptev Sea region. *Biogeosciences* 10, 4297–4318. doi: 10.5194/bg-10-4297-2013

Hoque, M. A., and Pollard, W. H. (2009). Arctic coastal retreat through block failure. *Can. Geotech. J.* 46, 1103–1115. doi: 10.1139/T09-058

Hoque, M. A., and Pollard, W. H. (2016). Stability of permafrost dominated coastal cliffs in the Arctic. *Polar Sci.* 10, 79–88. doi: 10.1016/j.polar.2015.10.004

Hughes, Z. (2016). *Erosion Threat Are Remote Military Radars Decades Ahead of Schedule*. Alaska Public Media. Available online at: https://www.alaskapublic.org/2016/07/04/erosion-threat-at-remote-military-radars-decades-ahead-of-schedule/ (accessed April 30, 2020).

Jones, B. M., Arp, C. D., Jorgenson, M. T., Hinkel, K. M., Schmutz, J. A., and Flint, P. L. (2009). Increase in the rate and uniformity of coastline erosion in Arctic Alaska. *Geophys. Res. Lett.* 36:L03503. doi: 10.1029/2008GL036205

Jones, B. M., Farquharson, L. M., Baughman, C. A., Buzard, R. M., Arp, C. D., Grosse, G., et al. (2018). A decade of remotely sensed observations highlight complex processes linked to coastal permafrost bluff erosion in the Arctic. *Environ. Res. Lett.* 13:115001. doi: 10.1088/1748-9326/aae471

Jorgenson, M. T., and Brown, J. (2005). Classification of the Alaskan Beaufort Sea Coast and estimation of carbon and sediment inputs from coastal erosion. *Geo Mar. Lett.* 25, 1432–1157. doi: 10.1007/s00367-004-0188-8

Kanevskiy, M., Shur, Y., Jorgenson, M. T., Ping, C. L., Michaelson, G. J., Fortier, D., et al. (2013). Ground ice in the upper permafrost of the Beaufort Sea coast of Alaska. *Cold Reg. Sci. Technol.* 85, 56–70. doi: 10.1016/j.coldregions.2012.08.002

Kobayashi, N. (1985). Formation of thermoerosional niches into frozen bluffs due to storm surges on the Beaufort Sea Coast. *J. Geophys. Res.* 90, 11983–11988. doi: 10.1029/JC090iC06p11983

Kobayashi, N., and Aktan, D. (1986). Thermoerosion of frozen sediment under wave attack. *J. Waterway Port Coastal Ocean Eng.* 112, 140–158. doi: 10.1061/(ASCE)0733-950X(1986)112:1(140)

Kruse, A. M., and Darrow, M. M. (2017). Adsorbed cation effects on unfrozen water in fine-grained frozen soil measured using pulsed nuclear magnetic resonance. *Cold Reg. Sci. Technol.* 142, 42–54. doi: 10.1016/j.coldregions.2017.07.006

Lantuit, H., Overduin, P. P., Couture, N., Wetterich, S., Aré, F., Atkinson, D., et al. (2012). The Arctic coastal dynamics database: a new classification scheme and statistics on Arctic permafrost coastlines. *Estuaries Coasts* 35, 383–400. doi: 10.1007/s12237-010-9362-6

Larsen, P. H., Goldsmith, S., Smith, O., Wilson, M. L., Strzepek, K., Chinowsky, P., et al. (2008). Estimating future costs for Alaska public infrastructure at risk from climate change. *Glob. Environ. Change* 18, 442–457. doi: 10.1016/j.gloenvcha.2008.03.005

Loague, K., Heppner, C. S., Ebel, B. A., and VanderKwaak, J. E. (2010). The quixotic search for a comprehensive understanding of hydrologic response at the surface: Horton, Dunne, Dunton, and the role of concept-development simulation. *Hydrol. Process.* 24, 2499–2505. doi: 10.1002/hyp.7834

Lu, N., Sener-Kaya, B., Wayllace, A., and Godt, J. W. (2012). Analysis of rainfall-induced slope instability using a field of local factor of safety. *Water Resour. Res.* 48:9524. doi: 10.1029/2012WR011830

Mars, J. C., and Houseknecht, D. W. (2007). Quantitative remote sensing study indicates doubling of coastal erosion rate in past 50 yr along a segment of the Arctic coast of Alaska. *Geology* 35, 583–586. doi: 10.1130/G23672A.1

Maslanik, J. A., Fowler, C., Stroeve, J., Drobot, S., Zwally, J., Yi, D., et al. (2007). A younger, thinner Arctic ice cover: increased potential for rapid, extensive sea-ice loss. *Geophy. Res. Lett.* 34:L24501. doi: 10.1029/2007GL032043

Overeem, I., Anderson, R. S., Wobus, C. W., Clow, G. D., Urban, F. E., and Matell, N. (2011). Sea ice loss enhances wave action at the Arctic coast. *Geophys. Res. Lett.* 38:L17503. doi: 10.1029/2011GL048681

Ping, C., Michaelson, G. J., Guo, L., Jorgenson, M. T., Kanevskiy, M., Shur, Y., et al. (2011). Soil carbon and material fluxes across the eroding Alaska Beaufort Sea coastline. *J. Geophys. Res. Biogeosci.* 116:G02004. doi: 10.1029/2010JG001588

Randhawa, K. S. (2018). *The measurement of the Young's modulus of ice with ultrasonic waves* (thesis). Hamburg University of Technology, Hamburg, Germany, 75. doi: 10.15480/882.1656

Rao, S. S. (2007). "Basic equations of elasticity" in *Vibrations of Continuous Systems, 2nd Edn,* ed S. S. Rao (Hoboken, NJ: John Wiley and Sons, Inc.), 700–706.

Ravens, T. M., Jones, B. M., Jinlin, Z., Arp, C. D., and Schmutz, J. A. (2012). Process-based coastal erosion modeling for Drew Point, North Slope, Alaska. *J. Waterway Port Coastal Ocean Eng.* 138, 122–130. doi: 10.1061/(ASCE)WW.1943-5460.0000106

Reimnitz, E., Graves, S. M., and Barnes, P. W. (1988). *Beaufort Sea Coastal Erosion, Shoreline Evolution, and Sediment Flux*. Reston, VA: U.S. Geological Survey Miscellaneous Investigations Series, Report I-1182-G, 22. doi: 10.3133/i1182G

Russell-Head, D. D. (1980). The melting of free-drifting icebergs. *Ann. Glaciol.* 1, 119–122. doi: 10.3189/S0260305500017092

Salinger, A. G., Bartlett, R. A., Bradley, A. M., Chen, Q., Demeshko, I. P., Gao, X., et al. (2016). Albany: using component-based design to develop a flexible, generic multiphysics analysis code. *Int. J. Multiscale Comput. Eng.* 14, 415–438. doi: 10.1615/IntJMultCompEng.2016017040

Sandia National Laboratories (2017). *Sandia's Open Source Software Portal, "Albany."* Available online at: https://software.sandia.gov/drupal/software/ (accessed January 17, 2020).

Schulson, E. M. (1999). The structure and mechanical behavior of ice. *J. Miner. Metals Mater. Soc.* 51, 21–27. doi: 10.1007/s11837-999-0206-4

Serreze, M. C., Holland, M. M., and Stroeve, J. (2007). Perspectives on the Arctic's shrinking sea-ice cover. *Science* 315, 1533–1536. doi: 10.1126/science.1139426

Simmonds, I., and Rudeva, I. (2012). The great Arctic cyclone of August 2012. *Geophys. Res. Lett.* 39:23709. doi: 10.1029/2012GL054259

Stammerjohn, S., Massom, R., Rind, D., and Martinson, D. (2012). Regions of rapid sea ice change: an inter-hemispheric seasonal comparison. *Geophys. Res. Lett.* 39:L06501. doi: 10.1029/2012GL050874

Thomas, M. A., and Loague, K. (2016). Landscape change as recorded by the Ocean Shore Railroad. *Eng. Environ. Geol.* 22, 209–223. doi: 10.2113/gseegeosci.22.3.209

U.S. Government Accountability Office (2004). *Alaska Native Villages: Villages Affected by Flooding and Erosion Have Difficulty Qualifying for Federal Assistance.* Washington, DC: U.S. Government Accountability Office, GAO 04-895T, 17.

U.S. Government Accountability Office (2009). *Alaska Native Villages: Limited Progress Has Been on Relocating Villages Threatened by Flood and Erosion.* Washington, D.C.: U.S. Government Accountability Office, GAO 09-551, 53.

Vermaire, J. C., Pisaric, M. F. J., Thienpont, J. R., Courtney, M., Colin, J., Kokelj, S. V., et al. (2013). Arctic climate warming and sea ice declines lead to increased storm surge activity. *Geophys. Res. Lett.* 40, 1386–1390. doi: 10.1002/grl.50191

Vonk, J. E., Sánchez-García, L., van Dongen, B. E., Alling, V., Kosmach, D., Charkin, A., et al. (2012). Activation of old carbon by erosion of coastal and subsea permafrost in Arctic Siberia. *Nature* 489, 137–140. doi: 10.1038/nature11392

White, F. M., Spaulding, M. L., and Gominho, L. (1980). *Theoretical Estimates of Various Mechanism Involved in Iceberg Deterioration in the Open Ocean Environment*. Washington, DC: U.S. Coast Guard Technical Service Information Service Publication CG-D-62-8081-20571, 126.

Wobus, C., Anderson, R., Overeem, I., Matell, N., Clow, G., and Urban, F. (2011). Thermal erosion of a permafrost coastline: improving process-cased models using time-lapse photography. *Arctic Antarctic Alpine Res.* 43, 474–484. doi: 10.1657/1938-4246-43.3.474

Young, A. P., and Ashford, S. A. (2008). Instability investigation of cantilevered seacliffs. *Earth Surface Process. Landforms* 33, 1661–1677. doi: 10.1002/esp.1636

Conflict of Interest: The authors declare that the research was conducted in the absence of any commercial or financial relationships that could be construed as a potential conflict of interest.

frontiers in Earth Science

ORIGINAL RESEARCH
published: 21 August 2020
doi: 10.3389/feart.2020.00336

Rapid Fluvio-Thermal Erosion of a Yedoma Permafrost Cliff in the Lena River Delta

Matthias Fuchs[1], Ingmar Nitze[1], Jens Strauss[1], Frank Günther[2,3], Sebastian Wetterich[1], Alexander Kizyakov[4], Michael Fritz[1], Thomas Opel[1], Mikhail N. Grigoriev[5], Georgii T. Maksimov[5] and Guido Grosse[1,2]*

[1] Alfred Wegener Institute Helmholtz Centre for Polar and Marine Research, Potsdam, Germany, [2] Institute of Geosciences, University of Potsdam, Potsdam, Germany, [3] Laboratory Geoecology of the North, Faculty of Geography, Lomonosov Moscow State University, Moscow, Russia, [4] Department of Cryolithology and Glaciology, Faculty of Geography, Lomonosov Moscow State University, Moscow, Russia, [5] Laboratory of General Geocryology, Melnikov Permafrost Institute, Siberian Branch of the Russian Academy of Sciences, Yakutsk, Russia

OPEN ACCESS

Edited by:
Scott Raymond Dallimore, Geological Survey of Canada, Canada

Reviewed by:
Jannik Martens, Stockholm University, Sweden
Scott Zolkos, University of Alberta, Canada

***Correspondence:**
Matthias Fuchs
matthias.fuchs@awi.de

Specialty section:
This article was submitted to Cryospheric Sciences, a section of the journal Frontiers in Earth Science

Received: 21 March 2020
Accepted: 20 July 2020
Published: 21 August 2020

Citation:
Fuchs M, Nitze I, Strauss J, Günther F, Wetterich S, Kizyakov A, Fritz M, Opel T, Grigoriev MN, Maksimov GT and Grosse G (2020) Rapid Fluvio-Thermal Erosion of a Yedoma Permafrost Cliff in the Lena River Delta. Front. Earth Sci. 8:336. doi: 10.3389/feart.2020.00336

The degradation of ice-rich permafrost deposits has the potential to release large amounts of previously freeze-locked carbon (C) and nitrogen (N) with local implications, such as affecting riverine and near-shore ecosystems, but also global impacts such as the release of greenhouse gases into the atmosphere. Here, we study the rapid erosion of the up to 27.7 m high and 1,660 m long Sobo-Sise yedoma cliff in the Lena River Delta using a remote sensing-based time-series analysis covering 53 years and calculate the mean annual sediment as well as C and N release into the Lena River. We find that the Sobo-Sise yedoma cliff, which exposes ice-rich late Pleistocene to Holocene deposits, had a mean long-term (1965–2018) erosion rate of 9.1 m yr^{-1} with locally and temporally varying rates of up to 22.3 m yr^{-1}. These rates are among the highest measured erosion rates for permafrost coastal and river shoreline stretches. The fluvio-thermal erosion led to the release of substantial amounts of C (soil organic carbon and dissolved organic carbon) and N to the river system. On average, currently at least 5.2×10^6 kg organic C and 0.4×10^6 kg N were eroded annually (2015–2018) into the Lena River. The observed sediment and organic matter erosion was persistent over the observation period also due to the specific configuration of river flow direction and cliff shore orientation. Our observations highlight the importance to further study rapid fluvio-thermal erosion processes in the permafrost region, also because our study shows increasing erosion rates at Sobo-Sise Cliff in the most recent investigated time periods. The organic C and N transport from land to river and eventually to the Arctic Ocean from this and similar settings may have severe implications on the biogeochemistry and ecology of the near-shore zone of the Laptev Sea as well as for turnover and rapid release of old C and N to the atmosphere.

Keywords: permafrost, river delta, ice-rich, carbon, nitrogen, time series, Landsat

INTRODUCTION

Permafrost landscapes are sensitive to global temperature rise and may be affected by widespread degradation (Grosse et al., 2016; Biskaborn et al., 2019). Very ice-rich permafrost deposits such as the yedoma Ice Complex (Schirrmeister et al., 2013; Strauss et al., 2013, 2017) are particularly at risk to rapid, strong thaw processes and erosion. The thaw of ice-rich deposits leads to strong ground subsidence (Strozzi et al., 2018) and landscape reorganization (Morgenstern et al., 2011). Coasts and river banks in the Arctic are particularly fast changing permafrost features, which are characterized by high ground ice contents (e.g., Walker et al., 1987; Lantuit et al., 2011; Kanevskiy et al., 2016; Jones et al., 2018). These shores are affected by thermo-erosion processes induced by sea or river water combining mechanical erosion from waves, currents, and moving ice with thermal impacts of the water that is warmer than the permafrost (Are, 1983; Günther et al., 2013). The strong erosion of river banks and coastal segments leads to large sediment and organic matter inputs into Arctic river systems and the Arctic Ocean, respectively (e.g., Rachold et al., 2000; Couture et al., 2018; Rowland et al., 2018) with regional to global implications affecting the aquatic ecosystem and global C cycle (Gustafsson et al., 2011; Vonk and Gustafsson, 2013; Mann et al., 2015; Semiletov et al., 2016; Fritz et al., 2017). The C release upon permafrost thaw has been shown to have the potential to further increase atmospheric C resulting in a positive permafrost C climate feedback (Schuur et al., 2009). The deep mobilization of permafrost C caused by thermo-erosional processes along shores might add C to the atmosphere, which is not yet taken into account in current Earth System Models that include only top-down thaw (Turetsky et al., 2020). However, how much of the C released through shore erosion is re-buried on the Arctic shelf or in the deep Arctic Ocean versus is being mineralized and released into the atmosphere is still a matter of discussion (Vonk et al., 2012; Bröder et al., 2019; Grotheer et al., 2020).

Often, rapid erosion of ice-rich permafrost landscapes such as retrogressive thaw slumping (Lantz and Kokelj, 2008; Balser et al., 2014) and river bank erosion (Walker et al., 1987; Kanevskiy et al., 2016) occurs on local spatial scales and is therefore challenging to include in permafrost C feedback models (Turetsky et al., 2020). Nevertheless, observations of increasing air and river water temperatures (van Vliet et al., 2013), decreasing sea ice cover (Stroeve and Notz, 2018), extended thaw season length (Serreze et al., 2000; Barichivich et al., 2012), and an increase in Arctic river discharge (Holmes et al., 2015; Box et al., 2019) and therefore a higher sediment transport capacity all point at a high probability for accelerated erosion rates along permafrost coasts and river shorelines in the Arctic. Several studies already indicate that acceleration of erosion is taking place over the recent decades in different regions (e.g., Günther et al., 2015; Irrgang et al., 2018; Jones et al., 2018) in response to large scale drivers such as changing sea-ice cover (Nielsen et al., 2020). It is therefore important to understand and quantify the dynamics and C mobilization of permafrost shore erosion across a range of environmental and geographical settings.

Several segments of the Arctic coast (e.g., Jorgenson and Brown, 2005; Jones et al., 2008, 2009; Lantuit et al., 2011; Ping et al., 2011; Günther et al., 2013; Obu et al., 2017; Couture et al., 2018; Irrgang et al., 2018; Jones et al., 2018) and some individual permafrost shore sites (e.g., Walker et al., 1987; Costard et al., 2003; Günther et al., 2015; Kanevskiy et al., 2016; Stettner et al., 2018) affected by thermo-denudation and thermo-erosion have been previously studied in terms of erosion rates and organic matter flux. Here we study the fluvio-thermal erosion dynamics of a carbon-rich and fast-eroding river bank in the eastern Lena Delta, Siberia, using remote sensing image analysis and geochemical field data from sediment samples. The Sobo-Sise Cliff in the eastern Lena Delta is composed of ice-rich yedoma permafrost and strongly eroded by a main branch of the Lena River. With our study, we aim (1) to assess the cliff erosion rates of this yedoma Ice Complex exposure and (2) to quantify the sediment, C and N loss from yedoma deposits due to river bank erosion. Our study highlights the potential for continued and very rapid erosion in permafrost regions under certain environmental and geological conditions by Arctic rivers and the related environmental impacts of such a high organic matter export.

STUDY SITE

Sobo-Sise Island is located in the eastern part of the Lena River Delta at the Sardakhskaya Lena river channel (**Figure 1**), which is one of the main Lena Delta river channels with a width of around 2 km and a water discharge of ∼8000 m^3 s^{-1} during the summer low-water period (Fedorova et al., 2015). The Lena River is ice-covered for about 8 months (October–May) during wintertime where presumably very little or no erosion happens on the subaerial frozen deposits along the river. However, ice thickness on the Lena River is up to 2 m while the water depth at the onset of the Sardakhskaya channel can reach 22 m (Fedorova et al., 2015) and around 11 m in front of Sobo-Sise Cliff (see **Supplementary Figure S1**) allowing constant water flow underneath also in winter. The delta island Sobo-Sise is characterized by late Pleistocene, ice-rich yedoma Ice Complex deposits with Holocene cover deposits. The yedoma deposits at Sobo-Sise are affected by rapid thaw processes such as thermokarst lake dynamics and thermo-erosional valley formation (Morgenstern et al., 2011; Nitze and Grosse, 2016) as well as thaw subsidence (Chen et al., 2018). Only 19% of the area of Sobo-Sise Island consist of largely un-affected yedoma uplands, whereas the remaining area of the island consists of degraded thermokarst basins (alases) and fluvial deposits (Fuchs et al., 2018). Most of the year, snow and ice cover the landscape and water bodies, respectively. With a mean annual air temperature of −11.7°C (1998–2017) and a mean summer rainfall of 145 mm (weather station on Samoylov Island 63 km to the southwest, Boike et al., 2019), Sobo-Sise is dominated by a polar tundra climate (Peel et al., 2007).

The Sobo-Sise Cliff (72°32 N, 128°17 E) is a 1,660 m long riverbank stretch in the central North of Sobo-Sise Island, with a northeast exposition. The vertical cliff erodes into yedoma uplands with heights up to 27.7 m above mean river water level, exposing yedoma Ice Complex and overlying Holocene deposits,

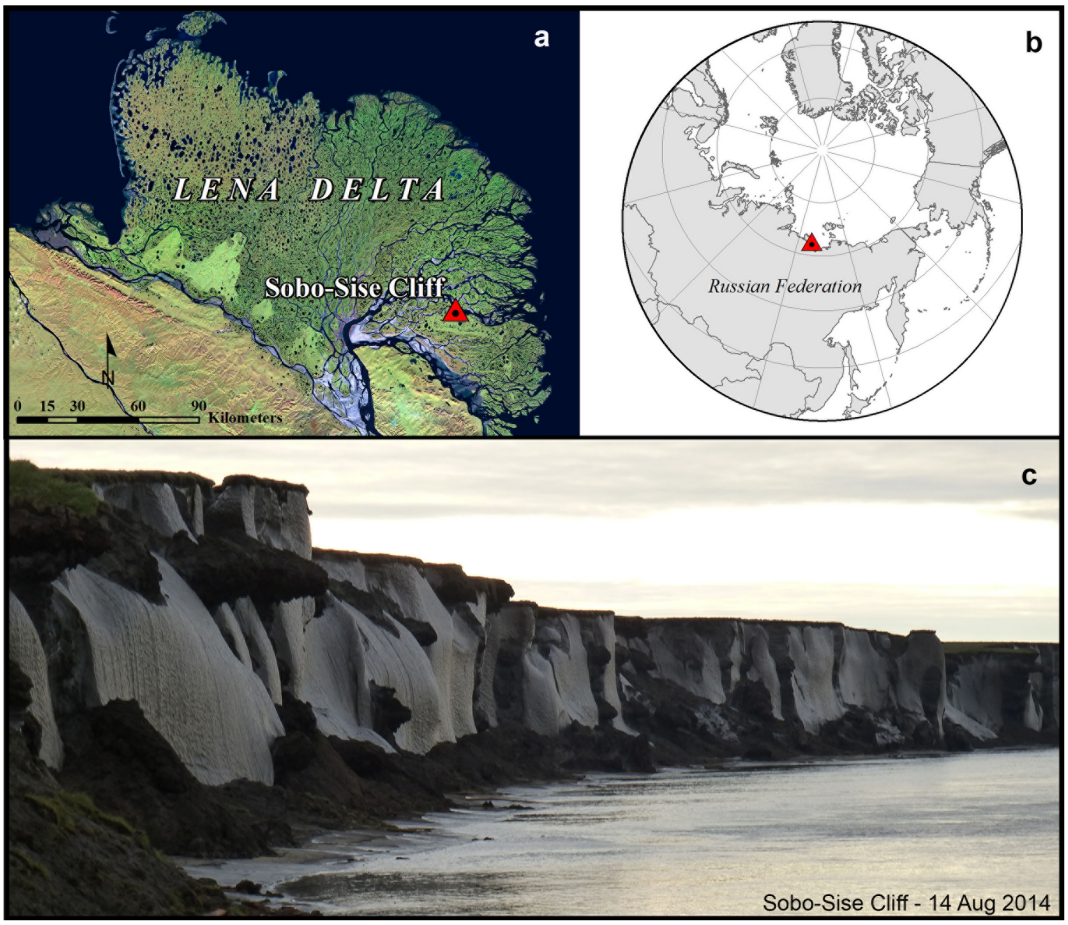

FIGURE 1 | Overview of the study site. The red triangle shows the location of Sobo-Sise Cliff in the eastern Lena River Delta **(a)** in the north of East Siberia, Russia **(b)**. [Lena Delta map is a mosaic compiled of six Landsat 5 scenes (bands 6-5-4) from 2009 to 2010.] Panel **(c)** shows the very ice-rich and up to 27.7 m high Sobo-Sise Cliff in August 2014 (photo: I. Nitze).

which can reach a thickness of up to two meters (Fuchs et al., 2018). Pavlova and Dorozhkina (2000) report that yedoma in the eastern part of the Lena Delta reaches to 8 to 10 m below sea level, resulting in ice-rich permafrost being exposed directly to above and underwater thermal erosion dynamics. Large syngenetic ice wedges, which dissect the entire height of the exposure, dominate the cross section exposed by erosion. The Sobo-Sise Cliff is directly exposed to the river flow of the Sardakhskaya channel, which hits the cliff at an angle of ∼30°. The position of the thick ice-rich deposits at this bend of the channel causes favorable conditions for erosion, removal of large sediment masses, and the formation of a steep cliff.

MATERIALS AND METHODS

Calculation of Total and Annual Erosion Rates

For the detection and analysis of recent and historic cliff retreat rates, we used remote sensing imagery from a variety of high to medium resolution optical sensors with different spatial resolution.

Image Data Sets

For historical long-term analysis, we used Corona and Hexagon satellite images from 1965 and 1975 (**Table 1**). For the following time steps, we used Landsat data (L5, L7, L8) for the years 2000, 2005, 2010, and 2015. Unfortunately, Landsat data from before 1999 is only sparsely available over large parts of NE Siberia due to the lacking on-board memory on the platform and the region being outside of footprints of high latitude satellite receiving stations (Goward et al., 2006). Spatially very high-resolution imagery from the DigitalGlobe constellation was available for 2014 (GeoEye). Additionally, we used Planet cube-sat imagery (Planet Team, 2017) from September 2018 to finalize the long-term erosion analysis.

While Landsat data is already delivered as geometrically and radiometrically corrected data, the Corona, Hexagon and high-resolution images were orthorectified and georeferenced using the GeoEye image from 2014 as a base image (see **Table 1**) and projected to WGS84 UTM 52N. The matching between

TABLE 1 | Images used for calculation of erosion rates.

	Image dates	Ground resolution (m)	Scale used for shoreline digitization
Corona KH-4A	1965-10-01	2.5	1:2500
Hexagon KH-9	1975-07-16	10	1:5000
Landsat 7 ETM+	2000-07-29	30	1:10000
Landsat 7 ETM+	2005-07-02	30	1:10000
Landsat 5 TM	2010-09-19	30	1:10000
Landsat 8 OLI	2015-09-08	30	1:10000
GeoEye[a]	2014-08-07	0.5	1:2500
PlanetOrthoTile	2018-09-13	3.15	1:5000

[a]*Master image for georeferencing. This image was not used for the calculation of erosion rates.*

images for the georeferencing was done by selecting features that we considered most stable in a landscape that is affected by change and does not contain artificial human-made structures. Such features included the centers of small circular thaw ponds that largely expand radially or polygonal ponds and ice wedge junctions that are rather stable over the decadal time scales analyzed with this imagery.

Calculation of Erosion Rates

Since the Sobo-Sise Cliff is a nearly vertical cliff with up to 27.7 m height, it was sufficient to manually digitize the upper cliff line on the selected imagery at an appropriate image scale (see **Table 1**) to quantify the cliff retreat rates between several points in time. Using the oldest image in the time-series, we also digitized the boundaries between yedoma uplands and thermokarst basin based on the Corona image to determine the volume of yedoma deposits, which was eroded since 1965 and to separate it from non-yedoma deposits.

For calculating erosion rates, we used the Digital Shoreline Analysis System 5.0 (DSAS; Himmelstoss et al., 2018) in ArcGIS 10.5. DSAS calculates erosion rates between given shorelines along defined transects perpendicular to a defined baseline. In DSAS the "baseline" was defined as the straight middle line between the 1965 and 2000 cliff lines. We then cast transects at an interval of 50 m for the entire 1,660 m coastal section (resulting in 32 transects) to calculate erosion rates for individual cliff segments. We calculated erosion rates for the entire period between 1965 and 2018, as well as several sub-periods, including 1965–1975, 1975–2000, 2000–2005, 2005–2010, 2010–2015, and 2015–2018. Erosion rates are given as end point rates (EPR) of DSAS. The digitized cliff fronts for each time step as well as the erosion rates for each of the 32 segments are available on the PANGAEA data set repository (Nitze et al., 2020).

For volumetric erosion estimates, we extracted 10 m ARCTIC DEM elevation data (Mosaic v3.0 10m: tile 59_43) (Porter et al., 2018), based on representative sample areas in proximity to the cliff line for yedoma areas and the eastern and western alases as well as the river water level. We extracted elevation statistics for these training areas (see **Supplementary Figure S3**) and transformed absolute elevation to relative elevation above the mean water level. However, as we do not have any height information for the older time steps (prior to 2000) and assume, based on topographic maps and the Corona scene, that there existed a down-slope toward the Sardakhskaya channel sometime prior to 2000, we do not calculate volumetric, C and N erosion rates prior to 2000.

Calculation of Total and Annual C and N Loss

Elemental Composition and Stock Calculations

Frozen sediment samples were taken by rope climbing across the entire vertically exposed yedoma sequence at 0.5 m intervals at three locations in close proximity and overlapping vertical profiles during an expedition to Sobo-Sise in July 2018 (Wetterich et al., 2019, 2020). In total, 60 permafrost samples were used for analyses of organic matter properties. The gravimetric segregated and pore ice content was measured in the field as difference between wet and dry weights after careful drying on a wood oven. The ice content is expressed as weight percentage (wt%, van Everdingen, 2005).

Gravimetric ice content for the samples was then converted into volumetric ice content by assuming ice saturation if the ice content is >20% (following Strauss et al., 2012) and an ice density of 0.917 g cm^{-3}. For estimating the segregated and pore ice volume in %, we assumed a 3-component model of the cliff consisting of ice, a mineral component of the sediment and organic matter, and assuming component densities of 2.65 g cm^{-3} (Lide et al., 2008) and 0.25 g cm^{-3} (Adams, 1973) for the latter two components, respectively. We used this for estimating the total volume of ice and organic matter at the Sobo-Sise Cliff.

The total C and total N content of the sediment samples were measured with a Vario EL III and total organic C with a Vario Max C elemental analyzer (Elementar Analysesysteme, 2007, 2011). Results are expressed as weight percentage (wt%) of the dry sediment samples. The soil organic carbon (SOC) density, which is organic C content per soil volume unit (kg C m^{-3}), was quantified following Strauss et al. (2012). Prior to conversion of the measured weight-based total organic C values to the volume-based SOC, the bulk density was estimated according to Strauss et al. (2012). More details on the bulk density calculation are presented in the **Supplementary Material** (section 2).

In addition, dissolved organic carbon (DOC) concentrations (mg L^{-1}) of segregated and pore ice were measured in 29 samples from throughout the cliff. Therefor meltwater was filtered in the field with gum-free syringes equipped with glass fiber filters (Whatman GF/F; pore size: 0.7 µm), which were rinsed with ≥20 ml of sample, and acidified with 20 µL HCl suprapur (30%) to pH < 2 in order to prevent microbial conversion. In the laboratory, samples were analyzed with a high-temperature (680°C) combustion total organic C analyzer (Shimadzu TOC-VCPH). This allows us to make a complete estimation of C loss through erosion of Sobo-Sise Cliff. For N we refer to the N loss, without differentiation between particulate and dissolved N or the form of N (e.g., organic or inorganic).

Ice Wedge Content Estimation

For the estimation of ice wedge content (IWC) we used photographs with frontal views of the Sobo-Sise Cliff taken

during field visits in summer 2014, 2015, and 2019. All analyzed photographs and front cliff sections are provided in the **Supplementary Figure S4**. In these photographs, we identified vertically continuous sediment sections and ice wedges to quantify volumetric ratios between sediment and ice wedge. We correlated the width of ice wedge sections with the width of the adjacent sediment section assuming that ice and sediment segments dissecting the entire cliff were eroded perpendicular to the polygon structure (**Figure 2**). This ice wedge to sediment column width ratio ($I{:}S_{width}$) was calculated according to Eq. (1).

$$I : S_{width} = Width_{ICE} / Width_{SED} \quad (1)$$

Further, assuming an ideal polygonal distribution in the landscape prior to erosion, the size of sediment columns (inner polygon) was related to adjacent ice wedges (outer polygon) (**Figure 2**). The $I{:}S_{width}$ was then used to calculate the volume of both inner (V_{IP}; Eq. 2) and outer polygon (V_{OP}; Eq. 3) and in a final step to calculate the amount of ice wedge content (IWC; Eq. 4) within the landscape.

$$V_{IP} = \left(\frac{a}{2}\right)^2 * 2\sqrt{3} * h \quad (2)$$

$$V_{OP} = \left(\left(\frac{1}{2} * \left(\frac{a}{I : S_{width}} + a\right)\right)^2 * 2\sqrt{3} * h\right) - V_{IP} \quad (3)$$

$$IWC\ [vol\%] = \left(\frac{V_{OP}}{V_{OP} + V_{IP}}\right) * 100 \quad (4)$$

For the diameter of the inner polygon (a) and the vertical height (h) of a polygon any reasonable realistic number for known polygon diameters and vertical heights can be chosen, since we calculate with a ratio, this does not change the final result of ice wedge content. $I{:}S_{width}$ for the 10 analyzed sections varied from 0.28 to 1.21 (see **Supplementary Table S1**). For each section, we calculated the ice wedge content and then calculated the average ice content over all our ten measured sections. In addition, to get an estimate for the total landscape ice volume we used Eq. (5):

$$total\ ice\ volume\ \left[vol\%\right] = IWC\left[vol\%\right] + \frac{100 - IWC\ [vol\%]}{100} * segregated\ and\ pore\ ice\ [vol\%] \quad (5)$$

Calculation of Annual C and N Loss

The data on ice volume and the mass of the mineral and organic components of the yedoma as well as the data on the retreat rates of the Sobo-Sise Cliff were used to estimate the amount of eroded sediments, SOC, DOC and N. According to Kanevskiy et al. (2016) we estimated the total volume (V) of frozen deposits (sediment and ice) transported annually to the river from the retreating bank using Eq. (6).

$$V[m^3 yr^{-1}] = L * H * R \quad (6)$$

L is the length of the cliff [m], H is the average height of the cliff [m above mean river water level], and R is the average retreat rate [m yr^{-1}] for the cliff during the period of observation. We then calculate the flux of the dry weight of sediments (Sed_{flux}), the flux of dry weight of soil organic carbon (SOC_{flux}) and the flux of dissolved organic carbon (DOC_{flux}) lost by erosion and transported to the river (Eqs 7–9):

$$Sed_{flux}[kg\ yr^{-1}] = \text{sediment density} * V * (1 - IWC) \quad (7)$$

$$SOC_{flux}[kg\ yr^{-1}] = \text{organic matter density} * V * (1 - IWC) \quad (8)$$

$$DOC_{flux}[kg\ yr^{-1}] = \text{DOC concentration} * V * (1 - IWC) * \text{ice content} * 0.917 \quad (9)$$

The flux of the dry weight of nitrogen (N_{flux}) was calculated like SOC_{flux} following Eq. (8) by replacing organic matter density by the N density. For DOC_{flux} (Eq. 9) the segregated and pore ice volume (ice content) was considered. In addition, the volume of ice was converted in volume of water with the density difference between ice and water of 0.917. In order to get the complete DOC loss from Sobo-Sise Cliff, ice wedge DOC flux was calculated including the mean DOC concentration of 11.1 mg L^{-1} for yedoma ice wedges based on Fritz et al. (2015), since we do not have own DOC concentrations from ice wedges at Sobo-Sise Cliff. This was combined with the total volume of ice wedges at Sobo-Sise Cliff derived from the ice wedge content estimation (see section "Ice Wedge Content Estimation"). As a result, the DOC_{flux} of Sobo-Sise Cliff is the sum of the DOC_{flux} from segregated and pore ice and the DOC_{flux} from eroded ice wedges for each investigated time period. In consequence, the total C flux from the yedoma Sobo-Sise Cliff includes the SOC, DOC from segregated and pore ice, and DOC from ice wedges. For this study, we only focus on C and N loss for the yedoma cliff. The two alas basins in the east and west of Sobo-Sise Cliff are eroding as well but were not considered here.

Bathymetric Survey Along the Sobo-Sise Cliff

In order to better understand how the fluvial erosion processes contribute or drive the cliff retreat a bathymetric survey was done in August 2016 during calm weather and at low speed (<4 km h^{-1}) with a Humminbird 899cxi HD SI COMBO to detect the water depth in front of Sobo-Sise Cliff. Along four parallel and one zigzag profile lines, about 9200 depth measurements were collected. The surveyed area in the Sardakhskaya channel captured the entire cliff length and included parts of the adjacent alas basins. Bathymetric profiles covered a zone of typically 50 m width off the lower cliff base. Average water depth was 7.2 ± 4.9 m.

RESULTS

Sobo-Sise Cliff Characteristics

According to the Arctic DEM, the Sobo-Sise Cliff (**Figure 3a**) has an average height of 22.3 m above mean river water

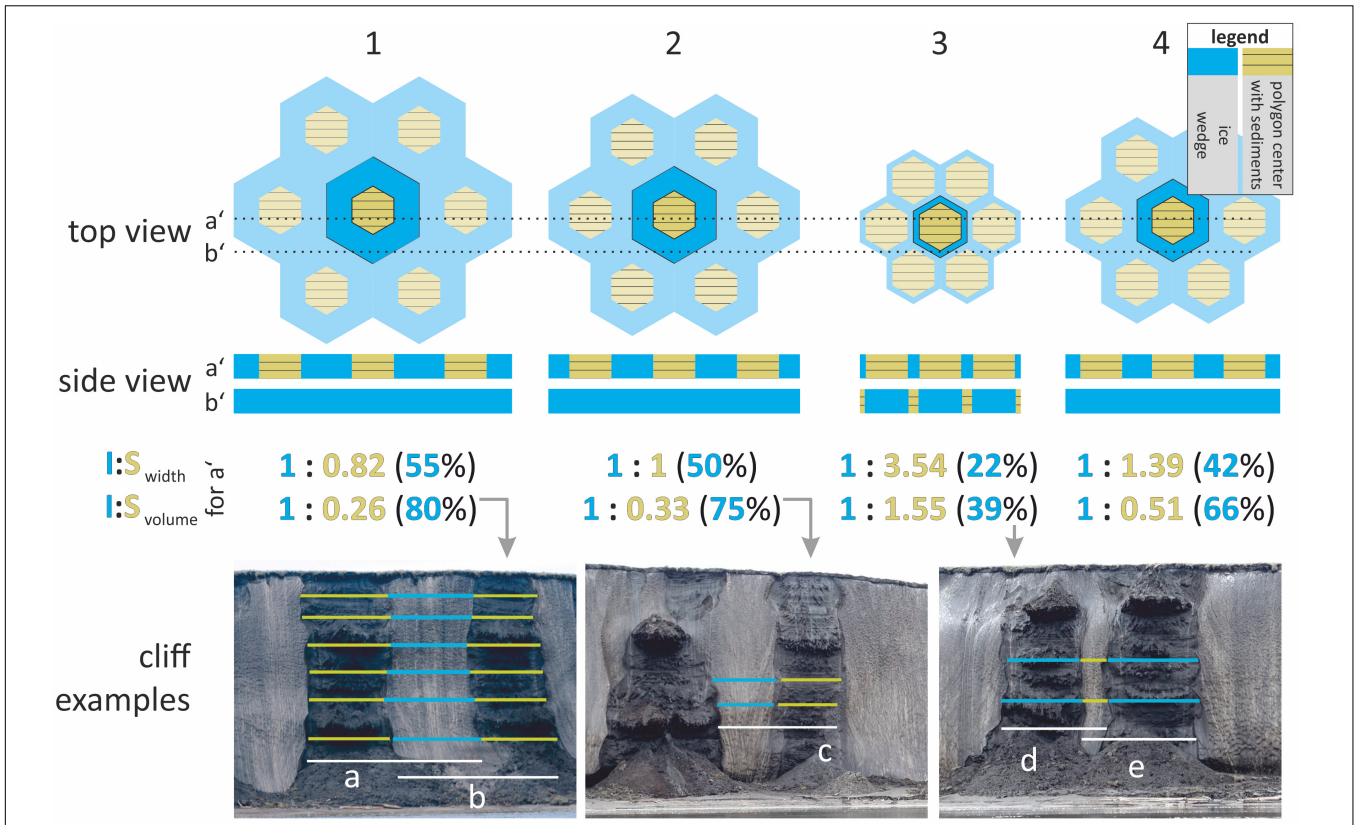

FIGURE 2 | Quantification of ice wedge to sediment ratio for the yedoma exposed at Sobo-Sise Cliff. **Top view** shows an ideal distribution of polygons in the landscape, where inner polygons (sediment, yellow) are surrounded by ice wedge containing outer polygons (blue). In the panels 1–3, the size of ice wedges is declining from left (1) to right (3), whereas column 1 shows the maximum width of ice wedges at Sobo-Sise Cliff; column 2 shows an equal ice to sediment ratio (1:1) and column 3 shows the minimum ice wedge width at Sobo-Sise Cliff. Column 4 shows the calculated average ice wedge content at Sobo-Sise Cliff (no cliff example photograph). The **side view** (or cliff view) shows a cross section of the polygons where profile a′ indicates an ideal cross section cutting the polygon centers at true width (leading to sediment sections which dissect the entire Sobo-Sise Cliff from top to bottom), whereas b′ shows a cross section with masked polygon centers leading to an ice-dominated cliff wall. The **I:S$_{width}$** (width ice: width sediment) was determined based on photographs from the cliff front visible in the lowermost cliff example panels according to the sections a–e. The percentage in brackets indicates the relation between the width of the ice wedge in relation to the width of the sediment section. This allowed calculating the **I:S$_{volume}$** (volume outer polygon: volume inner polygon) at the Sobo-Sise Cliff according to Eqs 1–3 and in a final step the ice wedge content (blue numbers in percentage). The **cliff examples** show three photographs with typical side views of the Sobo-Sise Cliff which match the top and side view of columns 1, 2, and 3 (photographs by T. Opel (left) and A. Fricke (middle and right). The lower case letters a–e indicate the analyzed I:S$_{width}$ across difference depths of the Sobo-Sise Cliff. More details on the analyzed sections are given in the **Supplementary Table S1** and **Supplementary Figure S4**. The average ice wedge content at Sobo-Sise Cliff is 66 vol% with an I:S$_{width}$ of 1:1.39 (or 0.72). This case is shown in column no. 4.

level (maximum height: 27.7 m) extending for 1,660 m from 72°32′34 N/128°15′59 E to 72°32′06 N/128°18′21 E in a concave shape along the Sardakhskaya channel in the Eastern Lena River Delta. The cliff emerged and has developed its shape from a formerly undisturbed yedoma upland gently downsloping to the Sardakhskaya Lena River channel. Interpreting topographic maps that are based on aerial surveys from the early 1950s, the riverbank next to the yedoma hill was lower than 10 m and likely consisted of alas deposits. Over time riverbank erosion reached the yedoma upland triggering the formation of the cliff likely during the early 1970s. The cliff front is dominated by late Pleistocene ice wedges stretching the entire height of the cliff. Our ice wedge volume estimation resulted in an average of 66 vol% of wedge ice at Sobo-Sise Cliff and 34 vol% of sediments (**Figure 2**) with high segregated and pore ice contents. The base of the cliff is often not visible due to sediment debris falling from the cliff onto the beach, forming piles that are rapidly removed by the river.

The sediment columns have an average segregated and pore ice content of 65.7 ± 9.0 vol%. This results in a total ice volume of 88.4 vol%. The segregated and pore ice content is included in the dry bulk density of the sediment and is therefore integrated in the calculation for mean SOC and N contents. Average dry bulk density of the Sobo-Sise Cliff sediments is 0.7 ± 0.2 g cm^{-3} resulting in average SOC and N contents of 26.2 ± 16.8 kg C m^{-3} and 2.1 ± 1.1 kg N m^{-3}, respectively. If accounted for ice wedge volume (66 vol%) on Sobo-Sise Cliff, average SOC and N contents are 8.9 ± 5.7 kg C m^{-3} and 0.7 ± 0.4 kg N m^{-3}. Beside SOC, DOC was analyzed from segregated and pore ice within the sediment column. Mean DOC content for Sobo-Sise Cliff is 315.5 ± 188.0 mg L^{-1} or 0.316 kg m^{-3}. For comparison,

FIGURE 3 | (a) Sobo-Sise Cliff in August 2014 with person for scale (photo: T. Opel, 11 August 2014), **(b)** Sobo-Sise Cliff in April 2019 with snow drifts (photo: J. Strauss, 5 April 2019), **(c)** cliff-top with a large crack (photo: G. Grosse, 12 August 2014), **(d)** cliff-top with thin snow cover (photo: J. Palmtag, 5 April 2019), **(e)** collapsing sediment block at the Sobo-Sise Cliff (photo: G. Grosse, 12 August 2014), **(f)** thermo-erosional niche and peat blocks at the base of the cliff (photo: M. Fuchs, 12 August 2014).

the average DOC content for yedoma ice wedges from Fritz et al. (2015) is 11.1 mg L^{-1} or 0.011 kg m^{-3}.

During the ice-free months (June–September), the cliff is prone to erosion mainly by flowing river water and air temperatures above freezing. Thermo-erosional niches (**Figure 3f**) form at the base of the cliff leading to collapse and failure of large ice and sediment blocks (**Figures 3c,e**). In winter (October–May), low negative air temperatures and presence of a stable ice cover on the river prevent ground ice melt and permafrost thaw on the subaerial part of cliff, while below river ice permafrost thaw continues undercutting the cliff during the winter providing favorable conditions for block collapse in the following summer. The wind exposed cliff top is covered by a thin snow cover (<20 cm; April 2019), whereas

large snow packs accumulate in windblown drifts at the cliff base (**Figures 3b,d**).

Dense bathymetric surveys in front of Sobo-Sise Cliff were combined with synchronous topographic survey data. The interpolated surface shows an almost immediate downward extension of the steep Sobo-Sise Cliff slope below river level (**Figure 4**). Within a 20 m wide shoreface zone water depths were 2.2 ± 1.2 m, while the adjacent 50 m of the cliff had mean depths of 10.3 ± 3.7 m, while maximum depths were recorded down to 19.1 m. These data suggest a narrow zone next to the cliff base, where river ice may freeze down to the bottom. Because the bathymetric survey was conducted in August several months after river ice breakup, the shoreface configuration might have changed considerably, potentially allowing for configurations during winter with a negligible bottom fast ice formation that enables direct contact of the river water flow with the cliff base and permafrost thaw throughout the winter.

Total and Annual Erosion Rates

The total erosion of the Sobo-Sise Cliff from 1965 to 2018 ranged from 322 to 679 m (**Figure 5**). The highest mean annual erosion rates (ER_{max}) occurred in the downstream section of the cliff with a rate of 12.8 m yr^{-1} whereas the upstream edge has a mean annual erosion rate of 6.1 m yr^{-1}. This results in an overall mean annual erosion rate (ER_{mean}) for the entire Sobo-Sise Cliff of 9.1 m yr^{-1} ranging from 4.8 to 15.7 m yr^{-1} for the mean values of the different periods. The cliff's planimetric shape changed from convex in 1965 to its present concave shape and the length of the cliff with exposed yedoma is ∼610 m longer in 2018 than in 1965. The point of maximum erosion gradually moved upstream over time. However, ER_{mean} since 2005 are more uniform along the Sobo-Sise Cliff compared to the period before 2000.

Over the entire period from 1965 to 2018 a total area of 0.88 km^2 was eroded, of which 0.77 km^2 (87.9%) were yedoma and 0.11 km^2 (12.1%) drained lake basin. In general, erosion rates increased over time but also show short term variation (**Table 2**). The ER_{mean} increased considerably from 4.8 m yr^{-1} in 1965–1975 to 15.7 m yr^{-1} in 2015–2018, while the ER_{max} increased from 8.2 to 21.1 m yr^{-1}.

The recent multi-year periods 2000–2005, 2005–2010, 2010–2015, and 2015–2018 exhibited a strong variation of erosion rates. The early period from 2000 to 2005 was characterized by less erosion with ER_{mean} of 5.7 m yr^{-1} and ER_{max} of 11.8 m yr^{-1}. During 2005–2010 erosion rates accelerated to ER_{mean} of 15.1 m yr^{-1} and ER_{max} of 22.3 m yr^{-1}, the highest measured erosion rate. From 2010 to 2015 erosion rates slightly receded to ER_{mean} of 13.8 m $yr^{-1}$and ER_{max} of 19.3 m yr^{-1}, which still exceeded long-term mean erosion rates (1965–2018) by 51%. For the most recent period (2015–2018) ER_{mean} increased again to 15.7 m yr^{-1}.

Total and Annual Sediment, C and N Loss

Even though the total volume of ice is 88 vol% at the Sobo-Sise Cliff, large amounts of yedoma sediments have been eroded since 2000 (**Table 3**). The average eroded sediment flux range from 47.1–154.4 $\times 10^6$ kg yr^{-1} leading to a loss of 1.7–5.6 $\times 10^6$ kg SOC yr^{-1} and 0.1–0.4 kg N yr^{-1} for the different time periods between 2000 and 2018. When splitting into different time periods, the highest SOC_{flux} and N_{flux} occurred between 2005 and 2010 with 5.6 $\times 10^6$ kg SOC yr^{-1} and 0.4 $\times 10^6$ kg N yr^{-1}. However, even after 2010 the erosion rates remained on a very high level with annual erosion rates of ∼5 $\times 10^6$ kg SOC yr^{-1} (**Table 3**). For the time period 2015–2018 in total 0.59 $\times 10^6$ m^3 of yedoma sediments (including segregated and pore ice but not including the adjacent shores along drained lake basins and the deposits below water level) were eroded into the Sardakhskaya channel, which led to a loss of $15.4 \pm 9.9 \times 10^6$ kg SOC.

In addition to SOC and N, DOC is released from Sobo-Sise Cliff. Average DOC fluxes (including ice wedge as well as segregated and pore ice DOC) range from 13.6 to 44.8 $\times 10^3$ kg DOC yr^{-1} for the different time periods between 2000 and 2018 (**Table 3**). Like sediment, SOC and N fluxes, highest DOC fluxes were estimated for the time period 2005–2010. However, compared to the SOC flux, DOC only contributes a minor amount of the total C flux of Sobo-Sise Cliff. For the four investigated time periods, DOC accounts for 0.8% of the total C lost through erosion. Nevertheless, this still accounts for a loss of 41,265 kg DOC yr^{-1} in the most recent investigated time period (2015–2018). As a result, the flux ratio of DOC vs. SOC is 1:125. In total, SOC and DOC combined, $15.5 \pm 9.9 \times 10^6$ kg C were eroded during 2015–2018. This leads to an average C flux of $5.2 \pm 3.3 \times 10^6$ kg C yr^{-1} or divided by meter coastline to an average of 3,131 kg C m^{-1} yr^{-1} along Sobo-Sise Cliff. However, the overall contribution of yedoma ice wedge DOC is relatively small. For the time period 2015–2018, 11.74 $\times 10^3$ kg DOC from ice wedges were eroded, which accounts for 9.5% of the total DOC flux and 0.08% of the total C flux from Sobo-Sise Cliff. Ice wedge DOC fluxes for the different time periods are presented in the **Supplementary Table S2**.

DISCUSSION

Comparison to Other Key Sites

The presence of a very ice-rich yedoma upland at a location where a major channel of the Lena Delta develops a large bend is certainly a key factor for the exceptional high erosion rates of the Sobo-Sise Cliff. These site characteristics favor high erosion rates and the local dynamics suggest that a wide range of permafrost shore erosion rates, including very high maximum rates may develop not only along wave-dominated sea coasts, but also along rivers. Maximum annual shore erosion rates of 22 m yr^{-1} on this Lena river bank exceeds all previously observed rates for Arctic rivers. Erosion dynamics along the cliff rival some of the most rapid permafrost coastal erosion rates in the Arctic and as it is the case for some sections at sea coasts (e.g., Günther et al., 2013; Irrgang et al., 2018; Jones et al., 2018), erosion of the Sobo-Sise Cliff is accelerating in the last decades.

The warm water transported by the large Lena River from further south can be considered as a contributing factor for the erosion. Water temperatures up to 15°C were measured in August 2019 (see **Supplementary Figure S1**). The warm and rapidly flowing water in front of the Sobo-Sise Cliff triggers the

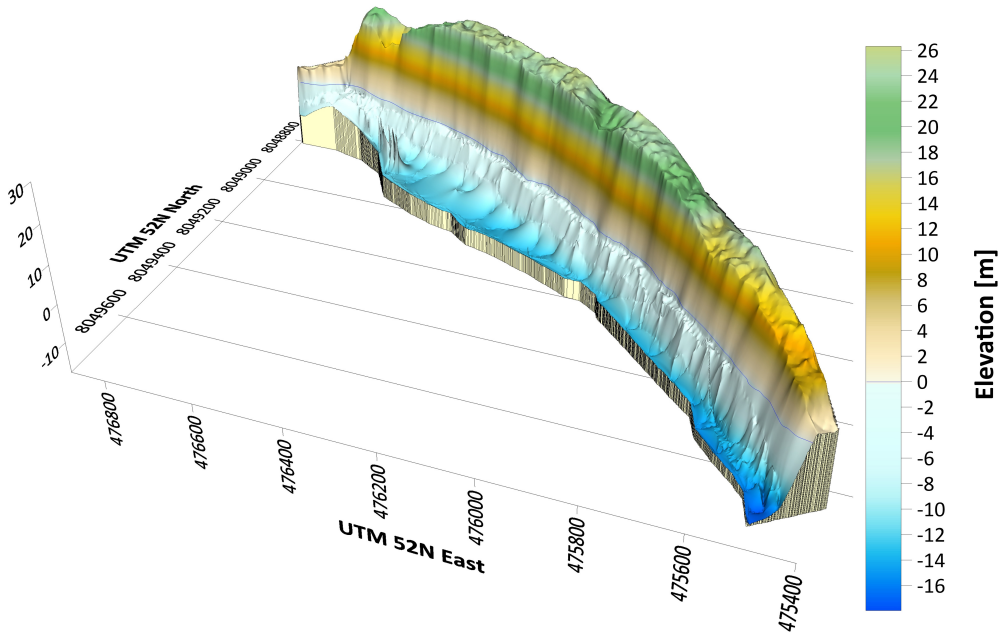

FIGURE 4 | 3D-view of combined topographic and bathymetric surveys at Sobo-Sise Cliff in August 2016 showing cliff height configuration and steep bathymetric gradients directly off the riverbank.

formation of thermo-erosional niches at the base of the ice-rich cliff and continuously removes eroded debris from the base during summertime. The lack of a beach and a water depth of ∼10 m directly in front of the cliff indicate that sediment entering the river is rapidly eroded also at depth and not accumulating. All this leads to formation of a nearly perfectly vertical cliff front where hardly any thaw slump-like features are developing at the cliff top due to the very rapid thermo-erosion of the cliff base.

For comparison, another yedoma cliff on Kurungnakh Island in the central Lena Delta has much smaller erosion rates with 4.1 to 6.9 m yr^{-1} (Stettner et al., 2018). On Kurungnakh Island, the yedoma is located on top of ice-poor fluvial sand layers (Wetterich et al., 2008), which limits erosion rates at the cliff base. Most of the erosion here currently takes place by thermo-denudation, i.e., the retreat of the bluff top by thaw slumping and forming slump floors at the stratigraphic boundary between yedoma and underlying sands roughly at 17 m above river level. The Olenekskaya channel that flows around Kurungnakh Island has a low runoff rate and therefore weaker river currents compared to the Sardakhskaya channel (Fedorova et al., 2015). For comparison, in the Olenekskaya channel in the Lena Delta, Are (1983) also reported smaller erosion rates of 1.7–6 m per year in up to 9 m thick deposits dissected by wedge ice.

Another key site studied for riverine yedoma cliff erosion is the Itkillik exposure on the North Slope of Alaska (Kanevskiy et al., 2016). With up to 35 m height above river water level, this 680 m long cliff retreats by 11 m yr^{-1} and erodes 70 × 10^6 kg yr^{-1} of sediments and 880,000 kg C yr^{-1}. Similar to the Sobo-Sise Cliff, the Itkillik cliff is very ice-rich (total ice content of 86 vol%) and lies on a river bend (Kanevskiy et al., 2016). However, the Sobo-Sise Cliff is more than twice the length resulting in an even higher sediment input into the river compared to the Itkillik exposure. A similar ice-rich permafrost cliff was studied by Shur et al. (2002) on the Yana River close to the village Kazachye. This 15 m high cliff had erosion rates of 6.5 m yr^{-1} from 1975 to 1990.

However, not only yedoma dominated cliff retreat leads to high erosion of sediment and C. Along the Colville River and in the Colville Delta, erosion rates of up to 3.5 m yr^{-1} (Walker et al., 1987; Payne et al., 2018) lead to a continuous transport of organic matter into delta and near-shore zones of the Colville River. Likewise, the Lena River is also eroding permafrost along its course and mobilizing sediments and organic matter. Average bank erosion on a 300 km stretch of the Lena River close to Yakutsk is 2 m yr^{-1} for the period 1967–2002 (Costard et al., 2007). At the Indigirka and Yana rivers, strong erosion of permafrost shores averages 6.5 m yr^{-1} and 2 m yr^{-1}, respectively (Shur et al., 2002). All these observations highlight the importance of major Arctic rivers for the mobilization and redistribution of formerly frozen sediments and organic matter into the fluvial and further downstream environments such as deltas and Arctic shelves (e.g., Wild et al., 2019).

Similar to the Sobo-Sise Cliff with a yedoma Ice Complex base of at least 10 m below river level, these strongly erosion-susceptible yedoma deposits extend down to 10 m below sea level on Muostakh Island (Overduin et al., 2016) and 3 m on Cape Mamontov Klyk (Schirrmeister et al., 2008). Both coastlines feature above-average erosion rates that locally may reach 39.4 and 21 m yr^{-1} during exceptional years on Muostakh Island and Cape Mamontov Klyk, respectively (Günther et al., 2013, 2015). On the Laptev Sea coast, Günther et al. (2013) studied three ice-rich coastal zones (Oyogos Yar, Buor Khaya,

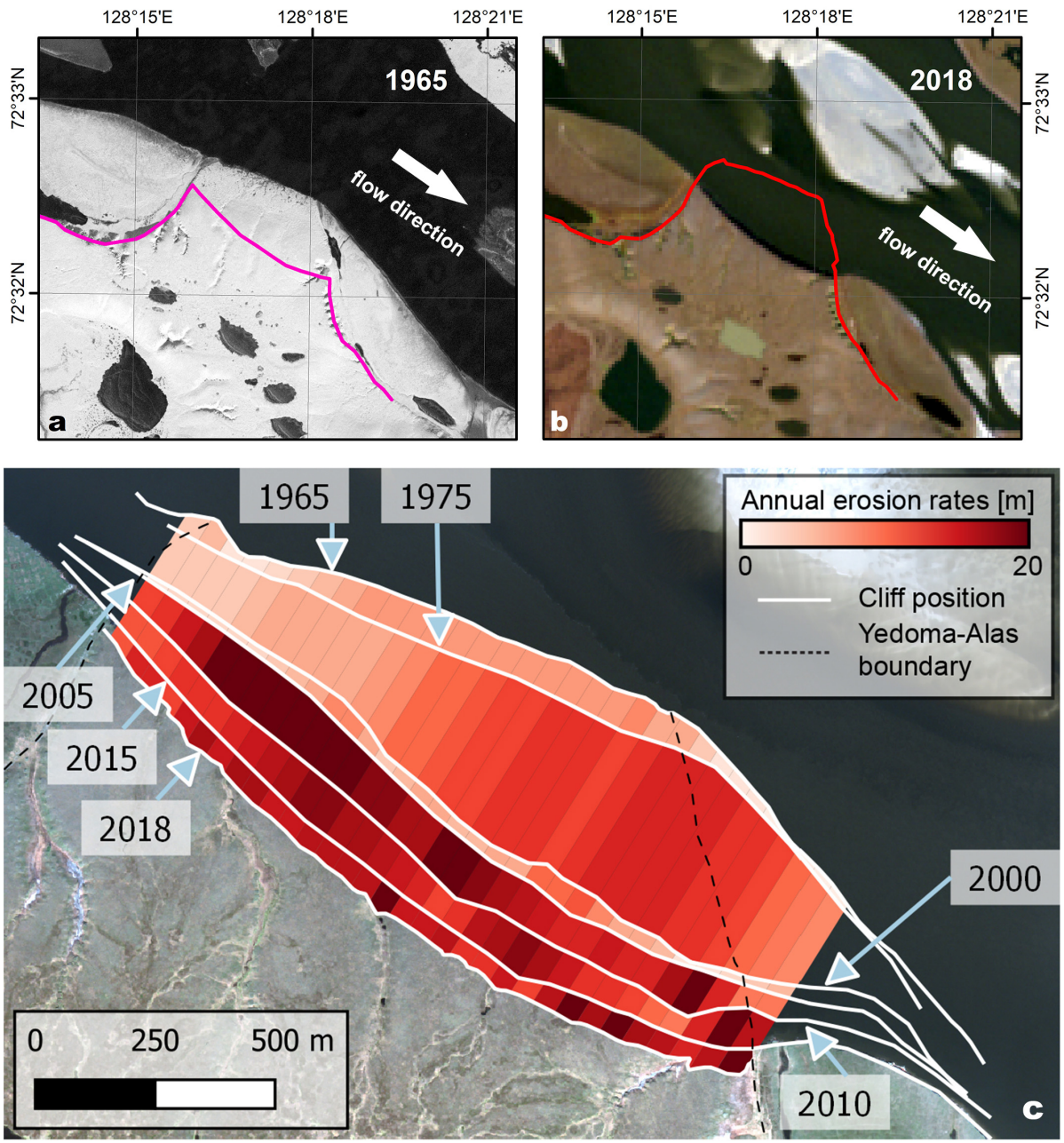

FIGURE 5 | Erosion rates at Sobo-Sise Cliff. **(a)** Corona image from 1965 showing the Sobo-Sise Cliff. Line in purple shows the cliff front in 2018. **(b)** Landsat 8 image from 2018 showing the Sobo-Sise Cliff. Line in red shows the cliff front in 1965. **(c)** Average annual erosion rates per segment and cliff lines for periods 1965–1975, 1975–2000, 2000–2005, 2005–2010, 2010–2015, and 2015–2018. Background image: GeoEye from 2014-08-07. Cliff lines were digitized on Corona (1965), Hexagon (1975), Landsat (2000, 2005, 2010, 2015), and Planet imagery (2018).

Mamontov Klyk) dominated by yedoma and alas deposits and found mean erosion rates of 0.9–2.9 m yr^{-1} for the yedoma dominated areas (**Figure 6**). Another example is the very ice-rich Alaskan Beaufort Sea coast between Drew Point and Cape Halkett with a mean erosion rate of 13.6 m yr^{-1} for the 2002–2007 period (Jones et al., 2009). Looking at a 9 km coastal segment at Drew Point only, average rates for the period 2007–2016 were even higher with 17.2 m yr^{-1} (Jones et al., 2018). Lower rates were reported from the Yukon coast with mean erosion rates of 1.3 m yr^{-1} (Irrgang et al., 2018), Herschel Island with 0.7 m yr^{-1} (Obu et al., 2016), the Chukchi Sea coast on the northern Seward Peninsula of Alaska with 1.3 m yr^{-1} (Farquharson et al., 2018), or Barter Island (Alaskan Beaufort Sea) with 1.3 m yr^{-1} (Gibbs et al., 2019), keeping in mind that these values are long term averages of areas, where local and temporal maxima can be substantial higher (e.g., 8.1 m yr^{-1} for

TABLE 2 | Erosion rates of Sobo-Sise Cliff from 1965 to 2018.

Period	$ER_{absolute}$(m)	Years	ER_{mean} (m yr^{-1})	Scaled factor vs. long term[a]	ER_{max} (m yr^{-1})	Eroded total area (km^2)	Eroded yedoma area (%)[b]	Eroded total volume (10^6 m^3)[b]	Eroded yedoma volume (10^6 m^3)[b]	Eroded yedoma volume per year (10^6 m^3 yr^{-1})[b]
1965–2018	321.8–679.2	53	9.13	1.00	12.83	0.878	n/a	n/a	n/a	n/a
1965–1975	6.4–80.6	10	4.76	0.52	8.24	0.082	n/a	n/a	n/a	n/a
1975–2000	110.0–371.5	25	9.24	1.01	14.84	0.406	n/a	n/a	n/a	n/a
2000–2005	11.8–58.2	5	5.73	0.63	11.82	0.046	0.043	0.972	0.961	0.192
2005–2010	49.5–116.1	5	15.12	1.66	22.26	0.145	0.141	3.165	3.150	0.630
2010–2015	47.6–96.0	5	13.79	1.51	19.32	0.121	0.118	2.648	2.636	0.527
2015–2018	34.3–63.7	3	15.67	1.72	21.21	0.078	0.078	1.743	1.743	0.581

All numbers are including ice wedges as well as segregated and pore ice, which means that 88% of all the yedoma volumes given here consist of ice. Eroded volumes are given in millions (10^6) of m^3. Eroded yedoma volumes excluding ice wedge volume are given in ***Table 3****.* [a]*This factor shows the ER_{mean} for the different time periods in comparison to the ER_{mean} 1965–2018. A value >1.00 indicates that the erosion is higher for this particular period compared with the long term average.* [b]*We did not estimate the volume loss for the periods 1965–2018, 1965–1975, and 1975–2000, because we have no information on the height of the yedoma cliff prior to 2000.*

TABLE 3 | Sediment (Sed_{flux}), soil organic carbon (SOC_{flux}), dissolved organic carbon (DOC_{flux}) and nitrogen (N_{flux}) erosion rates.

Period	Total eroded sediment[a] (10^6 m^3)	Total Sed_{flux}[b] (10^6 kg)	Mean annual Sed_{flux}[b] (10^6 kg yr^{-1})	Total SOC_{flux} (10^6 kg)	Mean annual SOC_{flux} (10^6 kg yr^{-1})	Total DOC_{flux} (10^6 kg)	Mean annual DOC_{flux} (10^3 kg yr^{-1})	Total eroded C (10^6 kg)	Mean annual eroded C (10^6 kg yr^{-1})	Total N_{flux} (10^6 kg)	Mean annual N_{flux} (10^6 kg yr^{-1})	Average annual C flux (SOC + DOC) per meter coast (kg C m^{-1} yr^{-1})[c]
2000–2018	2.87	2081.0	115.6	75.1 ± 48.2	4.2 ± 2.7	0.60 ± 0.33	33.5 ± 18.1	75.7 ± 48.2	4.2 ± 2.7	5.9 ± 3.2	0.3 ± 0.2	2631
2000–2005	0.32	235.5	47.1	8.5 ± 5.5	1.7 ± 1.1	0.07 ± 0.04	13.6 ± 7.4	8.6 ± 5.5	1.7 ± 1.1	0.7 ± 0.4	0.1 ± 0.1	1099
2005–2010	1.07	772.2	154.4	27.9 ± 17.9	5.6 ± 3.6	0.22 ± 0.12	44.8 ± 24.1	28.1 ± 17.9	5.6 ± 3.6	2.2 ± 1.2	0.4 ± 0.2	3546
2010–2015	0.89	646.2	129.2	23.3 ± 15.0	4.7 ± 3.0	0.19 ± 0.10	37.5 ± 20.2	23.5 ± 15.0	4.7 ± 3.0	1.8 ± 1.0	0.4 ± 0.2	2904
2015–2018	0.59	427.2	142.4	15.4 ± 9.9	5.1 ± 3.3	0.12 ± 0.07	41.3 ± 22.3	15.5 ± 9.9	5.2 ± 3.3	1.2 ± 0.6	0.4 ± 0.2	3131

All values are corrected for ice wedge volume. Total eroded sediment is given in millions (10^6) of m^3 and all other masses are given in 10^6 kg, except mean annual DOC_{flux} is given in 10^3 kg yr^{-1}. DOC fluxes include segregated and pore ice as well as ice wedge DOC flux estimations. Standard deviations are given for the eroded C and N, which are based on the variance in total organic C, dissolved organic C and total nitrogen measurements. [a]*Only accounting for the yedoma sediment. Ice wedge volume is excluded, however, segregated and pore ice is still included. The total eroded volume is presented in* ***Table 2****.* [b]*Assuming a mean dry bulk density of 0.7 g cm^{-3}. This is the dry mass of all sediments (including peat) eroded from Sobo-Sise Cliff, excluding all forms of ice.* [c]*An average cliff length was included in the calculation for each time period.*

central parts of a bluff on Barter Island (Gibbs et al., 2019), or 22 m yr^{-1} for active slumps from 2012 to 2013 on Herschel Island (Obu et al., 2017).

However, when comparing Sobo-Sise Cliff to other locations at the coast, it is important to point out that different factors affect fluvial thermo-erosion compared to coastal erosion. The moving river water, the annual ice breakup, the spring flood and the transport of warm river water from further south certainly favor erosion of cliffs along Arctic rivers. These factors lead to a different erosion setting when compared to coastal stretches, which are affected by thermo-denudation and thermo-abrasion (e.g., Are, 1983; Overduin et al., 2014; Günther et al., 2015). In particular, the moving river water of the Sardakhskaya channel leads to fast removal of eroded debris at the cliff base, allowing continuous erosion at the base by the warm river water in summer. This prevents the flattening of the Sobo-Sise Cliff front and is likely an important factor for the continuous high erosion rates.

Annual total C fluxes from rivers into the Laptev Sea have been estimated to 6,800 $\times$ 10^6 kg C yr^{-1} (Rachold et al., 2004). Despite its distinct height, very high ground ice content, and its fast fluvial erosion, by its local nature the Sobo-Sise Cliff contributes only a small portion (5.2 $\times$ 10^6 kg C yr^{-1}, 2015–2018) of this flux. Given the 1,660 m long river shore segment studied, a shoreline-length normalized C flux yields an average of 3,131 kg C m^{-1} yr^{-1} (2015–2018), which is significantly higher than C fluxes observed in other studies (**Figure 6**). Compared to the yedoma coasts studied by Günther et al. (2013), Sobo-Sise Cliff is distinct by its high annual erosion rate, which leads to an overall high sediment and C loss. However, the common practice of aggregating local observations over larger coastal stretches dilutes the substantial contribution of erosional hot spots such as the Sobo-Sise Cliff to overall C fluxes. Because comparable high erosion rates sustained over several decades as we report for the Sobo-Sise Cliff are not known from other locations, our study therefore contributes to a better picture of the upper end in organic matter flux total variability when compared with the mean values summarized in **Figure 6**.

Sobo-Sise Cliff Will Remain a Strong Source for Mobilized C and N

Future Sobo-Sise Cliff erosion rates are difficult to predict because they depend on dynamic factors such as ice cover thickness, timing of river-ice breakup, river discharge, air and water temperatures (Walker et al., 1987). Particularly the course of the main river bed of the Sardakhskaya channel is an important factor. In case the main channel might shift slightly or a sand bank forms in front of the Sobo-Sise Cliff, riverbank erosion would suddenly decrease due to accumulation of sediment load and eroded debris, reducing niche formation and subsequent erosion at the cliff base (Grigoriev, 2007). Although a major sudden shift of the Sardakhskaya channel in near future seems unlikely, the Sobo-Sise Cliff will not form an infinite bulge on the outer side of a river bend and only retreat at the pace of the neighboring river shoreline.

In our remote sensing time series for 1965–2018 we see an increase erosion rates at the Sobo-Sise Cliff (**Table 2**). Besides the increase in erosion rate, the length of the cliff itself increased by 58% from an initial length of 1,050 m in 1965 to a length of 1,660 m in 2018. The increase in length is due to continuous erosion from the initial convex shape to the concave shape of the Sobo-Sise Cliff and the progressing erosion into the crescent forms of eroded alases. With progressing erosion, the Sobo-Sise Cliff will likely further increase in length (**Figure 5**) and therefore would contribute an accordingly higher amount of sediment and organic C flux into the Lena River.

Our results show some variation in erosion rates of different time periods. Whereas the time period 2005–2010 is characterized by high mean erosion rates of 15.1 m yr^{-1}, the precedent period (2000–2005) showed almost three times smaller mean erosion rates of 5.7 m yr^{-1}. The reasons for this inconsistency in erosion rates are difficult to determine but likely are related to variable environmental conditions. Air temperature data (NOAA, Menne et al., 2012) from Tiksi show that from the late 1990s to the early 2000s mean monthly air temperatures were mostly below average and since then no extensive period with below-average mean monthly temperatures occurred anymore (see **Supplementary Figure S5**). However, air temperature is most likely not the only factor affecting Sobo-Sise Cliff erosion. Data on the Lena water level, the river discharge in the Sardakhskaya channel, duration and thickness of Lena River ice cover, or precipitation would be beneficial in determining the environmental conditions affecting Sobo-Sise Cliff erosion. Equally important, if not the major factor favoring high erosion rates, not only at the Sobo-Sise Cliff but also on outer coastal locations, is the position of the lower yedoma Ice Complex base that may have substantial variation in space due to an uneven paleo-relief prior to yedoma deposition.

We did not include erosion rates and volumes below the water surface, which makes our estimates of sediment, C, and N fluxes from the Sobo-Sise Cliff conservative. The ice-rich yedoma deposits in the eastern part of the Lena Delta are known to extend below the water surface (Pavlova and Dorozhkina, 2000) similar to the yedoma on nearby Bykovsky Peninsula (e.g., Schirrmeister et al., 2002). According to the bathymetrical survey in front of Sobo-Sise Cliff (**Figure 4**) mean water depth is 10.3 m. Assuming the below water deposits have a similar composition like the above-water deposits, the total volume as well as the C and N loss would increase by 46% compared to our estimates (2015–2018). However, we do not have sufficient data to characterize the deposits below the water surface nor the hydrological and erosional dynamics in the channel that would also include winter river flow, therefore this estimate remains highly speculative.

Exceptional DOC Fluxes From Ice-Rich Sobo-Sise Cliff

Up to 41.3 $\times$ 10^3 kg DOC is eroded annually (2015–2018) into the Sardakhskaya channel. Considering the length of Sobo-Sise Cliff of only 1,660 m this is a substantial amount of potentially bioavailable C, which is released into the riverine ecosystem. For comparison, Tanski et al. (2016) estimated an annual flux

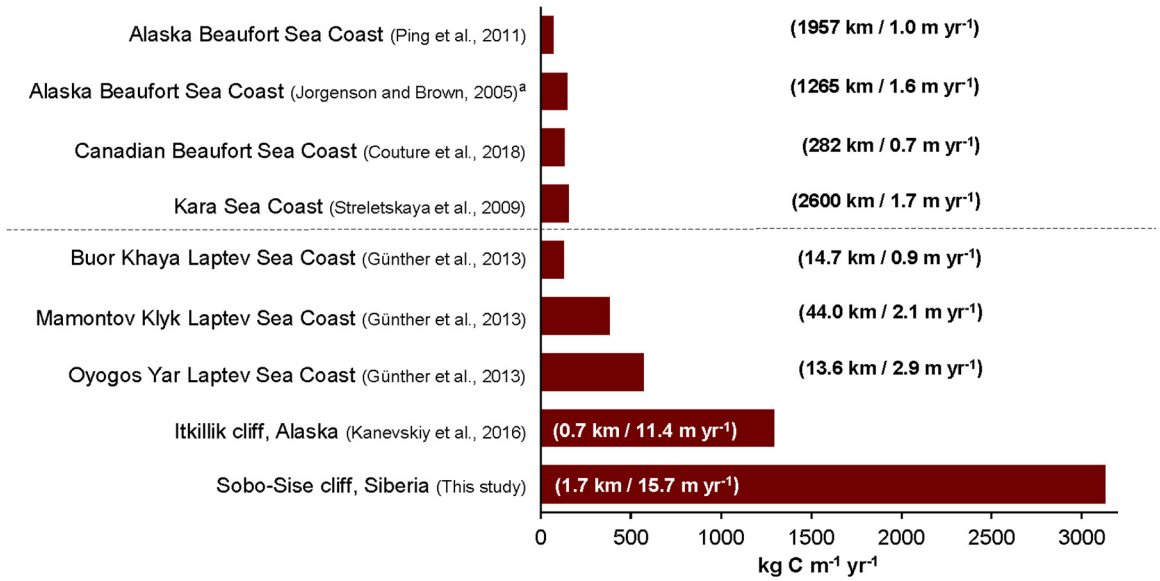

FIGURE 6 | Comparison of C fluxes in kg C m^{-1} yr^{-1} from studied coastal erosion sites. Numbers in brackets show the length of studied coast and the mean annual erosion for the studied coast. Studies below the dashed line focus on yedoma deposits. Only the two last studies investigate fluvial thermo-erosion, while all the other studies investigate coastal erosion processes. [a]In comparison to Ping et al. (2011); Jorgenson and Brown (2005) do not include delta areas along the Alaska Beaufort Sea Coast.

of 54.9 × 10^3 kg yr^{-1} from the 306 km long Yukon coast. The reasons for the very high DOC flux at Sobo-Sise Cliff are the high segregated and pore ice volume (65.7%), the dimensions of the cliff (up to 27.7 m high) and the high erosion rates. Nevertheless, the main factor is the high DOC concentration within the segregated and pore ice. Maximum DOC concentrations up to 786 mg L^{-1} and a DOC to SOC ratio of 1:125 are among the highest observed in the Arctic. Mann et al. (2015) and Vonk et al. (2013a) reported values of 131 mg L^{-1} and 196 mg L^{-1} for yedoma thaw streams, respectively. Schirrmeister et al. (2017) found similar high DOC concentrations in yedoma Ice Complex outcrops and drill cores of the Buor Khaya Peninsula in the east of the Lena Delta.

Although the DOC fluxes might still be small compared to the SOC fluxes from OC-rich sediments, DOC from permafrost is chemically labile (Dou et al., 2008; Vonk et al., 2013a,b) and may directly enter local food webs (bioavailability). This means that DOC can become quickly mineralized by microbial communities and photochemical reactions (Battin et al., 2008; Vonk et al., 2013a,b; Cory et al., 2014) and returned to the atmosphere when released due to permafrost degradation (Schuur et al., 2009, 2011; Tanski et al., 2019).

Fate of Eroded Organic Matter and Implications for the Ecosystem

The high amount of organic matter eroded from the Sobo-Sise Cliff enters the Lena River and is transported downstream to the outer parts of the delta or likely to the near-shore zone of the Laptev Sea that is only about 40 km to the east. Previous studies indicated that the Lena River has an organic C flux of 0.9 Tg C yr^{-1} coming from permafrost and peat deposits (Wild et al., 2019). However, Wild et al. (2019) measured C concentration approximately 800 km upstream from Sobo-Sise Cliff. Therefore, it is difficult to infer on the C concentration and export at Sobo-Sise Cliff from these values. Nevertheless, this indicates that high amounts of permafrost C are transported toward the Laptev Sea.

The consequences of permafrost erosion and the subsequent organic matter input from the Lena River catchment into the Laptev Sea are not fully understood yet. Increased terrestrial C fluxes to the Arctic Ocean might affect food webs in the near-shore zone (e.g., Dunton et al., 2006, 2012; Casper et al., 2015) or lead to an increased acidification (Semiletov et al., 2016). The latter is seen in waters of the East Siberian Arctic Shelf that become more acidic due to the high CO_2 concentrations in river water input, which is affected by degradation of terrestrial organic matter. In fact, the study by Semiletov et al. (2016) stated that 57% of the terrestrial organic C in the East Siberian Shelf originates from old Pleistocene age permafrost C like the deposits from the Sobo-Sise Cliff.

However, Bröder et al. (2019) reported on slow C degradation rates of terrestrial C in the top layer of seafloor sediments, of which a majority was considered even resistant to degradation. In addition, a large amount of the permafrost C might become re-buried in marine sediments of the Laptev and East Siberian Sea shelf (Vonk et al., 2012; Vonk and Gustafsson, 2013; Bröder et al., 2019). Nevertheless, terrestrial organic C on the Laptev Sea shelf is exposed for degradation for millennia so that these areas might become a C source for ocean acidification and atmospheric export on long timescales (Bröder et al., 2018).

Also, Tanski et al. (2019) showed in an incubation study that high amounts of CO_2 are produced from thawing permafrost C in seawater, potentially leading to high CO_2 production along

permafrost coasts and near-shore zones. Another aspect raised by Sánchez-García et al. (2014) is the potential correlation of decay intensity of the organic matter in relation to active erosion of yedoma deposits, where fast erosion rates and high moisture content during summer thaw seem to favor microbial activity. In another study, Winterfeld et al. (2018) suggest that fluvial export of old (Pleistocene) C from degrading permafrost was potentially an important process for high C mobilization at the Pleistocene-Holocene transition around 11.5 kyrs BP, leading to changes in atmospheric CO_2, and indicating the significance of eroding yedoma in the Arctic. Similar findings are provided by Tesi et al. (2016) and Martens et al. (2019), who report a much higher permafrost C transport to the Laptev and Chukchi Sea at the end of the last deglaciation, indicating high permafrost C mobilization during times of rapid climate warming.

DOC from late Pleistocene permafrost as an especially bioavailable form of C due to its fraction size and molecular composition could play a crucial role for microbial use and general food web impacts. For example, Vonk et al. (2013b) showed that yedoma ice wedge meltwater can increase the degradation of organic matter due to co-metabolizing effects. At the Duvanny Yar yedoma exposure on the Kolyma river, Vonk et al. (2013a) and Mann et al. (2014) found that DOC originating from ancient yedoma deposits is highly bioavailable and therefore important to consider in a potential permafrost C feedback. The origin of organic matter and the sequestration process into ground ice plays an important role in the concentration and bioavailability of DOC (Fritz et al., 2015). Sequestration of DOC into ground ice is a complex process that is dependent on water source, freezing process, organic matter quality and even the inorganic geochemical composition of the ambient water to form ground ice. Tundra-steppe vegetation, reduced organic matter degradation rates and syngenetic permafrost aggradation were characteristic for the cold stages of the last ice age. Late Pleistocene yedoma deposits and associated ground ice are therefore the ideal reservoir for the fresh and most bioavailable DOC components, where the chemical character is preserved because of rapid incorporation into permafrost.

In summary, while we quantified the amount to C and N mobilized from the Sobo-Sise Cliff the actual fate of the eroded terrestrial material is not yet clear and further studies are needed to investigate the state (dissolved, particulate) and the lability of the C and N released from Sobo-Sise Cliff and similar shores in the Lena River and Delta. The Sobo-Sise Cliff (this study) and other permafrost-shores characterized by rapid erosion in the Lena River (Costard et al., 2003, 2007; Dupeyrat et al., 2018; Stettner et al., 2018) contribute to an enhanced fluvial transport of terrestrial organic matter and nitrogen to the Arctic Ocean. McClelland et al. (2016) estimated that the Lena River exports 0.8 Tg particulate organic C and 0.1 Tg particulate N per year into the Arctic Ocean. In addition, Holmes et al. (2012) reported of an annual DOC and total dissolved N export of 5.7 Tg and 0.2 Tg, respectively. Combining particulate and dissolved organic C fluxes results in a total export of 6.5 Tg C yr^{-1} and 0.3 Tg N yr^{-1} by the Lena River. Understanding the sources of this flux and the processes behind its mobilization from permafrost is key to estimate current and project future impacts of changing river runoff regimes on biogeochemical cycling processes in permafrost rivers and the Arctic Ocean.

CONCLUSION

The 1,660 m long and 27.7 m high Sobo-Sise Cliff is one of the fastest eroding permafrost features in the Arctic, releasing a significant amount of C and N on a local scale. Erosion rates of up to 22 m per year and an average loss of 5.2×10^6 kg C (SOC and DOC) and 0.4×10^6 kg N per year (2015–2018) highlight the magnitude of biogeochemical fluxes from this individual erosional feature in the Lena River Delta. To study rapid permafrost shore erosion processes and resulting sediment fluxes at an extraordinary location such as the Sobo-Sise Cliff is extremely helpful to gain a better understanding of current and future impacts of permafrost thaw, interdependencies of permafrost erosion with runoff changes, and fluvial and marine biogeochemistry. In particular regarding the latter, our observations of current erosion dynamics at the Sobo-Sise Cliff provide an outlook of C and N fluxes from permafrost for the anticipated future accelerated coastal erosion in the course of global sea level rise, when it reaches the lower base of Ice Complex deposits in the yedoma upland along the northeast Siberian coastline.

DATA AVAILABILITY STATEMENT

The data for this study has been archived on the PANGAEA (www.pangaea.de) data set repository. Erosion rates and digitized cliff fronts are available on doi: 10.1594/PANGAEA.918507 (Nitze et al., 2020), and the geochemical results from Sobo-Sise Cliff samples are available on doi: 10.1594/PANGAEA.919470 (Wetterich et al., 2020).

AUTHOR CONTRIBUTIONS

MFu and IN contributed equally to this study. MFu, IN, JS, FG, and GG designed the study. GG, JS, and SW acquired funding. AK, SW, and MFr collected and analyzed sediment data. MFr collected and analyzed the samples for DOC. GM and SW made the bathymetric survey. IN, FG, and GG processed the remote sensing imagery. IN calculated erosion rates and cliff heights. MFu and JS calculated C and N stocks. All authors participated in field investigations. MFu wrote the original draft of the manuscript. All authors contributed in writing, reviewing, and editing the manuscript.

FUNDING

This work was supported by NERC-BMBF project CACOON [#03F0806A, Changing Arctic Ocean (CAO) program], the ERC starting grant PETA-CARB (#338335), the HGF impulse and network fund (ERC_0013), the BMBF project KoPf (#3F0764B), the ESA GlobPermafrost project, RFBR grant (#18-05-60221),

DAAD and EU Marie Curie Actions under REA grant agreement #605728 (PRIME), the EU Horizon 2020 project Nunataryuk (#773421), and MSU (#AAAA-A16-116032810095-6). Further support was provided by the Deutsche Forschungsgemeinschaft (Grant No. WE4390/7-1 to SW). MG and GM were supported by grants from the Russian Foundation for Basic Research (Grant Nos. RFBR 18-05-70091 and RFBR 18-45-140057).

ACKNOWLEDGMENTS

We thank Aleksey Aksenov, Lutz Schirrmeister, and the great support by the Hydrobaza Tiksi for help with field work in 2018 and 2019, Dyke Scheidemann for support with sample analysis in the AWI laboratories, Andreas Fricke and Juri Palmtag for providing photographs, and Sebastian Laboor for the support in preparing the data set publication. Fieldwork on Sobo-Sise Island was conducted in the framework of the joint Russian-German expeditions *Lena 2014*, *2015*, *2016*, *2018*, and *2019* supported by the Samoylov Research Station. Planet data were provided freely through Planet's Education and Research program. The Arctic DEM is provided by the Polar Geospatial Center under NSF-OPP awards 1043681, 1559691, and 1542736.

SUPPLEMENTARY MATERIAL

The Supplementary Material for this article can be found online at: https://www.frontiersin.org/articles/10.3389/feart.2020.00336/full#supplementary-material

REFERENCES

Adams, W. A. (1973). The effect of organic matter on the bulk and true densities of some uncultivated podzolic soils. *J. Soil Sci.* 24, 10–17. doi: 10.1111/j.1365-2389.1973.tb00737.x

Are, F. E. (1983). "Thermal abrasion of coasts," in *Proceedings of the 4th International Conference on Permafrost* (Washington D.C: National Academy Press), 24–28.

Balser, A. W., Jones, J. B., and Gens, R. (2014). Timing of retrogressive thaw slump initiation in the Noatak Basin, northwest Alaska, USA. *J. Geophys. Res. Earth Surf.* 119, 1106–1120. doi: 10.1002/2013JF002889

Barichivich, J., Briffa, K. R., Osborn, T. J., Melvin, T. M., and Caesar, J. (2012). Thermal growing season and timing of bisopheric carbon uptake across the Northern Hemisphere. *Global Biogeochem. Cycles* 26:GB4015. doi: 10.1029/2012GB004312

Battin, T. J., Kaplan, L. A., Findlay, S., Hopkinson, C. S., Marti, E., Packman, A. I., et al. (2008). Biophysical controls on organic carbon fluxes in fluvial networks. *Nat. Geosci.* 1, 95–100. doi: 10.1038/ngeo101

Biskaborn, B. K., Smith, S. L., Noetzli, J., Matthes, H., Vieira, G., Streletskiy, D. A., et al. (2019). Permafrost is warming at a global scale. *Nat. Commun.* 10:264. doi: 10.1038/s41467-018-08240-4

Boike, J., Nitzbon, J., Anders, K., Grigoriev, M., Bolshiyanov, D., Langer, M., et al. (2019). A 16-year record (2002–2017) of permafrost, active-layer, and meteorological conditions at the Samoylov Island Arctic permafrost research site, Lena River delta, northern Siberia: an opportunity to validate remote-sensing data and land surface, snow, and permafrost models. *Earth Syst. Sci. Data* 11, 261–299. doi: 10.5194/essd-11-261-2019

Box, J. E., Colgan, W. T., Christensen, T. R., Schmidt, N. M., Lund, M., Parmentier, F.-J., et al. (2019). Key indicators of arctic climate change: 1971-2017. *Environ. Res. Lett.* 14:045010. doi: 10.1088/1748-9326/aafc1b

Bröder, L., Andersson, A., Tesi, T., Semiletov, I., and Gustafsson, Ö. (2019). Quantifying degradative loss of terrigenous organic carbon in surface sediments across the Laptev and East Siberian Sea. *Global Biogeochem. Cycles* 33, 85–99. doi: 10.1029/2018GB005967

Bröder, L., Tesi, T., Andersson, A., Semiletov, I., and Gustafsson, Ö. (2018). Bounding cross-shelf transport time and degradation in Siberian-Arctic land-ocean carbon transfer. *Nat. Commun.* 9:806. doi: 10.1038/s41467-018-03192-1

Casper, A. F., Rautio, M., Martineau, C., and Vincent, W. F. (2015). Variation and assimilation of Arctic riverine sestonin the pelagic food web of the Mackenzie River Delta and Beaufort Sea transition zone. *Estuaries Coast* 38, 1656–1663. doi: 10.1007/s12237-014-9917-z

Chen, J., Günther, F., Grosse, G., Liu, L., and Lin, H. (2018). Sentinel-1 InSAR measurements of elevation changes over Yedoma Uplands on Sobo-Sise Island, Lena Delta. *Remote Sens.* 10:1152. doi: 10.3390/rs10071152

Cory, R. M., Ward, C. P., Crump, B. C., and Kling, G. W. (2014). Sunlight controls water column processing of carbon in arctic fresh waters. *Science* 345, 925–928. doi: 10.1126/science.1253119

Costard, F., Dupeyrat, L., Gautier, E., and Carey-Gailhardis, E. (2003). Fluvial thermal erosion investigations along a rapidly eroding river bank: application to the Lena River (central Siberia). *Earth Surf. Process. Landf.* 28, 1349–1359. doi: 10.1002/esp.592

Costard, F., Gautier, E., Brunstein, D., Hammadi, J., Fedorov, A., Yang, D., et al. (2007). Impact of the global warming on the fluvial thermal erosion over the Lena River in Central Siberia. *Geophys. Res. Lett.* 34:L14501. doi: 10.1029/2007gl030212

Couture, N. J., Irrgang, A., Pollard, W., Lantuit, H., and Fritz, M. (2018). Coastal erosion of permafrost soils along the Yukon Coastal Plain and fluxes of organic carbon to the Canadian Beaufort Sea. *J. Geophys. Res. Biogeosci.* 123, 406–422. doi: 10.1002/2017JG004166

Dou, F., Ping, C.-L., Guo, L., and Jorgenson, T. (2008). Estimating the impact of seawater on the production of soil water-extractable organic carbon during coastal erosion. *J. Environ. Qual.* 37, 2368–2374. doi: 10.2134/jeq2007.0403

Dunton, K. H., Schonberg, S. V., and Cooper, L. W. (2012). Food web structure of the Alaskan nearshore shelf and estuarine lagoons of the Beaufort Sea. *Estuaries Coast* 35, 416–435. doi: 10.1007/s12237-012-9475-1

Dunton, K. H., Weingartner, T., and Carmack, E. C. (2006). The nearshore western Beaufort Sea ecosystem: circulation and importance of terrestrial carbon in arctic coastal food webs. *Prog. Oceanogr.* 71, 362–378. doi: 10.1016/j.pocean.2006.09.011

Dupeyrat, L., Hurault, B., Costard, F., Marmo, C., and Gautier, E. (2018). Satellite image analysis and frozen cylinder experiments on thermal erosion of periglacial fluvial islands. *Permafr. Periglac. Process.* 29, 100–111. doi: 10.1002/ppp.1973

Elementar Analysesysteme (2007). *Vario Max C, Makro-Elementaranalysator, Bedienungsanleitung*. Hanau: Elementar Analysesysteme.

Elementar Analysesysteme (2011). *Vario EL III, CHNOS Elementaranalysator, Bedienungsanleitung*. Hanau: Elementar Analysesysteme.

Farquharson, L. M., Mann, D. H., Swanson, D. K., Jones, B. M., Buzard, R. M., and Jordan, J. W. (2018). Temporal and spatial variability in coastline response to declining sea-ice in northwest Alaska. *Mar. Geol.* 404, 71–83. doi: 10.1016/j.margeo.2018.07.007

Fedorova, I., Chetverova, A., Bolshiyanov, D., Makarov, A., Boike, J., Heim, B., et al. (2015). Lena Delta hydrology and geochemistry: long-term hydrological data and recent field observations. *Biogeosciences* 12, 345–363. doi: 10.5194/bg-12-345-2015

Fritz, M., Opel, T., Tanski, G., Herzschuh, U., Meyer, H., Eulenburg, A., et al. (2015). Dissolved organic carbon (DOC) in Arctic ground ice. *Cryosphere* 9, 737–752. doi: 10.5194/tc-9-737-2015

Fritz, M., Vonk, J. E., and Lantuit, H. (2017). Collapsing Arctic coastlines. *Nat. Clim. Change* 7, 6–7. doi: 10.1038/nclimate3188

Fuchs, M., Grosse, G., Strauss, J., Günther, F., Grigoriev, M., Maximov, G. M., et al. (2018). Carbon and nitrogen pools in thermokarst-affected permafrost landscapes in Arctic Siberia. *Biogeosciences* 15, 953–971. doi: 10.5194/bg-15-953-2018

Gibbs, A. E., Nolan, M., Richmond, B. M., Snyder, A. G., and Erikson, L. H. (2019). Assessing patterns of annual change to permafrost bluffs along the North Slope coast of Alaska using high-resolution imagery and elevation models. *Geomorphology* 336, 152–164. doi: 10.1016/j.geomorph.2019.03.029

Goward, S., Arvidson, T., Williams, D., Faundeen, J., Irons, J., and Franks, S. (2006). Historical record of Landsat global coverage. *Photogramm. Eng. Remote Sens.* 72, 1155–1169. doi: 10.14358/PERS.72.10.1155

Grigoriev, M. N. (2007). "Shore erosion studies on the Ice Complex Islands in the South-East Lena Delta," in *Russian-German Cooperation System Laptev Sea: The expedition LENA 2006*, Vol. 566, eds J. Boike, D. Y. Bolshiyanov, and M. N. Grigoriev (Bremerhaven: Alfred Wegener Institute for Polar and Marine Research), 31.

Grosse, G., Goetz, S., McGuire, A. D., Romanovsky, V. E., and Schuur, E. A. G. (2016). Review and synthesis: changing permafrost in a warming world and feedbacks to the Earth System. *Environ. Res. Lett.* 11:040201. doi: 10.1088/1748-9326/11/4/040201

Grotheer, H., Meyer, V., Riedel, T., Pfalz, G., Mathieu, L., Hefter, J., et al. (2020). Burial and origin of permafrost-derived carbon in the nearshore zone of the Southern Canadian Beaufort Sea. *Geophys. Res. Lett.* 47:e2019GL085897. doi: 10.1029/2019GL085897

Günther, F., Overduin, P. P., Sandakov, A. V., Grosse, G., and Grigoriev, M. N. (2013). Short- and long-term thermo-erosion of ice-rich permafrost coasts in the Laptev Sea region. *Biogeosciences* 10, 4297–4318. doi: 10.5194/bg-10-4297-2013

Günther, F., Overduin, P. P., Yakshina, I. A., Opel, T., Baranskaya, A. V., and Grigoriev, M. N. (2015). Observing Muostakh disappear: permafrost thaw subsidence and erosion of a ground-ice-rich island in response to arctic summer warming and sea ice reduction. *Cryosphere* 9, 151–178. doi: 10.5194/tc-9-151-2015

Gustafsson, Ö., van Dongen, B. E., Vonk, J. E., Dudarev, O. V., and Semiletov, I. P. (2011). Widespread release of olc carbon across the Siberian Arctic echoed by its large rivers. *Biogeosciences* 8, 1737–1743. doi: 10.5194/bg-8-1737-2011

Himmelstoss, E. A., Henderson, R. E., Kratzmann, M. G., and Farris, A. S. (2018). *Digital Shoreline Analysis System (DSAS) Version 5.0 User Guide*. US Geological Survey Open-File Report No. 2018-1179. Reston, VA: US Geological Survey. doi: 10.3133/ofr20181179

Holmes, R. M., McClelland, J. W., Peterson, B. J., Tank, S. E., Bulygina, E., Eglinton, I., et al. (2012). Seasonal and annual fluxes of nutrients and organic matter from large rivers to the Arctic Ocean and surrounding seas. *Estuaries Coast* 35, 369–382. doi: 10.1007/s12237-011-9386-6

Holmes, R. M., Shiklomanov, A. I., Tank, S. E., McClelland, J. W., and Tretiakov, M. (2015). *River Discharge*. Available online at: https://Arctic.noaa.gov/Report-Card/Report-Card-2015/ArtMID/5037/ArticleID/227/River-Discharge (accessed July 27, 2020).

Irrgang, A. M., Lantuit, H., Manson, G. K., Günther, F., Grosse, G., and Overduin, P. P. (2018). Variability in rates of coastal change along the Yukon Coast, 1951 to 2015. *J. Geophys. Res. Earth Surf.* 123, 779–800. doi: 10.1002/2017JF004326

Jones, B. M., Arp, C. D., Jorgenson, M. T., Hinkel, K. M., Schmutz, J. A., and Flint, P. L. (2009). Increase in the rate and uniformity of coastline erosion in Arctic Alaska. *Geophys. Res. Lett.* 36:L03503. doi: 10.1029/2008gl036205

Jones, B. M., Farquharson, L. M., Baughman, C. A., Buzard, R. M., Arp, C. D., Grosse, G., et al. (2018). A decade of remotely sensed observations highlight complex processes linked to coastal permafrost bluff erosion in the Arctic. *Environ. Res. Lett.* 13:115001. doi: 10.1088/1748-9326/aae471

Jones, B. M., Hinkel, K. M., Arp, C. D., and Eisner, W. R. (2008). Modern erosion rates and loss of coastal features and sites, Beaufort Sea coastline, Alaska. *Arctic* 61, 361–372.

Jorgenson, M. T., and Brown, J. (2005). Classification of the Alaskan Beaufort Sea Coast and estimation of carbon and sediment inputs from coastal erosion. *Geo Mar. Lett.* 25, 69–80. doi: 10.1007/s00367-004-0188-8

Kanevskiy, M., Shur, Y., Strauss, J., Jorgenson, T., Fortier, D., Stephani, E., et al. (2016). Patterns and rates of riverbank erosion involving ice-rich permafrost (yedoma) in northern Alaska. *Geomorphology* 253, 370–384. doi: 10.1016/j.geomorph.2015.10.023

Lantuit, H., Atkinson, D., Overduin, P. P., Grigoriev, M., Rachold, V., Grosse, G., et al. (2011). Coastal erosion dynamics on the permafrost-dominated Bykovsky Peninsula, north Siberia, 1951–2006. *Polar Res.* 30:7341. doi: 10.3402/polar.v30i0.7341

Lantz, T. C., and Kokelj, S. V. (2008). Increasing rates of retrogressive thaw slump activity in the Mackenzie Delta region, N.W.T., Canada. *Geophys. Res. Lett.* 35:L06502. doi: 10.1029/2007gl032433

Lide, D. R., Baysinger, G., Kehiaian, H. V., Berger, L. I., Kuchitsu, K., Goldberg, R. N., et al. (eds) (2008). "Properties of ice and supercooled water," in *CRC Handbook of Chemistry and Physics* (Boca Raton, FL: CRC Press), 1101.

Mann, P. J., Eglington, T. I., McIntyre, C. P., Zimov, N., Davydova, A., Vonk, J. E., et al. (2015). Utilization of ancient permafrost carbon in headwaters of Arctic fluvial networks. *Nat. Commun.* 6:7856. doi: 10.1038/ncomms8856

Mann, P. J., Sobczak, W. V., LaRue, M. M., Bulygina, E., Davydova, A., Vonk, J. E., et al. (2014). Evidence for key enzymatic controls on metabolism of Arctic river organic matter. *Global Change Biol.* 20, 1089–1100. doi: 10.1111/gcb.12416

Martens, J., Wild, B., Pearce, C., Tesi, T., Andersson, A., Bröder, L., et al. (2019). Remobilization of old permafrost carbon to Chukchi Sea sediments during the end of the last deglaciation. *Global Biogeochem. Cycles* 33, 2–14. doi: 10.1029/2018GB005969

McClelland, J. W., Holmes, R. M., Peterson, B. J., Raymond, P. A., Striegl, R. G., Zhulidov, A. V., et al. (2016). Particulate organic carbon and nitrogen export from major Arctic rivers. *Global Biogeochem. Cycles* 30, 629–643. doi: 10.1002/2015GB005351

Menne, M. J., Durre, I., Korzeniewski, B., McNeal, S., Thomas, K., Yin, X., et al. (2012). *Global Historical Climatology Network - Daily (GHCN-Daily), Version 3*. Asheville, NC: NOAA National Climatic Data Center.

Morgenstern, A., Grosse, G., Günther, F., Fedorova, I., and Schirrmeister, L. (2011). Spatial analyses of thermokarst lakes and basins in Yedoma landscapes of the Lena Delta. *Cryosphere* 5, 849–867. doi: 10.5194/tc-5-849-2011

Nielsen, D. M., Dobrynin, M., Baehr, J., Razumov, S., and Grigoriev, M. (2020). Coastal erosion variability at the southern Laptev Sea linked to winter sea ice and the Arctic Oscillation. *Geophys. Res. Lett.* 47:e2019GL086876. doi: 10.1029/2019GL086876

Nitze, I., Fuchs, M., Strauss, J., Günther, G., Wetterich, S., Kizyakov, A., et al. (2020). Erosion rates of the Sobo-Sise yedoma permafrost cliff in the Lena River Delta derived from remote sensing imagery. *PANGAEA*. doi: 10.1594/PANGAEA.918507

Nitze, I., and Grosse, G. (2016). Detection of landscape dynamics in the Arctic Lena Delta with temporally dense Landsat time-series stacks. *Remote Sens. Environ.* 181, 27–41. doi: 10.1016/j.rse.2016.03.038

Obu, J., Lantuit, H., Fritz, M., Pollard, W. H., Sachs, T., and Günther, F. (2016). Relation between planimetric and volumetric measurements of permafrost coast erosion: a case study from Herschel Island, western Canadian Arctic. *Polar Res.* 35:30313. doi: 10.3402/polar.v35.30313

Obu, J., Lantuit, H., Grosse, G., Günther, F., Sachs, T., Helm, V., et al. (2017). Coastal erosion and mass wasting along the Canadian Beaufort Sea based on annual airborne LiDAR elevation data. *Geomorphology* 293, 331–346. doi: 10.1016/j.geomorph.2016.02.014

Overduin, P. P., Strzelecki, M. C., Grigoriev, M. N., Couture, N., Lantuit, H., St-Hilaire-Gravel, D., et al. (2014). Coastal changes in the Arctic. *Geol. Soc. Lond. Spec. Publ.* 388:103. doi: 10.1144/SP388.13

Overduin, P. P., Wetterich, S., Günther, F., Grigoriev, M. N., Grosse, G., Schirrmeister, L., et al. (2016). Coastal dynamics and submarine permafrost in shallow water of the central Laptev Sea, East Siberia. *Cryosphere* 10, 1449–1462. doi: 10.5194/tc-10-1449-2016

Pavlova, E. Y., and Dorozhkina, M. (2000). "Geological-Geomorphological studies in the western and central sectors of the Lena Delta," in *Russian-German Cooperation SYSTEM LAPTEV SEA 2000: The Expedition LENA 1999*, eds V. Rachold and M. N. Grigoriev (Bremerhaven: Alfred Wegener Institute for Polar and Marine Research), 354.

Payne, C., Panda, S., and Prakash, A. (2018). Remote sensing of river erosion on the Colville River, North Slope Alaska. *Remote Sens.* 10:397. doi: 10.3390/rs10030397

Peel, M. C., Finlayson, B. L., and McMahon, T. A. (2007). Updated world map of the Köppen-Geiger climate classification. *Hydrol. Earth Syst. Sci.* 11, 1633–1644. doi: 10.5194/hess-11-1633-2007

Ping, C. L., Michaelson, G. J., Guo, L., Jorgenson, M. T., Kanevskiy, M., Shur, Y., et al. (2011). Soil carbon and material fluxes across the eroding Alaska Beaufort Sea coastline. *J. Geophys. Res. Biogeosci.* 116:G02004. doi: 10.1029/2010JG001588

Planet Team (2017). *Planet Application Program Interface: In Space for Life on Earth*. San Francisco, CA: Planet Team.

Porter, C., Morin, P., Howat, I., Noh, M.-J., Bates, B., Peterman, K., et al. (2018). *ArcticDEM*. Available online at: https://doi.org/10.7910/DVN/OHHUKH (accessed October 21, 2019).

Rachold, V., Eicken, H., Gordeev, V. V., Grigoriev, M. N., Hubberten, H. W., Lisitzin, A. P., et al. (2004). "Modern terrigenous organic carbon input to the Arctic Ocean," in *The Organic Carbon Cycle in the Arctic Ocean*, eds R. Stein and R. W. MacDonald (Berlin: Springer), 33–55. doi: 10.1007/978-3-642-18912-8_2

Rachold, V., Grigoriev, M. N., Are, F. E., Solomon, S., Reimnitz, E., Kassens, H., et al. (2000). Coastal erosion vs riverine sediment discharge in the Arctic Shelf seas. *Int. J. Earth Sci.* 89, 450–460. doi: 10.1007/s005310000113

Rowland, J. C., Schwenk, J., Shelef, E., Mishra, U., Muss, J., and Stauffer, S. (2018). "Pan-arctic flux of soil organic carbon to rivers by river bank erosion," in *Proceedings of the AGU Fall Meeting Abstracts*, Washington, DC.

Sánchez-García, L., Vonk, J. E., Charkin, A. N., Kosmach, D., Dudarev, O. V., Semiletov, I. P., et al. (2014). Characterisation of three regimes of collapsing Arctic ice complex deposits on the SE Laptev Sea Coast using biomarkers and dual carbon isotopes. *Permafr. Periglac. Process.* 25, 172–183. doi: 10.1002/ppp.1815

Schirrmeister, L., Froese, D., Tumskoy, V., Grosse, G., and Wetterich, S. (2013). "Yedoma: late Pleistocene ice-rich syngenetic permafrost of Beringia," in *The Encyclopedia of Quaternary Science*, ed. S. A. Elias (Amsterdam: Elsevier), 542–552. doi: 10.1016/b978-0-444-53643-3.00106-0

Schirrmeister, L., Grosse, G., Kunitsky, V., Magens, D., Meyer, H., Dereviagin, A., et al. (2008). Periglacial landscape evolution and environmental changes of Arctic lowland areas for the last 60 000 years (western LaptevSea coast, Cape Mamontov Klyk). *Polar Res.* 27, 249–272. doi: 10.1111/j.1751-8369.2008.00067.x

Schirrmeister, L., Schwamborn, G., Overduin, P. P., Strauss, J., Fuchs, M. C., Grigoriev, M., et al. (2017). Yedoma Ice Complex of the Buor Khaya Peninsula. *Biogeosciences* 14, 1261–1283. doi: 10.5194/bg-14-1261-2017

Schirrmeister, L., Siegert, C., Kuznetsova, T., Kuzmina, S., Andreev, A. A., Kienast, F., et al. (2002). Paleoenvironmental and paleoclimatic records from permafrost deposits in the Arctic region of Northern Siberia. *Quat. Int.* 89, 97–118. doi: 10.1016/s1040-6182(01)00083-0

Schuur, E. A. G., Abbott, B. W., Bowden, W. B., Brovkin, V., Camill, P., Canadell, J. P., et al. (2011). High risk of permafrost thaw. *Nature* 480, 32–33. doi: 10.1038/480032a

Schuur, E. A. G., Vogel, J. G., Crummer, K. G., Lee, H., Sickman, J. O., and Osterkamp, T. E. (2009). The effect of permafrost thaw on old carbon release and net carbon exchange from tundra. *Nature* 459, 556–559. doi: 10.1038/nature08031

Semiletov, I., Pipko, I., Gustafsson, Ö., Anderson, L. G., Sergienko, V., Pugach, S., et al. (2016). Acidification of East Siberian Arctic Shelf waters through addition of freshwater and terrestrial carbon. *Nat. Geosci.* 9, 361–365. doi: 10.1038/ngeo2695

Serreze, M. C., Walsh, J. E., Chapin, F. S. I. I. I., Osterkamp, T., Dyurgerov, M., Romanovsky, V., et al. (2000). Observational evidence of recent change in the Northern High-Latitude environment. *Clim. Change* 46, 159–207. doi: 10.1023/a:1005504031923

Shur, Y., Vasiliev, A., Kanevsky, M., Maximov, V., Pokrovsky, S., and Zaikanov, V. (2002). "Shore Erosion in Russian Arctic," in *Cold Regions Engineering – Cold Regions Impacts on Transportation and Infrastructure*, ed. K. Merrill (Reston, VA: American Society of Civil Engineers), 736–747.

Stettner, S., Beamish, L. A., Bartsch, A., Heim, B., Grosse, G., Roth, A., et al. (2018). Monitoring Inter- and intra-seasonal dynamics of rapidly degrading ice-rich permafrost riverbanks in the lena delta with TerraSAR-X time series. *Remote Sens.* 10:51. doi: 10.3390/rs10010051

Strauss, J., Schirrmeister, L., Grosse, G., Fortier, D., Hugelius, G., Knoblauch, C., et al. (2017). Deep yedoma permafrost: a synthesis of depositional characteristics and carbon vulnerability. *Earth Sci. Rev.* 172, 75–86. doi: 10.1016/j.earscirev.2017.07.007

Strauss, J., Schirrmeister, L., Grosse, G., Wetterich, S., Ulrich, M., Herzschuh, U., et al. (2013). The deep permafrost carbon pool of the Yedoma region in Siberia and Alaska. *Geophys. Res. Lett.* 40, 6165–6170. doi: 10.1002/2013GL058088

Strauss, J., Schirrmeister, L., Wetterich, S., Borchers, A., and Davydov, S. P. (2012). Grain-size properties and organic-carbon stock of Yedoma Ice Complex permafrost from the Kolyma lowland, northeastern Siberia. *Global Biogeochem. Cycles* 26:GB3003. doi: 10.1029/2011GB004104

Streletskaya, I. D., Vasiliev, A. A., and Vanstein, B. G. (2009). Erosion of sediment and organic carbon from the Kara Sea coast. *Arct. Antarct. Alp. Res.* 41, 79–87. doi: 10.1657/1523-0430-41.1.79

Stroeve, J., and Notz, D. (2018). Changing state of Arctic sea ice across all seasons. *Environ. Res. Lett.* 13:103001. doi: 10.1088/1748-9326/aade56

Strozzi, T., Antonova, S., Günther, F., Mätzler, E., Vieira, G., Wegmüller, U., et al. (2018). Sentinel-1 SAR interferometry for surface deformation monitoring in low-land Permafrost Areas. *Remote Sens.* 10:1360. doi: 10.3390/rs10091360

Tanski, G., Couture, N., Lantuit, H., Eulenburg, A., and Fritz, M. (2016). Eroding permafrost coasts release low amounts of dissolved organic carbon (DOC) from ground ice into the nearshore zone of the Arctic Ocean. *Global Biogeochem. Cycles* 30, 1054–1068. doi: 10.1002/2015GB005337

Tanski, G., Wagner, D., Knoblauch, C., Fritz, M., Sachs, T., and Lantuit, H. (2019). Rapid CO_2 release from eroding permafrost in seawater. *Geophys. Res. Lett.* 46, 11244–11252. doi: 10.1029/2019GL084303

Tesi, T., Muschitiello, F., Smittenberg, R. H., Jakobsson, M., Vonk, J. E., Hill, P., et al. (2016). Massive remobilization of permafrost carbon during post-glacial warming. *Nat. Commun.* 7:13653. doi: 10.1038/ncomms13653

Turetsky, M. R., Abbott, B. W., Jones, M. C., Anthony, K. W., Olefeldt, D., Schuur, E. A. G., et al. (2020). Carbon release through abrupt permafrost thaw. *Nat. Geosci.* 13, 138–143. doi: 10.1038/s41561-019-0526-0

van Everdingen, R. (2005). *Multi-Language Glossary of Permafrost and Related Ground-Ice Terms*. (Boulder, CO: National Snow and Ice Data Center), 159.

van Vliet, M. T. H., Franssen, W. H. P., Yearsley, J. R., Ludwig, F., Haddeland, I., Lettenmaier, D. P., et al. (2013). Global river discharge and water temperature under climate change. *Global Environ. Change* 23, 450–464. doi: 10.1016/j.gloenvcha.2012.11.002

Vonk, J., Sánchez-García, L., van Dongen, B. E., Alling, V., Kosmach, D., Charkin, A., et al. (2012). Activation of old carbon by erosion of coastal and subsea permafrost in Arctic Siberia. *Nature* 489, 137–140. doi: 10.1038/nature11392

Vonk, J. E., and Gustafsson, Ö. (2013). Permafrost-carbon complexities. *Nat. Geosci.* 6, 675–676. doi: 10.1038/ngeo1937

Vonk, J. E., Mann, P. J., Davydov, S., Davydova, A., Spencer, R. G. M., Schade, J., et al. (2013a). High biolability of ancient permafrost carbon upon thaw. *Geophys. Res. Lett.* 40, 2689–2693. doi: 10.1002/grl.50348

Vonk, J. E., Mann, P. J., Dowdy, K. L., Davydova, A., Davydov, S. P., Zimov, N., et al. (2013b). Dissolved organic carbon loss from Yedoma permafrost amplified by ice wedge thaw. *Environ. Res. Lett.* 8:035023. doi: 10.1088/1748-9326/8/3/035023

Walker, J., Arnborg, L., and Peippo, J. (1987). Riverbank Erosion in the Colville Delta, Alaska. *Geogr. Ann. Ser. A Phys. Geogr.* 69, 61–70. doi: 10.1080/04353676.1987.11880197

Wetterich, S., Kizyakov, A., Fritz, M., Aksenov, A., Schirrmeister, L., and Opel, T. (2019). "Permafrost research on Sobo-Sise Island (Lena Delta)," in *Russian-German Cooperation: Expeditions to Siberia in 2018*, Vol. 734, eds S. Kruse, D. Bolshiyanov, M. Grigoriev, A. Morgenstern, L. Pestryakova, L. Tsibizov, et al. (Bremerhaven: Alfred Wegener Institute for Polar and Marine Research), 102–113. doi: 10.2312/BzPM_0734_2019

Wetterich, S., Kizyakov, A., Fritz, M., Wolter, J., Mollenhauer, G., Meyer, H., et al. (2020). The cryostratigraphy of the Yedoma cliff of Sobo-Sise Island (Lena Delta) reveals permafrost dynamics in the Central Laptev Sea coastal region during the last about 52 ka. *Cryosphere Discuss.* doi: 10.5194/tc-2020-179

Wetterich, S., Kuzmina, S., Andreev, A. A., Kienast, F., Meyer, H., Schirrmeister, L., et al. (2008). Palaeoenvironmental dynamics inferred from late Quaternary permafrost deposits on Kurungnakh Island, Lena Delta, Northeast Siberia, Russia. *Quat. Sci. Rev.* 27, 1523–1540. doi: 10.1016/j.quascirev.2008.04.007

Wetterich, S., Meyer, H., Fritz, M., Opel, T., and Schirrmeister, L. (2020). Cryolithology of the Sobo-Sise Yedoma cliff (eastern Lena Delta). *PANGAEA*. doi: 10.1594/PANGAEA.919470

Wild, B., Andersson, A., Bröder, L., Vonk, J., Hugelius, G., McClelland, J. W., et al. (2019). Rivers across the Siberian Arctic unearth the patterns of carbon release from thawing permafrost. *Proc. Natl. Acad. Sci. U.S.A.* 116, 10280–10285. doi: 10.1073/pnas.1811797116

Winterfeld, M., Mollenhauer, G., Dummann, W., Köhler, P., Lembke-Jene, L., Meyer, V. D., et al. (2018). Deglacial mobilization of pre-aged terrestrial carbon from degrading permafrost. *Nat. Commun.* 9:3666. doi: 10.1038/s41467-018-06080-w

Conflict of Interest: The authors declare that the research was conducted in the absence of any commercial or financial relationships that could be construed as a potential conflict of interest.

frontiers in Earth Science

ORIGINAL RESEARCH
published: 27 August 2020
doi: 10.3389/feart.2020.00344

Mid-Winter Breakout of Landfast Sea Ice and Major Storm Leads to Significant Ice Push Event Along Chukchi Sea Coastline

Reyce Bogardus[1], Christopher Maio[1]*, Owen Mason[2], Richard Buzard[1], Andrew Mahoney[3] and Cary de Wit[4]*

[1] Arctic Coastal Geoscience Laboratory (ACGL), University of Alaska Fairbanks, Fairbanks, AK, United States, [2] Institute of Arctic and Alpine Research (INSTAAR), University of Colorado Boulder, Boulder, CO, United States, [3] Geophysical Institute, University of Alaska Fairbanks, Fairbanks, AK, United States, [4] Geography Program, University of Alaska Fairbanks, Fairbanks, AK, United States

During the winter of 2016, anomalous sea ice conditions and a powerful storm culminated in a destructive erosion event along the Chukchi Sea coastline of Cape Espenberg, Alaska. This event is commonly referred to as an "ice push" or "ivu," the Inupiat word for an ice ridging event. In this article, we report the process and impact of this event by combining traditional ecological knowledge, news accounts, meteorological data, remote sensing, and ground surveys. The midwinter detachment of shorefast ice was caused by a low-pressure system and wind-driven swell that destabilized shorefast ice, while northerly winds developed an open-water lead offshore to the eventual impact area. These conditions preceded the impact of an extratropical cyclone on December 31, 2016, when powerful southerly winds and the second largest storm surge in Kotzebue Sound since at least 2003 led to the compressional failure of the ice cover under uniaxial loading perpendicular to the southern coastline of the Cape, resulting in the ice push event. Ice-pushed debris was shoved up to 6.2 m above mean high water, with ∼3.5 km of coastline experiencing net erosion. The largest accumulation of ice-pushed debris had a volume of 1,000 m^3, and rose 3 + m above the surrounding ground surface even after roughly 6 months of melting. On low-lying areas, driftwood and other debris were deposited 130 m landward by the surge 5.0 m above mean high water, indicating the potential threat of such events to property, infrastructure, and, in this case, archeological sites and associated cultural resources. The anomalous environmental and sea ice conditions that preceded the ivu seem to suggest that such events may occur more frequently in a warmer Arctic.

Keywords: Cape Espenberg, sea ice, Kotzebue Sound, Arctic, storm surge, erosion, climate change, ivu

OPEN ACCESS

Edited by:
Annett Bartsch, b.geos, Austria

Reviewed by:
Aleksey Maslakov, Lomonosov Moscow State University, Russia
George Tanski, Vrije Universiteit Amsterdam, Netherlands

****Correspondence:***
Reyce Bogardus
rcbogardus@alaska.edu
Christopher Maio
cvmaio@alaska.edu

Specialty section:
This article was submitted to Cryospheric Sciences, a section of the journal Frontiers in Earth Science

Received: *17 December 2019*
Accepted: *24 July 2020*
Published: *27 August 2020*

Citation:
Bogardus R, Maio C, Mason O, Buzard R, Mahoney A and de Wit C (2020) Mid-Winter Breakout of Landfast Sea Ice and Major Storm Leads to Significant Ice Push Event Along Chukchi Sea Coastline. Front. Earth Sci. 8:344. doi: 10.3389/feart.2020.00344

INTRODUCTION

Contemporary warming in the Chukchi and Beaufort Seas is contributing toward coastal change in Alaska, especially related to the decline in pack and landfast ice (Mahoney, 2018; Vermaire et al., 2013). Synthetic aperture radar (SAR) indicates that landfast ice is forming later and disappearing earlier by approximately 1 week per decade along the Chukchi and Beaufort Sea coasts (Mahoney et al., 2014). The implications of which are important to consider,

given that the increase in open water days leads to a greater likelihood of destructive coastal hazards, including ice push events (Mahoney et al., 2004).

These movements of sea ice onshore are termed "ice push," "ice shove," or "ice ride-up" events (Kovacs, 1984; Shapiro et al., 1984; Kovacs and Sodhi, 1988; Mahoney et al., 2004) and are referred to in this article generally as either "ivu" or "ice push" (Mason et al., 1997b). Documented impacts of these events include destruction of property and cultural resources (Kinsman and DeRaps, 2012) and impeding safe travel (Sodhi et al., 1983). There is also archeological evidence suggesting an ivu may have caused loss of life (Zimmerman and Aufderheide, 1984). An extensive survey of ice push events by Kovacs and Sodhi (1980) indicates they span a scale between what are called ice ride-ups and ice pile-ups. Ice *ride-up* events are characterized by largely intact sheets of ice advancing up the shoreface, sometimes hundreds of meters inland (Brower, 1960). However, ice *pile-up* events involve the build-up of fragmented blocks of sea ice incorporated with nearshore sediments and debris into elevated piles. Compared to ride-up events, they have a limited landward extent and are typically greater in elevation (Sodhi et al., 1983). Both processes often occur in combination, depending on the friction of the littoral zone, beach slope, and topography, as well as the integrity, or thickness, of the ice (Sodhi et al., 1983; Barker and Timco, 2016). Ice ride-up and pile-up events can occur throughout the year but are more common in the fall (October–November) or spring (May–June) when there are less stable ice conditions (Leffingwell, 1919; Kovacs and Sodhi, 1980). On local scales, the seasonal evolution of landfast ice formation, stabilization, and break-up is heavily influenced by both geographic setting and pronounced interannual variability (Mahoney et al., 2014).

The destabilization of shorefast ice is a complex interaction of many dynamic processes, including wind forces, currents, local sea-level change, and pack ice interaction (e.g., Gilbert and Glew, 1986; Gilbert, 1991; George et al., 2004; Mahoney et al., 2007; Jones et al., 2016). Once the landfast ice is destabilized along a given stretch of coastline, a number of physical processes must take place in order for an ice push to occur. Most importantly, landward momentum must be transferred to the ice at the shoreline such that resistive forces in the nearshore (e.g., gravity, friction) are overcome (Sodhi et al., 1983; Mahoney et al., 2004). This can be caused by stresses due to wind and/or current or a drifting ice floe with substantial kinetic energy (Christensen, 1994; Barker and Timco, 2017). The morphology of the coast may also concentrate momentum transfer at particular stretches of shoreline (Kovacs and Sodhi, 1980).

Because of the episodic occurrence of ivu and the remoteness of Arctic coastlines, they are selectively surveyed when they occur near natural resource and/or residential infrastructure in the region (Leffingwell, 1919; Barker and Timco, 2017). Accordingly, this article documents a significant ivu event (**Figure 1**) that occurred on a remote stretch of shoreline along the Chukchi Sea at Cape Espenberg, which advances the understanding of the occurrence and implications of these coastal hazards. Specific research objectives were as follows: (1) to map the spatial extent of the affected coastline and document its geomorphic impacts, (2) to determine the environmental conditions and chronology of events that led to the ivu, and (3) to contribute toward a better understanding of ice push events in regard to recent warming trends in the Arctic.

FIGURE 1 | Remnants of the ivu along the eastern portion of coastline as observed on July 22, 2017, 7 months after its occurrence. The ivu eroded nearshore and bluff sediments placing them in large piles along the coastline. A member of the science party is shown for scale.

STUDY SITE

The Cape Espenberg dune and beach ridge plain is a mainland-attached spit in a microtidal setting dominated by longshore currents that transport sediments along the Cape toward the northern tip of the Seward Peninsula (**Figure 2**). The site is part of the Bering Land Bridge National Preserve, managed by the National Park Service, and has a history of multidisciplinary research (National Park Service [NPS], 2020). Multiple stratigraphic and sedimentological investigations have been carried out at the site spanning over 25 years (Mason and Jordan, 1993; Mason et al., 1997a; Alix et al., 2017; Maio et al., 2017, 2018). The Cape has a mean annual temperature of about −5°C (23°F) (Stewart et al., 2013), favoring the development of permafrost 20–90 cm below the ground surface (Mason et al., 1997a; Hoffecker and Mason, 2010; Jones et al., 2012). There is persistent sea ice cover offshore between roughly November and May, which has been stable until recent decades (Mahoney et al., 2014). Annually, the shallow Espenberg Lagoon is among the first stretches of water to freeze within Kotzebue Sound (Mason et al., 1997a). The routes of cyclones that impact the area typically follow two tracks: (1) north/north–northeastward following the coast of Siberia; (2) northeastward, across the Aleutian Islands, into the Bering Sea and continuing northward through the central Bering Sea (Mesquita et al., 2010). These storms can produce winds up to 35 m s^{-1} (78 mph) with hurricane force gusts up to 45 m s^{-1} (100 mph), wind waves exceeding 10 m, and local surge plus wave water levels upward of 7 m (Sallenger, 1983; Kowalik, 1984; Johnson and Kowalik, 1986; Mason et al., 1996; Blier et al., 1997).

Generally speaking, the Cape Espenberg barrier is composed of fine to medium sand with the fines being easily mobilized from the beach landward by northwesterly winds during the fall storm season (Mason and Jordan, 1993; Mason et al., 1997a). The study site area is divided into three sections including eastern,

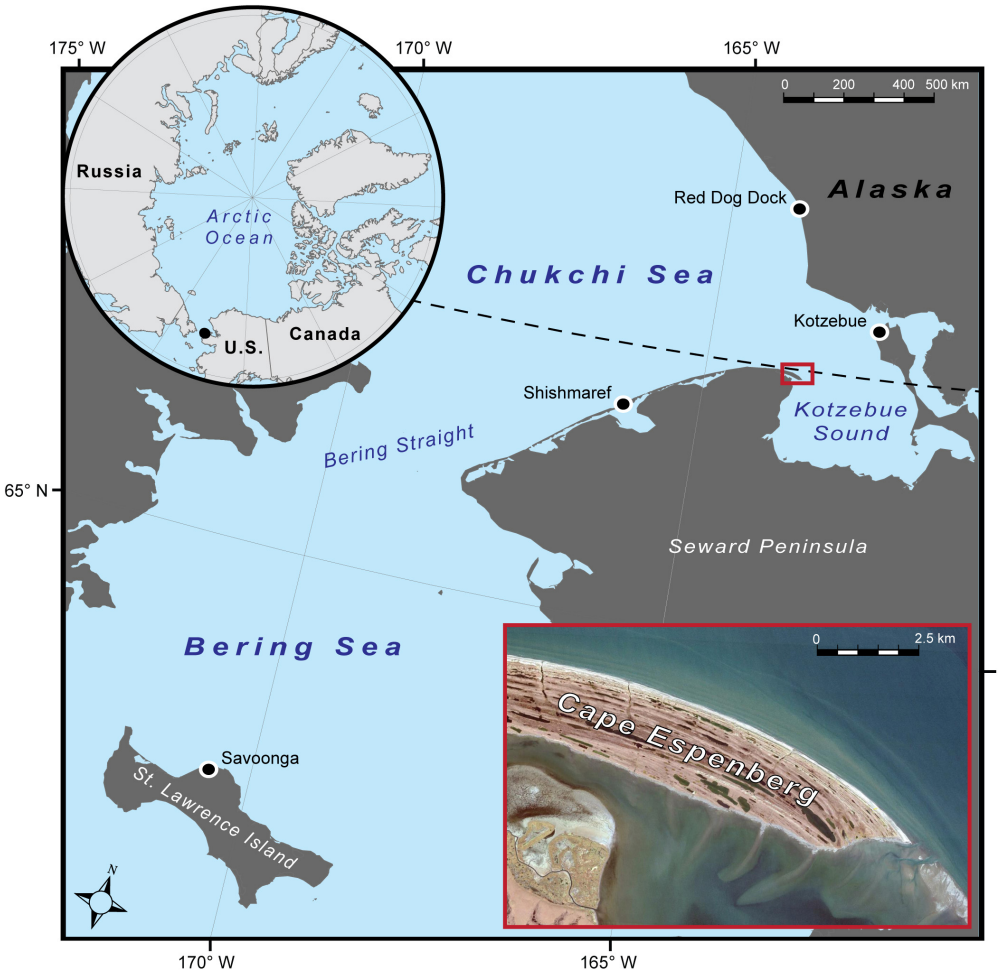

FIGURE 2 | Map showing the Cape Espenberg barrier spit. The Cape is located along the Arctic Circle (dashed line) on the northern tip of the Seward Peninsula, Alaska (red box), within Kotzebue Sound.

central, and western areas (**Figure 3**). The three sections were categorized based on clear differences in their morphology and the nature of geomorphic impacts imposed by the ice push event (**Figure 3**). The eastern section is marked by bluffs 3–5 m in height, alternating between cross-shore dune ridges and lower elevation swales that primarily consist of unconsolidated wind-blown sand, fronted by a very shallow offshore tidal flat (<1 m water depth for at least 2 km seaward) (Mason et al., 1997a). The central area is also fronted by shallow water (<1 m) and lacks the higher elevation beach ridges of the eastern and western sections. This lower elevation trough has only a few low relief dune ridges, with most of the area covered by a marsh and series of small ponds (Mason et al., 1997a). The sediment stratigraphy in the central area generally includes marine sand capped by 10–70 cm of marsh peat (Alix et al., 2017). Along the western section, there are greater offshore water depths (≤3 m) and a considerably steeper bluff face, which runs alongshore the Cape's dune ridges in places truncating these high relief features. There are much older and more developed soil horizons in the western section, with the upper 50–90 cm being primarily composed of organic rich peat with an underlying matrix of wind-blown sand and silt (Mason et al., 1997a; Alix et al., 2017). The active layer at this location loosely corresponds to this organic (peat) to inorganic (sand and silt) stratigraphic horizon (Mason et al., 1997a).

MATERIALS AND METHODS

To identify the specific timing of the ivu event and place it in the context of locally observed coastal processes, we utilized a combination of ground surveys; traditional ecological knowledge; news reports; and meteorological, water level, and SAR data. Field work and mapping were conducted in July 2017. This involved photographing and surveying the linear and vertical extent of the ivu deposits. The research team also interviewed a local environmental knowledge holder from the Alaska Native community of Shishmaref, to provide a longer-term context for sea ice–related disturbances in the area. Following the field work, we obtained remotely sensed sea ice data, local news accounts, and meteorological data and held discussions with National

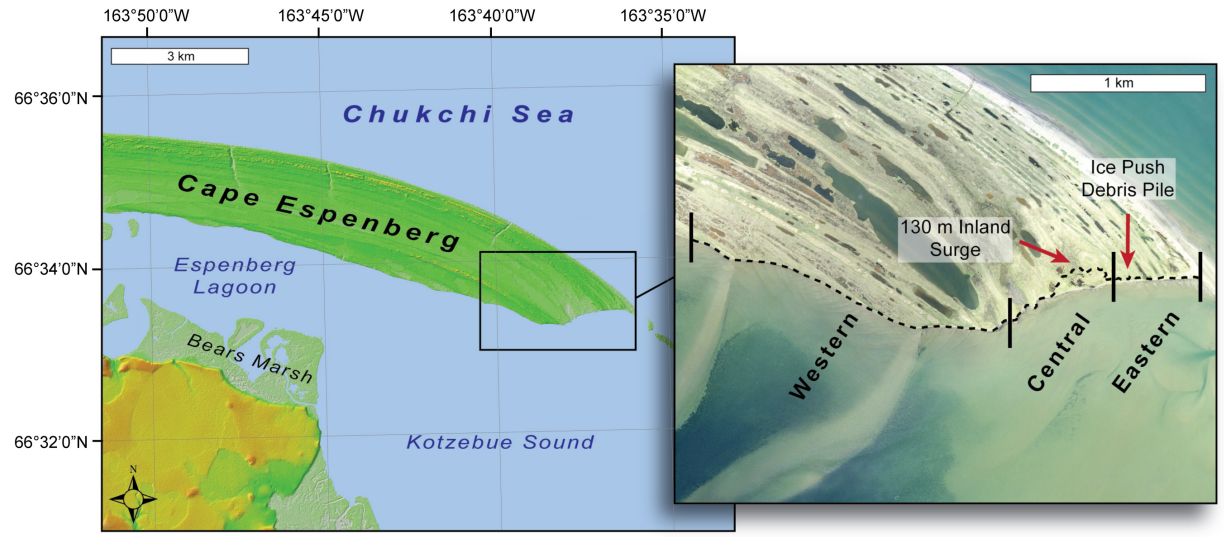

FIGURE 3 | Map showing the area impacted by the 2017 Cape Espenberg ivu. The map on the left uses elevation data from the ArcticDEM, created by the Polar Geospatial Center from DigitalGlobe, Inc., imagery (Porter et al., 2018). The insert map on the right shows the surveyed, spatial extent of the impacted coastline (dashed line) and denotes the Eastern, Central, and Western sections discussed in the text with vertical black lines. The 1,000 m^3 ice-push debris pile that impacted cultural resources and the maximum inland extent of the storm surge is marked with the red arrows.

Weather Service (NWS) meteorologists to elucidate when and how this event occurred.

Ground Survey and Tidal Datum

The inland extent of the storm surge and volume of the main ice push feature was quantified using a Real-Time Kinematic Global Navigation Satellite System (RTK-GNSS) (**Figure 3**). To determine the maximum inland extent and area of the ice push, continuous rover data (1-s intervals) were collected along the well-defined wrack line and/or sediment deposits overlaying terrestrial vegetation. A gridded survey was carried out to calculate the volume of the largest ice-shoved debris pile, located within the eastern section. Empirical Bayesian kriging was used to interpolate the 4,234 postprocessed elevation points over the 3,429 m^2 area, equating to an average sampling density of 1.2 points per m^2. The interpolated elevation surface was then compared to a 20 cm^2 resolution 2016 Digital Surface Model provided by Fairbanks FODAR (Fairbanks FODAR, 2020). To relate survey elevations to local mean high water (MHW), a tidal datum was produced by JOA Surveys, LLC (Joa Surveys LLC, 2020) based on 3 weeks of HOBO water-level data collected during the 2017 field work season. The National Oceanic and Atmospheric Administration (NOAA) tide station at the Red Dog Dock (9491094) was used as the control (National Oceanic and Atmospheric Administration [NOAA], 2020). In addition to the elevation data, more than 300 photographs were taken to document the physical remnants and impacts of the ivu, and a thaw depth probe was used along the stretch of impacted coastline to verify active layer thickness. Sediment type and relative grain size were noted as was the presence of marine debris such as shells, driftwood, and eelgrass. Additional photographs were taken to capture morphological changes that had occurred since the event, including drainage patterns and thermokarst features.

Shoreline Change Analysis

To quantify shoreline change caused by the ivu, the vegetation line (vegline) was selected as the shoreline indicator as it is easily discernable on the ground and in aerial imagery, and there is no inherent error due to tidal fluctuations and/or swash action as is the case with other indicators such as the high water line (Pajak and Leatherman, 2002; Boak and Turner, 2005; Buzard et al., submitted). Along the south-facing tip of Cape Espenberg, the vegline closely corresponds to the bluff edge, and a loss of vegetation often correlates to erosion, especially when it is related to individual storm events (e.g., Boak and Turner, 2005; Maio et al., 2012). A drawback in using the vegline for remote-sensing analyses is that there is a lag time between beach accretion and the seaward expansion of insipient vegetation (e.g., Boak and Turner, 2005; Keijsers et al., 2015; Buzard et al., submitted), although this phenomenon is accounted for in our case, given that the 2017 vegline was derived from the ground surveys and is supplemented with field observations and photographs.

To create a 2017 vegline, the feature was surveyed with the RTK-GNSS during the summer 2017 field work (e.g., Zarillo et al., 2008). The 2016 vegline was manually delineated within a geographic information system over a 10 cm^2 orthorectified aerial mosaic collected in August 2016 (Fairbanks FODAR, 2020). Net shoreline movement (NSM) (total distance of shoreline movement) was calculated using the USGS Digital Shoreline Analysis System (DSAS) by casting cross-shore virtual transects at 5 m intervals between the 2016 and 2017 veglines (Himmelstoss et al., 2018). Error estimates in NSM values

were calculated using the "square root of the sum of squares" method considering the digitizing uncertainty with regard to the 2016 orthomosaic (10 cm), as well as horizontal movements of the GNSS receiver antenna during the 2017 survey (up to 25 cm) (Ruggiero et al., 2013; Weaver et al., 2015). The same uncertainty range (± 0.27) is used for each transect, given that our analysis used veglines from only two dates and that the sources of uncertainty listed above were not spatially variable. DSAS analysis was only carried for the central and eastern sections, as the western stretch was not included in the extent of the 2016 aerial imagery. Observations along the western stretch are based off field surveys and photography, as described below. Because of the lack of any significant (>1 m) surge events between when the Cape Espenberg coast became ice-free and when the RTK survey was carried out (National Oceanic and Atmospheric Administration [NOAA], 2016), it is assumed that the calculated shoreline change is primarily attributable to the 2016 ice push event.

SAR Analysis

Satellite-derived copolarized vertical transmission and reception (VV) and horizontal transmission and reception (HH) SAR data (**Table 1**) from the Alaska Satellite Facility's data portal[1] (Alaska Satellite Facility [ASF], 2019) was used to analyze sea ice conditions in Kotzebue Sound from the time of first ice formation until after the ice push event at Cape Espenberg (**Figure 4**). We distinguished ice from open water based on backscatter signatures in the C-band (5.6 cm wavelength), using the principles described and illustrated by Jackson and Apel (2004). Because ice and ocean surfaces can exhibit similar backscatter magnitudes depending on wind conditions and ice type, we based our analysis on the geometry and textures of features in the imagery and their relationship to the coastline, rather than the values of individual pixels. Landfast ice was distinguished by its adjacency to the shoreline and lack of discernible motion between consecutive SAR scenes, which ranged between 2 and 15 days (e.g., Mahoney et al., 2014). Ridges and rubble piles were recognized as curvilinear features with high backscatter in both HH and VV caused by multiple surfaces oriented toward the SAR sensor (Onstott and Carsey, 1992; Jackson and Apel, 2004). Cracks in the ice were identified as high backscatter features when the exposed ice faces on the far side of the cracks were oriented perpendicular to the sensor relative to the orbit or view direction of the SAR satellite (Jackson and Apel, 2004; Dammann et al., 2018).

Water-Level Data

Water-level data for NOAA tide station 9491094 at the Red Dog Dock, 115 km to the north of Cape Espenberg (**Figure 2**), were compiled from NOAA's Tides and Currents web viewer[2]. The Red Dog Dock station is the closest to Cape Espenberg and has been the only continuously operating, vertically referenced water-level sensor in Kotzebue Sound since it was installed in August 2003 (National Oceanic and Atmospheric Administration [NOAA], 2020). The station also provided further control for the tidal datum computed from the 3 week HOBO water level survey collected for this study. Water-level elevations at 6 min intervals were plotted relative to MHW between 1 October 2016 and 31 January 2017 in order to show the extent of surge during the 31 December storm relative to the rest of the 2016 storm season (**Figure 5**). To provide context to this event, the 31 December water-level extent was also compared with the entire operating history of the station over the last 17 years.

Given the distance between Cape Espenberg and the Red Dog Dock, it is difficult to verify the timing and magnitude of the storm surge at Cape Espenberg. However, it has been well documented that debris line elevations provide an accurate estimate for *total* water levels, which include all individual components that contribute to water level: wave setup, wave run-up, barometric bulge, and astronomical tide (Sallenger, 1983; Blier et al., 1997). At Cape Espenberg, the surveyed debris line served as a proxy for the *total* water levels from the storm event (Blier et al., 1997).

TABLE 1 | Selected synthetic aperture radar datasets used to identify changes to sea ice conditions around the time of the ivu.

Image date	Platform	Mode	Wavelength	Polarization	GSD (m)
2016.11.04	Sentinel-1B	IW	C-band	VV	10
2016.11.08	Sentinel-1B	IW	C-band	VV	10
2016.11.28	Sentinel-1B	IW	C-band	VV	10
2016.12.24	Sentinel-1B	IW	C-band	VV	10
2016.12.27	Sentinel-1B	EW	C-band	HH	40
2016.12.29	Sentinel-1B	EW	C-band	HH	40
2016.12.31	Sentinel-1B	IW	C-band	VV	10
2017.01.15	Sentinel-1B	IW	C-band	VV	10
2017.03.13	Sentinel-1B	IW	C-band	VV	10

GSD, Ground sample distance; IW, interferometric wide swath; EW, extra wide swath; C-band, 5.6 cm; VV, vertical transmission vertical reception; HH, horizontal transmission horizontal reception.

Meteorological Data

To contextualize the oceanographic and meteorological conditions that forced the onshore movement of sea ice at Cape Espenberg, mean sea-level pressure (MSLP) and wind direction and speed (**Figures 6**, **7**) were obtained from the ERA-5 atmospheric reanalysis provided by the European Centre for Medium-Range Weather Forecasts[3] (Copernicus Climate Change Service (C3S), 2017). MSLP plots were derived by contouring sea-level atmospheric pressure at 2 hPa intervals over an area bounded between 68.7077° to 63.3131° N and −177.5301° to −161.5125°W. To represent atmospheric structure and dynamics between 18 December 2016 and 1 January 2017, a single time each day (23:00 Zulu time) was selected for visualization. Wind rose diagrams were derived by making daily histograms from the combined hourly zonal and meridional wind vector components at 10 m altitude of one ERA-5 cell at the Cape (66.5500°N, −163.6400°W) over

[1]https://search.asf.alaska.edu/#/

[2]https://tidesandcurrents.noaa.gov/stationhome.html?id=9491094

[3]https://cds.climate.copernicus.eu/cdsapp#!/dataset/reanalysis-era5-single-levels?tab=form

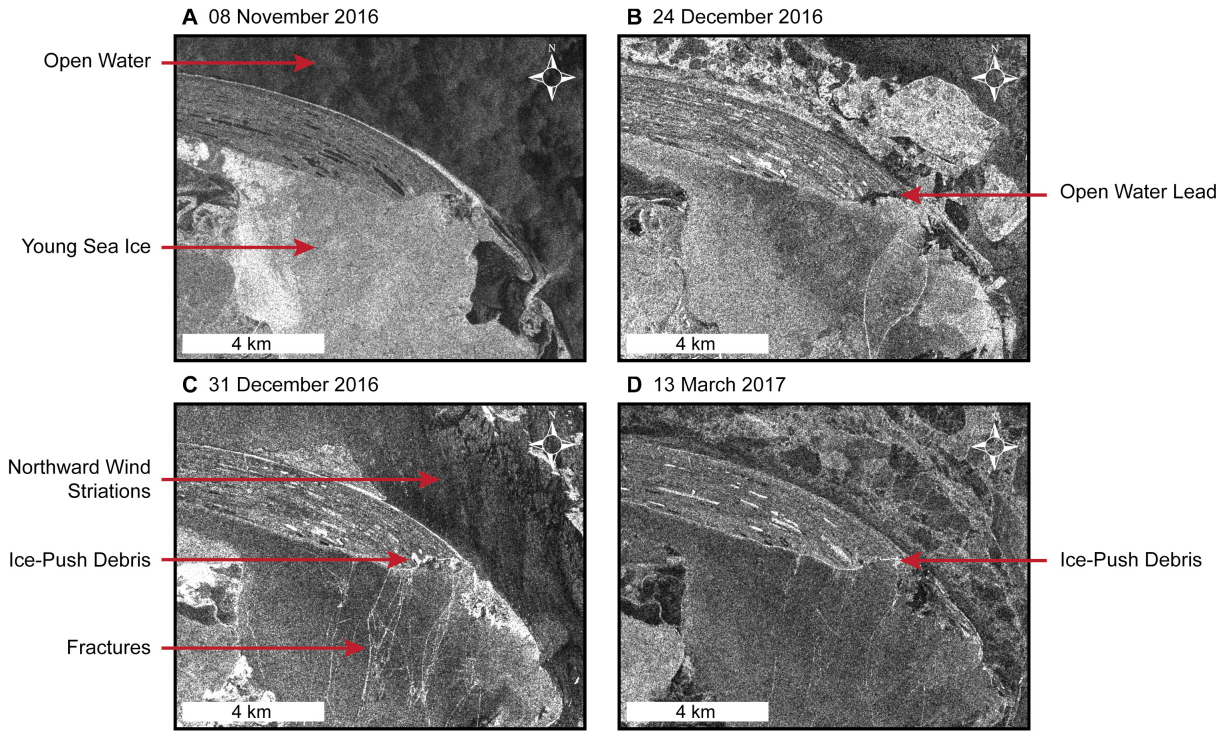

FIGURE 4 | Wide swath VV-polarized C-band synthetic aperture radar (SAR) data of the Cape Espenberg area. Backscatter intensity (unitless) is stretched over a continuous 16-bit black (low) to white (high) color gradient. A standard deviation (n = 2) and gamma stretch (0.832) has also been applied to highlight relative differences in backscatter intensity. **(A)** On November 8, open water is observed along the outer coastline, while within the Espenberg Lagoon the first sea ice of the season begins to form. **(B)** On 24 December, an open-water lead is visible along the affected coastline on the southern tip of Cape Espenberg, as well as bright linear features in the sea ice within the lagoon. **(C)** On 31 December, wind striations indicate a northward wind direction, whereas ice push debris is clearly visible (white areas) in the area landward of the open-water lead shown in **(B)**. Large ice fractures are also visible indicating the direction of ice movement. **(D)** On March 13, ice push debris is still visible approximately 6 weeks after deposition.

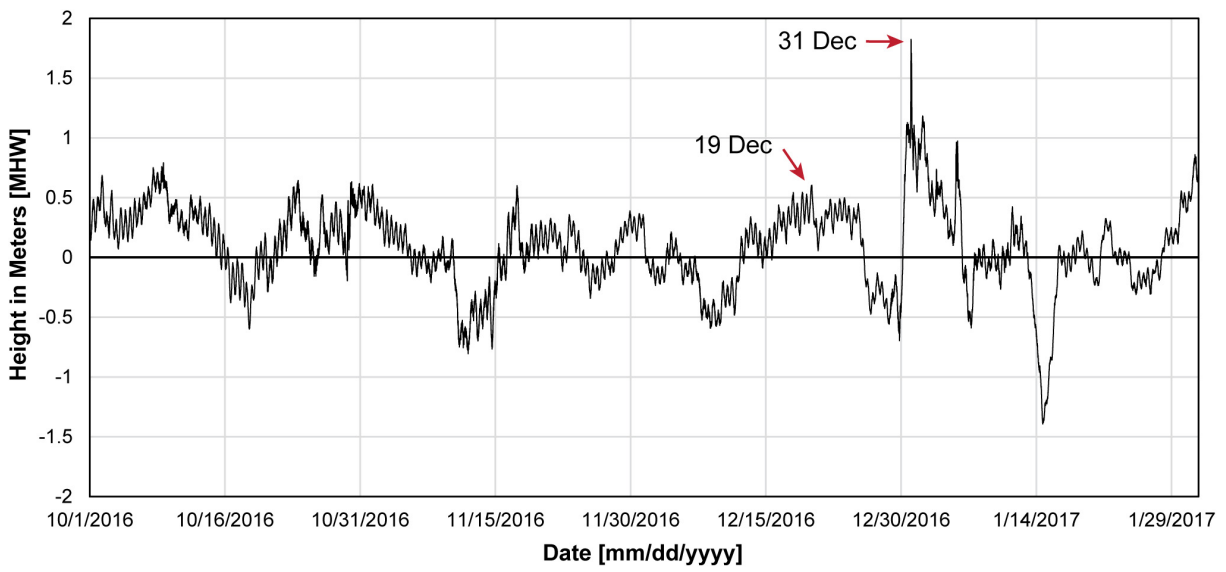

FIGURE 5 | Water-level data for NOAA tide station 9491094 at the Red Dog Dock, located 115 km to the north of Cape Espenberg, between 1 October 2016 and 31 January 2017. Water levels are shown in meters relative to mean high water (MHW), the average of all the high water heights at the station observed over the current national tidal datum epoch (NTDE) (1983–2001). The 31st December surge is the second largest recorded since the station began operation in August 2003 (National Oceanic and Atmospheric Administration [NOAA], 2020).

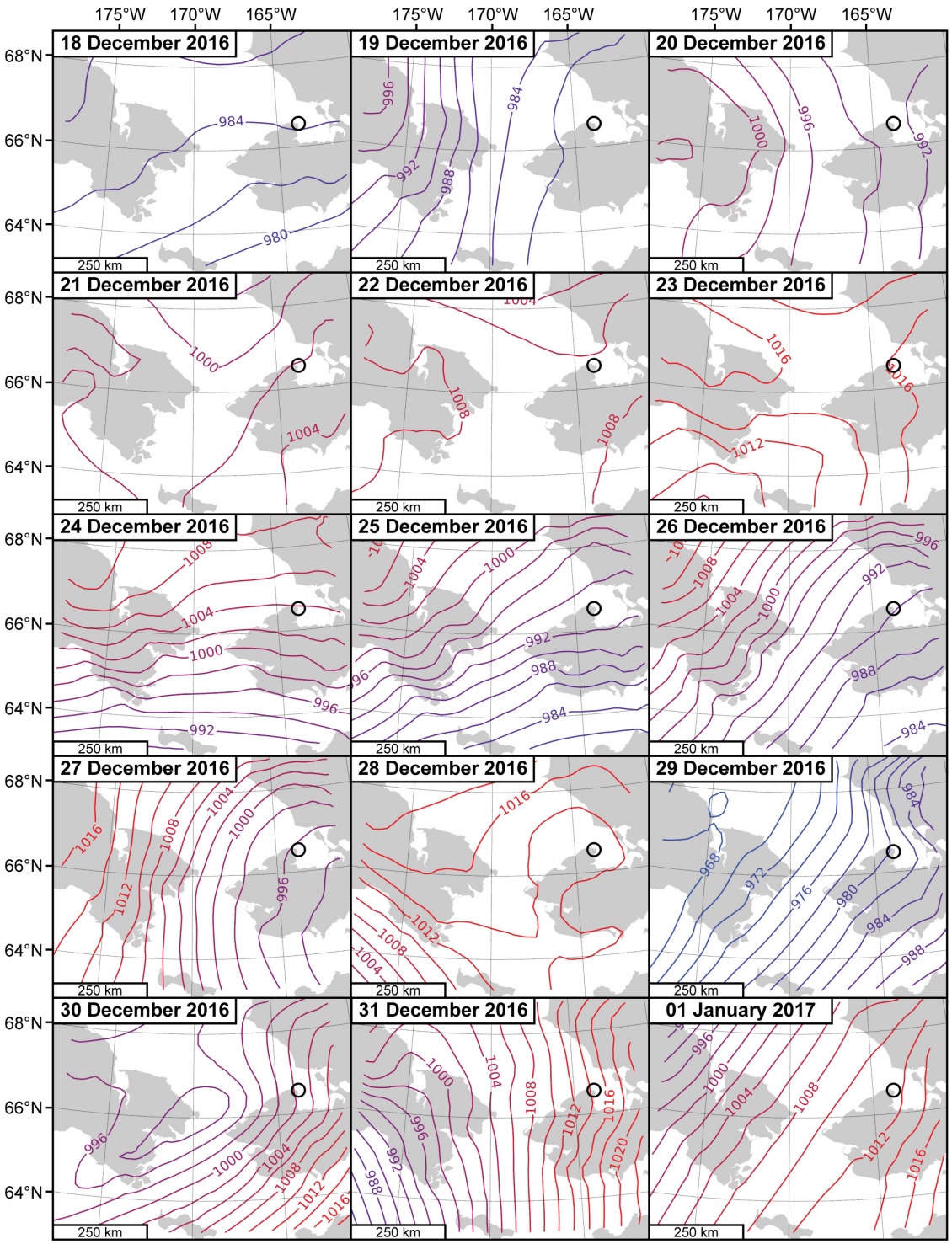

FIGURE 6 | Mean sea-level pressure (MSLP) contour maps derived from the ERA-5 atmospheric reanalysis provided by the European Centre for Medium-Range Weather Forecasts (ECMWF). MSLP is shown in hectopascals (hPa) at 2 hPa intervals between 18 December 2016 and 1 January 2017 (23:00 Zulu time each day). Lower pressure values are shown in cooler (blue) colors, whereas higher pressures are shown in hotter (red) colors. The location of Cape Espenberg is identified with the black circle. Notice the low pressures observed on both 19 December and 29 December that were major factors in the destabilization of shorefast ice and passage of the severe winter storm on 31 December.

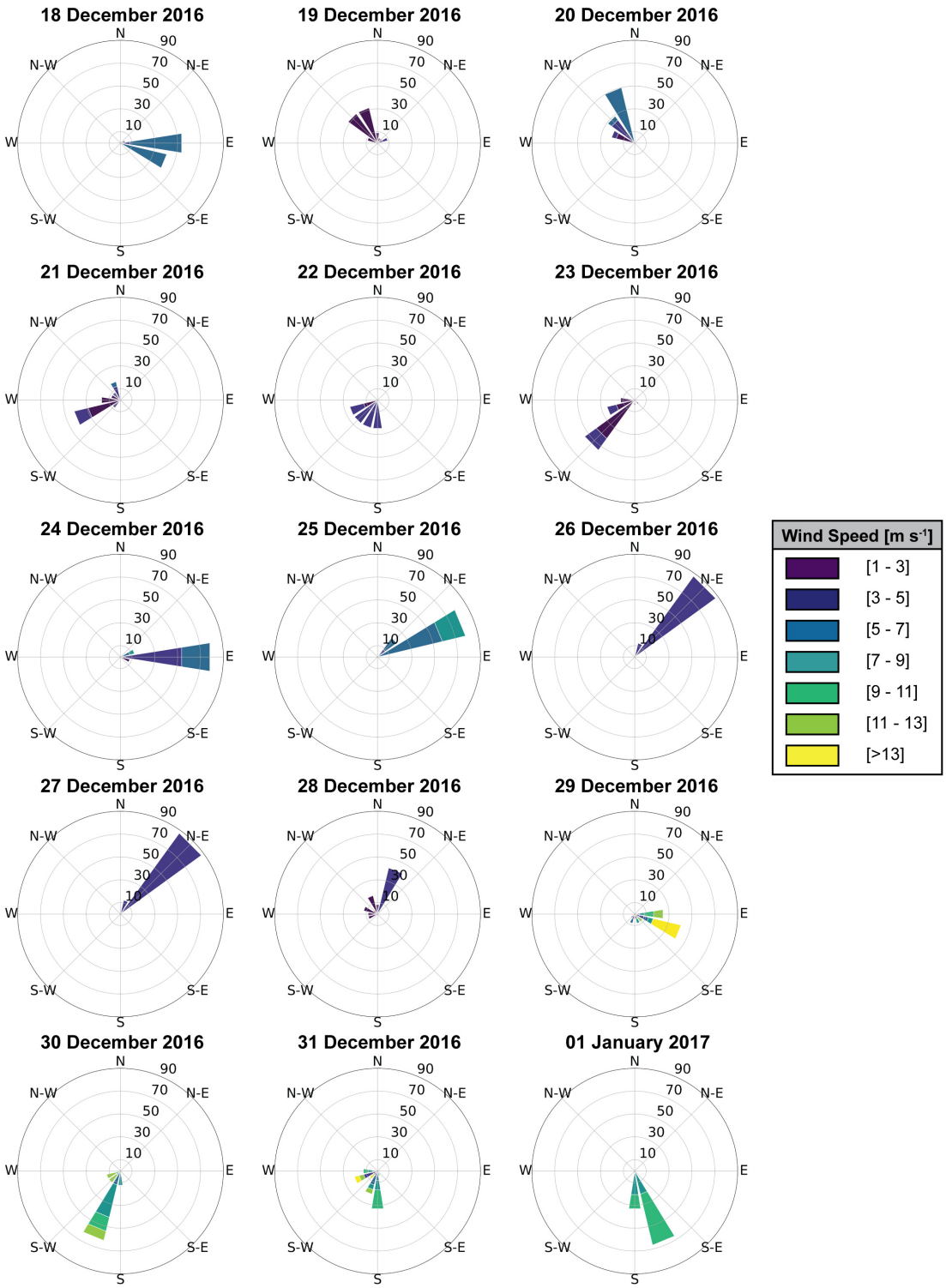

FIGURE 7 | Wind rose diagrams derived from the ERA-5 atmospheric reanalysis provided by the European Centre for Medium-Range Weather Forecasts (ECMWF) between 18 December 2016, and 1 January 2017. Wind at 10 m altitude from one ERA-5 cell at the Cape (66.5500°N, –163.6400°W) is shown. The circular format of the wind rose shows the direction the winds blew from and the length of each "spoke" around the circle shows how often the wind blew from that direction (here we use a fixed scale up to 90%). The different colors of each spoke provide details on the speed, in m s^{-1}, of the wind toward each direction. Notice the northwesterly winds on 19 and 20 December, which accompanied the low-pressure system and developed the open-water lead south of the Cape. Easterly and/or northeasterly winds between 24 and 29 December kept the ice pack within Kotzebue Sound pushed up against the western shore, south of the Cape. Southerly winds between 30 December and 1 January, combined with significant surge, resulted in the ice push event at Cape Espenberg.

the same timeframe. Daily temperature observations recorded by the NWS meteorological station at Ralph Wien Memorial Airport (PAOT) in Kotzebue, AK (66.9°N, 162.59°W), between 1 December 2016 and 31 January 2017 were compiled using Weather Underground's web viewer[4].

Traditional Ecological Knowledge

Traditional ecological knowledge was provided by Mr. Fred Goodhope, an Inupiat elder from Shishmaref, a community 70 km south of the impacted area (**Figure 2**). Mr. Goodhope, whose family has herded reindeer and gathered subsistence resources in the area for a generation, is an ongoing collaborator with scientists working at the Cape Espenberg archeological site. He has visited the Cape regularly over the last 50 years, as it is considered a sacred burial ground for his ancestors. For this study, we visited the disturbed coastline with Mr. Goodhope and held an unstructured oral discussion to determine any precedence on the timing and magnitude of the event.

TABLE 2 | Chronology of events and supporting datasets.

Date	Event	GNSS survey	SAR data	Met. data	Tidal data
08 Nov	Continuous sea ice forms in Espenberg Lagoon		✓		
18–20 Dec	Low pressure, surge, and wind cause open-water lead at Cape Espenberg		✓	✓	✓
24–29 Dec	Easterly winds compile drift ice along western Kotzebue Sound		✓	✓	
30 Dec	Strong southerly winds are observed at Cape Espenberg			✓	
31 Dec	Strong southerly winds and surge, cause ice push up to 130 m inland. N-S cracks in ice	✓	✓	✓	✓
01 Jan	Strong southerly winds and surge			✓	✓
24 Jul	Field survey finds 3.5 km of coastline affected, debris rafted (>5 m above MHW	✓			

These include global navigation satellite system (GNSS), synthetic aperture radar (SAR), meteorological (Met.), and tidal datasets.

RESULTS

Chronology of the Ice Push Event

Continuous sea ice first appeared along the shallow shores of Kotzebue Sound by 8 November (**Table 2** and **Figure 4A**). Over the next several weeks, the ice south of Cape Espenberg became landfast, whereas highly mobile pack ice developed in the central Sound by 28 November. The newly formed landfast ice was grounded based on its continuous position as observed over multiple SAR scenes. The shallow waters (<3 m water depth) immediately south of Cape Espenberg were among the first of the offshore areas to freeze up (**Figure 4A**).

A low-pressure system (980 hPa) moved into the eastern Chukchi coastline between 18 and 20 December (**Figure 6**). SAR imagery before and after these dates show that the low-pressure system, coupled with the northerly wind regime (**Figure 7**), floated (**Figure 5**) and transported nearshore ice away from the southern coastline at Cape Espenberg, forming an open-water lead along its southern tip (**Figure 4B**). This mote-like feature is still apparent in the SAR scenes up to 29 December, just prior to the ice push event (**Figure 4B**). In the same SAR scene, there is also open water with highly mobile sea ice within Kotzebue Sound. Predominant easterly winds between 24 and 29 December kept the fragmented ice floe within the Sound packed against the landfast ice that had formed along the western mainland shoreline (**Figure 7**).

During the 31 December storm event, NWS and public accounts from local media reported major storm surges and hurricane force wind gusts throughout northwestern Alaska (i.e., Alaska Dispatch News, 2017; Arctic Sounder, 2019). At Kotzebue, the NWS meteorological station (PAOT) recorded high winds of up to 20 m s^{-1} (45 mph), with maximum wind gusts of up to 27 m s^{-1} (60 mph) (National Oceanic and Atmospheric Administration [NOAA], 2016). The worst damage was reported in Savoonga (**Figure 2**), an Alaska Native Village on St. Lawrence Island, where several roofs were ripped off, windows were blown out, and rain flooded into homes through openings around foundations attributed to recent permafrost collapse (Alaska Dispatch News, 2017). A Savoonga resident noted the absence of sea ice in the northern Bering Sea around St. Lawrence Island and reported that the storm had the biggest impacts on the local coastline and infrastructure that he could remember in the past 57 years (Alaska Dispatch News, 2017).

As the storm continued moving northeast and approached Kotzebue Sound on 31 December 2016, weather station PAOT recorded temperatures exceeding 2°C (36°F), which tied previous records from 1982, 2013, 2015, and 2017 for the warmest temperature recorded in December for Kotzebue (National Oceanic and Atmospheric Administration [NOAA], 2016). The SAR image from that day shows a region of open water on the ocean-side northern coastline of the Cape with strong southerly winds apparent (**Figure 4C**) and several new cracks in the continuous sea ice south of the Cape (**Figure 4C**) that did not appear in the earlier scenes (i.e., Onstott and Carsey, 1992; Jackson and Apel, 2004). The cracks were caused by compressional failure of the ice cover under uniaxial force perpendicular to the southern coastline of the Cape and are aligned approximately north–south up to 6 km long and 1 km apart (**Figure 4C**). The onshore winds (**Figure 7**) and storm surge (**Figure 5**) on 31 December 2016 pushed the unfastened ice sheet north along these slip planes into the tip of Cape Espenberg where the open-water lead present in the 24 December SAR scene occurred. This open-water lead provided accommodation space, which lessened resistive forces and predisposed stress release along this stretch of coastline (e.g., Gilbert and Glew, 1986; Mahoney et al., 2004). A bright radar signature confirmed the presence of ice on top of the beach ridges at the tip of Cape Espenberg directly landward of the previously open stretch of

[4]https://www.wunderground.com/weather/us/ak/kotzebue/PAOT

water. This new relief feature matched the surveyed extent of the impacted coastline and is clearly visible on the landscape in SAR scenes through the winter and spring (**Figure 4D**).

Geomorphic Impacts

The geomorphic impacts of the ivu were first reported after an archeological crew that had been working on the spit in summer 2016 returned in late spring of 2017. They observed extensive erosional scarps with substantial piles of sand, ice, and other marine debris perched atop their field sites. Earlier in the spring, a local air taxi pilot had also observed anomalous "house-sized" piles of sand and ice while passing the site, noting clear disturbances along the 3.5 km tip of Cape Espenberg. Mr. Goodhope reported seeing similar features during his time in Shishmaref, Kotzebue, and Nome, but had never observed an ivu of this magnitude at this location. Mr. Goodhope's account did not provide the specific date of the event, but instead placed it within a range between mid-November 2016 (when sea ice first formed off of Shishmaref) and March 2017 when he passed by on a snow machine. These local testimonies helped to constrain the date of the event and its geomorphic impacts along an otherwise remote stretch of coastline.

The results of the field surveys and observations document the impacts of block erosion, surge-driven marine flooding, impounding of storm surge and sea ice melt waters, and the landward deposition of eroded material (**Figures 8–11**). Clear differences in geomorphic impacts, related to variability in coastline topography and stratigraphic characteristics, were apparent between the eastern, central, and western portions of the Cape's shore (**Figure 3**) (e.g., Sodhi et al., 1983; Barker and Timco, 2016). Geomorphic impacts, by section, are discussed below using field observations as well as the results from the shoreline change analysis.

Geomorphic Impacts: Eastern

The greatest amount of ice pile up material was along the southeastern tip of the Cape (**Figures 1**, **11A,B**). The main ice push feature along this stretch was made up of ice blocks as large as ∼50 cm^3 mixed with sand, shells, driftwood, and other marine debris with melt water pools and channels present (**Figures 11A,B**). It was concentrated over a 30 × 200 m area in close proximity to the active archeological site. Based on the survey data, this deposit had a volume of 1,000 m^3 (**Figure 3**). The elevation of the pile was 6.2 m (MHW) and rose 3 m above the surrounding land surface at the time of the survey (>6 months after its formation). This unconsolidated relief feature had a greater number of ice blocks, but lacked the well-defined organic-rich stratigraphic structure observed in the more western deposits (**Figure 8**).

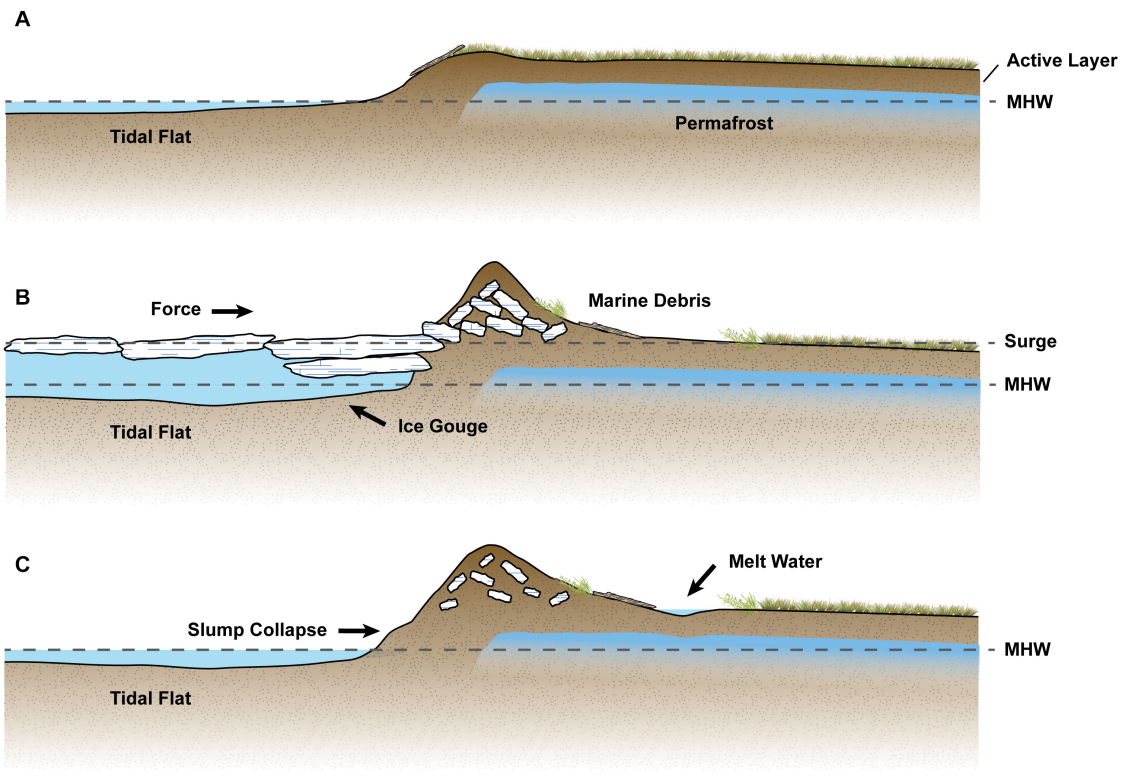

FIGURE 8 | Conceptual diagram showing the before **(A)**, during **(B)**, and after **(C)** cross-sections of the Eastern portion of the coastline (**Figure 3**). Key features are annotated with the arrows. **(A)** Undisturbed coastline prior to the ivu depicting bluff consisting primarily of unconsolidated wind-blown sand. **(B)** During the event, ice, sediments, and other marine debris were piled on top of the bluff. **(C)** Ivu debris pile as it was surveyed and documented 5 months after the ice push. MHW, mean high water.

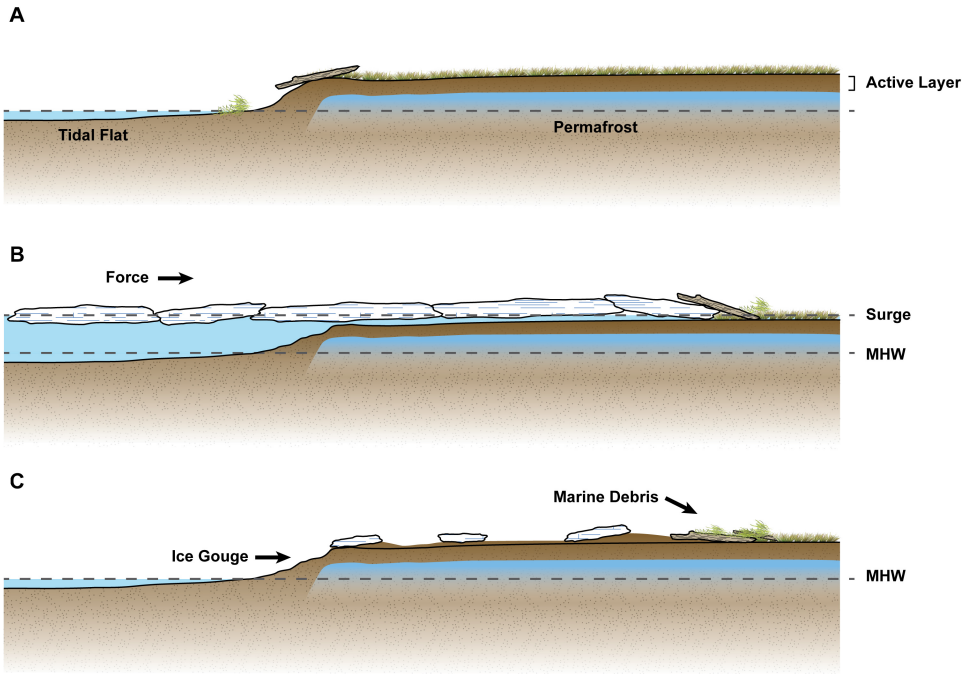

FIGURE 9 | Conceptual diagram showing the before **(A)**, during **(B)**, and after **(C)** cross-sections of the Central portion of coastline (**Figure 3**). Key features are annotated with the arrows. **(A)** Undisturbed coastline prior to the ivu depicting lower elevation trough and marsh. **(B)** Given the lower elevation of the central area, there was an ice ride-up where ice was floated or pushed inland by the storm surge waters but did not leave the distinct debris piles as observed along the Eastern and Western sections. **(C)** After the event, a clear wrack line marking the maximum inland extent of the event (130 m). MHW, mean high water.

The primarily sand and silt sediment matrix of the debris pile originated from both the wind-blown sands of the eroded bluff face and nearshore tidal flats made evident by the presence of marine shells.

The DSAS analysis for the eastern section revealed variable patterns of shoreline change predominately controlled by the alternating dune ridges and troughs alongshore. The eastern stretch had an average NSM of -1.6 ± 0.27 m, with highly variable values ranging between 1.4 and -18 ± 0.27 m. The larger piles of eroded material corresponded to sections of the shoreline with a steeper bluff face (cross-shore dune ridges), which were subject to significant abrasion by rafted sea ice during the 31 December storm (**Figures 11A,B**). The greatest amount of erosion (18 m) was observed seaward of the 1,000 m^3 ice shove feature mentioned previously. Although this analysis identified that there were three locations with positive NSM, field observations and photographs from this area document a clear erosional scarp along the entire coastline with marine debris and overwash deposits across the bluff edge. Two of the locations that observed positive NSM fell within the uncertainty range of the analysis ($\pm$ 0.27 m) and were therefore considered negligible (0 m). The third location that observed positive NSM (1.4 m) had still been reworked by the ice push event, but deposits of unconsolidated material intermixed with vegetation made identification of the vegline uncertain at this location. This positive NSM of the vegline could also be attributed to the growth of new vegetation seaward of the erosional scarp.

Geomorphic Impacts: Central

The low-lying central section had an average NSM of -0.9 ± 0.27 m, with values ranging between -0.1 and -2.5 ± 0.27 m. It is inferred that the upper range of NSM in the central section (-0.1 m) is negligible (0 m), as it falls within the uncertainty range of the shoreline change analysis. Analogous to the eastern section, the entire central coastline also appeared disturbed and truncated. Overwash sand and marine debris were deposited up to 130 m inland (**Figures 9**, **11C**). This maximum inland extent of the surge in the central low-lying swale was delineated by the well-defined rack line (**Figure 11C**). In this area, the storm surge covered an area of 37,000 m^2 and extended 130 m inland (**Figure 3**), terminating just 60 m from the archeological site. The maximum elevation of the storm debris line was surveyed at 5.0 m above MHW providing an accurate estimate for the maximum elevation reached by storm water.

Geomorphic Impacts: Western

Along the older and more ice rich (Mason et al., 1997a) beach ridge complex to the west, the ivu impacts were considerably different (**Figures 10**, **11E**). The ice push appears to have detached and transported fragmented sections of the active layer upwards and inland. These roughly $2 \times 4 \times 1$ m sediment blocks were deposited on top of the dune ridge as high as 5.0 m above MHW, with some blocks being completely flipped on end (**Figures 11D,E**). When surveyed, these blocks were intact with well-defined soil horizons unlike the unconsolidated debris

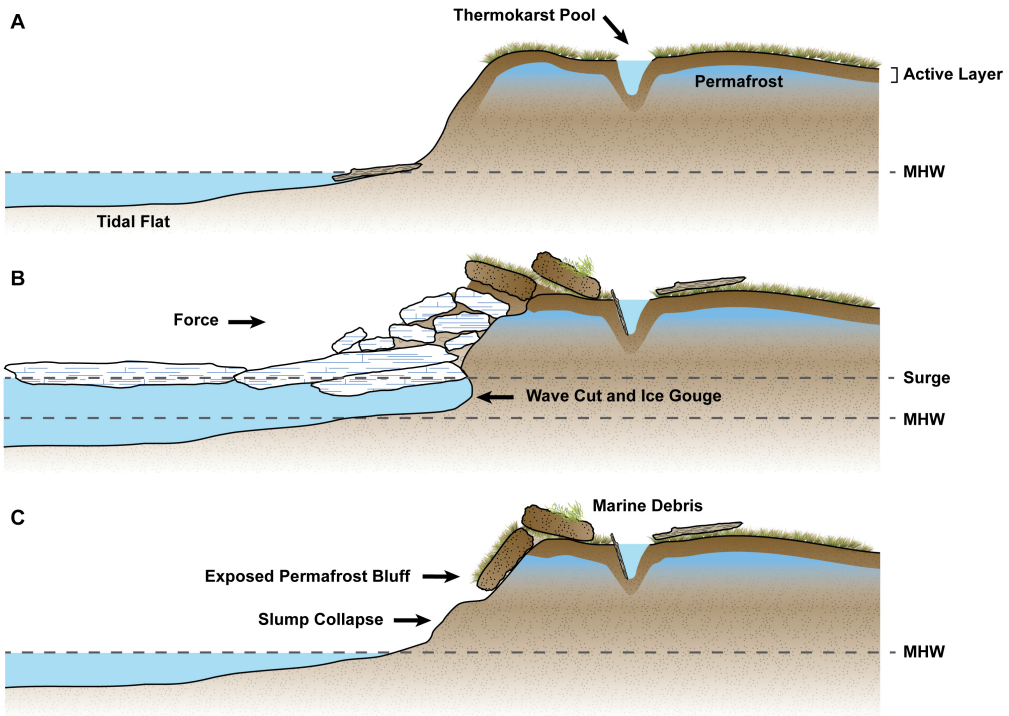

FIGURE 10 | Conceptual diagram showing the before **(A)**, during **(B)**, and after **(C)** cross-sections of the Western portion of coastline (**Figure 3**). Key features are annotated with arrows. **(A)** Prior to the event, there were shore parallel thermokarst cracks approximately 10 m inland from the bluff edge. Note the steeper bluff face and deeper offshore water when compared to the Eastern section (**Figure 8**). **(B)** During the event, ice was shoved into the steep bluff face gouging the bluff toe and sheering off large blocks of sediment along the bottom of the active layer. Notice how the lateral abrasion from the ice push leads to the exposure of permafrost at the bluff, compounding further erosion. **(C)** After the ice push, it was evident that the bluff face had slumped onto the beach with the large sediment blocks and thermokarst features remaining along the top of the bluff (**Figures 11E,F**). MHW, mean high water.

piles observed along the eastern section. While the bluff showed disturbance up to 10–15 m inland over the 1 km stretch, it was evident, from the lack of a defined marine debris line as observed along the eastern and central stretches of coastline, that the storm surge did not reach as far inland along the western ridge.

As previously stated, DSAS analysis was not carried out along the western stretch because of it falling outside the extent of the 2016 orthomosaic, but based on field photographs and observations, it is estimated that this section experienced approximately 2–4 m of erosion with more uniform patterns of disturbance compared to the other two sections. During the field campaign, cross-shore melt run-off channels and shore-parallel thermokarst crevices were also observed and photographed (**Figure 11F**). The presence of marine debris (e.g., shells, drift wood, marine algae) within these channels and crevices at the time of the ground survey indicates an input of marine water at these locations. Field observations also revealed slumping of the disturbed bluff face and exposure of ice-rich permafrost.

DISCUSSION

Ivu of varying degrees are fairly common along Arctic coastlines during seasonally driven periods of destabilized landfast sea ice conditions (Kovacs and Sodhi, 1980, 1988; Kovacs, 1984; Mahoney et al., 2004). However, local observers have never seen an ivu occur at Cape Espenberg, and there are few recent scientific accounts of their occurrence in the region, especially in late December. To address this gap in knowledge, this article documents a significant ivu event (**Figure 1**) that occurred on a remote stretch of shoreline along the Chukchi Sea at Cape Espenberg to advance the understanding of the occurrence and implications of these coastal hazards. These novel results serve to highlight the environmental conditions that lead to destructive ivu, its geomorphic impacts, and potential linkages between this event and regional trends in sea ice decline.

Spatial Extent and Geomorphic Impacts

Upon mapping and noting the characteristics of disturbance along the 3.5 km stretch, it became evident that the variability in foreshore and backshore morphology between the three sections (e.g., beach slope, insipient dune crest elevation, etc.) played a major role in controlling the degree of disturbance. Specifically, the orientation of dune ridges along the Cape relative to the affected coastline resulted in the differing geomorphic impacts between the eastern and central sections compared to the western section. The western section's coastline runs parallel to the dune ridges and is likely why the nature of disturbance and erosion was uniform along this stretch. Conversely, the eastern and central sections run perpendicular to the dune

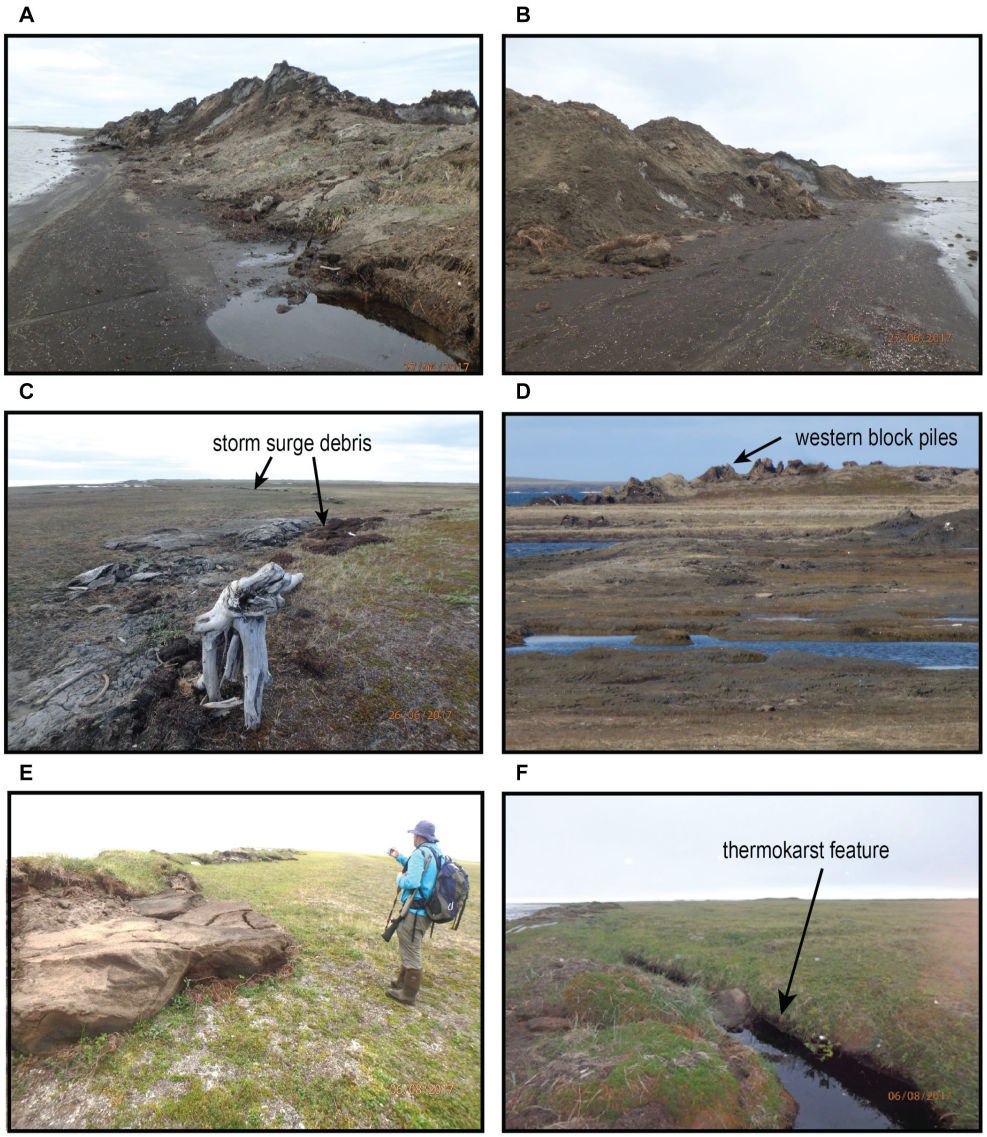

FIGURE 11 | Photographs of ivu impacts along the eastern, central, and western portions of Cape Espenberg (**Figure 3**). **(A)** Photo taken from the foreshore looking east with small erosional scarp and large ice pile-up debris. **(B)** Looking west toward the tip of the cape with ice blocks and eroded sediments shown. **(C)** Storm surge debris line in central low-lying area adjacent to archeological site. **(D)** Photo looking east across central low-lying swale with large piles of sediment blocks along western coastline. **(E)** Along this western portion of the coastline, large blocks of bluff material were cast landwards. **(F)** Parallel to the impacted western coastline, 20–50 m longshore parallel thermoerosional cracks were observed filled with water and ivu debris.

ridges and explain the highly variable nature of geomorphic impacts and erosion along these two sections. This agrees with previous studies that identify coastal morphology as a first-order controller on the nature and extent of coastal change (e.g., Manson et al., 2005; Overduin et al., 2014; Farquharson et al., 2018). Similarly, the shoreline configuration seems to have played a role in controlling where the ice push occurred (e.g., Wagner, 1970; Zagórski et al., 2015). In other words, the sea ice within the lagoon was constrained by the mainland to the west and offshore bars to the east, which concentrated stress release to the north when forced with southerly winds. These constraining features are made evident in SAR scenes preceding the ice push event, as they delineate the shallow waters south of the spit where sea ice began forming in early November (**Figure 4A**). These two factors, combined with the differing substrates along the three sections (see *Study Site*), likely explain the spatial patterns of erosion quantified by the shoreline change analysis (i.e., Barnhart et al., 2014).

The largest NSM (18 m of erosion) identified by the shoreline change analysis occurred along the eastern section, coming within meters of an active archeological site containing the remains of 1,000-year-old driftwood houses and irreplaceable artifactual records (Alix et al., 2017). Although it is important to reiterate that the elevations, erosion rates, and volumetric

change statistics reported in the sections above were measured 6 months after the ice push occurred, with this in mind, the volume and height of the debris pile are surely underestimated, as roughly 2.5 months of melting had occurred preceding the field campaign (National Oceanic and Atmospheric Administration [NOAA], 2016). This melting was made evident by the presence of melt water pools and channels along the affected coastline, predominately in the western and eastern sections. The western section had large blocks ripped from the bluff face and cast upward and landward onto the ridge crest, exposing subsurface permafrost along the bluff (**Figure 11**). Marine debris along the western ridge crest flooded existing thermokarst features and indicates that storm water, likely from wave run-up, reached this elevation (5 m MHW). These impacts have likely led to a further destabilization of bluff structure and the acceleration of erosion rates at this location (e.g., Jones et al., 2009; Jorgenson and Ely, 2001; Fritz et al., 2017). A repeat survey is needed to quantify the extent to which exposed permafrost has exacerbated secondary erosion.

The substantial forces behind these geomorphic impacts demonstrate the potential threat of such events to property, infrastructure, archeological sites, and cultural resources. Regionally speaking, the widespread damage to infrastructure from the 31 December storm was mainly caused by storm surge and/or hurricane-force winds, rather than ice push, as was predominantly the case at Cape Espenberg (Alaska Dispatch News, 2017; Arctic Sounder, 2019), although the major drivers of infrastructural damage from the 31 December storm differed with geographic setting. In Kotzebue, substantial winds caused power outages and damaged multiple buildings, whereas further south in Norton Sound, storm surge led to some of the highest sea levels observed in living memory for the month of December (Arctic Sounder, 2019). St. Lawrence Island took a direct hit from the storm. Damage from storm surge flooding and wind was reported to have occurred at 25 homes on the island, with one house being completely ripped in half and another being blown off its foundation (Arctic Sounder, 2019). Gambell, located on the northwest side of the island, saw its runway flooded and had more infrastructural damage than any other location (Arctic Sounder, 2019). The wind-turbine power plant in Gambell also had to be shut down, due to wind gusts reportedly exceeding 55 m s^{-1} (125 mph) (Alaska Dispatch News, 2017). Unfortunately, few empirical data regarding coastal change and other damage were collected. This point exemplifies the contribution of this study and the need of increased meteorological and water-level instrumentation in the region.

Chronology and Environmental Conditions

The SAR and meteorological data were especially helpful in interpreting the quasi-daily changes in sea ice and weather conditions that culminated in the ivu. This portion of the analysis made it apparent that the ivu at Cape Espenberg was made possible through a "perfect alignment" of sea ice dynamics, atmospheric forcing, and geomorphic setting. Identifying these preceding conditions to an ice push event at a given location is particularly useful to inform sea ice modeling and forecasting, given that ice push events are so episodic in nature (Mahoney et al., 2004). Additionally, although ivu events have been recorded at all times during the ice season, additional mechanisms must be active to incur an ice push event during the colder months (Mahoney et al., 2004), as was the case at Cape Espenberg. Thus, lead-up conditions are discussed in further detail below.

In the days preceding the arrival of the first low-pressure system on 18 December, temperatures rose from −23 to −3°C between 09 and 17 December as recorded at NWS meteorological station PAOT at Kotzebue airport (National Oceanic and Atmospheric Administration [NOAA], 2016). It is likely that this increase in temperature resulted in thermal cracking and weakening of the landfast sea ice due to differential thermal expansion (e.g., Cox, 1983; Johnson and Metzner, 1990). After this rise in temperature, a low-pressure system moved over the Cape between 18 and 20 December, contributing to the 0.6 m (MHW) water level observed at the Red Dog Dock on 19 December due to the inverse barometer effect (Ponte, 2006; National Oceanic and Atmospheric Administration [NOAA], 2020). In fact, the water level observed on 19 December was the highest that had occurred since 17 November (0.6 m MHW) and before the 31 December storm surge (1.9 m MHW) (National Oceanic and Atmospheric Administration [NOAA], 2020). These factors, combined with the northerly winds observed between 19 and 20 December, likely destabilized the landfast ice directly south of the Cape, resulting in the open-water lead and, possibly, the bright curvilinear features evident in the 24 December SAR scene (**Figure 4B**).

Another precursor to the ice push event was the expanse of open water in the Bering and Chukchi Seas as the 31 December storm moved to the northeast along its track. This factor likely contributed to the extreme nature of the storm in terms of wind, surge, and resultant infrastructural damage (Wicks, 2015; Alaska Dispatch News, 2017; Arctic Sounder, 2019). Storms of this or greater magnitude are projected to become more common in the region (Sepp and Jaagus, 2011). Recent atmospheric studies in the Arctic report an increase in the frequency and intensity of storm activity, generally attributed to regional warming and enhanced thermal contrast between the land and sea along the Arctic Frontal Zone (Zhang et al., 2004; Sepp and Jaagus, 2011; Day and Hodges, 2018). Specifically, a study by Sepp and Jaagus (2011) found that the trend in the annual total number of cyclones in the Arctic shows an increase of 55.8 cyclones over the period 1948–2002 and that the greatest increase in the frequency of cyclones was during the winter. There was a significant increase in the frequency of cyclones that specifically moved into the Arctic basin through the Bering Strait, as was the case for the 31 December storm (Sepp and Jaagus, 2011). Moreover, the same study identified that the sea-level pressure of Arctic cyclones showed a significant decreasing trend of 2.5 hPa (stronger storms) over the same study period. These findings align with other atmospheric studies on cyclone intensity and frequency in the region (McCabe et al., 2001;

Atkinson, 2005; Vermaire et al., 2013). A lack of continuous, long−term data extending beyond a few decades has made it difficult to adequately assess these trends and project any future impacts (Manson and Solomon, 2007; Vermaire et al., 2013).

Potential Linkages to Arctic Warming

Taken individually, the factors that culminated in the ivu (e.g., midwinter breakout event, low sea ice extent in Bering Sea, storm surge, hurricane force winds, etc.) do not necessarily seem anomalous. However, the culmination of these forces at the end of December suggests a linkage between this event and the decrease in local and regional sea ice extent associated with a warming Arctic. One of the key factors that contributed to the 31 December ice push event was the midwinter breakout of landfast ice around the tip of Cape Espenberg, which has been a rare phenomenon until recent decades (Mahoney et al., 2014). Historically, most ice push events are constrained to the late fall or spring when warmer temperatures result in ice being less stable (Mahoney et al., 2004). During these shoulder seasons, areas of open water directly adjacent to the beach may form a condition that has been shown to increase the likelihood of ice push given the reduction of resistive forces in the nearshore (i.e., Mahoney et al., 2004). For this reason, the formation of the open-water lead along the affected coastline of Cape Espenberg around 24 December (**Figure 4**) corresponding to both a low-pressure system and close to freezing temperatures increased the likelihood that an ice push could occur at that location. Recently, these midwinter breakout events have been occurring more frequently in northwestern Alaska and are predicted to occur throughout the winter season in the future (Fienup-Riordan and Rearden, 2010; Dammann et al., 2016). This point is made all the more relevant, given the temperature during the 31 December storm tied 1982, 2013, 2015, and 2017 as the warmest temperature recorded in December for Kotzebue (National Oceanic and Atmospheric Administration [NOAA], 2016). If these historically rare breakouts become a normal occurrence, the chance of ivu will likely increase.

Another factor that contributed to the ivu was the lack of continuous sea ice in the Northern Bering Sea prior to the event, which directly contributed to the 1.9 m (MHW) storm surge (observed minus predicted water level) measured on 31 December at the Red Dog Dock, the highest recorded surge in the month of December and second highest overall in the station's 17-year operating history (Wicks, 2015). As a testament to the extreme nature of the 31 December surge at Red Dog Dock, it exceeded that of the notoriously destructive November 2011 storm (1.46 m MHW), which impacted the entire western Alaska coastline (Herndon, 2011; Wicks, 2015; National Oceanic and Atmospheric Administration [NOAA], 2020) and caused widespread coastal inundation, destroying critical infrastructure such as airports and sewage treatment facilities (Herndon, 2011; Terenzi et al., 2014; Buzard et al., submitted). The surge on 31 December was considerably higher at Cape Espenberg with the combined surge and wave run-up height measured at 5 m MHW. This decline in the duration and extent of sea ice in the Bering and Chukchi Seas has been well-documented in the literature (e.g., Douglas, 2010; Mahoney, 2018; Overland et al., 2018; Petty et al., 2018; Walsh et al., 2018; Thoman et al., 2020). According to the Alaska Ocean Observatory Network (AOOS) Sea Ice Atlas, sea ice concentration at the mouth of Kotzebue Sound (67.00°N 164.50°W) in December 2016 was the 17th lowest over the entire 168-year record for the month of December (Alaska Ocean Observing System [AOOS], 2014; **Figure 12**). Recent analyses of historical sea ice trends show that sea ice duration has declined, on average, 1 day per year since 1980 and that the seaward

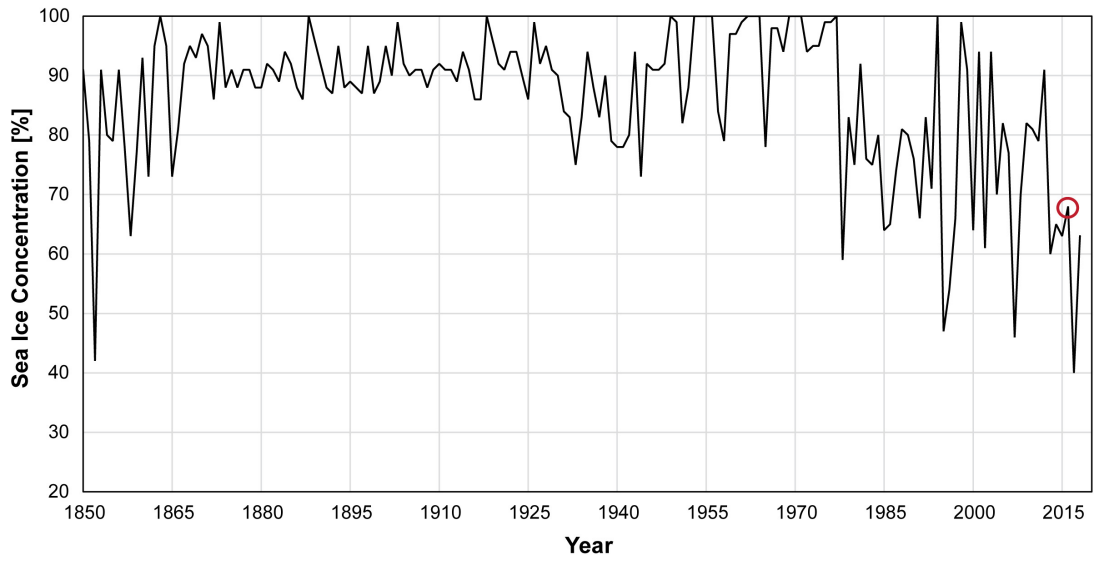

FIGURE 12 | Sea ice concentration compiled from the Alaska Ocean Observatory Network (AOOS) Sea Ice Atlas for the month of December between 1850 and 2018 at the mouth of Kotzebue Sound (67.00°N, -164.50°W). (0–30%) Open Water to very open drift, (30–90%) open drift to close pack, (90–100%) very close pack to compact. December 2016 (noted by the red circle) represents the 17th lowest December sea ice concentration over the entire 168-year record (Alaska Ocean Observing System [AOOS], 2014).

edge of the landfast ice around the mouth of Kotzebue Sound now lies over 30 km closer to shore than it did during the late 1970s (Mahoney et al., 2014; Farquharson et al., 2018). The negative trends in sea ice extent and duration are leading to a greater number of days with longer fetch distances (Farquharson et al., 2018). These findings, which equate to 2 additional months of open water in 2018 compared with 1979, are in line with comparable decadal changes in the length of the landfast sea ice season elsewhere on the Chukchi coast (Mahoney et al., 2014) and highlight the potential for increased open-water fetch and significant surge events in the future. Coastal permafrost erosion in the region has also accelerated in response to the increase in open water, which increases wave impact hours and thermoerosional processes (Farquharson et al., 2018; Jones et al., 2018). Thus, the same sea ice conditions that contributed to the ice push event at Cape Espenberg have likely exacerbated thermoerosion along the affected coastline, especially along the western stretch where the ice-rich permafrost along the bluff was exposed (Mason et al., 1997a).

CONCLUSION

In winter 2016, anomalous sea ice conditions and an extreme midwinter storm culminated in a powerful ivu along the coastline of Cape Espenberg. The ice push event was reconstructed by using ground surveys; traditional ecological knowledge; news reports; and meteorological, water level, and SAR data. Between 18 and 20 December, a low-pressure system coupled with offshore winds destabilized the shorefast ice, which led to the formation of an open-water lead along the impacted coastline. On 31 December, an extreme storm tracked through the Bering Strait and into Kotzebue Sound leading to a significant storm surge brought about by open water and long fetch distances in the Northern Bering Sea. The strong onshore winds and storm surge pushed the unfastened ice sheet in Kotzebue Sound northward onto the exposed tip of the Cape. The ice push affected ∼3.5 km of coastline and was predominantly an ice pile-up, with some ice ride-up occurring in the low-lying central areas. Additionally, along the western section, the exposure of ice-rich permafrost along the bluff and flooding of existing thermokarst features by storm surge may enhance bluff destabilization at this location. The anomalous local and regional sea ice conditions documented by this study are characteristic of wider trends in the region. If temperatures continue to rise in the Arctic along with the number of open water days, coastal hazards such as ivu may become more common in the future.

DATA AVAILABILITY STATEMENT

The datasets generated for this study are available on request to the corresponding author.

AUTHOR CONTRIBUTIONS

CM and RBo led field work activities and the design and execution of the manuscript. RBo processed and interpreted project data and created visualizations. OM contributed field observations, photographs, and expert interpretations of the event and also provided background information and context regarding the geomorphic evolution of Cape Espenberg as well as the occurrence of ice push events in northwestern Alaska. RBu processed and interpreted remotely sensed sea ice data and contributed to related sections in the manuscript. AM provided expert consultation on the use of SAR data and other components of the manuscript related to sea ice dynamics. CW contributed editorial expertise and ensured clear scientific communication throughout the writing of the manuscript. All authors contributed to the article and approved the submitted version.

FUNDING

The project was funded by the National Science Foundation, Arctic Social Science Program – Grants # ARC-1523160 to Drs. Claire Alix, OM, and Nancy Bigelow at the University of Alaska Fairbanks.

ACKNOWLEDGMENTS

We would like to express our gratitude to Sarah Thunberg, UAF MSc student, for providing the data and scripts to make the atmospheric plots included in this manuscript. We would also like to thank Mr. Fred Goodhope for his observations and discussions regarding the ivu event. Dr. Alix facilitated all field work activities and provided photographs for this paper. We also thank Dr. Nancy Bigelow for her extensive work in the field and lab. We also acknowledge the contributions made by the entire Cape Espenberg research and support team. Edward Plumb and Jonathan Chriest from the NWS were gracious with their time and provided first hand meteorological information regarding the storm event. Detailed comments and feedback from two reviewers greatly improved this manuscript. Nathan Wardwell of JOA Surveys assisted with the production of the tidal datum. Matt Nolan of Fairbanks Fodar provided the digital surface model used in coastal change detection. **Figure 3** DEM provided by the Polar Geospatial Center under NSF-OPP awards 1043681, 1559691, and 1542736. We would like to thank the National Science Foundation PerCSNet project, NSF-OISE 1927553, for the support of this publication. We also thank the University of Alaska Fairbanks Vice Chancellor of Research office for financially supporting this publication.

REFERENCES

Alaska Dispatch News (2017). *Winter Storm in Savoonga Draws Experts in Weather Emergencies*. Available online at: https://www.adn.com/alaska-news/2017/01/05/winter-storm-in-savoonga-draws-experts-in-weather-emergencies/ (accessed June 1, 2019).

Alaska Ocean Observing System [AOOS] (2014). *Data from: Historical Sea Ice Atlas: Alaska Sea Ice, Mid-1800s to the Present*. Fairbanks: University of Alaska.

Alaska Satellite Facility [ASF] (2019). Available online at: https://search.asf.alaska.edu/#/ (accessed November 24, 2019).

Alix, C., Mason, O. K., Norman, L., Grieve-Rawson, S., Bigelow, N. H., Lincoln, A., et al. (2017). "The cape espenberg birnirk Project-A report on the 2016 field season of archaeology, geomorphology and anthropology," in *Proceedings of the 44th Annual Meeting Alaska Anthropological Association* Fairbanks.

Arctic Sounder (2019). *Winter Storm Lams Western Alaska Coast*. Available online at: http://www.thearcticsounder.com/article/1701winter_storm_slams_western_alaska_coast (accessed June 1, 2019).

Atkinson, D. E. (2005). Observed storminess patterns and trends in the circum-Arctic coastal regime. *Geo Mar. Lett.* 25, 98–109. doi: 10.1007/s00367-004-0191-0

Barker, A., and Timco, G. (2016). Beaufort Sea rubble fields: characteristics and implications for nearshore petroleum operations. *Cold Regions Sci. Technol.* 121, 66–83. doi: 10.1016/j.coldregions.2015.09.016

Barker, A., and Timco, G. W. (2017). Maximum pile-up heights for grounded ice rubble. *Cold Regions Sci. Technol.* 135, 62–75. doi: 10.1016/j.coldregions.2016.12.001

Barnhart, K. R., Overeem, I., and Anderson, R. S. (2014). The effect of changing sea ice on the physical vulnerability of Arctic coasts. *Cryosphere* 8, 1777–1799. doi: 10.5194/tc-8-1777-2014

Blier, W., Keefe, S., Shaffer, W. A., and Kim, S. C. (1997). Storm surges in the region of western Alaska. *Monthly Weather Rev.* 125, 3094–3108. doi: 10.1175/1520-0493(1997)125<3094:ssitro>2.0.co;2

Boak, E. H., and Turner, I. L. (2005). Shoreline definition and detection: a review. *J. Coast. Res.* 21, 688–703. doi: 10.2112/03-0071.1

Brower, C. D. (1960). *Fifty Years Below Zero: A Lifetime of Adventure in the Far North*. New York, NY: DoodMead Co.

Christensen, F. T. (1994). Ice ride-up and pile-up on shores and coastal structures. *J. Coast. Res.* 10, 681–701.

Copernicus Climate Change Service (C3S) (2017). *Data from: ERA5 Fifth generation of ECMWF Atmospheric Reanalyses of the Global Climate*. Available online at: https://cds.climate.copernicus.eu/cdsapp#!/home (accessed May 8, 2020).

Cox, G. F. (1983). Thermal expansion of saline ice. *J. Glaciol.* 29, 425–432. doi: 10.3189/S0022143000030343

Dammann, D. O., Eicken, H., Mahoney, A. R., Meyer, F. J., Freymueller, J. T., and Kaufman, A. M. (2018). Evaluating landfast sea ice stress and fracture in support of operations on sea ice using SAR interferometry. *Cold Regions Sci. Technol.* 149, 51–64. doi: 10.1016/j.coldregions.2018.02.001

Dammann, D. O., Eicken, H., Meyer, F. J., and Mahoney, A. R. (2016). Assessing small-scale deformation and stability of landfast sea ice on seasonal timescales through L-band SAR interferometry and inverse modeling. *Remote Sens. Environ.* 187, 492–504. doi: 10.1016/j.rse.2016.10.032

Day, J. J., and Hodges, K. I. (2018). Growing land-sea temperature contrast and the intensification of Arctic cyclones. *Geophys. Res. Lett.* 45, 3673–3681. doi: 10.1029/2018GL077587

Douglas, D. C. (2010). *Arctic Sea Ice Decline: Projected Changes in Timing and Extent of Sea Ice in the Bering and Chukchi Seas*. U.S. Geological Survey Open-File Report 2010-1176. Reston: U.S. Geological Survey.

Fairbanks FODAR (2020). Available online at: https://fairbanksfodar.com/ (accessed June 1, 2020).

Farquharson, L. M., Mann, D. H., Swanson, D. K., Jones, B. M., Buzard, R. M., and Jordan, J. W. (2018). Temporal and spatial variability in coastline response to declining sea-ice in northwest Alaska. *Mar. Geol.* 404, 71–83. doi: 10.1016/j.margeo.2018.07.007

Fienup-Riordan, A., and Rearden, A. (2010). "The ice is always changing: yup'ik understandings of sea ice, past and present," in *SIKU: Knowing Our Ice*, eds I. Krupnik, C. Aporta, S. Gearheard, G. Laidler, and L. Kielsen Holm (Dordrecht: Springer), 295–320. doi: 10.1007/978-90-481-8587-0_13

Fritz, M., Vonk, J. E., and Lantuit, H. (2017). Collapsing Arctic coastlines. *Nat. Clim. Change* 7, 6–7. doi: 10.1038/nclimate3188

George, J. C., Huntington, H. P., Brewster, K., Eicken, H., Norton, D. W., and Glenn, R. (2004). Observations on shorefast ice dynamics in Arctic Alaska and the responses of the Iñupiat hunting community. *Arctic* 57, 363–374.

Gilbert, R. (1991). Ice pile-up on shores in northwestern Lake Ontario during winter 1990. *Géographie Phys. Quatern.* 45, 241–244. doi: 10.7202/032863ar

Gilbert, R., and Glew, J. R. (1986). A wind-driven ice-push event in Eastern Lake Ontario. *J. Great Lakes Res.* 12, 326–331. doi: 10.1016/S0380-1330(86)71733-4

Herndon, R. (2011). Storm Data and unusual weather phenomena with late reports and corrections. *NatL. Clim. Data Center* 53, 1–184.

Himmelstoss, E. A., Henderson, R. E., Kratzmann, M. G., and Farris, A. S. (2018). *Digital Shoreline Analysis System (DSAS) version 5.0 user guide (No. 2018-1179)*. Reston: US Geological Survey.

Hoffecker, J. F., and Mason, O. K. (2010). *Human Response to Climate Change at Cape Espenberg: AD 800e1400. Field Investigations at Cape Espenberg*. Available online at: https://instaar.colorado.edu/uploads/publications/cape-espenberg-2010-preliminary-report-to-nps.pdf (accessed May 5, 2020).

Jackson, C. R., and Apel, J. R. (2004). *Synthetic Aperture Radar: Marine User's Manual*. Washington, DC: U.S. Department of Commerce.

Joa Surveys LLC (2020). Available online at: https://joasurveys.com/services/tidal-datum-services/ (accessed June 1, 2020).

Johnson, J. B, and Metzner, R. C. (1990). Thermal expansion coefficients for sea ice. *J. Glaciol.* 36, 343–349. doi: 10.3189/002214390793701327

Johnson, W. R., and Kowalik, Z. (1986). Modeling of storm surges in the Bering Sea and Norton Sound. *J. Geophys. Res. Oceans* 91, 5119–5128. doi: 10.1029/JC091iC04p05119

Jones, B. M., Arp, C. D., Beck, R. A., Grosse, G., Webster, J. M., and Urban, F. E. (2009). Erosional history of Cape Halkett and contemporary monitoring of bluff retreat, Beaufort Sea coast, Alaska. *Polar Geography* 32, 129–142. doi: 10.1080/10889370903486449

Jones, B. M., Bull, D. L., Farquharson, L. M., Buzard, R. M., Arp, C. D., Grosse, G., et al. (2018). A decade of annual permafrost coastal observations indicate changes in the Arctic System. *Environ. Res. Lett.* 13, 1–13. doi: 10.1088/1748-9326/aae471

Jones, J., Eicken, H., Mahoney, A., Rohith, M., Kambhamettu, C., Fukamachi, Y., et al. (2016). Landfast sea ice breakouts: stabilizing ice features, oceanic and atmospheric forcing at Barrow, Alaska. *Cont. Shelf Res.* 126, 50–63. doi: 10.1016/j.csr.2016.07.015

Jones, M. C., Grosse, G., Jones, B. M., and Walter Anthony, K. (2012). Peat accumulation in drained thermokarst lake basins in continuous, ice-rich permafrost, northern Seward Peninsula, Alaska. *J. Geophys. Res. Biogeosci.* 117:G001766.

Jorgenson, T., and Ely, C. (2001). Topography and flooding of coastal ecosystems on the Yukon-Kuskokwim Delta, Alaska: implications for sea-level rise. *J. Coast. Res.* 17, 124–136.

Keijsers, J. G. S., De Groot, A. V., and Riksen, M. J. P. M. (2015). Vegetation and sedimentation on coastal foredunes. *Geomorphology* 228, 723–734. doi: 10.1016/j.geomorph.2014.10.027

Kinsman, N. E. M., and DeRaps, M. R. (2012). *Coastal hazard field investigations in response to the November 2011 Bering Sea storm DGGS RI 2012-2 v. 1.1*.

Kovacs, A. (1984). *Shore Ice Ride-Up and Pile-Up Features. Part 2. Alaska's Beaufort Sea Coast–1983 and 1984 (No. CRREL-84-26*. Hanover, NH: Cold Regions Research And Engineering Lab.

Kovacs, A., and Sodhi, D. S. (1980). Shore ice pile-up and ride-up: field observations, models, theoretical analyses. *Cold Regions Sci. Technol.* 2, 210–288. doi: 10.1016/0165-232X(80)90076-2

Kovacs, A., and Sodhi, D. S. (1988). "Onshore ice pile-up and ride-up: observations and theoretical assessment," in *Arctic Coastal Processes and Slope Protection Design*, eds A. T. Chen and C. B. Leidersdorf (Reston: ASCE), 108–142.

Kowalik, Z. (1984). Storm surges in the Beaufort and Chukchi seas. *J. Geophys. Res. Oceans* 89, 10570–10578. doi: 10.1029/JC089iC06p10570

Leffingwell, E. (1919). *The Canning River region, northern Alaska, U.S. Geological Survey Professional paper 109*. Reston: U.S. Geological Survey.

Mahoney, A., Eicken, H., Shapiro, L., and Grenfell, T. C. (2004). Ice motion and driving forces during a spring ice shove on the Alaskan Chukchi coast. *J. Glaciol.* 50, 195–207. doi: 10.3189/172756504781830141

Mahoney, A. R. (2018). *Landfast Sea Ice in a Changing Arctic, in Arctic Report Card 2018*. Silver Spring, MD: NOAA.

Mahoney, A. R., Eicken, H., Gaylord, A. G., and Gens, R. (2014). Landfast sea ice extent in the Chukchi and Beaufort Seas: the annual cycle and decadal variability. *Cold Regions Sci. Technol.* 103, 41–56. doi: 10.1016/j.coldregions.2014.03.003

Mahoney, A. R., Eicken, H., and Shapiro, L. (2007). How fast is landfast sea ice? A study of the attachment and detachment of nearshore ice at Barrow, Alaska. *Cold Regions Sci. Technol.* 47, 233–255. doi: 10.1016/j.coldregions.2006.09.005

Maio, C. V., Bigelow, N., and Combs, E. (2017). "Sand, peat, and sediment cores: addressing unanswered questions at Cape Espenberg to provide environmental context to the Birnirk-Thule transition," in *Proceedings of the 44th Annual Meeting of the Alaska Anthropological Association, February 27th – March 2nd, 2017* Fairbanks.

Maio, C. V., Bogardus, R. C., Bigelow, N. H., Buzard, R. M., and Roberts, J. W. (2018). "A 3000-year sediment proxy record of extreme storm surges, chukchi coastline, Alaska," in *Proceedings of the AGU Fall Meeting Abstracts 2018. Abstract retrieved from the SAO/NASA Astrophysics Data System* Washington, DC.

Maio, C. V., Gontz, A. M., Tenenbaum, D. E., and Berkland, E. P. (2012). Coastal hazard vulnerability assessment of sensitive historical sites on Rainsford Island, Boston Harbor, Massachusetts. *J. Coast. Res.* 28, 20–33. doi: 10.2112/JCOASTRES-D-10-00104.1

Manson, G. K., and Solomon, S. M. (2007). Past and future forcing of Beaufort Sea coastal change. *Atmos. Ocean* 45, 107–122. doi: 10.3137/ao.450204

Manson, G. K., Solomon, S. M., Forbes, D. L., Atkinson, D. E., and Craymer, M. (2005). Spatial variability of factors influencing coastal change in the western Canadian Arctic. *Geo Mar. Lett.* 25, 138–145. doi: 10.1007/s00367-004-0195-9

Mason, O. K., Hopkins, D. M., and Plug, L. (1997a). Chronology and paleoclimate of storm-induced erosion and episodic dune growth across Cape Espenberg Spit, Alaska, USA. *J. Coast. Res.* 13, 770–797.

Mason, O. K., and Jordan, J. W. (1993). Heightened North Pacific storminess during synchronous late Holocene erosion of Northwest Alaska beach ridges. *Quatern. Res.* 40, 55–69. doi: 10.1006/qres.1993.1056

Mason, O. K., Neal, W. J., Pilkey, O. H., Bullock, J., Fathauer, T., and Pilkey, D. (1997b). *Living with the Coast of Alaska*. Durham: Duke University Press.

Mason, O. K., Salmon, D. K., and Ludwig, S. L. (1996). The periodicity of storm surges in the Bering Sea from 1898 to 1993, based on newspaper accounts. *Clim. Change* 34, 109–123. doi: 10.1007/BF00139256

McCabe, G. J., Clark, M. P., and Serreze, M. C. (2001). Trends in Northern Hemisphere surface cyclone frequency and intensity. *J. Clim.* 14, 2763–2768. doi: 10.1175/1520-0442(2001)014<2763:tinhsc>2.0.co;2

Mesquita, M. S., Atkinson, D. E., and Hodges, K. I. (2010). Characteristics and variability of storm tracks in the North Pacific, Bering Sea, and Alaska. *J. Clim.* 23, 294–311. doi: 10.1175/2009JCLI3019.1

National Oceanic and Atmospheric Administration [NOAA] (2016). *Data from: National Weather Service (NWS) Station PAOT, Kotzebue*. Silver Spring, MD: NOAA.

National Oceanic and Atmospheric Administration [NOAA] (2020). *Data from: Water Levels - NOAA Tides, and Currents*. Silver Spring, MD: NOAA.

National Park Service [NPS] (2020). Available online at: https://www.nps.gov/bela/learn/historyculture/cape-espenburg.html (accessed May 12, 2020).

Onstott, R. G., and Carsey, F. D. (1992). SAR and scatterometer signatures of sea ice. *Microwave Remote Sens. Sea Ice* 68, 73–104. doi: 10.1029/gm068p0073

Overduin, P. P., Strzelecki, M. C., Grigoriev, M. N., Couture, N., Lantuit, H., St-Hilaire-Gravel, D., et al. (2014). Coastal changes in the Arctic. *Geol. Soc.* 388, 103–129. doi: 10.1144/SP388.13

Overland, J. E., Wang, M., and Ballinger, T. J. (2018). Recent increased warming of the Alaskan marine Arctic due to midlatitude linkages. *Adv. Atmos. Sci.* 35, 75–84. doi: 10.1007/s00376-017-7026-1

Pajak, M. J., and Leatherman, S. (2002). The high water line as shoreline indicator. *J. Coast. Res.* 18, 329–337.

Petty, A. A., Stroeve, J. C., Holland, P. R., Boisvert, L. N., Bliss, A. C., Kimura, N., et al. (2018). The Arctic sea ice cover of 2016: a year of record-low highs and higher-than-expected lows. *Cryosphere* 12, 433–452. doi: 10.5194/tc-12-433-2018

Ponte, R. M. (2006). Low-frequency sea level variability and the inverted barometer effect. *J. Atmos. Ocean. Technol.* 23, 619–629. doi: 10.1175/JTECH1864.1

Porter, C., Morin, P., Howat, I., Noh, M., Bates, B., Peterman, K., et al. (2018). *Data from: "ArcticDEM" Harvard Dataverse, V1*. Minneapolis, MN: University of Minnesota.

Ruggiero, P., Kratzmann, M. G., Himmelstoss, E. A., Reid, D., Allan, J., and Kaminsky, G. (2013). *National Assessment of Shoreline Change: Historical Shoreline Change Along the Pacific Northwest Coast*. Reston: US Geological Survey.

Sallenger, A. H. (1983). *Measurements of Debris-Line Elevations and Beach Profiles Following A Major Storm; Northern Bering Sea Coast of Alaska (No. 83-394)*. Reston: US Geological Survey.

Sepp, M., and Jaagus, J. (2011). Changes in the activity and tracks of Arctic cyclones. *Clim. Change* 105, 577–595. doi: 10.1007/s10584-010-9893-7

Shapiro, L. H., Metzner, R. C., Hanson, A., and Johnson, J. B. (1984). "Fast ice sheet deformation during ice-push and shore ice ride-up," in *the Alaskan Beaufort Sea*, eds E. Reimnitz, P. W. Barnes, and D. M. Schell (Cambridge, MA: Academic Press), 137–157. doi: 10.1016/b978-0-12-079030-2.50013-7

Sodhi, D. S., Hirayama, K., Haynes, F. D., and Kato, K. (1983). Experiments on ice ride-up and pile-up. *Ann. Glaciol.* 4, 266–270. doi: 10.3189/S0260305500005589

Stewart, B. C., Kunkel, K. E., Stevens, L. E., Sun, L., and Walsh, J. E. (2013). *Regional Climate Trends and Scenarios for the US National Climate Assessment: Part 7. Climate of Alaska*. Silver Spring, MD: NOAA. NOAA Technical Report NESDIS.

Terenzi, J., Jorgenson, M. T., Ely, C. R., and Giguère, N. (2014). Storm-surge flooding on the Yukon-Kuskokwim delta, Alaska. *Arctic* 360–374. doi: 10.14430/arctic4403

Thoman, R. L., Bhatt, U. S., Bieniek, P. A., Brettschneider, B. R., Brubaker, M., Danielson, S. L., et al. (2020). The record low bering sea ice extent in 2018: context, impacts, and an assessment of the role of anthropogenic climate change. *Bull. Am. Meteorol. Soc.* 101, S53–S55. doi: 10.1175/BAMS-D-19-0175.1

Vermaire, J. C., Pisaric, M., Thienpont, J. R., Mustaphi, C. J., Kokelj, S. V., and Smol, J. P. (2013). Arctic climate warming and sea ice declines lead to increased storm surge activity. *Geophys. Res. Lett.* 40, 1386–1390. doi: 10.1002/grl.50191

Wagner, W. P. (1970). Ice movement and shoreline modification, Lake Champlain, Vermont. *Geol. Soc. Am. Bull.* 81, 117–126.

Walsh, J. E., Thoman, R. L., Bhatt, U. S., Bieniek, P. A., Brettschneider, B., Brubaker, M., et al. (2018). The high latitude marine heat wave of 2016 and its impacts on Alaska. *Bull. Am. Meteorol. Soc.* 99, S39–S43. doi: 10.1175/BAMS-D-17-0105

Weaver, S. A., Ucar, Z., Bettinger, P., and Merry, K. (2015). How a GNSS receiver is held may affect static horizontal position accuracy. *PLoS One* 10:e0124696. doi: 10.1371/journal.pone.0124696

Wicks, A. J. (2015). *Coastal Storm Surge Identification, Classification, and Evaluation at Red Dog Dock, Alaska, 2004-2014*. dissertation/master's thesis, University of Victoria Victoria, BC.

Zagórski, P., Rodzik, J., Moskalik, M., Strzelecki, M., Lim, M., Błaszczyk, M., et al. (2015). Multidecadal (1960–2011) shoreline changes in Isbjørnhamna (Hornsund, Svalbard). *Polish Polar Res.* 36, 369–390. doi: 10.1515/popore-2015-0019

Zarillo, G. A., Kelley, J., and Larson, V. (2008). *A GIS Based Tool for Extracting Shoreline Positions from Aerial Imagery (BeachTools) revised (No. ERDC/CHL-CHETN-IV-73)*. Vicksburg, MS: Engineer Research And Development Center Vicksburg Ms Coastal And Hydraulics Lab.

Zhang, X., Walsh, J. E., Zhang, J., Bhatt, U. S., and Ikeda, M. (2004). Climatology and interannual variability of Arctic cyclone activity: 1948–2002. *J. Clim.* 17, 2300–2317. doi: 10.1175/1520-0442(2004)017<2300:caivoa>2.0.co;2

Zimmerman, M. R., and Aufderheide, A. C. (1984). The frozen family of Utqiagvik: the autopsy findings. *Arctic Anthropol.* 21, 53–64.

Conflict of Interest: The authors declare that the research was conducted in the absence of any commercial or financial relationships that could be construed as a potential conflict of interest.

frontiers in Environmental Science

METHODS
published: 08 September 2020
doi: 10.3389/fenvs.2020.00143

Feasibility Study for the Application of Synthetic Aperture Radar for Coastal Erosion Rate Quantification Across the Arctic

Annett Bartsch[1,2,3]*, *Sarah Ley*[1,2], *Ingmar Nitze*[4], *Georg Pointner*[1,2] *and Gonçalo Vieira*[5]

[1] b.geos, Korneuburg, Austria, [2] Cryosphere and Climate, Austrian Polar Research Institute, Vienna, Austria, [3] Department of Geodesy and Geoinformation, Vienna University of Technology, Vienna, Austria, [4] Permafrost Research Section, Alfred Wegener Institute Helmholtz Centre for Polar and Marine Research, Potsdam, Germany, [5] CEG/IGOT, University of Lisbon, Lisbon, Portugal

The applicability of optical satellite data to quantify coastal erosion across the Arctic is limited due to frequent cloud cover. Synthetic Aperture Radar (SAR) may provide an alternative. The interpretation of SAR data for coastal erosion monitoring in Arctic regions is, however, challenging due to issues of viewing geometry, ambiguities in scattering behavior and inconsistencies in acquisition strategies. In order to assess SAR applicability, we have investigated data acquired at three different wavelengths (X-, C-, L-band; TerraSAR-X, Sentinel-1, ALOS PALSAR 1/2). In a first step we developed a pre-processing workflow which considers viewing geometry issues (shoreline orientation, incidence angle relationships with respect to different landcover types). We distinguish between areas with foreshortening along cliffs facing the sensor, radar shadow along cliffs facing away and traditional land-water boundary discrimination. Results are compared to retrievals from Landsat trends. Four regions which feature high erosion rates have been selected. All three wavelengths have been investigated for Kay Point (Canadian Beaufort Sea Coast). C- and L-band have been studied at all sites, including also Herschel Island (Canadian Beaufort Sea Coast), Varandai (Barents Sea Coast, Russia), and Bykovsky Peninsula (Laptev Sea coast, Russia). Erosion rates have been derived for a 1-year period (2017–2018) and in case of L-band also over 11 years (2007–2018). Results indicate applicability of all wavelengths, but acquisitions need to be selected with care to deal with potential ambiguities in scattering behavior. Furthermore, incidence angle dependencies need to be considered for discrimination of the land-water boundary in case of L- and C-band. However, L-band has the lowest sensitivity to wave action and relevant future missions are expected to be of value for coastal erosion monitoring. The utilization of trends derived from Landsat is also promising for efficient long-term trend retrieval. The high spatial resolution of TerraSAR-X staring spot light mode (< 1 m) also allows the use of radar shadow for cliff-top monitoring in all seasons. Derived retreat rates agree with rates available from other data sources, but the applicability for automatic retrieval is partially limited. The derived rates suggest an increase of erosion at all four sites in recent years, but uncertainties are also high.

Keywords: Arctic, erosion, SAR, radar, coast, permafrost

OPEN ACCESS

Edited by:
Louise Farquharson, University of Alaska Fairbanks, United States

Reviewed by:
Melanie Engram, University of Alaska Fairbanks, United States
Ann Gibbs, United States Geological Survey, United States
Philipp Bernhard, ETH Zürich, Switzerland

***Correspondence:**
Annett Bartsch
annett.bartsch@bgeos.com

Specialty section:
This article was submitted to Environmental Informatics and Remote Sensing, a section of the journal Frontiers in Environmental Science

Received: *03 May 2020*
Accepted: *28 July 2020*
Published: *08 September 2020*

Citation:
Bartsch A, Ley S, Nitze I, Pointner G and Vieira G (2020) Feasibility Study for the Application of Synthetic Aperture Radar for Coastal Erosion Rate Quantification Across the Arctic. Front. Environ. Sci. 8:143. doi: 10.3389/fenvs.2020.00143

1. INTRODUCTION

Arctic regions are some of the most rapidly changing environments on Earth, and their coastlines are especially vulnerable to climate change due to permafrost thaw and marine changes (Lantuit, 2008; Overland et al., 2019; Nielsen et al., 2020). The latter includes decrease in sea ice extent due to warming temperatures and change in wave action (driven by length of open water season and sea ice concentration anomalies, Nielsen et al., 2020). They impact thermo-denudation and thermo-abrasion along the coast. The annual erosion rates at the Alaskan and northwest Canadian Arctic coastlines are among the highest in the world, but Siberian coastlines also show high rates (Frederick et al., 2016). These irreversible coastal changes are a threat to communities and wildlife in those areas. Communities have needed to be relocated, and houses and archaeological sites have been damaged (Jones et al., 2008; Arp et al., 2010; Frederick et al., 2016; Radosavljevic et al., 2016; Irrgang et al., 2019). In addition to these directly visible effects, the erosion mobilizes significant amounts of carbon and contaminants (e.g., Steele et al., 2008; Couture et al., 2018; Schuster et al., 2018; Overland et al., 2019). There is a clear need to quantify erosion regularly on circumpolar scale, but available studies focus on local to regional level. A first account for circumpolar rates has been published in 2012 (Lantuit et al., 2012). It is based on published rates from *in situ* measurements and partially from satellite data from a wide range of studies, which have been aggregated for coast segments to tackle scale differences. That study provides a first account of circumpolar coastal dynamics, but is inconsistent. Moreover, global initiatives on quantification of shore line changes based solely on satellite data omit the Arctic (e.g., Mentaschi et al., 2018).

Arctic coastal erosion has been monitored through airborne and spaceborne optical imagery or *in situ* measurements (e.g., Obu et al., 2016; Irrgang et al., 2018; Cunliffe et al., 2019). *In situ* measurements only cover small areas, and optical images can be unreliable due to frequent cloud cover in the Arctic (Stettner et al., 2017; Zwieback et al., 2018). Microwave radiation on the other hand is barely affected by the atmosphere, and does not rely on solar illumination, which can be especially useful for monitoring Arctic regions (Jones and Vaughan, 2010). This has motivated recent interest in using microwave technologies like Synthetic Aperture Radar (SAR) to monitor Arctic regions. The interpretation of SAR data for coastal erosion in Arctic regions is, however, challenging (Stettner et al., 2017). Differential SAR interferometry (DInSAR) and SAR interferometry (InSAR) have been successfully used to measure gradual surface displacement in Arctic environments (e.g., Liu et al., 2012; Strozzi et al., 2018). However, detecting mass movements is difficult, because repeat-pass interferometry methods are not effective in rapidly changing terrain such as the Arctic coasts. The changes between the satellite revisit times are too large in comparison to the SAR wavelength, and no useful correlation can be found between the images (Short et al., 2011; Zwieback et al., 2018). Therefore, Stettner et al. (2017) introduced a backscatter-based threshold method with TerraSAR-X images to classify and evaluate inter- and intra-annual cliff-top erosion rates. The high backscatter difference between tundra, water and steep cliffs facing the sensor justifies the simple approach. Unfortunately, only a limited number of high spatial resolution (in respect to the erosion rates) SAR acquisitions of the Arctic region exist. A further challenge is the limitation of the approach to steep cliffs facing toward the sensor. A different method is needed for cliffs facing away and coasts without steep cliffs. As an alternative, to cover also all other parts of the coastline, the separability between the land-water boundary needs to be investigated. Banks et al. (2014) analyzed the backscatter characteristics of Arctic shore and near-shore landcover types for C-band images in various incidence angle ranges and polarizations. They found that the separability between sand and water backscatter in C-band strongly depends on the incidence angle and polarization. Differences in applicability of certain wavelengths are also to be expected due to their varying sensitivity to waves on the water and surface roughness (modified by vegetation and snow; examples from Arctic sites in Stettner et al., 2018; Bartsch et al., 2020) on land, which leads to ambiguities. Wet snow appears similar to water (low backscatter), as do radar shadow areas. Waves and sea ice show similar or even higher backscatter than typical undisturbed tundra. An additional challenge poses the variation of spatial resolution across commonly used SAR spaceborne missions.

This study tests the accuracy and transferability of the threshold-based method proposed by Stettner et al. (2017) for comparably low resolution PALSAR/PALSAR-2 L-band and Sentinel-1 C-band images in addition to high-resolution TerraSAR-X X-band acquisitions. The overall goal is to identify options for operational mapping of coastal erosion along Arctic coasts. This requires the analyses of the land-water boundary in addition to represent all coast types.

The first objective is therefore to implement and demonstrate a landcover classification scheme for X-, C- and L-band data building on the approach suggested by Stettner et al. (2017). Specifically, the classification should correctly identify steep coasts, land, and water surfaces for applicability across various coast types. To achieve this, the classification approach must account for the landcover specific angular dependence in the classification step. Where available, different polarization needs to be assessed. Previously, thresholds have been determined only visually (Stettner et al., 2017). A quantitative approach is, however, required.

The second objective is to demonstrate the use of the proposed classifications to analyze coastline change in the Arctic. Specifically, annual coastline movement rates are calculated for steep cliff coastlines. The accuracy of these estimates is assessed by comparison with trends derived from multi-spectral data, published results from previous studies, and by cross-comparisons between sensors within this study.

2. MATERIALS AND METHODS

2.1. Study Areas and Reference Data for Coastal Erosion Rates

In order to judge the utility of different SAR parameters to detect and measure coastal erosion, we conducted our analysis in areas where coastal erosion has been measured before. This

study focuses on four coastal sites in three regions with existing records of comparably high erosion rates from previous studies: two sites at the Canadian Beaufort Sea (Herschel Island, 139.3°W 69.6°N; Kay Point, 138.4°W 69.3°N), one at the Russian Laptev Sea (Bykovsky Peninsula, 129.3°E 71.8°N), and one at the Barents Sea Coast (Varandai, 58.3°E 68.9°N) (**Figure 1**). Satellite image acquisitions of two further areas along the Beaufort Sea coast are considered for calibration purposes (King Point, 138°W 69.1°N and Stokes Point, 138.7°W 69.3°N).

Erosion dynamics in Arctic shorelines relate to cold climate and geomorphic impacts of permafrost, ground-ice, snow, and sea-ice. The evolution of coastal features occurs during the thawing and sea-ice-free seasons (Kroon, 2014). Depending on the morphology of the coastline and the ground ice content, thermo-abrasion (block failures) or thermo-denudation (retrogressive thaw slumps) are the main erosion processes (Lantuit, 2008; Hoque and Pollard, 2009). Coastal zones with horizontal thermo-erosional niches, especially when combined with large surface areas separated by ice wedges, are prone to block failures (Hoque and Pollard, 2004). The thermal-mechanical erosion undercuts the frozen cliff, and under the force of gravity, the heavy overhanging blocks of soil detaches from the coast (Lantuit, 2008). On average the erosion rate on Arctic coasts is 0.5 m/year, but in the Laptev East Siberian and the US and Canadian Beaufort Seas the rates are much higher (3 m/year and more) (Lantuit et al., 2012, see also **Figure 1**). The Barents Sea coast also includes low-gradient sandy shores with comparably high erosion rates (2–5 m/yr, Sinitsyn et al., 2020).

2.1.1. Canadian Beaufort (Yukon) Sea Coast

The approximately 280 km long Yukon Coast lies between the Alaskan border and the Mackenzie Delta in Canada, in the continuous permafrost zone. The climate has a continental character in winter and maritime influences in summer. Herschel Island is located approximately in its center. Komakuk Beach, around 40 km west of Herschel Island, is the closest weather station in this area (Obu et al., 2016). From 1971 to 2000 the mean air temperature was −11.3°C. The coldest temperatures were measured in February and the warmest in July, with averages of −25.3°C and 7.8°C, respectively (Government Canada, 2019). The coastal areas of the Beaufort Sea are typically ice-covered from October to June. From late August to September, storms become increasingly frequent and can generate significant high waves greater than 4 m (Solomon, 2005). Tides are in the order of 0.3 to 0.5 m in this region (Hequette et al., 1995). The coastal erosion processes mainly take place during this ice-free storm season (Obu et al., 2016).

In this area, low-relief landforms like beaches, barrier islands and spits, inundated tundra, tundra flats and slopes, and active cliffs are common (Irrgang et al., 2018). Around 33% of the coast shows active slumps, and 13% shows high bluffs with no slumping. Such slumps as well as bluffs exist, for example, on Herschel Island. A site with active slumps on the west coast (Avadlek as described in Obu et al., 2016) with a length of about 700 m and bluff heights of 10–25 m has been selected for analyses (**Figure 2A**). The slope orientation of the Avadlek site favors tests for the cliff-top detection approach as the majority of available satellite data is acquired by right looking system set ups and from ascending orbits (see **Table 1**).

In 2006 around 78% of the Yukon coastline, including Herschel Island, was affected by coastal erosion processes (Obu et al., 2016). Excluding Herschel Island, the mean annual rate of shoreline change from 1950 to 2011 was −0.7± 0.2 m/year. The highest erosion rates were measured at shorelines characterized by spits (Irrgang et al., 2018) and capes. One example is Kay Point (**Figure 2B**). It includes a NE facing coastline stretch of approximately 2km length characterized by approximately 4 m high bluffs, but no thaw slumps. This coast segment has been selected for analyses, since it is a long-term monitoring site of the Geological Survey of Canada (Forbes et al., 1995, site 5280), as well as due to satellite data availability (**Table 1**), specifically very high spatial resolution SAR, which allows investigation of radar shadow occurrence. Reference erosion rates with geospatial information is available from Irrgang et al. (2017) for this region. Both sites (Avadlek on Herschel Island and Kay Point) are located in areas with comparably high Soil Organic Carbon (SOC) mobilization (Couture et al., 2018).

2.1.2. Bykovsky Peninsula, Laptev Sea Coast

The Bykovsky peninsula is located southeast of the Lena Delta in northeastern Siberia, and lies within the zone of continuous permafrost. The weather has an almost continental character, although it is surrounded by the Laptev sea (Lantuit et al., 2011). The mean annual temperature is −11.5°C with long harsh winters and short cold summers. The open water season is between July and September, but can begin as early as late May (Lantuit et al., 2011; Günther et al., 2013). The length of the open water season at the Laptev Sea Coast has a strong influence on annual rates and is conditioned by the Arctic Oscillation in winter and summer (Nielsen et al., 2020). Concurrent with the open water season, the highest storm activity takes place in these months (Lantuit et al., 2011). Storms are in general the largest driver of erosion in the Arctic, and therefore the coastal erosion is mostly limited to the open water season in July to September. However, even during this period chunks of sea ice can reduce the wave activity (Lantuit, 2008).

The relief of the peninsula is dominated by flat elevated areas up to 40 m above sea level and thermokarst depressions near sea level (Grosse et al., 2005). At the over 150 km long shoreline, various coastal landforms exist, such as sandbars, lagoon barriers, ice complex cliffs, thermokarst basins (alases), and thaw slump coasts according to Lantuit et al. (2011). Between 1951 and 2006, alases and retrogressive thaw slumps underwent erosion at a rate of 1.02 and 0.91 m/year, respectively (Lantuit et al., 2011). These rates are significantly higher than the other coast types on the Bykovsky Peninsula, which underwent erosion at rates between 0.40 and 0.47 m/year (Lantuit et al., 2011). A three kilometer long stretch along the west coast, which is characterized by retrogressive thaw slumps has been selected for this study (**Figure 3A**). Similarly to the Herschel Island site, the slope orientation favors testing the cliff-top detection approach.

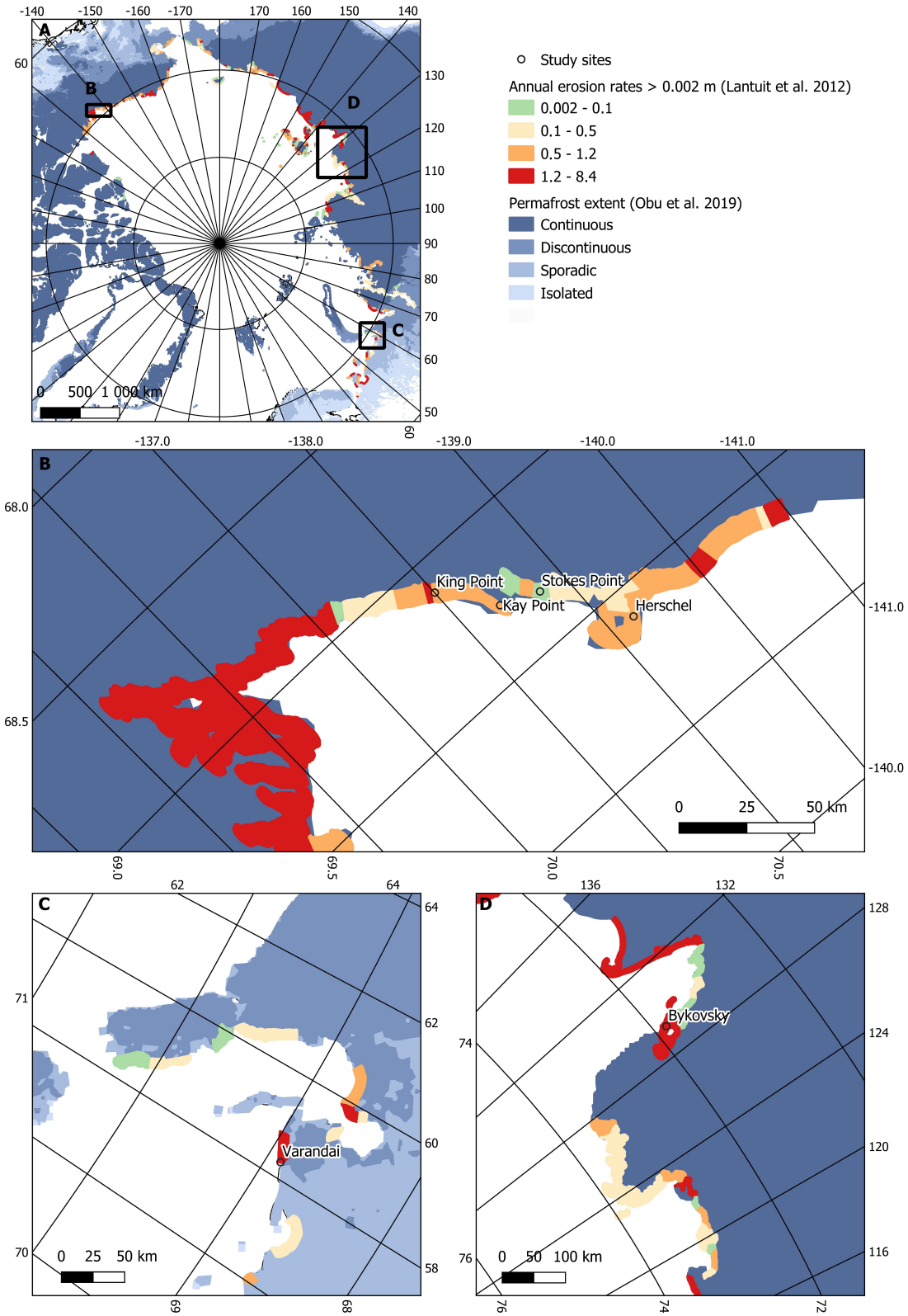

FIGURE 1 | (A) Location of study areas, annual erosion rates (source: Lantuit et al., 2012) and permafrost zones (source: Obu et al., 2019b). **(B)** zoom for Beaufort Sea coast, **(C)** zoom for Barents Sea Coast, **(D)** zoom for Laptev Sea Coast.

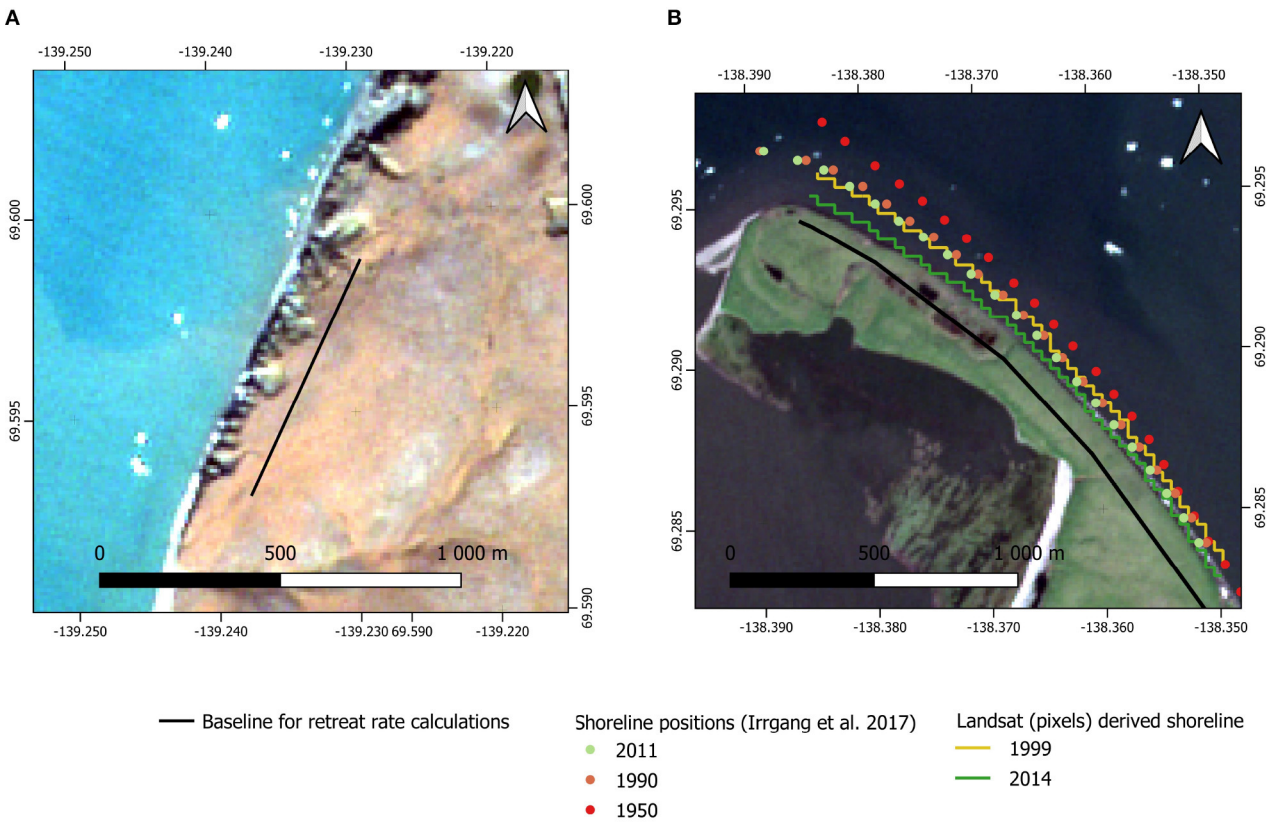

FIGURE 2 | Study sites along the Beaufort Sea Coast, Canada: **(A)** Avadlek on Herschel Island, **(B)** Kay Point, including shoreline points for rate calculations from Irrgang et al. (2017) and Landsat trend data based on probability of land to water change between 1999 and 2014 (Nitze et al., 2018) (visualization based on vectorized 30 × 30 m pixels). The baseline for rate calculations in this paper is shown in addition. Background: RGB (band 4, 3, and 2) composite of Sentinel-2 (optical, multi-spectral), Sep 20 2018.

2.1.3. Varandai, Barents Sea Coast

The study region at the Barents sea coast in the northwest of Russia is warmer regarding ground and air temperatures than the other sites. It lies in the zone of sporadic to discontinuous permafrost (**Figure 1**). Le et al. (2018) report a mean annual air temperature between −3.8 and −4.8°C in 2012–2014. The coldest air temperature of −39.4°C was measured in January, and the warmest, 30°C, in July. Storm surges with magnitudes of 1.5–2 m, and tides with high amplitudes of 0.5 m are common (Leont'yev, 2003).

In general, the landscape varies from wide, low-gradient sandy shores with dune belts to sub-vertical ice-rich bluffs and narrow beaches (Guégan and Christiansen, 2016). The coast is formed by a marine terrace 2 to 6 km wide, and the sediment body is predominantly sand. The coastal cliffs, where present, are mostly between 3 and 10 m high. Thermal erosion only occurs locally, and does not play a large role in the coastal dynamics. Coastal erosion rates of 1 to 4 m/year are common (Leont'yev, 2003). This applies to specifically the area near Varandai, which has been selected as example for low relief coast with an extensive sandy beach area (approximately 700 m, **Figure 3B**). Sinitsyn et al. (2020) report on average −1.8 m/year from 1951 to 2013 in the proximity. Several buildings have been destroyed between 2004 and 2012. This period included a storm surge which occurred in summer 2010.

2.2. Synthetic Aperture Radar Data

Three different wavelengths from SAR sensors from four different satellite missions have been investigated. This also included the analyses of different polarization combinations. The choice of acquisition dates and wavelengths was determined by data availability. A further issue is also spatial resolution. Although a long history of C- and L-band SAR acquisition exists, older platforms such as ERS-1/2 (European remote sensing satellites 1 and 2, 1991–2011) or JERS-1 (Japanese Earth Resources Satellite 1) offer only comparably coarse spatial resolution (about 30 and 18 m, respectively) and limited polarization combinations. Open access and continuous acquisitions only exist for C-band (Sentinel-1 Copernicus mission). X-band and L-band availability and access is in general limited. **Table 1** provides an overview of used sensors, their specifications and dates. Recent annual erosion rates were determined for 2017 to 2018 using L-band and C-band data and for part of the open water season of 2018 in case of X-band data. A longer time period (decadal time scale) could be only investigated for L-band as only in this case consecutive missions

TABLE 1 | List of available Synthetic Aperture Radar acquisitions grouped by sensor and study area.

Sensor (band, polarization, incidence angle range)	Region	Date	Nominal resolution [m]	Pass	Site specific incidence angle [°]
PALSAR/ PALSAR-2 (L-band, HH, HV; 33–43°)	Herschel Island & Kay Point	2007-08-31	12.5	Ascending	37.5 & 39
		2008-09-02	12.5	Ascending	38 & 39.5
		2017-07-26	10	Ascending	34.3 & 36
		2018-07-25	10	Ascending	34.5 & 36
	Bykovsky Peninsula	2007-09-04	12.5	Ascending	38
		2008-09-06	12.5	Ascending	38.5
		2017-09-05	10	Ascending	40
		2018-08-07	10	Ascending	40
	Varandai	2007-08-01	12.5	Ascending	38
		2008-08-03	12.5	Ascending	38
		2017-09-23	10	Ascending	41
		2018-07-14	10	Ascending	41
Sentinel-1 (C-band, VV, VH; 34–42.5°)	Herschel Island & Kay Point	2017-07-15	10	Ascending	40 & 40.5
		2018-07-22	10	Ascending	40 & 40.5
		2017-07-29	10	Descending	43.2 &40.2
		2018-07-24	10	Descending	43.2 &40.2
	Bykovsky Peninsula	2017-07-25*	10	Descending	39.8
		2018-07-20*	10	Descending	39.8
	Varandai	2017-07-28	10	Descending	38
		2018-07-23	10	Descending	38
TerraSAR-X (X-band, HH; 19–53°)	King Point	2018-06-15*	0.62	Descending	51
		2018-07-07*	0.62	Descending	51
	Kay Point	2018-07-13	0.69	Ascending	40
		2019-01-27	0.69	Ascending	40
		2018-08-12*	1.35	Descending	19.5
	Stokes Point	2018-07-16*	0.96	Descending	29.5

**indicates use for incidence angle and landcover analyses only.*

with similar acquisition properties are existing. The years 2007 and 2008 have been therefore analyzed for L-band in addition to 2017 and 2018. The actual dates varied from sensor to sensor also due to acquisition strategies, revisit intervals and image quality. The availability of polarization combinations also varies across the sensors. At maximum two types of combinations have been available for the study sites, including HH (horizontally sent and horizontally received), VV (vertically sent and vertically received) as well as HV and VH.

The Phased Array type L-band Synthetic Aperture Radar (PALSAR) and PALSAR-2 are L-band SARs with a center frequency around 1.2 GHz (JAXA, 2008, 2018). They are follow-on missions of JERS-1. PALSAR was launched on board the Advanced Land Observation Satellite (ALOS) in January 2006 and sent information until its failure in April 2011. ALOS was replaced in May 2014 by ALOS-2, carrying the PALSAR-2. Both satellites have a sun-synchronous, sub-recurrent orbit, but the 14-day revisit time of ALOS-2 is much shorter than the ALOS revisit time of 46 days (Shimada, 2009; JAXA, 2018). Due to their duration and orbits, the PALSAR datasets are suitable for long-term studies of the Arctic. Two sets of data were used from the PALSAR satellites. First, PALSAR Fine Beam (FB) dual polarization images with 12.5 m nominal resolution in HH and HV polarizations were analyzed. Second, PALSAR-2 Stripmap mode 3 (SM3) images with 10 m nominal resolution, also in HH and HV polarizations, were investigated. In total four images with the same orbit, one image per year, for each area of interest were used.

The Sentinel-1 mission is part of the European Union's Copernicus program. The mission consists currently of two satellites with a near-polar, sun-synchronous orbit, 180 degrees apart from each other. The two earth observation satellites Sentinel-1A (launched in April 2014) and Sentinel-1B (launched in April 2016) have an identical C-band SAR sensor on board (Schubert et al., 2017). The Interferometric Wide Swath (IW) mode combines a swath width of 250 km with a medium-high ground resolution of 5 × 20 m. Products in ground range are distributed with 10 m nominal resolution. The incidence angle range is potentially 31° to 46°. Images can be captured in dual polarization (HH+HV or VV+VH). Only VV+VH is available for the study areas for this mode and resolution. Like the PALSAR/PALSAR-2 data sets, one image per year with the same relative orbit for every area of interest was analyzed. The years 2017 and 2018 were chosen to enable the comparison of the

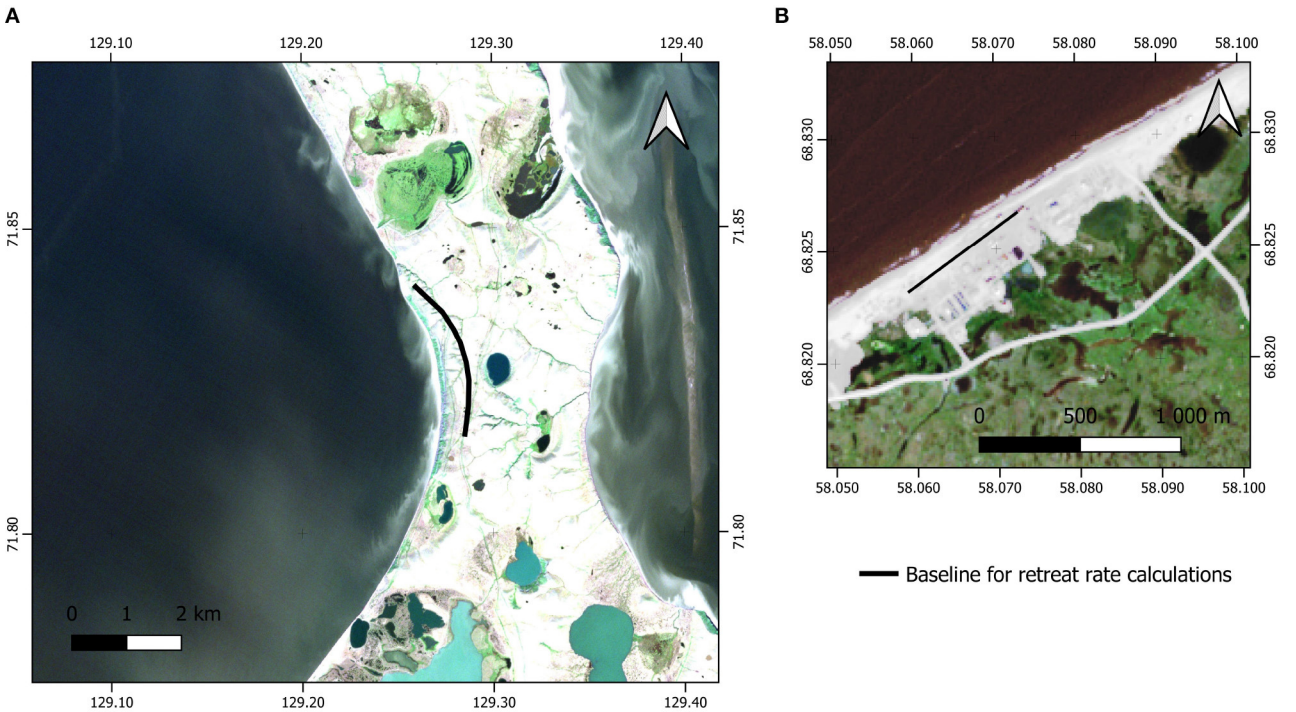

FIGURE 3 | Russian study sites: **(A)** West coast of the Bykovsky Peninsula, **(B)** Varandai, Barents Sea Coast. The baseline for rate calculations in this paper is shown in addition. Background: RGB (band 4, 3, and 2) composite of Sentinel-2 (optical, multi-spectral), Aug 28 2018 and Aug 8 2019.

coastal erosion rates with the PALSAR/PALSAR-2 images. Images with ascending and descending pass directions were available for the Canadian Beaufort Sea Coast, and both were used for this study.

TerraSAR-X was launched in June 2007, and is a commercial German X-band SAR earth observation satellite. It has a sun-synchronous orbit and a repeat period of 11 days. The standard operational mode is the single receive antenna mode, which can be used in three different modes: SpotLight (SL), StripMap (SM) and ScanSAR (SC). The SpotLight mode uses phased array beam steering in azimuth direction to increase the illumination time. It can further be divided in the High Resolution SpotLight (HS) and Staring SpotLight (ST) mode. The ST scene size and resolution is highly dependent on the incidence angle, because the antenna footprint depends on the scene, and the scene length corresponds to the length of the antenna footprint. The Spotlight mode achieves an azimuth resolution up to 0.24 m. For this mode only single polarization acquisitions are available (HH). In this study TerraSAR-X images in ST mode with incidence angles between 19° and 51° as well as ascending and descending acquisitions are available for parts of the Beaufort Sea Coast (Kay point, King Point and Stokes Point). The incidence angle impacts the spatial resolution. The applied nominal resolution for the used images therefore ranges from 0.62 to 1.35 m (see **Table 1**). The only image pair which allows for time series analyses has an ascending pass designation and covers only Kay Point. In addition, the second acquisition is from winter time which may affect the classification results (accuracy) as well as annual rates (disproportional representation of thaw period).

The PALSAR/PALSAR-2 L-band and Sentinel-1 C-band data sets used in this study were recorded in the most likely open water months, from June to September. This time frame was chosen to take advantage of the backscatter difference between land and water, which is greater than the difference between land and sea ice. The high-resolution TerraSAR-X X-band data sets were available for June, July, August and October 2018 and January 2019. For calibration, only data from the sea ice free season/areas were used. **Table 1** summarizes the used acquisitions.

The availability of ascending and descending image pairs by L-band and C-band data allows the comparison of cliff-top classification based results and land-water boundary based results for the Herschel site. C-band was found not applicable for Bykovsky, due to constant high wave action in the proximity. Therefore only L-band has been investigated at this site.

Data from all three bands are available at the Kay Point site only. Continuous stretches of steep cliffs facing the sensor are not present in acquisitions for this area. Therefore only the land-water boundary is investigated. A specific feature in this area is the occurrence of radar shadows in X-band where the bluffs are steep and face away from the sensor, due to the comparably high spatial resolution. The land-water boundary only is also investigated in case of Varandai; here due to the absence of steep coast.

2.3. Auxiliary Multi-Spectral Data and Derived Products

A landcover classification provided by Bartsch et al. (2019b) was used to define the coastline and to calculate the coastline orientation with respect to the sensor. This classification is based on a combined approach of supervised and unsupervised classification using SAR (Sentinel-1 VV, IW mode) and multi-spectral data (Sentinel-2). Sentinel-2 is an European mission to deploy wide-swath, high-resolution, multi-spectral observation satellites. It deployed two twin satellites, Sentinel-2A and -2B, in a sun-synchronous orbit 180° apart from each other. Sentinel-2A was launched in June 2015 and Sentinel-2B in March 2017. The optical sensor samples 13 spectral bands. The spatial resolution depends on the used band: four bands have a spatial resolution of 10 m, six bands of 20 m, and three bands of 60 m (ESA, 2015). Bands 3 (green, 10 m resolution), 4 (red, 10 m), 8 (near infrared, 10 m), 11 (SWIR, 20 m), and 12 (SWIR, 20 m) from July/August 2015–2018 have been used for the classification (Bartsch et al., 2019a,b).

Sentinel-2 images are further used for visualization purposes as well as to aid validation and calibration sample selection. True color RGB composites (band 4, 3, and 2) with a spatial resolution of 10 m have been prepared. The images were acquired on Jun 14, Jul 23, Sep 20 2018 (Beaufort Sea Coast), Aug 28 2018 (Bykovsky Peninsula), and Aug 8 2019 (Varandai).

A Landsat-derived product was used for the assessment of the SAR retrievals. Data from this mission are commonly used for change detection and Arctic landcover classification (Bartsch et al., 2016). NASA's Landsat mission deployed a series of land observation satellites. Landsat 5, 7, and 8 were launched in 1984, 1999, and 2013, respectively. They provide visible-, and infrared–wavelength images of all land and near-coast areas on Earth in 30 m spatial resolution. Landsat 7 and 8 have additional thermal bands in 60 m resolution and a panchromatic band in 15 m resolution. These datasets formed the basis for trend analyses described in Nitze et al. (2017, 2018). Trends from various multi-spectral indices in combination with the random forest machine-learning algorithm allow the retrieval of land surface change probabilities. They have been already applied for land-water change for lakes (Nitze et al., 2017, 2018). Resulting products are available open access (Nitze, 2018) for selected Arctic regions at 30 m spatial resolution spanning 1999–2014. For this study, we expanded the dataset extent along the Beaufort Sea Coast to Herschel and Kay Point, which were not covered in previous analyses.

2.4. Pre-processing of SAR Data

The Sentinel-1, PALSAR-2, and TerraSAR-X data were preprocessed in ESA's SNAP toolbox (ESA, 2019b). The PALSAR data was processed in the ASF MapReady software (ASF, 2019).

Pre-processing included radiometric calibration as well as multi-looking in case of the PALSAR-2 and TerraSAR-X images (1:4 and 1:2, respectively, range:azimuth), since the data were available as single-look complex images. This step was not necessary for the Sentinel-1 data, because Ground Range Detected (GRD) products were used. GRD products are detected, multi-looked, and projected to ground range using an Earth ellipsoid model (ESA, 2012).

To reduce speckle, a filtering step was added. The Lee Sigma filter was applied (sigma = 0.9, window = 7×7, and target window size = 3×3). This filter assumes that 95.5% of the pixels are distributed within the two-sigma range from its mean. It replaces the center pixel of a scanning window with the average of those pixels within the two-sigma range of the center pixel. Pixels outside the two-sigma range are not included into the sample mean computing, and a speckle reduction is achieved (Lee et al., 2009).

The third step was ellipsoid correction of the data (as suggested in Stettner et al., 2017). For areas of continuous erosion a terrain correction cannot be applied, when a precise Digital Elevation Model (DEM) for the constantly changing coastline area is not available. Therefore only images with the same orbit constellation are comparable to each other. These steps were carried out with the SNAP (Sentinel Application Platform) toolbox provided by the European Space Agency and the scattering coefficient σ^0 was derived. During the ellipsoid correction, the local incidence angle (based on ellipsoid) was extracted. The final step involved converting σ^0 to decibels. The resulting nominal resolution is provided in **Table 1**.

In case of PALSAR data, ellipsoid correction was carried out first in the ASF MapReady software, and afterwards the Lee Sigma filter was applied in the SNAP toolbox.

2.5. Identification of Steep Coasts Facing the Sensor

Samples for calibration and validation are required for all three target classes: water, land and steep coasts facing the sensor. Water and land reference data are available through the existing land cover classifications and the Sentinel-2 images. Steep coasts can be also partially identified with Sentinel-2 (visible thaw slumps), but they are only of relevance when they are facing the sensor.

Steep coasts that are facing the sensor have a relatively high backscatter coefficient. This is mainly caused by the foreshortening effect and occurs only when the cliff faces the sensor. Therefore it is important for the threshold determination proposed by Stettner et al. (2017) to consider the orientation of the coast relative to the incoming signal.

Calculating the coastline orientation means calculating the intersection angle between the coastline and the line of sight (LOS) of the sensor. For threshold determination, the coastline of the Beaufort Sea coast was extracted from a land cover classification provided by Bartsch et al. (2019b) and divided into segments. The raster (20 × 20 m) was vectorized, the land water boundary vector manually extracted and simplified using the Douglas-Peucker algorithm (Douglas and Peucker, 1973) with a smoothing distance of 30 m. The resulting vector was split at every second vertex to create the segments. The coordinates of each segment's midpoint and endpoints were then derived.

The midpoints were moved 40 m toward the satellite to test whether the coast was facing toward or away from the satellite.

The moved point lies outside the land area (over the ocean) if the coastline faces the satellite and inside (over the land surface) if it faces away.

Finally the angle between the LOS of the sensor and the coast segment was calculated. The gradient of the LOS, m_2, was derived from the inclination of the satellite's orbit. The angle α was calculated

$$\tan\alpha = \frac{m_1 - m_2}{1 + m_1 m_2} \quad (1)$$

where m_1 is the gradient of the coast segment. This gradient is calculated based on the start and end point of the respective line vector. Results served for choice of analyses segments, including calibration sites for the classification threshold determination as well as for erosion rate retrieval.

2.6. Threshold Determination and Classification

In general, we followed the approach by Stettner et al. (2017) but extended it in order to consider local incidence angle dependencies as necessary for transferability of the approach. Also the case for land-water boundary detection as an alternative is included. A threshold method which considers three surface types (water, land and steep cliff) as well as incidence angles is required. The assumption is that thresholds differ for each sensor type/ wavelength. Ellipsoid derived incidence angles can be assumed to be of limited applicability for local incidence estimation at steep cliffs (are in general smaller at cliffs facing the sensor), but are nevertheless treated similarly to the other classes and are discussed.

Radar shadow needs to be taken into consideration as a fourth class in case of the TerraSAR-X staring spotlight mode images, due to their high spatial resolution (less than 1 m). Radar shadow occurs at cliffs facing away from the sensor resulting in an about five meter wide affected area at Kay Point. This effect is always present at this viewing geometry which allows utilization of data from winter acquisitions. **Figure 4A** shows an example of a summer and a winter image. The determined backscatter for radar shadow is in the same order as for smooth water surfaces (appr. −20 dB, **Figure 4B**). The backscatter characteristics for open water (threshold function separating open water from land) are therefore also used for application during winter in case of the selected coastal stretch at Kay Point. The example also includes typical values for cliffs collected from the W and NW facing parts of the Babbage Estuary, which is located SW from Kay Point within the TerraSAR-X scene extent. They demonstrate that thresholds separating cliffs from the "land" class determined from summer images are not applicable for the category cliffs facing to the sensor in winter (exposed soils are wet and therefore exhibit a strong frozen-unfrozen difference), but all cliffs at the selected coastal segment at Kay Point are facing away from the sensor.

Samples were taken to analyze the dependence of σ^0 on incidence angle for each of the three surface classes. The samples were manually selected using the auxiliary datasets. The landcover classification from Bartsch et al. (2019b) was used to identify sample locations for land and water areas. Potential areas with steep cliffs facing the sensor have been identified supported by the coast orientation dataset which was created in the preceding step. The incidence angle range was different for each satellite. The PALSAR/PALSAR-2 range varied from 33° to 43°, Sentinel-1 from 34° to 42.5°, and TerraSAR-X from 19° to 51°. Nearly all images were used (except January acquisition from TerraSAR-X), and samples that cover the maximum possible incidence angle range were selected. This required the use of data from two additional sites with differing viewing geometry (King Point, 20 km south of Kay Point and Stokes Point, 20 km to the North) in case of TerraSAR-X. Regions with sea-ice were excluded from the water class sampling. The sample sets were grouped by satellite, surface class, and polarization. Each group was divided into a training set (to calculate the threshold function) and a testing set (to test the quality of the classification results). The separation was made based on the rasterized training polygons. Every second pixel in the sequence (row by row) was excluded from the training and used for validation later on. The sample sizes of the three classes reflect approximately the occurrence in the images. The sample size (area covered) of steep cliff features is therefore much smaller than for the other classes (less than 1% of the complete sample dataset). Approximately 15–17% for land and 83–84% for water are contained in the sample datasets for each of the wavelengths. The sample dataset covers in total about 617 km^2.

In order to classify the images, a functional relationship between σ^0 and the incidence angle θ was calculated following a similar approach as suggested by Bartsch et al. (2017) but applying a linear function as only a limited range is used (see also Widhalm et al., 2018; Bartsch et al., 2020; with a being the slope and b the intercept).

$$\sigma^0 = a\theta + b \quad (2)$$

In general, the water samples show the lowest backscatter values, and the coast samples the highest (example for X-band, see **Figure 4**). For this reason threshold functions were calculated to differentiate the water from land and land from steep cliffs (but not water from steep cliffs). The parameters a and b have been derived for each wavelength and polarization combination separately. The standard deviation for the different landcover types are also expected to differ. To derive more precise threshold functions, the standard deviation of the absolute residuals was therefore considered (**Table 2**). The threshold between water and land was calculated as:

$$\sigma^0_{w/l}(\theta) = \frac{(\sigma^0_{water} + std_{water}) + (\sigma^0_{land} - std_{land})}{2} \quad (3)$$

where σ^0_{water} and σ^0_{land} are the function fitted to the water and land samples and their standard deviations are std_{water} and std_{land}. Similarly, the threshold function between the land and steep cliff classes was calculated as:

$$\sigma^0_{l/c}(\theta) = \frac{(\sigma^0_{land} + std_{land}) + (\sigma^0_{cliff} - std_{cliff})}{2} \quad (4)$$

where σ^0_{cliff} is the function fitted to the land samples and its standard deviation is std_{cliff}.

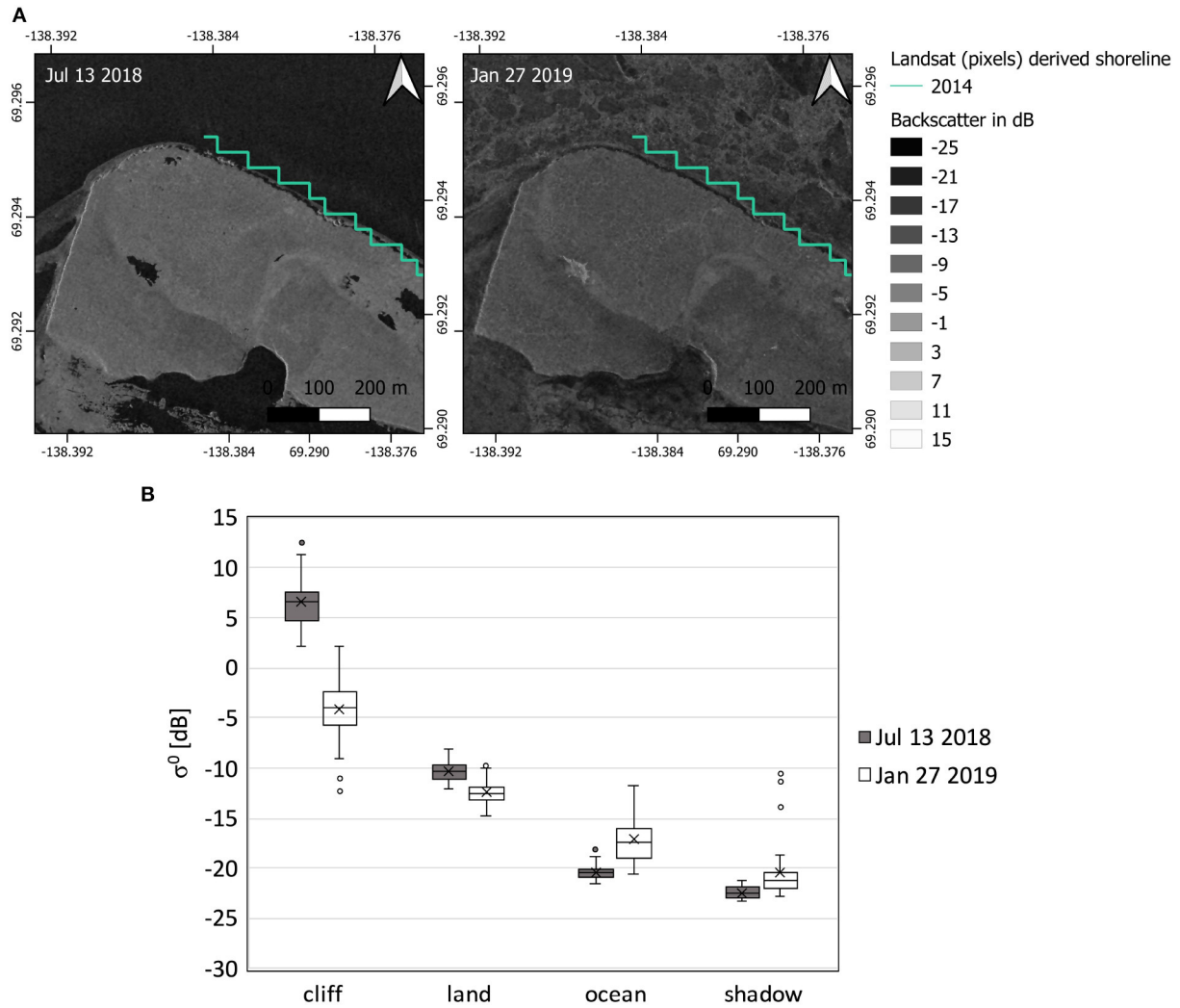

FIGURE 4 | Backscatter characteristics (σ^0 in dB) of TerraSAR-X at Kay Point: **(A)** Example of a summer and a winter acquisition including the Landsat derived coastline for demarcation of the analysed coast segment (using) trend data based on probability of land to water change between 1999 and 2014 (Nitze et al., 2018); visualization based on vectorized 30 × 30 m pixels), **(B)** boxplots of backscatter samples for all relevant classes (cliffs facing toward the sensor, land, ocean, and radar shadow) at 40 degree incidence angle for summer and winter.

TABLE 2 | Standard deviation of absolute residuals for water, land and cliff for each satellite and polarization (σ^0 in dB) for use in equation 3 and 4.

Sensor	Polarization	Water	Land	Cliff
PALSAR	HH	0.69	0.76	0.96
	HV	0.56	0.45	0.75
PALSAR-2	HH	0.64	0.87	1.36
	HV	0.59	1.31	0.83
Sentinel 1	VH	0.92	0.81	0.69
	VV	1.88	0.77	0.78
TerraSAR-X	HH	1.44	0.78	1.36

These threshold functions were used to classify the image pixels. During the classification process it was calculated whether the σ^0 pixel values lie below or above the threshold functions. If the σ^0 pixel value was below the σ_w/l threshold it was classified as water. Otherwise, it was tested whether the σ^0 values lie below or above the σ_l/c threshold. Every pixel above the threshold was classified as steep cliff, every value below as land.

The error evaluation was carried out separately for the different polarizations. The "producer's accuracy" and the "user's accuracy" have been derived.

The classification results were then used to derive vectors representing the land-water boundaries and cliff-land boundaries, respectively. The classification raster was vectorized

and then all vectors, which represent such boundaries within the areas of interest manually extracted. These vectors were then split perpendicular to the relevant baseline (at their end and start point, see **Figures 2**, **3** for baseline locations) for the erosion rate calculation.

2.7. Post-processing of the Landsat Landsurface Trend Products

Probabilities of erosion and accretion (change of land to water and visa versa) as well as no change are available for the time period 1999–2014. Samples of probabilities have been taken for published coastline positions at Kay Point for 1950, 1990, and 2011 [Irrgang et al. (2017), see **Figure 5**]. The extracted values (mean and median) indicate that a probability threshold between 0.4 and 0.6 could be applicable for retrieval of land to water conversion. Probabilities drop sharply in front of the NE oriented coastal erosion area at Kay Point (**Figure 6**, left). Differences between thresholds of 0.45, 0.5, and 0.55 are small (**Figure 6**, right). A probability threshold of 0.5 has been therefore selected based on these samples in order to derive potential areas of erosion at the Beaufort Sea Coast sites and at the Bykovsky peninsula. The resulting raster has been vectorized along the selected coastal segments and segments selected as for the SAR classification results (see section 2.6).

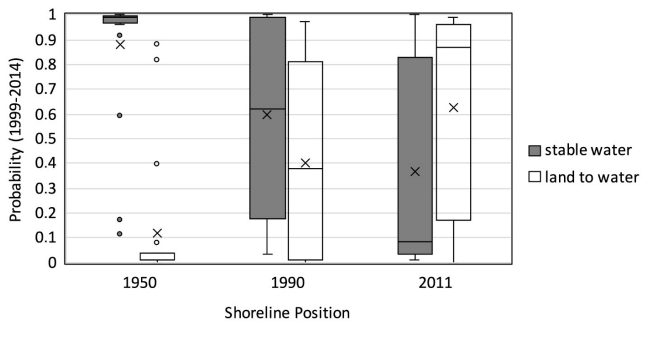

FIGURE 5 | Probabilities for stable water and land to water conversion derived from Landsat (1999–2014) for shore line positions 1950, 1990, and 2011 at Kay Point (source Irrgang et al., 2017, see also **Figure 2B**).

2.8. Erosion Rate Estimation

In line with Stettner et al. (2017) the Digital Shoreline Analysis System (DSAS), an ArcGIS extension provided by the United States Geological Survey (Himmelstoss et al., 2018), was used to derive the coastline erosion rates. DSAS calculates rate-of-change statistics for a chronological series of shoreline vectors. For the erosion rate calculation, baselines and transects were defined. Considering the spatial resolution, a transect distance of 10 m was used for the PALSAR/PALSAR-2 and Sentinel-1 shorelines, and a distance of 1 m was used for the TerraSAR-X shorelines. The shoreline uncertainty values (*unc*) were chosen to be equal to the spatial resolution of the image (PALSAR 12.5 m, Sentinel-1 10 m, PALSAR-2 6.8–8.2 m, and TerraSAR-X 0.69 m).

Three statistics and their uncertainty were calculated: the net shoreline movement (NSM), the end point rate (EPR), and the weighted linear regression (WLR). For the WLR calculation, shorelines from three or more dates are necessary.

The NSM is the distance in meters between the oldest and the most recent shoreline positions for each transect. This NSM value was used to determine the EPR and the associated uncertainty as documented in Himmelstoss et al. (2018).

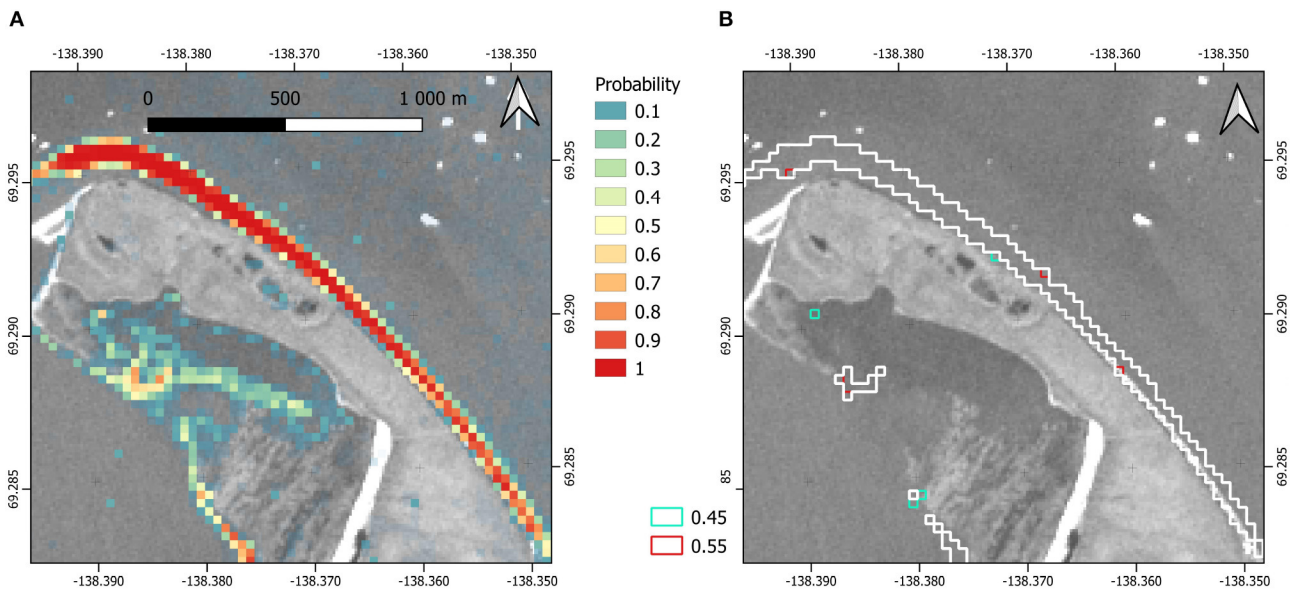

FIGURE 6 | Probabilities for land to water conversion derived from Landsat (1999–2014) at Kay Point (see also **Figure 2B**). **(A)** overlay of probabilities for each pixel, **(B)** vectorized classifications for >0.5 (white), >0.45 (blue), and >0.55 (red). Background: Band 2 (blue) of Sentinel-2 Sep 20 2018.

The WLR was calculated by using least-squares regression to fit a line through the transect points. Data points with a small spatial uncertainty, were given more weight (Himmelstoss et al., 2018). Like the EPR, the WLR expresses a shoreline change rate for each transect. The EPR is the change between pairs of sequential observations, and the WLR is the overall trend.

The WLR could only be calculated for the PALSAR/PALSAR-2 shoreline time series because the other datasets only have two timepoints. The NSM and EPR were calculated for the Sentinel-1 and TerraSAR-X data sets. The 2017–2018 EPR for the PALSAR/PALSAR-2 coastlines that overlap with the Sentinel-1 data set were calculated for comparison.

TABLE 3 | Threshold parameters for each satellite and polarization.

Sensor	Polarization	Threshold	*a*	*b*
PALSAR-2	HH	Cliff–Land	-0.203	4.353
		Land–Water	-0.382	-0.620
	HV	Cliff–Land	-0.245	-4.467
		Land–Water	-0.203	-18.753
Sentinel-1	VH	Cliff–Land	-0.055	-9.898
		Land–Water	-0.220	-13.224
	VV	Cliff–Land	0.059	-7.266
		Land–Water	-0.303	-3.070
TerraSAR-X	HH	Cliff–Land	-0.023	-2.029
		Land–Water	$-1.041\ 10^{-4}$	-15.73

The parameters a and b refer to Equation (2). PALSAR is omitted because its images were classified based on the PALSAR-2 threshold.

3. RESULTS

3.1. Threshold Functions for Classification

The standard deviation of backscatter for water is highest for C- and X-band, which reflects wave action and the comparably short radar wavelength with respect to wave height. Deviations are in general high for all steep sensor facing cliffs as affected areas are comparably small (mixed pixels) and topography varies locally. The standard deviation is below 1 dB in most cases with exceptions not exceeding 2dB. **Table 3** summarizes the parameters of the threshold functions grouped by satellite and polarization. A slope (*a*) close to zero indicates low incidence angle dependence. This is the case for the cliff-land threshold in case of C- and X-band for all tested polarizations due to low dependence of the land and cliff class. The same applies to the land-water boundary for X-band. In all other cases, including all L-band polarizations (**Figure 7**), the incidence angle needs to be considered for the threshold determination, which is in general driven by the properties of water surfaces in case of C- and X-band.

The Sentinel-1 VV polarized samples show higher backscatter values than the VH polarized samples, which is reflected in the threshold functions in **Figure 7**. The same applies to L-HH compared to L-HV. The PALSAR-2 samples were eventually used to calculate the threshold functions for both PALSAR and PALSAR-2, because of the wider incidence angle range available from the PALSAR-2 data.

3.2. Classification Accuracy

The threshold based classification results show the highest classification accuracy for co-polarized acquisition (**Table 4**). This can be shown for L-band as well as C-band.

The producer's accuracy of the cliff classification is 100% for every polarization. In other words, all cliff samples were correctly

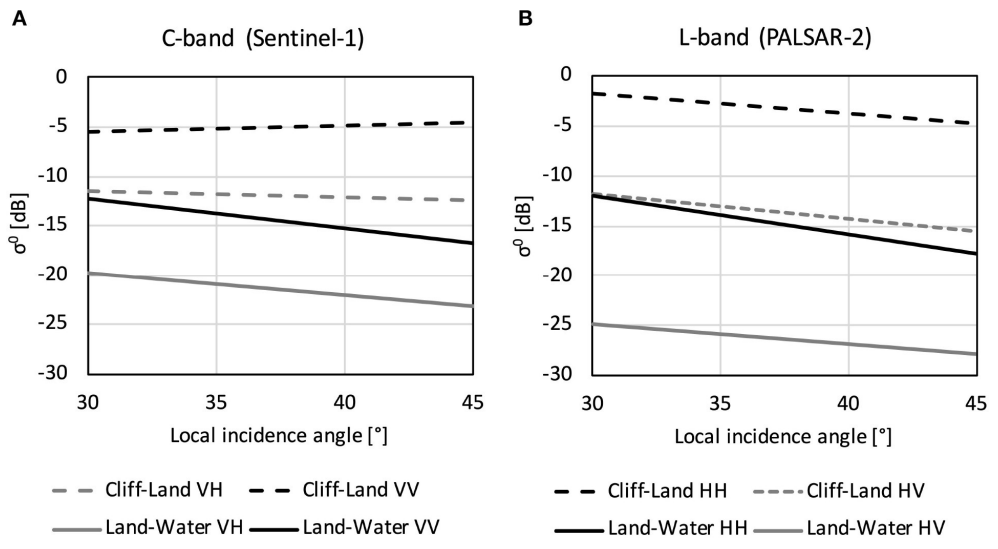

FIGURE 7 | Threshold functions derived for **(A)** C-band (Sentinel-1, Interferometric Wide Swath mode) and **(B)** L-band (PALSAR-2, Fine Beam mode). Local incidence angles (x-axis) are derived with respect to the ellipsoid. For equation parameters see **Table 3**.

TABLE 4 | User's and producers accuracy of landcover classifications.

Classified data		Reference data			Users accuracy
		Cliff	Land	Water	
PALSAR/PALSAR 2 HH	Cliff	**100**	0	0	100.00
	Land	0	**71.51**	0.3	93.70
	Water	0	28.49	**99.7**	97.43
PALSAR/PALSAR 2 HV	Cliff	**100**	0.03	0	88.34
	Land	0	**77.14**	14.14	52.76
	Water	0	22.83	**85.86**	94.84
Sentinel-1 VV	Cliff	**100**	0.13	0	18.39
	Land	0	**97.56**	4.13	78.47
	Water	0	2.31	**95.87**	99.63
Sentinel-1 VH	Cliff	**100**	0.43	0	7.32
	Land	0	**66.34**	0	100
	Water	0	33.23	**100**	95.13
TerraSAR-X HH	Cliff	**100**	0	0	100
	Land	0	**99.87**	0.6	97.41
	Water	0	0.13	**99.4**	99.97

"Cliff" refers to steep coasts facing the sensor. Producer's accuracy values are highlighted in bold. All values are in %.

classified as cliff, regardless of sensor. This is especially important for assessing coastal erosion based on cliff-top lines derived from steep sensor-facing coast classifications.

The Sentinel 1 user's accuracy values in case of the cliff class (areas with foreshortening), ranging from 7 to 18%, are relatively low. Independent from the polarization, only land samples were misclassified as cliffs. TerraSAR-X user's accuracy is also 100%. The area covered by the acquisitions is comparably small and does not include any mountain ranges. Water–land misclassification occurs for all sensors and polarizations due to wave action. The magnitude can be expected to vary with meteorological conditions and therefore results cannot be generalized.

3.3. Coastal Change Rates

All of the results show erosion, which indicates that the selected areas were predominately eroding as expected (**Table 5**). The calculated rates for the same regions based on images from different sensors are mostly in the same order of magnitude. Values range mostly between 3 and 9 m/year. Uncertainty values reflect the impact of spatial resolution and time interval. Values are small (less than one meter) for TerraSAR-X and comparably low for PALSAR/PALSAR-2 retrievals for 2007–2018 (0.4–4.3m) compared to annual changes (mostly more than 10 m).

Short term (year to year) rates are often higher than the long-term rates but have much higher uncertainties. Deviations from Landsat derived rates and values published in the literature are in general higher for the land-water boundary estimates compared to the cliff-top derived rates. In case of the Bykovsky peninsula, all satellite derived rates (radar as well as optical) are higher than reported before. Kay Point estimates agree with the maximum recorded for this area for 1990–2011 (Irrgang et al., 2018). The differences suggest also higher rates in recent years for this site. Cliff-top retreat rates are lower than the corresponding land-water boundary changes at the Herschel site. They are largely similar in case of Bykovsky.

4. DISCUSSION

4.1. SAR Capabilities for Separation of Relevant Landcover Types

Our results indicate the utility of SAR data for the identification of the land-water boundary in addition to cliff-top identification as suggested by Stettner et al. (2017). The latter approach is limited to sensor facing coasts, what means that only coastal segments with orientation toward West or East can be investigated as SAR satellites are acquiring data from polar orbits. The extension of SAR application to the land-water boundary identification enables broader use. Various further issues need to be, however, considered.

In addition to the general spatial resolution issue of satellite images (pixel size usually exceeding annual retreat), implications for using SAR include the specific viewing geometry and weather conditions (specifically wind and subsequent wave action). The use of acquisitions from several sites allowed for the assessment of the maximum possible incidence angle range of the used satellites. The impact of wave action on the separability between water and land is reflected in the classification accuracy. In one case, acquisitions could not be used for erosion rate retrievals (Sentinel-1 for Bykovsky). A constraint with respect to the extent of the used Sentinel-1 acquisitions is inland steep terrain

TABLE 5 | Summary of the shoreline movement results grouped by region.

Region	Sensor	Coastline Type	Years	Mean Change Rate m/year	Ref. Change Rate m/year	Ref. Years	Refernces
Herschel Island, Avadlek	P., P.-2	Cliff-Top	07–08	-9.68 ± 17.53	-6.8±8.6	2012-2013	Obu et al., 2016
	P., P.-2	Land–Water	07–08	-45.06± 17.53			
	P., P.-2	Cliff-Top	07–18	-3.42 ± 4.32			
	P., P.-2	Land–Water	07–18	-7.02±2.65			
	P.-2	Cliff–Top	17–18	-2.61± 14.83			
	P.-2	Land–Water	17–18	-9.52 ± 11.2			
	S.-1	Cliff–Top	17–18	-0.9 ± 8.01			
	S.-1 Asc.	Land–Water	17–18	-3.26 ± 13.88			
	S.-1 Desc.	Land–Water	17–18	-27.63 ± 14.34			
	Landsat	Land–Water	99–14	-4.19 ± 2.8			
Kay Point East Coast	P.	Land–Water	07–08	-14.51 ± 8.77	-1.7 (-0.8 – -4.1)	1990-2011	Irrgang et al., 2018
	P., P.-2	Land–Water	07–18	-5.90 ± 0.41			
	P.-2	Land–Water	17–18	-3.93 ± 5.61			
	S.-1	Land–Water	17–18	-4.44 ± 6.94			
	TSX	Land–Shadow	18–19[a]	-2.58 ± 0.90			
	Landsat	Land–Water	99–14	-3.94 ± 1.4			
Bykovsky Peninsula West Coast	P.	Cliff-Top	07–08	-9.42 ± 6.06	-1 – -2	1951-2006	Lantuit et al., 2011
	P.	Land–Water	07–08	-9.84 ± 17.53			
	P., P.-2	Cliff-Top	07–18	-4.81 ± 1.37			
	P., P.-2	Land–Water	07–18	-2.69 ± 0.58			
	P.-2	Cliff–Top	17–18	-10.53 ± 10.45			
	P.-2	Land–Water	17–18	-11.75 ± 10.6			
	Landsat	Land–Water	99–14	-5.83 ± 2.8			
Varandai	P., P.-2	Land–Water	07–08	-2.9 ± 17.53	-3 – -5	2003-2013	Leont'yev, 2003
	P., P.-2	Land–Water	07–18	-5.41 ± 2.64			
	P.-2	Land–Water	17–18	-2.51 ± 14.39	-1.8	1951-2013	Sinitsyn et al., 2020
	S.-1	Land–Water	17–18	-3.00 ± 14.34			

The shoreline movements were calculated based on PALSAR (P.), PALSAR-2 (P.-2), Sentinel-1 (S.-1), and TerraSAR-X (TSX) image classifications (HH Polarization). A mean change rate <0 indicates erosion.

[a]*Classified data spanned July 2018 to January 2019.*

(Buckland Hills at the Beaufort Sea Coast site), for which the foreshortening effect is also characteristic. The extraction of cliff areas should be applied in proximity to the coast only. Sentinel-1 VH polarization is also affected by an intrinsic processing artifact called scalloping effect. This effect causes wavelike modulation of the image intensity in near-azimuth direction, and could potentially be reduced with another filtering routine (Romeiser et al., 2013), which may improve VH performance.

The rate estimates seem to have failed in two cases for the Herschel site. Both occurred for estimates from the land–water boundary. This includes PALSAR estimates for 2007–2008 and Sentinel-1 retrievals for 2017–2018. **Figure 8** demonstrates this for the case of the acquisitions of Sentinel-1. PALSAR-2 images from 2017 and 2018 are shown for comparison. The most impacted scene was acquired on the 24th of July 2018 (**Figure 8B**). Ice floes were present (visible in Sentinel-1 as well as PALSAR-2) and an area of low backscatter can be observed in the Sentinel-1 image on the base of the thaw slump affected slopes. This might be the result of late lying snow or high water level (tides or storm surge). This effect is not visible in a PALSAR-2 acquisition on the following day. In case of PALSAR-2, the coast is facing toward the sensor (ascending orbit) and that may have an impact on the backscatter level due to the foreshortening effect.

Misclassifications can be also caused by infrastructure. Buildings show high backscatter values due to foreshortening and the double-bounce effect. Smooth streets scatter almost no signal back toward the sensor (Balz and Liao, 2010). This causes misclassifications of buildings and metallic objects as steep coast and misclassifications of streets as water. The Beaufort Sea Coast and Bykovsky study areas are, however, not affected as they do not include settlements. In the Varandai region, the infrastructure misclassifications did not affect the erosion analysis because the coast is not a steep cliff. There, the land–water border was used

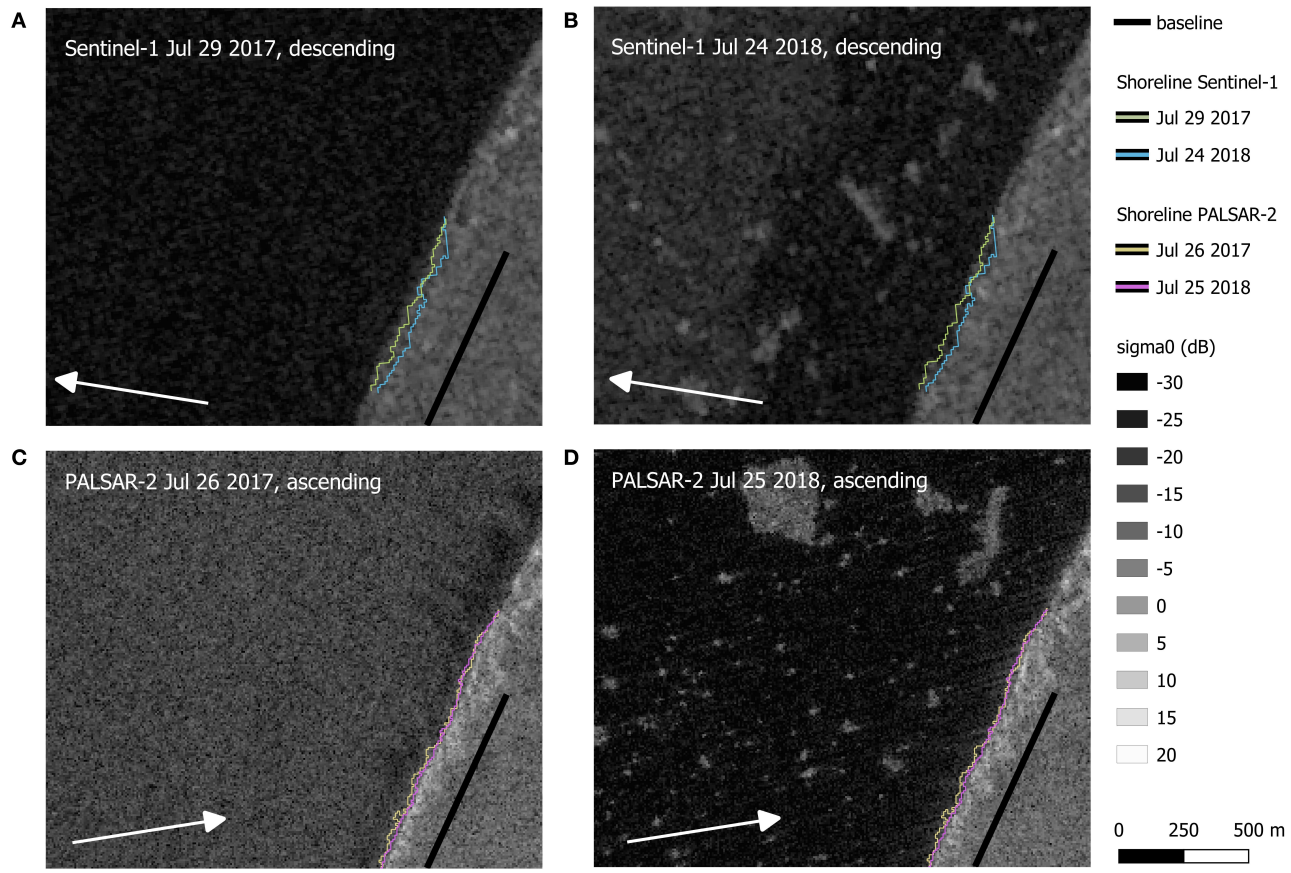

FIGURE 8 | Backscatter of Sentinel-1 (top panels **(A)** and **(B)**, acquired on descending orbit, VV polarization) and PALSAR-2 (bottom panels, **(C)** and **(D)**, acquired on ascending orbit, HH polarization) acquisitions at Avadlek (Herschel Island) for 2017 and 2018. Dates represent closest acquisitions between the two sensors for each year. Images are ellipsoid corrected only. Sensor viewing direction is indicated by arrows. Derived shorelines represent the land-water boundary. The baseline for retreat rate calculations corresponds to **Figure 2A**.

as the coastline for the erosion analysis. This issue needs to be considered for applications over larger regions.

Wide, smooth sand beaches are in general difficult to classify, especially for longer wavelengths. The roughness of the material in comparison to the wavelength is the main factor whether a specular reflection or a scattering of the wave takes place (Jones and Vaughan, 2010). Like calm water, sand is a relatively smooth surface in comparison to the C- and L-band wavelengths, and the microwave signal is reflected in a single beam that is not directed toward the sensor. Furthermore, the radar backscatter depends on the geometric and dielectric properties of the surface. Sand has in general a very low dielectric constant, so the microwaves penetrate deep into the material. This effect further reduces the backscatter signal (Stephen and Long, 2005). This makes SAR classification of sandy areas, like parts of the Barents Sea coast, challenging. The temporal stability of the low surface roughness of these areas may, however, be of benefit for separation of sandy areas from water affected by wave action (rough surface).

Banks et al. (2014) found that for C-band the best separability of sandy areas from water was given with images in HH polarization with shallow (45.3°–49.5°) and medium (39.3°) incidence angles. However, images with steep (20.9°–24.2°) incidence angles tend to bring better separability results in VV and HV polarizations. This incidence angle range is however not available from Sentinel-1.

Wet snow can impact the classification result as shown in **Figure 9** for TerraSAR-X near King Point. Snow has been still present at the June acquisition date in 2018. A comparison with the Sentinel-2 optical images demonstrates that some pixels, which were classified as water, correspond to the location of late lying snow patches. The mean temperature around 2018-06-15 in that area hovered slightly above 0°C (Government Canada, 2019), indicating that the snow was melting. Like open water, wet snow is characterized by low backscatter. Wet snow typically absorbs the microwave signal and reduces the backscatter intensity significantly (further TerraSAR-X examples in similar settings: Antonova et al., 2016; Mora et al., 2017; Stettner et al., 2018), which caused the false classification result.

Results indicate that also radar shadow areas can be used to quantify erosion rates in case that the spatial resolution allows clear separation. This enables identification of the cliff tops in

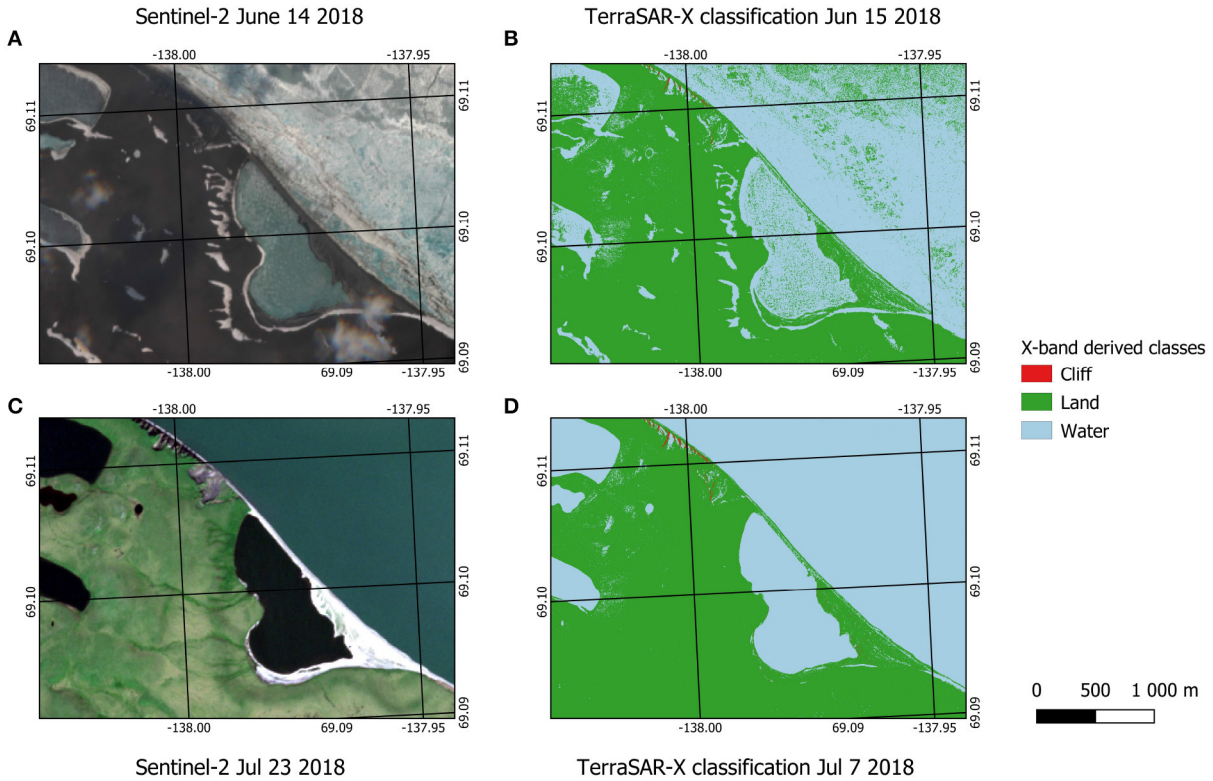

FIGURE 9 | The influence of snow and ice on the classification result of TerraSAR-X at King Point (20 km south of Kay Point). Left **(A)** and **(C)**: RGB (band 4, 3, and 2) composites of Sentinel-2; right **(B)** and **(D)**: TerraSAR-X derived classes. Snow on land is classified as water (wet snow - low backscatter) and sea ice is partially classified as land (higher backscatter than open water). Sentinel-2 acquisitions represent closest available to TerraSAR-X acquisition.

case of bluffs facing away from the sensor in summer as well as winter. Retrievals for X-band indicate that identification of cliff-tops facing the sensor (separation from land) might be more reliable with acquisitions from the unfrozen and snow-free period as not only the foreshortening effect plays a role for the higher backscatter. Exposed wet soils contribute as well, leading to a drop in backscatter in winter (see **Figure 5**). The winter- summer difference at Kay Point is larger than reported in Stettner et al. (2017).

The limitation of the analysis to the ellipsoid correction allows to account for the lack of accurate digital elevation model time series. Direct comparisons between results from different viewing geometries, however, can not be made. Only the quantification of relative change is feasible, which impacts combinations with other data sources and an exact assignment to coastlines. A characterization of coastal segments (as in Lantuit et al., 2012) should be nevertheless feasible.

The high uncertainty values of the PALSAR-2 and Sentinel-1 results might be caused by the spatial resolution, which also affects which erosion processes can be monitored. Choosing a transect distance much lower than the spatial resolution will not improve the calculation results. Therefore, only erosion features larger or equal to the spatial resolution of the image can be captured. The differences in derived rates between the sensors may be also explained by the fact that the calculations assess slightly different areas due to their comparably coarse spatial resolution (mixed pixel effects) and differences in classification accuracy. The different acquisition timing also adds to that.

It would be interesting to compare change rates based on 2007–2018 C-band data with the calculated rates based on 2007–2018 PALSAR/PALSAR-2 L-band data. Unfortunately, only coarse resolution (30 m) data for the areas of interest are available for ENVISAT and ERS-1/2 (the predecessor satellites of Sentinel-1) (ESA, 2019a). Both of these SAR missions acquired data in VV polarization, which we could show to be suitable for the identification of the land-water boundary. Such data could be therefore used to derive long-term trends similar to Landsat, going back as far as 1991. Coverage across the Arctic is, however, limited due to the acquisition strategies of these missions. Future studies could include data from the operationally focused Canadian RADARSAT-2 satellite. Images with a higher resolution than 30 m were acquired for some study areas (e.g., Herschel Island) between 2008–2019 (MDA, 2019).

4.2. Erosion Rates

The only available study to date using SAR data for Arctic erosion rates was carried out for a river bank with TerraSAR-X. Stettner et al. (2017) calculated 22-day cliff-top movements based on a threshold classification for an ice-rich riverbank situated in the Lena Delta. The statistically determined threshold (cliff vs. land)

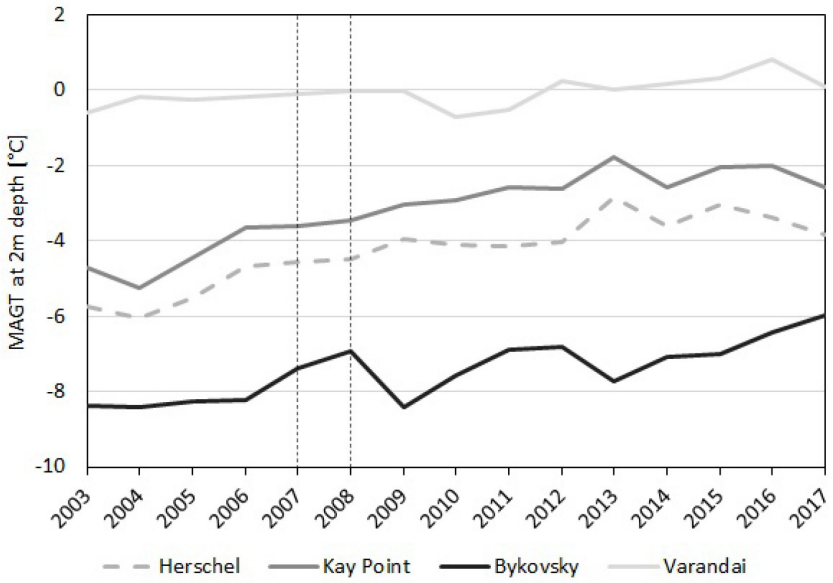

FIGURE 10 | Mean annual ground temperature (MAGT) at 2 m depth for 2003–2017 (source: Obu et al., 2019a). Vertical dashed lines indicate years with PALSAR acquisitions.

for this study (approximately −2.5 dB for 31°) is higher than in Stettner et al. (2017) which determined −7.8 dB for HH (31°) based on visual evaluation. This difference may relate to mode characteristics (staring spot light in this study vs. stripmap mode in Stettner et al., 2017), strength of the foreshortening effect, and surface wetness apart from the consideration of surface type specific noise. The −7.8 dB threshold is still well above the land (tundra) average (∼ −11 dB), but within one standard deviation.

Results for the Beaufort Sea Coast (Kay Point) are similar to results published by Irrgang et al. (2018) (**Table 5**). They calculated shoreline movements of the Yukon Coast based on aerial and satellite images between the years 1951 and 2011. Average rates for the entire coast segment are in the order of the maximum in case of all sensors, specifically PALSAR-1/2 and Landsat which provide long-term rates with lower uncertainties than the annual retrievals. The differences suggest higher rates in recent years for this site, but the uncertainties (±−0.4 m and ±−1.4 m, respectively) are still high compared to the observed range in Irrgang et al. (2018, −0.8 to −4.1 m).

Obu et al. (2016) used aerial lidar elevation data from 2012 and 2013 with a horizontal resolution of 1 m to study short-term coastal erosion at the Yukon Coast including Herschel Island. Rates are reported for the land-water boundary. The results are also consistent with this study. Their calculated coastline movement for this area is −6.8 m/year (Obu et al., 2016), which is similar to the long-term results (2007–2018) of this study (−7.02 m/year). Landsat estimates are, however, lower with −4.19 m/year for the period 1999–2014. Mean annual ground temperature has been increasing by 3°C from 2003 to 2017 (**Figure 10**). This may suggest higher rates in recent years, but differences in spatial resolution may reduce the comparability of results. Larger fluctuations from year to year within the different analyses periods could also contribute to this difference.

Coastal erosion dynamics on Bykovsky Peninsula were calculated between 1951 and 2006 by Lantuit et al. (2011). They analyzed airborne and spaceborne optical images and calculated the annual erosion rates. Rates of up to 2 m/year (Lantuit et al., 2011) were determined at the coastal stretch selected in our study. The agreement among the sensors for the recent development (up to about 10 m/year) suggests an increase of erosion activity at this site as well, but uncertainties are also very high (**Table 5**). However, this agrees with findings by Günther et al. (2015) at the nearby Muostakh island for 2010–2013. The time series of mean annual ground temperature indicates an increase of 2°C in this region between 2003 and 2017 (**Figure 10**).

While cliff-top retreat (thermo-denudation) was faster than the land-water boundary change (thermo-abrasion) at Muostakh (10.2 m vs. 3.4 m/year), it appears rather similar at the Bykovsky site (**Table 5**). The analyzed Muostakh sections face mostly North-East, whereas the Bykovsky site exposition is West. As thermo-abrasion conditions thermo-denudation (Günther et al., 2015), the differences among the sites (also compared to Herschel where the land-water boundary change exceeds cliff top retreat) may represent different stages of interaction. The analyses of longer time series with annual resolution might provide more insight into the related mechanisms and dependencies.

Leont'yev (2003) predicted that the open coast of Varandai would retreat 300 to 500 m over the next century, or 3 to 5 m/year. This study's calculated 2007–2018 erosion rate of 5.41 m/year is slightly faster than Leont'yev's rate, but matches within the uncertainty. Surprisingly, the two year-to-year rates calculated in this study were very close to Leont'yev's rate, even though their

uncertainties are still extremely large. As mentioned before, it is challenging to distinguish between tidal and wave motion and erosion processes in sand areas without vegetation or cliffs. The tidal motion can cause calculation errors as the position of the land-water boundary is affected. Rates for 1951–2013 as reported by Sinitsyn et al. (2020) are lower with 1.8 m/years. Rates seem to have increased at Varandai as well. The rates in 2007/8 and 2017/18 are similar (about 3m) as was also mean annual ground temperature (**Figure 10**).

5. CONCLUSIONS

In general, the calculation of long-term shoreline movements of sensor facing steep coasts in the Arctic based on a threshold classification seems to be a promising approach. The calculated rates based on PALSAR/PALSAR-2 L-band images between 2007 and 2018 seem to bring reasonable results. The uncertainties are, however, high for the prediction of short-term trends based on Sentinel-1 and PALSAR-2 images, which have comparably low-resolution (10 and 12.5 m nominal resolution, respectively) with respect to actual erosion rates. This may be improved by using more than one image per year. Another limitation of such resolution is that only erosion features equal to or greater than the resolution of the image can be detected.

In addition to Stettner et al. (2017), who focused on cliffs facing the sensor, we demonstrated the utility of SAR data for separation of the land-water boundary at Arctic coasts. This expands the potential of SAR application, as sensor facing cliffs are only relevant in case of (1) presence of cliffs and (2) coast orientation toward the West or the East. The identification of such coastal segments can be based on using existing landcover datasets in conjunction with orbit inclination information as presented in this paper.

The comparison of the classification results with optical data revealed several issues: snow, wide sand beaches, and infrastructure. In the classification results, wet snow was misclassified as water, which made classifications during snow melt difficult. Late lying snow patches can also occur at North-facing slopes. In future work, including a threshold function to determine snow melt may help avoid possible misclassifications.

Classification is also complicated by smooth sand beaches. The sand backscatter values of long-wave C-band and L-band microwaves are relatively low, which makes the distinction between water and sand challenging. Future studies may overcome this by introducing an additional class for land, by distinguishing between sandy areas and undisturbed tundra.

A comparison of the PALSAR/PALSAR-2 L-band long-term results of this study with RADARSAT-2 C-band long-term results would be an interesting approach for future studies. Also, the calculation of seasonal trends with TerraSAR-X data in a region with more active erosion would be a promising application, which should be investigated. The threshold based method can help to better understand the seasonal, annual, and inter-annual Arctic coastline dynamics, and it provides additional information that complements the optical and *in situ* methods. In a further step machine-learning methods can be introduced to analyze coastlines with a higher degree of automation and reliability.

The consideration of incidence angles to distinguish relevant surface types is required for cliff-land as well as land-water discrimination in case of L-band. In case of C-band it is only required for land-water discrimination. The variation of backscatter in X-band data is specifically high for water. But our results suggest that incidence angle dependencies are not required to be considered for this type of application of X-band data at HH polarization. High incidence angles might be of benefit due to the impact of incidence angle on spatial resolution in staring spot light mode.

Specifically L-band data could be shown of benefit due to their lower sensitivity to wave action. C-band, specifically Sentinel-1, can be, however, also utilized and provides similar estimates like other sensors in case of calm sea. Several future L-band SAR missions are currently in planning [NISAR, ROSE-L NASA (2019), Pierdicca et al. (2019)] which could be of interest for coastal erosion studies over larger areas in the future. The post processed Landsat derived trends provide an additional source for longterm monitoring, specifically for automatic retrieval across the entire Arctic. This could be complemented by ENVISAT and ERS-1/2 C-band SAR data for the period 1991 to 2012. Superior regarding spatial resolution and at the same time also illumination independence is TerraSAR-X. The nominal resolution of 1 m or better may not only allow determination of sub-seasonal retreat rates at some of the sites, but also the separation of radar shadow at high bluffs enables the identification of the cliff-top position.

DATA AVAILABILITY STATEMENT

The raw data supporting the conclusions of this article will be made available by the authors, without undue reservation.

AUTHOR CONTRIBUTIONS

AB contributed conception and design of the study. SL organized the database. SL, AB, and GP performed the SAR data and statistical analysis. IN performed the Landsat data trend analysis, AB the post-processing. AB and SL wrote the first draft of the manuscript. GV supported procurement and selection of TerraSAR-X sites and acquisitions. All authors contributed to manuscript revision, read and approved the submitted version.

FUNDING

The authors acknowledge financial support by the HORIZON2020 (BG-2017-1) project Nunataryuk, ESA's DUE GlobPermafrost project (Contract Number 4000116196/15/I-NB), ESA's CCI+ Permafrost (4000123681/18/I-NB), the FFG FemTech projects CoastSAR (874213) and CoastAIMap (880182).

ACKNOWLEDGMENTS

We acknowledge the coordination of TerraSAR-X acquisitions through the WMO Polar Space Task Group, specifically Achim Roth. All TerraSAR-X data were made available by the German Aerospace Center (DLR) through PI agreement COA3645. All ALOS PALSAR and PALSAR-2 data were made available by the Japanese Space Agency (JAXA) through PI agreement 3068002. Results are partially based on modified Copernicus data from 2017 to 2018. We further thank Aleksandra Efimova (b.geos) for supporting part of the GIS tasks.

REFERENCES

Antonova, S., Duguay, C., Kaab, A., Heim, B., Langer, M., Westermann, S., and Boike, J. (2016). Monitoring bedfast ice and ice phenology in lakes of the Lena River delta using TerraSAR-X backscatter and coherent time series. *Remote Sens.* 8:903. doi: 10.3390/rs8110903

Arp, C. D., Jones, B. M., Schmutz, J. A., Urban, F. E., and Jorgenson, M. T. (2010). Two mechanisms of aquatic and terrestial habitat change along an Alaskan Arctic coastline. *Polar Biol.* 33, 1629–1640. doi: 10.1007/s00300-010-0800-5

ASF (2019). *MapReady*. Version 3.1.24. Available online at: https://www.asf.alaska.edu/data-tools/mapready

Balz, T., and Liao, M. (2010). Building-damage detection using post-seismic high-resolution SAR satellite data. *Int. J. Remote Sens.* 31, 3369–3391. doi: 10.1080/01431161003727671

Banks, S. N., King, D. J., Merzouki, A., and Duff, J. (2014). Assessing RADARSAT-2 for mapping shoreline cleanup and assessment technique (SCAT) classes in the Canadian Arctic. *Can. J. Remote Sens.* 40, 243–267. doi: 10.1080/07038992.2014.968276

Bartsch, A., Höfler, A., Kroisleitner, C., and Trofaier, A. M. (2016). Land cover mapping in northern high latitude permafrost regions with satellite data: achievements and remaining challenges. *Remote Sens.* 8:979. doi: 10.3390/rs8120979

Bartsch, A., Leibman, M., Strozzi, T., Khomutov, A., Widhalm, B., Babkina, E., et al. (2019a). Seasonal progression of ground displacement identified with satellite radar interferometry and the impact of unusually warm conditions on permafrost at the Yamal Peninsula in 2016. *Remote Sens.* 11:1865. doi: 10.3390/rs11161865

Bartsch, A., Pointner, G., Leibman, M. O., Dvornikov, Y. A., Khomutov, A. V., and Trofaier, A. M. (2017). Circumpolar mapping of ground-fast lake ice. *Front. Earth Sci.* 5:12. doi: 10.3389/feart.2017.00012

Bartsch, A., Widhalm, B., Leibman, M., Ermokhina, K., Kumpula, T., Skarin, A., et al. (2020). Feasibility of tundra vegetation height retrieval from Sentinel-1 and Sentinel-2 data. *Remote Sens. Environ.* 237:111515. doi: 10.1016/j.rse.2019.111515

Bartsch, A., Widhalm, B., Pointner, G., Ermokhina, K., Leibman, M., and Heim, B. (2019b). *Landcover Derived From Sentinel-1 and Sentinel-2 Satellite Data (2015-2018) for Subarctic and Arctic Environments*. PANGAEA. doi: 10.1594/PANGAEA.897916

Couture, N. J., Irrgang, A., Pollard, W., Lantuit, H., and Fritz, M. (2018). Coastal erosion of permafrost soils along the yukon coastal plain and fluxes of organic carbon to the Canadian Beaufort Sea. *J. Geophys. Res. Biogeosci.* 123, 406–422. doi: 10.1002/2017JG004166

Cunliffe, A. C., Tanksi, G., Radosavljevic, B., Palmer, W. F., Sachs, T., Lanuit, H., et al. (2019). Rapid retreat of permafrost coastline observed with aerial drone photogrammetry. *Cryosphere* 13, 1513–1528. doi: 10.5194/tc-13-1513-2019

Douglas, D. H., and Peucker, T. K. (1973). Algorithms for the reduction of the number of points required to represent a digitized line or its caricature. *Cartographica* 10, 112–122. doi: 10.3138/FM57-6770-U75U-7727

ESA (2012). *Sentinel-1. ESA's Radar Observatory Mission for GMES Operational Services*. Technical report.

ESA (2015). *Sentinel-2 User Handbook*. Technical report.

ESA (2019a). *ESA Online Catalogue*. Available online at: http://esar-ds.eo.esa.int/socat/ASA_IMP_1P (accessed September 1, 2019).

ESA (2019b). *Sentinel Application Platform (SNAP)*. Available online at: http://step.esa.int/main/toolboxes/snap

Forbes, D. L., Solomon, S. M., and Frobel, D. (1995). *Report of 1992 Coastal Surveys in the Beaufort Sea*. Technical report. doi: 10.4095/203482

Frederick, J. M., Thomas, M. A., Bull, D. L., Jones, C. A., and Roberts, J. D. (2016). *The Arctic Coastal Erosion Problem*. Technical report, Sandia National Laboratories. doi: 10.2172/1431492

Government Canada (2019). *Historical Climate Data*. Available online at: http://climate.weather.gc.ca/historical_data/search_historic_data_e.html (accessed July 15, 2019).

Grosse, G., Schirrmeister, L., Kunitsky, V. W., and Hubberten, H.-W. (2005). The use of CORONA images in remote sensing of periglacial geomorphology: an illustration from the NE Sibirian Coast. *Permafrost Periglacial Process.* 16, 163–172. doi: 10.1002/ppp.509

Guégan, E. B. M., and Christiansen, H. H. (2016). Seasonal arctic coastal bluff dynamics in Adventfjorden, Svalbard. *Permafrost Periglacial Process.* 28, 18–31. doi: 10.1002/ppp.1891

Günther, F., Overduin, P. P., Sandakov, A. V., Grosse, G., and Grigoriev, M. N. (2013). Short- and long-term thermo-erosion of ice-rich permafrost coasts in the Laptev Sea region. *Biogeosciences* 10, 4297–4318. doi: 10.5194/bg-10-4297-2013

Günther, F., Overduin, P. P., Yakshina, L. A., Opel, T., Baranskaya, A. V., and Grigoriev, M. N. (2015). Observing Muostakh disappear: permafrost thaw subsidence and erosion of a ground-ice-rich island in response to arctic summer warming and sea ice reduction. *Cryosphere* 9, 151–178. doi: 10.5194/tc-9-151-2015

Hequette, A., Ruz, M.-H., and Hill, P. R. (1995). The effects of the Holocene sea-level rise on the evolution of the southeastern coast of the Canadian Beaufort Sea. *J. Coast. Res.* 11, 494–507.

Himmelstoss, E. A., Henderson, R. E., Kratzmann, M. G., and Farris, A. S. (2018). *Digital Shoreline Analysis System (DSAS)*. Version 5.0 User Guide. USGS. doi: 10.3133/ofr20181179

Hoque, M. A., and Pollard, W. H. (2004). "Modeling block failures of vertical cliffs in the Arctic Coast. Arctic Coastal Dynamic," in *Report of the 5th International Workshop* (Montreal, QC: McGill University), 60–64.

Hoque, M. A., and Pollard, W. H. (2009). Arctic coastal retreat through block failure. *Can. Geotech. J.* 46, 1103–1115. doi: 10.1139/T09-058

Irrgang, A. M., Lantuit, H., Gordon, R. R., Piskor, A., and Manson, G. K. (2019). Impacts of past and future coastal changes on the Yukon coast-threats for cultural sites, infrastructure, and travel routes. *Arctic Sci.* 5, 107–126. doi: 10.1139/as-2017-0041

Irrgang, A. M., Lantuit, H., Manson, G. K., Günther, F., Grosse, G., and Overduin, P. P. (2017). Quantification of shoreline movements along the Yukon territory mainland coast between 1951 and 2011, supplement to: Irrgang, anna maria; lantuit, hugues; manson, gavin k; guenther, frank; grosse, guido; overduin, pier paul (2018): Variability in rates of coastal change along the yukon coast, 1951 to 2015. *J. Geophys. Res. Earth Surface* 123, 779–800. doi: 10.1594/PANGAEA.874343

Irrgang, A. M., Lantuit, H., Manson, G. K., Günther, F., Grosse, G., and Overduin, P. P. (2018). Variability in Rates of Coastal Change Along the Yukon coast, 1951 to 2015. *J. Geophys. Res. Earth Surface* 123, 779–800. doi: 10.1002/2017JF004326

JAXA (2008). *ALOS Data Users Handbook. Revision C*. Tokyo.

JAXA (2018). *ALOS-2 Solution Book. Proposals for 'DAICHI 2' SAR Data Utilization, 3rd Edn*. Tokyo.

Jones, B., Hinkel, K. M., Arp, C. D., and Eisner, W. R. (2008). Modern erosion rates and loss of coastal features and sites, Beaufort Sea Coastline, Alaska. *Arctic* 61, 361–372. doi: 10.14430/arctic44

Jones, G. H., and Vaughan, R. A. (2010). *Remote Sensing of Vegetation. Principles, Techniques and Applications*. New York, NY: Oxford University Press.

Kroon, A. (2014). "Chapter 14: High-Latitude Coasts," in *Coastal Environments and Global Change*, eds G. Masselink and R. Gehrels (Chichester: John Wily & Sons), 338–353. doi: 10.1002/9781119117261.ch14

Lantuit, H. (2008). *The modification of arctic permafrost coastlines* (Ph.D. thesis). Universität Potsdam, Potsdam, Germany.

Lantuit, H., Atkinson, D., Overduin, P. P., Grigoriew, M., Rachold, V., Grosse, G., and Hubberten, H.-W. (2011). Coastal erosion dynamics on the permafrost-dominated Bykovsky Peninsula, north Siberia, 1951-2006. *Polar Res.* 30:7341. doi: 10.3402/polar.v30i0.7341

Lantuit, H., Overduin, P. P., Couture, N., Wetterich, S., Aré, F., Atkinson, D., et al. (2012). The Arctic Coastal Dynamics Database: A New Classification Scheme and Statistics on Arctic Permafrost Coastlines. *Estuar. Coasts* 35, 383–400. doi: 10.1007/s12237-010-9362-6

Le, T. M. H., Depina, I., Guegan, E., and Sinitsyn, A. (2018). Thermal regime of permafrost at Varandey Settlement along the Barents Sea Coast, North West Arctic Russia. *Eng. Geol.* 246, 69–81. doi: 10.1016/j.enggeo.2018.09.026

Lee, J.-S., Wen, J.-W., Ainsworth, T. L., Chen, K.-S., and Chen, A. (2009). Improved sigma filter for speckle filtering of SAR imagery. *IEEE Trans. Geosci. Remote Sens.* 47, 202–213. doi: 10.1109/TGRS.2008.2002881

Leont'yev, I. O. (2003). Modeling erosion of sedimentary coasts in the western Russian Arctic. *Coast. Eng.* 47, 413–429. doi: 10.1016/S0378-3839(02)00145-X

Liu, L., Schaefer, K., Zhang, T., and Wahr, J. (2012). Estimating 1992-2000 average active layer thickness on the Alaskan north slope from remotely sensed surface subsidence. *J. Geophys. Res. Earth Surface* 117:F01005. doi: 10.1029/2011JF002041

MDA (2019). *MDA's RADARSAT-2 Portal*. Available online at: https://mdacorporation.com/geospatial/international/radarsat-portal (accessed September 1, 2019).

Mentaschi, L., Vousdoukas, M. I., Pekel, J.-F., Voukouvalas, E., and Feyen, L. (2018). Global long-term observations of coastal erosion and accretion. *Sci. Rep.* 8:12876. doi: 10.1038/s41598-018-30904-w

Mora, C., Jiménez, J. J., Pina, P., Catalão, J., and Vieira, G. (2017). Evaluation of single-band snow-patch mapping using high-resolution microwave remote sensing: an application in the maritime Antarctic. *Cryosphere* 11, 139–155. doi: 10.5194/tc-11-139-2017

NASA (2019). *NASA-ISRO SAR (NISAR) Mission Science Users' Handbook*. CL# 18-1893, JPL 400-1707 08/19. California, CA: Jet Propulsion Laboratory; California Institute of Technology Pasadena.

Nielsen, D. M., Dobrynin, M., Baehr, J., Razumov, S., and Grigoriev, M. (2020). Coastal erosion variability at the southern Laptev Sea linked to winter sea ice and the Arctic oscillation. *Geophys. Res. Lett.* 47:e2019GL086876. doi: 10.1029/2019GL086876

Nitze, I. (2018). *Trends of Land Surface Change Fromlandsat Time-Series 1999-2014*. PANGAEA - Data Publisher for Earth & Environmental Science. doi: 10.1594/PANGAEA.884137

Nitze, I., Grosse, G., Jones, B., Arp, C., Ulrich, M., Fedorov, A., et al. (2017). Landsat-based trend analysis of lake dynamics across northern permafrost regions. *Remote Sens.* 9:640. doi: 10.3390/rs9070640

Nitze, I., Grosse, G., Jones, B. M., Romanovsky, V. E., and Boike, J. (2018). Remote sensing quantifies widespread abundance of permafrost region disturbances across the Arctic and Subarctic. *Nat. Commun.* 9:5423. doi: 10.1038/s41467-018-07663-3

Obu, J., Lantuit, H., Grosse, G., Günther, F., Sachs, T., Helm, V., et al. (2016). Coast erosion and mass wasting along the Canadian Beaufort Seas based on annual airborne LiDAR elevation data. *Geomorphology* 293, 331–346. doi: 10.1016/j.geomorph.2016.02.014

Obu, J., Westermann, S., Barboux, C., Bartsch, A., Delaloye, R., Grosse, G., et al. (2019a). *ESA Permafrost Climate Change Initiative (Permafrost_cci): Permafrost Ground Temperature for the Northern Hemisphere*, Centre for Environmental Data Analysis (CEDA). doi: 10.5285/9A333481E9A34C7A8F78902F77AD3FE7

Obu, J., Westermann, S., Bartsch, A., Berdnikov, N., Christiansen, H. H., Dashtseren, A., et al. (2019b). Northern hemisphere permafrost map based on TTOP modelling for 2000-2016 at 1 km2 scale. *Earth Sci. Rev.* 193, 299–316. doi: 10.1016/j.earscirev.2019.04.023

Overland, J., Dunlea, E., Box, J. E., Corell, R., Forsius, M., Kattsov, V., et al. (2019). The urgency of Arctic change. *Polar Sci.* 21, 6–13. doi: 10.1016/j.polar.2018.11.008

Pierdicca, N., Davidson, M., Chini, M., Dierking, W., Djavidnia, S., Haarpaintner, J., et al. (2019). "The Copernicus L-band SAR mission ROSE-L (Radar Observing System for Europe) (Conference Presentation)," in *Proc. SPIE 11154, Active and Passive Microwave Remote Sensing for Environmental Monitoring III*. doi: 10.1117/12.2534743

Radosavljevic, B., Lantuit, H., Pollard, W., Overduin, P., Couture, N., Sachs, T., et al. (2016). Erosion and flooding–threats to coastal infrastructure in the Arctic: a case study from Herschel Island, Yukon Territory, Canada. *Estuar. Coasts* 39, 900–915. doi: 10.1007/s12237-015-0046-0

Romeiser, R., Horstmann, J., Caruso, M. J., and Graber, H. C. (2013). A descalloping postprocessor for ScanSAR images of ocean scenes. *IEEE Trans. Geosci. Remote Sens.* 51, 3259–3272. doi: 10.1109/TGRS.2012.2222648

Schubert, A., Miranda, N., Geudtner, D., and Small, D. (2017). Sentinel-1A/B combined product geolocation accuracy. *Remote Sens.* 9:607. doi: 10.3390/rs9060607

Schuster, P. F., Schaefer, K. M., Aiken, G. R., Antweiler, R. C., Dewild, J. F., Gryziec, J. D., et al. (2018). Permafrost stores a globally significant amount of mercury. *Geophys. Res. Lett.* 45, 1463–1471. doi: 10.1002/2017GL075571

Shimada, M. (2009). "Advance land-observation satellite (ALOS) and its follow-on satellite, ALOS-2," in *Proceedings of the 4th International POLinSAR 2009 Workshop, ESA/ESRIN* (Frascati).

Short, N., Brisco, B., Couture, N., Pollard, W., Murnaghan, K., and Budkewitsch, P. (2011). A comparison of TerraSAR-X, RASARSAT-2 and ALOS-PALSAR interferometry for monitoring permafrost environments, case study from Herschel Island, Canada. *Remote Sens. Environ.* 115, 3491–3506. doi: 10.1016/j.rse.2011.08.012

Sinitsyn, A. O., Guegan, E., Shabanova, N., Kokin, O., and Ogorodov, S. (2020). Fifty four years of coastal erosion and hydrometeorological parameters in the Varandey region, Barents Sea. *Coast. Eng.* 157:103610. doi: 10.1016/j.coastaleng.2019.103610

Solomon, S. M. (2005). Spatial and temporal variability of shoreline change in the Beaufort-Mackenzie region, northwest territories, Canada. *Geomar. Lett.* 25, 127–137. doi: 10.1007/s00367-004-0194-x

Steele, M., Ermold, W., and Zhang, J. (2008). Arctic Ocean surface warming trends over the past 100 years. *Geophys. Res. Lett.* 35:L02614. doi: 10.1029/2007GL031651

Stephen, H., and Long, D. G. (2005). Microwave backscatter modeling of erg surfaces in the Sahara Desert. *IEEE Trans. Geosci. Remote Sens.* 43, 238–247. doi: 10.1109/TGRS.2004.840646

Stettner, S., Beamish, A., Bartsch, A., Heim, B., Grosse, G., Roth, A., et al. (2017). Monitoring inter- and intra-seasonal dynamics of rapidly degrading ice-rich permafrost riverbanks in the Lena Delta with TerraSAR-x time series. *Remote Sens.* 10:51. doi: 10.3390/rs10010051

Stettner, S., Lantuit, H., Heim, B., Eppler, J., Roth, A., Bartsch, A., et al. (2018). TerraSAR-X time series fill a gap in spaceborne snowmelt monitoring of small arctic catchments–a case study on Qikiqtaruk (Herschel Island), Canada. *Remote Sens.* 10:1155. doi: 10.3390/rs10071155

Strozzi, T., Antonova, S., Günther, F., Mätzler, E., Vieira, G., Wegmüller, U., et al. (2018). Sentinel-1 SAR interferometry for surface deformation monitoring in low-land permafrost areas. *Remote Sens.* 10:1360. doi: 10.3390/rs10091360

Widhalm, B., Bartsch, A., and Goler, R. (2018). Simplified normalization of C-band synthetic aperture radar data for terrestrial applications in high latitude environments. *Remote Sens.* 10:551. doi: 10.3390/rs10040551

Zwieback, S., Kokelj, S. V., Günther, F., Boike, J., Grosse, G., and Hajnsek, I. (2018). Sub-seasonal thaw slump mass wasting is not consistently energy limited at the landscape scale. *Cryosphere* 12, 549–564. doi: 10.5194/tc-12-549-2018

Conflict of Interest: The authors declare that the research was conducted in the absence of any commercial or financial relationships that could be construed as a potential conflict of interest.

frontiers in Earth Science

ORIGINAL RESEARCH
published: 08 October 2020
doi: 10.3389/feart.2020.561322

Effective Monitoring of Permafrost Coast Erosion: Wide-scale Storm Impacts on Outer Islands in the Mackenzie Delta Area

Michael Lim[1], Dustin Whalen[2], Paul J. Mann[1], Paul Fraser[2], Heather Bay Berry[3], Charlotte Irish[4], Kendyce Cockney[4] and John Woodward[1]*

[1]Engineering and Environment, Northumbria University, Newcastle Upon Tyne, United Kingdom, [2]Natural Resources Canada, Geological Survey of Canada–Atlantic, Dartmouth, NS, Canada, [3]Department of Earth and Environmental Sciences, Dalhousie University, Halifax, NS, Canada, [4]Tuktoyaktuk Climate Resilience Project, Tuktoyaktuk, NWT, Canada

Permafrost coasts are extensive in scale and complex in nature, resulting in particular challenges for understanding how they respond to both long-term shifts in climate and short-term extreme weather events. Taking examples from the Canadian Beaufort Sea coastline characterized by extensive areas of massive ground ice within slump and block failure complexes, we conduct a quantitative analysis of the practical performance of helicopter-based photogrammetry. The results demonstrate that large scale (>1 km^2) surface models can be achieved at comparable accuracy to standard unmanned aerial vehicle surveys, but 36 times faster. Large scale models have greater potential for progressive alignment and contrast issues and so breaking down image sequences into coherent chunks has been found the most effective technique for accurate landscape reconstructions. The approach has subsequently been applied in a responsive acquisition immediately before and after a large storm event and during conditions (wind gusts >50 km h^{-1}) that would have prohibited unmanned aerial vehicle data acquisition. Trading lower resolution surface models for large scale coverage and more effective responsive monitoring, the helicopter-based data have been applied to assess storm driven-change across the exposed outer islands of the Mackenzie Delta area for the first time. These data show that the main storm impacts were concentrated on exposed North orientated permafrost cliff sections (particularly low cliffs, >20 m in height) where cliff recession was 43% of annual rates and in places up to 29% of the annual site-wide erosion volume was recorded in this single event. In contrast, the thaw-slump complexes remained relatively unaffected, debris flow fans were generally more resistant to storm erosion than the ice-rich cliffs, perhaps due to the relatively low amounts of precipitation that occurred. Therefore, the variability of permafrost coast erosion rates is controlled by interactions between both the forcing conditions and local response mechanisms. Helicopter-based photogrammetric surveys have the potential to effectively analyze these controls with greater spatial and temporal consistency across more representative scales and resolutions than has previously been achieved, improving the capacity to adequately constrain and ultimately project future Arctic coast sensitivity.

OPEN ACCESS

Edited by:
Davide Tiranti, Agenzia Regionale per la Protezione Ambientale (ARPA), Italy

Reviewed by:
Fabio Matano, National Research Council (CNR), Italy
Frank Günther, University of Potsdam, Germany

***Correspondence:**
Michael Lim
michael.lim@northumbria.ac.uk

Specialty section:
This article was submitted to Quaternary Science, Geomorphology and Paleoenvironment, a section of the journal Frontiers in Earth Science

Received: *13 May 2020*
Accepted: *16 September 2020*
Published: *08 October 2020*

Citation:
Lim M, Whalen D, J. Mann P, Fraser P, Berry HB, Irish C, Cockney K and Woodward J (2020) Effective Monitoring of Permafrost Coast Erosion: Wide-scale Storm Impacts on Outer Islands in the Mackenzie Delta Area. Front. Earth Sci. 8:561322. doi: 10.3389/feart.2020.561322

Keywords: arctic storms, permafrost coasts, volumetric erosion monitoring, photogrammetric surveys, regional scale impacts, arctic community resilience

INTRODUCTION

An increase in storm intensity resulting from rising air temperatures has been widely reported across the Arctic (Pisaric et al., 2011; Small et al., 2011), and has potentially shifted the Beaufort Sea to a "new normal" climatic state (Wood et al., 2013). Despite a limited ice-free season when erosion can occur, pan-Arctic long-term recession rates are high relative to other coastlines (Lantuit et al., 2012). Concerns have been raised over the potential for accelerated rates of erosion in permafrost coasts in particular (Wobus et al., 2011; Radosavljevic et al., 2016), but both the spatial (Maslakov and Kraev, 2016; Overduin et al., 2016) and the temporal (Günther et al., 2013; Nielsen et al., 2020) variability noted have proven challenging to accurately model and assess (Fritz et al., 2017). A key element of uncertainty within the quantification of erosion rates originates in the approaches used to monitor change. There is generally a dichotomy of scales of investigation based on frequent, local and detailed studies, or infrequent (annual at best) wide-scale assessments that simplify the coastal zone into a single retreating line, usually denoted by the shore or cliff top (Günther et al., 2013). Position mapping from satellite images often focuses on landward recession rates as the primary indicator of coastal change, but volume estimates can be derived if surface topography is accounted for (Novikova et al., 2018), and these metrics have been comprehensively investigated by (Obu et al., 2016). Satellite imagery is limited for responding to short-term events such as storms (Cunliffe et al., 2019), although visual data is available at increasingly high frequency (Nitze and Grosse, 2016).

The capacity to consistently measure detailed volumetric change over wide regions or large coherent sites is generally limited to lidar surveys (Obu et al., 2017), which are effective but require a dedicated survey vehicle and are cost-prohibitive for frequent or responsive surveys. Long-range fixed wing unmanned aerial vehicle (UAV) systems such as the Griffon Aerospace Outlaw Seahunter, with a maximum possible range of 100 km, are being used to map the Inuvik to Tuktoyaktuk highway but require restrictive pre-arranged notice to be filed with the aviation authority and are generally limited to fair weather conditions. The current state of the art coastal monitoring approach for the challenging and expansive Beaufort Sea coastline is to access remote outer islands and key community or type sites via helicopter in order to undertake detailed photogrammetric UAV surveys of failure complexes (Cunliffe et al., 2019). This approach provides vital data on these sensitive geoindicators of climatic change and helps inform community resilience and decision making (Van der Sluijs et al., 2018). However, it relies on the expert knowledge to identify which areas to concentrate on and leads to a fragmented patchwork of detailed monitoring sites rather than a coherent picture of processes of geomorphic change (Grosse et al., 2016).

Single storm events have the potential to produce short-term order of magnitude increases in erosion rates (Solomon, 2005), but questions remain over how localized these impacts are, whether specific sites are more susceptible to storm-driven change and if storm characteristics (duration, precipitation, wind speed and direction) result in quantifiable differences in landscape responses. The effects of both short-term, high magnitude events and long-term trends on processes beyond the landward retreat of the coast, such as thaw-induced subsidence or transitions to new failure mechanisms, cannot be convincingly addressed with current datasets. Here we examine the potential of helicopter-based SfM surveys as a new, effective approach for wide-scale volumetric coastal change monitoring. Applications using helicopter platforms for photogrammetric surveys remain very limited, particularly repeat surveys for change detection, but have achieved notable successes in generating topographic maps of inaccessible hazardous areas (Neri et al., 2017) or long linear riverscapes (Dietrich, 2016). We evaluate helicopter-based photogrammetric surveys of a key ice-rich permafrost coast type site against a model produced using standard high-resolution UAV captured images. We then apply a wide-scale pre- and post-storm survey across exposed outer islands of the Mackenzie Delta area, which is undergoing significant erosion rates (Solomon, 2005) and threatening communities (Irrgang et al., 2019).

MATERIALS AND METHODS

Field Site

The MacKenzie River Delta area of the Beaufort Sea coast is significant within the Arctic due to its rapidly changing hydrology and ecosystem dynamics (Lesack and Marsh, 2007, Lesack and Marsh, 2010); it is sea-ice and river discharge interactions (Dean et al., 1994); and its significance in supplying sediments to the Beaufort Shelf (Goñi et al., 2000). It is thought to be the largest single source of sediments in the Arctic (Rachold et al., 2000). Although future climate projections in the area contain substantial variability, a study of 18 future projections to 2,039 showed continued temperature and precipitation increases and many are already being exceeded (Bonsal and Kochtubajda, 2009), with significant trends in deeper thaw penetration also noted from 1991–2016 (O'Neill et al., 2019). Recent concerns have centered on the potentially under-estimated (O'Rourke, 2017) and accelerating rates of coastal erosion in the area (Lantuit et al., 2012; Irrgang et al., 2018), and particularly the vulnerability of communities (Alvarez et al., 2020), infrastructure (Warren et al., 2005), ecosystems (Waugh et al., 2018) and significant archaeological sites across the Inuvialuit area (O'Rourke, 2017).

Tuktoyaktuk is one of the major population centers within the Inuvialuit Regional Settlement Region (Waugh et al., 2018), and is a key area of concern due to unprecedented recent development

following the completion of the Northwest Territories Highway 10 that connects the coastal settlement to Inuvik by permanent road. Homes in Tuktoyaktuk have already been destroyed or relocated in response to coastal erosion. Erosion processes are particularly effective in the area resulting in retreat rates in excess of 0.7 m a^{-1} and high susceptibility to storms is typically observed (Solomon, 2005). Adjacent to the Tuktoyaktuk community is the Pingo National Landmark, a 16 km^2 designated site that includes massive ground ice structures at a range of scales, from microscale (<2 m height) patterned ground, through mesoscale (generally 2–30 m high) plateaus of ice layered cliffs to macroscale (>20 m high) pingos that dominate the landscape. The area is within the zone of continuous permafrost (Burn and Kokelj, 2009) and Peninsula Point is a well-documented type site for massive ground ice (Mackay and Dallimore, 1992; Lim et al., 2020) that has been used to develop and evaluate the approaches in this paper. On the evening of August 4, 2019 a storm (wind gusts >50 km h^{-1}) resulted in a surge that breached parts of the Tuktoyaktuk community and caused extensive damage to sea defenses. Both pre- and post-storm helicopter-based surveys have been conducted to quantify the changes occurring at Peninsula Point (an area of 0.27 km^2) and across the outer islands in the delta (**Figure 1**), including Pelly Island (27.29 km^2), Hooper Island (8.35 km^2) and Pullen Island (5.6 km^2).

Field Methods

For the past several decades Natural Resources Canada (NRCan) has had the responsibility of monitoring the rapid changes occurring along the Beaufort Sea coast (Solomon et al., 1994; Forbes et al., 1995). Long-term erosion rates can be approximated by mapping the cliff or shoreline position, but to address the spatial and temporal limitations of this approach, NRCan conducts frequent (annual or sub-annual) monitoring of key sites across the region using helicopter access and then detailed UAV surveys of local areas of concern. A new helicopter-based photogrammetric survey approach was developed and tested at Peninsula Point, using a UAV survey of the island undertaken the following day as a ground truth model for comparison.

Helicopter-Based Surveys: Collection and Evaluation

In order to assess the feasibility and performance of wide-scale (>1 km^2) helicopter-based photogrammetry for effective coastal monitoring, certain criteria have been used to constrain the approach development. Firstly, only non-specialist equipment has been used. Any professional surveying systems that attach to the outside of the helicopter are unlikely to be an option for long-term monitoring practice as they are prohibitively expensive, require special permission and testing for specific aircraft and would take time to install, preventing effective response times. Additionally, only survey geometry (view angles) achievable using a digital single-lens reflex camera aimed through the open window (the Bell 206B and LR and Airbus AS350B2 and AS350B3 helicopter models have been tested) because, although the door can sometimes be removed this is not always possible and often not practical for responsive monitoring data collection flights that may have multiple objectives beyond topographic surveys. Secondly, the aim of developing and evaluating a helicopter survey method is not to replicate the established procedure for UAV surveys because the approach needs to be effectively upscaled. Capturing oblique images from a helicopter negates the usual nadir images achieved from UAV surveys and the time consuming and detailed use of ground control networks is not practicable. However, check point targets, separate to reduced natural feature ground control, have been used to evaluate both helicopter and UAV based models.

A range of data collection approaches have been tested ranging from high (200 m) and steep (20° from vertical) to low (40 m) and shallow (70° from vertical) but the most successful involved high-level oblique image collection. A flying height of 120 m was used for terrain with an elevation range within approximately 20 m (and up to 150 m for cliff heights that reached 30 m). The digital

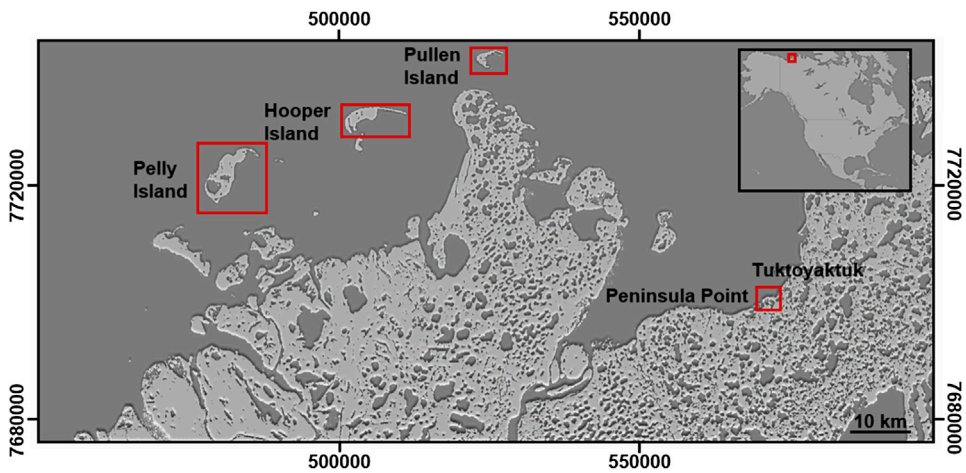

FIGURE 1 | Study area in the Mackenzie Delta area, key sites are highlighted.

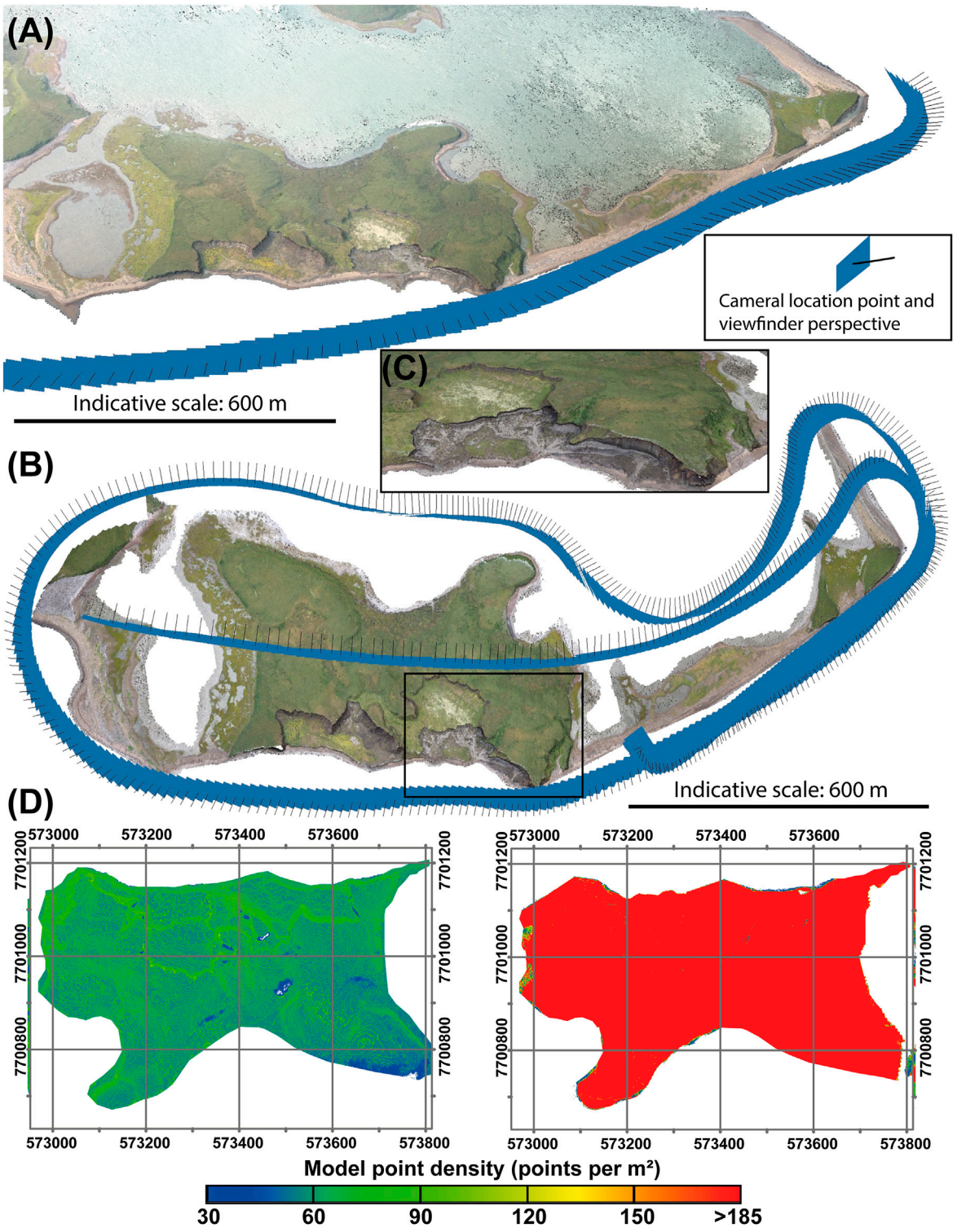

FIGURE 2 | Helicopter-based survey geometry and dense point cloud of Peninsula Point, NWT. **(A)** Coast parallel, single pass surveys produce sufficient quality digital surface point cloud models of the immediate coastal zone but beyond this model accuracies are based on increasingly oblique image matches and have greater potential for error. **(B)** In order to effectively survey the whole island a concentric collection pattern around the edge and then and oblique pass over the center of the island produced a high quality consistent DEM. **(C)** Processing has been broken down into coherent sequences of images and then iteratively converged to optimize the DEM from a combination of perspectives in areas of complex topography. **(D)** Visualization of point resolution differences in the models produced from the two helicopter survey approaches, showing the density reduction away from the coast produced by a single pass **(left)** and the denser and even coverage of the concentric survey collection **(right)**. A UTM grid is overlain for scale.

single-lens reflex used was a Sony DSC-RX10M2 linked to an intervalometer set to take images every second. With an average flying speed of 50–60 km h^{-1}, an image was captured approximately every 14–17 m. The use of this system with high speed (95 MB/s) and high capacity (64 GB) SD cards enabled long sequences (several hundred images) to be captured without buffering issues. Single passes of oblique images with an approximate angle of 40° (**Figure 2A**) generally produced enough overlap to achieve sufficient quality (i.e., they produced point cloud densities >30 ppm^2 on clearly identifiable surfaces with no doming, erroneous layers or clouds of non-surface points) DEMs of the eroding cliff and slump areas for testing. This allowed for long stretches of coastline to be surveyed in a single pass, if ground control and check points exist and the changes in coastline orientation are continuous (without sharp changes that lead to large differences in perspective between adjacent images). However, the edges (typically the outer 20%) of the swath area covered by the oblique images and resultant DEM lost image texture, point density and accuracy (**Figure 2D**). This had two implications. Firstly, a significant (Liu et al., 2015) but often poorly accounted for (Rowland and Coon, 2015) aspect of permafrost landscape response to environmental changes is subsidence (Morse et al., 2009), which would not be well constrained away from coastal focus area. Secondly, when interested in producing a model of a complete island these edge effects lead to registration errors between overlapping sections, resulting in erroneous change concentrated on the edges of overlapping sections that could mask or obscure genuine changes. The most effective approach to minimize this was to capture high level oblique data all around the coastline and then conduct a series (if necessary, to account for 20% edge effects) of flight lines over the island maintaining similar altitude and view angle (**Figure 2B**).

Sparse (>200 m separation) natural features have been surveyed using post-processed carrier phase GNSS measurements to establish ground control points with an accuracy within ±0.02 m. In order to externally check the accuracy of the helicopter-based model produced and to survey sites prior to helicopter-based collections, UAV surveys have been conducted with a DJI Matrice 210 RTK equipped with a vertically orientated Zenmuse X4S 20 MP camera. Parallel flight lines (45 m separation) produced an overlapping mosaic of nadir images from a flying height of 100 m. The more limited image footprint and longer collection time meant that lighting and contrast issues were generally more significant in reducing the quality of the UAV model. An even distribution of 12 specially designed temporary control targets were distributed across the survey areas at an approximate separate separation of >100 m. A summary of the survey collection platforms and dates is presented in **Table 1**.

TABLE 1 | Summary of survey collections used to analyze storm impacts on the outer islands in the Mackenzie Delta area.

Island site	Survey method	Surveyed area (km^2)	Date
Peninsula point	UAV	0.14	August 06, 2018
Peninsula point	UAV	0.27	August 02, 2019
Peninsula point	Helicopter	0.27	August 03, 2019
Peninsula point	Helicopter	0.27	August 07, 2019
Pullen	UAV	0.56	August 02, 2019
Pullen	Helicopter	0.56	August 07, 2019
Hooper	Helicopter	8.35	August 03, 2019
Hooper	Helicopter	Perimeter only	August 07, 2019
Pelly	Helicopter	27.29	August 03, 2019
Pelly	Helicopter	27.29	August 07, 2019

Data Processing

The image sequences have been processed in Agisoft Metashape Professional (version 1.5.5.9097) using a standard workflow (Verhoeven, 2011). Entire sequences of site images have successfully been used here to generate dense point cloud models of deltaic islands (see for example **Figure 3B**), but when surveying at these large (>km^2) scales there is greater potential for lighting contrasts during the survey and misalignments in overlapping areas. To account for this, processing has been broken down into sequences or "chunks" defined by visual differences in lighting and at points of notably different perspectives. Images toward the edges of the sequence have been kept common to the next sequence to ensure overlap. The large sequences of images (a total of 574 images were used for Peninsula points but larger sites surveyed exceeded 1,300 images) processed efficiently (typically overnight) on a specialist workstation with 128 GB RAM and an 18 Core Intel Xeon Gold processor equipped with an 11 GB graphics card. The dense (average > 30 ppm^2) point clouds of sections of each site were then exported and iteratively converged in Cloud Compare (version 2.1). The point clouds were filtered for blunders, which were particularly associated with bodies of water in the surveyed scene and the most obliquely generated points (that had a notably lower resolution, typically <30 ppm^2) were deleted from overlapping areas. Finally, the point clouds were merged and georeferenced using the sparse distribution of control points (7 points were used for Peninsula Point). Independent check points produced an RMSE of 0.21 m planimetric accuracy and 0.41 m in vertical accuracy.

The UAV surveys were generally processed as a single sequence of 1,200 images but problematic areas of lighting contrast have been processed separately and areas of over exposure had notably higher noise levels. These areas have been filtered for over exposed pixels and any blunders removed manually, but some remained problematic (**Figure 3A**). The control target points were used directly in Agisoft to orientate and scale the models and separate check points produced a typical planimetric accuracy of 0.05 m and a vertical RMSE of 0.10 m (it is noted that this not representative of the errors within the over exposed flight lines, which have largely been discounted from subsequent analyses).

RESULTS

Evaluating Helicopter Surveys

The RMSE values indicate that the helicopter-based models are generally reflective of the surveyed topography, but a more rigorous evaluation has been achieved by analyzing the

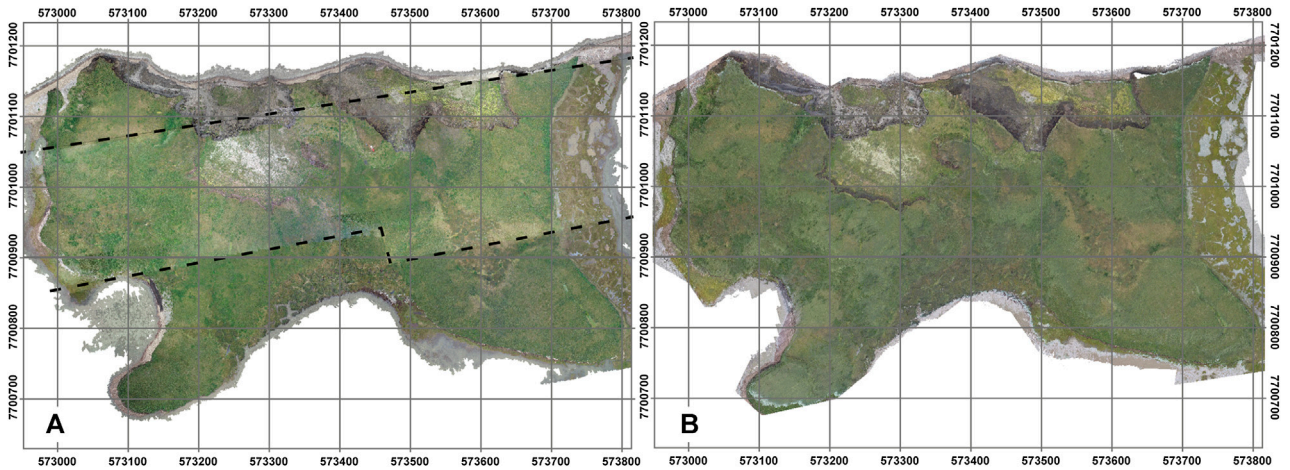

FIGURE 3 | Photogrammetric colored point clouds of Peninsula Point, NWT, one day apart. **(A)** Unmanned aerial vehicle survey of the island collected in flight lines, contrast changes over the course of the survey led to different noise levels and elevation errors across these differences, denoted by the dashed black lines. **(B)** Helicopter-based survey of the island that was sufficiently quick (5 min, including surrounding areas) that no significant contrast changes occurred. A UTM grid is overlain for scale.

difference to the higher resolution UAV model conducted with more ground control on the following day. The difference between the surveys should be minimal, limited to the changes occurring in the (24) hours between the surveys. This pattern is evident in the difference model with strong spatial agreement between the standard and widely adopted UAV survey data and the new helicopter-based data (**Figure 4A**). Additionally, the rapid data collection using a helicopter platform negated some of the flight line contrast noise and alignment errors that affected the slower UAV survey (**Figure 3B**). Beyond the contrast issue in the UAV survey, locations and quantities of change are consistent with observations from the site; primary activity areas were at a retreating backscarp terrace within a retrogressive thaw complex and at exposed permafrost cliffs at the shoreface **Figure 4C**. A total volumetric difference of 129.5 m^3 was recorded between the surveys, no thresholding has been applied so this may include error as well as genuine change.

The ability to effectively produce a surface model from oblique helicopter-based images demonstrates the potential to quantitatively monitor extensive (km^2) areas of coastline. Helicopter surveys using standard photographic equipment and sparse ground control data can account for the complexity of coastal systems such as those found across the Beaufort Sea coast, typified by both long linear sequences of sea-cliffs and dunes and also by numerous island and spit complexes, particularly prevalent in the MacKenzie Delta area. Helicopter-based surveys do not offer the resolution and precision of UAV surveys but the high rates of change across permafrost coastlines may not always warrant such detail. A comparison between the approaches shows that helicopter surveys are significantly more expensive than UAV surveys for a few locally accessible sites, but as soon as monitoring is required on more distant sites helicopter surveys become rapidly more cost-effective (**Table 2**). Helicopter surveys can now achieve effective quantitative erosion data over wide spatial scales using standard photographic equipment.

Annual Change at Peninsula Point, NWT

In order to apply the helicopter-based survey approach for longer term (annual) change quantification the helicopter-based surface model has been compared to a UAV survey conducted a year earlier (**Figure 5A**). The surface differences show that the currently active areas, principally the exposed cliff faces, dominate the annual signal, although other areas of difference are detected such as the vegetated back scarp of a higher level slump area that had appeared to be relict (**Figure 5B**; see also **Figure 2C**). The total annual surface loss at Peninsula Point recorded was 44,522 m^3. Over the area of the island (274,670 m^2) this is a low rate of change (0.16 m^3 per m^2) but this response has been concentrated at the exposed massive ice and permafrost cliffs within the island and these areas have receded by approximately 8 m in places (**Figure 5C**).

Storm Driven Change

After evaluating the performance of helicopter-based photogrammetry for erosion monitoring, a forecast of storm conditions provided the opportunity to apply the new approach at large (>km^2) scales. The storm was forecast for the evening of 4th August–morning of August 5, 2019. On the August 3, 2019 a single flight was used to survey seven key monitoring sites across a 150 km stretch of the Beaufort Sea coast. The flight also included stops for installation of time-lapse cameras for validation at key community sites and other research tasks. This meant that one key outer island, Pullen Island, was not surveyed but it had been surveyed using UAV-based photogrammetry the day before. The wind conditions on the third were already escalating (exceeding 50 km h^{-1}) and prohibited UAV surveys but all surveyed sites produced data of comparable accuracy to Peninsula Point, which was also included in the survey and used as a control site. The storm was not particularly exceptional in terms of magnitude, but the duration of higher significant wave heights was notably

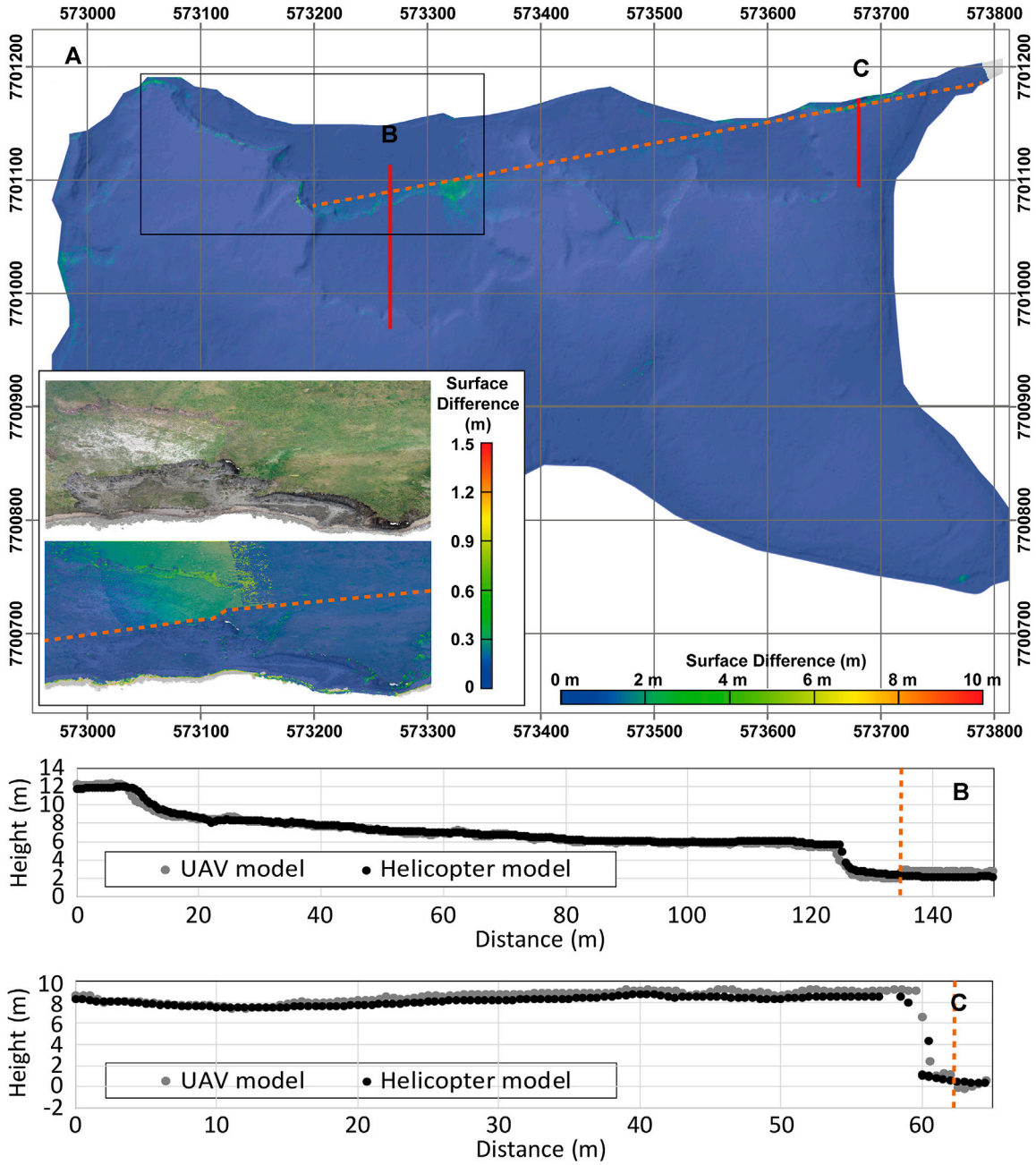

FIGURE 4 | DEM surface differences between next-day helicopter and unmanned aerial vehicle (UAV) surveys at Peninsula Point, NWT. **(A)** Overview of the differences recorded across the island showing no detectable change apart from at the actively eroding cliff faces. This is complicated by an error in the UAV data where lighting contrasts between flight lines resulted in an alignment error denoted by the orange dashed line. Fine scale oblique views are inset (at a different surface difference scale for detail) and a UTM grid is overlain for scale. **(B)** Profile through a retrogressive thaw slump area shows little discernible change other than the stepped contrast error (dashed orange line). **(C)** Profile through a section of sea-exposed cliff shows minor (<1 m) recession of the cliff top, the stepped contrast error in the UAV data is also visible (dashed orange line).

longer than any preceding events within the 2019 open water season (**Figure 6**). A repeat flight was undertaken on 7th August when storm conditions had largely abated, but wind speeds (20–30 km h^{-1}) still made UAV surveys challenging. The post-storm data capture included the previous seven sites and other sites of interest such as Pullen Island. Here we present the results from the storm-related differences at the massive ice type site Peninsula Point and then the three outermost islands (highlighted in **Figure 1**) surveyed in the delta area to quantify the short-term storm related changes occurring.

The storm-related change at Peninsula Point resulted in the volumetric loss of 12,800 m^3, with change concentrated at the

TABLE 2 | Comparison of helicopter surveys against the current approach of unmanned aerial vehicle-based monitoring (cost in Canadian dollars).

Description	UAV based surveys	Helicopter-based surveys
Cost per day	$1,200 (covers a field crew of pilot and spotter)	$6,600 (helicopter plus camera operator)
Coverage per day	Using boat access: 2–4 km^2	70 km^2
	Using helicopter access: 5–8 km^2	—
Access to site via helicopter	Helicopter: $6,000/day	Not applicable
Access to site via boat	Boat $600	Not applicable
Survey time per km	3 h per km^2	Island survey: 5 min per km^2
	—	Linear coastline survey: 2 min per km^2
Survey cost per km	$225 using boat access to nearby locations	$94
	$6,150 using helicopter access to remote locations	—
Maximum operating conditions (wind speed)	40 km h^{-1}	70 km h^{-1}
Pre-site requirements	None	Ground control network or a pre-existing DEM

cliffs exposed directly to sea waves. This accounted for 29% of the annual total erosion (compared to UAV survey data collected a year earlier; **Figure 5**) and was disproportionately high given the relatively modest magnitude of the storm, although the storm had sustained high wind and wave conditions and a longer duration than previous events since the sea-ice break-up (**Figure 6**). The storm was able to remove much of the material that had accumulated at the base of the coastal slope during the previous year (note the lower level of the mud drape in front of the cliff toe in **Figure 7B**) in addition to a strong response of the cliffs exposed directly to storm surge contact (**Figure 7C**). In an environment where erosion is concentrated to the ice-free season, the impact of storms on sea cliffs is clear, and can lead to dramatic event-based erosion rates, but slump back scarps at the site were much less affected **(Figure 7A)**. The storm response at Peninsula Point emphasizes the importance of geomorphic context in applying and interpreting both annual rates of loss and the impact of specific events such as extreme weather.

Storm Change Across Outer Islands

The outer islands of the MacKenzie Delta are the most exposed to storm conditions, and their responses may inform projections of future coastal dynamics elsewhere. The surveyed outer islands had varied amounts of pre-existing survey information. Pullen Island (the most exposed site) had a volumetric loss (assumed to be dominated by storm-driven responses) of 12,056 m^3. The response was comparable to the storm-induced surface loss that occurred at Peninsula Point but concentrated over a shorter 525 m north-orientated coastal section (relative to 700 m of north orientated exposed coast and several raised back scarps at Peninsula Point). In common with Peninsula Point, the retrogressive thaw slumps showed minimal significant change during the storm and a dramatic impact on the sea cliff sections that receded, steepened and were undercut in places (**Figure 8**).

At Hooper Island the pre-storm data captured the whole island but the post-storm resurvey data focused only on the coastal zone given that little detectable change was expected inland due to the lack of rainfall associated with the storm (that may trigger inland slope failures), and to simulate the most efficient survey capture method for coastal monitoring (single pass flights). Covering an area of 8.35 km^2, Hooper Island **(Figure 9A)** is much larger than the islands at Pullen or Peninsula and recorded a storm related erosion volume of 132,385 m^3 from the coastal zone. Despite the larger total eroded volume, the erosion from the storm was lower than that at Pullen when accounting for the 5.6 km stretch of north coastline over which most surface loss was concentrated; the muted response was characterized by relatively smaller losses at the base of exposed cliffs (**Figure 9C**). Prior to the pre-storm flight, NRCan's 3D monitoring program had not surveyed Hooper Island before and so it is not possible to set these valuable new event-based data in a wider temporal context.

The largest outer island surveyed was Pelly Island, encompassing a spatial footprint of 27.29 km^2, although approximately 23% (6.14 km^2) of the island is lake surface. In order to assess the ability of helicopter surveys at large scale the entire island was repeat surveyed. The storm resulted in a loss of 545,394 m^3. In common with the other islands, the storm impact was concentrated on the northern shores, but due to its orientation, erosion occurred throughout the island's 25 km coastline, particularly along its eastern flank (**Figure 10**). These are high-end measures of surface loss because no thresholding has been applied in order to aid comparability across sites and so there is the potential to incorporate error in addition to the genuine changes detected. However, a principle advantage of the photogrammetric process is that color orthoimages enable visual validation of detected changes if higher accuracy change detection and specific process detailing is required.

The sea-exposed cliff faces on the northern shores were most significantly affected by the storm process conditions. When normalized by both coastline length and cliff height to produce an effective landward volumetric recession, these areas showed peak storm responses in the lower cliff top elevation sea-exposed cliffs at Peninsula Point (3.4 m) and Pullen Island (3.2 m) relative to the much taller cliff sections at Hooper Island (1.5 m) and Pelly Island (2.0 m). These values show that the variability of storm responses are not always captured well by single profiles and that higher cliffs may have potentially greater immediate resistance to storm effects but the large undercuts noted in the photogrammetry are likely to separate the cantilever collapse and true erosion response from the primary driving event.

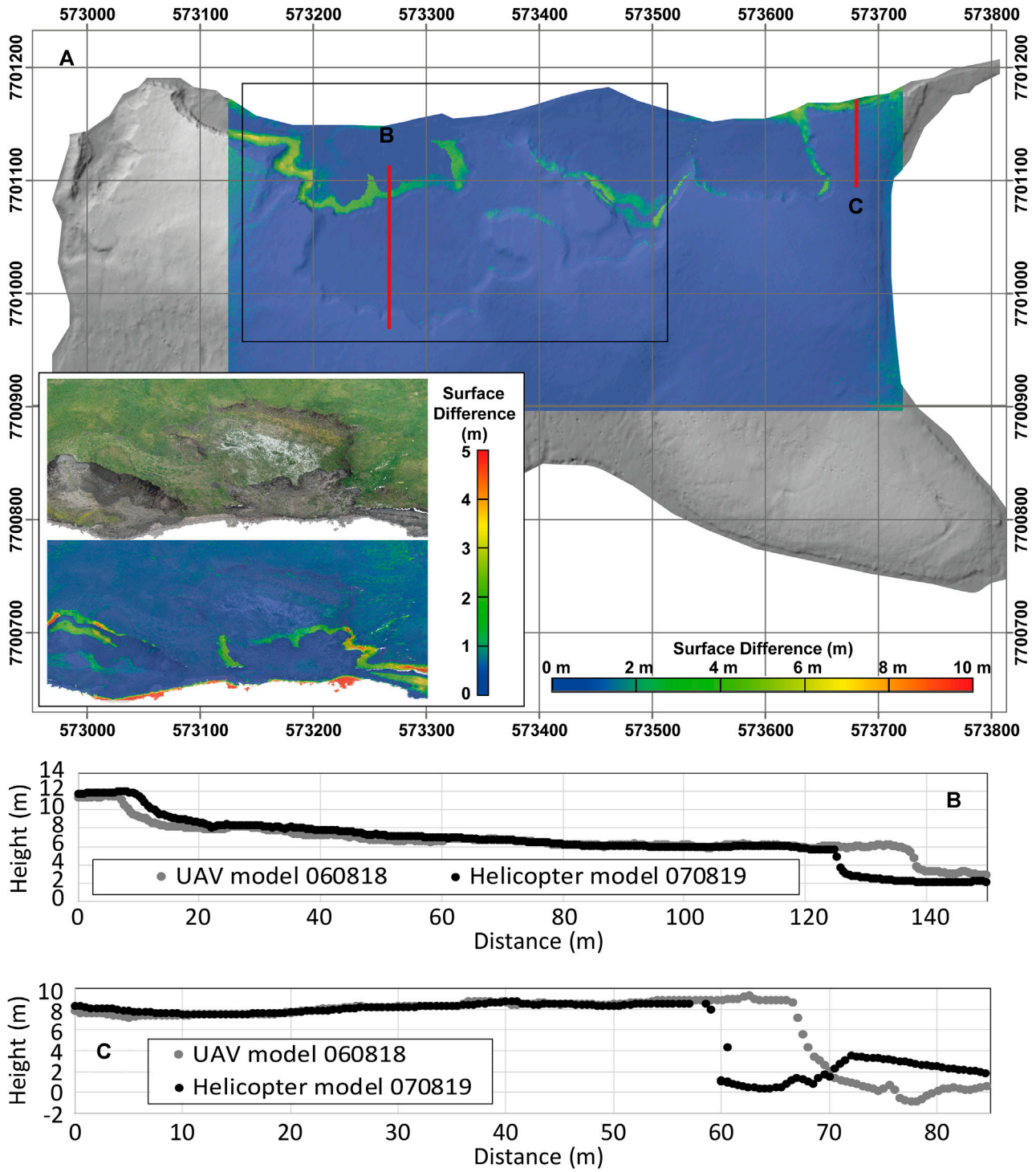

FIGURE 5 | DEM surface differences between helicopter and UAV photogrammetric surveys a year apart at Peninsula Point, NWT. **(A)** Overview of the differences recorded across the island (the UAV data did not capture the whole site) showing change concentrated on retreating slump back scarps and exposed cliffs. Fine scale oblique views are inset (at a different surface difference scale for detail) and a UTM grid is overlain for scale. **(B)** Profile through a retrogressive thaw slump area shows back scarp retreat and slope toe erosion. **(C)** Profile through a section of sea-exposed cliff shows approximately 8 m of recession at the cliff top.

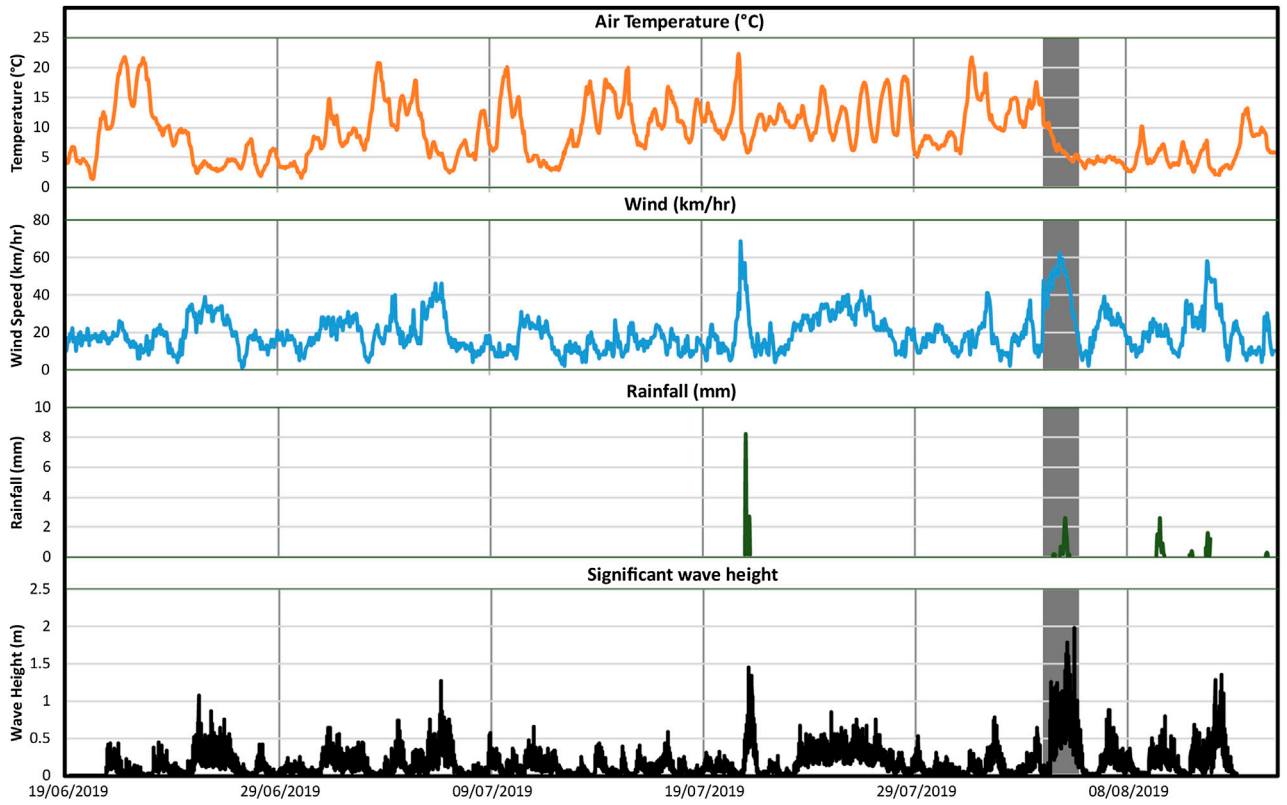

FIGURE 6 | Storm conditions (highlighted in gray from 4–5August, 2019) show high wind speeds and sustained high significant wave heights but limited rainfall relative to the rest of the open water season.

DISCUSSION

The paucity of high-resolution (>1 m^2), quantitative data on the regional variability of responses (on both annual timescales and to extreme events), has limited assessments of future climatic changes (Overduin et al., 2014). We have evaluated and then applied new helicopter-based surveys for assessing the significance of storm-related morphological change across outer islands in the Mackenzie Delta area, NWT.

Helicopter-Based Photogrammetric Surveys

The performance of helicopter-based surveys for monitoring wide-scale (>km^2) coastal processes has been evaluated at a type-site for massive ground ice (Lim et al., 2020), thought to be a dominant control on coastal sensitivity to change (Farquharson et al., 2019). The resolution of the helicopter models are generally lower than that of conventional UAV survey approaches resulting from the coarser ground sample distances achieved in the raw imagery: each pixel typically represented <0.05 m in helicopter images relative to 0.01 m in the UAV derived images. There is potential for accuracy issues with continuous surveys over such large areas, but the scale and rate of Arctic coast erosion may not always warrant such high levels of precision and the accuracy of large-scale surveys has been improved by segmenting large image sequences and using ground control from both existing datasets and specially collected sparsely distributed points. Error thresholds have not been applied here but the check point assessments suggest that a conservative detection difference of 0.50 m would be achievable for responsive pre- and post-storm surveys (change detection models typically identified genuine, visually validated, differences beyond approximately 0.25 m) when no significant lighting or contrast issues have been noted. This level of detection is potentially acceptable given the dynamism of permafrost coast landscapes and the propensity for processes such as thaw-induced surface deformation, which can account for comparable or greater amounts of subsidence through the thaw season (Morse et al., 2009).

The ability to survey in high (up to 70 km h^{-1}) wind conditions and to produce new repeat and responsive sub-meter resolution three-dimensional data at scales not previously achievable, using non-specialist equipment has demonstrable advantages. The time savings are dramatic in the field and more advanced computers have meant processing large datasets is now viable and practical. While helicopter-based platforms remain an expensive option, the cost-effectiveness per kilometer is a fraction of widely applied UAV surveys for

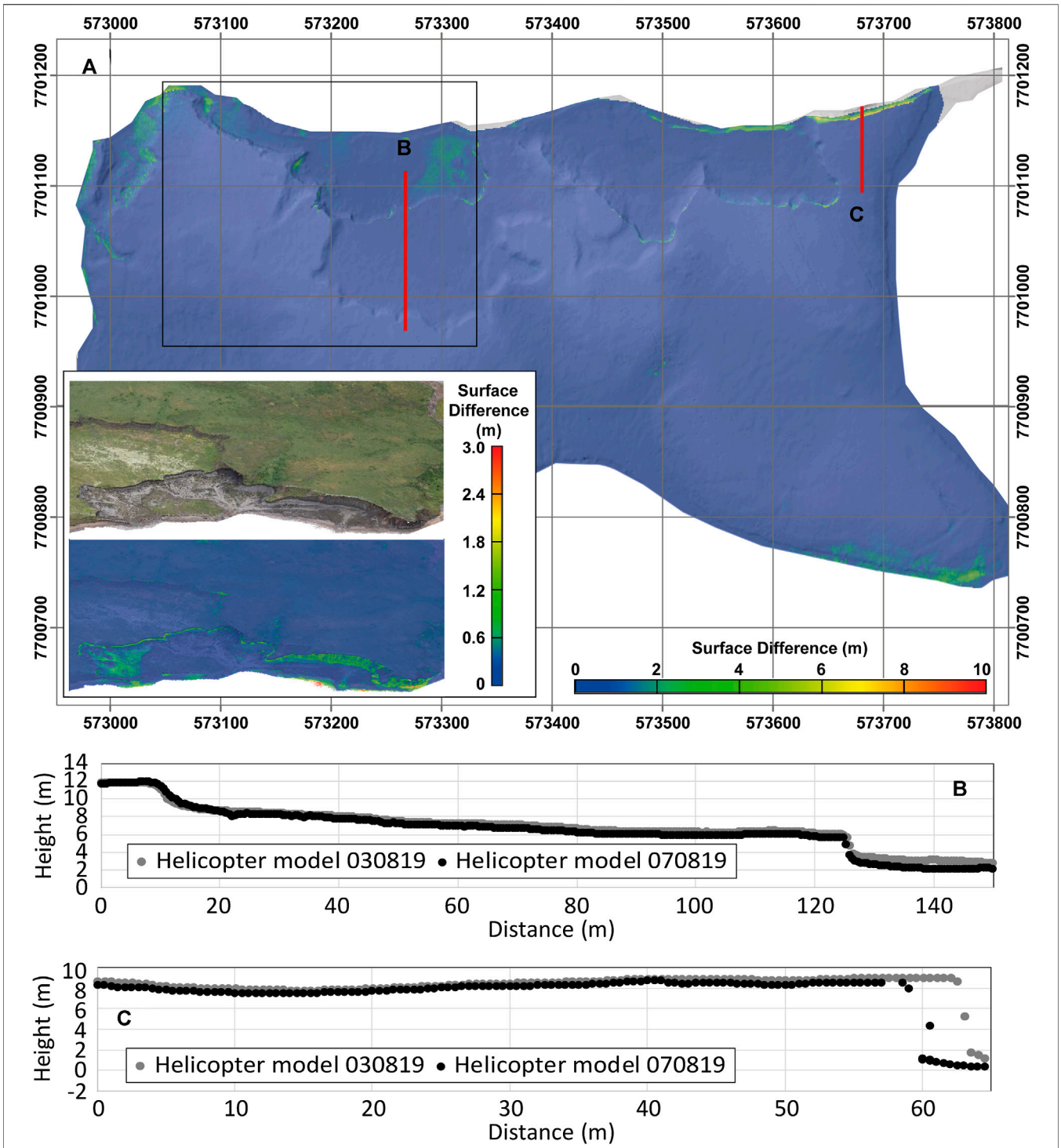

FIGURE 7 | DEM differences between helicopter photogrammetric surveys before and after a storm at Peninsula Point, NWT. **(A)** Overview of the differences recorded across the island showing spatial distribution of change. Fine scale oblique views are inset (at a different surface difference scale for detail) and a UTM grid is overlain for scale. **(B)** Profile through a retrogressive thaw slump area shows erosion of the mud drape in front of the slope toe but little change elsewhere. **(C)** Profile through a section of sea-exposed cliff shows approximately 4 m of recession at the cliff top.

all but the most readily accessible sites. Additionally, the survey geometry can be adapted to capture the range of environments found in permafrost coasts from continuous linear stretches of cliffs, dunes and bars to complex topographic features such as islands and pingoes. However, it is likely that this new approach for permafrost coast monitoring will be best applied in

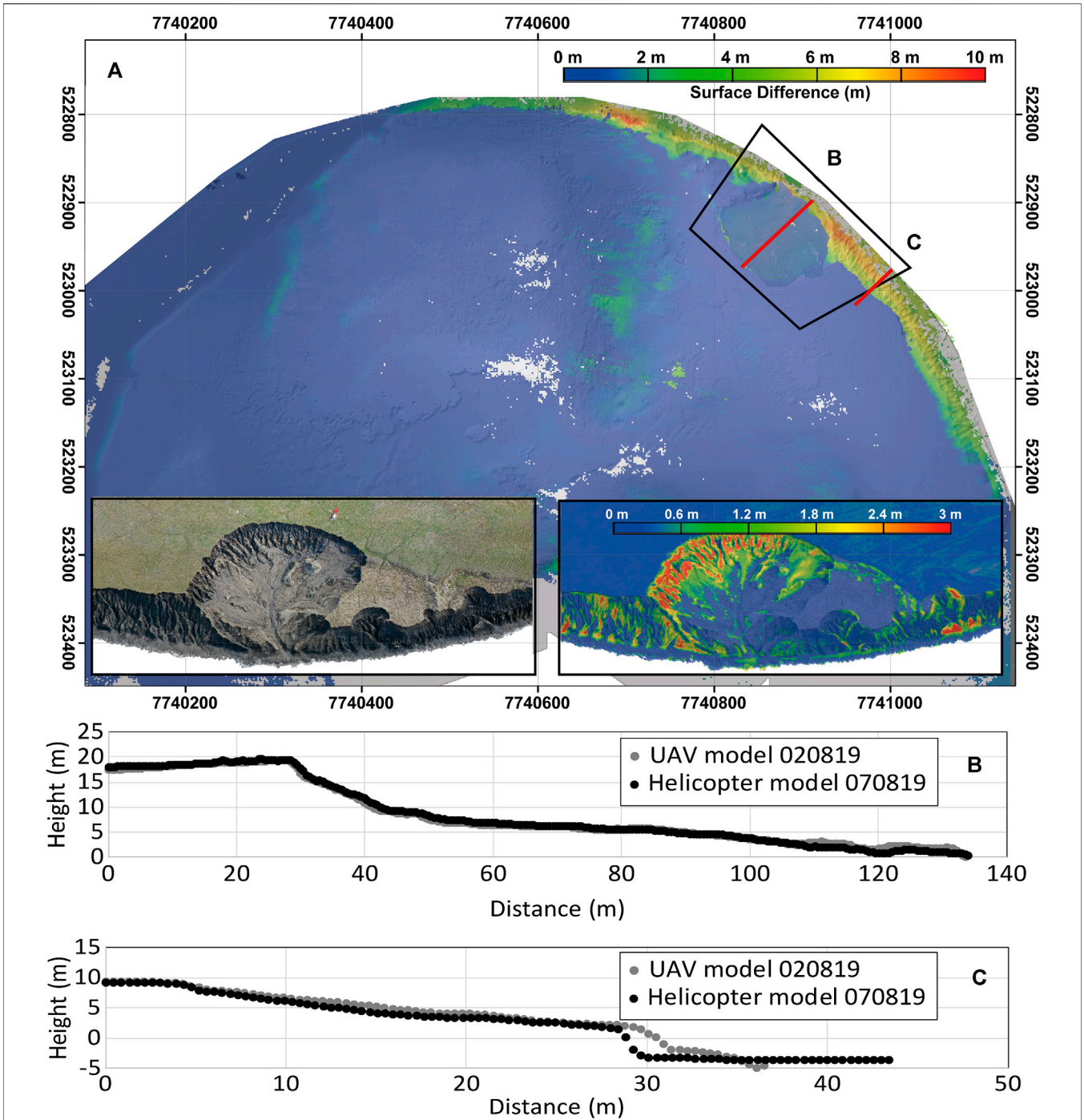

FIGURE 8 | DEM surface differences between pre-storm UAV and post-storm helicopter-based photogrammetric surveys at Pullen Island, NWT. Note: the geospatial data have been rotated through 90° for presentation purposes, effectively transposing the UTM Eastings and Northings. **(A)** Overview of the differences recorded across the island showing spatial distribution of change and fine scale oblique views are inset (at a different surface difference scale for detail). **(B)** Profile through a retrogressive thaw slump area shows only minor areas of significant change. **(C)** Profile through a section of sea-exposed cliff shows approximately 3 m of recession at the cliff top.

combination with more detailed UAV surveys (there were no unaccountable and therefore erroneous surface differences over the same island site, surveyed by both approaches a day apart) and will be particularly valuable in situations such as the those across the Beaufort Sea coast where helicopters already play a vital role in site accessibility. The installation of a (semi) permanent sparse network of recognisable ground control, potentially more concentrated in critical areas, could be surveyed once and then

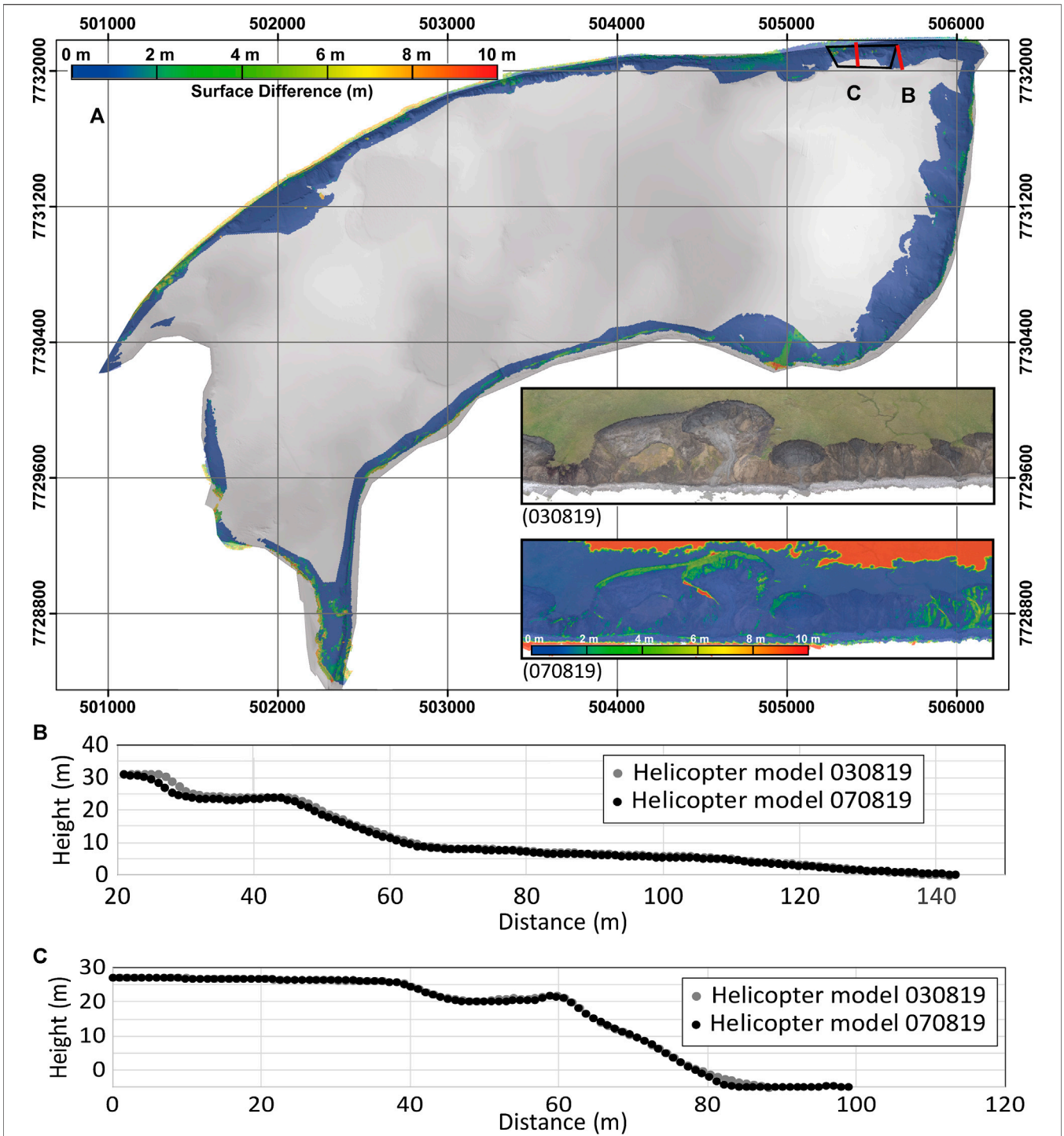

FIGURE 9 | DEM surface differences between pre-storm (whole island) and post-storm (coastline) helicopter-based photogrammetric surveys at Hooper Island, NWT. **(A)** Overview of the differences recorded across the island showing spatial distribution of change and fine scale oblique views are inset (at a different surface difference scale for detail); note that the red upper area in the difference model is where there is no overlap between DEMs. **(B)** Profile through a retrogressive thaw slump area shows only minor areas of significant change. **(C)** Profile through a section of sea-exposed cliff shows approximately 2 m of recession at a very confine area at the base of the cliff.

used throughout the season to generate wide coverage volumetric monitoring. Ultimately, helicopter-based photogrammetry is comparable to and complementary with the UAV surveys currently used to monitor these sites (see **Figure 8**). Analyzing these datasets together, potentially with new expansive satellite monitoring (e.g., Zwieback et al., 2018), improves understanding

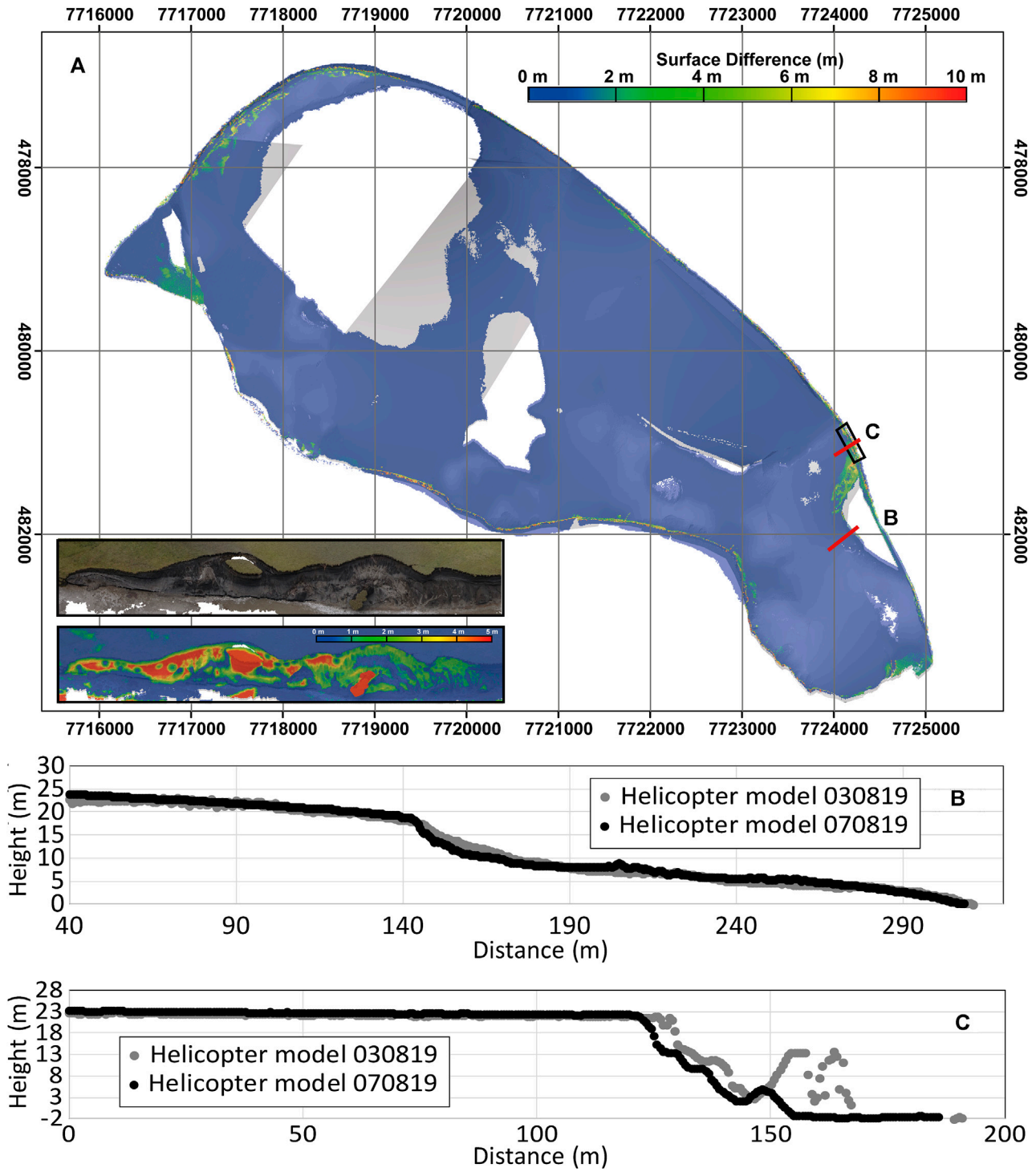

FIGURE 10 | DEM surface differences between pre- and post-storm helicopter-based photogrammetric surveys at Pelly Island, NWT. Note: the geospatial data have been rotated through 90° for presentation purposes, effectively transposing the UTM Eastings and Northings. **(A)** Overview of the differences recorded across the island showing spatial distribution of change and fine scale oblique views are inset (at a different surface difference scale for detail). **(B)** Profile through a retrogressive thaw slump area shows some flattening of the coastal slope through head scarp erosion and subsidence and in filling of the mud and debris flow area. **(C)** Profile through a section of sea-exposed cliff shows large stacks were removed during the storm in addition to approximately 6 m of recession at the cliff top in places where large blocks collapsed.

of errors within each dataset and enables a versatile and effective monitoring approach across key spatial and temporal scales.

Storm Impacts in a Morpho-Climatic Context

Lengthening open water seasons have extended the exposure of Arctic coastlines to storm conditions (Stroeve et al., 2012), which may also be increasing in intensity and duration (Vermaire et al., 2013). The impacts of extreme weather events, and wider climatic patterns in the Beaufort Sea (Wood et al., 2013), are already being felt by northern communities (Pearce et al., 2010) and impacting the key species they depend upon (Scharffenberg et al., 2019). However, the geomorphic significance of storms and the spatial variability of their effects are poorly quantified across Arctic regions. The ability to generate new and responsive 3D morphological data at regional scales enables a former fragmented mosaic of detailed local studies of erosion patterns to be linked (both temporally and through more consistent resolution) and set in wider context.

Evaluating the wide-scale changes associated with a relatively long duration (15 h) storm revealed that retrogressive thaw slumps were generally much less affected (see for example **Figure 9B**), with most erosion concentrated on exposed cliffs within the storm-surge contact zone. Where slump material entered this zone the erosion was detectable but less than within the intact cliffs, which were deeply undercut. This is perhaps reflective of the lack of ground ice within the debris fan material (Gilbert et al., 2016) or the higher relative resistance of silty material, which was often desiccated and hard set. Additionally, lower elevation (<20 m) cliffs recorded an average recession of 3.3 m whereas higher (>20 m) cliffs receded by an average of 1.75 m but with the true response potentially lagged until undercut areas collapse. These cross-site data demonstrate both the spatial and temporal complexity of storm responses and how coastal geometry (height and orientation), material properties and failure modes all influence the sensitivity and responses of permafrost coasts. The role of intense precipitation events has also been demonstrated in coarse (30 m pixel) but expansive (5,000 km^2) and frequent (11 days) elevation change monitoring using satellite interferometry (Zwieback et al., 2018). The ability to quantify distinct geomorphic responses due to specific local controls (Lim et al., 2020), during specific events as we show here, or across sub-seasonal timescales (Zwieback et al., 2018) has the potential to provide a more detailed appreciation of permafrost landscapes.

At Peninsula Point the exposed coast is dominated by retrogressive thaw complexes bordered by shorter sections of coastal cliffs. Canadian Global Coupled Model ensembles have determined that air temperatures in the region have risen by approximately 4°C between 1960 and 2020 (Manson and Solomon, 2007) and historic patterns of retreat at the site show a progressive shift from a convex cross shore profile to generally flat shoreline from 1935 to 1989 (Mackay and Dallimore, 1992). That morphology has since been maintained at a relatively consistent rate of approximately 3.5 m a^{-1}. Therefore, the first significant storm (>36 km h^{-1} for longer than 10 h, adjusted from Scharffenberg et al., 2019) event during the 2019 open water season directly resulted in a cliff line step-back comparable to the long-term mean annual rates (although some areas receded landwards by up to 8 m between 2018 and 2019 summers). Furthermore, an average of 2.2 m cliff retreat across the most exposed sections of the MacKenzie Delta outer islands during the storm represents a key geomorphic event that impacted multiple sites. This agency has the potential to cause fundamental shifts in long-term erosion rates if projected and currently monitored increases in storminess and open water seasons continue (Manson and Solomon, 2007). However, in this morpho-climatic context, it should also be noted that more sheltered coastal sections recorded no detectable change in places.

It is evident that true morphodynamic responses to both short-term extreme events and potentially longer-term climatic signals rely on the ability to detail surface differences consistently and across wide scales in a practical manner. Tailored helicopter-based photogrammetric surveys provide a systematic, responsive and potentially cost-effective and accessible approach to achieve wide-scale topographic monitoring in order to more adequately understand the regional responses to specific weather events. This approach has direct implications for assessing the immediate and short-term impacts of storms in terms of erosion volumes, infrastructure damage, and the release of significant material such as carbon bearing layers or contaminants (Fritz et al., 2017), and if applied routinely may help address questions of the spatial variability that cannot be resolved by long-term observations (Obu et al., 2017). In particular, the complex sensitivities of block failures from permafrost cliffs of different sizes (Hoque and Pollard, 2016) and potentially increasing effects of retrogressive thaw slumps (Ward Jones et al., 2019) need to be accounted for to improve projections and models of future Arctic coastal behavior.

CONCLUSION

In the context of concerns regarding heightened storm intensity (Small et al., 2011), increased open water seasons (Stroeve et al., 2012) and accelerated erosion of permafrost coasts across the Arctic (Radosavljevic et al., 2016), here we have evaluated the use of helicopter-based photogrammetric surveys to quantify volumetric changes for both regular and responsive monitoring purposes. Constrained by the use of standard camera equipment for data collection, the savings in terms of time (97–99% quicker per km) and cost efficiency (58–98% cheaper per km) are potentially large when assessing sites that are large and not easily accessible. However, the most significant contribution of this approach will be new data and an improved understanding of high resolution permafrost coast responses at much larger scales than has previously been possible. Applying the approach to a 150 km transect of sites (including new sites, not preciously surveyed by NRC and UAV monitoring) before and after a storm event, in conditions not suitable for standard UAV surveys has detailed and quantified key coastal responses. Erosion was concentrated on the exposed

north orientated coastlines, and particularly on the permafrost and ground ice cliff sections. The storm accounted for over a quarter of the annual total volumetric surface losses at a type-site for massive ice, and the coastal cliff areas receded at amounts comparable to typical annual retreat rate in places. There was a consistently greater immediate volumetric response in low (<20 m) relative to high (>20 m) elevation cliffs, but further monitoring would be required to assess the long-term impacts when deep undercuts finally result in cantilever collapse (Hoque and Pollard, 2016). Retrogressive thaw slumps were much less affected, perhaps due to the lack of high intensity rain associated with the storm, and these data indicate that where debris flow material had solidified within the coastal zone the erosion volumes were relatively less than those of intact permafrost cliff material. The need for detailed observations such as these and the potential for retrogressive thaw slumps to become decoupled from environmental drivers has been noted elsewhere (Zwieback et al., 2018; Ward Jones et al., 2019). Therefore, quantifying the geomorphic agency of both annual and extreme weather events at wider, more representative scales provides a more holistic and consistent approach to assessing current and future changes to Arctic coastlines.

DATA AVAILABILITY STATEMENT

The data supporting the conclusions of this manuscript but not presented above will be made available by the authors to any qualified researcher. These data include the raw images, storm meteorological conditions or digital elevation models.

AUTHOR CONTRIBUTIONS

ML, PM, CI, CC, and JW planned, collected and processed the helicopter-based surveys and ML wrote the manuscript and DW, PF, and JW reviewed it. DW, PF, HB, and CI conducted and processed the UAV surveys.

FUNDING

The authors thank and acknowledge the support of the NERC Arctic office UK-Canada Bursary scheme and Polar Continental Shelf Program for helicopter survey support, without which this research would not have been possible. This work was supported by the Natural Resources Canada's Climate Change Geoscience program and is linked to and received funds from the Beaufort Sea Regional Strategic Environmental Assessment (BRSEA) and Climate Change Preparedness in the North Fund (CCPN) both of Indigenous and Northern Affairs Canada.

ACKNOWLEDGMENTS

We particularly thank and acknowledge the Inuvik and Tuktoyaktuk Hunters and Trappers Committee, the Hamlet of Tuktoyaktuk and members of the Tuktoyaktuk Climate Change Resilience Project who have actively supported this work. We owe our gratitude to Parks Canada who have granted unprecedented access to the Pingo Canadian Landmark, within which a large portion of the study takes place and thank the editor and reviewers for their insightful comments.

REFERENCES

Alvarez, J., Yumashev, D., and Whiteman, G. (2020). A framework for assessing the economic impacts of Arctic change. *Ambio* 49 (2), 407–418. doi:10.1007/s13280-019-01211-z

Bonsal, B. R., and Kochtubajda, B. (2009). An assessment of present and future climate in the Mackenzie Delta and the near-shore Beaufort Sea region of Canada. *Int. J. Climatol.* 29 (12), 1780–1795. doi:10.1002/joc.1812

Burn, C. R., and Kokelj, S. V. (2009). The environment and permafrost of the Mackenzie Delta area. *Permafr. Periglac. Process.* 20 (2), 83–105. doi:10.1002/ppp.655

Cunliffe, A., Tanski, G., Radosavljević, B., Palmer, W., Sachs, T., Lantuit, H., et al. (2019). Rapid retreat of permafrost coastline observed with aerial drone photogrammetry. *The Cryosphere 13,* 1513–1528.

Dean, K. G., Stringer, W. J., Ahlnäs, K., Searcy, C., and Weingartner, T. (1994). The influence of river discharge on the thawing of sea ice, Mackenzie River Delta: albedo and temperature analyses. *Polar Res.* 13 (1), 83–94. doi:10.1111/j.1751-8369.1994.tb00439.x

Dietrich, J. T. (2016). Riverscape mapping with helicopter-based structure-from-motion photogrammetry. *Geomorphology* 252, 144–157. doi:10.1016/j.geomorph.2015.05.008

Farquharson, L. M., Romanovsky, V. E., Cable, W. L., Walker, D. A., Kokelj, S. V., and Nicolsky, D. (2019). Climate change drives widespread and rapid thermokarst development in very cold permafrost in the Canadian high arctic. *Geophys. Res. Lett.* 46 (12), 6681–6689. doi:10.1029/2019gl082187

Forbes, D. L., Solomon, S. M., and Frobel, D. (1995). Report of the 1992 coastal surveys in the Beaufort Sea. *Geol. Survey Canada Open File.* 3053, 53. doi:10.4095/203482

Fritz, M., Vonk, J. E., and Lantuit, H. (2017). Collapsing Arctic coastlines. *Nat. Clim. Change.* 7 (1), 6–7. doi:10.1038/nclimate3188

Günther, F., Overduin, P., Sandakov, A., Grosse, G., and Grigoriev, M. (2013). Short- and long-term thermo-erosion of ice-rich permafrost coasts in the Laptev Sea region. *Biogeosciences* 10, 4297–4318. doi:10.5194/bg-10-4297-2013

Gilbert, G. L., Kanevskiy, M., and Murton, J. B. (2016). Recent advances (2008-2015) in the study of ground ice and cryostratigraphy. *Permafr. Periglac. Process.* 27 (4), 377–389. doi:10.1002/ppp.1912

Goñi, M. A., Yunker, M. B., Macdonald, R. W., and Eglinton, T. I. (2000). Distribution and sources of organic biomarkers in arctic sediments from the Mackenzie River and Beaufort Shelf. *Mar. Chem.* 71 (1), 23–51. doi:10.1016/s0304-4203(00)00037-2

Grosse, G., Goetz, S., McGuire, A. D., Romanovsky, V. E., and Schuur, E. A. G. (2016). Changing permafrost in a warming world and feedbacks to the Earth system. *Environ. Res. Lett.* 11 (4), 040201. doi:10.1088/1748-9326/11/4/040201

Hoque, M. A., and Pollard, W. H. (2016). Stability of permafrost dominated coastal cliffs in the Arctic. *Polar Sci.* 10 (1), 79–88. doi:10.1016/j.polar.2015.10.004

Irrgang, A. M., Lantuit, H., Gordon, R. R., Piskor, A., and Manson, G. K. (2019). Impacts of past and future coastal changes on the Yukon coast—threats for cultural sites, infrastructure, and travel routes. *Arct. Sci.* 5 (2), 107–126. doi:10.1139/as-2017-0041

Irrgang, A. M., Lantuit, H., Manson, G. K., Günther, F., Grosse, G., and Overduin, P. P. (2018). Variability in rates of coastal change along the Yukon coast, 1951 to 2015. *J. Geophys. Res. Earth Surf.* 123 (4), 779–800. doi:10.1002/2017jf004326

Lantuit, H., Overduin, P. P., Couture, N., Wetterich, S., Aré, F., Atkinson, D., et al. (2012). The Arctic coastal dynamics database: a new classification scheme and statistics on Arctic permafrost coastlines. *Estuar. Coast.* 35 (2), 383–400. doi:10.1007/s12237-010-9362-6

Lesack, L. F. W., and Marsh, P. (2007). Lengthening plus shortening of river-to-lake connection times in the Mackenzie River Delta respectively via two global change mechanisms along the arctic coast. *Geophys. Res. Lett.* 34 (23), L23404. doi:10.1029/2007gl031656

Lesack, L. F. W., and Marsh, P. (2010). River-to-lake connectivities, water renewal, and aquatic habitat diversity in the Mackenzie River Delta. *Water Resour. Res.* 46 (12), 1–16. doi:10.1029/2010wr009607

Lim, M., Whalen, D., Martin, J., Mann, P. J., Hayes, S., Fraser, P., et al. (2020). Massive ice control on permafrost coast erosion and sensitivity. *Geophys. Res. Lett.* 47 (17), e2020GL087917. doi:10.1029/2020gl087917

Liu, L., Schaefer, K. M., Chen, A. C., Gusmeroli, A., Zebker, H. A., and Zhang, T. (2015). Remote sensing measurements of thermokarst subsidence using InSAR. *J. Geophys. Res. Earth Surf.* 120 (9), 1935–1948. doi:10.1002/2015jf003599

Mackay, J. R., and Dallimore, S. R. (1992). Massive ice of the Tuktoyaktuk area, western Arctic coast, Canada. *Can. J. Earth Sci.* 29 (6), 1235–1249. doi:10.1139/e92-099

Manson, G. K., and Solomon, S. M. (2007). Past and future forcing of Beaufort Sea coastal change. *Atmos. Ocean.* 45 (2), 107–122. doi:10.3137/ao.450204

Maslakov, A., and Kraev, G. (2016). Erodibility of permafrost exposures in the coasts of Eastern Chukotka. *Polar Sci.* 10 (3), 374–381. doi:10.1016/j.polar.2016.04.009

Morse, P. D., Burn, C. R., and Kokelj, S. V. (2009). Near-surface ground-ice distribution, Kendall Island Bird Sanctuary, western Arctic coast, Canada. *Permafr. Periglac. Process.* 20 (2), 155–171. doi:10.1002/ppp.650

Neri, M., De Maio, M., Crepaldi, S., Suozzi, E., Lavy, M., Marchionatti, F., et al. (2017). Topographic maps of Mount Etna's Summit Craters, updated to December 2015. *J. Maps.* 13 (2), 674–683. doi:10.1080/17445647.2017.1352041

Nielsen, D. M., Dobrynin, M., Baehr, J., Razumov, S., and Grigoriev, M. (2020). Coastal erosion variability at the southern Laptev sea linked to winter sea ice and the Arctic oscillation. *Geophys. Res. Lett.* 47 (5), e2019GL086876. doi:10.1029/2019gl086876

Nitze, I., and Grosse, G. (2016). Detection of landscape dynamics in the Arctic Lena Delta with temporally dense Landsat time-series stacks. *Remote Sens. Environ.* 181, 27–41. doi:10.1016/j.rse.2016.03.038

Novikova, A., Belova, N., Baranskaya, A., Aleksyutina, D., Maslakov, A., Zelenin, E., et al. (2018). Dynamics of Permafrost coasts of Baydaratskaya bay (Kara sea) based on multi-temporal remote sensing data. *Rem. Sens.* 10 (9), 1481. doi:10.3390/rs10091481

O'Neill, H. B., Smith, S. L., and Duchesne, C. (2019). Long-term permafrost degradation and thermokarst subsidence in the Mackenzie delta area indicated by thaw tube measurements. *Cold Regions Eng.* 2019, 643–651. doi:10.1061/9780784482599.074

O'Rourke, M. J. E. (2017). Archaeological site vulnerability modelling: the influence of high impact storm events on models of shoreline erosion in the western Canadian Arctic. *Open Archaeol.* 3 (1), 1–16. doi:10.1515/opar-2017-0001

Obu, J., Lantuit, H., Fritz, M., Pollard, W. H., Sachs, T., and Günther, F. (2016). Relation between planimetric and volumetric measurements of permafrost coast erosion: a case study from Herschel Island, western Canadian Arctic. *Polar Res.* 35 (1), 30313. doi:10.3402/polar.v35.30313

Obu, J., Lantuit, H., Grosse, G., Günther, F., Sachs, T., Helm, V., et al. (2017). Coastal erosion and mass wasting along the Canadian Beaufort Sea based on annual airborne LiDAR elevation data. *Geomorphology* 293, 331–346. doi:10.1016/j.geomorph.2016.02.014

Overduin, P. P., Strzelecki, M. C, Grigoriev, M. N, Couture, N., Lantuit, H., St-Hilaire-Gravel, D., et al. Geological Society, London, Special Publications 388, 103–129, 12 February 2014, doi:10.1144/SP388.13.

Overduin, P. P., Wetterich, S., Günther, F., Grigoriev, M. N., Grosse, G., Schirrmeister, L., et al. (2016). Coastal dynamics and submarine permafrost in shallow water of the central Laptev Sea, East Siberia. *Cryosphere* 10 (4), 1449–1462. doi:10.5194/tc-10-1449-2016

Pearce, T., Smit, B., Duerden, F., Ford, J. D., Goose, A., and Kataoyak, F. (2010). Inuit vulnerability and adaptive capacity to climate change in Ulukhaktok, Northwest Territories, Canada. *Polar Record.* 46 (2), 157–177. doi:10.1017/s0032247409008602

Pisaric, M. F. J., Thienpont, J. R., Kokelj, S. V., Nesbitt, H., Lantz, T. C., Solomon, S., et al. (2011). Impacts of a recent storm surge on an Arctic delta ecosystem examined in the context of the last millennium. *Proc. Natl. Acad. Sci. U.S.A.* 108 (22), 8960–8965. doi:10.1073/pnas.1018527108

Rachold, V., Grigoriev, M. N., Are, F. E., Solomon, S., Reimnitz, E., Kassens, H., et al. (2000). Coastal erosion vs riverine sediment discharge in the Arctic Shelf seas. *Int. J. Earth Sci.* 89 (3), 450–460. doi:10.1007/s005310000113

Radosavljevic, B., Lantuit, H., Pollard, W., Overduin, P., Couture, N., Sachs, T., et al. (2016). Erosion and flooding-threats to coastal infrastructure in the Arctic: a case study from Herschel island, Yukon territory, Canada. *Estuar. Coast.* 39 (4), 900–915. doi:10.1007/s12237-015-0046-0

Rowland, J., and Coon, E. (2015). From documentation to prediction: raising the bar for thermokarst research. *Hydrogeol. J.* 24, 645–648. doi:10.1007/s10040-015-1331-5

Scharffenberg, K. C., Whalen, D., MacPhee, S. A., Marcoux, M., Iacozza, J., Davoren, G., et al. (2019). Oceanographic, ecological, and socio-economic impacts of an unusual summer storm in the Mackenzie Estuary. *Arct. Sci.* 6 (2), 62–76. doi:10.1139/as-2018-0029

Small, D., Atallah, E., and Gyakum, J. (2011). Wind regimes along the Beaufort Sea coast favorable for strong wind events at Tuktoyaktuk. *J Appl. Meteorol. Climatol.* 50 (6), 1291–1306. doi:10.1175/2010jamc2606.1

Solomon, S. M., Forbes, D. L., and Kierstead, B. (1994). Coastal impacts of climate change: Beaufort Sea erosion study. *Geol. Survey Canada Open File.* 2890, 85. doi:10.4095/194148

Solomon, S. M. (2005). Spatial and temporal variability of shoreline change in the Beaufort-Mackenzie region, northwest territories, Canada. *Geo Mar. Lett.* 25 (2), 127–137. doi:10.1007/s00367-004-0194-x

Stroeve, J. C., Serreze, M. C., Holland, M. M., Kay, J. E., Malanik, J., and Barrett, A. P. (2012). The Arctic's rapidly shrinking sea ice cover: a research synthesis. *Clim. Change.* 110 (3), 1005–1027. doi:10.1007/s10584-011-0101-1

Van der Sluijs, J., Kokelj, S., Fraser, R., Tunnicliffe, J., and Lacelle, D. (2018). Permafrost terrain dynamics and infrastructure impacts revealed by UAV photogrammetry and thermal imaging. *Rem. Sens.* 10 (11), 1734. doi:10.3390/rs10111734

Verhoeven, G. (2011). Taking computer vision aloft - archaeological three-dimensional reconstructions from aerial photographs with photoscan. *Archaeol. Prospect.* 18 (1), 67–73. doi:10.1002/arp.399

Vermaire, J. C., Pisaric, M. F. J., Thienpont, J. R., Courtney Mustaphi, C. J., Kokelj, S. V., and Smol, J. P. (2013). Arctic climate warming and sea ice declines lead to increased storm surge activity. *Geophys. Res. Lett.* 40 (7), 1386–1390. doi:10.1002/grl.50191

Ward Jones, M. K., Pollard, W. H., and Jones, B. M. (2019). Rapid initialization of retrogressive thaw slumps in the Canadian high Arctic and their response to climate and terrain factors. *Environ. Res. Lett.* 14 (5), 055006. doi:10.1088/1748-9326/ab12fd

Warren, J. A., Berner, J. E., and Curtis, T. (2005). Climate change and human health: infrastructure impacts to small remote communities in the north. *Int. J. Circumpolar Health.* 64 (5), 487–497. doi:10.3402/ijch.v64i5.18030

Waugh, D., Pearce, T., Ostertag, S. K., Pokiak, V., Collings, P., and Loseto, L. L. (2018). Inuvialuit traditional ecological knowledge of beluga whale (Delphinapterus leucas) under changing climatic conditions in Tuktoyaktuk, NT. *Arct. Sci.* 4 (3), 242–258.

Wobus, C., Anderson, R., Overeem, I., Matell, N., Clow, G., and Urban, F. (2011). Thermal erosion of a permafrost coastline: improving process-based models using time-lapse photography. *Arctic Antarct. Alpine Res.* 43 (3), 474–484. doi:10.1657/1938-4246-43.3.474

Wood, K. R., Overland, J. E., Salo, S. A., Bond, N. A., Williams, W. J., and Dong, X. (2013). Is there a "new normal" climate in the Beaufort Sea? *Polar Res.* 32 (1), 19552. doi:10.3402/polar.v32i0.19552

Zwieback, S., Kokelj, S. V., Günther, F., Boike, J., Grosse, G., and Hajnsek, I. (2018). Sub-seasonal thaw slump mass wasting is not consistently energy limited at the landscape scale. *Cryosphere* 12 (2), 549–564. doi:10.5194/tc-12-549-2018

Conflict of Interest: The authors declare that the research was conducted in the absence of any commercial or financial relationships that could be construed as a potential conflict of interest.

frontiers in Earth Science

ORIGINAL RESEARCH
published: 15 December 2020
doi: 10.3389/feart.2020.582103

Microbial Greenhouse Gas Dynamics Associated With Warming Coastal Permafrost, Western Canadian Arctic

Laura L. Lapham[1], Scott R. Dallimore[2], Cédric Magen[1], Lillian C. Henderson[1], Leanne C. Powers[1], Michael Gonsior[1], Brittany Clark[1], Michelle Côté[2], Paul Fraser[2] and Beth N. Orcutt[3]*

[1]Chesapeake Biological Laboratory, University of Maryland Center for Environmental Science, Solomons, MD, United States, [2]Geological Survey of Canada, Natural Resources Canada, Sidney, BC, Canada, [3]Bigelow Laboratory for Ocean Sciences, East Boothbay, ME, United States

OPEN ACCESS

Edited by:
Benjamin M. Jones, University of Alaska Fairbanks, United States

Reviewed by:
Kathy Kelsey, University of Colorado Denver, United States
Matthias Fuchs, Alfred Wegener Institute Helmholtz Centre for Polar and Marine Research (AWI), Germany

***Correspondence:**
Laura L. Lapham
lapham@umces.edu

Specialty section:
This article was submitted to Biogeoscience, a section of the journal Frontiers in Earth Science

Received: *10 July 2020*
Accepted: *03 November 2020*
Published: *15 December 2020*

Citation:
Lapham LL, Dallimore SR, Magen C, Henderson LC, Powers LC, Gonsior M, Clark B, Côté M, Fraser P and Orcutt BN (2020) Microbial Greenhouse Gas Dynamics Associated With Warming Coastal Permafrost, Western Canadian Arctic. Front. Earth Sci. 8:582103. doi: 10.3389/feart.2020.582103

Permafrost sediments contain one of the largest reservoirs of organic carbon on Earth that is relatively stable when it remains frozen. As air temperatures increase, the shallow permafrost thaws which allows this organic matter to be converted into potent greenhouse gases such as methane (CH_4) and carbon dioxide (CO_2) through microbial processes. Along the Beaufort Sea coast in the vicinity of the Tuktoyaktuk Peninsula, Northwest Territories, Canada, warming air temperatures are causing the active layer above permafrost to deepen, and a number of active periglacial processes are causing rapid erosion of previously frozen permafrost. In this paper, we consider the biogeochemical consequences of these processes on the permafrost sediments found at Tuktoyaktuk Island. Our goals were to document the *in situ* carbon characteristics which can support microbial activity, and then consider rates of such activity if the permafrost material were to warm even further. Samples were collected from a 12 m permafrost core positioned on the top of the island adjacent to an eroding coastal bluff. Downcore CH_4, total organic carbon and dissolved organic carbon (DOC) concentrations and stable carbon isotopes revealed variable *in situ* CH_4 concentrations down core with a sub-surface peak just below the current active layer. The highest DOC concentrations were observed in the active layer. Controlled incubations of sediment from various depths were carried out from several depths anaerobically under thawed (5°C and 15°C) and under frozen (–20°C and –5°C) conditions. These incubations resulted in gross production rates of CH_4 and CO_2 that increased upon thawing, as expected, but also showed appreciable production rates under frozen conditions. This dataset presents the potential for sediments below the active layer to produce potent greenhouse gases, even under frozen conditions, which could be an important atmospheric source in the actively eroding coastal zone even prior to thawing.

Keywords: permafrost, methanogenesis, carbon, thaw, coastal erosion

INTRODUCTION

The Arctic coast of western North America and northern Eurasia is undergoing rapid change due to sea level rise, reduction in seasonal sea ice extent and accelerated rates of coastal erosion (AMAP, 2019). Air temperatures in these regions are increasing at a rate that surpasses the average global temperature increase (GISTEMP, 2019; Lenssen et al., 2019) and projections suggest that this trend will continue into the future (Christensen et al., 2013; AMAP, 2019; Bush and Lemmen, 2019). Permafrost that is widespread and ubiquitous to most Arctic settings is responding to this warming with changes in near surface processes, such as a thickening of the active layer (Biskaborn et al., 2019). Warming permafrost can lead to the release of previously stored dissolved organic carbon (DOC), which could act as a labile carbon source for microbial metabolisms. Microbial incubation studies where permafrost material is thawed to above freezing temperatures, have shown the potential for the formation of potent greenhouse gases, such as CH_4 and CO_2 (Treat et al., 2015; Schädel et al., 2016; Knoblauch et al., 2018). Understanding how temperature affects microbial production rates of these gases, under realistic temperature scenarios, is key to projecting the role permafrost may play in future climate change.

Incubation studies assessing the rates of microbial processes in Arctic soils often concentrate on these near-surface sediments and the top of permafrost as an area most vulnerable to thaw in the future (Elberling and Brandt, 2003; Treat et al., 2014; Treat et al., 2015). Yet, microbial processes could still occur deeper within the permafrost that ultimately end in the production of the same greenhouse gases (Wagner et al., 2007; Knoblauch et al., 2013). Microbial activity in the frozen state is certainly recognized and studies are moving toward understanding the mechanisms for specific processes, such as methanogenesis (Hultman et al., 2015; Nikrad et al., 2016). Studies specifically incubating frozen permafrost with isotope labeled substrates such as bicarbonate or acetate, show that these methanogens are actively producing radiative gases under frozen conditions (Rivkina et al., 2007). Such activity could occur in unfrozen water found in the permafrost (Romanovsky and Osterkamp, 2000), possibly as cryopegs (sodium-chloride brines) which remain liquid down to −11°C (Gilichinsky et al., 2005), although this remains unclear.

In response to climate warming, a changing mean annual ground surface temperature regime (Biskaborn et al., 2019) could manifest in greater microbial activity within the permafrost, even if temperatures remain below freezing. But warming temperatures are not the only factor. Frozen sediments at depth can also experience rapid thaw triggered from coastal erosion and landslides. In these cases, warming, or abrupt thaw (Turetsky et al., 2020), can occur from the top down, or from the sides of exposed cliff faces. If there are accumulated greenhouse gases within this newly exposed permafrost, it could be abruptly released to the atmosphere.

In this paper, we consider the biogeochemical consequences of warming (yet still frozen) and thawing (no longer frozen) of permafrost from an eroding coastal setting near Tuktoyaktuk, Northwest Territories (N.W.T.), Canada, on the Beaufort Sea coast. This area has experienced prolonged atmospheric warming and coastal erosion (Hynes et al., 2014). Based on previous permafrost studies, we hypothesize that there are active microbial processes occurring in these coastal sediments that generate CO_2 and CH_4 as permafrost is warmed *in situ* or exposed to rapid thawing by geomorphic processes such as coastal retreat, landslides or nearshore transgression. We characterize the baseline conditions of a 12 m permafrost core by measuring physical properties, *in situ* CH_4 concentrations, and organic carbon quantity and quality. Laboratory incubation studies document CH_4 and CO_2 release from frozen permafrost core samples as the they are warmed at negative temperatures and after thawing.

SAMPLE COLLECTION AND METHODS

Geologic and Permafrost Setting

The study area (**Figure 1**) is part of the Tuktoyaktuk Coastlands physiographic region, which is characterized by thick occurrences of unconsolidated sediments (Rampton, 1988). The landscape is covered by a low arctic tundra vegetation with dwarf birch, willow, grasses and moss. The climate is characterized by long cold winters and short cool summers, with low precipitation. The Tuktoyaktuk area lies within the continuous permafrost zone, with permafrost thicknesses of ~400 m (Hu et al., 2013). Ground ice, including ice lenses, ice wedges, and extensive bodies of massive ice, is common (Mackay and Dallimore, 1992). The only community in the area is the Hamlet of Tuktoyaktuk, which was originally an Inuvialuit seasonal harvesting site and was established as a harbor by the Hudson's Bay Company in 1934. The Hamlet presently has a population of ~900 people (Statistics Canada, 2017).

The coastal environment of the Tuktoyaktuk area is experiencing relatively rapid coastal retreat. The seaward side of Tuktoyaktuk Island, located approximately 1 km from the Hamlet, has eroded at an average rate of ~2.5 m/a since 1950 (**Figure 1**; Hynes et al., 2014). The majority of the erosion occurs during wind-induced storm surge events. Although storm surges can occur at any time of the year, the largest erosional impact is during the late summer and early fall when the Beaufort Sea coast is ice free, the dominant storm winds are from the northwest and fetch length is at its maximum (Manson and Solomon, 2007). Increases in mean annual air temperatures from approximately −11°C to −8.5°C have been recorded over the past 5 decades (**Figure 2**; GISTEMP, 2019). A linear fit to this trend gives an increase of 0.52°C/decade, about twice the global average for this same period (Hansen et al., 2010). Changing permafrost conditions are affecting building foundations and other infrastructure, storm surges are causing flooding, and accelerated coastal retreat is forcing the relocation of buildings (Gruben, 2018; Zingel, 2019).

Core Collection

The permafrost core utilized for our study was collected from a drilling program, conducted by the Geological Survey of Canada in March 2018, to document the properties of the eroding

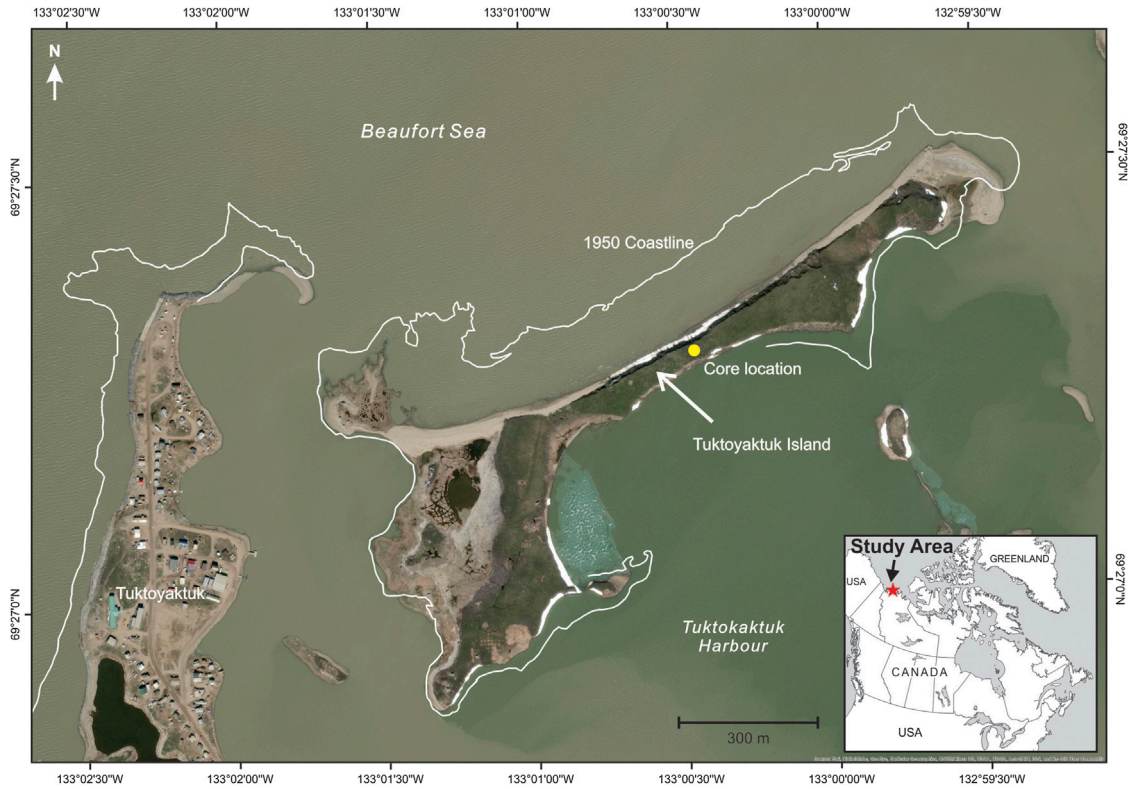

FIGURE 1 | Location of 12 m borehole collected from Tuktoyaktuk, Northwest Territories, Canada (69.442°N, 133.031°W). The Hamlet of Tuktoyaktuk is marked on left.

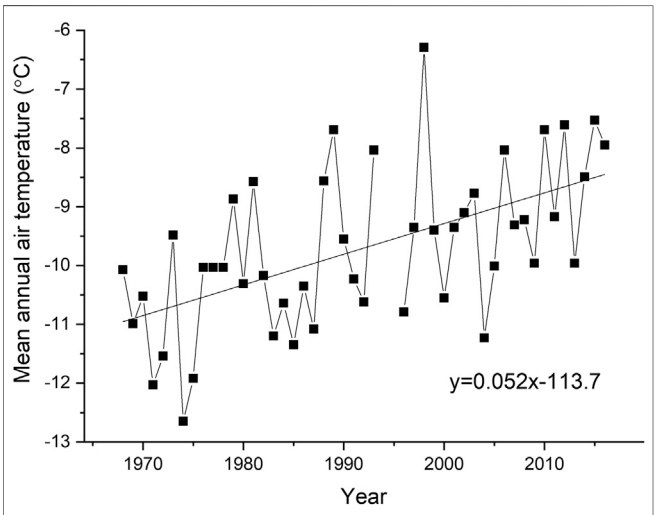

FIGURE 2 | Mean annual air temperature at Tuktoyaktuk from 1968–2018. Linear fit shows positive slope of 0.052°C/year. Data from GISTEMP (2019).

permafrost as a basis to assess the consequences of ongoing warming and erosion of Tuktoyaktuk Island (**Figure 1**). Four drill holes were completed using a CRREL core barrel (10 cm diameter, Midnight Sun Drilling, Whitehorse, CA, **Figure 3A**) for frozen sediments and a solid stem auger for unfrozen sediments. The CRREL core barrel was specifically designed to collect permafrost samples with minimal contamination or thermal disturbance to the core. The core samples utilized for this project (**Figures 3B,C**) were retrieved from a terrestrial borehole positioned at the surface of the Island, ~6 m above sea level ~30 m from the eroding coastal bluff (**Figure 4A**). In August 2018, a thermistor cable was installed in a borehole to measure ground temperatures. The thermistor sensor depths ranged from just below ground surface to a maximum depth of 14 m with a data logger (RBR XR-420, 8 channel) set to record temperatures hourly. In July 2019, the temperature data was recovered and presented here.

Samples used in this study were collected from 10 cm length whole round core sections selected from 10 depth intervals representing a range of *in situ* ground temperatures (0.6, 0.9, 1.5, 1.7, 2.2, 2.8, 3.4, 3.9, 7.8, and 11.6 m). The drilling was undertaken in March with air temperatures <−25°C and samples were stored in plastic bags and maintained at *in situ* air temperature until transportation to the Aurora Research Institute in Inuvik, N.W.T. Care was taken to minimize contamination by handling sediment sections with nitrile gloves. Cores were then transferred frozen to the Chesapeake Biological Laboratory (Solomons, MD, USA), and stored at −20°C until further analysis. Given the care to prevent contamination or warming during coring, storage and transport we assume that

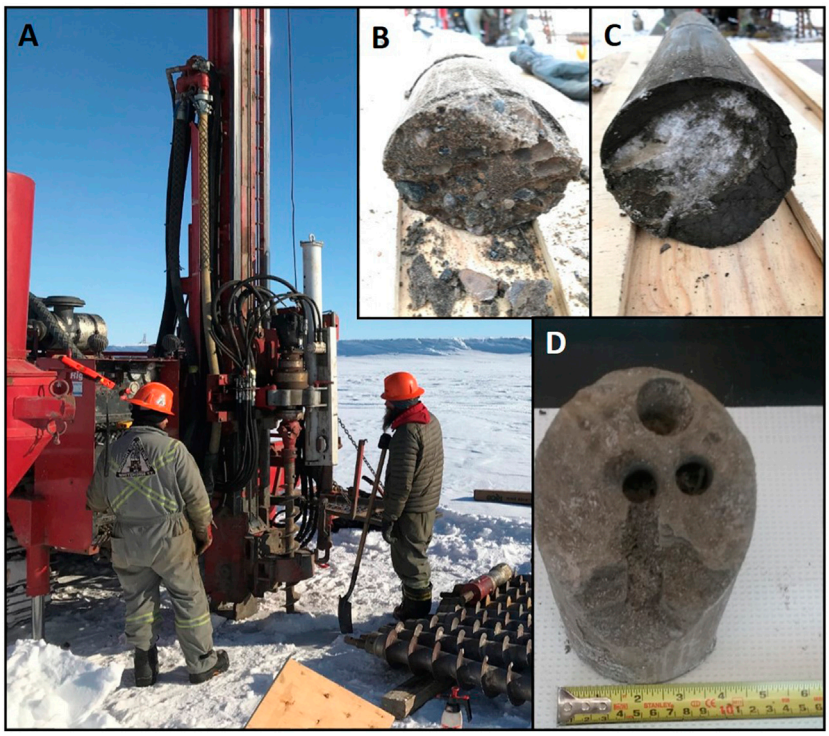

FIGURE 3 | (A) Picture of field operations, **(B)** the surface sediments at this site consisted mainly of pebbly sands which were very slow to core, **(C)** deeper in the section some fine grained sediments with clasts and nodules of pure ground ice were encountered, and **(D)** a sub-section sampled for the analyses described in study. Pictures from Paul Fraser.

measured physical and geochemical parameters reasonably reflect *in situ* conditions of the subsurface permafrost.

Chemical and Physical Characterization of the Core

In situ CH_4 Content

Within 1 month of collection, the 10 core sections were subsampled under frozen conditions by drill with a flame sterilized hole saw (3 cm long, 1.5 cm outer diameter) from the center of the section to obtain ~3–6 g of undisturbed sediment (**Figure 3D**). Material was placed into pre-weighed 20 ml glass serum vials and capped with black butyl rubber stoppers and aluminum caps, in a manner similar to CH_4 determination in marine sediments (Lapham et al., 2008). Vials were weighed to determine the mass of each sample, and basified to arrest further microbial activity (3 ml 1M potassium hydroxide). CH_4 concentrations were determined via a headspace equilibration method, and 6 ml of headspace gas were injected into a gas chromatograph (SRI 8620 Multi Gas, thermal conductivity and flame ionization detectors, 3′ HaysepD and 6′ mol sieve 13X columns). Concentrations were corrected for solubility, as previously described in Magen et al. (2014), and analytical precision is 2%.

Physical Parameters

Fresh subsamples were drilled from each depth, in triplicate, to determine porosity, wet bulk density and gravimetric water content. Determinations were made on ~6 ml of drilled sediment that was pre-weighed and then placed into a pre-weighed volumetric cylinder with ~10 ml of prefiltered deionized water to determine the volume. The cylinder was then dried at 60°C until constant weight was obtained after seven days. Porosity, wet bulk density, and gravimetric water content was then calculated from these masses and volumes. Analytical accuracy was around 5%.

Organic Matter, Sulfate (SO_4^{2-}) and Chloride (Cl^-) Contents

After the physical parameter testing, the remaining sediment was ground and then treated with acid (1 M HCl) to remove carbonates and measured for total organic carbon (TOC) and organic nitrogen (TON) concentrations, as well as stable isotope ratios (δ^{13}C-TOC, δ^{15}N-TON). Aliquots of sediment were measured on an elemental analyzer (Costech elemental combustion system) interfaced to a Delta V Plus Isotope Ratio Mass Spectrometer (Thermo Scientific, Waltham, MA, USA). The δ^{13}C and δ^{15}N values were reported in ‰ vs VPDB and ‰ vs Air, respectively. Precision on the stable isotope measurement was ±0.1‰ for δ^{13}C and 0.2‰ for δ^{15}N. Carbon to nitrogen (C:N) ratios are also reported.

On a freshly drilled sediment sample, DOC concentrations were analyzed by placing sediment subcores in a 10 ml centrifuge tube and diluting with ~3.5 ml milli-Q water. After centrifugation (3000 RPM, 30 min, 20°C, Sorvall® RT 6000D), the supernatant

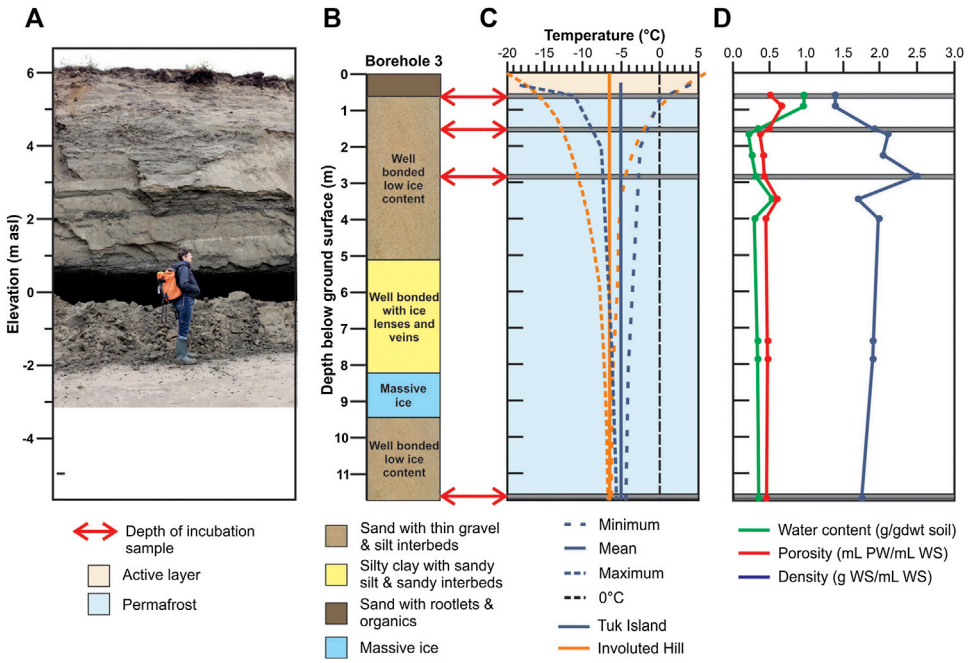

FIGURE 4 | Down core physical properties. **(A)** Photograph of coastal exposure near field site. **(B)** Core description. Red arrows and gray bars indicate depths chosen for incubation experiments. **(C)** Permafrost annual temperature range presented in this study (blue line Tuk Island 2018-2019) and a close location (orange line Involuted Hill (IH88-2) in 1995). **(D)** Physical properties measured of core: water content (green line), porosity (red line) and wet bulk density (blue line). PW = porewater, WS = wet sediment.

liquid was filtered using 0.2 μm pore size Whatman 25 mm GD/X syringe filters and diluted 1:2 with milli-Q water for DOC and optical property analyses. Samples were acidified to pH 2 with concentrated HCl (Sigma Aldrich 32%, *pura*) and analyzed on a total organic carbon analyzer (Shimadzu TOC-V_{CPH}) using potassium hydrogen phthalate solution as DOC standards. Final DOC concentrations were corrected for dilutions and reported in volume of pore-water present at each depth. An aliquot of this water was then used to determine SO_4^{2-} and Cl^- concentrations on an ion chromatograph (IC, Dionex ICS1000) at 13.5 times dilution with milli-Q water. Concentrations were calculated from IC response compared to standard curve made from IAPSO seawater (35 ppt) and dilutions down to 0.35 ppt. Precision of the measurement was 3% for these samples. Final SO_4^{2-} and Cl^- concentrations are reported after correcting for two dilutions made during manipulations for DOC measurements.

Dissolved organic matter (DOM) optical properties were measured on the above diluted pore water samples (not acidified) by recording ultraviolet (UV)-visible (VIS) absorbance (A(λ)) spectra and excitation emission matrix (EEM) fluorescence spectra (Horiba Aqualog Spectrofluorometer). Excitation or A(λ) spectra were collected at 3 nm intervals between 240 and 700 nm and emission spectra were collected at fixed 3 nm intervals between 245 and 600 nm. Milli-Q water served as the absorbance and fluorescence blank and the water Raman peak (excitation = 350 nm) was measured to normalize all EEM data. Thus, fluorescence intensities are expressed in water Raman units (RU). EEM spectra were also corrected for Raleigh scattering following a method established previously (Zepp et al., 2004). Raw absorbance data was corrected for any offsets between pore water and the pure water blank or instrument drift by subtracting all spectra by their absorbance value at 700 nm. From the A(λ) spectra scans, we only report specific UV absorbance at 254 nm ($SUVA_{254}$; m^{-1} L mg^{-1}), which is the A (254) normalized to pathlength (m) and DOC concentration (mg L^{-1}). A(254) is reported in Supplemental Figure 1. $SUVA_{254}$ has been used as an indicator of DOM aromatic content (Weishaar et al., 2003) and thus the quality of the organic carbon (i.e., higher aromatic content indicating lower quality). The full EEM dataset was further examined for organic matter quality using Parallel Factor Analysis (PARAFAC) (Stedmon and Bro, 2008; Murphy et al., 2013). However, since this analysis is beyond the scope of this paper, the methods, results, and discussion associated with this analysis are presented in the supplemental material.

Anaerobic Incubations

Laboratory incubations lasting ~6 weeks were carried out on sub-samples from four depths. For each depth, the incubations were conducted under anaerobic conditions at different temperatures, and compared to killed (basified) controls to determine if any abiotic processes contributed to CH_4 release. The depths were chosen to document the range of sediment, permafrost and chemical characteristics down core: 0.6 m corresponded to the only sample at the base of the active layer, 1.5 m corresponded to a

peak in CH_4 concentrations, 2.8 m corresponded to a peak in DOC concentrations, and 11.6 m was the deepest sample collected which was near the depth of zero annual temperature amplitude.

For each incubation, approximately 6–9 g of freshly drilled sediment was placed into six pre-combusted (550°C) 10 ml glass serum vials and capped with black butyl rubber septa and aluminum cap. Vials were then flushed with nitrogen (UHP Airgas) to obtain an anaerobic headspace and placed back at −20°C. To obtain replication within treatments, to three of these vials, 3 ml of a 1M KOH solution was added to arrest microbial activity and referred to as the "killed control" (in triplicate). Since flushing the vials with nitrogen may have removed any *in situ* CH_4, the killed controls act as a way to follow the diffusion of remaining CH_4 to the headspace, which is an abiotic process. The remaining three vials were not amended with base and referred to as the "experimental treatment" to examine the gross potential of microbial production of CH_4 and/or CO_2 during the incubation (also done in triplicate). As the vials were devoid of oxygen, there was no electron acceptor for aerobic microbial CH_4 oxidation, so the CH_4 production rates should be considered a high-end for gross production potential, and not net rates expected under real-world conditions where oxygen would likely be present.

All vials were then placed in temperature-controlled chambers maintained at specific temperatures within 1°C. For 0.6 m, incubations were carried out at −20 and 15°C, to replicate natural range in temperature conditions in the active layer at this site (**Figure 4**). For 1.5 and 11.6 m, incubations were carried out at −20°C (coldest surface temperatures sediments experience), −5°C (average air temperature), and +5°C (to replicate modest warming comparable to other studies). For 2.8 m, incubations were carried out at the same frozen temperatures (−20 and -5°C); for the warm treatment, 15°C was chosen for comparison to other studies incubating active layer sediments (Treat et al., 2015). All treatment and temperature pairings were carried out in triplicate. During the incubation, vials were stored in the dark and upside down in a small tub of water (or ice) at their respective temperatures to prevent gases from escaping the septa (although independent experiments show this process would be minimal during the incubations (Magen et al., 2014)).

Time points were collected as discrete headspace samples, approximately once a week, to determine the CH_4 and CO_2 concentrations. To do this, 6 ml of nitrogen (UHP Airgas) was injected into the vial to displace 6 ml of the headspace, and this aliquot was injected onto the gas chromatograph described above. Vials never experienced an overpressure of gas. Sample areas were compared to certified standards (Airgas, 30 ppm CH_4, 2000 ppm CO_2) and converted to ppmv in the headspace. Analytical precision was 3%. CH_4 concentrations were averaged between the three triplicates and reported as an average +/− standard deviation. Concentrations were then converted to cumulative production for CH_4 and CO_2 and reported as μmol CH_4 or CO_2 carbon per gram dry weight (μmol CH4−or CO_2−C/gdw) and plotted against incubation time. To calculate a rate of CH_4 generation on a per carbon basis, a line was fitted to the linear portion of the cumulative production time-series and converted to a per carbon basis by multiplying by the %TOC measured for each depth. It should be noted that while CO_2 concentrations were measured in the killed controls, the values were expected to be 0 since base drives gaseous CO_2 into the water phase. The results are still shown as a way to verify our basic assumptions.

Modeling Diffusion

When the sediment plugs are first placed in the vials and flushed with N_2 gas, it is possible that CH_4 dissolved in the sediment interstial spaces will diffuse out and be measured as an increase in CH_4 concentrations over time due to the concentration gradient present at the beginning of the incubations. This theoretical diffusion can be estimated using a one-dimension model to calculate how much CH_4 could diffuse from the sediment plug in the incubation vials to the headspace over the time of the incubations (Lapham et al., 2014). We used a diffusion coefficient of 8.6×10^{-6} cm^2/sec for CH_4, which is corrected for temperature, salinity, and pressure in the vials (Riley and Skirrow, 1975). We estimated salinity based on the Cl^- concentrations reported in *Organic Matter, Sulfate (SO_4^{2-}) and Chloride (Cl^-) Contents*. The starting CH_4 concentration was the *in situ* value we measured from the triplicate sub-sections (*In situ CH_4 Content*). The results of this model will thus be an overestimate, since CH_4 was most likely lost in the vials during headspace flushing. We assumed the distance for diffusion was 3 cm, the distance in the vials.

RESULTS

Physical and Chemical Parameters of *in situ* Permafrost

Cored sediments consisted of bedded glaciofluvial sands with interbeds of gravel and silt, thought to have been deposited during the waning stages of the late Wisconsinan glaciation (~12,000 years before present; Rampton, 1988). The stratigraphy consisted of a near surface organic-rich interval (containing rootlets) that extended to ~60 cm depth, ice-bonded fine sands with occasional pebble and silt-rich layers and intervals of massive ice with >80% excess ice by volume (**Figure 4B**). Thermistor data shows that sediment temperature fluctuates annually to a depth of ~11.5 m, with a mean annual ground surface temperature of approximately −5°C. The active layer is interpreted to be within the upper 0.6 m based on where the maximum temperature crosses 0°C (**Figure 4C**). Similar ground temperature measurements from a nearby site (~15 km east of Tuktoyaktuk 69.4736°N, 132.6285°W) carried out in 1995 (Dallimore et al., 1996; **Figure 4C**), show that mean annual ground temperatures may have increased 3–4°C in the past 25 years.

The *in situ* sediment physical properties varied with depth (**Figure 4D**) reflecting changes in the geology at the site (mainly grain size) and ground ice content. Permafrost sediment porosity averaged 0.48 ± 0.09 down core (**Figure 4D**). Gravimetric water content was ~1.0 g/gdwt (grams dry weight) near the surface and at ~2 m, decreased to ~0.25 for the remainder of the core (**Figure 4D**). We observed an ice-rich interval at 3.5 m sediment depth (**Figure 4B**), which corresponded to an increase in both gravimetric water content and porosity. There was no indication of gas bubbles in the ice. Wet bulk density mirrored the other physical parameters (**Figure 4D**). Compared

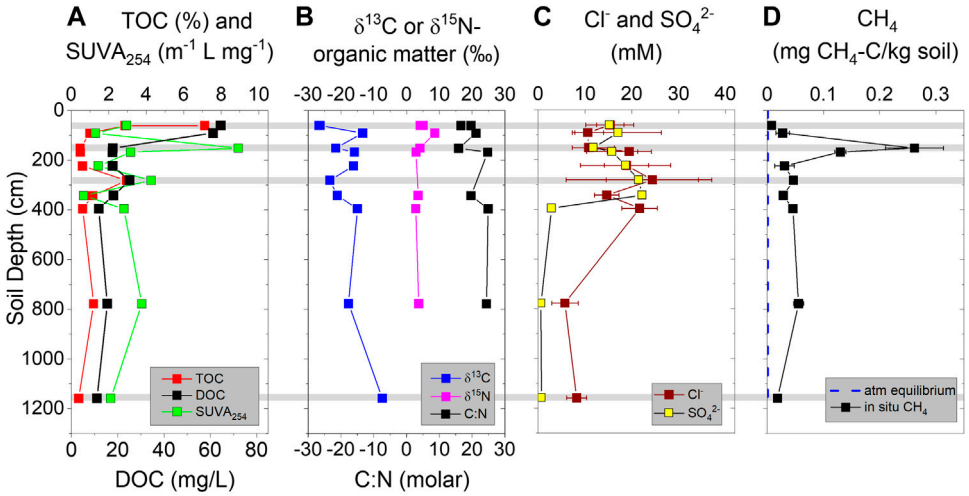

FIGURE 5 | Downcore profiles from permafrost core: **(A)** Total organic carbon (TOC), $SUVA_{254}$, and dissolved organic carbon (DOC). **(B)** Stable carbon and nitrogen isotopes of organic matter and C:N ratio. **(C)** Chloride and sulfate concentrations within thawed permafrost interstitial waters. **(D)** Methane concentrations (mg methane per kg wet soil) compared to concentrations equilibrated with two ppmv CH_4 atmosphere (0.001 mg/kg soil). Gray horizontal bars indicate depths chosen for incubation experiments.

to unfrozen settings, the permafrost samples had very low bulk densities and high porosities, especially those with elevated ground ice content.

TOC concentrations (given in weight %) in the uppermost surface sample (~0.6 m deep) was 2% in one replicate and 7% in the other two replicates, indicating heterogeneity of material in the active layer (**Figure 5A**). TOC then decreased to ~0.5% by 1 m, exhibited a sub-surface peak at 2.8 m (3%) and decreased again to 0.5% for the remainder of the core. Similar to TOC, DOC concentrations were highest in the surface sample (60 mg/L) and exhibited a sub-surface peak of 25 mg/L at 2.8 m depth (**Figure 5A**). DOC concentrations remained at 11–17 mg/L for the remainder of the core. Specific UV absorbance $SUVA_{254}$ values of the DOM throughout the core ranged from 1.3 to 8.9 m^{-1} L mg^{-1} (**Figure 5A**). The values were variable down core with two small sub-surface peaks which corresponded to the highest CH_4 values (highest SUVA value of 8.9 ± 2.5 m^{-1}) and the TOC/DOC sub-surface peak (4.3 ± 2.2 m^{-1} L mg^{-1}).

δ^{13}C-TOC values ranged between −26.7 and −7.4‰ and average -18.6 ± 5.9‰ (**Figure 5B**). The highest δ^{13}C-TOC value of −7.4‰ was found at the deepest depth. δ^{15}N-TON values ranged between 2–5‰ for the whole core with a sub-surface peak of 8.6‰ at ~1 m. TON concentrations were highest at the surface (0.4%) and decreased to 0.06% at 3.4 m and was undetected at our deepest depth (data not graphed). C:N values ranged between 15–24 for the whole core (**Figure 5B**). SO_4^{2-} and Cl^- concentrations were between 10 and 20 mM in the upper 3 m with large variability within replicate samples (**Figure 5C**), likely indicating variable ice concentrations in subsamples. Below 3 m, concentrations decreased to ~2 mM SO_4^{2-} and 6 mM Cl^-.

CH_4 concentrations in the core samples exhibited a sub-surface peak at ~1.5 m of 0.28 mg CH_4 per kg sediment (**Figure 5D**). Above this sub-surface peak, the two shallowest samples collected within or just below the modern active layer (0.6 and 0.9 m depth) had the lowest CH_4 concentrations, despite having the highest TOC values. Beneath the sub-surface peak, CH_4 concentrations decreased and became constant at ~0.03 CH_4 per kg sediment down to 11.6 m in the core (**Figure 5D**).

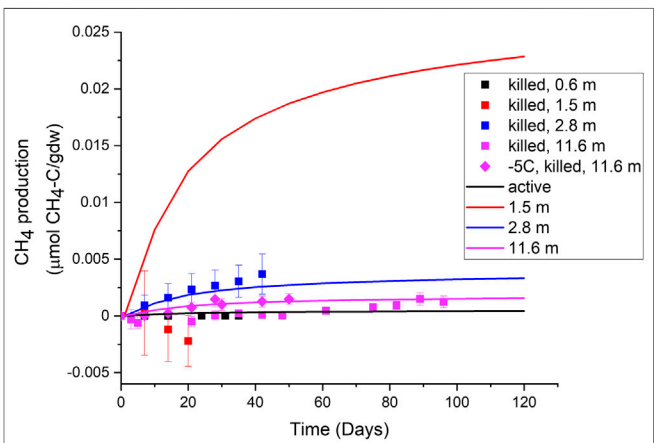

FIGURE 6 | Methane production rates in killed controls (symbols), compared to modeled diffusion rates at 5°C starting with measured *in situ* concentrations (solid lines). The 1.5 m depth diffusion line is much higher because the *in situ* methane concentrations were also so much higher.

Incubation Results

Sediment incubations were carried out at four depths (0.6, 1.5, 2.8, and 11.6 m) that had varied *in situ* geochemistry and physical properties. As shown on **Figure 4C**, these depths also experience different seasonal permafrost temperature regimes. CH_4 concentrations in the killed control treatments slightly

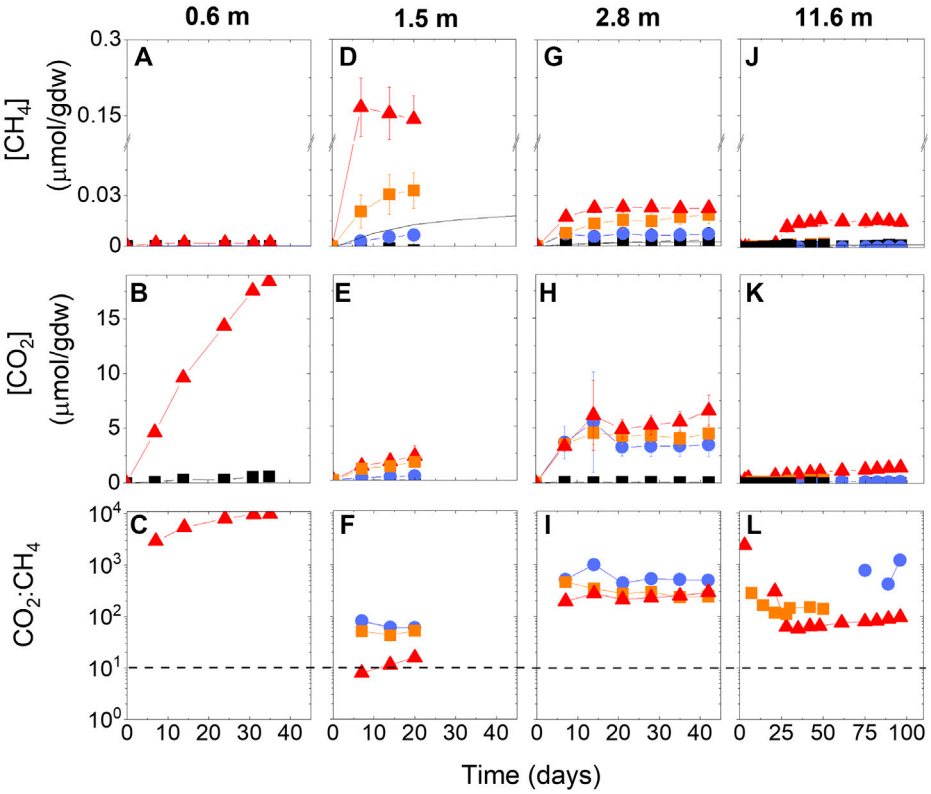

FIGURE 7 | Cumulative CH_4 and CO_2 production rates and CO_2:CH_4 ratios from incubations at **(A–C)** 0.6 m, **(D–F)** 1.5 m, **(G–I)** 2.8 m, and **(J–L)** 11.6 m. Red triangles denote warmest treatment (either +15°C or +5°C), orange squares are −5°C, and blue circles are −20°C. Black squares are average of all killed controls across all temperatures. Black solid line in panel D denotes production rates as calculated from diffusion. Note *x*-axis for 11.6 m depth is different than other depths and *y*-axis scale is broken in CH_4 production rates to show all data on one scale. The black dashed line in CO_2:CH_4 panels shows the 1:1 line. Error bars are standard deviation of triplicates.

increased over time for all the depths except 1.5 m, which decreased over time (data points in **Figure 6**). When a simple 1-D diffusion model was applied to the incubation results, for all depths except the 1.5 m, the slight increase was explained by simple diffusion of *in situ* CH_4 out of the sediment plug upon incubation set-up (model lines in **Figure 6**). The results from these controls gave us confidence that any values above those measured in the killed controls could be interpreted as the gross potential for microbial CH_4 production stimulated by the incubations.

For all depths of the incubations, CH_4 and CO_2 concentrations increased over time in all treatments (including some of the frozen treatments; **Figure 7**). The gross production rates were faster at the higher temperatures than at the lower temperatures. The cumulative gross production rates increased linearly at first, indicative of the growth phase, and then plateaued, indicative of sustained production. The active layer incubation (i.e., 0.6 m) had the lowest CH_4 production rates of any incubation at +15°C (0.0012 µmol CH_4 per gdw, **Figure 7A**). At −20°C, the rate is 0.000012 µmol CH_4 per gdw (**Figure 7A**). This active layer also had the highest CO_2 production rates (**Figure 7B**), with the CO_2:CH_4 ratio reaching 10,000 at the end of the experiment (**Figure 7C**). The incubation of sediment with the highest *in situ* CH_4 concentration (i.e., 1.5 m) exhibited the highest gross CH_4 production rates of any incubation (0.15 µmol CH_4 per gdw at 5°C and 0.03 µmol CH_4 per gdw at −5°C; **Figure 7D**). The CO_2 production rates in this sample were similar for the +5°C and −5°C treatments at about 3 µmol CO_2 per gdw (**Figure 7E**), resulting in CO_2:CH_4 ratios less than 100 for all temperatures and a pattern where ratios were higher at the colder temperatures (**Figure 7F**). The incubation of sediment from the sub-surface organic carbon peak (i.e., 2.8 m) had the highest CO_2 production rates at frozen temperatures compared to the other depths (averaging µmol CO_2 per gdw at all temperatures, even in the 15°C treatment; **Figure 7H**). Gross potential CH_4 production rates reached as high as 0.024 µmol CH_4 per gdw at +15°C in this sample (**Figure 7G**). Rates decreased with colder temperatures but remained above the killed controls even at −20°C. The CO_2:CH_4 ratios in this sample showed a similar pattern as the above depth but were an order of magnitude higher (**Figure 7I**). In the deepest permafrost sediment incubation (i.e., 11.6 m), gross potential rates of CH_4 production were near the diffusion line for the frozen temperatures, indicating no microbial production, and there was a ~25 days lag phase before rates increased to 0.015 µmol CH_4 per gdw in the 5°C incubation (**Figure 7J**). CO_2 production rates were the lowest observed in the incubations

(**Figure 7K**), resulting in CO_2:CH_4 ratios that showed no pattern with time (**Figure 7L**) and that were negative at times (data not shown). Negative ratios mean that CH_4 production exceeded CO_2 production.

DISCUSSION

The main objective of this study was to assess microbial greenhouse gas dynamics associated with a permafrost type section that is presently experiencing the effects of climate warming and coastal erosion. The motivation derives from the fact that release of these gases may accelerate the pace of global warming, but the magnitude of gas release from settings typical of the geology of the Beaufort Sea coast is not well constrained. We carried out the study on a permafrost core drilled on Tuktoyaktuk Island, where increased ground temperatures are documented. The site also experiences event driven, coastal erosion primarily by undercutting of an eroding cliff face, which exposes frozen permafrost to relatively warm air temperatures resulting in rapid thawing. At current erosion rates, the core site presented here could be exposed to the sea in ~12 years. Our experiments document significant potential for microbially-mediated greenhouse gas release under still-frozen conditions and after thawing (**Figure 7**). Here we discuss the implications of the *in situ* conditions of the permafrost and for microbial processes to occur in frozen and unfrozen soils.

Geochemistry of Carbon Reservoir

While most of the permafrost sediment depths analyzed had relatively low organic carbon content (TOC: ~0.5 weight%; DOC: ~10 mg/L), as might normally be expected for glaciofluvial sediments, we observed some depths with high TOC (2–7 weight%) and DOC (20–60 mg/L) contents (**Figure 5**). The active layer had the highest TOC and DOC concentrations, and a secondary peak was observed at ~3 m depth. This depth may represent an organic-rich (not peat) paleo-active layer formed under warmer temperature conditions in the past. Indeed, other studies conducted in this area have documented the presence of older and deeper organic horizons thought to have formed during the Hypsithermal warm period in the early Holocene (Burn, 1997).

The permafrost organic matter observed in the core samples suggested possible terrestrial and marine sources, based on the ^{13}C and ^{15}N signatures of organic matter (**Figure 5B**). Terrestrial ecosystems (dominated by C3 plants) typically have ^{13}C values that range from −23 to −34‰, whereas marine systems range from −10 to −25‰ (Ehleringer et al., 1993). Values measured in our core are slightly enriched in ^{13}C, compared to sediments from the Lena River Delta ranged from −29 to −26‰ (Knoblauch et al., 2013). The ^{13}C-organic matter in the surface samples was −26‰, suggesting a predominantly C3 terrestrial source, whereas more positive ^{13}C values of deeper layers indicate mixed C3 terrestrial and marine sources. The ^{13}C-organic matter value of −7.4‰ for the deepest layer does not reflect either of these sources. Such heavy values have been measured when the terrestrial system is dominated by C4 plants, which are typically tropical and warm-temperate plants. Certainly tropical plants are not supported at this site; however, unconsolidated Tertiary strata, which were deposited during much warmer climate conditions, do occur at shallow depth in the Tuktoyaktuk area, and reworked Tertiary pollen is often seen in Quaternary sediments (Ritchie, 1974). This may be a possible source for the enriched isotope values observed in this sample.

The stable isotope values give us a bulk view of the organic matter available to the microbial community, but microorganisms typically access carbon from the dissolved pool. Therefore, to compliment the stable isotope work, we also assessed the quality of the DOM with optical methods (Supplementary Material). We focus the discussion on $SUVA_{254}$, which relates to the aromatic content of the molecules in the dissolved pool (Traina et al., 1990; Weishaar et al., 2003; Fellman et al., 2008). We recognize that this parameter has limitations in that there is no way to distinguish between a low concentration of highly absorbing material and a high concentration of low absorbing material. Furthermore, permafrost pore waters may have a very different chemical composition than the organic matter isolates analyzed in previous studies, so the relationship to DOM aromatic content may be different here. But, as a generalization, the higher the aromatic content, the less "labile" and more "refractory" the organic carbon is for microbial processes. Given the debate in the literature now with such labels as "labile" and "refractory" (Hansell, 2013) we use this measurement here only as an indicator of organic matter quality and not a definitive measurement. The permafrost sediment layer with the highest *in situ* CH_4 concentration (**Figure 5A**), the highest potential for CH_4 production (**Figure 7D**), and some of the lowest CO_2 production potential (**Figure 7E**), had the highest $SUVA_{254}$ value (**Figure 5A**). This indicates that the labile carbon to fuel microbial heterotrophic or fermentative respiration (i.e., producing CO_2) is less available at this depth, and that methanogens are likely using more refractory carbon to produce CH_4. Likewise, the deeper permafrost sediment layer with a subsurface TOC peak also had relatively high $SUVA_{254}$ values (**Figure 5A**), the second highest CH_4 production potential (**Figure 7G**), and modest CO_2 production potential (**Figure 7H**). By contrast, the sediment from the active layer had low $SUVA_{254}$ values (i.e., was more labile) and the lowest and highest CH_4 and CO_2 production potentials, respectively (**Figures 7A, B**). Overall, these patterns support the observation that permafrost carbon quality, in addition to quantity, plays an important role in determining greenhouse gas production potential (Schädel et al., 2014; Kuhry et al., 2020).

In situ CH_4 Present in Permafrost and Potential for Atmospheric Release

We detected *in situ* CH_4 in all frozen core samples with values ranging from 0.03 to 0.28 mg CH_4 per kg sediment (**Figure 5A**). The highest value was measured in the organic-rich layer just below the modern active layer. These values are consistent with published values from other permafrost settings with low organic contents. For example, Alaskan discontinuous permafrost

sediments contained ~0.001–22 mg CH_4 per kg sediment (Kvenvolden and Lorensen, 1993), and silty sediments with ground ice near Prudhoe Bay, Alaska, had 0.2–11 mg CH_4 per kg sediment (Rasmussen et al., 1993). Higher values have been observed in organic-rich active layer sediments with lacustrine vegetation (15 mg CH_4 per kg sediment (Rivkin, 1998); in the active layer of a permafrost floodplain and within a polygon center (6.5 and 8,656 mg CH_4 per kg sediment, respectively Ganzert et al. (2007)), and Lena Delta permafrost setting (4.8 mg CH_4 per kg sediment (Wagner et al., 2007)). Our study adds to the body of work on this topic and demonstrates that *in situ* CH_4 is common in Arctic permafrost in a variety of sediments and geologic settings.

In addition to the concentration of *in situ* CH_4 in permafrost, the state of CH_4 (i.e., as bubbles trapped in ice, free gas in the sediment, and/or dissolved) is important when evaluating the potential for greenhouse gas release from these environments and for understanding operative geologic processes. Given that all of our core samples were collected in the winter when ground temperatures were well below −5°C, and that they were stored at −20°C until testing, we envisage that the CH_4 detected was residing within a heterogeneous matrix consisting of sediment grains (sand, minor silt and some organics), pore ice and possibly a very small fraction of liquid water [even in sand, small amounts of unfrozen water can occur at negative temperatures (Watanabe et al., 2011)]. By comparing the *in situ* ice content (as estimated visually and from gravimetric water content and density determinations) vs. CH_4 concentrations, we can estimate if CH_4 existed as bubbles within ice. The highest ground ice contents within the samples investigated were within the active layer and at 3.5 m depth (**Figure 4D**), where the lowest CH_4 concentrations were measured (**Figure 5D**). This indicates that the CH_4 is not dominantly residing as bubbles in the ground ice, as coarse-grained sands are almost completely frozen at temperatures slightly below 0°C (Williams, 1967). Thus, we envisage that a significant fraction of the *in situ* CH_4 may reside within the sediment matrix as free gas, and a small amount dissolved within unfrozen water. While the presence of free gas in permafrost settings is poorly studied, free gas was detected in permafrost research wells in the Mackenzie Delta (Dallimore and Collett, 1995), and has been implicated in the formation of permafrost craters in coastal settings in Siberia (Leibman et al., 2014). Likewise, some active geomorphic features may be associated with free gas release (Mackay, 1965). As finer-grained, organic rich sediments may be more conducive to free gas occurrence, additional studies are needed to constrain the physics and chemistry of CH_4 residing with the pore space of permafrost sediments.

We envisage that a number of coastal processes could cause direct release to the atmosphere of the *in situ* CH_4 observed in the Tuktoyaktuk Island permafrost. Tuktoyaktuk Island is undergoing rates of coastal erosion of ~2.5 m per year, mostly during storm events which is significant when compared to other Arctic coastal settings (Lantuit et al., 2012). These storms can cause erosional niche formation creating block failures (**Figure 8** upper left photo). When these events occur, the *in situ* CH_4 can be immediately exposed to the atmosphere on the cliff faces. The permafrost away from the cliff faces can also rapidly thaw over a period of hours or days. Because the thawing is very rapid we speculate that the *in situ* CH_4 could be released without being oxidized to form CO_2. At Tuktoyaktuk Island coast, 6 m of permafrost is exposed on the exposed cliff edge (see **Figure 4A**). If we assume an average concentration of 0.15 mg CH_4 per kg sediment in this upper 6 m, and an erosion rate of 2 m/yr, we estimate an annual CH_4 flux rate from the eroding sediments could be ~3,500 g CH_4/yr/km of shoreline. Eroding coastal areas in the Canadian Beaufort Sea comprise at least 1,000 km in length (Solomon and Gareau, 2003; Manson et al., 2019) thus, if similar sediments were encountered elsewhere in the region, there is potential for atmospheric release of 3.5×10^6 g CH_4/yr. While this is a relatively small amount compared to the ~1×10^{12} g CH_4 estimated to be released from the global permafrost reservoir annually (Saunois et al., 2020), it should be noted that the glaciofluvial sediments we have studied from Tuktoyaktuk Island are not particularly organic rich. A full assessment of the potential for release of CH_4 to the atmosphere from this process is only possible with further testing of the different types of eroding sediments along the coast. Other eroding sedimentary deposits commonly found along the Beaufort coast include glacial till, lacustrine and deltaic sediments (Rampton, 1988) which may contain higher *in situ* CH_4 concentrations and therefore result in increased atmospheric release from event driven erosion.

Microbial Greenhouse Gas Production Associated With Warming Ice-Bonded Permafrost

The observation of *in situ* CH_4 in permafrost environments raises the question of how this CH_4 was formed and if *in situ* CH_4 concentrations could be increasing in association with warming of the permafrost due to climate change? Our incubation experiments clearly document that microbial activity remediate permafrost organic matter producing CO_2 and CH_4 with warming under still frozen conditions. Previous studies have documented the presence of viable microorganisms (Ganzert et al., 2007; Jansson and Taş, 2014; Stapel et al., 2016; Altshuler et al., 2017; Margesin and Collins, 2019) and active bacteria (Elberling and Brandt, 2003; Wagner et al., 2007; Mykytczuk et al., 2013) in frozen permafrost. Our incubations support these findings that there is an active, viable population of microorganisms producing CH_4 at below freezing temperatures. We can not, however, speculate on the mechanism driving methanogenesis without further experiments with isotope labeled substrates (as done in Rivkina et al., 2004).

In terms of the geothermal setting of the cores from Tuktoyaktuk Island, we note the geothermal environment of the sediments is within the interval that experiences annual seasonal fluctuations in temperatures with warming and cooling that ranges from perhaps >10°C at 1 m depth to only a 1–2°C at 10 m depth. At *in situ* temperatures, our results demonstrate that CH_4 and CO_2 is potentially produced when the upper intervals of sediment experience seasonal warming. Indeed the *in situ* CH_4 concentrations we observed likely result

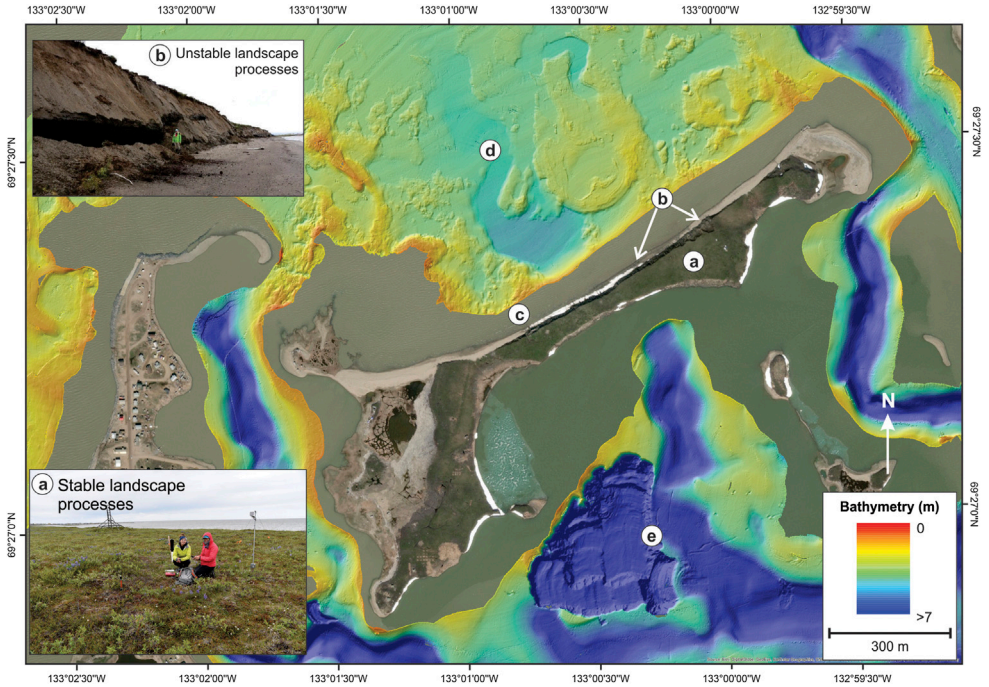

FIGURE 8 | Potential biotic and geologic CH_4 and CO_2 feedbacks for an actively eroding coastline. This map shows Tuktoyaktuk Island currently and four geological settings that could release CH_4 and CO_2 and induce climate warming. **(A)** Indicates an area of stable landscape where the release of CH_4 and CO_2 to the sediment system and atmosphere is from deepening of the active layer and warming of permafrost at depth (lower left inset photo by Caroline Duchesne). **(B)** Closer to the coast, there are unstable landscape processes where the release of CH_4 and CO_2 to the atmosphere is from rapid deposition of thawed permafrost caused by coastal erosion and thaw slumps (upper left inset photo by Nicole Couture). **(C)** In the near shore, release of CH_4 and CO_2 to the atmosphere is from rapid deposition of thawed permafrost. **(D)** Offshore processes could involve release of CH_4 and CO_2 to the sediment system and atmosphere from thawing of seabed and warming of frozen permafrost at depth and **(E)** eroding materials could also be deposited into deep, anoxic basins to produce CH_4 and CO_2.

from slow but repetitive seasonal formation of biogenic gas, that is then trapped within the ice bonded sediment matrix.

Our experiments may also have implications when considering future climate warming and its impact on *in situ* greenhouse gas concentrations and geomorphic processes. While the pace of warming of subsurface permafrost is clearly somewhat slower than the pace of atmospheric warming, our work suggests that temperature increases of only a few degrees can enhance activity of the *in situ* microbial communities, generating greenhouse gases. This creates the potential for build-up of CH_4 and CO_2 under warming permafrost conditions than might be expected from seasonal temperature variations alone. This points to the potential for subsurface biogenic gas accumulations which are continually being charged or pressurized over time. Such conditions may create the potential for the *in situ* pressure regime to exceed the confining pressure of the permafrost cover. This in turn could cause the trapped gas to leak to the surface through cracks in the permafrost or even cause more catastrophic pressure release as is inferred for the formation of permafrost craters described in Siberia (Leibman et al., 2014). There is also the potential for the formation of intrapermafrost CH_4 gas hydrate within the permafrost interval at depth (Dallimore and Collett, 1995).

Microbial Greenhouse Gas Production Associated With Thawing Ice-Bonded Permafrost

At incubation temperatures above freezing, the amount of CH_4 produced in the Tuktoyaktuk Island samples, in terms of moles CH_4 per weight sediment or petagrams CH_4 per gram carbon (**Figure 9**) was comparable to rates observed in incubations with sediments from other settings with higher organic carbon contents (Roy Chowdhury et al., 2015; Treat et al., 2015). These results suggest that glaciofluvial sediments found along the coast of the Beaufort Sea, which might not normally be considered as candidates for high greenhouse gas production upon thawing, could be contributing significant amounts of modern microbial greenhouse gases in association with ongoing climate warming. A key consideration for our experiments however is that they were conducted under anaerobic conditions. If sediment processes associated with thawing change the *in situ* biogeochemical environment from anaerobic to aerobic conditions, of course there is potential for oxidation of CH_4 to form CO_2.

We anticipate a number of settings, found within a landscape such as Tuktoyaktuk Island, that experience greenhouse gas release from coastal processes. The first, and most widespread

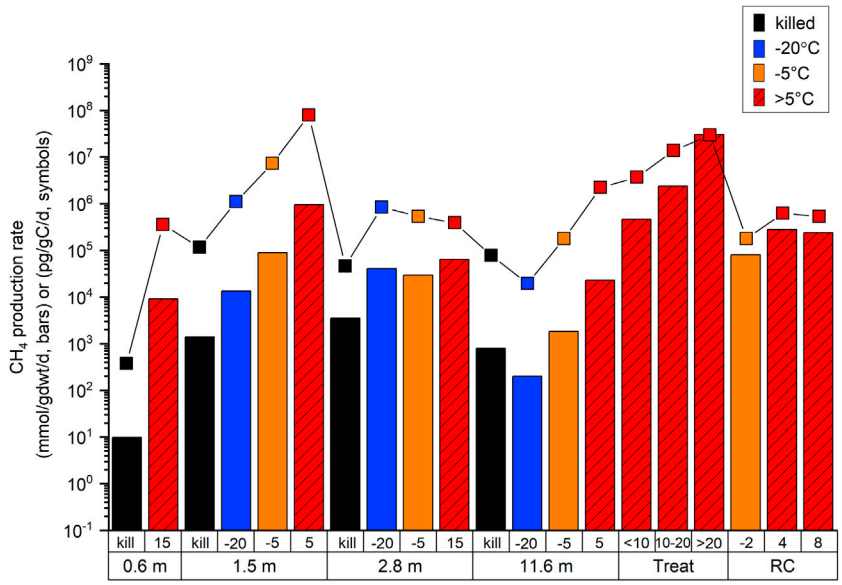

FIGURE 9 | Comparison of measured CH_4 production rates compared to published literature in two different units: colored bars (mmol CH_4/gdwt/d) and black symbols (pg CH_4/gC/d). For the colored bars, black represents killed controls, red is >0°C treatments, orange is −5°C treatment, and blue is −20°C treatment. Depths of sediment are given in meters. "Treat" refers to Treat et al., 2015 and "RC" refers to Roy Chowdry et al., 2015.

setting, is in association with a deepening of the active layer due to atmospheric warming along the coast (**Figure 8A**). In this case, CH_4 and CO_2 can be generated under anaerobic conditions similar to our experiments at the base of the active layer by microorganisms that already exist within the permafrost but become more active under thawed conditions. In addition, if new labile organic material thaws at the base of the active layer, there is potential for new microbial communities to become active and generate CH_4. If CH_4 and CO_2 concentrations at the base of the active layer are substantive there is potential for free gas migration through the active layer quickly without oxidation. However, as observed in other settings, it is likely that at least some of the CH_4 is oxidized to CO_2 in the upper portion of the active layer which is likely to be oxygenated (Oh et al., 2020 and references within). The second candidate geologic setting relate to the possible mobility of organic material through an unstable landscape as it thaws and is re-deposited in new sedimentary environments (**Figures 8B–E**). At Tuktoyaktuk Island, this might include terrestrial landslide deposits, beach sediments or shallow nearshore settings on the north side of the Island, which are in oxygenated waters. Our experiments, conducted under anoxic conditions do not directly address this environment, however new studies (Tanski et al., 2019) are beginning to better characterize these conditions demonstrating potential for CO_2 production and potential atmospheric release. However, we note that in Tuktoyaktuk Harbor on the south side of Tuktoyaktuk Island, deep water pockets allow for anoxic conditions to form year round creating conditions similar to our incubation experiments (**Figure 8E**; Lawrence et al., 1993). Local CH_4 and CO_2 production may possibly be quite vigorous in this setting. And finally, as the coastal setting is inundated with sea level rise, organic matter can accumulate in the offshore setting and host similar microbial processes to release CH_4 and CO_2 to the overlying waters (**Figure 8D**).

CONCLUSION AND FUTURE DIRECTIONS

At a broader scale, this study emphasizes the value of characterizing *in situ* geology and biogeochemistry for understanding greenhouse gas dynamics, as highlighted by others recently (Barbier et al., 2012). Permafrost sediments are thought to contain an enormous amount of trapped carbon that could be converted to CH_4 and CO_2 by microbial activity. In fact, many previous incubation studies reveal significant CH_4 production when permafrost is thawed, as might be expected in the case of a deepening active layer. However, current global CH_4 budgets consider terrestrial permafrost sediments only as a small source of atmospheric CH_4 release (~1 Tg/yr; Saunois et al., 2020). This is in part because CH_4 can be consumed within the oxygenated portion of the active layer. Our study characterizes a field example that is experiencing atmospheric warming and rapid coastal erosion and reveals that there is considerable potential for the greenhouse gas generation under anoxic conditions, even with modest concentrations of organic carbon. We envisage that these gases within the frozen permafrost could be rapidly released to the atmosphere when episodic coast erosion causes sediment block failures. There is also potential for the generation of free gas within the permafrost that could trigger unique permafrost processes or indeed migrate to

the surface where it could be released to the atmosphere. While the observation of CH_4 dynamics in frozen sediments needs to be verified across a variety of permafrost sediment types, there are several biogeochemical questions it opens: How are microbes functioning at freezing temperatures? Are there microzones of liquid water within the pore spaces that are enriched in active microbes? What organic matter source is being used? Future work could characterize the small organic acids that could be used in CH_4 and CO_2 production; along with the total DOM pool change over the time scale of an incubation.

Our study also highlights the need for more characterization of *in situ* CH_4 and CO_2 concentrations and production potential within permafrost sediments, especially in the coastal zone where such sediments could soon erode into the ocean. Notably, in our experiments, microbial degradation of organic matter to CO_2 was generally 100–1,000 times higher than CH_4 production, to make the CO_2 release from these warming soils also a significant component of the greenhouse gas potential. In order to move toward a better constraint on the potential release rates in global models, *in situ* greenhouse gas concentrations within permafrost sediments across a variety of geologically distinct areas is necessary. Currently, the global CH_4 model (Saunois et al., 2020) uses the potential release of CH_4 from permafrost sediments from very few actual measurements (Kvenvolden and Lorensen, 1993; Rasmussen et al., 1993). By measuring more environments, and even repeating measurements in these early papers, we can confirm this flux currently estimated in global budgets.

DATA AVAILABILITY STATEMENT

The datasets presented in this study can be found in online repositories. The names of the repository/repositories and accession number(s) can be found below: https://arcticdata.io/catalog/view/doi:10.18739/A2MP4VN5F.

ETHICS STATEMENT

Written informed consent was obtained from the individual(s) for the publication of any potentially identifiable images or data included in this article.

AUTHOR CONTRIBUTIONS

LL and SD conceived of the experiments, planned field work, wrote the initial draft of the paper, and interpreted interdisciplinary data; CM and PF carried out field work to obtain samples; LH and BC carried out incubation experiments; CM provided stable isotope data and interpretation; LP and MG provided DOC characterization data and interpretation; and LL supervised and validated all geochemical data analyzed. MC provided high quality maps and figures; CD collected *in situ* temperature profile; and LL, BO, and SD acquired funding for the project. All authors contributed to the manuscript revision, read and approved the submitted version.

FUNDING

We thank our funding sources: Public Safety Geoscience Program, Geological Survey of Canada, Natural Resources Canada; Beaufort Regional Strategic Environment Assessment, Indigenous and Northern Affairs Canada (AGR-4935-ILOA-INAC); Maryland Sea Grant REU program (NSF grant OCE-1262374); and U.S. National Science Foundation grants PLR-1417128 (LLL) and PLR-1416961 (BNO).

ACKNOWLEDGMENTS

We thank the staff of Midnight Sun drilling who conducted the drilling and the Hamlet of Tuktoyaktuk who assisted with logistics, Dustin Whalen who helped with community liaison and field logistics, and Edwin Amos and Joel McAlister (Aurora Research Institute) who assisted with lab activities in Inuvik and sample storage and transport. Special thanks also goes to the contractors in Tuktoyaktuk who helped remedy a small incident that happened when the drill rig arrived in the community. We thank Kathy Kelsey and Matthias Fuchs who provided insightful comments to improve this manuscript. The field work was conducted under science license #16286 issued by the Government of Northwest Territories, http://data.nwtresearch.com/Scientific/16286. This is UMCES contribution #5927.

SUPPLEMENTARY MATERIAL

The Supplementary Material for this article can be found online at: https://www.frontiersin.org/articles/10.3389/feart.2020.582103/full#supplementary-material.

REFERENCES

Altshuler, I., Whyte, L., and Doordial, J. (2017). "Chapter 8, microbial life in permafrost," in *Psychrophiles: from biodiversity to biotechnology*. Editor R. Margesin (Springer International Publishing), 153–179.

AMAP (2019). AMAP climate change update 2019: an update to key findings of snow, water, ice and permafrost in the arctic (SWIPA) 2017. Arctic monitoring and assessment programme (AMAP). Oslo, Norway. Available at: https://www.amap.no/documents/download/3295/inline (Accessed May 6 2019).

Barbier, B. A., Dziduch, I., Liebner, S., Ganzert, L., Lantuit, H., Pollard, W., et al. (2012). Methane-cycling communities in a permafrost-affected soil on Herschel Island, Western Canadian Arctic: active layer profiling of mcrA and pmoA genes. *FEMS Microbiol. Ecol.* 82, 287–302. 10.1111/j.1574-6941.2012.01332.x

Biskaborn, B. K., Smith, S. L., Noetzli, J., Matthes, H., Vieira, G., Streletskiy, D. A., et al. (2019). Permafrost is warming at a global scale. *Nat. Commun.* 10, 1–11. 10.1038/s41467-018-08240-4

Burn, C. R. (1997). Cryostratigraphy, paleogeography, and climate change during the early Holocene warm interval, western Arctic coast, Canada. *Can. J. Earth Sci.* 34, 912–925. 10.1139/e17-076

Bush, E. and D. S. Lemmen (Editors) (2019). Canada's changing climate report. Ottawa, ON: Government of Canada. Available at: https://www.nrcan.gc.ca/sites/www.nrcan.gc.ca/files/energy/Climate-change/pdf/CCCR_FULLREPORT-EN-FINAL.pdf (Accessed July 29 2020).

Christensen, J. H., Krishna Kumar, K., Aldrian, E., An, S.-I., Cavalcanti, I. F. A., De Castro, M., et al. (2013). "Climate phenomena and their relevance for future regional climate change," in *Climate change 2013: the physical science basis. Contribution of working group I to the fifth assessment report of the intergovernmental panel on climate change*. Editors T. F. Stocker, D. in, G.-K. Plattner, M. Tignor, S. K. Allen, J. Boschung, et al. (Cambridge: Cambridge University Press), 1585.

Dallimore, S. R., and Collett, T. S. (1995). Intrapermafrost gas hydrates from a deep core hole in the Mackenzie Delta, Northwest Territories. Canada. *Geology.* 23, 527–530. 10.1130/0091-7613(1995)023<0527:IGHFAD>2.3.CO;2

Dallimore, S. R., Nixon, F. M., Egginton, P. A., and Bisson, J. G. (1996). Deep-seated creep of massive gound ice, Tuktoyaktuk, NWT. *Permafr. Periglac. Process.* 7, 337–347. 10.1002/(SICI)1099-1530(199610)7:4<337::AID-PPP232>3.0.CO;2-3

Ehleringer, J. R., Hall, A. E., and Farquhar, G. D. (1993). *Stable isotopes and plant carbon/water relations.* San Diego, CA: Academic Press.

Elberling, B., and Brandt, K. K. (2003). Uncoupling of microbial CO2 production and release in frozen soil and its implications for field studies of arctic C cycling. *Soil Biol. Biochem.* 35, 263–272. 10.1016/S0038-0717(02)00258-4

Fellman, J. B., D'Amore, D. V., Hood, E., and Boone, R. D. (2008). Fluorescence characteristics and biodegradability of dissolved organic matter in forest and wetland soils from coastal temperate watersheds in southeast Alaska. *Biogeochemistry.* 88, 169–184. 10.1007/s10533-008-9203-x

Ganzert, L., Jurgens, G., Munster, U., and Wagner, D. (2007). Methanogenic communities in permafrost-affected soils of the Laptev Sea coast, Siberian Arctic, characterized by 16S rRNA gene fingerprints. *FEMS Microbiol. Ecol.* 59, 476–488. 10.1111/j.1574-6941.2006.00205.x

Gilichinsky, D., Rivkina, E., Bakermans, C., Shcherbakova, V., Petrovskaya, L., Ozerskaya, S., et al. (2005). Biodiversity of cryopegs in permafrost. *FEMS Microbiol. Ecol.* 53, 117–128. 10.1016/j.femsec.2005.02.003

GISTEMP (2019). Version 4. *GISS surface temperature analysis (GISTEMP) [Online]*. Available at: https://data.giss.nasa.gov/gistemp/ (Accessed February 27 2020).

Gruben, M. (2018). "On behalf of councillors of the Hamlet of Tuktoyaktuk: a Mayor's assessment of a community threatened by coastal erosion," in *Arctic Net*. Ottawa, Canada.

Hansell, D. (2013). Recalcitrant dissolved organic carbon fractions. *Annual Review in Marine Science.* 5, 421–445.

Hansen, J., Ruedy, R., Sato, M., and Lo, K. (2010). Global surface temperature change. *Rev. Geophys.* 48, 1–29. 10.1029/2010RG000345

Hu, K., Issler, D. R., Chen, Z., and Brent, T. A. (2013). Open file 6956. Permafrost investigation by well logs, and seismic velocity and repeated shallow temperature surveys, Beaufort-Mackenzie Basin. Canada: Geological Survey of Canada. Available at: https://doi.org/10.4095/293120 (Accessed June 18 2013).

Hultman, J., Waldrop, M. P., Mackelprang, R., David, M. M., Mcfarland, J., Blazewicz, S. J., et al. (2015). Multi-omics of permafrost, active layer and thermokarst bog soil microbiomes. *Nature.* 521, 208–212. 10.1038/nature14238

Hynes, S., Solomon, S. M., and Whalen, D. (2014). Open file report 7685. GIS compilation of coastline variability spanning 60 years in the Mackenzie Delta and Tuktoyaktuk in the Beaufort Sea. Ottawa: Geological Survey of Canada, 7. Available at: https://doi.org/10.4095/295579 (Accessed December 12 2014).

Jansson, J. K., and Taş, N. (2014). The microbial ecology of permafrost. *Nat. Rev. Microbiol.* 12, 414–425. 10.1038/nrmicro3262

J. P. Riley and G. Skirrow (Editors) (1975). *Chemical oceanography*. 2nd edition (New York: Academic Press), Vol. 4.

Knoblauch, C., Beer, C., Liebner, S., Grigoriev, M. N., and Pfeiffer, E.-M. (2018). Methane production as key to the greenhouse gas budget of thawing permafrost. *Nat. Clim. Change.* 8, 309–312. 10.1038/s41558-018-0095-z

Knoblauch, C., Beer, C., Sosnin, A., Wagner, D., and Pfeiffer, E.-M. (2013). Predicting long-term carbon mineralization and trace gas production from thawing permafrost of Northeast Siberia. *Global Change Biol.* 19, 1160–1172. 10.1111/gcb.12116

Kuhry, P., Bárta, J., Blok, D., Elberling, B., Faucherre, S., Hugelius, G., et al. (2020). Lability classification of soil organic matter in the northern permafrost region. *Biogeosciences.* 17, 361–379. 10.5194/bg-17-361-2020

Kvenvolden, K. A., and Lorensen, T. D. (1993). Methane in permafrost—Preliminary results from coring at Fairbanks, Alaska. *Chemosphere.* 26, 609–616. doi:10.1016/0045-6535(93)90446-C

Lantuit, H., Overduin, P. P., Couture, N., Wetterich, S., Aré, F., Atkinson, D., et al. (2012). The arctic coastal dynamics database: a new classification scheme and statistics on arctic permafrost coastlines. *Estuar. Coast.* 35, 383–400. 10.1007/s12237-010-9362-6

Lapham, L. L., Chanton, J. P., Martens, C. S., Sleeper, K., and Woolsey, J. R. (2008). Microbial activity in surficial sediments overlying acoustic wipe-out zones at a Gulf of Mexico cold seep. *Geochem. Geophys. Geosyst.* 9, Q06001. doi:06010.01029/02008GC001944

Lapham, L. L., Wilson, R. M., Macdonald, I. R., and Chanton, J. P. (2014). Gas hydrate dissolution rates quantified with laboratory and seafloor experiments. *Geochem. Cosmochim. Acta.* 125, 492–503. 10.1016/j.gca.2013.10.030

Lawrence, M. J., Bergmann, M. A., Hopky, G. E., and Chiperzak, D. B. (1993). Report No.: 859. NOGAP [northern Oil and gas program] B. 2; Chemical data from Tuktoyaktuk Harbour and mason Bay, 1984 to 1988. Winnipeg, MB: Central and Arctic Region. Available at: https://waves-vagues.dfo-mpo.gc.ca/Library/149492.pdf (Accessed 1993).

Leibman, M. O., Kizyakov, A. I., Plekhanov, A. V., and Streletskaya, I. D. (2014). New permafrost feature- Deep crater in central Yamal (West Siberia, Russia) as a reponse to local climate fluctuations. *Geography Environ. Sustain.* 7, 68–79. 10.15356/2071-9388_04v07_2014_05

Lenssen, N., Schmidt, G., Hansen, J., Menne, M., Persin, A., Ruedy, R., et al. (2019). Improvements in the GISTEMP uncertainty model. *J. Geophys. Res. Atmos.* 124, 6307–6326. 10.1029/2018JD029522

Mackay, J. R., and Dallimore, S. R. (1992). Massive ice of the Tuktoyaktuk area, western Arctic coast, Canada. *Can. J. Earth Sci.* 29, 1235–1249. 10.1139/e92-099

Mackay, J. R. (1965). Gas-domed mounds in permafrost, Kendall Island, N.W.T. *Geogr. Bull.* 7, 105–115.

Magen, C., Lapham, L. L., Pohlman, J., Marshall, K., Bossman, S., and Chanton, J. P. (2014). A simple headspace equilibration method for measuring dissolved methane. *Limnol Oceanogr. Methods.* 12, 637–650. 10.4319/lom.2014.12.637

Manson, G. K., Couture, N. J., and James, T. S. (2019). Open File 8551. CanCoast 2.0: data and indices to describe the sensitivity of Canada's marine coasts to changing climate. Canada: Geological Survey of Canada. Available at: https://doi.org/10.4095/314669 (Accessed June 5 2019).

Manson, G. K., and Solomon, S. M. (2007). Past and future forcing of Beaufort Sea coastal change. *Atmos.-Ocean.* 45, 107–122. 10.3137/ao.450204

Margesin, R., and Collins, T. (2019). Microbial ecology of the cryosphere (glacial and permafrost habitats): current knowledge. *Appl. Microbiol. Biotechnol.* 103, 2537–2549. 10.1007/s00253-019-09631-3

Murphy, K. R., Stedmon, C. A., Graeber, D., and Bro, R. (2013). Fluorescence spectroscopy and multi-way techniques. PARAFAC. *Anal. Methods.* 5, 6557–6566. 10.1039/c3ay41160e

Mykytczuk, N. C., Foote, S. J., Omelon, C. R., Southam, G., Greer, C. W., and Whyte, L. G. (2013). Bacterial growth at −15 °C; molecular insights from the permafrost bacterium Planococcus halocryophilus Or1. *ISME J.* 7, 1211–1226. 10.1038/ismej.2013.8

Nikrad, M. P., Kerkhof, L. J., and Häggblom, M. M. (2016). The subzero microbiome: microbial activity in frozen and thawing soils. *FEMS Microbiol. Ecol.* 92, fiw081. 10.1093/femsec/fiw081

Oh, Y., Zhuang, Q., Liu, L., Welp, L. R., Lau, M. C. Y., Onstott, T. C., et al. (2020). Reduced net methane emissions due to microbial methane oxidation in a warmer Arctic. *Nat. Clim. Change.* 10, 317–321. 10.1038/s41558-020-0734-z

Rampton, V. N. (1988). Memoir 423. *Quaternary geology of the Tuktoyaktuk Coastlands, Northwest Territories*. Canada: Geological Survey of Canada. Available at: https://doi.org/10.4095/126937.98 (Accessed 1988).

Rasmussen, R. A., Khalil, M. a. K., and Moraes, F. (1993). Permafrost methane content: 1. experimental data from sites in northern Alaska. *Chemosphere.* 26, 591–594. doi:10.1016/0045-6535(93)90444-A

Ritchie, J. C. (1974). Modern pollen assemblages near the arctic tree line, Mackenzie Delta region, Northwest Territories. *Can. J. Bot.* 52, 381–396. 10.1139/b74-050

Rivkin, F. M. (1998). Release of methane from permafrost as a result of global warming and other disturbances. *Polar Geogr.* 22, 105–118. 10.1080/10889379809377640

Rivkina, E., Laurinavichius, K., Mcgrath, J., Tiedje, J. M., Shcherbakova, V., and Gilichinsky, D. (2004). Microbial life in permafrost. *Adv. Space Res.* 33, 1215–1221. doi:10.1016/j.asr.2003.06.024

Rivkina, E., Shcherbakova, V., Laurinavichius, K., Petrovskaya, L., Krivushin, K., Kraev, G., et al. (2007). Biogeochemistry of methane and methanogenic archaea in permafrost. *FEMS Microbiol. Ecol.* 61, 1–15. 10.1111/j.1574-6941.2007.00315.x

Romanovsky, V. E., and Osterkamp, T. E. (2000). Effects of unfrozen water on heat and mass transport processes in the active layer and permafrost. *Permafr. Periglac. Process.* 11, 219–239. 10.1002/1099-1530(200007/09)11:3<219::AID-PPP352>3.0.CO;2-7

Roy Chowdhury, T., Herndon, E. M., Phelps, T. J., Elias, D. A., Gu, B., Liang, L., et al. (2015). Stoichiometry and temperature sensitivity of methanogenesis and CO_2 production from saturated polygonal tundra in Barrow, Alaska. *Global Change Biol.* 21, 727–737. doi:10.1111/gcb.12762

Saunois, M., Stavert, A. R., Poulter, B., Bousquet, P., Canadell, J. G., Jackson, R. B., et al. (2020). The global methane budget 2000–2017. *Earth Syst. Sci. Data.* 12, 1561–1623. 10.5194/essd-12-1561-2020

Schädel, C., Bader, M. K.-F., Schuur, E. A. G., Biasi, C., Bracho, R., Capek, P., et al. (2016). Potential carbon emissions dominated by carbon dioxide from thawed permafrost soils. *Nat. Clim. Change.* 6, 950–953. 10.1038/nclimate3054

Schädel, C., Schuur, E. A. G., Bracho, R., Elberling, B., Knoblauch, C., Lee, H., et al. (2014). Circumpolar assessment of permafrost C quality and its vulnerability over time using long-term incubation data. *Global Change Biol.* 20, 641–652. 10.1111/gcb.12417

Solomon, S., and Gareau, P. (2003). "Beaufort Sea coastal mapping and the development of an erosion hazard index," in Proceedings of the 8th international conference on permafrost, Zurich, Switerland, July 21–25, 2003, 1091–1096. Available at: https://www.arlis.org/docs/vol1/ICOP/55700698/Pdf/Chapter_191.pdf (Accessed 2003).

Stapel, J. G., Schirrmeister, L., Overduin, P. P., Wetterich, S., Strauss, J., Horsfield, B., et al. (2016). Microbial lipid signatures and substrate potential of organic matter in permafrost deposits: implications for future greenhouse gas production. *J. Geophys. Res. Biogeosci.* 121, 2652–2666. 10.1002/2016JG003483

Statistics Canada (2017). Catalogue no.: 98-316-X2016001. Tuktoyaktuk, HAM [census subdivision], Northwest Territories and Northwest Territories [territory] (table). Census profile. 2016 census. (Ottawa, Canada: Statistics Canada.). Available at: https://www12.statcan.gc.ca/census-recensement/2016/dp-pd/prof/index (Accessed February 8 2017).

Stedmon, C. A., and Bro, R. (2008). Characterizing dissolved organic matter fluorescence with parallel factor analysis: a tutorial. *Limnol Oceanogr. Methods.* 6, 572–579. doi:10.4319/lom.2008.6.572

Tanski, G., Wagner, D., Knoblauch, C., Fritz, M., Sachs, T., and Lantuit, H. (2019). Rapid CO_2 release from eroding permafrost in seawater. *Geophys. Res. Lett.* 46, 11244–11252. 10.1029/2019GL084303

Traina, S. J., Novak, J., and Smeck, N. E. (1990). An ultraviolet absorbance method of estimating the percent aromatic carbon content of humic acids. *J. Environ. Qual.* 19, 151–153. 10.2134/jeq1990.00472425001900010023x

Treat, C. C., Natali, S. M., Ernakovich, J., Iversen, C. M., Lubascu, M., Mcguire, A. D., et al. (2015). A pan-arctic synthesis of CH_4 and CO_2 production from anoxic soil incubations. *Global Change Biol.* 21, 2787–2803. 10.1111/gcb.12875

Treat, C. C., Wollheim, W. M., Varner, R. K., Grandy, A. S., Talbot, J., and Frolking, S. (2014). Temperature and peat type control CO_2 and CH_4 production in Alaskan permafrost peats. *Global Change Biol.* 20, 2674–2686. 10.1111/gcb.12572

Turetsky, M. R., Abbott, B. W., Jones, M. C., Anthony, K. W., Olefeldt, D., Schuur, E. A. G., et al. (2020). Carbon release through abrupt permafrost thaw. *Nat. Geosci.* 13, 138–143. 10.1038/s41561-019-0526-0

Wagner, D., Gattinger, A., Embacher, A., Pfeiffer, E.-M., Schloter, M., and Lipski, A. (2007). Methanogenic activity and biomass in Holocene permafrost deposits of the Lena Delta, Siberian Arctic and its implication for the global methane budget. *Global Change Biol.* 13, 1089–1099. 10.1111/j.1365-2486.2007.01331.x

Watanabe, K., Kito, T., Wake, T., and Sakai, M. (2011). Freezing experiments on unsaturated sand, loam and silt loam. *Ann. Glaciol.* 52, 37–43. doi:10.3189/172756411797252220

Weishaar, J. L., Aiken, G. R., Bergamaschi, B. A., Fram, M. S., Fujii, R., and Moper, K. (2003). Evaluation of specific ultraviolet absorbance as an indicator of the chemical composition and reactivity of dissolved organic carbon. *Environ. Sci. Technol.* 37, 4702–4708. doi:10.1021/es030360x

Williams, P. J. (1967). DBR-RP-359. Properties and behaviour of freezing soils. Available at: https://publications-cnrc.canada.ca/fra/voir/objet/?id=ff43e8e1-9da1-4bd4-8b13-7ec7fe9ad47d (Accessed July 24 2012).

Zepp, R. G., Sheldon, W. M., and Moran, M. A. (2004). Dissolved organic fluorophores in southeastern U.S. coastal waters: correction method for eliminating Rayleigh and Raman scattering peaks in excitation-emission matrices. *Mar. Chem.* 89, 15–36. doi:10.1016/j.marchem.2004.02.006

Zingel, A. (2019). Protecting Tuktoyaktuk from coastal erosion could cost $50M, says mayor. Ottawa, Canada: CBC news online. Available at: https://www.cbc.ca/news/canada/north/coastal-erosion-tuktoyaktuk-needs-more-money-1.5095115 (Accessed April 12 2019).

Conflict of Interest: The authors declare that the research was conducted in the absence of any commercial or financial relationships that could be constructed as a potential conflict of interest.

The handling editor is currently organizing a Research Topic with one of the authors SRD.

frontiers in Earth Science

ORIGINAL RESEARCH
published: 08 January 2021
doi: 10.3389/feart.2020.598933

Geochemistry of Coastal Permafrost and Erosion-Driven Organic Matter Fluxes to the Beaufort Sea Near Drew Point, Alaska

Emily M. Bristol[1], Craig T. Connolly[1], Thomas D. Lorenson[2], Bruce M. Richmond[2], Anastasia G. Ilgen[3], R. Charles Choens[4], Diana L. Bull[5], Mikhail Kanevskiy[6], Go Iwahana[7], Benjamin M. Jones[6] and James W. McClelland[1]*

[1] Marine Science Institute, University of Texas at Austin, Port Aransas, TX, United States, [2] Pacific Coastal and Marine Science Center, United States Geological Survey, Santa Cruz, CA, United States, [3] Geochemistry Department, Sandia National Laboratories, Albuquerque, NM, United States, [4] Geomechanics Department, Sandia National Laboratories, Albuquerque, NM, United States, [5] Strategic Futures and Policy Analysis Department, Sandia National Laboratories, Albuquerque, NM, United States, [6] Institute of Northern Engineering, University of Alaska Fairbanks, Fairbanks, AK, United States, [7] International Arctic Research Center, University of Alaska Fairbanks, Fairbanks, AK, United States

OPEN ACCESS

Edited by:
Alexandra V. Turchyn, University of Cambridge, United Kingdom

Reviewed by:
Laura Lapham, University of Maryland Center for Environmental Science (UMCES), United States
Ronny Lauerwald, Université Paris-Saclay, France

***Correspondence:**
Emily M. Bristol
bristol@utexas.edu

Specialty section:
This article was submitted to Biogeoscience, a section of the journal Frontiers in Earth Science

Received: *25 August 2020*
Accepted: *19 November 2020*
Published: *08 January 2021*

Citation:
Bristol EM, Connolly CT, Lorenson TD, Richmond BM, Ilgen AG, Choens RC, Bull DL, Kanevskiy M, Iwahana G, Jones BM and McClelland JW (2021) Geochemistry of Coastal Permafrost and Erosion-Driven Organic Matter Fluxes to the Beaufort Sea Near Drew Point, Alaska. Front. Earth Sci. 8:598933. doi: 10.3389/feart.2020.598933

Accelerating erosion of the Alaska Beaufort Sea coast is increasing inputs of organic matter from land to the Arctic Ocean, and improved estimates of organic matter stocks in eroding coastal permafrost are needed to assess their mobilization rates under contemporary conditions. We collected three permafrost cores (4.5–7.5 m long) along a geomorphic gradient near Drew Point, Alaska, where recent erosion rates average 17.2 m $year^{-1}$. Down-core patterns indicate that organic-rich soils and lacustrine sediments (12–45% total organic carbon; TOC) in the active layer and upper permafrost accumulated during the Holocene. Deeper permafrost (below 3 m elevation) mainly consists of Late Pleistocene marine sediments with lower organic matter content (~1% TOC), lower C:N ratios, and higher $\delta^{13}C$ values. Radiocarbon-based estimates of organic carbon accumulation rates were 11.3 ± 3.6 g TOC m^{-2} $year^{-1}$ during the Holocene and 0.5 ± 0.1 g TOC m^{-2} $year^{-1}$ during the Late Pleistocene (12–38 kyr BP). Within relict marine sediments, porewater salinities increased with depth. Elevated salinity near sea level (~20–37 in thawed samples) inhibited freezing despite year-round temperatures below 0°C. We used organic matter stock estimates from the cores in combination with remote sensing time-series data to estimate carbon fluxes for a 9 km stretch of coastline near Drew Point. Erosional fluxes of TOC averaged 1,369 kg C m^{-1} $year^{-1}$ during the 21st century (2002–2018), nearly doubling the average flux of the previous half-century (1955–2002). Our estimate of the 21st century erosional TOC flux $year^{-1}$ from this 9 km coastline (12,318 metric tons C $year^{-1}$) is similar to the annual TOC flux from the Kuparuk River, which drains a 8,107 km^2 area east of Drew Point and ranks as the third largest river on the North Slope of Alaska. Total nitrogen fluxes via coastal erosion at Drew Point were also quantified, and were similar to those from the Kuparuk River. This study emphasizes that coastal erosion represents a significant pathway for carbon and nitrogen trapped in permafrost to enter modern biogeochemical cycles, where it may fuel food webs and greenhouse gas emissions in the marine environment.

Keywords: coastal erosion, carbon flux, nitrogen flux, porewater chemistry, permafost, biogeochemistry, Alaskan Beaufort Sea

INTRODUCTION

Rising permafrost temperature (Romanovsky et al., 2010), declines in sea ice extent (Overeem et al., 2011), and longer ice-free seasons (Stammerjohn et al., 2012) are increasing the vulnerability of Arctic coasts to erosion (Manson and Solomon, 2007). Arctic coastlines, which make up roughly one third of the global coastline extent, are retreating at an average rate of 0.5 m $year^{-1}$ (Lantuit et al., 2012). The long-term mean annual erosion rate (1940–2000s) of Alaska's 1,957 km of Beaufort Sea coastline is 1.7 m $year^{-1}$, but there is high spatial and temporal variability in erosion rates (Gibbs and Richmond, 2015). Not only is this coast retreating on average, but erosion rates along the Alaska Beaufort Sea coast are also increasing, from 0.6 m $year^{-1}$ circa 1950–1980 to 1.2 m $year^{-1}$ circa 1980–2000 (Ping et al., 2011). Some sections of the Alaska Beaufort Sea coast retreat more than 22 m in a single year, which is on par with the fastest eroding coasts worldwide (Gibbs and Richmond 2015; Jones et al., 2009; Jones et al, 2018). Rapid erosion along northern Arctic coastlines threatens infrastructure and cultural heritage sites of local communities (Jones et al., 2008). Erosion also delivers sediment, organic matter, and inorganic nutrients to the Arctic Ocean (Ping et al., 2011; Lantuit et al., 2012).

Soils in northern Alaska contain ~40–150 kg total organic carbon (TOC) m^{-2} in the top 3 m (Strauss et al., 2013; Hugelius et al., 2014; Schuur et al., 2015; Fuchs et al., 2019). Most of this TOC is sequestered in permafrost; however, coastal erosion can rapidly liberate large quantities of this frozen organic matter into the coastal ocean (Vonk et al., 2012; Vonk and Gustafsson, 2013; Fritz et al., 2017; Stein and MacDonald, 2004). An estimated 4.9–14.0 Tg of organic carbon is released to the Arctic Ocean each year from coastal erosion (Wegner et al., 2015), similar in magnitude to river-borne particulate organic carbon (POC) export to the Arctic Ocean (5.8 Tg; McClelland et al., 2016). Eroded material may be deposited as nearshore marine sediments, resuspended in the water column as POC, or produce dissolved organic carbon (DOC) through physical leaching processes (Dou et al., 2008; Vonk et al., 2012; Fritz et al., 2017). Previous work has shown that organic matter in coastal permafrost along Herschel Island, Canada is rapidly decomposed upon entering seawater, thereby producing carbon dioxide via microbial metabolism (Tanski et al., 2019). In addition to heterotrophic bacteria, higher organisms in nearshore marine food webs also incorporate terrestrial organic matter from along the Beaufort Sea coast (Dunton et al., 2012; Bell et al., 2016; Harris et al., 2018).

TOC storage varies widely along the northern coast of Alaska due to differences in geomorphology and surficial depositional history, making it difficult to constrain estimates of erosional organic matter fluxes to the ocean (Jorgenson and Brown, 2005; Dou et al., 2010; Ping et al., 2011). For instance, Ping et al. (2011) estimates that TOC storage on the Alaska Beaufort Sea coast is highest for exposed bluffs and bays (92–99 kg TOC m^{-2}) and lowest in tapped lake basins and deltas (41–46 kg TOC m^{-2}). When paired with measurements of coastline loss, TOC storage estimates translate into erosional fluxes of 153–180 Gg TOC to the Alaska Beaufort Sea annually (Jorgenson and Brown, 2005; Ping et al., 2011).

In this study, we estimate organic matter and inorganic nutrient fluxes from a 9 km length of coastline near Drew Point, located approximately 100 km east of Utqiaġvik (formerly known as Barrow), AK. The exposed coast between Drew Point and Cape Halkett has the highest rates of erosion along the northern coast of Alaska (Gibbs and Richmond 2015). Jones et al. (2018) reports that erosion along this 9 km segment has more than doubled since the mid-20th century, with recent (2007–2016) annual erosion rates averaging 17.2 m yr^{-1}. This region of Alaska's North Slope is underlain by continuous permafrost, where the upper several meters of permafrost are characterized by high ground-ice content (up to 90% in some locations), with an abundance of wedge ice (Kanevskiy et al., 2013). Throughout the Holocene, widespread thermokarst lake formation and drainage in this region left roughly 84% of the landscape covered by lakes or drained thermokarst lake basins (DTLBs) (Hinkel et al., 2005; Jones and Arp, 2015). Below reworked lacustrine sediments, permafrost material is composed of marine sediments that were deposited during late-Pleistocene marine transgressions (Black, 1983; Rawlinson, 1993; Brigham-Grette and Hopkins, 1995). The coastline consists of north-facing, exposed bluffs that reach elevations of 1.6–7.1 m above sea level (Jones et al., 2018). Along these bluffs, the primary mechanism for erosion occurs via thermo-mechanical development of niches from wave-action during storms that cause large blocks of permafrost to collapse into the ocean (Jones et al., 2009).

Estimates of organic matter stocks in eroding soils along the Alaska Beaufort Sea coast are currently based on only a few studies. We constructed geochemical profiles extending from the tundra surface to below sea level using coastal permafrost cores (4.5–7.5 m) to better constrain organic matter and nutrient stock estimates along one of Alaska's most rapidly eroding stretches of shoreline. This is one of the first studies to compare stocks of bulk organic matter with porewater dissolved organic matter in eroding permafrost. Additionally, ^{14}C data from core sediments provide new insight on landscape geomorphology and carbon accumulation rates over time. We used geospatial imagery and LiDAR data to calculate volumetric erosion rates over three time intervals from 1955 through 2007 and over annual time steps from 2008 through 2017 for a 9 km length of coastline. These erosion rates were combined with geochemical data to estimate TOC and other constituent fluxes to the Beaufort Sea from this study coastline. While the results of this study are particularly relevant to the Drew Point area, they also serve as a benchmark for improving regional-scale estimates of erosional organic matter inputs to Arctic coastal waters.

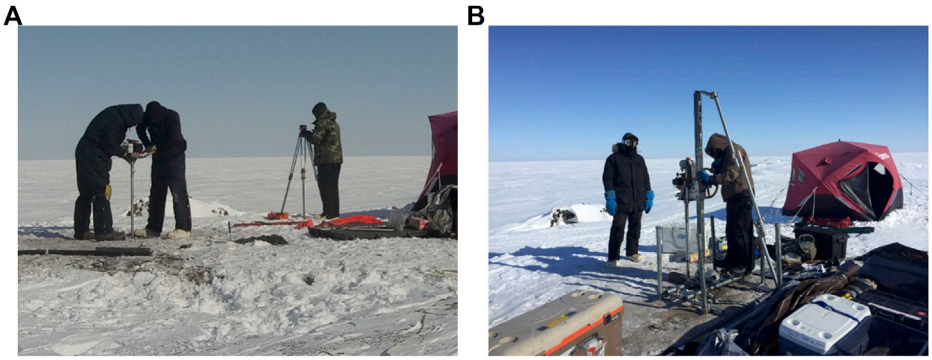

FIGURE 1 | Coring activities were conducted near Drew Point, AK in April 2018 using a **(A)** SIPRE coring system to collect near-surface (top 4–6 m) cores and a **(B)** Geoact coring system to retrieve cores at depth.

FIGURE 2 | Oblique aerial photographs of landscape characteristics. **(A)** Primary Surface (i.e. landscape that has not been reworked by thaw-lakes), **(B)** an ancient drained thermokarst lake basin (Ancient DTLB) that drained ~5 kyr BP, and **(C)** a young drained thermokarst lake basin (Young DTLB) that most recently drained ~0.5 kyr BP.

METHODS

Field Campaign

We acquired permafrost cores at Drew Point in April 2018 using two coring systems (**Figure 1**). Near-surface cores (upper 4–6 m) were acquired using a SIPRE corer (7.5 cm diameter) and cores at depth were acquired using a Geoact coring system (7.5 cm diameter). To capture variations in near-surface permafrost characteristics, we sampled each of the three dominant geomorphic terrain units present in the Drew Point region (**Figure 2**): primary surface material that has not been reworked by thermokarst lake formation and drainage, an ancient DTLB which drained approximately 5 kyr BP (Hinkel et al., 2003; Jones et al., 2012), and a young DTLB that drained approximately 0.5 kyr BP (Jones et al., 2012). Each core spanned from the tundra surface to below local mean sea level. The core from the primary surface spanned from 6.7 to −0.5 m elevation, the ancient DTLB core spanned from 5.2 to −2.5 m elevation, and the young DTLB core spanned from 3.9 to −0.5 m elevation. Cores were collected in air temperatures between −10 and −20°C. They were photographed and described in the field, packed into coolers for transport back to Utqiaġvik, Alaska and then flown frozen to the University of Alaska in Fairbanks where the cores were stored in a −20°C freezer room prior to shipping them frozen to Sandia National Lab in Albuquerque, NM for processing. Core descriptions and photographs are included in **Supplementary Tables S1–S3** and **Supplementary Figures S1–S7**.

Sectioning and Sampling of Permafrost Cores

Core sections for chemical analyses were 6–15 cm long. We sectioned the cores at higher resolution near the tundra surface: intervals ranged from 0–40 cm within the top meter of the core and 21–101 cm with increasing depth. Sections from the frozen cores were cut using a band saw that was cleaned with Milli-Q water and ethanol after each use. Core material was then thawed in acid-washed glass beakers at room temperature in preparation for sampling. Aqueous sampling was initiated immediately after the frozen cores were fully thawed. In a few cases, core sections were kept in a refrigerator (4°C) to thaw overnight and sampled the following day. Rhizon samplers were used to collect and filter porewater from thawed core sections. The mean pore size of the filter was 0.15 μm. Following porewater extraction, thawed soil was placed in Whirl-packs and frozen for bulk soil organic carbon and nitrogen content and bulk soil stable carbon and radiocarbon analysis.

Soil/Sediment Organic Matter and Radiocarbon

Measurements of total organic carbon (TOC) and total nitrogen (TN) content, stable carbon isotope ratios ($\delta^{13}C$) and radiocarbon

(^{14}C) analyses of bulk soils/sediments were conducted on 45 samples at the Woods Hole Oceanographic Institution (WHOI), National Ocean Sciences Accelerator Mass Spectrometer (NOSAMS) facility. Bulk samples were dried at 60°C then finely ground using a mortar and pestle. Ground samples went through a vapor fumigation acid/base treatment step to remove inorganic carbon. This step involved placing samples in a vacuum-sealed desiccator in a drying oven (60°C) with a beaker of concentrated HCl for 24 h. Samples were then removed and placed in another vacuum-sealed desiccator with a dish of NaOH pellets, and again stored in a drying oven at 60°C for another 24 h. This latter step neutralized excess HCl. Samples were combusted using an Elementar el Vario Cube C/N analyzer. TOC and TN (% by weight) were quantified during this step. The resulting CO_2 was transferred to a vacuum line and cryogenically purified. The purified CO_2 gas samples were converted to graphite targets by reducing CO_2 with an iron catalyst under 1 atm H_2 at 550°C. Targets were subsequently analyzed for stable and radiocarbon isotopes ($\delta^{13}C$ as ‰ and ^{14}C as fraction modern carbon). All $\Delta^{14}C$ data (in ‰) were corrected for isotopic fractionation using measured $\delta^{13}C$ values that were quantified during the ^{14}C-AMS procedure. We measured $\delta^{13}C$ in these samples separately on a VG Prism Stable Mass Spectrometer at NOSAMS. $\Delta^{14}C$ and radiocarbon age were determined from percent modern carbon using the year of sample analysis according to Stuiver and Polach (1977). The analytical error associated with the radiocarbon ages increases with age: samples assigned an age between modern and 20 kyr BP had an error up to ±85 years, and samples assigned an age greater than 20 kyr BP had an error ranging from ±110 to ±3,700 years.

Porewater Chemistry

Dissolved organic carbon (DOC) and total dissolved nitrogen (TDN) concentrations were measured from filtered porewater samples without any added preservatives, which were kept frozen until analysis. Due to limited sample volume and anticipated high concentrations of dissolved organic carbon and nitrogen, pore water samples were diluted either 1:10 or 1:15 with ultrapure (18 MΩ cm^{-1}) water prior to analysis. Concentrations of DOC and TDN were measured at the University of Texas Marine Science Institute using a Shimatzu TOC-V CSH analyzer equipped with a TNM-1 total nitrogen detector. Porewater remaining after DOC and TDN analysis was used to measure conductivity. Conductivity was measured using a Myron L Ultrameter II and converted to the practical salinity scale (PSS-78). Nitrate (NO_3^-) concentrations were determined using high-performance ion chromatography (HP-ICE) on a Dionex DX-500 ion chromatography system equipped with an AS-1 column at the USGS in Menlo Park, CA, United States. The eluent was a solution of 1.0 mM octanesulfonic acid in 2% isopropanol and using 5.0 mM tetrabutyl ammonium hydroxide as a chemical suppressor. Analyses of ratios of the isotopes strontium-87 (^{87}Sr) to strontium-86 (^{86}Sr) were also done at the USGS laboratories in Menlo Park, California with methods consistent with those reported by Bayless et al. (2004). Values are reported as the dimensionless ratio of ^{87}Sr and ^{86}Sr concentrations ($^{87}Sr/^{86}Sr$). The ratios of $^{87}Sr/^{86}Sr$ isotopes were measured with a multicollector thermal-ionization mass spectrometer in positive-ion mode (PTIMS; Finnigan MAT 261).

A suite of other porewater constituents (aluminum, barium, bromide, calcium, chloride, iron, manganese, silicon, sulfate, and strontium) were also analyzed. These data are not presented and discussed in detail herein, but can be found in **Supplementary Table S4**.

Geospatial Analyses and Remote Sensing

We combined historic aerial photography and recent high-resolution satellite imagery to reconstruct the bluff position at Drew Point between 1955 and 2018 (Jones et al., 2018). A tundra landform geospatial data layer was created by manual delineating features visible (scale of 1:5,000) in a georeferenced aerial photo dataset from 1955 in a Geographic Information System (GIS) framework. Our geomorphic terrain unit classification scheme identified primary surfaces (not altered by thermokarst lake activity), three ages of drained lake basins following Hinkel et al. (2003), modern thermokarst lakes, and sizeable drainage corridors (**Figure 3**). The geomorphic terrain unit dataset was then clipped according to the area of land lost between a particular period in which we had bluff line position information between 1955 and 2018. Total land area lost per geomorphic terrain unit was then summed for each time period. An airborne LiDAR dataset acquired in 2011 provided information on the height of the terrain relative to local sea level that we used to assign a volume of land loss for each time period between 2012 and 2018. To estimate volume lost before 2012, we averaged terrain heights within each geomorphic terrain unit in the 2011 LiDAR dataset and combined average bluff heights with area lost per geomorphic terrain unit to estimate volumetric erosion rates from 1955 to 2011. These data can be found in **Supplementary Table S5**.

Soil/Sediment Organic Matter and Porewater Constituent Stocks

Soil/sediment bulk densities were calculated from core sections by measuring water volumes displaced by vacuum sealed frozen core samples. These samples were weighed before and after drying at 50°C to determine dry bulk density (ρ_b; g solids/cm^3) and water content (g H_2O/cm^3). These measurements were completed for 53 samples which encompassed a range of depths.

Soil/sediment (dry solids) accumulation rates and TOC accumulation rates were calculated independently for each of the three permafrost cores. Accumulation rates were calculated as the slope of a linear regression between cumulative stocks and radiocarbon age. Stocks were calculated in bins between radiocarbon dates, where the soil stock in a bin is ρ_b * height of bin, and the TOC stock in a bin is %TOC/100 * ρ_b * height of bin. Since bulk density was measured from different core sections than geochemical data, bulk density values for a given height were estimated using a linear model of ρ_b vs. elevation ($R^2 = 0.68$) for elevations between 0 and 6 m, and using an average value for elevations above 6 m (**Supplementary Figure S8**). We only calculated accumulation rates between present and 38 kyr BP due to age depth inversions in sediments with older ^{14}C ages.

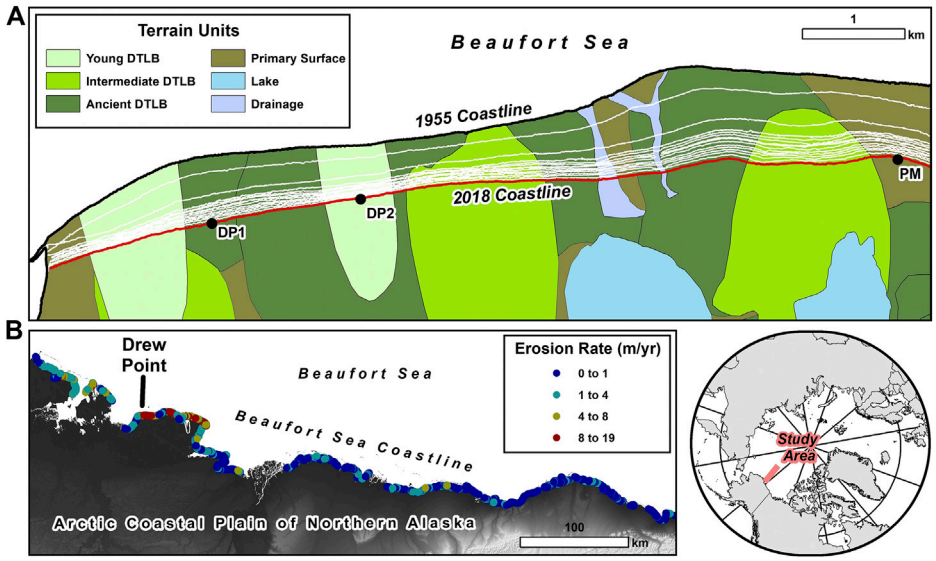

FIGURE 3 | (A) Map of 9 km study coastline denoting coastline lost from 1955 (bold black line) and 2018 (bold red line). White lines show bluff line position for timesteps between 1955 and 2018. Geomorphic terrain units indicate surface waters, primary material never re-worked by thaw lakes, and the age-classification of drained thermokarst lake basins. Thermokarst lakes were drained throughout the mid-Holocene (ancient) to late- Holocene (young). Coring locations are indicated by PM (primary surface), DP1 (ancient DTLB), and DP2 (young DTLB). **(B)** Map of Alaskan Beaufort Sea coast with erosion rates from circa 1940s to circa 2010s (adapted from Gibbs and Richmond, 2017).

To calculate stocks of TOC, TN, and dissolved porewater constituents in eroding bluffs and scale these measurements to the coastline, we binned our data based on downcore patterns. Since downcore patterns were similar between cores of different geomorphic terrain units, we averaged data across the three cores. Based on patterns in organic matter concentrations (presented in the Results section) we created three bins: permafrost 0–3 m above sea level, permafrost >3 m above sea level, and active layer. We assumed an average active layer depth of 40 cm, based on visual inspection of the three cores (**Supplementary Tables S1–S3**) and other active layer measurements reported from the region (Bockheim and Hinkel, 2007; Urban and Clow, 2018). Within each bin, we averaged our measured dry bulk density, water content, TOC, TN, DOC, TDN, and nitrate concentrations. Since we cored permafrost near the center of ice-wedge polygons, our measured ice content is representative of ground ice in sediments between ice wedges, including pore and segregated ice, but not wedge ice. Values of gravimetric moisture content and effective porosity (which is equal to volumetric ice content) of frozen sediments are presented in **Supplementary Figure S8** and **Supplementary Table S6**. We did not measure excess-ice content of sediments in the laboratory, but it was estimated visually in the field (**Supplementary Tables S1–S3**). Our estimates showed that segregated ice in ice-rich sediments with ataxitic (suspended) cryostructure comprised up to 70% of volume (**Supplementary Figures S2, S3, and S5**). To account for wedge-ice content, we used values from a study of ground ice on the Alaska Beaufort Sea coast by Kanevskiy et al. (2013). We assumed that the primary surface at this location had 28% wedge ice, ancient DTLBs had 11% wedge ice, intermediate age DTLBs had 7% wedge ice, and young DTLBs had 3% wedge ice (Kanevskiy et al., 2013). Since wedge ice contains much lower concentrations of TOC compared to soils and pore ice (Tanski et al., 2016), we neglected the potential TOC content in wedge ice. With these data, the mass of TOC (M_C, kg m^{-2}) in a column was calculated as the sum of the mass of TOC in each bin using the following equation:

$$M_C = \sum_{b=1}^{n}\left(\rho_b \times \mathrm{h} \times \frac{\mathrm{TOC}}{100} \times (100 - V_i)\right)$$

where ρ_b is the average dry bulk density (kg m^{-3}), h is the height (thickness) of the sediment bin (m), TOC is the average total organic carbon (% by weight), and V_i is the wedge ice content (% by volume). The height of the bin below the active layer was calculated as the difference between the bluff height, active layer depth, and lower elevation bins. With this methodology, the lowest elevation bluffs had only two bins: 0–3 m above sea level and active layer. Nitrogen stocks were calculated with this same method, replacing TOC with TN. Stocks of porewater constituents were calculated similarly, replacing ρ_b in the above equation with our measured porewater content (kg H_2O m^{-3} soil) and replacing TOC with solute concentration (mg solute kg^{-1} H_2O).

Land-to-Ocean Flux Calculations

Fluxes of organic carbon to the ocean were calculated as the sum of fluxes from each geomorphic terrain unit during each time step using the following equation

$$Flux_C = \sum\left(M_{C_g} \times \frac{A_g}{t}\right)$$

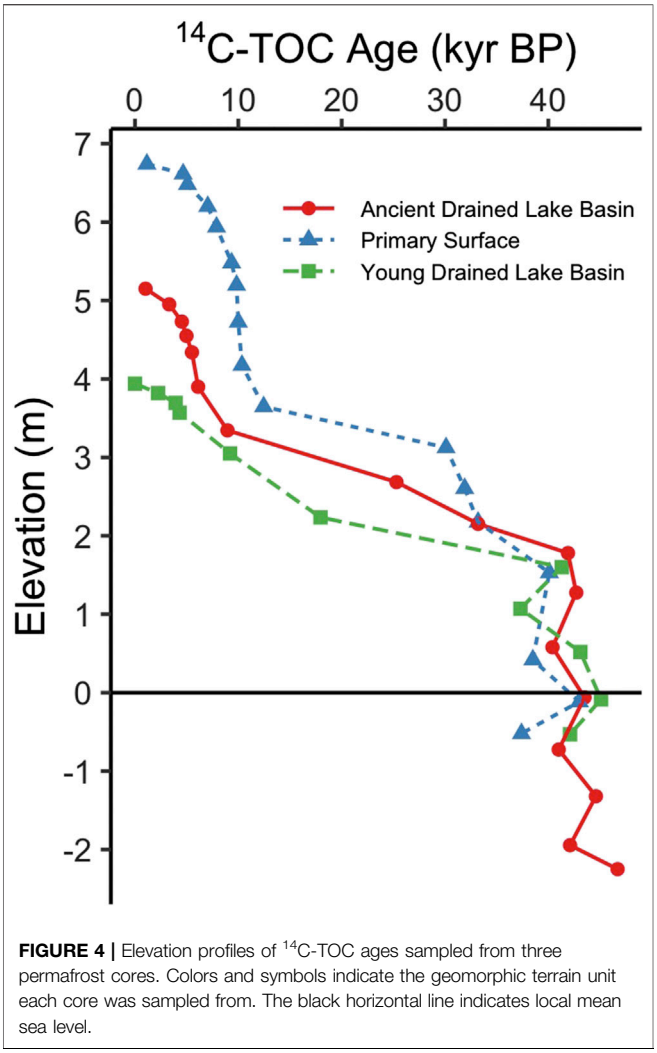

FIGURE 4 | Elevation profiles of ^{14}C-TOC ages sampled from three permafrost cores. Colors and symbols indicate the geomorphic terrain unit each core was sampled from. The black horizontal line indicates local mean sea level.

where M_{C_g} is the calculated carbon stock (kg m^{-3}, see *Soil/Sediment Organic Matter and Porewater Constituent Stocks*) for a geomorphic terrain unit based on measured bluff height, A_g is the area (m^2) eroded from that geomorphic terrain unit in the timestep, and t is the length of the timestep in years. We only calculated fluxes from bluffs, so terrain classified as drainages and lakes were not included in our flux calculations. Since only 3% of the eroding coastline was classified as a lake or drainage (**Figure 3**), excluding these two geomorphic units should only result in a slight underestimate of organic matter fluxes from our study coastline. This same equation was used to calculate fluxes of nitrogen and porewater constituents, replacing MCg with the appropriate mass stock.

RESULTS

Soil/Sediment Organic Matter Characteristics

In each core, bulk ^{14}C-TOC ranged in age from modern to over 45 thousand years before present (kyr BP; i.e., before 1950). While the primary surface, young DTLB, and ancient DTLB differed in total elevation, we observe similar down core patterns in ^{14}C-TOC age for all the terrain units when plotted with respect to sea level (**Figure 4**). Soil/sediment and TOC accumulation rates were higher during the Holocene (<12 kyr BP) than the Late Pleistocene (12–38 kyr). Soil/sediment accumulation averaged 102.7 ± 3.6 g m^{-2} year^{-1} across the three cores during the Holocene, and 55.9 ± 6.5 g m^{-2} year^{-1} from 12 to 38 kyr BP. TOC accumulation averaged 11.3 ± 3.6 g m^{-2} year^{-1} during the Holocene and 0.5 ± 0.1 g m^{-2} year^{-1} from 12 to 38 kyr BP. Below 1.5 m elevation, ^{14}C-TOC age oscillates between 37 and 47 kyr BP.

The chemical characteristics of soil/sediment organic matter change markedly with elevation, exhibiting a particularly strong transition around 3 m (**Figure 5**). TOC and TN profiles are similar among cores, particularly below 3 m elevation (**Figure 5**). Organic matter content is high and variable above an elevation of 3 m, with TN generally tracking TOC patterns downcore. From the landscape surface to an elevation of 3 m, organic matter content across the three cores average 12.1 ± 1.9% TOC and 0.66 ± 0.09% TN. Below 3 m elevation, organic matter content is much lower and less variable, averaging 1.2 ± 0.1% TOC and 0.10 ± 0.01% TN. TOC to TN molar ratios (C:N) ranged from 7.2 to 21.7, declining from highest values at the tundra surface to the lowest values around 3 m elevation, then gradually increasing again with depth. There is also a distinct shift in δ^{13}C-TOC values that aligns with the shift from higher to lower TOC content at 3 m elevation. Above 3 m, the average for δ^{13}C-TOC was −27.9 ± 0.2‰; below 3 m the average for δ^{13}C-TOC was −26.0‰ ± 0.2.

To estimate bluff organic carbon and nitrogen stocks, we paired TOC and TN measurements with soil/sediment dry bulk density measurements. Dry bulk density generally increases down core, averaging 0.4 g cm^{-3} in permafrost above 3 m elevation and 1.1 g cm^{-3} below 3 m elevation (**Supplementary Figure S8**). A table of density measurements (dry bulk density, water content, gravimetric water content, effective porosity) can be found in **Supplementary Table S6**. Since TOC and TN stocks vary by bluff height, we calculated stocks for each geomorphic terrain unit (young DTLB, intermediate age DTLB, ancient DTLB, primary surface) based on the average bluff height of eroding material and estimated wedge-ice content (%). The primary surface classification has the tallest bluffs (4.8 ± 0.1 m) and stores an estimated 106.3 kg m^{-2} TOC and 6.9 kg m^{-2} TN. Young DTLBs have an average bluff height of 4.1 ± 0.1 m and store 101.0 kg m^{-2} TOC and 6.9 kg m^{-2} TN. Ancient DTLBs have a lower elevation of 3.7 m and store 81.1 m^{-2} TOC and 5.6 kg m^{-2} TN. Intermediate age DTLBs have the lowest elevation bluffs (3.0 ± 0.1 m) and store an estimated 67.1 kg m^{-2} TOC and 4.6 kg m^{-2} TN. For a 4 m bluff (average along this coastline), the average ^{14}C-TOC age of eroding organic matter is ~16 kyr BP when weighted by TOC stocks.

Porewater Chemistry

In general, porewater chemistry varies greatly with depth, but elevation profiles demonstrate relatively similar trends among the three cores (**Figure 6**). Like total organic matter, there are distinct

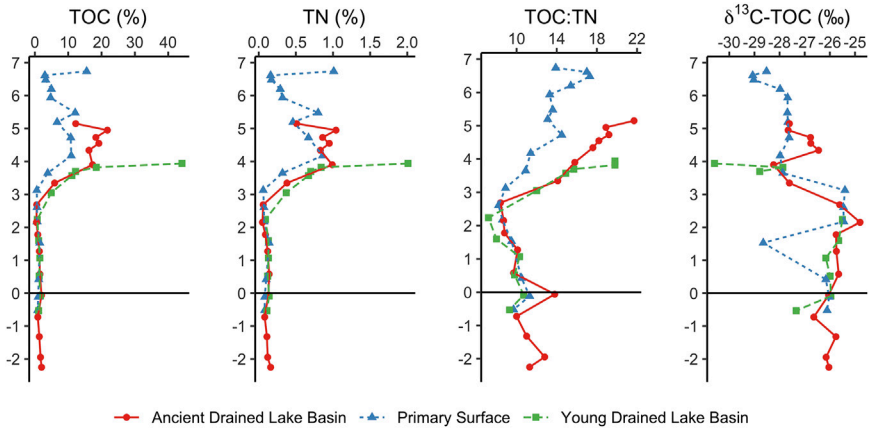

FIGURE 5 | Total organic carbon (TOC; wt%), total nitrogen (TN; wt%), organic carbon to nitrogen molar ratio (C:N), and δ^{13}C-TOC (‰) profiles for three permafrost cores. Colors and symbols indicate the geomorphic terrain unit each core was sampled from. The black horizontal lines indicate mean local sea level.

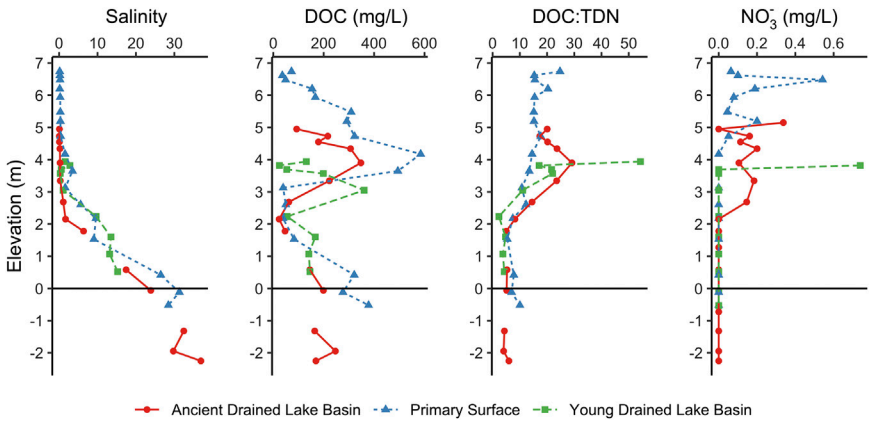

FIGURE 6 | Porewater salinity, dissolved organic carbon (DOC; mg C L^{-1}), dissolved organic carbon to total dissolved nitrogen molar ratio (DOC:TDN), and nitrate (NO_3^-; mg NO_3^- L^{-1}) profiles for three permafrost cores. Colors and symbols indicate the geomorphic terrain unit each core was sampled from. The black horizontal line indicates mean local sea level.

trends above and below an elevation of 3 m. Above 3 m, salinities of thawed porewaters are under 3.5 (**Figure 6**). Below 3 m, salinities of thawed porewaters increase nearly linearly with depth to a maximum of 36.9 at an elevation of −2.3 m. We observed that with increasing salt content, there was a phase change in the core: permafrost with porewater salinities greater than ~25 at room temperature was also partially or completely unfrozen at ground temperatures as low as −8°C. These salty, unfrozen cryotic sediments (sometimes referred to as a cryopeg; Tolstikhin and Tolstikhin 1974; van Everdingen 1998) occurred within ±0.5 m of sea level and extended to the bottom of each core. Dissolved organic matter concentrations in porewater vary greatly down core (**Figure 6**), and TDN generally tracks DOC (see **Supplementary Table S4** for TDN concentrations). DOC concentrations range between 23 and 585 mg L^{-1} (**Figure 6**), with the lowest concentrations occurring near the soil surface and near an elevation of 2 m. DOC:TDN molar ratios range from 15 to 54 in the top 40 cm of the cores and decline to ~6 below 3 m elevation. Nitrate concentrations reach 0.7 mg NO_3^- L^{-1} above 3 m elevation, and no nitrate was detected below an elevation of 2.5 m. Data from a subset of samples that were analyzed for strontium isotope ratios showed that $^{87}Sr/^{86}Sr$ ranged between 0.7092 and 0.7115. Samples with salinities greater than 10 were notably more depleted in $^{87}Sr/^{86}Sr$, with ratios below 0.7095 (**Figure 7**).

While this paper focuses on the abovementioned porewater constituents that are most relevant to understanding of organic C and N fluxes, a broader suite of geochemical data, including porewater aluminum, barium, bromide, calcium, chloride, iron, manganese, silicon, sulfate, and strontium are available for interested readers in **Supplementary Table S4**. Downcore changes in these constituents are highly variable, with some tracking patterns observed for salinity (e.g. bromide, chloride) and others showing unique patterns. For example, porewater dissolved iron generally remained between 0.1 and 20 mg L^{-1}, with the exception of a distinct spike in concentration occurring

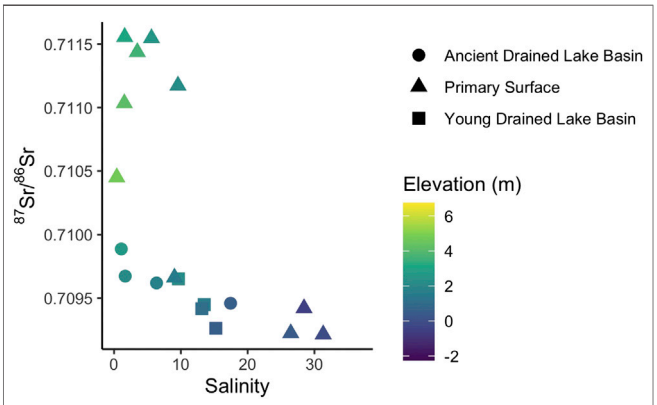

FIGURE 7 | Relationship between porewater $^{87}Sr/^{86}Sr$ and porewater salinity. Color indicates elevation (m) relative to mean local sea level and symbols indicate the geomorphic terrain unit.

at about 4 m elevation in each core where iron reached a maximum of 84.8 mg L^{-1} (**Supplementary Figure S9**).

Coastal Erosion Rates and Fluxes of Carbon and Nitrogen From Land to Ocean

Coastal erosion rates and associated fluxes of TOC have increased markedly since the 1950s (**Table 1**). Between 1955 and 1979, an average area of 58,673 m^2 eroded from the 9 km study section each year. From 2008 to 2018, area lost more than doubled, averaging 148,586 m^2 $year^{-1}$. Along with this increase in areal erosion rates, TOC fluxes to the ocean more than doubled, from 5,340 metric tons TOC $year^{-1}$ between 1955–1979 to 12,331 metric tons TOC $year^{-1}$ in the past decade (**Figure 8**). Note that since our calculations account for the area eroded from geomorphic classifications of various elevation, TOC fluxes scale similarly but not exactly with area lost. Annual resolution data from 2008 to 2018 show how TOC fluxes vary over shorter time steps, and also demonstrate a continued increase in TOC flux within the most recent decade. TN fluxes follow the same trend as TOC fluxes, but are approximately an order of magnitude lower, consistent with our reported C:N (**Figure 5**). Porewater DOC and TDN fluxes are approximately two orders of magnitude lower than TOC and TN fluxes, respectively (**Table 1**).

DISCUSSION

Our geochemical analyses show that two distinct permafrost layers are eroding into the ocean near Drew Point, AK: 1) organic-rich Holocene-era terrestrial soils and lacustrine sediments and 2) late-Pleistocene marine sediments. The upper layer, found above 3 m elevation, contains TOC with ^{14}C ages as old as ~12 kyr BP. The $\delta^{13}C$-TOC values in this layer (averaging −27.9‰) are consistent with contributions from C3-dominated tundra vegetation in the Arctic (Stein and Macdonald 2004). Higher C:N ratios above 3 m elevation (**Figure 5**) are also indicative of vascular plant contributions. Studies have shown that thaw lake development in this region was initiated by the Holocene Thermal Maximum approximately 9–11 kyr BP (Jones and Yu 2010; Kaufman et al., 2004), which aligns with the rapid accumulation of organic-rich material in our cores since 12 kyr BP. Below 3 m elevation, the shift to higher $\delta^{13}C$-TOC values (**Figure 5**) reflects an increase in marine-derived organic matter. The lower TOC content (<2%) and C:N (~8–14) of organic matter in the lower layer are also indicative of its marine origin, having similar values to organic matter in nearshore sediments of the Beaufort Sea (Stein and Macdonald, 2004; Couture et al., 2018; Goni et al., 2000). Other studies along Beaufort Sea coastal bluffs report permafrost containing marine microfauna and refer to this silty, unconsolidated sediment as the Flaxman Member of the Gubik Formation (Black, 1983; Carter et al., 1988; Rawlinson, 1993). Thermoluminescence dates on Flaxman Member sediments suggest that this material accumulated during the Simpsonian marine transgression approximately 70–80 kyr BP (Dinter et al., 1990; Rawlinson, 1993; Brigham-Grette and Hopkins, 1995). Another study inland from Drew Point also provides evidence for a late Pleistocene marine transgression occurring between 113 and 71 kyr BP (Farquharson et al., 2018). The relatively young (~40 kyr BP) radiocarbon ages of bulk OM that we measured below 2 m elevation suggest that these marine sediments have been reworked and subject to homogenization across depths. Our estimated net accumulation rates were comparatively low between 12 and 38 kyr BP, corresponding to colder, drier conditions in the late Pleistocene before rapid development of peatlands (MacDonald et al., 2006; Jones and Yu, 2010). A study by Meyer et al. (2010) showed similar sedimentology near Utqiaġvik, AK, where high-salinity sediments at depth were assigned a ^{14}C–TOC age of 39.5 kyr BP, and there was a geochronological gap between 21.7 and 12.4 kyr BP that suggests there was little deposition or reworking during this time.

The unfrozen, brine-rich permafrost (cryopeg) that we encountered near sea level is consistent with findings by Brown (1969) and Meyer et al. (2010) near Utqiaġvik, AK. Proposed mechanisms for brine formation include 1) rejection and concentration of salts in porewaters of soils and lacustrine sediments during permafrost aggradation and 2) residual seawater from relict marine sediments (Brown, 1969; Cascoyne, 2000). Our results showing a decrease in strontium isotope ratios in porewaters with a salinity above ~10 (**Figure 7**) suggest that both mechanisms are likely involved. In porewater samples with salinities greater than 10, Sr isotope ratios of 0.7094–0.7095 are similar to values of ~0.0792 found in modern seawater (Krabbenhoft et al., 2010; Peucker-Ehrenbrink et al., 2010). In porewater samples with salinities less than 10, on the other hand, Sr isotope ratios transition from values close to those expected for seawater to values expected for North American fresh waters (>0.71; Krabbenhoft et al., 2010; Peucker-Ehrenbrink et al., 2010). This points to a mixture of marine and freshwater-derived ions, with the marine source dominating at porewater salinities above 10. Regardless of the mechanism of formation, the existence of a cryopeg along the base of bluffs has implications for coastal erosion, as unfrozen

TABLE 1 | Average area lost to coastal erosion, TOC and TN fluxes, and porewater DOC, TDN, and NO_3^- fluxes for our 9 km study coastline over four time steps from 1955 to 2018 and over annual time steps from 2008 to 2018.

Year		Soil/sediment				Porewater					
		TOC		TN		DOC		TDN		NO_3^-	
	Area lost	tons C	kg C	tons N	kg N	tons C	kg C	tons N	kg N	tons N	kg NO_3^-
	m^2 $year^{-1}$	$year^{-1}$	m^{-1} $year^{-1}$	$year^{-1}$	m^{-1} $year^{-1}$	$year^{-1}$	m^{-1} $year^{-1}$	$year^{-1}$	m^{-1} $year^{-1}$	$year^{-1}$	m^{-1} $year^{-1}$
1955–1979	58,673	5,340	593	359	40	15.5	1.7	2.3	0.26	0.006	0.0007
1979–2002	80,178	7,040	782	476	53	19.9	2.2	3.1	0.35	0.008	0.0008
2002–2008	143,084	12,297	1,366	832	92	34.3	3.8	5.4	0.60	0.013	0.0015
2008–2018	148,586	12,331	1,370	838	93	33.5	3.7	5.4	0.61	0.013	0.0014

and unconsolidated cryotic soils may be more susceptible to erosion by wave action (Jones et al., 2018).

Most of the landscape near Drew Point has been reworked by thermokarst lake formation and drainage, where ice-rich permafrost degradation and ground ice melt lead to lake formation, followed by drainage and subsequent soil organic matter accumulation and ice-wedge growth (Bockheim et al., 2004; Jorgenson and Shur, 2007; Jones et al., 2012). Thermokarst lakes have been shown to drain quickly, releasing large quantities of water and dissolved organic matter (Jones and Arp, 2015). Post drainage, a study from the Seward Peninsula, Alaska showed that peat accumulates rapidly as productive species colonize the newly exposed surface (Jones et al., 2012). Although peat accumulation slows over time as surface conditions change, TOC stocks tend to increase with lake basin age (Hinkel et al., 2003; Jones et al., 2012). Our cores span a gradient in landscape geomorphology, representing a site where lake formation and drainage did not occur during the Holocene (primary surface), an ancient lake basin that formed and drained about 5 kyr BP, and a young basin where two lakes formed and drained with the last draining occurring in the last 0.5 kyr BP (Hinkel et al., 2003; Jones et al., 2012). We do not explicitly report geomorphic terrain unit-specific carbon stocks in this study because more replication of primary surface, young DTLB, and ancient DTLB coring would be needed to do so. However, there is a general trend of increasing surface elevation with landscape age that translates into differences in carbon storage among geomorphic terrain units. Due to differences in surface elevation, our estimates of carbon storage from local sea level to the tundra surface range from 67.1 kg TOC m^{-2} (3.0 m bluff typical of an intermediate age DTLB) to 106.3 kg TOC m^{-2} (4.8 m bluff typical of primary surface). These storage estimates bracket values reported by Ping et al. (2011) for exposed bluffs with an average height of 3.2 ± 0.5 m along the Alaskan Beaufort Sea coast (92 ± 35 kg TOC m^{-2}).

Our geochemical profiles demonstrate that sampling at elevations from near sea level to the active layer is necessary to account for variability in TOC stocks when calculating erosional fluxes. For example, if we calculate TOC stocks for a typical 4 m bluff using TOC and bulk density data from the top meter alone, we overestimate TOC stocks by ~90% relative to those calculated using data from the full profile. We get closer if we use data from the top 3 m of soil, but still overestimate TOC stocks by ~8%. Only when we fully account for down-core variations do the estimates completely converge. At least where marine transgressions come into play, accounting for the presence of relict marine sediments as well as organic-rich Holocene age soils and lacustrine sediments allows for more accurate quantification of TOC stocks.

The approximate doubling of TOC flux over the timeframe of our analysis (**Figure 8**) is associated with accelerating coastline erosion rates rather than a shift in landscape classification or surface elevation. The accelerated erosion rates translate into a higher estimated TOC flux (1,370 kg TOC m^{-1} $year^{-1}$) than previously reported by Jorgenson and Brown (2005) or Ping et al. (2011) for the Drew Point coastline (818–848 kg TOC m^{-1} $year^{-1}$). Ping et al. (2011) estimated that, on average,

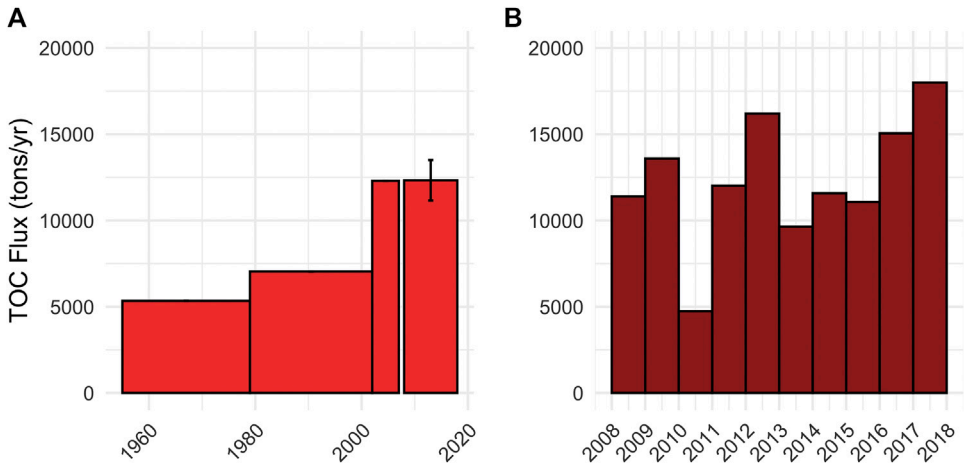

FIGURE 8 | Estimation of total organic carbon fluxes to the ocean (metric tons TOC year^{-1}) from the 9 km study section **(A)** over four time steps from 1955 to 2018 and **(B)** over annual time steps from 2008 to 2018. The error bar shows standard error.

exposed bluffs contribute 163 kg TOC m^{-1} year^{-1} to the Beaufort Sea. Our estimates suggest that TOC fluxes from Drew Point are nearly an order of magnitude higher than the typical exposed bluffs along the Beaufort Sea coast. As mentioned previously, this is explained by higher erosion rates at Drew Point (17.2 m year^{-1}) compared to the average 1.8 m year^{-1} (1950–2000) from exposed bluffs reported by Ping et al. (2011). For additional context, it is also noteworthy that annual TOC erosion from our 9 km study section at Drew Point (12,331 tons year^{-1}) is now on par with annual TOC inputs to the Beaufort Sea from the Kuparuk River (12,387 tons year^{-1}; McClelland et al., 2014). Arctic rivers are known to transport large quantities of organic matter and strongly influence the Arctic Ocean (Holmes et al., 2012; McClelland et al., 2016). These results are impressive considering the Kuparuk drains 8,107 km^2 of land extending from the Brooks mountain range to the Beaufort Sea coast and is the third largest river on the North Slope of Alaska (McClelland et al., 2014). The Kuparuk River empties into the Beaufort Sea near Deadhorse, approximately 200 km east of Drew Point.

Erosional TN fluxes follow similar trends to TOC, indicating that erosion also contributes a substantial amount of nitrogen to nearshore Arctic coastal waters. Over the past decade, we estimate that erosion from this coastline supplies 838 tons TN year^{-1} to the ocean, similar to the TN flux (particulate organic nitrogen, dissolved organic nitrogen, ammonium, and nitrate) from the Kuparuk River (641 tons N year^{-1}; McClelland et al., 2014). While this eroding nitrogen is mostly in the particulate organic form, a fraction of it is likely remineralized to inorganic forms in the nearshore environment and supports marine primary production (Tank et al., 2012). It is also important to consider the timing of these nitrogen fluxes. Riverine fluxes peak during the spring snowmelt period, compared to erosion that peaks during the summer open-water season (Holmes et al., 2012; Jones et al., 2018). Therefore, coastal erosion likely supplies nitrogen to nearshore coastal environments during a time of nutrient depletion following spring phytoplankton blooms (Connelly et al., 2015; Kellogg et al., 2019).

Similar to down-core patterns in organic matter, the profiles of DOC, TDN and NO_3^- show differences in concentrations between Holocene age soils and lacustrine sediments and late-Pleistocene marine sediments. TDN (**Supplementary Table S4**) tracks DOC, and NO_3^- concentrations are <1% of TDN, indicating that the bulk of porewater nitrogen is in the organic form. Increasing DOC concentrations with depth from the tundra surface to the bottom of the Holocene age material, and again from ~2 m elevation to the bottom of the core (**Figure 6**) could be attributed to leaching of particulate organic matter over time and the concentration of solutes during freeze-thaw cycles. NO_3^- concentrations decline with depth within terrestrial-derived soils to undetectable concentrations within relict marine sediments. Lower DOC: TDN molar ratios in porewater below 3 m elevation is also reflective of the transition to relict marine sediments. Despite the large volumes of pore and segregated ice that can be found in permafrost, porewater DOC and nutrient concentrations are a small fraction of the total mass fluxes of carbon and nitrogen. DOC and TDN accounted for less than 1% of the total mass fluxes of TOC and TN, respectively (**Table 1**). However, particulate organic matter eroding into the ocean may be quickly solubilized to dissolved organic forms (Dou et al., 2008) and remineralized to inorganic forms of nitrogen in the nearshore environment (Tank et al., 2012).

CONCLUSION

In this study, we evaluate the role of coastal erosion in mobilizing ancient stocks of organic carbon and nitrogen to the nearshore Beaufort Sea. Our estimates for carbon storage in the bluffs are comparable to previous studies, but our calculated annual fluxes of material are higher than previous estimates due to the rapid, increasing erosion rates in this region. This suggests that future

studies should continue to monitor shoreline loss over time, particularly for sections of coast with high erosion rates or tall bluffs that contribute the greatest volumes of material. The unique, high-resolution depth profiles of TOC, ^{14}C, and other geochemical constituents in this study highlight the need to consider landscape geomorphology and TOC content at depth to prevent overestimating carbon storage in deeper soil horizons. While permafrost contains large volumes of porewaters, we show that dissolved organic carbon and nitrogen are a small fraction of the total flux. Providing detailed estimates of eroding TOC and nutrient fluxes in a warming Arctic will inform our understanding of nearshore carbon and nutrient cycling. Arctic rivers are understood to deliver large quantities of terrestrially-derived organic matter to the ocean (Holmes et al., 2012; McClelland et al., 2016). This study emphasizes coastal erosion as another important driver of organic carbon and nitrogen fluxes to the ocean. Eroding coasts supply organic matter mostly in the particulate form; however, it is likely that dissolved organic matter is leached from eroding material in seawater and can be used by heterotrophic bacteria in the water column or marine sediments. Therefore, estimates of erosional organic carbon and nutrient fluxes, in combination with studies of organic matter lability, are necessary to assess CO_2 production as well as marine productivity in the Arctic Ocean.

DATA AVAILABILITY STATEMENT

The original contributions presented in the study are publicly available. This data can be found here: doi: 10.6073/pasta/cc4d53a91ed873765224fcb6d09f5eb7.

AUTHOR CONTRIBUTIONS

All authors were involved in developing the concept and design of this study. MK, GI, and BJ conducted field work. EB, CC, TL, AI, DB, and RC were involved in sample processing. EB, CC, TL, BR, and AI contributed to geochemical analyses. BJ provided geospatial analyses. EB, CC, BJ, and JM wrote the initial draft of the manuscript, and all authors contributed to subsequent revisions.

FUNDING

This project was primarily supported by the Laboratory Directed Research and Development program at Sandia National Laboratories. Additionally, the National Science Foundation provided support for BMJ (OPP-1806213, OISE-1927553), JWM (OPP-1656026), and MK (OPP-1820883). USGS personnel were supported by the USGS Coastal Hazards Program and the Alaska Coastal Processes and Hazards Project team. The Beaufort Lagoon Ecosystems LTER program (funded by OPP-1656026) also provided travel support for EMB's field work, and provided assistance with data archiving.

ACKNOWLEDGMENTS

We thank A. Turetskaia, B. Cardenas, R. Hladyniuk, and P. Garlough at the University of Texas at Austin, and C. Conaway and J. Fitzpatrick at the USGS in Menlo Park, CA for assisting with chemical analyses. This work was supported by a NOSAMS Graduate Student Internship. We thank the NOSAMS facility and its members at the Woods Hole Oceanographic Institution for their invaluable assistance and generosity in our efforts to estimate ^{14}C and ^{13}C of our sediment samples. Lastly, we thank the two reviewers and the associate editor for their helpful insights.

SUPPLEMENTARY MATERIAL

The Supplementary Material for this article can be found online at: https://www.frontiersin.org/articles/10.3389/feart.2020.598933/full#supplementary-material.

REFERENCES

Bayless, E. R., Bullen, T. D., and Fitzpatrick, J. A. (2004). Use of 87Sr/86Sr and delta11B to identify slag-affected sediment in southern Lake Michigan. *Environ. Sci. Technol.* 38, 1330–1337. doi:10.1021/es0347843

Bell, L. E., Bluhm, B. A., and Iken, K. (2016). Influence of terrestrial organic matter in marine food webs of the Beaufort Sea shelf and slope. *Mar. Ecol. Prog. Ser.* 550, 1–24. doi:10.3354/meps11725

Black, R. F. (1983). "Three superposed systems of ice wedges at McLeod Point, northern Alaska, may span most of the Wisconsin stage and Holocene," in Proceedings of the permafrost Fouth International Conference, 68–72

Bockheim, J. G., and Hinkel, K. M. (2007). The importance of "deep" organic carbon in Permafrost-affected soils of Arctic Alaska. *Soil Sci. Soc. Am. J.* 71, 1889–1892. doi:10.2136/sssaj2007.0070N

Bockheim, J. G., Hinkel, K. M., Eisner, W. R., and Dai, X. Y. (2004). Carbon pools and accumulation rates in an age-series of soils in drained thaw-lake basins, Arctic Alaska. *Soil Sci. Soc. Am. J.* 68, 697–704.

Brigham-Grette, J., and Hopkins, D. M. (1995). Emergent marine record and paleoclimate of the last interglaciation along the northwest Alaskan coast. *Quat. Res.* 43 (2), 159–173.

Brown, J. (1969). Ionic concentration gradients in permafrost: Barrow, Alaska, U.S. Army Corps Engineers Cold Regions Research and Engineering Laboratory Research Report, 272.

Carter, L. D., Brouwers, E. M., and Marincovich, L. (1988). "Nearshore marine environment of the Alaska Beaufort Sea during deposition of the Flaxman member of the Gubik Formation," in *In Geologic studies in Alaska by the U.S. Geological Survey during 1987*. Editors J.P Galloway and T.D. Hamilton, 27–30.

Cascoyne, M. (2000). "A review of published literature on the effects of permafrost on the hydrogeochemistry of bedrock," in POSIVA—00-09.

Connelly, T. L., McClelland, J. W., Crump, B. C., Kellogg, C. T. E., and Dunton, K. H. (2015). Seasonal changes in the quantity and composition of suspended particulate organic matter in lagoons of the Alaskan Beaufort Sea. *Mar. Ecol. Prog. Ser.* 527, 31–45. doi:10.3354/meps11207

Couture, N. J., Irrgang, A., Pollard, W., Lantuit, H., and Fritz, M. (2018). Coastal erosion of Permafrost soils along the Yukon coastal Plain and fluxes of organic

carbon to the Canadian Beaufort Sea. *J Geophys Res-Biogeo* 123 (2), 406–422. doi:10.1002/2017JG004166

Dinter, D. A., Cater, L. D., and Brigham-Grette, J. (1990). "Late Cenozoic geoloic evolution of the Alaskan North Slope and adjacent continental shelves," in *The Arctic Ocean Region: Geology of North America*. Editors A. Grantz, L. Johnson, and J.F. Sweeney (Boulder, CO: The Geological Society of North America), 459–490.

Dou, F., Ping, C. L., Guo, L., and Jorgenson, T. (2008). Estimating the impact of seawater on the Production of soil water-extractable organic carbon during coastal erosion. *J. Environ. Qual.* 37, 2368–2374. doi:10.2134/jeq2007.0403

Dou, F., Yu, X., Ping, C. L., Michaelson, G., Guo, L. D., and Jorgenson, T. (2010). Spatial variation of tundra soil organic carbon along the coastline of northern Alaska. *Geoderma* 154 (3–4), 328–335. doi:10.1016/j.geoderma.2009.10.020

Dunton, K. H., Schonberg, S. V., and Cooper, L. W. (2012). Food web structure of the alaskan nearshore shelf and estuarine Lagoons of the Beaufort Sea. *Estuar. Coast* 35 (2), 416–435. doi:10.1007/s12237-012-9475-1

Farquharson, L., Mann, D., Rittenour, T., Groves, P., Grosse, G., and Jones, B. (2018). Alaskan marine transgressions record out-of-phase Arctic Ocean glaciation during the last interglacial. *Geology* 46 (9), 783–786. doi:10.1130/G40345.1

Fritz, M., Vonk, J. E., and Lantuit, H. (2017). Collapsing arctic coastlines. *Nat. Clim. Change* 7 (1), 6–7. doi:10.1038/nclimate3188

Fuchs, M., Lenz, J., Jock, S., Nitze, I., Jones, B. M., Strauss, J., et al. (2019). Organic carbon and nitrogen stocks along a thermokarst lake sequence in Arctic Alaska. *J Geophys Res Biogeosci* 124, 1230–1247. doi:10.1029/2018JG004591

Gibbs, A. E., and Richmond, B. M. (2015). National assessment of shoreline change — historical shoreline change along the North coast of Alaska, U.S. — Canadian Border to Icy Cape. *U.S. Geologial Survey Open File Report 2015—1048*. doi:10.3133/ofr20151048

Gibbs, A. E., and Richmond, B. M. (2017). National assessment of shoreline change—summary statistics for updated vector shorelines and associated shoreline change data for the north coast of Alaska, U.S.-Canadian Border to Icy Cape. U.S. Geological Survey Open-File Report. doi:10.3133/ofr20171107

Goñi, M. A., Yunker, M. B., Macdonald, R. W., and Eglinton, T. I. (2000). Distribution and sources of organic biomarkers in arctic sediments from the Mackenzie River and Beaufort Shelf. *Mar. Chem.* 71 (1-2), 23–51. doi:10.1029/2001GL014047

Harris, C., McTigue, N., McClelland, J., and Dunton, K. (2018). Do high Arctic coastal food webs rely on a terrestrial carbon subsidy?. *Food Webs* 15, e0081 doi:10.1016/j.fooweb.2018.e00081

Hinkel, K. M., Eisner, W. R., Bockheim, J. G., Nelson, F. E., Peterson, K. M., and Dai, X. (2003). Spatial extent, age, and carbon stocks in drained thaw lake basins on the Barrow Peninsula, Alaska. *Arctic Antarct. Alpine Res.* 35 (3), 291–300.

Hinkel, K. M., Frohn, R. C., Nelson, F. E., Eisner, W. R., and Beck, R. A. (2005). Morphometric and spatial analysis of thaw lakes and drained thaw lake basins in the western Arctic Coastal Plain, Alaska. *Permafr. Periglac. Process.* 16 4, 327–341. doi:10.1007/s41063-016-0025-0

Holmes, R. M., McClelland, J. W., Peterson, B. J., Tank, S. E., Bulygina, E., Eglinton, T. I., et al. (2012). Seasonal and annual fluxes of nutrients and organic matter from large rivers to the Arctic Ocean and surrounding seas. *Estuar. Coast* 35 (2), 369–382. doi:10.1007/s12237-011-9386-6

Hugelius, G., Strauss, J., Zubrzycki, S., Harden, J. W., Schuur, E. A. G., Ping, C. L., et al. (2014). Estimated stocks of circumpolar permafrost carbon with quantified uncertainty ranges and identified data gaps. *Biogeosciences* 11 (23), 6573–6593. doi:10.5194/bg-11-6573-2014

Jones, B. M., Arp, C. D., Jorgenson, M. T., Hinkel, K. M., Schmutz, J. A., and Flint, P. L. (2009). Increase in the rate and uniformity of coastline erosion in Arctic Alaska. *Geophys. Res. Lett.* 26, 3. doi:10.1029/2008GL036205

Jones, B. M., and Arp, C. D. (2015). Observing a catastrophic thermokarst lake drainage in northern Alaska. *Permafr. Periglac. Process.* 26 (2), 119–128. doi:10.1002/ppp.1842

Jones, B. M., Farquharson, L. M., Baughman, C. A., Buzard, R. M., Arp, C. D., Grosse, G., et al. (2018). A decade of remotely sensed observations highlight complex processes linked to coastal permafrost bluff erosion in the Arctic. *Environ. Res. Lett.* 13 (11), 1274. doi:10.1088/1748-9326/aae471

Jones, B. M., Hinkel, K. M., Arp, C. D., and Eisner, W. R. (2008). Modern erosion rates and loss of coastal features and sites, Beaufort Sea coastline, Alaska. *Arctic* 61 (4), 361–372. doi:10.1029/2008GL036205

Jones, M. C., and Yu, Z. (2010). Rapid deglacial and early Holocene expansion of peatlands in Alaska. *Proc. Natl. Acad. Sci. U.S.A.* 107 (16), 7347–7352. doi:10.1073/pnas.0911387107

Jones, M. C., Grosse, G., Jones, B. M., and Walter Anthony, K. (2012). Peat accumulation in drained thermokarst lake basins in continuous, ice-rich permafrost, northern Seward Peninsula, Alaska. *J. Geophys. Res.: Biogeo* 117, 1567. doi:10.1029/2011JG001766

Jorgenson, M. T., and Brown, J. (2005). Classification of the Alaskan Beaufort Sea Coast and estimation of carbon and sediment inputs from coastal erosion. *Geo Mar. Lett.* 25 (2–3), 69–80. doi:10.1007/s00367-004-0188-8

Jorgenson, M. T., and Shur, Y. (2007). Evolution of lakes and basins in northern Alaska and discussion of the thaw lake cycle. *J. Geophys. Res.: Earth Surface* 112 F2. doi:10.1029/2006JF000531

Kanevskiy, M., Shur, Y., Jorgenson, M. T., Ping, C. L., Michaelson, G. J., Fortier, D., et al. (2013). Ground ice in the upper permafrost of the Beaufort Sea coast of Alaska. *Cold Reg. Sci. Technol.* 85, 56–70. doi:10.1016/j.coldregions.2012.08.002

Kaufman, D. S., Ager, T. A., Anderson, N. J., Anderson, P. M., Andrews, J. T., Bartlein, P. T., et al. (2004). Holocene thermal maximum in the western Arctic (0-180°W). *Quat. Sci. Rev.* 23 (5–6), 529–560. doi:10.1016/j.quascirev.2003.09.007

Kellogg, C. T. E., McClelland, J. W., Dunton, K. H., and Crump, B. C. (2019). Strong seasonality in Arctic estuarine microbial food webs. *Front. Microbiol.* 29, 189. doi:10.3389/fmicb.2019.02628

Krabbenhoft, A., Eisenhauer, A., Bohm, F., Vollstaedt, H., Fietzke, J., Liebetrau, V., et al. (2010). Constraining the marine strontium budget with natural strontium isotope fractionations (87Sr/86Sr*, d88/86Sr) of carbonates, hydrothermal solutions and river waters. *Geochem. Cosmochim. Acta* 74, 4097–4109. doi:10.1016/j.gca.2010.04.009

Lantuit, H., Overduin, P. P., Couture, N., Wetterich, S., Are, F., Atkinson, D., et al. (2012). The arctic coastal dynamics database: a new classification scheme and statistics on arctic Permafrost coastlines. *Estuar. Coast* 35 (2), 383–400. doi:10.1007/s12237-010-9362-6

Macdonald, G. M., Beilman, D. W., Kremenetski, K. V., Sheng, Y., Smith, L. C., and Velichko, A. A. (2006). Rapid early development of circumarctic Peatlands and atmospheric CH4 and CO2 variations. *Science* 314 (5797), 285–288. doi:10.1126/science.1131722

Manson, G. K., and Solomon, S. M. (2007). Past and future forcing of Beaufort sea coastal change. *Atmos.-Ocean* 45 (2), 107–122. doi:10.3137/ao.450204

McClelland, J. W., Holmes, R. M., Peterson, B. J., et al. (2016). Particulate organic carbon and nitrogen export from major Arctic rivers. *Global Biogoechem Cycles* 30, 629–643. doi:10.1002/2015GB005351

McClelland, J. W., Townsend-Small, A., Holmes, R. M., Pan, F., Stieglitz, M., Khosh, M., et al. (2014). River export of nutrients and organic matter from the North slope of Alaska to the Beaufort Sea. *Water Resour. Res.* 50, 1823–1839. doi:10.1002/2013WR014722

Meyer, H., Schirrmeister, L., Andreev, A., Wagner, D., Hubberten, H. W., Yoshikawa, K., et al. (2010). Late glacial and Holocene isotopic and environmental history of northern coastal Alaska—Results from a buried ice-wedge system at Barrow. *Quat. Sci. Rev.* 29, 3720–3735. doi:10.2204/iodp.sd.11.03.2011

Overeem, I., Anderson, R. S., Wobus, C. W., Clow, G. D., Urban, F. E., and Matell, N. (2011). Sea ice loss enhances wave action at the Arctic coast. *Geophys. Res. Lett.* 38, 127 doi:10.1029/2011GL048681

Peucker-Ehrenbrink, B., Miller, M. W., Arsouze, T., and Jeandel, C. (2010). Continental bedrock and riverine fluxes of strontium and neodymium isotopes to the oceans. *G-cubed* 11, 3. doi:10.1029/2009GC002869

Ping, C. L., Michaelson, G. J., Guo, L. D., Jorgenson, M. T., Kanevskiy, M., Shur, Y., et al. (2011). Soil carbon and material fluxes across the eroding Alaska Beaufort Sea coastline. *J Geophys Res-Biogeo* 116, G2. doi:10.1029/2010JG001588

Rawlinson, S. E. (1993). Surficial geology and morphology of the alaskan central arctic coastal Plain.*Alaska Div. Geol. Geophys. Surv. Rep. Invest.* 93. 1. doi:10.14509/2484

Romanovsky, V. E., Smith, S. L., and Christiansen, H. H. (2010). Permafrost thermal state in the Polar Northern hemisphere during the international Polar Year 2007-2009: a synthesis. *Permafrost Periglac* 21 (2), 106–116. doi:10.1002/ppp.689

van Everdingen, R.O. (Editor) (1998). Multi-language glossary of Permafrost and related ground-ice terms," in *International Permafrost Association* (Calgary: The Arctic Institute of North America, University of Calgary).

Schuur, E. A., McGuire, A. D., Schädel, C., Grosse, G., Harden, J. W., Hayes, D. J., et al. (2015). Climate change and the permafrost carbon feedback. *Nature* 520 (7546), 171–179. doi:10.1038/nature14338

Stammerjohn, S., Massom, R., Rind, D., and Martinson, D. (2012). Regions of rapid sea ice change: an inter-hemispheric seasonal comparison. *Geophys. Res. Lett.* 39, 6. doi:10.1029/2012GL050874

Stein, R., and Macdonald, R. M. (2004). *The organic carbon cycle in the Arctic Ocean*. Berlin, UK: Springer.

Strauss, J., Schirrmeister, L., Grosse, G., Wetterich, S., Ulrich, M., Herzschuh, U., et al. (2013). The deep permafrost carbon pool of the Yedoma region in Siberia and Alaska. *Geophys. Res. Lett.* 40 (23), 6165–6170. doi:10.1002/2013gl058088

Tank, S. E., Manizza, M., Holmes, R. M., McClelland, J. W., and Peterson, B. J. (2012). The Processing and impact of dissolved riverine nitrogen in the Arctic Ocean. *Estuar. Coast* 35, 401–415. doi:10.1007/s12237-011-9417-3

Tanski, G., Couture, N., Lantuit, H., Eulenburg, E., and Fritz, M. (2016). Eroding permafrost coasts release low amounts of dissolved organic carbon (DOC) from ground ice into the nearshore zone of the Arctic Ocean. *Global Biogeochem. Cycles* 30 (7), 1054–1068. doi:10.1002/2015GB005337

Tanski, G., Wagner, D., Knoblauch, C., Fritz, M., Sachs, T., and Lantuit, H. (2019). Rapid CO2 release from eroding Permafrost in seawater. *Geophys. Res. Lett.* 46, 1047. doi:10.1029/2019GL084303

Tolstikhin, N. I., and Tolstikhin, O. N. (1974). in *"Groundwater and surface water in the permafrost region" in General Permafrost Studies.* Editors P.I. Melnikov and O.N. Tolstikhin (Novosibirsk: U.S.S.R. Academy of Sciences)), 192–229.(In Russian.)

Urban, F. E., and Clow, G. D. (2018). GTN-P climate and active-layer data acquired in the National Petroleum Reserve–Alaska and the Arctic National Wildlife Refuge, 1998–2016, *U.S. Geological Survey Data Series*. 1092, 28. doi:10.3133/ds1092 [Supersedes USGS Data Series 1021]

Vonk, J. E., Sánchez-García, L., van Dongen, B. E., Alling, V., Kosmach, D., Charkin, A., et al. (2012). Activation of old carbon by erosion of coastal and subsea permafrost in Arctic Siberia. *Nature* 489 (7414), 137–140. doi:10.1038/nature11392

Vonk, J. E., and Gustafsson, O. (2013). Permafrost-carbon complexities. *Nat. Geosci.* 6, 675–676.

Wegner, C., Bennett, K. E., de Vernal, A., Forwick, M., Fritz, M., Heikkila, M., et al. (2015). Variability in transport of terrigenous material on the shelves and the deep Arctic Ocean during the Holocene. *Polar Res.* 34, 157. doi:10.3402/polar.v34.24964

Conflict of Interest: Sandia National Laboratories is a multimission laboratory managed and operated by National Technology and Engineering Solutions of Sandia, LLC, a wholly owned subsidiary of Honeywell International Inc., for the U.S. Department of Energy's National Nuclear Security Administration under contract DENA0003525. Honeywell International Inc. was not involved in the study design, collection, analysis, interpretation of data, the writing of this article or the decision to submit it for publication.

This paper describes objective technical results and analysis. Any subjective views or opinions that might be expressed in the paper do not necessarily represent the views of the U.S. Department of Energy or the United States Government. Any use of trade, firm, or product names is for descriptive purposes only and does not imply endorsement by the U.S. Government.

frontiers in Earth Science

ORIGINAL RESEARCH
published: 19 January 2021
doi: 10.3389/feart.2020.566227

The Role of Thermal Denudation in Erosion of Ice-Rich Permafrost Coasts in an Enclosed Bay (Gulf of Kruzenstern, Western Yamal, Russia)

Alisa Baranskaya[1,2]*, *Anna Novikova*[1], *Natalya Shabanova*[1], *Nataliya Belova*[1,3], *Stepan Maznev*[1], *Stanislav Ogorodov*[1] and *Benjamin M. Jones*[4]

[1]Laboratory of Geoecology of the North, Faculty of Geography, Lomonosov Moscow State University, Moscow, Russia, [2]Laboratory of Environmental Paleoarchives, Institute of Geography, Russian Academy of Sciences, Moscow, Russia, [3]Earth Cryosphere Institute, Tyumen Scientific Centre, SB RAS, Russia, [4]Institute of Northern Engineering, University of Alaska Fairbanks, Fairbanks, AK, United States

OPEN ACCESS

Edited by:
Valerio Acocella,
Roma Tre University, Italy

Reviewed by:
Mikhail Dobrynin,
German Weather Service, Germany
Michael Lehning,
École Polytechnique Fédérale de Lausanne, Switzerland
David Marcolino Nielsen,
University of Hamburg, Germany, in collaboration with reviewer MD

***Correspondence:**
Alisa Baranskaya
baranskaya@geogr.msu.ru

Specialty section:
This article was submitted to Cryospheric Sciences, a section of the journal Frontiers in Earth Science

Received: 27 May 2020
Accepted: 30 November 2020
Published: 19 January 2021

Citation:
Baranskaya A, Novikova A, Shabanova N, Belova N, Maznev S, Ogorodov S and Jones BM (2021) The Role of Thermal Denudation in Erosion of Ice-Rich Permafrost Coasts in an Enclosed Bay (Gulf of Kruzenstern, Western Yamal, Russia). Front. Earth Sci. 8:566227. doi: 10.3389/feart.2020.566227

Coastal erosion in the Arctic has numerous internal and external environmental drivers. Internal drivers include sediment composition, permafrost properties and exposure which contribute to its spatial variability, while changing hydrometeorological conditions act as external drivers and determine the temporal evolution of shoreline retreat. To reveal the relative role of these factors, we investigated patterns of coastal dynamics in an enclosed bay in the southwestern Kara Sea, Russia, namely the Gulf of Kruzenstern, which is protected from open-sea waves by the Sharapovy Koshki Islands. Using multitemporal satellite imagery, we calculated decadal-scale retreat rates for erosional segments of the coastal plain from 1964 to 2019. In the field, we studied and described Quaternary sediments and massive ground-ice beds outcropping in the coastal bluffs. Using data from regional hydrometeorological stations and climate reanalysis (ERA), we estimated changes in the air thawing index, sea ice-free period duration, wind-wave energy and total hydrometeorological stress for the Gulf of Kruzenstern, and compared it to Kharasavey and Marre-Sale open-sea segments north and south of the gulf to understand how the hydrometeorological forcing changes in an enclosed bay. The calculated average shoreline retreat rates along the Gulf in 1964–2010 were 0.5 ± 0.2 m yr^{-1}; the highest erosion of up to 1.7 ± 0.2 m yr^{-1} was typical for segments containing outcrops of massive ground-ice beds and facing to the northwest. These retreat rates, driven by intensive thermal denudation, are comparable to long-term rates measured along open-sea sites known from literature. As a result of recent air temperature and sea ice-free period increases, average erosion rates rose to 0.9 ± 0.7 m yr^{-1} in 2010–2019, with extremes of up to 2.4 ± 0.7 m yr^{-1}. The increased mean decadal-scale erosion rates were also associated with higher spatial variability in erosion patterns. Analysis of the air thawing index, wave energy potential and their total effect showed that inside the Gulf of Kruzenstern, 85% of coastal erosion is attributable to thermal denudation associated with the air thawing index, if we suppose that at open-sea locations, the input of wave energy and air thawing index is equal. Our findings highlight the importance of permafrost degradation and thermal denudation on increases in ice-rich permafrost bluff erosion in the Arctic.

Keywords: coastal erosion, permafrost, thermoabrasion, wave energy, massive ice beds, coastal retreat rates, thermal denudation

INTRODUCTION

Coasts in permafrost regions are extremely sensitive to environmental changes; coastal erosion is among the major destructive geomorphic processes in the Arctic, with circum-Arctic average shoreline retreat rate reaching 0.5 m yr^{-1} (Lantuit et al., 2013). While coastal erosion in low latitudes mainly depends on wind and wave energy and sediment composition of the shores (e.g., Luijendijk et al., 2018), as well as sea level rise (Meyssignac and Cazenave, 2012) and human impacts, drivers of the Arctic coastal dynamics are unique with respect to the added influence of permafrost and ground-ice (internal drivers) and sea-ice dynamics (external drivers). Together, they comprehend such highly variable processes as thermal abrasion, or thermal and mechanical destruction of permafrost coasts by waves, and thermal denudation, or thawing of the frozen ground at the bluffs and slumping of material due to gravity (Aré, 1988; Razumov, 2001; Leontiev, 2003).

The temporal evolution of coastal erosion rates in permafrost areas mainly depends on changing hydrometeorologic factors, such as air temperature, wind-wave energy, ice-free period, etc. (Vasiliev et al., 2005; Vasiliev et al., 2006; Shabanova et al., 2018). As the frozen cliffs thaw in contact with warmer air and water, shoreline retreat rates are sensitive to air temperature changes (Jones et al., 2009), increasing along with the modern warming in the Arctic (Overland et al., 2019), which exceeds the average world trends (IPCC, 2014; Savo et al., 2016) and trends for the Northern Hemisphere (Serreze et al., 2008). The thawed sediments are further removed by waves, the energy of which depends on wind speed and wind direction. Sea ice is a considerable limiting factor as well, protecting the coasts in winter, and controlling the length of the wave fetch in the sea ice-free period (Barnhart et al., 2014; Ogorodov et al., 2016). With the sea ice reduction in the Arctic since the early 2000s (Kay et al., 2011; Overeem et al., 2011; Stroeve et al., 2014; Barber et al., 2017), the sea ice-free period has become longer (Barnhart et al., 2016), and the length of the wave fetch has increased. As a result, stronger waves affect the coast for a longer period of time each year (Ogorodov et al., 2013; Nielsen et al., 2020), while at the same time there has been an increase in storm frequency (Atkinson, 2005) and positive wave height anomalies have been forecasted (Dobrynin et al., 2015). All of these hydrometeorologic drivers influence shoreline retreat; however, changes in one parameter do not always result in changes in other parameters. In order for a chain reaction to occur they have to act simultaneously, amplifying each other (Baranskaya et al., 2017). For example, an increase in the sea ice-free period duration will only result in active coastal erosion if there are considerable storms coinciding with it. Such complex patterns make correlations of hydrometeorological parameters with temporal evolution of coastal erosion a challenging task (Jones et al., 2018; Shabanova et al., 2018).

The spatial variability of shoreline retreat in the Arctic is determined by coastal morphology, lithology, exposure, ground ice and permafrost properties (Jones et al., 2009; Konopczak et al., 2014; Maslakov and Kraev, 2016; Obu et al., 2016). In the West Siberian Arctic, one of the typical permafrost features is the presence of massive ground-ice beds associated with Late Pleistocene deposits (Streletskaya et al., 2001; Belova, 2015; Vasil'chuk, 2012), large layers of ground-ice inside frozen sediments. Contrary to the East Siberian Arctic, where deposits of the Ice Complex (ice-rich permafrost with numerous ice wedges) compose quickly eroding coastal plains (Lantuit et al., 2012; Günther et al., 2015), massive ice beds are a typical feature of the Yamal and Gydan peninsulas. They are often exposed in coastal bluffs, and their rapid thawing increases rates of retreat of ice-rich segments in comparison with the adjacent areas with little or no ground ice (Belova, 2015). Because of this, they often factor into the development of retrogressive thaw slumps (or thermocirques) (Leibman and Kizyakov, 2007; Lantuit et al., 2012; Khomutovm and Leibman, 2016; Belova et al., 2018) or promote subsidence of coastal plain surface (Lim et al., 2020). The spatial variability of coastal erosion within segments with different morphological and permafrost properties imposed on the temporal evolution of climate parameters creates the rapidly changing and highly variable spatial patterns of coastal dynamics in the Arctic.

The southwestern Kara Sea is among the best-studied polar regions in terms of coastal dynamics. Field observations of coastal erosion began in the 1980s along the coasts of the Baydaratskaya Bay (Kamalov et al., 2006; Novikova et al., 2018), near Kharasavey (Yuriev, 2009; Belova et al., 2017) and Marre-Sale settlements (Vasiliev et al., 2006; Vasiliev et al., 2011); additional remote sensing based studies followed (Kritsuk et al., 2014; Belova et al., 2017; Belova et al., 2018; Novikova et al., 2018; Isaev et al., 2019). They showed average long-term shoreline retreat rates ranging from 0.3 to 3.0 m yr^{-1}; these values are generally lower compared to Eastern Siberia, with its Ice Complex coastal bluffs retreating with rates from 0.9 to 9.0 m yr^{-1} with extremes exceeding 15 m yr^{-1} (Günther et al., 2013, 2015; Pizhankova, 2016; Grigoriev, 2019; Nielsen et al., 2020). However, these shoreline retreat rates are comparable to some sites along the Beaufort Sea with average shoreline retreat rates from the 1970s to the early 2000s ranging from 0.5 to 2 m yr^{-1} (Brown et al., 2003; Radosavljevic et al., 2016; Irrgang et al., 2018), with extremes up to 9.4 m (Jones et al., 2018), increasing in the 2000s–2010s. In this light, shoreline retreat rates of Western Siberia, often exceeding 2 m yr^{-1} are considerable taking into account that they are long-term average values, representing sites of several kilometers (Kritsuk et al., 2014; Novikova et al., 2018). We use the term "sites" identifying areas of coastal dynamics monitoring of several kilometers' length with varying coastal morphology and other properties (e.g., Gulf of Kruzenstern, Kharasavey, etc.). By "segments" we mean short patches of coastline within these sites with relatively uniform morphology, exposure, permafrost properties, etc. All of the previously studied sites face toward the open sea and are directly exposed to waves of different directions. Wave energy is therefore one of the most important drivers of the erosion for these segments, as rates of coastal erosion showed an increase in years with longer sea ice-free period and stronger storms, an example being the period between 2005 and 2012–2013 for two stretches of coast of the Baydaratskaya Bay (Novikova et al., 2018; Isaev et al., 2019).

However, so far there have been no attempts to quantify the relative role of abrasion driven by the wave factor, and thermal denudation, resulting from air temperature increase and permafrost thawing. One possible way to estimate the role of thermal denudation in eroding the Kara Sea coasts is comparing the results of monitoring at known open-sea sites with shoreline retreat rates of coasts in an enclosed bay with less wave action. In addition, observing spatial variability of coastal erosion in such a bay is a tool to link it to coastal morphology, sediment composition and permafrost properties and assess their influence on shoreline retreat.

In this study, we chose the shallow Gulf of Kruzenstern, Western Yamal, protected by the Sharapovy Koshki Islands, as a test site to compare to erosion studies being conducted along bluffs facing toward the open sea in the same region (Kritsuk et al., 2014; Belova et al., 2017; Novikova et al., 2018). Here, we address the questions related to the relative contribution of factors driving spatial and temporal differences in shoreline retreat rates across sections of coast that are exposed to direct wave action to different degrees. Using multitemporal satellite imagery, we estimate decadal-scale shoreline retreat rates since the 1960s for the Gulf of Kruzenstern, and compare the patterns of erosion in the Gulf to the spatial distribution of outcrops of massive ice beds observed in the field. We also analyze the temporal evolution of the hydrometeorological parameters since the 1970s, and compare them, along with shoreline retreat rates, to the areas of long-term coastal erosion monitoring situated from 70 to 150 km away from the gulf in open-sea settings in the Western Yamal study region (Kritsuk et al., 2014; Belova et al., 2017; Novikova et al., 2018). Our aim is to study the naturally isolated effect of thermal denudation and make the first attempt to quantitatively compare it to areas where its influence is combined with the effect of wave abrasion.

STUDY AREA AND REGIONAL SETTING

The Gulf of Kruzenstern is situated in the western part of the Kara Sea, near the western Yamal Peninsula (**Figure 1**). It is protected from the open sea from the west and northwest by a chain of low accumulative sandy barrier islands named Sharapovy Koshki Islands. The size of enclosed part of the lagoon between Yamal peninsula and the Sharapovy Koshki Islands is about 50 × 30 km; the deepest part is near its southern entrance, where depths reach slightly more than 10 m. Most of the bathymetry is very shallow, with average depths of 2–3 m. Areas of less than 1vm depth stretch 200–400 m into the Gulf. The eastern coast of the Gulf consists of several levels of terraces with heights of 10–15 and 25–40 m, with steep bluffs, and low floodplains and deltaic laidas (salt marshes) of not more than 1–2 m elevation. The floodplains stretch for 10–15 km.

The climate of the region is cold, with a long winter lasting up to 9 months, and a cool, short summer. Mean annual air temperatures in the second half of the 20th century varied from −8 to −10°C (RIHMI-WDC, 2020). Mean annual accumulated positive air temperatures (thawing degree days) crucial for permafrost thawing and, hence, coastal dynamics, rose from 485 to 700°C-days in 1977–2013 at Kharasavey station, 70 km north of the Gulf (Belova et al., 2017), and from about 600 to 780°C-days in 1979–2013 at Marre-Sale, 90 km south of the Gulf (Shabanova et al., 2018). These values are smaller compared to the Barents Sea coasts, where they increased from ~800°C-days to ~1,000°C-days since the 1950s at Kolguev Island, and higher compared to stations at high latitudes both in the Kara and Laptev seas such as Dikson, (from ~300 to ~500°C-days since the 1970s), Terpiay-Tumsa or Shalaurova, (from ~200 to ~300°C-days since the 1960s) (Ogorodov et al., 2020). Average yearly precipitation varied from 300 to 350 mm in the 1950s–1970s (Trofimov et al., 1975) with a recent trend to increase to ~370 mm in Amderma (Aleksandrov et al., 2005). The wind conditions of the Kara Sea are driven by the monsoon effect: in winter, the Siberian winter high pressure center determines southerly winds (Wu and Jia, 2002), while in summer, northerly and northwesterly winds prevail (Trofimov et al., 1975).

The thickness of Quaternary sediments in the western part of Yamal can reach 200 m (German et al., 1963). Terrestrial permafrost is continuous, with temperatures at the depth of zero annual amplitude varying from −5 to −10°C. The thickness of permafrost varies from 50 m at river mouths to 150 m in interfluvial areas. Depths of the active layer on the coastal plains varies from 0.6 to 1.5 m, depending on sediment composition and slope exposure (Melnikov et al., 2004). One of the typical features of permafrost is the presence of abundant massive ground-ice beds in the form of large horizontal ice bodies. The ground-ice outcrops in coastal exposures on the Ural coast of the Baydaratskaya Bay (Belova et al., 2008; Belova, 2015; point 4, **Figure 1B**), near Marre-Sale station (Tarnogradskiy, 1982; Astakhov et al., 1996; Forman et al., 2002; Kanevskiy et al., 2005; Kritsuk, 2010; Shpolyanskaya, 2015; Streletskaya et al., 2018, etc.; point 3, **Figure 1B**) and Cape Kharasavey (Belova et al., 2017; point 2, **Figure 1B**). The presence of similar massive ice beds at the Bovanenkovo gas site, documented by numerous boreholes and outcrops over a large area (Dubikov and Koreisha, 1964; Tarasov, 1990; Solomatin and Koniakhin, 1993; Baulin et al., 1996; Kondakov et al., 2001; Romanenko et al., 2001; Dubikov, 2002; Vasil'chuk et al., 2009; Vasil'chuk, 2012; Fotiev, 2012; Vasil'chuk et al., 2014) provides evidence that massive ice beds are typical for Western Yamal and are present under most of its plains, occasionally outcropping in coastal bluffs or thermocirques. The origin of these massive ice beds has a broad range of interpretations, from intrasedimental (Dubikov and Koreisha, 1964; Streletskaya et al., 2001; Streletskaya et al., 2009; Slagoda et al., 2010; Slagoda et al., 2012; Vasil'chuk, 2012; Streletskaya et al., 2013; Streletskaya et al., 2018) to buried glacial ice (Astakhov et al., 1996; Astakhov and Nazarov, 2010).

On the southwestern Kara Sea coasts, long-term, high-resolution monitoring of coastal dynamics has been conducted by several research teams. Instrumental measurements have been made since 1988 on the Ural and Yamal coasts of the underwater pipeline crossing of the Baydaratskaya Bay (Ogorodov et al., 2016; Kamalov et al., 2006; points 4 and 5, **Figure 1B**). Since 1981, they have been made near Kharasavey settlement (Belova et al., 2017; point 2, **Figure 1B**) and since 1978 near Marre-Sale (Vasiliev et al., 2011; point 3, **Figure 1B**). Application of multitemporal satellite imagery allowed for the determination of shoreline

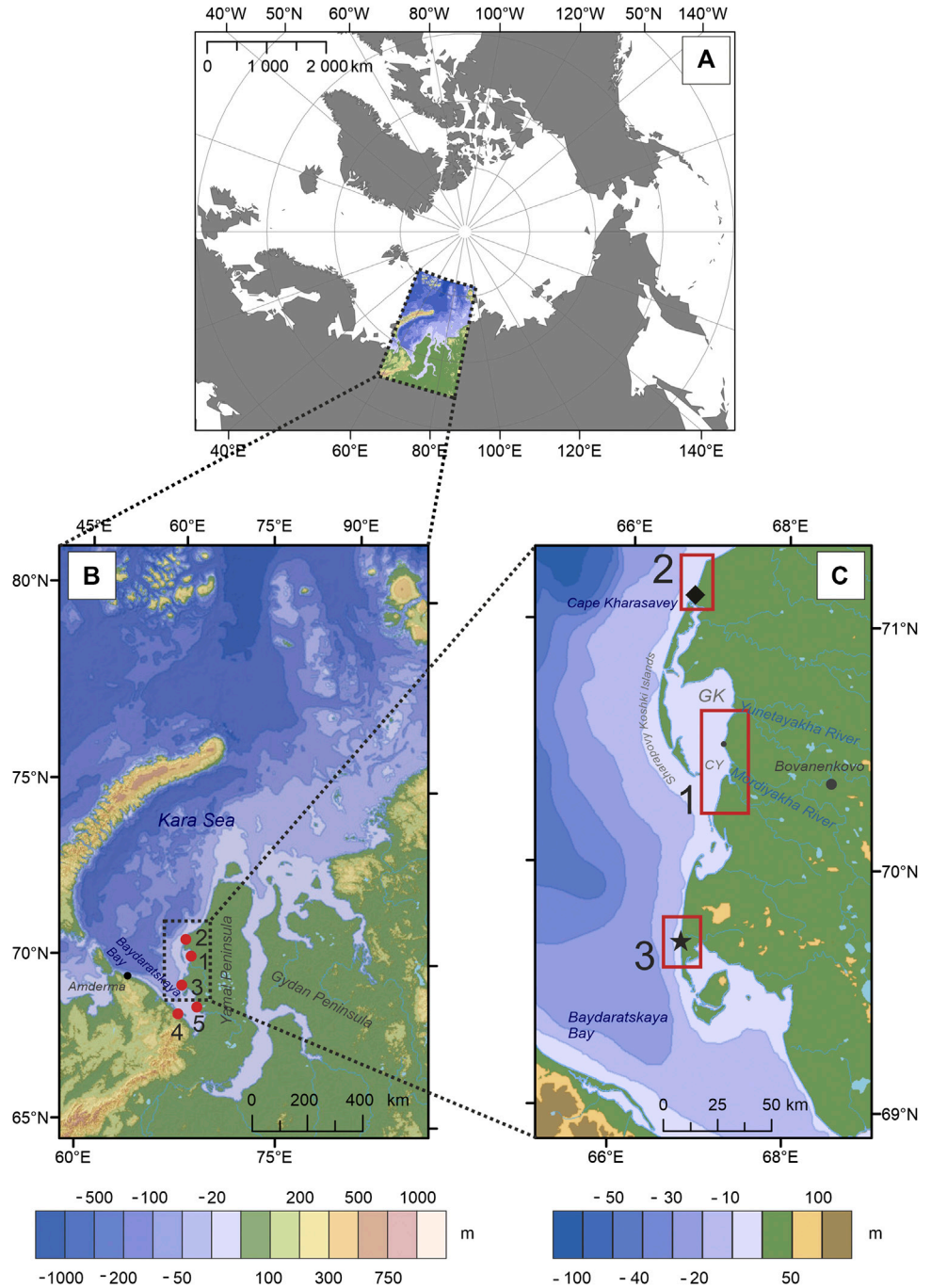

FIGURE 1 | Position of the study area and other key sites of coastal dynamics' monitoring mentioned in the text. 1—Gulf of Kruzenstern, Eastern Coast; 2—Kharasavey, 3—Marre-Sale, 4—Ural coast of the Baydaratskaya Bay, 5—Yamal coast of the Baydaratskaya Bay. Marresalya hydrometeorological station at Marre-Sale is shown with an asterisk; Kharasavey hydrometeorological station is shown with a diamond. Abbreviations: GK—Gulf of Kruzenstern, CY—Cape Yasalya.

retreat rates for contiguous segments of the study regions and to extend the period of investigations to since 1969 for Marre-Sale (Kritsuk et al., 2014), since 1964 for the Yamal coast of the Baydaratskaya Bay and since 1968 for the Ural coast of the Baydaratskaya Bay (Novikova et al., 2018) because of the use of Corona satellite imagery from the 1960s.

METHODS

Fieldwork

Field investigations on the morphology and sediment composition of the coastal bluffs of the eastern coast of the Gulf of Kruzenstern were carried out in July 2016. The

topography and geomorphic processes were described at key points, distributed along the coast every 400 m; the total length of the explored shoreline was about 50 km. Geomorphic profiles were made; in separate outcrops, exposures of Quaternary sediments were cleaned and described. Samples for grain size analysis, diatom analysis and radiocarbon dating were collected. Sections up to 2 m wide were described. Cryogenic structure and permafrost properties were documented; outcrops of massive ice beds were described; their position was marked with a handheld GPS unit Garmin Etrex Vista Hcx with a precision of up to 5 m. The position of thermocirques was also marked along the coast with the same GPS unit. High rates of thawing resulting from extreme summer temperatures of 2016 (up to +16°C) and destruction of the thermoabrasional niches did not allow detailed sampling of the massive ice beds, as the overhanging 10–15 m of sediments threatened to collapse during sample collection and excavation at the outcrops.

Conventional radiocarbon dating was made in the Laboratory of Palaeogeography and geomorphology of Polar Countries and the World Ocean named after V. Köppen, Institute of Earth Sciences, Saint-Petersburg State University. Grain size analysis was done at the Institute of Geography RAS, Moscow; diatom analysis was done in VNIIOkeangeologiya, Saint-Petersburg.

Satellite Imagery

To estimate changes in the position of the shoreline since the second half of the 20th century, multitemporal imagery was used for two coastal segments of ~20 and ~17 km length. We investigated erosional segments only, as the shoreline position on low accumulative segments highly depends on tides and surges and is therefore challenging to detect on multitemporal imagery. The accumulative coasts excluded from the analysis made about 30% of the study site. The decision whether the coast was accumulative or erosional was made based on coastal morphology determined during fieldwork in 2016 and on the images of 2010 and 2019. We analyzed recent changes in the position of the shoreline using a WorldView-1 (WV-1) image of 2010 with a spatial resolution of 0.5 m and a WorldView-2 (WV-2) image of 2019 with a spatial resolution of 0.6 m (DigitalGlobe, 2020). The WorldView-1 2010 image initially had Standard 2A level of processing: it was radiometrically corrected, sensor corrected, projected to a plane using the WGS 84 datum, and had a coarse DEM applied to it by the provider, to normalize for topographic relief with respect to the reference ellipsoid (Digital Globe Core Imagery Product Guide, 2016). The WorldView-2 2019 image was provided as Basic 1B level of processing: it was radiometrically corrected and sensor corrected, but not projected to a plane using a map projection or datum. Both images have a 5 m geolocation accuracy. The WV-2 2019 image was georeferenced to the WV-1 2010 image using 30 ground control points and the spline transformation in ArcGIS 10.6.1™. The accuracy of the georegistration of the 2019 imagery was assessed with 50 additional ground check points located within 100 m of the shoreline. The mean uncertainty of georeferencing of the image from 2019 to the image from 2010 imagery was 0.94 m, with a minimum and maximum error of 0.26 and 1.60 m, respectively.

To determine the position of the shoreline in 1964, Corona KH-4 satellite images were used. Corona is declassified military satellite imagery from 1960 to 1972 with global coverage, distributed by the U.S. Geological Survey (EarthExplorer, 2020) as scanned film strips 70 mm × 75.6 cm in size in four image tiles with a 7 μm (3,600 dpi) scan resolution. We used images from the 9th of August, 1964, with a spatial resolution of 2.7 m. The parts of the Corona images covering the area of the study were referenced to the 2010 WorldView-1 image with a spline transformation with 52 referencing points. For more precise georeferencing, additional points referenced by handheld GPS in field were applied. The accuracy of the referencing of Corona imagery (δ_r), estimated by manual comparison of 50 points across the study area, is equal to 4.2 m.

The WV-2 image of 2019 and the Corona image of 1964 that initially had no projection were projected using the respective UTM zone (42N) on a WGS-84 datum.

We digitized the shorelines in 1964 and 2010 manually in the ArcGIS 10.2 (ESRI) software at a sub-pixel accuracy equivalent to the scale from 1:300 to 1:2000. The shoreline was similarly digitized in the 2019 scenes using ArcGIS 10.6 (ESRI). We traced the edge of the cliff at erosional segments only, as the accumulative segments are difficult to interpret because of unstable vegetation position and considerable shoreline shifts depending on the tide.

To calculate the shoreline position changes, we used the Digital Shoreline Analysis System (DSAS) of Thieler et al. (2017), available as an extension to ArcGIS. The program automatically creates transects perpendicular to a previously drawn baseline. The position of the intersection points between the transects and the shorelines are consequently being used for calculating shoreline change statistics. For this study, a transect spacing of 500 m was chosen which resulted in 74 transects. The DSAS program measures the shoreline retreat rates as an offset from the baseline $L\ (t_i)$ for imagery acquisition dates t_i, and calculates statistics on the overall shoreline retreat rates and their uncertainty.

We calculated shoreline retreat rates for the time span between imagery acquisitions in m yr^{-1}:

$$r_L\,(t_{i-1}, t_i) = \Delta L/\Delta\tau = \left(L\,(t_i - L\,(t_{i-1}))\right)/\,(t_i - t_{i-1}), \qquad (1)$$

where r is the shoreline retreat rate, L is the distance of retreat, and t is time.

The volume of eroded deposits was assessed based on the obtained values of shoreline retreat (r_V) and altitudes of transects extracted from the ArcticDEM (Porter et al., 2018) (h_t) in cubic meters from 1 m of shoreline:

$$r_V = h_t \times r_L. \qquad (2)$$

Calculating the uncertainty of shoreline position on the WorldView-1 imagery, we took into consideration the topography-induced horizontal displacement (Toutin, 2004), which is

$$\delta_t = tg\alpha \times H, \qquad (3)$$

where α is the tilt angle of the spacecraft (14.1° in our case), and H is the maximum relative height at the territory (25 m), resulting in 6.25 m.

The uncertainty of shoreline position is calculated as:

$$\delta_x = \sqrt{\delta_t^2 + \delta_s^2} \quad (4)$$

for the WorldView-1 base image. For the referenced WorldView-2 2019 and KH-4 Corona 1964 images, the uncertainty of shoreline position was calculated as:

$$\delta_x = \sqrt{\delta_r^2 + \delta_s^2}, \quad (5)$$

where δt is the topography-induced uncertainty, δs is the uncertainty of shoreline digitization, which is one half of the imagery spatial resolution, and δr is the uncertainty of the referencing of Corona and WorldView-2 images to WorldView-1. The total uncertainty of the shoreline position results in 6.25 m for the WorldView-1 of 2010, 0.99 m for the WorldView-2 of 2019 and 4.46 m for the Corona imagery of 1964.

The uncertainty of the rate of linear shoreline retreat from x_1 to x_2 during the period from t_1 to t_2 was calculated as:

$$\delta_L = \frac{\sqrt{\delta x_1^2 + \delta x_2^2}}{t_1 - t_2}, \quad (6)$$

and results in 0.2 m yr^{-1} for 1964–2010, 0.7 m yr^{-1} for 2010–2019 and 0.1 m yr^{-1} for 1964–2019.

The volumetric approach utilizes heights of eroded surface *(h)* as well as rates of planar retreat *(r)*, so the total uncertainty of volumetric rates δ_V comprises:

$$\delta_V = \sqrt{h^2\delta_L^2 + r^2\delta_h^2}, \quad (7)$$

where δ_h is the uncertainty of estimation of the eroded surface height, depending on the surface roughness and equal to the height variance of the eroded surface at the current cliff.

Hydrometeorological Forcing

To estimate the changing hydrometeorological impact, the evolution of the air temperature, sea ice-free period duration and wind-wave energy was estimated. The potential of thermal denudation was assessed by the air thawing index (I_t) showing the number of positive/negative °C·days per year (Andersland and Ladanyi, 2004):

$$I_t = \sum_{i=1,}^{N} t_i,\ t > 0, \quad (8)$$

where t_i is the daily mean temperature, and N is the number of warm ($t > 0$°C) days per year. A similar parameter called positive degree-day (PDD) sums was used in Günther et al. (2015). This index is an evaluation of the annual amount of heat added to the ground and permafrost during warm periods. For its calculation, we used both observational data from Marre-Sale (Marreslaya hydrometeorological station) and Kharasavey (Kharasavey hydrometeorological station, **Figure 1C**) and ERA Interim reanalysis data on air temperature at a height of 2 m (Berrisford et al., 2009).

The Kharasavey hydrometeorological station was established in 1972; observations were made until 1986. We used the whole obsevation period. Data from Marre-Sale has gaps in 1973–1976, as well as in the 2000s. For the Gulf of Kruzenstern, the nearest cell of ERA Interim grid (1979–2018) with a grid resolution of 0.75° was used. Calculation of the air thawing index (It) at Marre-Sale and Kharasavey was done according to the procedure described in Shabanova et al. (2018) and Belova et al. (2017). To reconstruct thermal conditions in the Gulf of Kruzenstern, I_t from Marre-Sale and Kharasavey were weighted depending on their distance to the Gulf of Kruzenstern. The weights were calculated as the inversed linear distances:

$$t_k = \frac{t_m \cdot \frac{1}{d_{km}} + t_h \cdot \frac{1}{d_{hk}}}{\frac{1}{d_{km}} + \frac{1}{d_{hk}}} = t_m \cdot \frac{d_{hk}}{d} + t_h \cdot \frac{d_{km}}{d}, \quad (9)$$

where t_h, t_m and t_k are temperatures in Kharasavey, Marre-Sale and Kruzenstern respectively, d is the distance between Marre-Sale and Kharasavey ($d = d_{hk} + d_{km}$), where d_{hk} is the distance from Kharasavey to Kruzenstern, and d_{km} is the distance from Kruzenstern to Marre-Sale. As d_{km} is equal to ~100 km, and d_{hk} is equal to ~ 70 km, the weights $\frac{d_{hk}}{d}$ and $\frac{d_{km}}{d}$ make 0.4 for Kharasavey and 0.6 for Marre-Sale, respectively.

We chose eleven years in which data from both stations were available (1972 and 1977–1986). The obtained series were used to build the regression model with the ERA Interim data in the nearest "land" cell of the ERA grid, the size of the grid being equal to approximately 0.75°. The calculated regression coefficient was 0.82 and the determination coefficient was 0.94, showing sufficient agreement between the reanalysis and observational data.

The duration of the sea ice-free period was determined based on satellite imagery data. We used the sea ice concentration products of the EUMETSAT Ocean and Sea Ice Satellite Application Facility (OSI SAF) OSI-450 (EUMETSAT, 2017) for 1979—2015 and OSI-430-b for 2016–2018 (EUMETSAT, 2019). The products are provided by the Danish Meteorological Institute; their resolution is 25 km. Previous works based on OSI SAF products showed that the accuracy of the sea ice-free period start and end dates determination is comparable to NSIDC (Shabanov and Shabanova, 2019).

We determine the start and end dates of the sea ice-free period for the cells of OSI SAF data nearest to Marre-Sale, Kharasavey, the Gulf of Kruzenstern eastern coast and to the outer coast of the Sharapovy Koshki islands outside the Gulf of Kruzenstern. To detect the sea ice-free period start and end dates, the original rolling-window method (rolling-window approach or RWA) is used. The method is based on sea ice concentration (SIC) annual variation analysis and detects the robust SIC jumps, which are usually linked to water clearing-up (the last date of the downward jump) or freezing-up (the first date of the upward jump). The details of the RWA are published in Shabanov and Shabanova (2019). This method was introduced to avoid the disadvantages of the common 15%-method which is sometimes inapplicable in coastal zones due to SIC data contamination from land which results in high (20–40%) SIC values during the open water season.

The wave energy potential (WE), called "wave-energy flux" in earlier studies (Popov and Sovershaev, 1982), was calculated according to the Popov–Sovershaev method (Popov and Sovershaev, 1982; Ogorodov, 2002; Shabanova et al., 2018). The method is based on the wave processes theory and applies correlations between wind speed and parameters of wind-induced waves.

For deep-water conditions, when the sea floor does not affect wave formation, the wave energy potential, coming from 1 m of the wave front per second during a storm with the wind speed V_{ji} with a wind speed class j from a chosen wave direction i at the outer coastal zone boundary is proportional to the wind speed to the power of three and to the wave fetch:

$$WE_{ji} = 3 \times 10^{-6} V_{ji}^3 x_i, \quad (10)$$

where V_{ij} is the real wind speed of a chosen direction measured by anemometer at 10 m above sea level (m/s), x_i. is the wave fetch (km) along the current wind direction. The 3×10^{-6} coefficient is derived from the wind speed and wave parameters' empiric ratios and corresponds to the dimension of ρ/g, where ρ is density (kg/m^3), and g is gravitational acceleration (m/s^2). Thus, WE_{ji} has the dimension of kilograms per second:

$$\frac{kg}{m^3} \cdot \frac{s^2}{m} \cdot \frac{m^3}{s^3} \cdot m = \frac{kg}{s}. \quad (11)$$

The total wave energy potential, accumulated during the ice-free season, is calculated as:

$$WE = \sum_{i=1}^{M} \sum_{j=1}^{N} 3 \times 10^{-6} V_{ji}^3 x_i \cdot p_{ji} \cdot n, \quad (12)$$

where p_{ji} is the frequency of storm with the wave direction i and wind speed class j (calculated for the ice-free season only), n is the sea ice-free period duration in seconds, M is the number of wave-dangerous directions, and N is the number of wind speed classes. The wave energy potential is then expressed in kilograms (kg per season or kg yr^{-1}) and is the measure of the wave energy coming to the coastal zone, expressed as mass of incoming water.

Landward wave-dangerous directions of winds, wave fetches and depths were obtained from ETOPO1 digital elevation model, which also includes bathymetry (NOAA, 2017). The vertical resolution of ETOPO1 did not allow to take into account Sharapovy Koshki islands, because of their shallow topography being lower than the resolution of the DEM. For this reason, the wave energy potential evolution was calculated for the outer coast of the Gulf of Kruzenstern. The wave energy potential inside the Gulf was calculated separately using topographic maps. The frequency of wave-generating winds was estimated for the sea ice-free period only; winter months were not taken into account. For wind data, ERA Interim reanalysis was used (Berrisford et al., 2009); we took data on the wind speed and direction at a height of 10 m. The complete results of calculations of the air thawing index, ice-free period duration and wind-wave energy for the Gulf of Kruzenstern, its outer border at Sharapovy Koshki Islands, Kharasavey and Marre-Sale can be found in the **Supplementary material (Table S1)**

To estimate the relative role of wave destruction and thermal denudation in the total hydrometeorological forcing, the distribution of the values of the wave energy potential and air thawing index for four sites: Marre-Sale, Kharasavey, the Gulf of Kruzenstern eastern coast and to the outer coast of the Sharapovy Koshki islands outside the Gulf of Kruzenstern, was analyzed. The 0.975 quantile for the wave energy potential of all the four sites together made from 0 to $1{,}865 \times 10^6$ kg per year. The 0.975 quantile for the air thawing index made from 0 to 1,065 degree-days. All the values of WE and I_t were divided by these two values, respectively. Therefore all the transformed values had the range from 0 to 1 and no dimension. The transformed WE (WE_t) and I_t (It_t) values were further summed to calculate total hydrometeorological effect (stress or action) TE acting on the coasts:

$$TE = WE_t + It_t. \quad (13)$$

Based on these values, the relative role of the wave energy potential and air thawing index in the total hydrometeorological effect for each site could be quantitatively estimated. This estimation is relative, as it depends on the choice of sites for analysis, and shows the relation of the two factors between these sites only. It therefore helps to compare the conditions of neighboring sites only.

RESULTS

Quaternary Sediments and Massive Ice Beds

The sections exposed in the bluffs of the Gulf of Kruzenstern generally consist of three main units: Unit 1) brown silts at the top; Unit 2) poorly sorted silty thin sands in the middle and Unit 3) dark gray silts and clays with massive ground-ice beds at the bottom (**Figure 2**).

The upper unit (**Figure 2**, Unit 1) consists of brown silts which are non-laminated and deformed by cryoturbation, with the thickness of 1–2 m; they cover all the high plains of 10–35 m elevation. Their lower contact with Unit 2 is straight and horizontal, sometimes marked by thin (up to 5 cm) layers of peat debris. Separate benthic freshwater alkaphile diatom algae *Staurosira venter* were encountered, along with the extinct re-deposited diatoms *Paralia grunowii, Aulacoseira praegranulata*, fragments of *Grunowiella gemmata* and non-identifiable fragments of marine centric diatoms. Thin (2–3 cm) layers of peat at the lower boundary (**Figure 2A**), radiocarbon dated to 8,160 ± 80 years (LU-8457; 9,130 ± 120 cal. Years), give evidence that the upper brown silts formed in the Holocene; they are cover sediments accumulated in terrestrial conditions, derived from the presence of single freshwater diatoms and cryogenic deformations by multiple thawing and re-freezing events.

The middle unit (**Figure 2**, Unit 2) consists of poorly sorted silty thin sands with uneven lamination and traces of thawing and re-freezing. Separate freshwater boggy diatoms *Eunotia parallela* were documented, as well as single valves of the extinct Palaeogene *Paralia grunowii*, fragments of non-identifiable

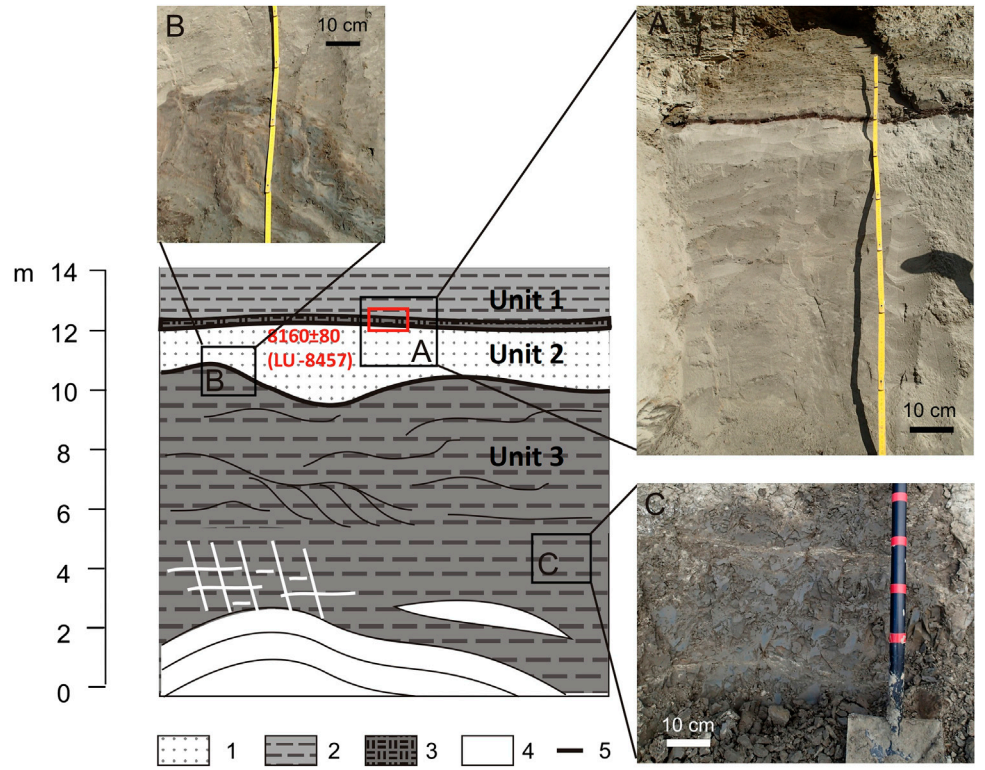

FIGURE 2 | General section of Quaternary sediments outcropping in the coastal bluffs of the Gulf of Kruzenstern. 1—sands, 2—silts, 3—peat, 4—ice, 5—geological interfaces. **(A)** Brown silts of the upper layer, underlain by peat; poorly sorted thin sands of the top of the middle layer. **(B)** Erosional contact between sands of the middle unit and silts and clays of the lower unit; deformations in the upper part of the lower unit. **(C)** Dark gray silts and clays of the bottom unit. The red box shows the position of material taken for radiocarbon dating; the radiocarbon age, error and sample number are shown in red color.

marine centric diatoms and sponge spicula. The presence of single freshwater diatoms, absence of distinct lamination implying sedimentation from water, and traces of thawing and re-freezing suggest sub-aerial or alluvial accumulation. This unit overlies the lower silts and clays of Unit 3 with an unconformity; its lower contact goes up and down, sometimes with a steep dip up to 60° (**Figure 2B**).

The lower unit (**Figure 2**, Unit 3) of dark gray and bluish gray silts and clays is exposed at elevations of up to 5–6 m a.s.l.; its bottom lies below sea level. The silts and clays are either non-laminated or have thin horizontal layers of gray sandy loam with deformed initial lamination; they have a splintered texture (**Figure 2C**) and a reticulate cryogenic structure, with up to 2 cm thick ice lenses. The upper part of the silts and clays contains layers of brownish sandy loams; this part is folded. The sediments contain few microfossils, including separate valves of the extinct diatom algae *Paralia grunowii*, non-identifiable fragments of marine centric diatoms, sponge spicula and separate cysts of freshwater *Chrysophyte* algae.

Massive ice beds, incorporated into the dark gray silts and clays, were noted in several thermoabrasional niches at elevations of up to 2–3 m a.s.l. The niches are steep, with an overhang of clays and silts above the ice. In the warm summer of 2016, the niches were very unstable: every few minutes, large volumes of thawed silts collapsed over the quickly melting ice, suggesting a very short lifetime of every massive ice exposure of not more than a few days. The shape and position of the ice outcrops probably changes every year, with some niches collapsing, and other ones becoming exposed.

The length of the ice exposures along the coast varies from 3 to 10 m; the visible thickness of ice is up to 2.5 m; its bottom is below sea-level. The ice is clean and transparent, with no bubbles and large (up to 2 cm) crystals. The massive ice beds have distinct layers of 0.3–0.5 m thickness; they form micro-steps in the outcrop. The upper contact of the ice with clays cuts these layers (**Figure 3**). From the contact, ice veins of up to 2 cm thick go up and sideways, creating the reticulate cryogenic structure in the dark gray silts and clays. Around the ice, they are non-laminated; layers of brown sandy loam are not seen. At 0.2–0.3 m above the massive ice beds with transparent clean ice, lenses of dirty turbid ice of up to 0.3 m thickness occur.

Massive ice beds mostly outcrop in steep erosional niches where the shoreline is relatively straight. However, they also exist under large thermocirques, spread along the shoreline, being the main reason of their formation. The ice is usually buried under the thawed grounds covering the flat bottom of the thermocirques. On the one hand, thawing of the ice, containing almost no sediments leads to considerable ground subsidence. On the other hand, the water saturates the sediments above the contact, while the remaining

FIGURE 3 | Coastal exposure of massive ice beds near Cape Yasalya. The dashed line shows the boundaries of the ice body.

FIGURE 4 | Thermocirque to the north of Cape Yasalya: **(A)** View from space in 2018 (Yandex Digital Maps, 2020 https://yandex.ru/maps/-/CCVtMVJd). **(B)** Field view in 2016; the cliff height is ~15 m.

ice acts like an aquiclude, leading to massive landslides streaming into the Gulf. The size of the thermocirques varies from 10 to 20 to 100–150 m in diameter; fresh recently formed thermocirques occur along with older ones. In the north of the area, the plant cover of a relatively old landslide by mayweed (*Matricaria inodora L.*) suggested its formation about 2 years ago, after which the landslide remained inactive. The distribution of the thermocirques and outcrops in niches (**Figure 4**) suggests that the massive ice beds are present almost everywhere along high coasts near Cape Yasalya.

Rates of Coastal Erosion

During the 46-years time period between 1964 and 2010, the eastern erosional coasts of the Gulf of Kruzenstern retreated on average by 23.3 ± 9.2 m (**Table 1**), resulting in an average shoreline retreat rate of 0.5 ± 0.2 m yr^{-1}. For active thermoabrasional segments not covered by vegetation in 2016, mean shoreline retreat rates reached 0.9 ± 0.2 m yr^{-1}. The area north of Cape Yasalya had the highest shoreline retreat rates of up to 1.5–1.7 ± 0.2 m yr^{-1} concentrated along 2 km of the shoreline facing to the northwest (**Figure 5**). Volumetric rates show more variability than the linear shoreline retreat rates; however, their values also increase toward the segments north of Cape Yasalya, reaching extremes up to 27.8 ± 3.1 m^3 m^{-1} yr^{-1}. The highest retreat of up to 80.0 ± 9.2 m was observed between the two largest outcrops of massive ice beds exposed in summer 2016 (**Figure 6**). Because of considerable planimetric retreat, the highest volumes of sediment were eroded from the terrace with heights of 10–15 m

TABLE 1 | Parameters of shoreline retreat for erosional coastal segments of the Gulf of Kruzenstern.

Parameter	1964–2010			2010–2019			1964–2019		
	Av	Max	Unc	Av	Max	Unc	Av	Max	Unc
Distance of shoreline retreat (m)	23.3	80.0	9.2	7.5	21.9	6.3	27.6	86.9	5.5
Rate of shoreline retreat (planimetric) (m yr^{-1})	0.5	1.7	0.2	0.9	2.4	0.7	0.5	1.6	0.1
Volumes of sediments eroded from a 1 m-wide segment of the shoreline (m^3 m^{-1})	283.6	1,277.2	142.6	98.1	370.3	103.7	83.7	1,333.3	126.5
Rate of retreat (volumetric) (m^3 m^{-1} yr^{-1})	6.2	27.8	3.1	11.1	41.1	11.6	9.3	24.2	2.3

immediately north from Cape Yasalya, and not from the high coastal bluffs of 25–40 m immediately south of Yunetayakha River or south of Mordiyakha River (**Figure 5**).

During the 9-years time period between 2010 and 2019, coastal erosion accelerated. The average retreat rate of the whole shoreline almost doubled: 0.5 ± 0.2 m yr^{-1} in 1964–2010 compared to 0.9 ± 0.7 m yr^{-1} in 2010–2019 (**Table 1**), although the increase in the uncertainty of the rates' calculation was considerable because of a shorter time period between observations. Peak erosion rates also increased by 40% (2.4 ± 0.7 m yr^{-1} compared to 1.7 ± 0.2 m yr^{-1} in 1964–2010). Overall, in nine years, the coast retreated by 21.9 ± 6.3 m. Volumetric retreat rates almost doubled making up to 41.1 ± 11.6 m^3 m^{-1} yr^{-1}. At the same time, the spatial variability of shoreline retreat increased, evidenced by higher RMSE values in 2010–2019 compared to 1964–2010 (**Table 1**). Segments with shoreline retreat rates exceeding 2 m yr^{-1} were documented not only north of Cape Yasalya, where most of the massive ice beds outcrop, but also to the south of it, and south of Mordiyakha River. The last two areas had relatively low erosion in 1964–2010, which became more active in the last nine years. The rates in 2010–2019 can be partly biased by their large uncertainty; however, a trend in the increase of both, the average and highest shoreline retreat rates, and considerable erosion at previously calm segments together suggest an intensification in erosion in the last decade.

During the entire 55-years observational period, from 1964 to 2019, mean erosion rates were 0.5 ± 0.1 m yr^{-1} on average, with extreme values up to 1.6 ± 0.1 m yr^{-1}, reflecting the effect of smoothening the extreme shoreline retreat rates through time: the longer period that is analyzed, the lower the mean erosion rates generally are. The greatest distance of shoreline retreat of 86.9 ± 5.5 m was typical for segments north of Cape Yasalya, between the two largest exposures of massive ice beds noted in the field (**Figure 6**). Areas with outcrops of massive ice beds and thermocirques marked in 2016 are generally destroyed faster than the adjacent segments; however, the outcrops do not exactly coincide with peak rates (**Figure 7**). Higher cliffs generally retreat faster than the lower segments, which is seen both in linear and volumetric erosion rates.

Evolution of Hydrometeorological Drivers of Coastal Dynamics

Along the coast of the Gulf of Kruzenstern, the air thawing index in 1979–2018 increased considerably (**Figure 8A**): its trend rose by more than 300 degree-days. Comparison of this parameter to Marre-Sale and Kharasavey shows that, according to the latitudes of these three points, temperatures at the Gulf of Kruzenstern are higher compared to Kharasavey and lower compared to Marre-Sale; therefore there are more positive degree days than at Kharasavey and less positive degree days than at Marre-Sale. From 1979 to 2000, the air thawing index showed no clear trend, fluctuating from 300 to slightly more than 800 degree-days. The coldest periods tend toward the end of the 1970s and the end of the 1990s; warm years were 1982–1985 and 1993–1995. From the beginning of the 2000s, a steady temperature rise was observed; the air thawing index reached its peak value of 1,358 degree-days in 2016.

The duration of the sea ice-free period also increased in the Gulf of Kruzenstern and adjacent areas (**Figure 8B**), as a result of both earlier breakup of the ice in spring and its later formation in autumn. This increase coincides with rising air temperatures in the last decades, although there could be a lag in ice conditions from temperature changes. Despite considerable fluctuations, a steady rise since the 1980s is seen at all sites. During this time, the sea ice-free period increased by more than 50 days. Contrarily to the air thawing index, the longest sea ice-free period was observed at Kharasavey and at the outer side of the Gulf of Kruzenstern (Sharapovy Koshki islands), situated in the northern and central part of the area (**Figure 1**). The longest sea ice-free period of 205 days was noted in 2012 at Kharasavey. At the outer side of the Gulf of Kruzenstern, near Sharapovy Koshki islands, the sea ice-free period on average lasted five to ten days longer compared to the coast inside the Gulf. In 1982, the difference exceeded 20 days. The enclosed lagoon becomes covered by ice faster than the open sea, and the ice holds for a longer time in the early summer. Many shallow areas freeze to the bottom, resulting in later ice breakup. In this way, the waves erode the coast of the Gulf of Kruzenstern for a shorter duration than they do at open-sea segments.

Fluctuations of the wind-wave energy potential (**Figure 8C**) generally agree with changes in the sea ice-free period duration and show a slight increase in storm intensity. Similarly to the ice-free period, the wind-wave energy potential at Kharasavey, the outer side of the Gulf of Kruzenstern (Sharapovy Koshki) and Marre-Sale shows an increase in 1995–1995 and between 2007 and 2013. The values in all three areas agree well; the wind-wave energy potential inside the Gulf of Kruzenstern is more than five times smaller than at the outer rim of the Sharapovy Koshki Islands. Such difference results from smaller wave fetch on the one hand, and shorter sea ice-free period on the other hand.

The total hydrometeorological forcing (TE) also shows a general increase since 1979 for all four sites (**Figure 9**). The graphs show similar

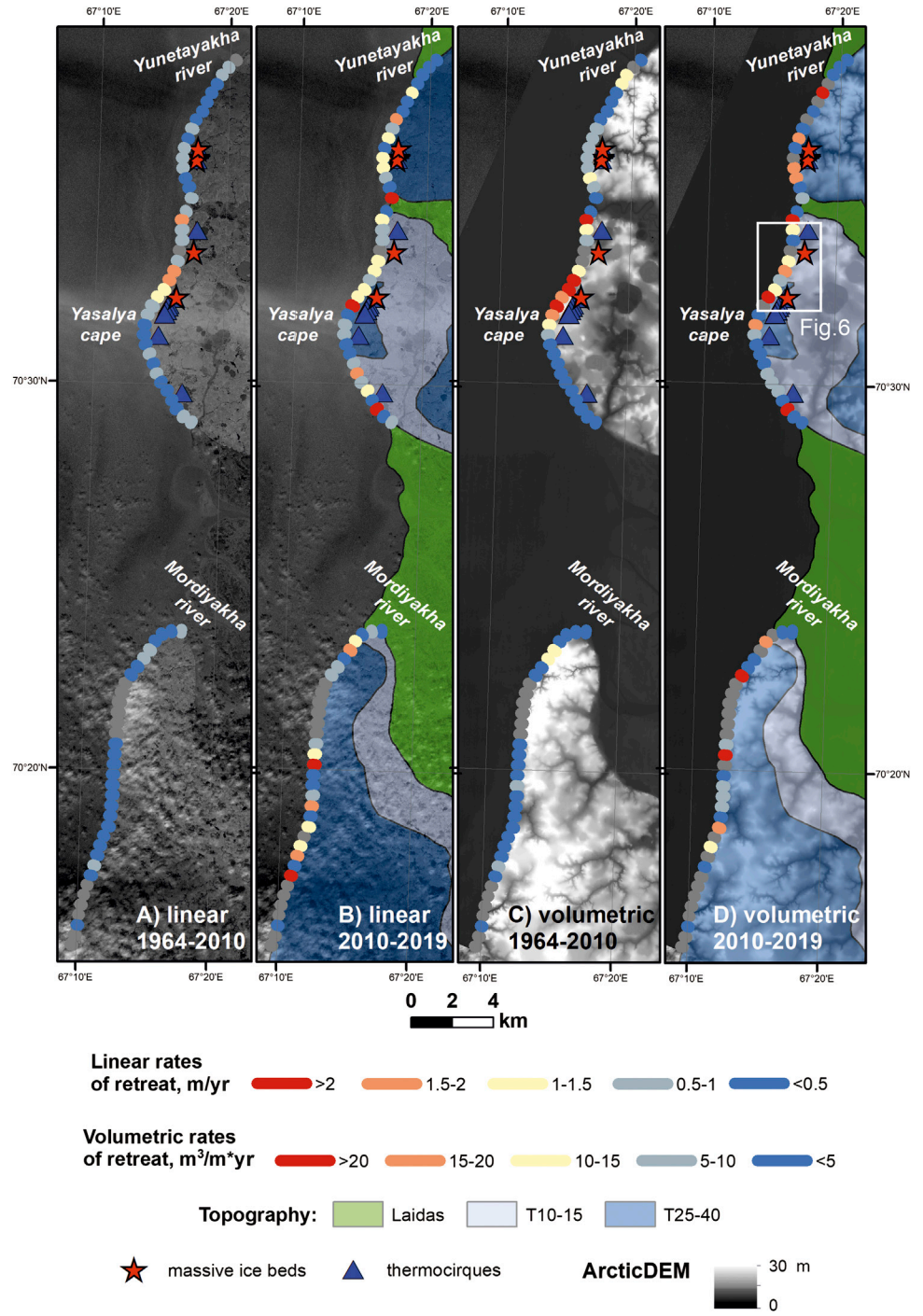

FIGURE 5 | Rates of retreat of the eastern coast of Gulf of Kruzenstern (area 1, **Figure 1C**), for 1964–2010 and 2010–2019. The dots indicate rates of shoreline retreat measured at every 500 m. Gray dots ("no data") correspond to areas covered by clouds where it was impossible to calculate retreat rates. "T10–15"—coastal plain (terrace) with heights of 10–15 m; "T25–40"—coastal plain (terrace) with heights of 25–40 m. The position of **Figure 6** is shown as a white rectangle.

distributions with the same highs and lows, although the values of these highs and lows differ from site to site. For all open-sea sites (**Figures 9B–D**), the increase of TE was higher than for the Gulf of Kruzenstern.

In 1992 and 1999, at all sites TE was lowest, resulting from relatively cool summers. The two positive peak years were 1994 and 2016. The reasons of increased TE were different: in 1994, the temperature was close to its average values, while the wind-wave energy showed a considerable increase, increasing mechanical erosion. On the contrary, in 2016, the wind-wave energy was slightly lower than usual, and TE mainly

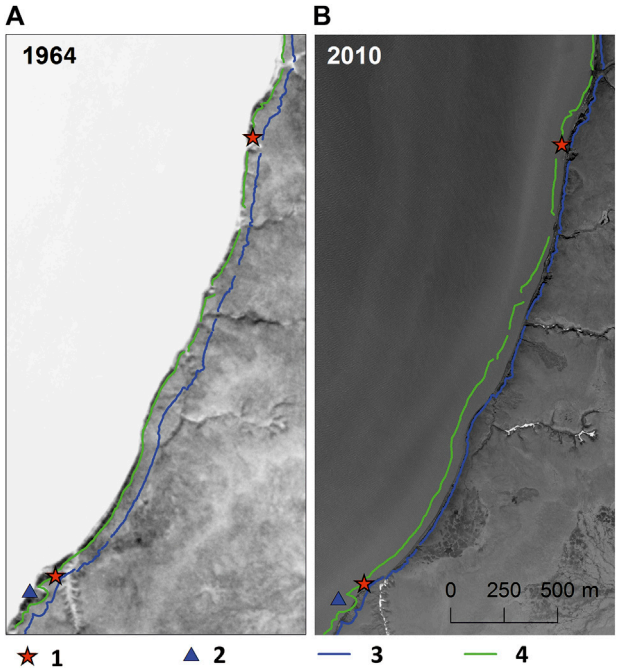

FIGURE 6 | Shorelines of 1964 and 2010 within the area of the fastest erosion and massive ice beds' exposure: **(A)** Corona image. **(B)** WorldView-1 image. 1—outcrops of massive ice beds in 2016, 2—outcrops of thermocirques in 2016, 3—shoreline of 2010. 4—Shoreline of 1964.

resulted from high air temperatures and thus intensified thawing of the frozen grounds.

Generally, the highest TE was recorded at Marre-Sale (**Table 2**) where its long-term mean was close to 1.3. The values for Kharasavey and the Sharapovy Koshki Islands outside the Gulf of Kruzenstern are slightly smaller (1.06 and 1.15 respectively), while inside the Gulf TE is 30% lower than at the Sharapovy Koshki Islands. The total forcing inside the Gulf is smaller than at open-sea locations because the Gulf of Kruzenstern receives 75% less wave energy as it is shielded by the Sharapovy Koshki islands. Therefore, variations in the air thawing index inside the Gulf have higher impact on coastal erosion relatively to other sites: the relation of I_t to the total effect is equal to 85%, while at other sites it makes 51–53% (**Table 3**). It should be taken into consideration, however, that the obtained ratios were based on the assumption that for open-sea segments, the thermal and wave factor have equal weights, which could in fact be more complex because of the ice content, cliff composition, morphology and other factors. Consequently, the percentage of coastal erosion attributed to the thermal denudation in the Gulf of Kruzenstern is a relative assessment in comparison to the other three sites.

DISCUSSION

Drivers of Spatial Variability in Coastal Erosion

Results of shoreline retreat measurements using remotely sensed data show considerable spatial variability in erosion rates: from 0.1 to 1.6 ± 0.1 m yr^{-1} or from 0.2 to 24.2 ± 2.3 m^3 m^{-1} yr^{-1} (1964–2019) at different segments, despite similar climatic and wave conditions within the eastern coast of the Gulf. The patterns of erosion rate distribution, showing faster retreat of the segment north from Cape Yasalya compared to the adjacent segment south of Cape Yasalya, with similar cliff heights, sediment composition and permafrost properties, indicate that the orientation of the coastal segment toward the potentially longest fetch and the most common wind direction is important for erosion intensity. Despite the small wave fetch in the Gulf of Kruzenstern, resulting in relatively low wind-wave energy potential compared to Kharasavey, Marre-Sale or to the coast seawards from the Sharapovy Koshki Islands, the most actively retreating coastal segment is the one that faces westerly and northwesterly winds. This gives evidence that even small amounts of wave energy can considerably influence coastal dynamics, depending on the coastal segment exposure toward waves. Such effect on larger scales was noted for Baydaratskaya Bay: while the Yamal coast faces to the southwest, and its average erosion rates were 0.3 ± 0.16 m yr^{-1} in 1968–2016, the Ural coast, exposed to northerly and northeasterly winds from the open sea

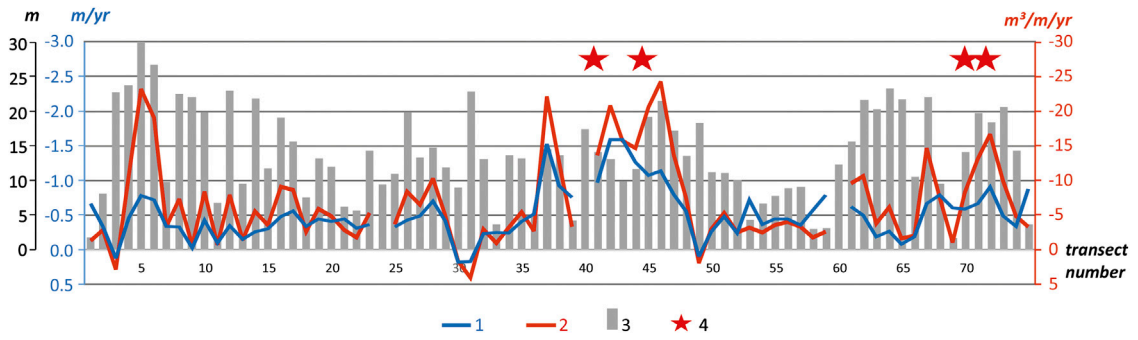

FIGURE 7 | Distribution of erosion rates in 1964–2019, cliff heights and position of outcrops of massive ice beds (summer 2016) along the shoreline. The *y* axes show (from left to right): bluff height, planimetric coastal erosion rates, volumetric coastal erosion rates; the *x* axis shows the number of transects from the south to the north. 1—linear erosion rates, 2—volumetric erosion rates, 3—cliff height, 4—outcrops of massive ice beds exposed in July 2016.

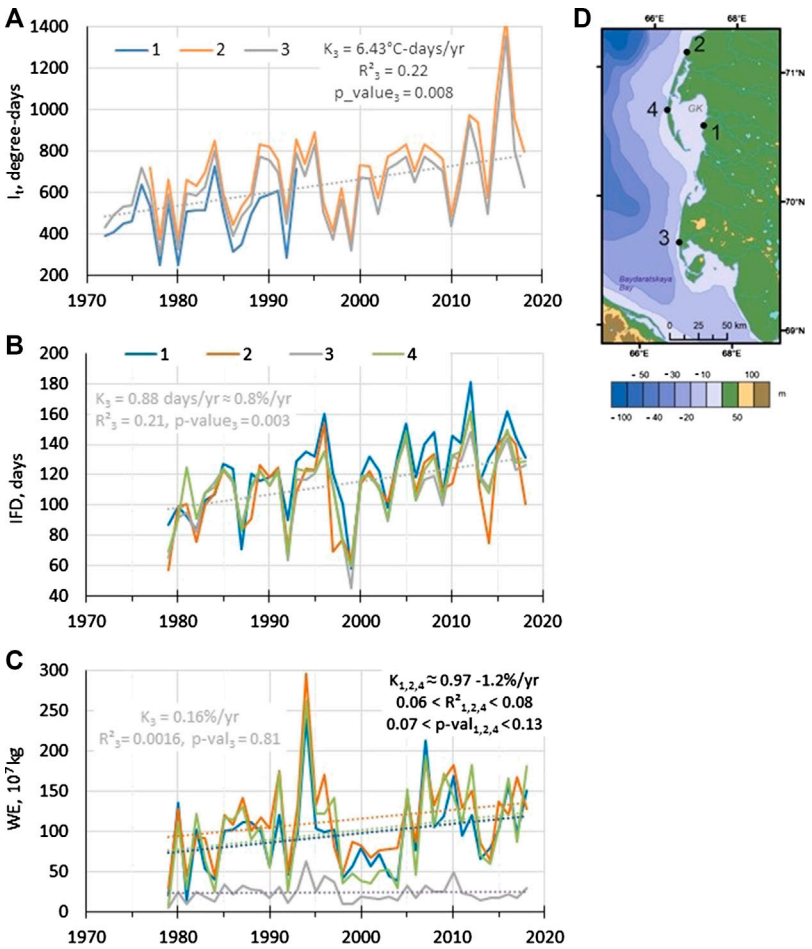

FIGURE 8 | (A) Air thawing index (I_t) according to observational data and ERA Interim reanalysis at the Gulf of Kruzenstern (1), Kharasavey (2), and Marre-Sale (3). **(B)** Sea ice-free period duration (IFD) at the Gulf of Kruzenstern eastern coast (1), Kharasavey (2), Marre-Sale (3) and outer side at Sharapovy Koshki Islands (4); **(C)** Wind-wave energy potential (WE) evolution at the Gulf of Kruzenstern eastern coast (1), Kharasavey (2), Marre-Sale (3) and outer side at Sharapovy Koshki Islands (4). The trends for the Gulf of Kruzenstern are shown as dotted lines together with their slope (K), determination coefficient (R^2) and *p*-value; **(D)** map showing the four sites for which the hydrometeorological parameters were calculated.

was characterized by average shoreline retreat rates of 1.2 ± 0.15 m yr^{-1} in 1964–2016 (Novikova et al., 2018). The orientation of the Ural coast toward the open sea leads to the reception of more wave energy than the Yamal coast (Shabanova et al., 2018). Our findings imply that even for small enclosed water areas, the orientation and exposure effect remains significant and can directly influence long-term coastal erosion patterns.

Another factor determining the spatial variability of erosion rates are permafrost properties (sediment composition and the presence of ground ice and massive ice beds). The massive ice beds exposed along the coast are similar to massive ice beds found near the Bovanenkovo settlement in terms of morphology and ice properties (Dubikov and Koreisha, 1964; Solomatin and Koniakhin, 1993; Vasil'chuk et al., 2009; Vasil'chuk et al., 2014). In Bovanenkovo, the massive ice beds are 1–2–28.5 m thick and are incorporated in silts of 2–12 m thickness or clays of 3–9 m thickness; the general composition of these silts and clays is similar to the ice containing dark gray silts of the Gulf of Kruzenstern. The ice is considered either as polygenetic: segregation, infiltration-segregation, injection-segregation, lacustrine, river and sea ice (Vasil'chuk, 2012) or buried glacial ice, relic from a land-based ice sheet (Solomatin and Koniakhin, 1993).

Despite varying interpretations of the origin of the massive ice beds, it is generally agreed that the massive ice beds are widely distributed under the lowlands in the central and western Yamal (see, e.g., Vasil'chuk, 2012). As the massive ice beds of the Gulf of Kruzenstern are similar to Bovanenkovo, they should also be largely present under the coastal plains of the Gulf, as confirmed by borehole data in the area (Baulin et al., 2003). The presence of numerous thermocirques confirms this assumption as their presence is indicative of ice-rich permafrost deposits. The distribution of erosion rates relative to the outcrops of the ground-ice (**Figure 7**) show that the peaks do not directly match with the exposures. However, according to field observations, segments of increased shoreline retreat rates generally correspond to areas with abundant ground-ice

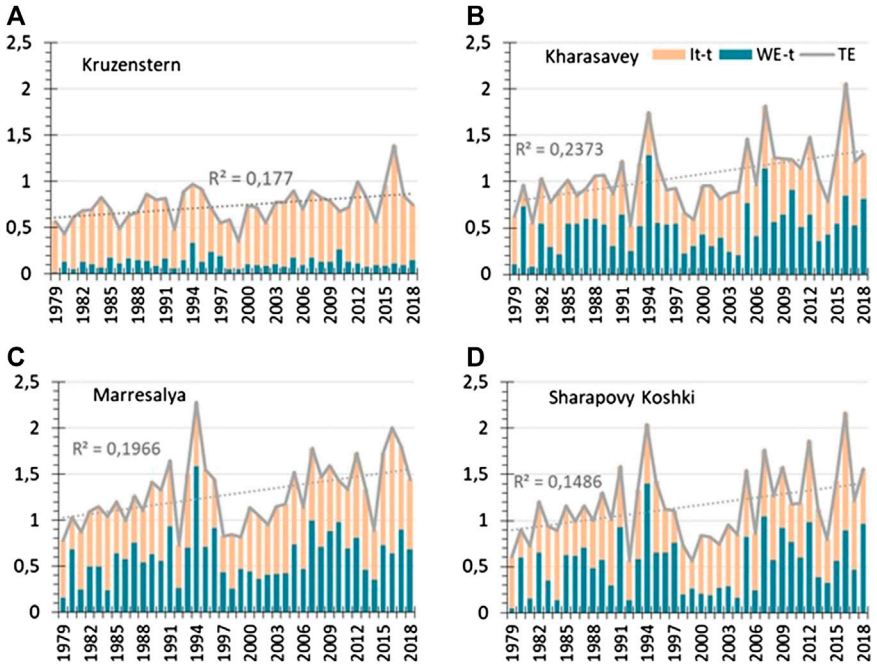

FIGURE 9 | Evolution of the normalized air thawing index (I_t) and wind-wave energy (WE), and their total effect (TE) showing the hydrometeorological forcing of coastal erosion of the Gulf of Kruzenstern **(A)**, Kharasavey **(B)**, Marre-Sale **(C)**, and Sharapovy Koshki Islands **(D)**. The trend of the total effect is shown as a dotted line. See **Figure 8D** for the map of the four sites.

TABLE 2 | Comparison of shoreline retreat at key sites of monitoring in the southwestern Kara Sea.

	(1) Gulf of Kruzenstern (this study)	(2) Kharasavey (Belova et al., 2017)	(3) Marre-Sale (Kritsuk et al., 2014)	(4) Ural coast of the Baydaratskaya Bay (Novikova et al., 2018)	(5) Yamal Coast of the Baydaratskaya Bay (Novikova et al., 2018)
Period of observations	1964–2019	1977–2016	1969–2009	1964–2016	1968–2016
Mean planimetric retreat rates (m yr-1)	0.5 ± 0.1	1.1 ± 0.1	2.0	1.2 ± 0.15	0.3 ± 0.16
Maximum planimetric retreat rates (m yr-1)	1.6 (2.4 in 2010–2019)	3.2 ± 0.1	3.0 (within a thermocirque)	2.5 ± 0.15	1.0 ± 0.16
Presence of massive ice beds	Yes	Yes	Yes	Yes	No

*The numbering of key sites corresponds to their numbering in **Figure 1**.*

TABLE 3 | I_t and WE long-term values transformed to 0–1 scale by dividing them by the 0.975 maximum values for four sites, their sum (TE), and the relative role of thermal denudation in coastal destruction (I_t-t/TE).

	Kharasavey	Sh. Koshki	Kruzenstern	Marre-Sale
I_t-t	0.55	0.62	0.62	0.68
WE-t	0.51	0.54	0.13	0.61
TE	1.06	1.15	0.74	1.29
I_t-t/TE	0.51	0.53	0.83	0.53

outcrops and thermocirques (**Figure 7**). As the thermoabrasional niches with the outcrops were actively collapsing in summer 2016, we suppose that the life span of such a niche is relatively short; they were carved and became buried many times in many locations along the coast between the acquisitions of the three satellite images of 1964, 2010, and 2019. Another important factor is the high ground-ice content of the silts and clays above the massive ice beds. A case study of the Kharasavey settlement gives evidence that segments where the coastal bluff is composed by ice-rich clays can retreat faster than segments with abundant massive ice beds (Belova et al., 2017). Not only the ice bodies themselves, but also silts and clays with ice-rich reticulate cryostructure can contribute to considerable rates of retreat of the segment north of Cape Yasalya (e.g., Baulin et al., 2003). Wide presence of massive ice beds generally enhances erosion in the region, although every single outcrop does not necessarily imply peak erosion rates in its every location.

In order to gain insight into regional coastal erosion patterns, we compared shoreline retreat rates from the Gulf of Kruzenstern to rates from coastal monitoring stations on the southwestern

Kara coast (**Table 2**). The highest average shoreline retreat rates were recorded at the Marre-Sale station and on the Ural coast of the Baydaratskaya Bay, where also the largest outcrops of massive ice beds are present (Kritsuk et al., 2014; Forman et al., 2002; Slagoda et al., 2012; Vasil'chuk, 2012). The average rates of the Gulf of Kruzenstern shoreline retreat are smaller; however, they exceed average shoreline change rates for the Yamal coast of the Baydaratskaya Bay, which is facing the open sea but does not contain massive ice beds. Comparing the long-term maximal shoreline retreat rates, we can conclude that the peaks for the Gulf of Kruzenstern were close to the values for the Ural coast, Marre-Sale and Kharasavey, and exceeded values for the Yamal coast. The average shoreline retreat rates along the Gulf of Kruzenstern in 1964–2010 (0.5 ± 0.1 m yr^{-1}) were lower compared to the Ural coast (1.2 ± 0.15 m yr^{-1} in 1964–2012, Novikova et al., 2018). However, in the last decade, these rates were comparable: 0.5 ± 0.3 m yr^{-1} in 2012–2016 at the Ural coast (Novikova et al., 2018), against 0.9 ± 0.7 m yr^{-1} in 2010–2019 at the Gulf of Kruzenstern. Higher rates at the Gulf of Kruzenstern in the most recent period partly result from the warm summer of 2016, the effect of which might not be included in the observations at the Ural coast. Nevertheless, due to the increases in the air thawing index, erosion of ice-rich coasts in the Gulf may occur at similar speed to the more exposed and wave-dependent open-sea sites in the region. At the same time, average rates over longer timescales exceed rates for the Yamal coast, but are lower in comparison to all the other open sea sites. This leads us to a conclusion that long-term dynamics are also influenced by the wind-wave energy and sea ice-free period duration.

For the Gulf of Kruzenstern, the presence of massive ice beds has a major impact on the erosional behavior of the coast, since rising air temperatures are leading to ground ice melt which in turn evokes that the coastal bluff faces degrade and slump. Even though wave development is hampered by the Sharapovy Koshki Islands which are sheltering the study site from the open sea, waves developing inside the Gulf are sufficient to remove the debris from the collapsed coastal bluffs. Similar patterns were noted by Vasiliev et al. (2006), suggesting that for gulfs and bays, sediment composition and permafrost properties are more important than the wave energy in these settings. Therefore, coastal erosion in the Gulf of Kruzenstern is mainly attributable to the high presence of ground ice, rather than to the exposure to high wave energy.

Another prominent feature of the Gulf of Kruzenstern is the increase in the spatial variability of erosion rates in 2010–2019 compared to 1964–2010. In other locations in the Arctic, such as Drew Point on the Beaufort coast of Arctic Alaska, the distribution of coastal erosion rates became more uniform along with their recent increase (Jones et al., 2009): different geomorphic levels composed by sediments of different ice content were eroding at nearly identical rates in 2002–2007, contrarily to the previous periods from 1955 to 2002. There seems to be a regional difference in these patterns, as other areas of long-term coastal erosion monitoring in the Kara Sea show more variable distribution of shoreline retreat rates in recent years, just like the Gulf of Kruzenstern. An example of this is the Ural coast of the Baydaratskaya Bay (**Figure 1B**; point 4), where shoreline retreat rates in 2005–2012 and 2012–2016 had higher spatial variability across different landforms compared to 1964–1988 (Novikova et al., 2018). Erosion became especially active on the 6–8 m terrace and got slower on the 12–16 m terrace in the recent years, while in 1964–1988, the 12–16 m terrace experienced higher retreat. This effect needs more investigations with higher temporal resolution than the present study, however, suggestions can be made that the increasing spatial variability of erosion at the Gulf of Kruzenstern is caused by the specific distribution of permafrost with large massive ice beds and relatively small and rare ice wedges. As the top of the massive ice beds typically has its highs and lows (Lim et al., 2020), their exposure usually differs from year to year, as the shoreline retreats. If the top of the massive ice is close to the surface, it crops out along the cliff, and erosion rates accelerate locally. If erosion rates are averaged over long-term periods (20 years or more), the effect of locally accelerated erosion due to ground ice presence is evened out, as massive ice beds are present in the sediments composing all topographic levels above 5–6 m. In case of shorter observational periods, spatial variations in massive ice presence along the coast can influence the speed of erosion and thus the distribution of erosion rates, leading to a high spatial variability.

Drivers of Temporal Variability in Coastal Erosion

The shoreline of the Gulf of Kruzenstern generally retreats faster than the shorelines of other gulfs and bays across the Kara Sea: 0.2–0.7 m yr^{-1} in all bays and gulfs (Vasiliev et al., 2006) against 0.5 ± 0.1 to 0.9 ± 0.7 m yr^{-1} in the Gulf of Kruzenstern. As previously shown, we suggest that this effect is caused by the presence of massive ice beds, which becomes especially important given that temperature variations provide 85% of the coastal erosion (**Table 3**) compared to 51–53% of it for open-sea sites. Because of this, temperature variations are especially important for the temporal evolution of erosion rates of the Gulf. The recent increase in TE in 2012–2017 (**Figure 9**) is a result of temperature rise, while the maximum of 2005–2009 seen at other sites (**Figure 9** b, c, d) is mainly caused by enhanced wind-wave energy and is not seen in the curve of TE for the Gulf of Kruzenstern (**Figure 9A**). The high erosion rates between 2010 and 2019 can be mainly attributed to the recent increase in the air thawing index. Similar patterns were observed in the last decade at Kharasavey, where shoreline retreat accelerated between 2006 and 2016 (Belova et al., 2017), on the Yamal coast of the Baydaratskaya Bay, where the shoreline retreated three times faster than earlier in the last decade (Novikova et al., 2018), and at Marre-Sale station, where erosion rates increased by roughly three times in 2010–2013 (Kritsuk et al., 2014). On the contrary, the Ural coast of the Baydaratskaya Bay experienced a decrease in coastal erosion in 2012–2016 (Novikova et al., 2018).

The above mentioned increase in the spatial variability of erosion rates in 2010–2019 also partly results from the high role of thermal denudation driven by the air thawing index increase. Segments of the

Gulf of Kruzenstern which contain massive ice beds but receive less wave energy started to retreat faster as a result of active thawing due to air temperature increases. Examples of these process are the segments south of Cape Yasalya and south of Mordiyakha River, which were relatively stable in 1964–2010 and retreated up to 21.9 ± 6.3 m in 2010–2019. With ongoing climate and permafrost warming (Biskaborn et al., 2019), it is reasonable to expect a further acceleration in coastal erosion along segments with high massive ice contents.

CONCLUSION

Multitemporal imagery analysis of a coastal segment of an enclosed bay (Gulf of Kruzenstern, Western Yamal, Kara Sea) showed erosion of coastal bluffs composed by ice-rich permafrost. The average rate of shoreline retreat from 1964 to 2010 was 0.5 ± 0.2 m yr^{-1}. The fastest erosion of up to 1.7 ± 0.2 m yr^{-1} was noted for segments with abundant outcrops of massive ice beds and numerous thermocirques. In 2010–2019, coastal erosion accelerated, reaching 0.9 ± 0.7 m yr^{-1} on average with peaks up to 2.4 ± 0.7 m yr^{-1}. This recent increase in erosion rates results from the increase in the air thawing index, especially noticeable in 2010–2019, along with increases in sea ice-free period duration and wind-wave energy, which together contribute to an intensification of hydrometeorological forcing in the recent decade. Compared to other sites of coastal dynamics monitoring at open-sea sites in the region (Marre-Sale, Kharasavey), the Gulf of Kruzenstern experiences 30% less hydrometeorological forcing. However, due to abundance of massive ground-ice beds exposed along the bluffs of the Gulf, its shoreline retreats at comparable rates, as the thermal factor is more important in driving erosion than the wind-wave energy factor, providing 85% of the variability in shoreline retreat. Based on these findings, projections of ongoing air temperature warming in the Arctic will likely result in a continuation of rapid coastal erosion in the Gulf of Kruzenstern, and generally along wave-sheltered shorelines with ice-rich permafrost. Such erosion is substantially less dependent on changes in wave dynamics: an increase in surface air temperature alone leads to higher coastal erosion rates in ice-rich permafrost bluffs in enclosed bays and lagoons in the Arctic.

DATA AVAILABILITY STATEMENT

The raw data supporting the conclusions of this article will be made available by the authors, without undue reservation.

AUTHOR CONTRIBUTIONS

Conceptualization, AB; methodology by AB, AN, and NS; validation by AB, AN, and NS; formal analysis by AN, BJ, and AB; investigation by AB, AN, and BJ; resources by AB; data curation by AN; writing—original draft preparation by AB; writing - review and editing by AB, NB, SM and BJ; visualization by AN, AB, and NS; supervision by SO; project administration by AB; funding acquisition by SO.

FUNDING

Studies were funded by the RSF Grant 16-17-00034. BJ was supported by the US National Science Foundation award OISE-1927553.

ACKNOWLEDGMENTS

We thank Digital Globe Foundation for the WorldView-1 satellite imagery. Additional geospatial support for this work provided by the Polar Geospatial Center under NSF-OPP awards 1043681 and 1559691. Investigations were made using the equipment obtained within the State Budget Theme AAAA-A16-116032810055-0. We thank the anonymous reviewers and the editors for comments and corrections which lead to substantial changes in the manuscript.

SUPPLEMENTARY MATERIAL

The Supplementary Material for this article can be found online at: https://www.frontiersin.org/articles/10.3389/feart.2020.566227/full#supplementary-material.

REFERENCES

Aleksandrov, Y., Bryazgin, N., Førland, E., Radionov, V., and Svyashchennikov, P. (2005). Seasonal, interannual and long-term variability of precipitation and snow depth in the region of the Barents and Kara seas. *Polar Res.* 24. doi:10.3402/polar.v24i1.6254

Andersland, O. B., and Ladanyi, B. (2004). *Frozen ground engineering*. 2nd Edn. Hoboken, NJ: John Wiley & Sons.

Aré, F. E. (1988). Thermal abrasion of sea coasts (part I). *Polar Geogr. Geol.* 12, 1. doi:10.1080/10889378809377343

Astakhov, V. I., Kaplyanskaya, F. A., and Tarnogradsky, V. D. (1996). Pleistocene permafrost of West Siberia as a deformable glacier bed. *Permafrost Periglac.* 7, 165–191. doi:10.1002/(SICI)1099-1530(199604)7:2<165::AID-PPP218>3.0.CO;2-S

Astakhov, V. I., and Nazarov, D. V. (2010). The stratigraphy of the upper neopleistocene of Western Siberia and its geochronometric justification. *Regional'naja geologija i metallogenija.* 43, 36–47 [in Russian].

Atkinson, D. E. (2005). Observed storminess patterns and trends in the circum-Arctic coastal regime. *Geo. Mar. Lett.* 25, 98–109. doi:10.1007/s00367-004-0191-0

Baranskaya, A. V., Belova, N. G., Kokin, O. V., Shabanova, N. N., Aleksyutina, D. M., and Ogorodov, S. A. (2017). "Coastal dynamics of the Barents and Kara seas in changing environment," in *Proceeding of the Thirteenth international MEDCOAST congress on coastal and marine science, engineering, management and conservation; Oct. 31 – Nov. 04 2017; mellieha, Malta. Dalyan*. Editor E. Özhan (Mediterranien Coastal Foundation), 281–292. doi:10.2118/166927-MS

Barber, D. G., Meier, W. N., Gerland, S., Mundy, C. J., Holland, M., Kern, S., et al. (2017). *Snow, water, ice and permafrost in the arctic (SWIPA) ed. C. Symon, Arctic sea ice*. Oslo, Norway: AMAP. 103–136.

Barnhart, K. R., Miller, C. R., Overeem, I., and Kay, J. E. (2016). Mapping the future expansion of Arctic open water. *Nat. Clim. Change.* 6 (3), 280–285. doi:10.1038/nclimate2848

Barnhart, K. R., Overeem, I., and Anderson, R. S. (2014). The effect of changing sea ice on the physical vulnerability of Arctic coasts. *Cryosphere.* 8 (5), 1777–1799. doi:10.5194/tc-8-1777-2014

Baulin, V. V., Aksenov, V. I., and Dubikov, G. I. (1996). *Engineering and geological monitoring of Yamal fisheries. Vol. II. Geocryological conditions of the Bovanenkovo field*. Tyumen: IPOS SB RAS [in Russian].

Baulin, V. V., Dubikov, G. I., Aksenov, G. I., Ivanova, N. V., Rivkin, F. M., Chernyadiev, V. P., et al. (2003). *Geocryological conditions of Kharasavey and kruzenstern gas Condensate fields (Yamal peninsula)*. Moscow: GEOS [in Russian].

Belova, N. G. (2015). Buried and massive ground ice on the West coast of Baidaratskaya Bay in the Kara Sea. *Ice Snow*. 55 (2), 93–102 [in Russian]. doi:10.15356/2076-6734-2015-2-93-102

Belova, N. G., Shabanova, N. N., Ogorodov, S. A., Baranskaya, A. V., Novikova, A. V., and Aleksyutina, D. M. (2018). "Coastal Erosion at Kharasavey gas condensate Field, Western Yamal Peninsula," in SPE Russian Petroleum Technology Conference 2018: Proceedings of the Society of Petroleum Engineers. Moscow, Russia: Society of Petroleum Engineers. doi:10.2118/191727-18RPTC-MS

Belova, N. G., Shabanova, N. N., Ogorodov, S. A., Kamalov, A. M., Kuznetsov, D. E., Baranskaya, A. V., et al. (2017). Erosion of permafrost coasts of the Kara Sea near Kharasavey Cape, Western Yamal. *Earths Cryosph.* 21 (6), 73–83. doi:10.21782/EC1560-7496-2017-6(73-83)

Belova, N. G., Solomatin, V. I., and Romanenko, F. A. (2008). "Massive ground ice on the ural coast of the Baydaratskaya Bay, Kara Sea," in *Proceedings of the 9th international Conference on permafrost, 2008 June 29–July 3*. Fairbanks, USA: Fairbanks: University of Alaska, 107–112.

Berrisford, P., Dee, D., Fielding, K., Fuentes, M., Kallberg, P., Kobayashi, S., et al. (2009). *The ERA-interim archive*. Available at: https://www.ecmwf.int/node/8173 (Accessed November 3, 2011).

Biskaborn, B. K., Smith, S. L., and Noetzli, J. (2019). Permafrost is warming at a global scale. *Nat. Commun.* 10 (1), 264. doi:10.1038/s41467-018-08240-4

DigitalGlobe Core Imagery Product Guide. (2016). *DigitalGlobe Core imagery product Guide. v. 2.0*. Available at: https://www.geosoluciones.cl/documentos/worldview/DigitalGlobe-Core-Imagery-Products-Guide.pdf (Accessed November 3, 2020).

DigitalGlobe (2020). *Extractinsights, validate critical decisions*. Available at: https://www.digitalglobe.com/. (Accessed May 1, 2020).

Dobrynin, M., Murawski, J., Baehr, J., and Ilyina, T. (2015). Detection and attribution of climate change signal in ocean wind waves. *J. Clim.* 28 (4), 1578–1591. doi:10.1175/JCLI-D-13-00664.1

Dubikov, G. I. (2002). *Composition and cryogenic structure of frozen Strata of western Siberia*. Moscow: GEOS. [in Russian].

Dubikov, G. I., and Koreisha, M. M. (1964). Injection fossil ice on the Yamal Peninsula. Izvestia AS USSR. *Series Geographical.* 5, 58–65. [in Russian].

EarthExplorer – Home (2020). Available at: https://earthexplorer.usgs.gov/ (Accessed May 1, 2020).

EUMETSAT (20172017). *EUMETSAT Ocean and Sea Ice Satellite Application Facility. Global sea ice concentration climate data record 1979-2015 (v2.0)*. Norwegian and Danish Meteorological Institutes. 10.15770/EUM_SAF_OSI_0008 2020). (Accessed May 1, 2020).

EUMETSAT(20192019). *EUMETSAT Ocean and Sea Ice Satellite Application Facility. Global sea ice concentration interim climate data record 2016 onwards (v2.0)Norwegian and Danish Meteorological Institutes*, 2020). (Accessed May 1, 2020).

Forman, S. L., Ingolfsson, O., Gataullin, V., Manley, W. F., and Lokrantz, H. (2002). Late quaternary stratigraphy, glacial limits, and paleoenvironments of the Marresale area, Western Yamal Peninsula. *Quat. Res.* 57, 355–370. doi:10.1006/qres.2002.2322

Fotiev, S. M. (2012). Chemical composition and genesis of water that formed the repeatedly injected massive ice beds on the area of the Bovanenkovo deposit. *Earths Cryosphere.* 3, 3–28. [in Russian].

German, E. V., Kislyakov, V. N., and Reinin, I. V. (1963). Geology and geomorphology of the Yamal Peninsula – new area perspective for oil and gas investigations. *Proceedings of VNIGRI.* 225, 311–329. [in Russian].

Grigoriev, M. (2019). Data from: coastal retreat rates at the Laptev Sea key monitoring sites. *PANGAEA*. 12, 11–37. doi:10.1594/PANGAEA.905519

Günther, F., Overduin, P. P., Sandakov, A. V., Grosse, G., and Grigoriev, M. N. (2013). Short- and long-term thermo-erosion of ice-rich permafrost coasts in the Laptev Sea region. *Biogeosciences.* 10, 4297–4318. doi:10.5194/bg-10-4297-2013

Günther, F., Overduin, P. P., Yakshina, I. A., Opel, T., Baranskaya, A. V., and Grigoriev, M. N. (2015). Observing Muostakh disappear: permafrost thaw subsidence and erosion of a ground-ice-rich island in response to arctic summer warming and sea ice reduction. *Cryosphere.* 9 (1), 151–178. doi:10.5194/tc-9-151-2015

IPCC (2014). *AR5 Synthesis report: climate change 2014*. Available at: https://www.ipcc.ch/report/ar5/syr/ (Accessed May 1 2020).

Irrgang, A. M., Lantuit, H., Manson, G. K., Günther, F., Grosse, G., and Overduin, P. P. (2018). Variability in rates of coastal change along the Yukon coast, 1951 to 2015. *J. Geophys. Res.: Earth Surf.* 123, 12. doi:10.1002/2017JF004326

Isaev, V. S., Koshurnikov, A. V., Pogorelov, A., Amangurov, R. M., Podchasov, O., Sergeev, D. O., et al. (2019). Cliff retreat of permafrost coast in south-west Baydaratskaya Bay, Kara Sea, during 2005–2016. *Permafrost Periglac.* 30 (1), 35–47. doi:10.1002/ppp.1993

Jones, B., Arp, C., Jorgenson, M., Hinkel, K., and SchmutzFlint, J. A. P. (2009). Increase in the rate and uniformity of coastline erosion in Arctic Alaska. *Geophysical Research Letters - Geophys Res. lett.* 36. doi:10.1029/2008GL036205

Jones, B., Farquharson, L., Baughman, C., Buzard, R., Arp, C., Grosse, G., et al. (2018). A decade of remotely sensed observations highlight complex processes linked to coastal permafrost bluff erosion in the Arctic. *Environ. Res. Lett.* 1, 38–45. doi:10.1088/1748-9326/aae471

Kamalov, A. M., Ogorodov, S. A., Birukov, V. Y., Sovershaeva, G. D., Tsvetsinsky, A. S., Arkhipov, V. V., et al. (2006). Coastal and seabed morpholithodynamics of Baydaratskaya Bay at the route of gas pipeline crossing. *Earths Cryosph.* 3, 3–14. [in Russian].

Kanevskiy, M. Z., Streletskaya, I. D., and Vasiliev, A. A. (2005). Formation of cryogenic structure of Quaternary sediments in Western Yamal (example of Marre-Sale area). *Earths Cryosph.* 3, 16–27. [in Russian].

Kay, J. E., Holland, M. M., and Jahn, A. (2011). Inter-annual to multi-decadal Arctic sea ice extent trends in a warming world. *Geophys. Res. Lett.* 38, 15. doi:10.1029/2011GL048008

Khomutovm, A. V., and Leibman, M. O. (2016). Rating of cryogenic translational landsliding hazard in the tundra of Central Yamal. *Earth`s Cryosphere.* 2, 45–54.

Kondakov, V. V., Yazynin, O. M., and Grachev, Yu. M. (2001). "Massive ice beds of the Yamal Peninsula," in *Proceedings of the second conference of geocryologists of Russia; 2001 June 6-8*. Editor R. M. Kamensky (Moscow, RussiaMoscow: MSU Publishers), 37–39.

Konopczak, A. M., Manson, G. K., and Couture, N. J. (2014). *Variability of coastal change along the western Yukon coast*. Ottawa: Geological Survey of Canada.

Kritsuk, L. N., Dubrovinm, V. A., and Yastreba, N. V. (2014). Results of complex study of the Kara Sea shore dynamics in the area of the meteorological station Marre-Sale, using GIS-technologies. *Earths Cryosph.* 18 (4), 59–69.

Kritsuk, L. N. (2010). *Ground ice of western Siberia*. Moscow: Science world. [in Russian].

Lantuit, H., Overduin, P. P., and Wetterich, S. (2013). Recent progress regarding permafrost coasts. *Permafrost Periglac.* 24 (2), 120–130. doi:10.1002/ppp.1777

Lantuit, H., Pollard, W. H., Couture, N., Fritz, M., Schirrmeister, L., Meyer, H., et al. (2012). Modern and late Holocene retrogressive thaw slump Activity on the Yukon coastal plain and Herschel island, Yukon territory, Canada. *Permafrost Periglac.* 23, 39–51. doi:10.1002/ppp.1731

Lantuit, J., Jorgenson, M. T., and SmithLee, O. P. W. (2003). "Long- term rates of erosion and carbon input, Elson Lagoon, Barrow, Alaska," in *ICOP permafrost: Proceedings of the 8th international conference on permafrost M. Phillips. A.A.* Editors S. M. Springman and L. U. Arenson (The Netherlands: Balkema Publishers), 101–106.

Leibman, M. O., and Kizyakov, A. I. (2007). *Cryogenic landslides of Yamal and the Ugorskiy peninsula*. Moscow: Institute of the Earth Cryosphere. [in Russian].

Leontiev, I. O. (2003). Modeling evolution of coastal thermo-abrasion. *Geomorfologiya.* 1, 15–24. [in Russian].

Lim, M., Whalen, D., Martin, J., Mann, P. J., Hayes, S., Fraser, P., et al. (2020). Massive ice control on permafrost coast erosion and sensitivity. *Geophys. Res. Lett.* 47, e2020GL087917. 10.1029/2020GL087917

Luijendijk, A., Hagenaars, G., Ranasinghe, R., Baart, F., Donchyts, G., and Aarninkhof, S. (2018). The state of the World's Beaches. *Sci. Rep.* 8, 6641. doi:10.1038/s41598-018-24630-6

Maslakov, A., and Kraev, G. (2016). Erodibility of permafrost exposures in the coasts of Eastern Chukotka. *Pol. Sci.* 10, 374–381. doi:10.1016/j.polar.2016.04.009

Melnikov, E. S., Leibman, M. O., Moskalenko, N. G., and Vasiliev, A. (2004). Active-layer monitoring in the cryolithozone of West Siberia. *Polar Geogr.* 28 (4), 267–285. doi:10.1080/789610206

Meyssignac, B., and Cazenave, A. (2012). Sea level: a review of present-day and recent-past changes and variability. *J. Geodyn.* 58, 96–109. doi:10.1051/e3sconf/202016407016

Nielsen, D. M., Dobrynin, M., Baehr, J., Razumov, S., and Grigoriev, M. (2020). Coastal erosion variability at the southern Laptev Sea linked to winter sea ice and the Arctic Oscillation. *Geophys. Res. Lett.* 47, e2019GL086876. doi:10.1029/2019GL086876

NOAA (2017). *ETOPO1 1 arc-minute global relief model: Procedures, data Sources and analysis*. Available at: https://data.nodc.noaa.gov/cgi-bin/iso?id=gov.noaa.ngdc.mgg.dem:316 (Accessed May 1, 2020).

Novikova, A., Belova, N., Baranskaya, A., Aleksyutina, D., Maslakov, A., Zelenin, E., et al. (2018). Dynamics of permafrost coasts of Baydaratskaya Bay (Kara Sea) based on multi-temporal remote sensing data. *Rem. Sens.* 10 (9), 1481. doi:10.3390/rs10091481

Obu, J., Lantuit, H., Fritz, M., Pollard, W. H., Sachs, T., and Günther, F. (2016). Relation between planimetric and volumetric measurements of permafrost coast erosion: a case study from Herschel Island, western Canadian Arctic. *Polar Res.* 35, 30313. doi:10.3402/polar.v35.30313

Ogorodov, S. A. (2002). "Application of wind-energetic method of Popov-Sovershaev for investigations of coastal dynamics in the Arctic," in *Report of an International Workshop: Proceedings of the Arctic Coastal Dynamic; 2001 Nov. 26–30; Potsdam, Germany. Bremerhaven: Berichte zur Polar- und Meeresforschung*. Editors V. Rachold, J. Brown, and S. Solomon, 82–85.

Ogorodov, S., Aleksyutina, D., Baranskaya, A., Shabanova, N., and Shilova, O. (2020). Coastal erosion of the Russian Arctic: an overview. *J. Coast Res.* 95, 599–604. 10.2112/SI95-117.1

Ogorodov, S., Baranskaya, A., Belova, N., Kamalov, A., Kuznetsov, D., Overduin, P., et al. (2016). Coastal dynamics of the Pechora and Kara seas under changing climatic conditions and human disturbances. *Geogr. Environ. Sustain.* 9 (3), 53–83. doi:10.15356/2071-9388_03v09_2016_04

Ogorodov, S., Kamalov, A., Belova, N., Baranskaya, A., Kuznetsov, D., Kopa-Ovdienko, N., et al. (2013). "Coastal Erosion monitoring at the Barents and Kara seas," in *Global congress on ICM: lessons learned to address New challenges. Proceedings of EMECS 10 MEDCOAST 2013 Joint conference; 2013 Oct. 30–Nov. 03; marmaris, Turkey*. Editor E. Özhan (Ankara: Middle East Technical University), 1335–1346.

Overeem, I., Anderson, R. S., Wobus, C. W., Clow, G. D., Urban, F. E., and Matell, N. (2011). Sea ice loss enhances wave action at the Arctic coast. *Geophys. Res. Lett.* 38, L17503. doi:10.1029/2011GL048681

Overland, J., Dunlea, E., Box, J. E., Corell, R., Forsius, M., Kattsov, V., et al. (2019). The urgency of Arctic change. *Polar Science* 21, 6–13. doi:10.1016/j.polar.2018.11.008

Pizhankova, E. I. (2016). Modern climate change at high latitudes and its influence on the coastal dynamics of the Dmitriy Laptev Strait area. *Earth`s Cryosphere.* XX (No. 1), 46–59.

Popov, B. A., and Sovershaev, V. A. (1982). Some features of the coastal dynamics in the Asian Arctic. *Vopr. Geogr.* 119, 105–116. [in Russian].

Porter, C., Morin, P., Howat, I., Noh, M.-J., Bates, B., Peterman, K., et al. (2018). *ArcticDEM. Harvard Dataverse, V1*. (Accessed May 1, 2020).

Radosavljevic, B., Lantuit, H., Pollard, W., Overduin, P., Couture, N., Sachs, T., et al. (2016). Erosion and flooding—threats to coastal infrastructure in the Arctic: a case study from Herschel Island, Yukon Territory. *Canada Estuaries and Coasts.* 39 (4), 900–915. doi:10.1007/s12237-015-0046-0

Razumov, S. O. (2001). Modeling arctic seas coastal erosion in the changing climatic conditions. *Earths Cryosphere.* 5 (1), 53–60. [in Russian].

RIHMI-WDC (2020). *Meteoru – data*. http://meteo.ru/english/data/ 01 May, 2020). Accessed

Romanenko, F. A., Voskresensky, K. S., Tarasov, P. E., Andreev, A. A., Nikolaev, V. I., and Sulerzhitsky, L. D. (2001). "Features of relief formation and loose sediments of western Yamal and the Baydaratskaya Bay coast (Kara Sea)," in *Problems of general and applied geoecology of the North*. Editor V. I. Solomatin (Moscow: MSU Publishers)), 41–68. [in Russian].

Savo, V., Lepofsky, D., Benner, J. P., Kohfeld, K. E., Bailey, J., and Lertzman, K. (2016). Observations of climate change among subsistence-oriented communities around the world. *Nat. Clim. Change.* 6, 462–473. doi:10.1038/nclimate2958

Serreze, M. C., Barrett, A. P., Stroeve, J. C., Kindig, D. N., and Holland, M. M. (2008). The emergence of surface-based Arctic amplification. *Cryosphere.* 3, 11–19. doi:10.5194/tc-3-11-2009

Shabanov, P. A., and Shabanova, N. N. (2019). *Open water season changes over the Kara Sea coastal zone: marresalya exampleIGARSS 2019 - 2019 IEEE international geoscience and remote sensing Symposium*. Yokohama, Japan, 4218–4221.2019.

Shabanova, N., Ogorodov, S., Shabanov, P., and Baranskaya, A. (2018). Hydrometeorological forcing of Western Russian Arctic coastal dynamics: XX-century history and current state. *Geography, Environment, Sustainability* 11 (1), 113–129. doi:10.24057/2071-9388-2018-11-1-113-129

Shpolyanskaya, N. A. (2015). *Pleistocene-Holocene history of the development of the permafrost zone of the Russian Arctic "through the eyes" of ground ice*. Moscow-Izhevsk: Institute for Computer Research. [in Russian].

Slagoda, E. A., Leibman, M. O., and Opokina, O. L. (2010). Origin of deformations in Holocene-Quaternary deposits with tabular ground ice on Yugorsky peninsula. *Earths Cryosphere.* 4, 30–41. [in Russian].

Slagoda, E. A., Opokina, O. L., Rogov, V. V., and Kurchatova, A. N. (2012). Structure and genesis of the underground ice in the neopleistocene-Holocene sediments of Marre-Sale Cape, Western Yamal. *Earths Cryosphere.* 2, 9–22. [in Russian].

Solomatin, V. I., and Koniakhin, M. A. (1993). "Stratigraphy, age and origin of massive ice, Yamal peninsula, West Siberia," in *Proceedings of the sixth international permafrost conference; 1993 july 5-9*. Editor C. Guodong (Beijing, ChinaGuangzhou: South China University of Technology Press), 103–115.

Streletskaya, I. D., Ukraintseva, N. G., and Drozdov, I. D. (2001). *Late Pleistocene history reconstruction based on the massive ground ice origin in the arctic coastal zone*. Available at: http://www.geogr.msu.ru/cafedra/crio/Tabular/ (Accessed May 1, 2020).

Streletskaya, I. D., Vasiliev, A. A., Oblogov, G. E., and Streletskiy, D. A. (2018). Methane content in ground ice and sediments of the Kara Sea coast. *Geosciences* 8, 434. doi:10.3390/geosciences8120434

Stroeve, J. C., Markus, T., Boisvert, L., Miller, J., and Barrett, A. (2014). Changes in Arctic melt season and implications for sea ice loss. *Geophys. Res. Lett.* 41 (4), 1216–1225. doi:10.1002/2013GL058951

Tarasov, A. M. (1990). *Experience of application of the isotopic-oxygen method of the ground ice study during the engineering-geological survey" in Engineering-geocryological survey methods*. Moscow: Vsegingeo Publishers, 118–133. [in Russian].

Tarnogradskiy, V. D. (1982). in *The origin of tabular bodies of ground ice on the Kara coast of the Yamal Peninsula" in Tabular ice in the cryolithozone*. Editor A. I. Popov (Yakutsk: Permafrost Institute)), 80–89. [in Russian].

Thieler, E. R., Himmelstoss, E. A., Zichichi, J. L., and Ergul, A. (2017). *Digital shoreline analysis System (DSAS) version 4.0—an ArcGIS extension for calculating shoreline change (ver. 4.4U.S. Geological survey open-file report 2008-1278*. Available at: https://pubs.er.usgs.gov/publication/ofr20081278 (Accessed May 1, 2020). doi:10.3133/ofr20081278

Toutin, Th. (2004). Comparison of stereo-extracted DTM from different highresolution sensors: SPOT-5, EROS-A, IKONOS-II, and QuickBird. *IEEE T. Geosci. Remote.* 42 (10), 2121–2129. doi:10.17122/ogbus-2016-2-7-24

Trofimov, V. T., Badu, Y. B., Kudriashov, V. G., and Firsov, N. G. (1975). *Yamal peninsula*. Moscow: MSU Publishers. [in Russian].

Vasiliev, A., Kanevskiy, M., Cherkashov, G., and Vanshtein, B. (2005). Coastal dynamics at the Barents and Kara Sea key sites. *Geo. Mar. Lett.* 25, 110–120. doi:10.1007/s00367-004-0192-z

Vasiliev, A. A., Shirokov, R. S., Oblogov, G. E., and Streletskaya, I. D. (2011). Coastal dynamics of western Yamal. *Earths Cryosphere.* 15 (4), 72–75. [in Russian].

Vasiliev, A. A., Streletskaya, I. D., Cherkashev, G. A., and Vanshtein, B. G. (2006). The Kara Sea coastal dynamics. *Earths Cryosphere.* 10 (2), 56–67. [in Russian].

Vasil'chuk, Y. K. (2012). *Isotope ratios in the environment*. in *Part 2: Stable isotope geochemistry of massive ice, Vol. 1*. Moscow: MSU Publishers. [in Russian].

Vasil'chuk, Yu. K., Vasil'chuk, A. C., Budantseva, N. A., Chizhova, Ju. N., Papesch, W., Podborny, Ye. Ye., et al. (2009). Oxygen isotope and

Deuterium indication of the origin and ^{14}C age of the massive ice, Bovanenkovo, central Yamal Peninsula. *Dokl. Earth Sci.* 8, 1326–1332. doi:10.1134/S1028334X09080194

Vasil'chuk, Y. K., Vasil'chuk, A. C., Budantseva, N. A., Chizhova, J. N., Papesch, W., and Podborny, Y. Y. (2014). ^{14}C age, stable isotope composition and pollen analysis of massive ice, Bovanenkovo gas field, Central Yamal Peninsula. *Geograph. Environ. Sustain.* 7 (2), 49–70. doi:10.24057/2071-9388-2014-7-2-49-70

Wu, B., and Jia, W. (2002). Possible impacts of winter Arctic Oscillation on Siberian high, the East Asian winter monsoon and sea–ice extent. *Adv. Atmos. Sci.* 19, 297–320. doi:10.1007/s00376-002-0024-x

Yandex Digital Maps (2020). *Maps: search for places, addresses, and public transport*. Available at: https://yandex.ru/maps/-/CCVtMVJd (Accessed May 1, 2020).

Yuriev, I. V. (2009). Problems of gas field exploitation in the coastal zone of Western Yamal. *Earths Cryosphere.* 13, 46–54. [in Russian].

Conflict of Interest: The authors declare that the research was conducted in the absence of any commercial or financial relationships that could be construed as a potential conflict of interest.

frontiers in Earth Science

ORIGINAL RESEARCH
published: 24 March 2021
doi: 10.3389/feart.2021.640580

Terrestrial Dissolved Organic Matter Mobilized From Eroding Permafrost Controls Microbial Community Composition and Growth in Arctic Coastal Zones

Anders Dalhoff Bruhn[1], Colin A. Stedmon[1], Jérôme Comte[2], Atsushi Matsuoka[3,4], Niek Jesse Speetjens[5], George Tanski[5,6], Jorien E. Vonk[5] and Johanna Sjöstedt[1,7]*

[1] National Institute of Aquatic Resources, Technical University of Denmark, Lyngby, Denmark, [2] Centre - Eau Terre Environnement, Institut National de la Recherche Scientifique, Québec, QC, Canada, [3] Takuvik Joint International Laboratory (CNRS-ULaval), Québec, QC, Canada, [4] Institute for the Study of Earth, Oceans, and Space, University of New Hampshire, Durham, NH, United States, [5] Department for Earth Sciences, Vrije Universiteit Amsterdam, Amsterdam, Netherlands, [6] Permafrost Research Section, Alfred Wegener Institute Helmholtz Centre for Polar and Marine Research, Potsdam, Germany, [7] Department of Biology, Aquatic Ecology, Lund University, Lund, Sweden

OPEN ACCESS

Edited by:
Louise Farquharson, University of Alaska Fairbanks, United States

Reviewed by:
Joanne K. Heslop, German Research Centre for Geosciences, Helmholtz Centre Potsdam, Germany
Alexander Michaud, Bigelow Laboratory for Ocean Sciences, United States
David E. Graham, Oak Ridge National Laboratory (DOE), United States

***Correspondence:**
Anders Dalhoff Bruhn
adbj@aqua.dtu.dk

Specialty section:
This article was submitted to Biogeoscience, a section of the journal Frontiers in Earth Science

Received: *11 December 2020*
Accepted: *24 February 2021*
Published: *24 March 2021*

Citation:
Bruhn AD, Stedmon CA, Comte J, Matsuoka A, Speetjens NJ, Tanski G, Vonk JE and Sjöstedt J (2021) Terrestrial Dissolved Organic Matter Mobilized From Eroding Permafrost Controls Microbial Community Composition and Growth in Arctic Coastal Zones. Front. Earth Sci. 9:640580. doi: 10.3389/feart.2021.640580

Climate warming is accelerating erosion along permafrost-dominated Arctic coasts. This results in the additional supply of organic matter (OM) and nutrients into the coastal zone. In this study we investigate the impact of coastal erosion on the marine microbial community composition and growth rates in the coastal Beaufort Sea. Dissolved organic matter (DOM) derived from three representative glacial deposit types (fluvial, lacustrine, and moraine) along the Yukon coastal plain, Canada, were used as substrate to cultivate marine bacteria using a chemostat setup. Our results show that DOM composition (inferred from UV-Visible spectroscopy) and biodegradability (inferred from DOC concentration, bacterial production and respiration) significantly differ between the three glacial deposit types. DOM derived from fluvial and moraine types show clear terrestrial characteristics with low aromaticity (S_r: 0.63 ± 0.02 and $SUVA_{254}$: 1.65 ± 0.06 L mg C^{-1} m^{-1} & S_r: 0.68 ± 0.01 and $SUVA_{254}$: 1.17 ± 0.06 L mg C^{-1} m^{-1}, respectively) compared to the lacustrine soil type (S_r: 0.71 ± 0.02 and $SUVA_{254}$: 2.15 ± 0.05 L mg C^{-1} m^{-1}). The difference in composition of DOM leads to the development of three different microbial communities. Whereas *Alphaproteobacteria* dominate in fluvial and lacustrine deposit types (67 and 87% relative abundance, respectively), *Gammaproteobacteria* is the most abundant class for moraine deposit type (88% relative abundance). Bacterial growth efficiency (BGE) is 66% for DOM from moraine deposit type, while 13 and 28% for DOM from fluvial and lacustrine deposit types, respectively. The three microbial communities therefore differ strongly in their net effect on DOM utilization depending on the eroded landscape type. The high BGE value for moraine-derived DOM is probably caused by a larger proportion of labile colorless DOM. These results indicate that the substrate controls marine microbial community composition and activities in coastal waters. This suggests that

biogeochemical changes in the Arctic coastal zone will depend on the DOM character of adjacent deposit types, which determine the speed and extent of DOM mineralization and thereby carbon channeling into the microbial food web. We conclude that marine microbes strongly respond to the input of terrestrial DOM released by coastal erosion and that the landscape type differently influence marine microbes.

Keywords: climate change, terrestrial dissolved organic matter, Arctic coastal zone, marine microbial community, chemostat, glacial deposits, permafrost

INTRODUCTION

The permafrost region in the northern hemisphere covers approximately 22% of the land surface which is not covered by glaciers and ice (Obu et al., 2019). A seasonally unfrozen active layer which thaws every year during the warm season is situated on top of the permafrost layer. The permafrost layer itself is permanently frozen, per definition, for at least 2 years in a row (Pollard, 2018). Recent estimates project that ∼1,000 ± 150Pg organic carbon (OC) are stored in the upper 3 m of the soils, plus 500 Pg C in deeper deposits such as yedoma and deltaic sediments (Hugelius et al., 2014; Schuur et al., 2015; McGuire et al., 2018). The amount of carbon stored in active and permafrost layers across the Northern Hemisphere is larger than the carbon storage of any other soil regions on Earth (e.g., temperate and tropical soils) and also surpasses that of the atmosphere (Jobbágy and Jackson, 2000; Strauss et al., 2017).

Due to climate change, permafrost is warming at a global scale (Biskaborn et al., 2019) and the increased loss in soil integrity primes Arctic coastlines for erosion (Günther et al., 2015; Hoque and Pollard, 2016; Obu et al., 2016; Fritz et al., 2017; Couture et al., 2018; Jones et al., 2018). Coastal erosion is further promoted by the reduction in landfast sea ice, making the shores vulnerable to environmental forcing, such as bathing of coastal bluffs in warm seawater and increased wave heights during storms (Overeem et al., 2011; Fritz et al., 2017). Dissolved organic matter (DOM), which is mobilized from permafrost compartments in Cryosols (i.e., soil type in cold regions which is affected by permafrost and cryoturbation processes), is highly biodegradable and directly available for microbial utilization upon permafrost thaw (Dou et al., 2008; Vonk et al., 2013; Abbott et al., 2014; Drake et al., 2015; Fritz et al., 2015; Spencer et al., 2015; Wologo et al., 2020). Increased release of DOM from degrading permafrost landscapes to the Arctic coastal zone (ACZ) can potentially lead to changes in OC processing by marine microbes (Colatriano et al., 2018). This can in turn influence marine primary production and higher trophic levels by increases in regenerated nutrients (Sipler et al., 2017), competition for mineral nutrients (Thingstad et al., 2008) and decreased light penetration (Arrigo and Brown, 1996). Utilization of dissolved organic carbon (DOC) (Tanski et al., 2019) and its offshore transport to deeper oceans (Belicka et al., 2002) will also be affected by the change in microbial carbon processing. This will ultimately affect the overall carbon cycle and thereby impact the carbon budget and aquatic ecosystems in the ACZ. Due to the magnitude of permafrost thaw (Romanovsky et al., 2010; Smith et al., 2010) and increase in coastal erosion (Günther et al., 2015; Fritz et al., 2017; Jones et al., 2018) a better estimate of marine microbial carbon processing of DOC from coastal erosion and its effect on microbial communities in ACZ is needed.

In this study we examine three different permafrost landscape units, which are omnipresent in our study region (Yukon coastal plain, western Canadian Arctic). The landscape units differ from their (post-)glacial genesis and OC storage and include fluvial (FLU) deposits (∼53 kg OC m^{-3} in the top meter of soil); lacustrine (LAC) deposits (∼47 kg OC m^{-3}); and moraine (MOR) deposits (∼40 kg OC m^{-3}) (Couture et al., 2018). Organic matter in FLU deposits comes from dispersed plant detritus mixed with mineral soil or peat layers that accumulated under stagnant water conditions in abandoned river channels (Rampton, 1982; Schirrmeister et al., 2011). Organic matter in LAC deposits was incorporated from the reworking and deposition of older material eroded from shore bluffs into lakes together with *in situ* production of fresh OM from aquatic plants and animals (Schirrmeister et al., 2011) along with talik formation (Wolter et al., 2017) and OC degradation in these lake sediments (Walter Anthony et al., 2018) due to permafrost thaw under the lakes. For the MOR deposit type, peat lenses and organic-rich silt is characteristic for the upper part of the deposits, where syngenetic formation and cryoturbation of permafrost has been the main driver behind the storage of OM (Rampton, 1982). This lead to high rates of accumulation and preservation of plant remains, which consists of less decomposed OM and high TOC (Schirrmeister et al., 2011). The organic matter incorporated into FLU and LAC has likely experienced Holocene decomposition since they were waterlogged during this period, whereas MOR likely been preserved since the Pleistocene and experienced very low decomposition (Strauss et al., 2017). During Holocene decomposition, labile OM, such as aliphatic and peptide-like compounds, in FLU and LAC deposits have been reworked by microbial activity, thereby leaving a higher amount of less labile compounds, such as aromatic compounds, when refrozen during the cooling of the middle Holocene (Stapel et al., 2017; Strauss et al., 2017; Heslop et al., 2019).

Terrestrial OM along permafrost coasts is released primarily as particulate organic carbon (POC) to the ACZ (Tanski et al., 2016). Although erosion of the coastline delivers relatively low amounts of DOC (annual flux of 55 Mg yr^{-1}) to the ACZ compared to Arctic rivers (34–38 Tg y^{-1} if the entire pan-Arctic watershed is considered) (Guo and Macdonald, 2006; Holmes et al., 2012; Tanski et al., 2016; Wild et al., 2019), the DOC

released by coastal erosion is highly biodegradable upon thaw (Vonk et al., 2013, 2015; Fritz et al., 2015; Spencer et al., 2015). In addition, upon exposure to seawater with high ionic strengths, ion exchange can release and further dissolve mineral-bound particulate OM or colloids, which can mobilize 19–50% of the bound OM (Kaiser and Guggenberger, 2000; Kawahigashi et al., 2006; Dou et al., 2008). The release of DOM from coastal erosion can therefore be assumed to have a large influence on microbes in coastal environments. Multiple studies have shown that the supply of permafrost-derived DOM can lead to rapid changes in marine microbial community composition and growth (Blanchet et al., 2017; Sipler et al., 2017; Müller et al., 2018) and it has recently been shown that the marine bacteria *Chloroflexi*, have the capacity to utilize terrestrial DOM (Colatriano et al., 2018). The effect of rapid mineralization of OC from permafrost thaw has been shown for freshwater bacterial communities, where microbes can degrade 34% of permafrost-derived DOC within 14 days of incubation (Vonk et al., 2013) or 47% within 28 days of incubation (Mann et al., 2015). However, there are knowledge gaps associated with the impact of DOM derived from coastal erosion of different glacial deposit types and how it affects marine microbial composition and carbon processing.

Here we study the bioavailability of DOM, released directly to marine microbes in the ACZ, through coastal erosion, using a chemostat approach. This allows the development of a stable microbial community under conditions where the constant supply of substrate could reflect conditions in coastal waters influenced by coastal erosion. We investigate the biodegradability of DOM derived from three representative glacial deposit types (FLU, LAC, and MOR) to test if differences in DOM character can induce differences in bacterial community composition (BCC) and bacterial growth efficiency (BGE). We also follow the changes in DOM character imparted by microbes using absorbance and fluorescence spectroscopy. We hypothesized that (i) the DOM provided by erosion of permafrost coasts is highly bioavailable for marine microbes and that (ii) different DOM characteristics among glacial deposit types induce different growth rates and the establishment of different bacterial communities.

MATERIALS AND METHODS

Study Area

The study area is located in the western Canadian Arctic on the Yukon coastal plain near Herschel Island - Qikiqtaruk (**Figure 1**). The Yukon coastal plain is about 282 km long and 10–30 km wide. Cliff heights are diverse, ranging from 2–3 m on the mainland across from Herschel Island to 60 m in the eastern part of the Yukon coastal plains (Couture et al., 2018). The mean annual air temperature is −11°C, with the highest temperature during July month reaching 7.8°C (1971–2000) (Environment Canada, 2016). The parent material of the Cryosols in the Yukon coastal plains originate from an ice-rich glacial margin and has been deposited by glacial transportation (ice and meltwater) of earth material and later on reworked by water during Holocene Thermal Maximum (higher than modern summer temperatures) (Fritz et al., 2012).

Sampling targeted fluvial, lacustrine, and moraine deposits since they represent the permafrost landscape on the Yukon coastal plain and differ the most in OC content and storage among all post-glacial landscape units (Couture et al., 2018). Fluvial sediments are poorly-drained floodplain deposits consisting of fine-grained sediments. The fluvial sediments used for this study were taken from the floodplains of the Babbage River Delta and may resemble other floodplain deposits in the study area. The fine-grained and ice-rich fluvial deposits are prone to erosion and can be mobilized with increasing river discharge, floods and deltaic or river bank erosion. Lacustrine sediments originate from thermokarst formation within moraine deposits (Krzic et al., 2010). These sediments accumulated with lake formation and have a fine-grained composition with peat layers present (Rampton, 1982). Lacustrine deposits are situated in flat and gently sloping terrain and have a poor surface drainage (Rampton, 1982). Moraine deposits are very common and cover approximately 50% of the formerly glaciated part of the Yukon coastal plain. Moraines are ice-rich and surfaces usually well drained due to a distinct topographic gradient with slopes of 5–25° (Rampton, 1982). The finer sediments in the upper layer of moraine soil were commonly washed away by meltwater from the glacier and moved to lacustrine and marine environments (Krzic et al., 2010).

Collection of Samples

Permafrost and active layer sediment samples as well as coastal seawater samples were collected in April and May 2019. The sediment samples were taken with a SIPRE corer at three sites with different glacial deposit types; (A) fluvial (FLU, fluvial deposits, 69.20686 N, 138.36730W), (B) lacustrine (LAC, lacustrine-wetland deposits, 69.33580 N, 138.8768W), and (C) moraine (MOR, moraine ridge-drained deposits, 69.46122N, 139.24230W). Subsamples were taken from the active layer (FLU: 9–24 cm, LAC: 4–14 cm, and MOR: 27–42 cm) and from the permafrost layer (FLU: 105–120 cm, LAC: 55–70 cm, and MOR: 90–105 cm) of the cores. All samples were stored frozen (−18°C) and in the dark.

Seawater samples were collected in the wider Mackenzie Bay in Herschel Basin through the sea ice using a Niskin water sampler (69.50978 N, 138.86278 W). A Conductivity, Temperature, and Depth (CTD) cast was taken to make sure seawater was collected from the main water body avoiding layers below the sea ice or close to the seabed. Seawater was stored in pre-leached 1 L Nalgene bottles, which were rinsed with the sample two to three times. Seawater was stored cold (4°C) in the dark for 1 month prior to the experiment. The seawater had a salinity of 31 ppt and was later used as a bacterial inoculum.

Preparation of Soil Medium and Bacterial Culture

All the equipment used in the experiment was acid cleaned. Soil extracts were prepared from the six soil cores from FLU, MOR, and LAC glacial deposit types. For each glacial deposit type, extracts were prepared by dissolving soils from the active layer (wet weight; FLU: 343 g, LAC: 331 g, and MOR: 282 g)

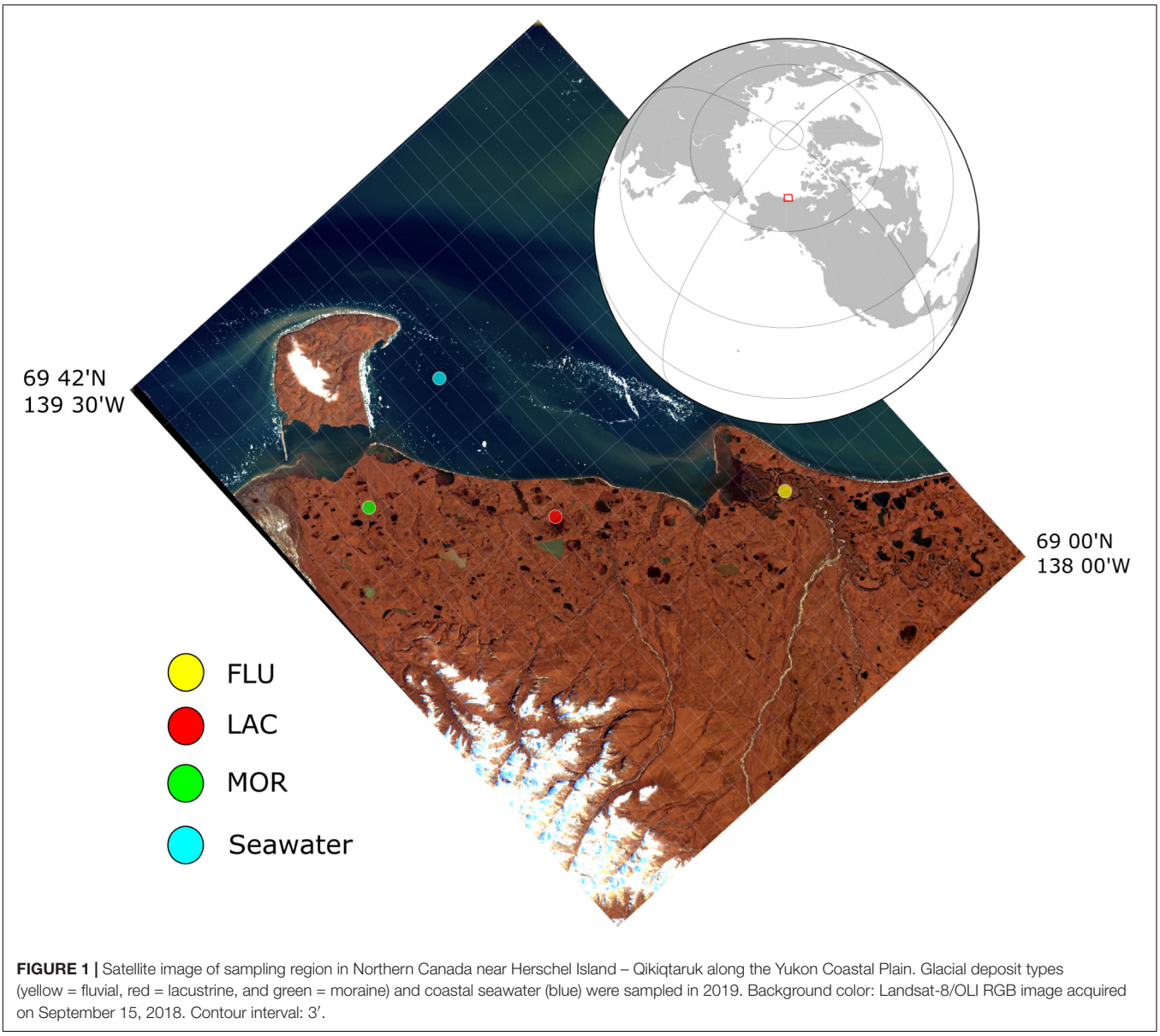

FIGURE 1 | Satellite image of sampling region in Northern Canada near Herschel Island – Qikiqtaruk along the Yukon Coastal Plain. Glacial deposit types (yellow = fluvial, red = lacustrine, and green = moraine) and coastal seawater (blue) were sampled in 2019. Background color: Landsat-8/OLI RGB image acquired on September 15, 2018. Contour interval: 3′.

or the permafrost layer (wet weight; FLU: 581 g, LAC: 192 g, and MOR: 222 g) separately into 8 L of ultrapure water (water extraction). The same volume of soil was added, which resulted in different mass due to differences in ice content between the glacial deposit types. The soil was kept in suspension overnight and then allowed to settle for 1 h before filtration through a 0.2 μm filter (AcroPak Capsules with Supor® Membrane, PALL). Salts were added (NaCl 21.1 g, $MgCl_2$ 4.5 g, Na_2SO_4 3.5 g, $CaCl_2$ 1 g, KCl 0.6 g, KBr 0.1 g, H_3BO_3 0.02 g, and $NaHCO_3$ 0.2 g per L) to a final salinity of 31 ppt (reflecting the same salinity and ratios as the sampled seawater). The water extractions from the soils were then stored at 20°C overnight to let the salts completely dissolve. For each glacial deposit type, the soil extract from the active layer was mixed with an equal volume of soil extract from the permafrost layer (2 × 7 L mixed soil extracts per glacial deposit type) and then autoclaved. We mixed the two layers to reflect what will happen during coastal erosion when the whole soil column collapses into the ACZ. After the first autoclaving, the mixed soil extracts were split into four replicates (4 × 3.5 L mixed soil extracts per deposit type). The extracts were then re-filtered through a 0.2 μm filter and KNO_3 and K_3PO_4 was added to a final concentration of 16 and 1 μM, respectively. The sterile soil extracts were then autoclaved a second time. The sterile soil extracts were stored overnight, in darkness at 4°C, until the start of the experiment, where they were used as medium for the chemostat cultures. The mixed and sterile soil extracts are hereafter referred to as medium/media.

The sampled seawater obtained from Herschel Basin was used as bacterial inoculum. To adapt the marine microbial communities to the DOM derived from the Cryosols and thereby get a faster establishment in the chemostats, 900 ml of seawater

was mixed with 200 ml from the respective autoclaved medium, 3 days before the start of each chemostat experiment. This formed the base of the culture to be used in the chemostat experiments.

Experimental Setup

Chemostats for each glacial deposit type were run in quadruplicates using the same approach as reported in Sjöstedt et al. (2012b). For each chemostat, 3.5 L of medium was used and 0.2 L of marine bacterial inoculum as culture. Medium was fed dropwise through a glass tube to prevent back growth (Hagstrom et al., 1984). Oxygen was supplied by passing air through a 0.2 μm pore-size polytetrafluoroethylene Acrodisc CR filter (Pall Corporation) (Zweifel et al., 1996). The chemostats were run for 14 days in the dark and at 20°C, which is standard temperature for biodegradation experiments (Vonk et al., 2015). The dilution rate was 1 day^{-1}, which is close to the median growth rate of marine bacteria ranging from polar to temperate regions (Moriarty, 1986).

Samples for bacterial abundance (BA) and optical measurements of DOM (absorbance and fluorescence) were taken both from the culture (once per day) and the medium (every 2 days). Bacterial community composition samples were taken from the culture every day. Samples for DOC and nutrient concentrations were taken from the culture daily and from the medium at day 0, 7 and 14. Samples from the culture were taken from the outflow of the chemostat, whereas samples from the medium were taken by carefully disconnecting the tubing feeding the culture with medium.

DOM Absorbance and Fluorescence

Samples (20 ml) were collected in acid washed and precombusted 40 ml glass vials with Teflon-lined caps and measured within 2 h of collection. The absorption spectrum of colored DOM (CDOM) and excitation-emission-matrix (EEM) of fluorescent DOM (FDOM) were measured on filtered samples (0.2 μm Supor Acrodisc, Pall Corporation). Both CDOM and FDOM was measured on an Aqualog fluorometer (HORIBA Jobin Yvon). The CDOM absorbance was measured in a 1 cm quartz cuvette between 239 and 800 nm, with increment of 3 nm and integration time of 0.1 s. The FDOM fluorescence was measured in the same 1 cm quartz cuvette immediately after the CDOM measurement. Emission wavelengths were 245–824 nm with increment of 2 nm and excitation wavelengths 240–450 nm with increment of 5 nm. The emission integration time was adjusted to account for varying FDOM fluorescence intensities between samples. An ultrapure water sample was used as a blank for both absorbance and fluorescence measurements.

The absorption spectrum of the ultrapure blank was subtracted from the absorption spectrum of the chemostat samples. This was performed by subtracting the absorption mean value between 590 and 800 nm. The absorption values were converted to the naperian absorption coefficient according to the following equation, $a_\lambda = 2.303^*A/L$, where A (unitless) is the optical density measured by the instrument and L (m) is the length of the cuvette and λ is wavelength. Fluorescence data was converted into Raman units (R.U) applying Raman calibration (Lawaetz and Stedmon, 2009), blank subtracted and then corrected for inner filter effects using the drEEM toolbox (Murphy et al., 2013). The quality of CDOM in the contrasting media were compared by using the spectral slope coefficients (Helms et al., 2008) and the carbon specific UV absorbance at 254 nm, $SUVA_{254}$ (based on decadic absorbance) (Weishaar et al., 2003). The intensity of CDOM absorption in the media and the cultures was compared using the absorption at 330 nm (highest observed degradation wavelength). The fluorescence intensities were summarized using the peak regions defined by Coble (1996). An attempt to characterize the fluorescence data using parallel factor analysis was unsuccessful. A robust result could not be obtained largely due to the fact that the changes in fluorescence occurring were very minor and that the sample dataset largely represented replicate samples of same medium, which invalidated the use of the commonly applied split half analysis for testing the result.

The steady state period for the cultures were determined based on achievement of a stable CDOM absorbance signal (330 nm) after initial flushing and establishment of the cultures during the first week (between days 7 and 13, **Supplementary Figure 1**).

DOC and Nutrients

After filtration, subsamples for DOC, total dissolved nitrogen (TDN), nitrate/nitrite and phosphate were collected in 30 mL acid-washed HDPE bottles and stored at −20°C until analysis. DOC and TDN concentrations were determined by high-temperature combustion (720°C) using a Shimadzu TOC-V CPH-TN carbon and nitrogen analyzer. The instrument was calibrated using acetanilide (Cauwet, 1999) and carbon determination was referenced to the community deep-sea reference (Hansell laboratory, Miami). DOC accuracy was assured by comparing to reference material provided by the Hansell Laboratory (Sargasso Sea water from 2,600 m near Bermuda; DOC concentration of 42–44 μM). Precision was estimated using a (more comparable) higher concentration sample of aged seawater. This was analyzed every 8 samples in the runs, and was determined to be ±7 μM. Nitrite, nitrate and phosphate were analyzed on a SmartChem200 discrete analyzer (AMS Alliance). The combined concentration of nitrate and nitrite was determined using the method described in Schnetger and Lehners (2014). Phosphate was measured using the manual method described in Hansen and Koroleff (1999). Nutrients standard kits from OSIL were used for calibration.

Bacterial Abundance

Samples (1.6 ml) for BA were fixed with glutaraldehyde (1% final conc.) and stored at −20°C until measured in the flow cytometer. Samples were stained with SybrGreen (Invitrogen) and cells were counted on a FACSCantoII flow cytometer (BD Biosciences), as previously described (Gasol and Del Giorgio, 2000). Fluorescent beads (BD Trucount Tubes, BD Biosciences) were used to calibrate the flow rate. The data was processed using FlowJo9.9.5. Average bacterial abundances were calculated for the steady state period (days 7–13). Bacterial carbon production

(BCP) was calculated based on the bacterial abundance as cells produced per day multiplied by a carbon constant ($1.6^{*}10^{-15}$ moles carbon $cell^{-1}$ (Lee and Fuhrman, 1987).

Bacterial Community Composition

Samples for BCC analysis were taken from the cultures from each deposit type every day. 100 ml of water was filtered through 0.2 μm Supor filters (25 mm; Pall Corporation) to collect bacterial biomass for DNA extraction. The filters were stored at −20°C until extraction. The samples from days 0, 9, 11, and 13 for each culture was selected for analysis. From these filters, DNA was extracted using the Qiagen Power Soil kit.

Amplification of the 16S rRNA gene, equimolar pooling and sequencing was performed at the Plateforme d'analyses génomiques (IBIS, Université Laval, Quebec City, QC, Canada). Amplification of the 16S V3–V4 regions was performed using the sequence specific regions (341F-805R) described in Herlemann et al. (2011) using a two-step dual-index PCR approach specifically designed for Illumina instruments. In the first step, the gene specific sequence is fused to the Illumina TruSeq sequencing primers and PCR was carried out in a total volume of 25 μL that contains 1× Q5 buffer (NEB), 0.25 μM of each primer, 200 μM of each dNTPs, 1 U of Q5 High-Fidelity DNA polymerase (NEB) and 1 μL of template DNA. The PCR started with an initial denaturation at 98°C for 30 s followed by 35 cycles of denaturation at 98°C for 10 s, annealing at 55°C for 10 s, extension at 72°C for 30 s and a final extension at 72°C for 2 min. The PCR reaction was purified using the Axygen PCR cleanup kit (Axygen). Quality of the purified PCR products was checked on a 1% agarose gel. A 50–100 fold dilution of this purified product was used as a template for a second PCR step with the goal of adding barcodes (dual-indexed) and missing sequence required for Illumina sequencing. Cycling for the second PCR were identical to the first PCR but with 12 cycles. PCR reactions were purified as above, checked for quality on a DNA7500 Bioanlayzer chip (Agilent) and then quantified spectrophotometrically with the Nanodrop 1000 (Thermo Fisher Scientific). Barcoded amplicons were pooled in equimolar concentration for sequencing on the Illumina Miseq.

Quality control of the sequences was performed by first removing the primer sequence using the Cutadapt 2.7 tool (Martin, 2011) and secondly by trimming the sequences at 260 bp (forward sequence) and 190 bp (reverse sequence). Sequence analysis was then performed using the IBIS computing infrastructure and the Dada2 algorithm (Callahan et al., 2016). In the end, 1,694,984 sequences were retained (median of 42,939 sequences per sample) following the different quality filters resulting in a total of 912 amplicon sequence variants (ASV). Taxonomic assignment was performed using the SILVA database (v.138) (Quast et al., 2013). DNA sequences have been deposited in the National Centre for Biotechnology Information (NCBI) Sequence Read Archive under accession number PRJNA675030.

A statistical method applied for differential gene expressions was used to rank ASVs consistently present in replicates as representative for each deposit type (Robinson and Smyth, 2008). In brief, a tagwise dispersion function [edgeR, R package (Robinson et al., 2010)] was used to rank ASVs according to their consistency among replicates and analyze which ASVs that differed significantly between deposit types. Differences were considered significant at $p < 0.01$. By using a generalized linear model, we tested for differential representation of ASVs between deposit types using the Toptag function, an analysis quite similar to an ANOVA. The analysis applies $\log_2$-counts per million (logCPM) that is used for estimating relative representation in the community, where low value within a range from 1 to 100 is considered high relative abundance. The analysis also reports logFC that is the x-fold change in ASV contribution to the community. The change in $\log_2$ CPM gives a measure of the consistency of replicates (Canelhas et al., 2016).

Richness (S.Obs, observed number of species) and evenness were calculated in R 3.0.2 using the package Vegan (Oksanen et al., 2019). Non-metric multidimensional scaling (NMDS) was performed using normalized data (relative abundances) of ASVs obtained from sequencing of the 16S rRNA gene. Distances were based on Bray–Curtis dissimilarity matrix to describe relationships in community composition among samples. Vectors representing significantly correlated (PERMANOVA, $p \leq 0.05$, df = 39, n = 999 permutations) DOM characteristics were plotted with the ordination [R 3.0.2, Vegan package (Oksanen et al., 2019)]. Vector length and direction reflects strength and direction of correlation between the DOM characteristics and community composition. Correlations between differences in community composition and differences in DOM utilization (BCP, BGE, and change in DOM characteristics between medium and culture) was investigated using Mantel tests [R 3.0.2, mvabund package, (Wang et al., 2012)].

Biological Oxygen Demand (BOD)

To investigate respiration rates, a sample from each culture replicate in each glacial deposit type (n = 12) was taken at the end of the experiment and incubated for 24 h. Oxygen consumption was measured using a Pyroscience Firesting four channel optode oxygen sensor equipped with 20 mL respiration vials and a temperature sensor. As the chemostats for each glacial deposit type were set up sequentially (1 day apart), the respiration measurements could all be carried out on day 13 (steady state period). Medium and culture from each glacial deposit type was mixed 1:1, to ensure adequate substrate supply during the respiration measurements. Respiration rates were calculated as the slope of oxygen concentration over time for two periods (2–12 h and 12–24 h) as for several of the incubations it was clear that there was a shift (flattening) of the oxygen concentrations during the BOD experiment. Data from the first 2 h were disregarded as it was clear there was a lag time before the establishment of stable respiration rates.

Data Analysis, Presentation, and Statistics

To simplify the data analysis only measurements from the steady state period were used to compare the growth and uptake rates of the cultures. For the optical measurements (absorption and fluorescence), the absorption spectrum and the EEM from the

culture were subtracted with the absorption spectrum and the EEM from their respective medium for each day in the steady state period. The newly created absorption spectra and EEMs from the subtraction could then be used to identify the net production or removal of CDOM and FDOM. A mean value per deposit type was calculated using replicates and days in the steady state.

To investigate the fate of bioavailable carbon from the glacial deposit types, four parameters were calculated; (1) total respiration (calculated from BOD experiments as the sum of respiration rates <12 h and >12 h multiplied by 12 h), (2) total bacterial carbon production [based on bacterial abundance as cells produced per day multiplied by a carbon constant of $1.6*10^{-15}$ moles carbon $cell^{-1}$ (Lee and Fuhrman, 1987)], (3) the total change in DOC concentration (calculated from the difference between medium and culture) and (4) BGE (calculated by dividing BCP by the DOC uptake).

In order to test for differences between glacial deposit types an analysis of variance (ANOVA) test was performed when criteria of normality and heterogeneity was met. If these criteria were not met, the Kruskal–Wallis test was applied. To resolve regions of the absorption spectra and fluorescence EEMs where medium and culture differed significantly, a two sample *t*-test was applied for each wavelength independently. The significance level was set to a *p*-value of 0.05. ANOVA and *t*-test ran in MatLab while Kruskal–Wallis test was applied in R.

The averages (mean) and standard deviations were calculated across the four replicates within each glacial deposit type. This was applied to all parameters using all measurements in the steady state (across days and replicates) unless else stated. Difference in samples number are due to missing data and outliers (defined from boxplots in R) and sample numbers will be stated after each parameter for each glacial deposit type.

RESULTS

Characteristics of DOM

The DOC concentration in the media was highest in LAC, followed by MOR and FLU with an average concentration of 632 (±34, $n = 8$), 543 (±36, $n = 8$), and 526 (±26, $n = 6$) μM DOC, respectively (**Figure 2**). DOC concentrations in the LAC medium were significantly higher than in both the MOR and FLU medium (ANOVA, $p < 0.01$), while MOR and FLU were not significantly different (ANOVA, $p = 0.16$). One replicate of FLU (2 out of 8 measurements) was removed when calculating the mean DOC concentration due to its anomalously low value (368 μM), while the source of the error could not be identified. The average DON concentration in the media was 28.7 (±4.5, $n = 8$), 25.2 (±1.9, $n = 8$), and 24.1 (±2.7, $n = 8$) μM DON for FLU, LAC, and MOR, respectively (**Figure 2**) and there was no significant difference among the three media (ANOVA, $p > 0.05$). The DOC:DON ratios for FLU, LAC, and MOR media were 17.0 (±1.2, $n = 8$), 25.1 (±1.4, $n = 8$), and 22.8 (±2.7, $n = 8$), respectively. The DOC:DON ratio for FLU was found to be significantly lower than those of LAC and MOR (ANOVA, $p < 0.01$), while LAC and MOR did not differ significantly between each other (ANOVA, $p > 0.05$).

The LAC medium had the highest absorption coefficients (**Figure 3**). The absorption coefficients values at 330 nm differed significantly between all three media and were 15.5 m^{-1} (±0.4, $n = 8$) for LAC, 9.2 m^{-1} (±0.5, $n = 12$) for FLU, and 7.3 m^{-1} (±0.5, $n = 11$) for MOR (**Figure 3**, ANOVA, $p < 0.01$). Spectral slopes (S) and $SUVA_{254}$ were used to assess the quality of the CDOM (**Table 1**). The S values for 275–295 nm (UVB) and 350–400 nm (UVA) ranged between 13.4–13.7 and 19.2–21.3 μm^{-1} in the three media. The spectral slopes for the UVB area did not differ significantly between the three media (ANOVA, $p > 0.05$), while the spectral slope of the UVA area was significantly higher in FLU medium than in the other two media (ANOVA, and $p < 0.05$). The spectral slope ratio (S_r) values differed significantly between all media (ANOVA, $p < 0.01$) and were highest for LAC followed by MOR and FLU. The $SUVA_{254}$ values (**Table 1**) were also significantly different between all media (ANOVA, $p < 0.01$) and were highest for LAC, followed by FLU and MOR.

The fluorescence characteristics of the media are shown in **Figure 3** and the fluorescence intensities for common peak regions (Coble, 1996) are reported in **Table 1**. As with the absorption spectra, the fluorescence intensities differed between the media. The visible wavelength peaks (peak A, C, and M) were significantly different between all media (ANOVA, $p < 0.01$) with highest values for LAC, followed by FLU and MOR (**Table 1**). For peak T, the fluorescence intensities did not differ between FLU and LAC (ANOVA, $p > 0.05$), while it was significantly lower for MOR compared to the other two (ANOVA, $p < 0.01$) (**Table 1**). For peak B the fluorescence intensities did not differ significantly between MOR and LAC (ANOVA, $p > 0.05$), while FLU had significantly higher intensity than the other two (ANOVA, $p < 0.01$) (**Table 1**).

Alteration of DOM in the Cultures

Inorganic nutrients were added to ensure replete conditions and carbon limitation in the chemostats. Measured nutrient concentrations in the media were on average 13–15 μM for combined nitrate and nitrite and 0.68–1.01 for phosphate, and remained above 6 and 0.3 μM, respectively in the water flowing out of the cultures.

There were a significant difference in the concentrations of DOC and DON between the medium and the culture for all glacial deposit types (ANOVA, $p < 0.05$). The total removal of DOC in FLU, LAC, and MOR cultures was 132 (±50, $n = 28$), 160 (±46, $n = 28$), and 158 (±48, $n = 28$) μM (**Table 2**) corresponding to 24% (±9%), 25% (±7%), and 29% (±8%) of the initial DOC, respectively. For DON, the highest removal was instead observed for FLU culture and was found to be 10 (±4, $n = 28$) μM corresponding to 36% (±8%) loss, whereas for LAC and MOR cultures it was found to be 4 (±2, $n = 28$) and 4 (±1, $n = 28$) μM corresponding to a loss of 17% (±6%) and 18% (±3%) respectively. The DOC:DON ratios in the cultures changed from their corresponding media and were calculated to be 22 (±4.5, $n = 28$), 22.6 (±1.9, $n = 28$) and 20.8 (±6.2, $n = 28$) for respectively FLU, LAC, and MOR cultures, however, the change was only found to be significant for the FLU deposit type (ANOVA, $p < 0.01$).

The change in the absorption spectra (**Figure 4**) reveals the spectral fingerprint on the CDOM imparted by the

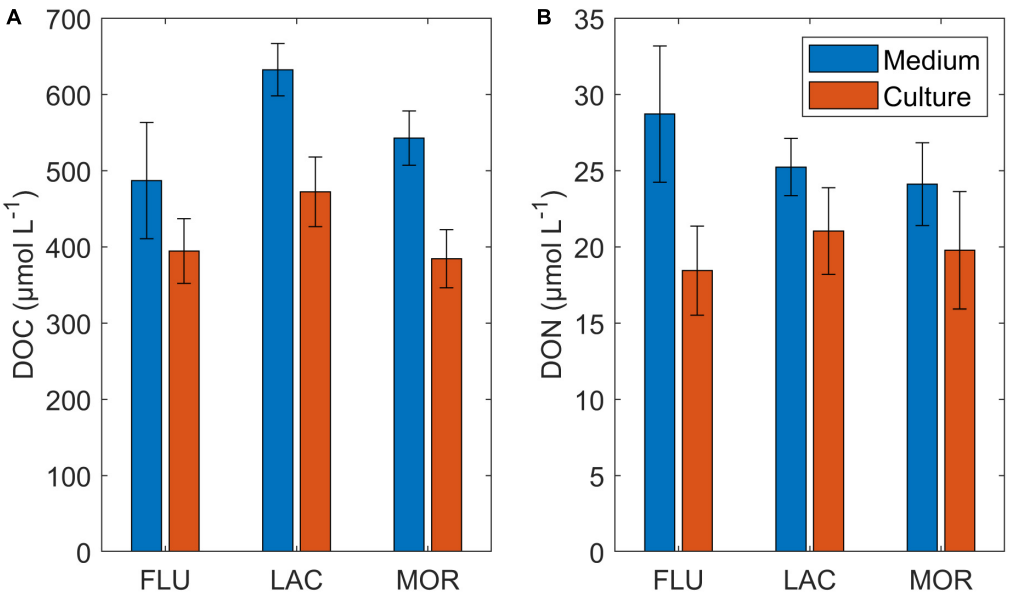

FIGURE 2 | Average DOC **(A)** and DON **(B)** Concentration (µmol L^{-1}) of soil media and cultures at steady state. NO_3^- and NO_2 are subtracted from DON, while ammonium is still included. Error bars represent the standard deviation.

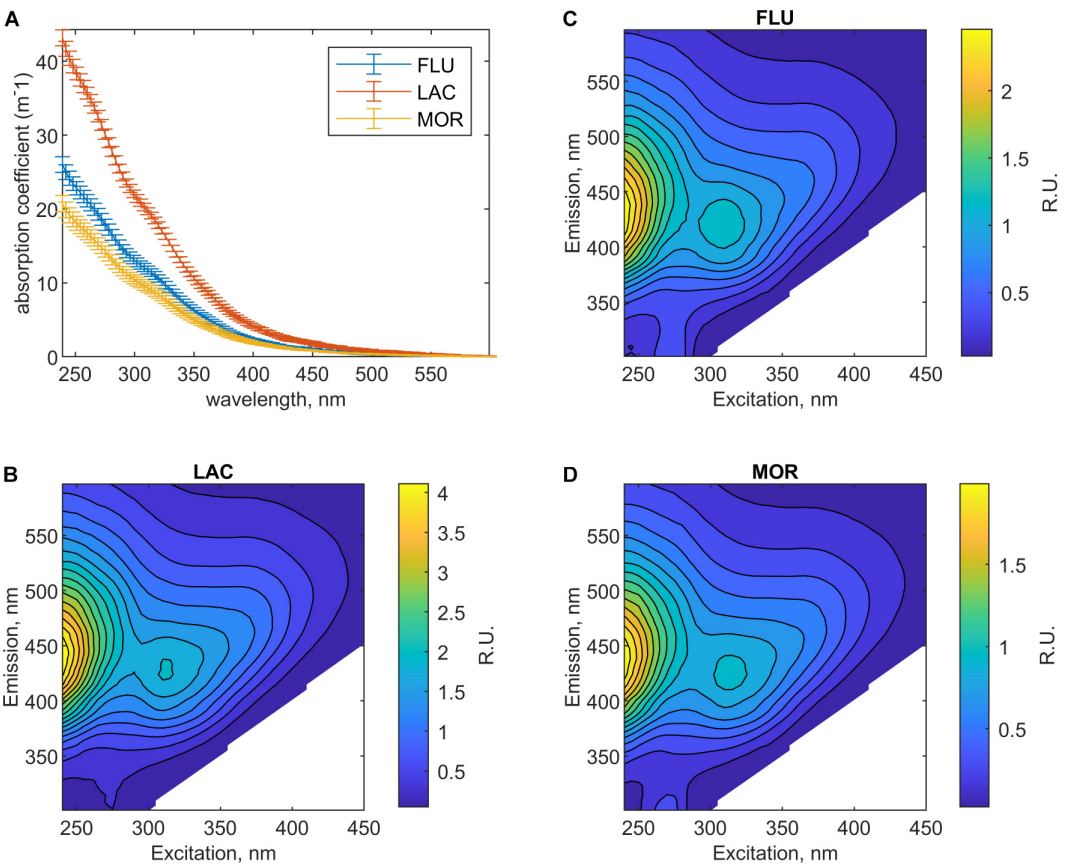

FIGURE 3 | Mean absorption spectra **(A)** and fluorescence EEMs (**B–D**, displayed as Raman units, R.U.) for the filtered media at steady-state. **(B)** LAC, **(C)** FLU, and **(D)** MOR.

TABLE 1 | Mean spectral slopes [*S*(275–295) and *S*(350–400)], slope ratios (S_r), $SUVA_{254}$ values (calculated from the soil medium CDOM spectra) and intensities of five commonly reported fluorescence peaks (Coble, 1996) (peak *A* = Ex/Em: 260/430, peak *B* = Ex/Em: 275/305, peak *C* = Ex/Em: 340/440, peak *M*: Ex/Em: 300/390, and peak *T* = Ex/Em: 275/340) for the three glacial deposit types.

DOM characteristics	Proxy	FLU	LAC	MOR
***S*(275–295) (μm^{-1})**	Molecular weight; photobleaching	**13.4** (±0.29)	**13.7** (±0.22)	**13.4** (±0.31)
***S*(350–400) (μm^{-1})**	Molecular weight; photobleaching	**21.3** (±0.69)	**19.2** (±0.59)	**19.6** (±0.70)
S_r	Molecular weight; origin of water	**0.63** (±0.02)	**0.71** (±0.02)	**0.68** (±0.00)
$SUVA_{254}$ (L mg C^{-1} m^{-1})	Aromaticity	**1.65** (±0.06)	**2.15** (±0.05)	**1.17** (±0.06)
Peak A (R.U.)	Humic-like compounds; terrestrial	**1.73** (±0.05)	**2.79** (±0.05)	**1.38** (±0.08)
Peak B (R.U.)	Tyrosine and protein-like compounds; autochthonous	**0.50** (±0.04)	**0.29** (±0.02)	**0.32** (±0.15)
Peak C (R.U.)	Humic-like compounds; terrestrial	**0.95** (±0.03)	**1.69** (±0.04)	**0.85** (±0.06)
Peak M (R.U.)	Marine humic-like compounds;	**1.07** (±0.04)	**1.42** (±0.03)	**0.76** (±0.05)
Peak T (R.U.)	Tryptophan and protein-like compounds; autochthonous	**0.40** (±0.03)	**0.39** (±0.01)	**0.24** (±0.03)

R.U. corresponds to Raman units. Numbers in bold represent mean values, while numbers in parentheses represent standard deviations.

TABLE 2 | Overview of the carbon processing at 24 h timescale due to microbial activity in the cultures.

Glacial deposit type	Respiration (μM O_2 d^{-1})	Bacterial carbon production (μM C d^{-1})	DOC uptake (μM C d^{-1})	BGE (%)
FLU	**90** (±12, *n* = 8)	**16** (±13, *n* = 26)	**132**(±50, *n* = 28)	**13**(±12, *n* = 25)
LAC	**57** (±20, *n* = 8)	**48** (±37, *n* = 26)	**160** (±46, *n* = 28)	**28**(±20, *n* = 23)
MOR	**111** (±17, *n* = 8)	**105** (±58, *n* = 28)	**158** (±48, *n* = 28)	**66**(±42, *n* = 26)

The numbers are calculated as the mean value over the whole steady state period. Numbers in bold represent mean values, while numbers in parentheses represent standard deviations. The standard deviation indicates the variation across all the samples measured from different days and replicates.

marine microbial communities in the cultures, with a negative change corresponding to degradation and a positive change to production of CDOM. For FLU, the absorption between 239 and 450 nm was significantly lower in the culture compared to the medium during the steady state period (*t*-test, $p < 0.05$). A similar yet weaker change was apparent for LAC and only significant at wavelengths between 308 and 371 nm (*t*-test, $p < 0.05$). The reduction in CDOM absorption at 330 nm, for FLU and LAC was respectively −1.32 (±0.28, $n = 23$) m^{-1} and −0.70 (±0.35, $n = 22$) m^{-1} and significantly different (ANOVA, $p < 0.01$). For MOR, there was a significant production in CDOM absorption between 239 and 296 nm (*t*-test, $p < 0.05$, $n = 24$) and no significant change at 330 nm (*t*-test, $p > 0.05$).

The fluorescence properties of DOM were altered by the marine microbial communities, but the extent to which the EEM area was altered differed in between all three glacial deposit types (**Figures 5A–C**). The change in fluorescence intensity between FLU medium and culture was significant for all peaks (*t*-test, $p < 0.05$) and the change in peak A, peak B, peak C, peak M, and peak T, corresponded, respectively, to −0.15 (±0.07, $n = 23$), −0.18 (±0.04, $n = 23$), −0.06 (±0.04, $n = 23$), −0.14 (±0.04, $n = 23$), and −0.05 (±0.05, $n = 23$) R.U. (**Figure 5A**). For LAC, the change in fluorescence intensity was only significant for peak B and peak M (*t*-test, $p < 0.05$) and corresponded, respectively, to 0.05 (±0.02, $n = 22$) and −0.07 (±0.04, $n = 22$) R.U. (**Figure 5B**). As seen from **Figures 5D,G**, both the spectral characteristics of the fluorescence loss in the peak A and M regions in the FLU and LAC deposit types was very similar, although the microbial community in FLU removed much more from the medium (**Table 1**). The spectral characteristics of the fluorescence change in peak B region was also similar between FLU and LAC cultures (**Figure 5E**), however, there was a large removal in the FLU culture, while there was a weak, but still significant production in the LAC culture. The fluorescence loss in the region of peak C was comparable in character and intensity of removal for both FLU and LAC cultures (**Figure 5F**), even though there were differing start concentrations in the respective media (**Table 1**). For MOR, we observed no significant removal of fluorescence but rather

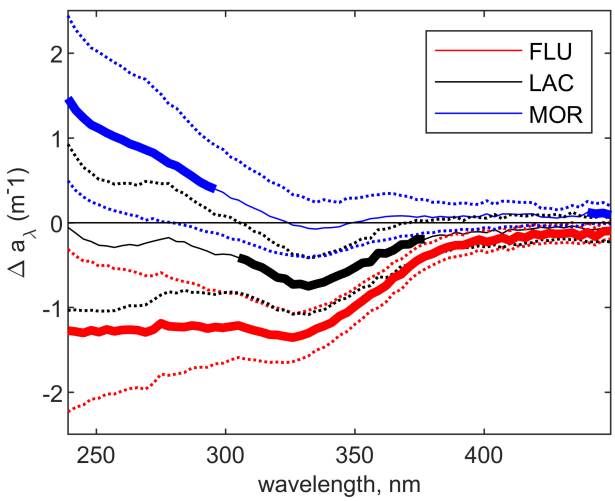

FIGURE 4 | Mean absorbance change between culture and medium at steady-state for each glacial deposit type. The dotted lines are displaying the standard deviation across all measurements in the steady-state period for each glacial deposit type ($n = 28$). The bold line is showing the area of the absorption spectrum that has significantly changed (*t*-test, $p < 0.05$).

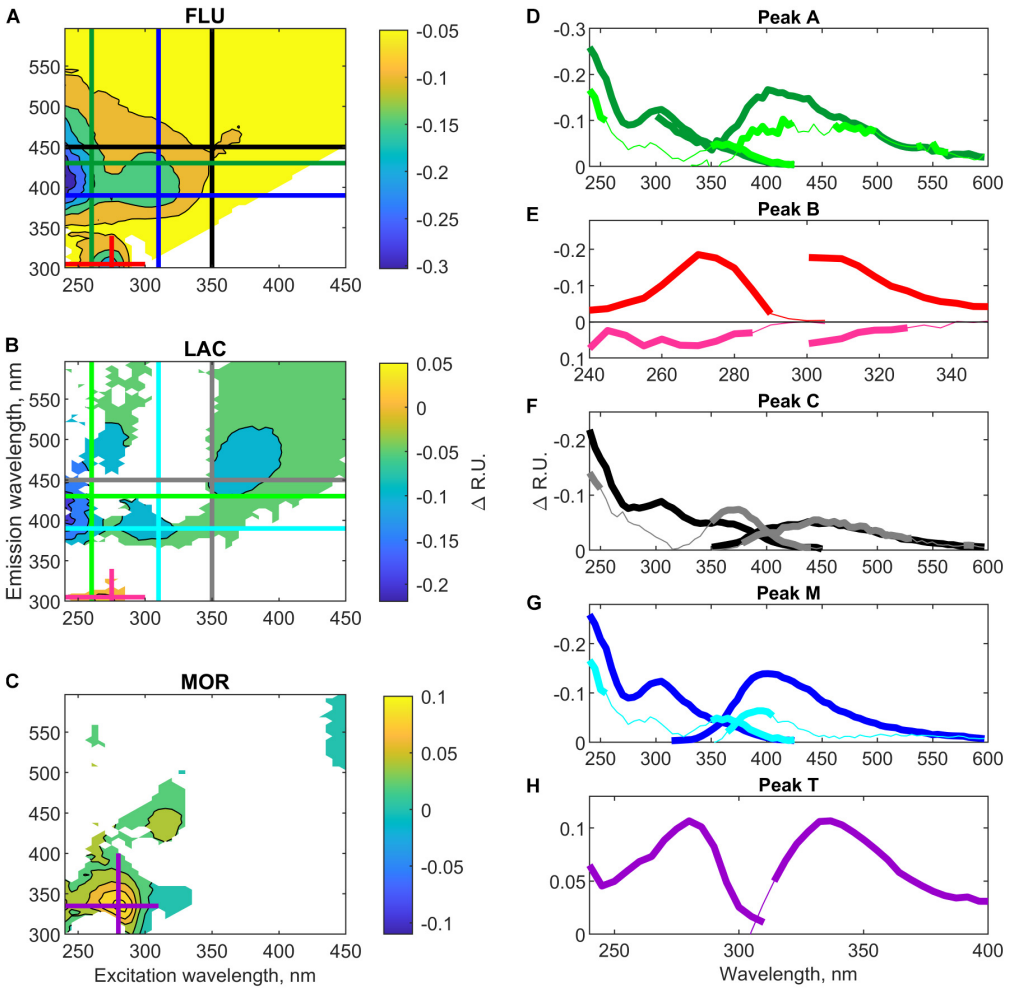

FIGURE 5 | Mean fluorescence change (Raman units, R.U.) between culture and medium at steady-state for each glacial deposit type. Panels **(A–C)** Shows the excitation-emission-matrix (EEM) with areas that are significant ($p < 0.05$) changed from the medium. **(A)** FLU, **(B)** LAC, and **(C)** MOR. Panels **(D–H)** Shows the excitation and emission spectra at specific emission and excitation wavelengths for different peaks. Panel **(D)** Peak A, **(E)** Peak B, **(F)** Peak C, **(G)** Peak M, and **(H)** peak T. The bold line shows which area is significant different from the soil medium. Note the *y*-axis changes, negative values represent a removal of fluorescence and positive values a production.

a significant production of peak T fluorescence by 0.10 (±0.03, $n = 24$) R.U. (**Figures 5C,H**).

Bacterial Growth and Bacterial Community Composition

At steady state the average BA was significantly different between all the three glacial deposit types (Kruskal–Wallis, $p < 0.005$) and the average abundance was 9.2 (±2.5, $n = 28$) 10^6 cell/mL in FLU culture, 32.1 (±14.6, $n = 28$) 10^6 cell/mL in LAC culture and 45.7 (±14.2, $n = 28$) 10^6 cell/mL in MOR culture.

Analysis of BCC was based on the % of reads. The BCC in the start cultures (**Figure 6A**) were dominated by *Gamma-* and *Alphaproteobacteria* in all cultures. In the FLU start culture, the bacterial community was composed of 48% *Gammaproteobacteria*, 42% *Alphaproteobacteria* and 10% *Bacteroidetes*. For LAC, the start culture had a BCC of 91% *Gammaproteobacteria*, 8% *Alphaproteobacteria* and 1% *Bacteriodetes*. Last, the MOR start culture had a BCC of 61% *Gammaproteobacteria*, 36% *Alphaproteobacteria*, and 3% *Bacteroidetes*. Other taxa contributed to less than 0.5% of the sequences in each of the three glacial deposit types. In the start cultures, the dominant order within *Alphaproteobacteria* was *Rhodobacterales* which contributed to 99, 87, and 98% of the *Alphaproteobacterial* reads in FLU, LAC, and MOR, respectively. In LAC start culture, the abundance of *Sphingomonadales* was 11% (**Supplementary Table 1**). Within *Gammaproteobacteria* the dominant orders in all treatments were *Oceanospirillales* and *Burkholderiales*. In the MOR start culture, *Cellvibrionales* and *Nitrosococcales* were also important and the abundance of each of these orders were 15% (**Supplementary Table 1**).

During the steady state period (**Figure 6B**), the bacterial community in the FLU and LAC cultures became dominated by *Alphaproteobacteria* [67% (±5, $n = 12$) and 87% (±13,

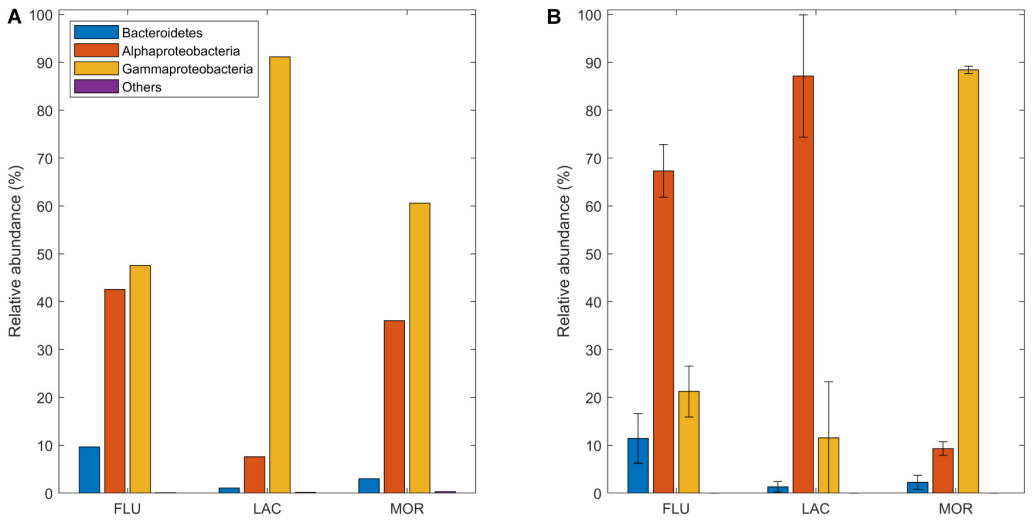

FIGURE 6 | Relative abundance of taxa (% of total number of reads) found in the culture for each glacial deposit type **(A)** Prior to the chemostat experiment and **(B)** During steady state of the chemostat experiment.

n = 12), for FLU and LAC, respectively]. In contrast the community in the MOR culture became more dominated by *Gammaproteobacteria* [88% (±1, n = 12)]. The abundance of other taxa remained very low in the cultures from all three glacial deposit types. At steady state, *Rhodobacterales* was the dominant order within *Alphaproteobacteria* within all glacial deposit types and contributed to between 79 and 98% of the Alphaproteobacterial reads. Other orders contributing to at least 1% of the reads in at least one of the glacial deposit types were *Sphingomonadales*, *Caulobacterales* and *Rhizobiales* (**Supplementary Table 1**). Within *Gammaproteobacteria*, *Oceanospirillales* was the dominant order in the cultures from all glacial deposit types and contributed to between 79 and 99% of the Gammaproteobacterial reads. In the FLU and LAC cultures the abundance of *Nitrosococcales* was 14% and 13% of the reads, respectively. Other orders with an abundance above 1% in at least one of the glacial deposit types were *Alteromonadales* and *Cellvibrionales* (**Supplementary Table 1**).

Based on tagwise dispersion analysis, 125 ASVs differed significantly in abundance between the MOR and the FLU cultures, 157 ASVs between the LAC and FLU cultures and 144 ASVs between the LAC and MOR cultures (**Supplementary Tables 2–4**). Based on the top 10 ASVs there was a significant higher abundance of ASVs belonging to the genus *Sulfitobacter* in the FLU cultures compared to both the LAC and MOR cultures (**Supplementary Tables 2**, **3**). In the LAC culture several of the ASVs with significantly higher abundance compared to the FLU and MOR cultures belonged to the genus *Pacificibacter* and *Polaribacter* (**Supplementary Tables 3**, **4**). Whereas in the MOR culture several of the ASVs belonged to the genus *Amphritea* and *Marinomonas* (**Supplementary Tables 2**, **4**).

During the development of all the cultures, bacterial community richness decreased, while community evenness either increased slightly (FLU and LAC) or decreased drastically (MOR) (**Supplementary Table 5**). During the steady state, both richness and evenness were significantly higher in FLU compared to both LAC and MOR (Kruskal–Wallis, $p < 0.05$).

During the steady state period the cultures from the different glacial deposit types formed three clearly distinct clusters (**Figure 7**) indicating that the composition of bacterial communities in cultures was significantly different between glacial deposit types (PERMANOVA, F = 36.75, $r2$ = 0.67, $p < 0.01$), despite starting with the same marine inoculum. Replicates from the same glacial deposit type were very similar indicating good reproducibility in the BCC. For MOR and LAC cultures, there was a clear development from the start community to the steady state community, whereas for the FLU culture the start and steady state communities were rather similar. Significant DOM characteristics plotted as vectors on the NMDS plot indicate that BCC is linked to DOM composition of the medium (**Figure 7B** and **Supplementary Table 6**) and that the different glacial deposit types were linked to different DOM characteristics. The strongest predictors are peak A and peak C (R^2 0.9521, respectively, 0.9503). The BCC in the LAC culture was positively correlated to peak A and peak C but also to peak M and $SUVA_{254}$. The BCC in the FLU culture was positively correlated to peak B and negatively correlated to DOC concentration and S_r. In contrast, the BCC in the MOR culture was not positively correlated to any of the included DOM characteristics but negatively correlated to peak T. Bacterial community composition was also correlated to DOM utilization. Differences in BCC was significant correlated to BCP, BGE, ΔpeakA, ΔpeakB, ΔpeakC, ΔpeakM, and ΔpeakT (where Δ refer to the change between medium and culture, Mantel test, $p < 0.05$, Pearson r = 11–46%, n = 36, **Supplementary Table 7**).

Carbon Processing

Average respiration rates were calculated for two time periods, <12 and >12 h, as there was a significant (ANOVA, $p < 0.01$) decrease in rates for FLU and LAC (**Figure 8**). Initial respiration

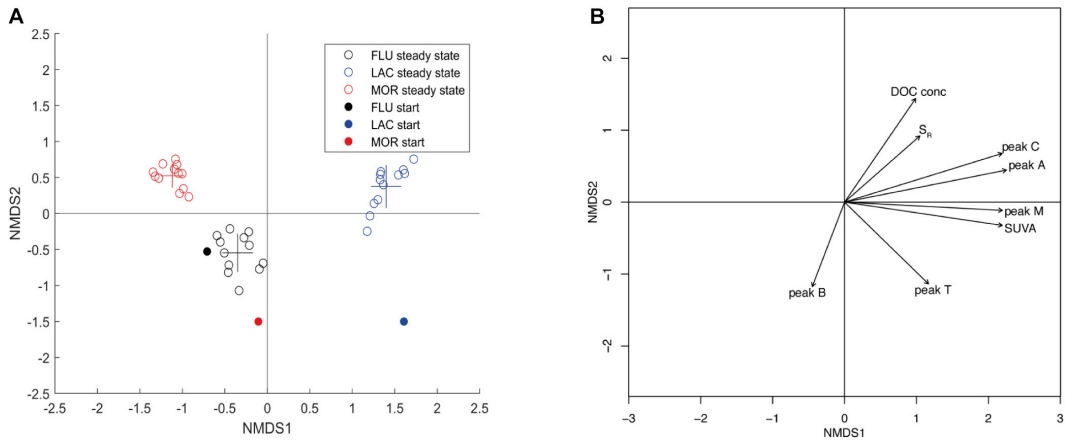

FIGURE 7 | (A) NMDS coordination plot based on 16S rRNA gene amplicon sequencing showing differences in bacterial community composition over time and between deposit types (Stress = 0.0903). Analysis is based on data from Illumina sequencing and Bray–Curtis dissimilarities. Glacial deposit type is indicated by color and time by filled and open circles (start and steady state). The center of the crosses represent the average (at steady-state) NMDS value of each glacial deposit type, while the length of the crosses represent the standard deviation. **(B)** NMDS coordination (as in **A**) with vectors indicating significant DOM characteristics of the medium. The direction of the vector indicate an increase of the variable and the length of the vector indicate the strength of the association.

rates were highest in FLU. For the second period (>12 h) FLU and LAC had comparable lower respiration rates while MOR maintained a respiration rate which was comparable to the initial stage (<12) (ANOVA, $p > 0.05$).

Bacterial carbon production rates were highest for the MOR culture, followed by the LAC and FLU cultures (**Table 2**) and the BCP rates differed significantly between all the glacial deposit types (Kruskal–Wallis, $p < 0.001$). Based on the change in DOC concentration (see section "Alteration of DOM in the Cultures") between medium and culture, the DOC uptake over 24 h (**Table 2**) was found to be similar between LAC and MOR, but significantly lower in FLU (ANOVA, $p < 0.01$, respectively). Bacterial growth efficiency (**Table 2**) was found to be significantly higher in the MOR culture (ANOVA, $p < 0.001$), while the BGE in the FLU and LAC cultures did not differ significant between each other (ANOVA, $p = 0.14$).

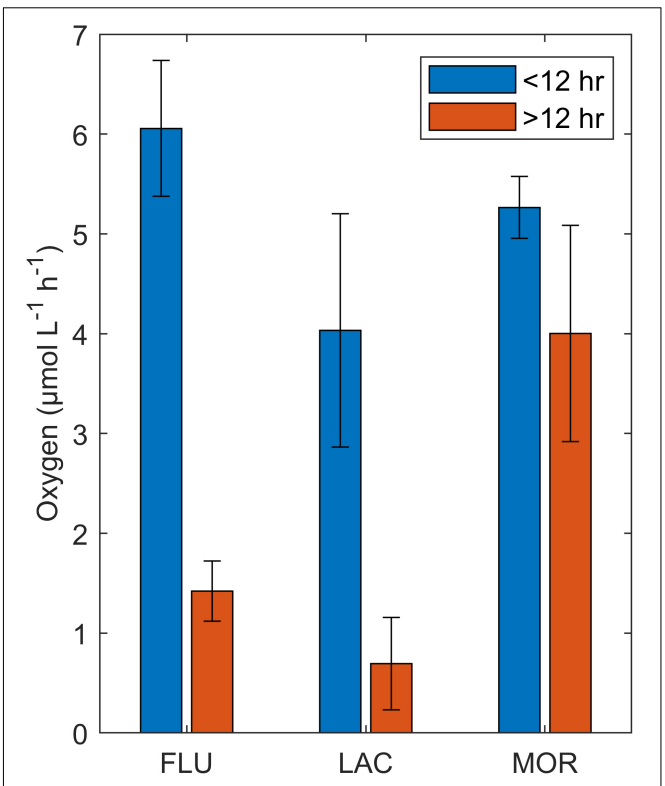

FIGURE 8 | Respiration rates (oxygen µmol L^{-1} h^{-1}) for each glacial deposit type, divided into two different categories <12 h (blue bar) and >12 h (red bar). Error bars represent standard deviation.

DISCUSSION

Characteristics of DOM in Media

Our results show that the composition and biodegradability of DOM differs between post-glacial landscape units and that these differences are related to the glacial processes. In agreement with our results, a recent study also found a coupling between permafrost soil formation and DOM character for different permafrost end-member types (tills, diamicton, lacustrine, peat, and Yedoma deposits) (MacDonald et al., 2021). In addition, different soil-forming factors such as ice content, permafrost extent and parent material (epigenetic vs. syngenetic formation) shape the biogeochemical response to permafrost thaw in aquatic systems (Tank et al., 2020). Factors such as grain size and the amount of minerals can also influence the OM content (Palmtag and Kuhry, 2018; Opfergelt, 2020). These findings underline that soil formation and erosion conditions play an important role when looking at DOM release due to coastal erosion, but at the same time highlight the complexity of studying biodegradation related to permafrost thaw. The differences in soil formation history, OC content, and grain size therefore likely

help explain some of the subtle differences we observed in DOM characteristics between our glacial deposit types.

The DOC:DON ratios (17–25) of the DOM in the media in this experiment indicate a high bioavailability of freshly eroded coastal permafrost soil. Ratios were on the whole lower than those for Arctic rivers [>50, (Dittmar and Kattner, 2003; Holmes et al., 2012)] but comparable to four different Arctic lagoons and coastal waters (16–19) near our sampling site (Dunton and Crump, 2014) as well as thermokarst feature outflows (19.5) (Abbott et al., 2014). Similarly to these studies, Dittmar and Kattner has reported an average DOC:DON ratio for the ACZ around the Laptev Sea of 21.4 (150 μM DOC and 7 μM DON). $SUVA_{254}$ is correlated to the aromatic content of DOM (Weishaar et al., 2003) and $SUVA_{254}$ from permafrost-derived DOM are expected to vary between 0.6 and 4.5 L mg C^{-1} m^{-1} (Ward and Cory, 2015; Raudina et al., 2017; Wickland et al., 2018; Coch et al., 2019; Fouché et al., 2020) depending on the OM content, with mineral soil types posing lower $SUVA_{254}$ values than organic soil types. In our study, the average $SUVA_{254}$ value across the three glacial deposit types was found to be 1.66 L mg C^{-1} m^{-1} and therefore fits with the reported average of 1.82 L mg C^{-1} m^{-1} obtained from 221 Arctic Canadian soil samples including active layer and permafrost layer (Fouché et al., 2020). Since the contribution of polyphenolic and condensed aromatic compounds leads to lower degradability of organic matter (Textor et al., 2019), we could therefore expect a higher bioavailability in MOR compared to FLU and LAC, based on the $SUVA_{254}$ values. As with the DOC:DON ratios, the $SUVA_{254}$ values are lower than that reported for DOM in Arctic rivers (Walker et al., 2013; Mann et al., 2016; O'Donnell et al., 2016; Coch et al., 2019). DOM is transformed during the transport along the river (Drake et al., 2018; Zhang et al., 2020) and according to the River Continuum Concept it can be expected that labile DOM from the catchment would be rapidly removed, while more recalcitrant DOM would be transported downstream (Vannote et al., 1980). This might explain the higher $SUVA_{254}$ and DOC:DON ratio in Arctic rivers compared to the media used in the experiment.

Slope ratio has shown to be inversely correlated to molecular weight, with low values (<1.0) typical for terrestrial DOM (Helms et al., 2008). DOM extracted from Canadian Arctic soil types expect to have S_r values that range between 0.58 and 3.24 (Fouché et al., 2020). Ward and Cory (2015) demonstrated that the CDOM in the active layer and permafrost layer from soils in Alaska had S_r values of 0.72 and 0.96, respectively, while Wickland et al. (2018) reported S_r values ranging between 0.73 and 1.13 across the active layer and permafrost layer for three other soil types in Alaska (Orthels, Histels, and Turbels). S_r values increase as DOM is processed in natural settings, particularly via photodegradation (Helms et al., 2008). However, since our media has been kept in dark during the whole experiment, the S_r values in this study relate to the composition of CDOM rather than processing. In addition, it has been shown that lower spectral slopes in the UVA area for Arctic coastal water is not correlated with photodegradation (Juhls et al., 2019), and that the lower spectral slope for UVA instead likely reflects lability of DOM (Matsuoka et al., 2015). Therefore, we conclude that the significant differences in S_r values between the three glacial deposit types underline differences in the DOM composition. The higher UVA spectral slope for FLU medium compared to LAC and MOR media (**Table 1**) indicates a lower bioavailability of the DOM pool in this glacial deposit type and fits with results from the BGE values (**Table 2**).

An important difference between the DOM from natural coastal erosion and the DOM in this experiment is the fact that the media was autoclaved. Autoclaving might cause changes in DOM composition due to hydrolysis and denaturation of various compounds and colloids (Dill and Shortle, 1991; Druart and De Wulf, 1993) and, therefore, also changes in bioavailability. However, all the parameters reported above were within natural ranges for soils found in the study region. In addition, it has been shown that even if autoclaving changed DOC in an unpredictable manner, it did not cause a convergence of the DOC pool from different lakes (Andersson et al., 2018). This means that although DOC is not identical to the initial conditions after autoclaving, the diversity of DOC is preserved.

Optical Signature of Microbial Degradation

The microbial degradation of the DOM in the media imparted an optical signature on the absorption and fluorescence properties of the DOM. Despite the fact that the initial spectral characteristics of the DOM in the media were only subtly different between glacial deposit types, the results show significant differences in DOM turnover. The high utilization rate of permafrost-derived DOM has been correlated to the relative high abundance of hydrogen-rich compounds, such as aliphatic molecules (amino acids, peptides, and protein) and carbohydrates (Spencer et al., 2015; Stapel et al., 2017; Textor et al., 2018, 2019). Lower degradability of organic matter in some soils has on the other hand been correlated with a greater contribution of polyphenolic and condensed aromatic compounds, often linked to decomposition processes of the overlying vegetation during unfrozen periods (Textor et al., 2019). Although harder for bacteria to utilize, compounds such as lignin phenols and related poly-phenolic compounds, can be metabolized or transformed into other compounds (Fasching et al., 2014).

Even though the highest amount of DOC was degraded in the MOR culture (**Figure 2**), the optical signature indicated a net production of CDOM and FDOM (**Figures 4**, **5**). Production of fluorescence peaks B and T in coastal waters are known to be correlated to amino acids produced by bacterial communities (Yamashita and Tanoue, 2003). This production of CDOM and FDOM, together with the high DOC removal, suggests that the DOM derived from the MOR deposit type contains a high amount of colorless labile DOM compounds (less conjugated aliphatic molecules). Since these compounds are easier for bacteria to utilize (Berggren et al., 2010), CDOM and FDOM would not be degraded as long as these labile DOM compounds are available. The high amount of colorless DOM can probably be explained by the glacial formation process behind MOR. Since the MOR deposit type was not submerged in water during glacial processes (Krzic et al., 2010), little prior decomposition of these

less conjugated aliphatic compounds has occurred. The upper permafrost layer of MOR may have thawed during the Holocene Thermal Maximum, where active layer depths reached more than 1 m (Burn, 1997), which could have resulted in intensive carbon degradation under aerobic conditions as a topographic gradient remained. However, this assumption remains speculative for our sampled sites.

From the optical signature (**Figures 4**, **5**), the FLU culture showed degradation of CDOM and FDOM compounds across the whole absorbance spectrum and fluorescence EEM. This suggests that only a very small amount of colorless bioavailable DOM was present and that the microbial community degraded the bioavailable CDOM and FDOM, such as labile conjugated aliphatic and aromatic compounds, immediately. This assumption fits well with the FLU deposit type, which potentially lacks less conjugated and colorless labile aliphatic compounds, previously leached from vegetation into the active layer (Textor et al., 2019). The lack of these compounds could be due to degradation when the FLU deposit type was submerged under stagnant waters during glacial processes in the Holocene Thermal Maximum (Krzic et al., 2010; Schirrmeister et al., 2011), thereby leaving a higher abundance of more conjugated aliphatic and aromatic compounds behind when the soil permanently refroze after this period.

For the LAC culture, we observed a production of peak B (**Figure 5**), which could indicate that the DOM derived from the LAC deposit type was transformed into FDOM compounds upon microbial degradation (Yamashita and Tanoue, 2003; Fasching et al., 2014). However, in contrast to the MOR culture, the LAC culture also degrades CDOM and FDOM compounds (**Figures 4**, **5**), such as labile conjugated aliphatic and aromatic compounds, probably as the competition for the colorless labile DOM increases. Similar to the FLU deposit type, the LAC deposit type was also submerged in water during glacial processes (Krzic et al., 2010), resulting in the degradation of less conjugated and colorless aliphatic compounds prior to our sampling (Walter Anthony et al., 2018). In contrast to the fluvial environment, the lacustrine environment has probably allowed a production of colorless aliphatic compounds (Meyers and Ishiwatari, 1995; Schirrmeister et al., 2011), such as OM excreted from phytoplankton and heterotrophic species which can be very labile compounds and often support bacterial growth (Rosenstock and Simon, 2001; Kinsey et al., 2018).

Our results suggest that the DOM composition in Cryosols with a different glacial geomorphic history, induce marine microbial communities to impart different optical degradation signatures, ultimately indicating differences in biodegradability among the glacial deposit types. The results also indicate that DOM in the media is more bioavailable than riverine terrestrial DOM, since several studies found no to very low degradation by marine microbial communities as the riverine terrestrial DOM enters coastal waters (Köhler et al., 2003; Amon and Meon, 2004; Herlemann et al., 2014; Blanchet et al., 2017). Large rivers have already lost most of the labile ancient soil DOM components at the time the material reach the ACZ, as degradation occurs mostly in uplands and headwaters (Drake et al., 2015; Spencer et al., 2015). Nonetheless, it can therefore be argued that DOM released from coastal erosion of Cryosols will have a larger impact on the coastal environment in the ACZ than that of riverine DOM.

Substrate Driven Community Differences

The observed distinct patterns in BCC between the three glacial deposit types, used in this experiment, reflect the subtle underlying differences in DOM quality (**Figure 7** and **Supplementary Table 1**). The grouping of the BCC across replicates (**Figure 7**) within each soil treatment indicates a systematic DOM control on BCC development from a common marine inoculum community. Interestingly, the community composition in the MOR culture was not positively correlated to any of the DOM characteristics included in the analysis which might indicate that this community is selected by the colorless DOC dominating the MOR medium. This agrees with the negative correlation to peak T and $SUVA_{254}$ for MOR soil, which indicates a response to less degraded DOM pool with a lower aromaticity. In contrast, the BCC of FLU and LAC cultures were positively correlated to one or several of the DOM characteristics (**Table 1**). The positive correlation to peak B in the FLU medium indicate a response to a higher relative amount of protein-like compounds, whereas the positive correlation to peak A, peak C, peak M, and $SUVA_{254}$ in the LAC soil show a response to humic-like compounds (Coble, 2007; Stedmon and Nelson, 2015).

Common for all of the three different cultures was the reduction in species richness between start and steady state, which essentially indicates that cultivation in the chemostat selected bacterial communities that were best suited to the specific DOM derived from the glacial deposit types. The rise and dominance of *Gammaproteobacteria* and *Alphaproteobacteria* in these chemostat cultures agrees with results from regrowth batch experiments (Sipler et al., 2017; Müller et al., 2018). However, *Gammaproteobacteria* are commonly found to dominate biodegradation experiments, as these bacterial taxa are known to be opportunistic with high growth rate and ability to exploit available DOM (Herlemann et al., 2014). This was clearly the case for the MOR culture (**Figure 6**) where the highest DOC uptake and respiration rates were measured (**Figure 8**), coupled with CDOM and FDOM production (**Figures 4**, **5**). Combined these results indicate that moraine soil DOM contains colorless labile DOM which is rapidly degraded and supporting the development of the *Gammaproteobacteria* community. In the FLU and LAC cultures, we instead observed a dominance of *Alphaproteobacteria* (**Figure 6**). This difference in BCC was paralleled with the notable difference in CDOM and FDOM signatures imparted by the communities (Mantel tests, **Supplementary Table 3**). In FLU and LAC cultures, there were a significant removal of CDOM and FDOM (**Figures 4**, **5**). Although both dominated by *Alphaproteobacteria*, the FLU and LAC communities were also distinct (**Figure 7**) and this apparently influenced the extent of CDOM and FDOM removal (**Figures 4**, **5**).

Alphaproteobacterial reads were dominated by the order *Rhodobacterales* in cultures from all glacial deposit types, whereas *Oceanospirillales* was the dominant order among Gammaproteobacterial reads. However, the difference in BCC

was verified at the genus level where several ASVs differed significantly in abundance between the three glacial deposit types (tagwise dispersion analysis). There was significant higher abundance of ASVs belonging to the genus *Sulfitobacter* in the FLU culture, and members from this genus have been isolated from similar environments (Park et al., 2019). The first isolate and type specie, *Sulfitobacter pontiacus*, is a sulfur-oxidizing chemoheterotrophic bacteria which utilizes mainly carboxyl and amino acids (Sorokin, 1995). In the LAC cultures several of the ASVs with significantly higher abundance belonged to the genus *Polaribacter* and *Pacificibacter*. *Polaribacter* belongs to *Flavobacteria* (*Bacteroidetes*) which have been ascribed to act as degraders of high molecular weight OM, such as proteins and carbohydrates (Thomas et al., 2011). The type specie for *Pacificibacter*, *Pacificibacter maritimus*, was isolated from shallow marine sediments and utilizes mostly sugars, amino acids and a few carboxylic acids (Romanenko et al., 2011). And last, in the MOR culture several of the ASVs belonged to the genera *Amphritea* and *Marinomonas*. The majority of the members of the genus *Amphritea* are closely associated with living marine organisms, however, some members of the genus has been isolated from marine sediments (Miyazaki et al., 2008). Species within *Amphritea* oxidize various sugars and carboxylic acids (Gärtner et al., 2008). Members of the genus *Marinomonas* have a widespread distribution in marine environments and have for example been found in seawater (Yoon et al., 2005), sea ice (Zhang et al., 2008) and seafloor sediment (Romanenko et al., 2011). Based on the characterization of *Marinomonas polaris* and *Marinomonas arctica* the species utilize sugars, amino acids, and sugar alcohols, but not complex carboxylic acids and aromatic compounds (Gupta et al., 2006; Zhang et al., 2008).

Although it is hard to link these ASVs to specific characteristics of the DOM, these analyses show that the presence and abundance of specific phylotypes might determine the utilization of DOM. Our results are therefore in line with the growing number of studies linking community composition to OM lability (Cottrell and David, 2003; Gómez-Consarnau et al., 2012; Nelson and Carlson, 2012; Logue et al., 2016; Balmonte et al., 2019) and shows that the bioavailability should be seen as an interaction between the chemical composition of DOM and the metabolic capacity of the microbial community (Nelson and Wear, 2014).

Microbial Carbon Processing

Climate change will intensify erosion of Arctic coasts (Günther et al., 2015; Hoque and Pollard, 2016; Obu et al., 2016; Couture et al., 2018; Jones et al., 2018) but the ultimate fate of this carbon source is still unknown (Fritz et al., 2017). Understanding how DOC from different glacial deposit types will be mobilized by bacteria in the ACZ could eventually help us quantify the fate of carbon export from eroding soils along Arctic coastlines. We acknowledge the important difference between natural coastal erosion and our experiment, where coastal erosion will add both OM and *in situ* microbial communities to the marine water. Recent studies along aquatic continua have shown that microbial communities in lakes and streams contain organisms with terrestrial origins (Crump et al., 2012; Ruiz-González et al., 2015; Hauptmann et al., 2016). However, it is not clear whether bacteria transported with soil will be active and thrive in sea water since salinity is one of the strongest environmental filters (Langenheder et al., 2003). In addition to 'species sorting' which probably will take place in response to this chemical limit (Van der Gucht et al., 2007) there will also be priority effects for well established communities (Svoboda et al., 2018). We therefore believe that most of the carbon reaching the ACZ due to coastal erosion will be processed by the marine bacterial community.

In this study we demonstrate that not only are colorless DOM compounds being mobilized by marine microbial communities when Cryosols are released into the ACZ, but also that CDOM and FDOM compounds are bioavailable to marine microbial communities. The DOC removal by marine microbial degradation is the sum of carbon used for bacterial production and carbon released through respiration (**Table 2**). The bacterial production achieved by the chemostat cultures is dependent on the dilution rate, the quality of substrate (DOM bioavailability) and the ability of the community to utilize the substrate (Del Giorgio and Cole, 1998). As the dilution rates were set constant, the differences observed here reflect a combination of community composition and DOM character. The FLU culture had the lowest removal of DOC (**Figure 2** and **Table 2**) and lowest BCP. MOR and LAC cultures achieved approximately 3–4 times higher BA than FLU and abundances were higher than those often achieved in bottle experiment (Sipler et al., 2017; Müller et al., 2018), where supply of substrate is limited. Although the DOC removal was similar between the MOR and LAC cultures, BCP was two times higher in the MOR cultures.

Differences in BCP will have consequences for bacterial growth efficiency (BGE) which is a measurement of how efficiently carbon is converted into biomass (Del Giorgio and Cole, 1998). BGE has been shown to be strongly correlated with the composition of terrestrial DOM (Berggren et al., 2007). BGE in our study varied between 13 and 66% with highest values in the MOR culture and lowest in the FLU culture. Estimates of BGE for natural aquatic bacterial communities range from 5 to 60% with the highest values usually found in coastal waters and estuaries (Del Giorgio and Cole, 1998). However, in the Arctic region other studies have found the BGE to be 19.5% within Arctic Rivers and between 7 and 10% within Arctic Fjords (Middelboe et al., 2012; Paulsen et al., 2017), while it has been found to be lower in Arctic Ocean with 6.3% in the Fram Strait (Kritzberg et al., 2010) and 2.2% in the Chucki Sea (Cota et al., 1996). The fact that the BGE results from our study exceeds what has been previously found within other aquatic ecosystems throughout the Arctic Ocean, therefore suggest that the DOC from freshly exposed Cryosols could be one of the most labile sources of carbon in this region. In addition, the high variation in BGE between glacial deposit types suggest that the lability of DOC depends heavily on the specific deposit type being eroded. The increased rate of coastal erosion and thereby release of highly bioavailable DOM can therefore have a huge impact on the marine microbial communities in the ACZ.

Several studies have shown that a potentially large amount of CO_2 is released during coastal erosion due to microbial processes (Vonk et al., 2012; Semiletov et al., 2013; Tanski et al., 2019). Our results on BCP and respiration show that carbon processing by the marine microbial communities will lead to different fates of the DOC depending on the glacial deposit type. With a lower BGE, lower amounts of bioavailable DOC are stored as biomass in the marine microbial communities and more of the carbon may be respired to the atmosphere as CO_2, as seen for the FLU deposit type. However, the majority of DOC was indeed refractory to biodegradation. This refractory DOC may be exported further out into ACZ where it may end up being buried in sediments or stored in the deep ocean.

Summary of Findings and Future Implications

Coastal erosion in the Arctic is intensifying and DOM from Cryosols will become an even more important source in the ACZ in the future. Here we show that the composition and biodegradability of DOM differs between post-glacial landscape units and that the differences in DOM composition and biodegradability are related to the glacial processes.

The three different DOM sources (FLU, LAC and MOR) supported the development of three different marine microbial communities, which was especially clear when comparing the MOR deposit type to FLU and LAC. These findings indicate a clear substrate-driven control on marine microbial community composition, especially where the input of organic carbon and DOM in the ACZ is dominated by release from coastal erosion of Cryosols. The bacterial communities imparted different spectral fingerprints on the absorption spectra and fluorescence EEMs of the DOM. Based on these fingerprints, we show that both colorless DOM and labile CDOM and FDOM fractions are being degraded. Also, the spectral results suggest that the more refractory CDOM and FDOM pool can be associated with CDOM and FDOM found in the open ocean after passing the ACZ. In addition, we show that absorbance at 330 nm could to be a proxy of microbial degradation of CDOM, especially produced in FLU and LAC deposit types during the Holocene Thermal Maximum.

The chemostat approach applied here provides a simulation of the constant substrate supply to coastal waters that can occur during summer open water conditions with maximum permafrost erosion rates. However, the results from this experiment will not fully represent what is happening in the natural environment. Important differences include the higher-than-natural incubation temperature at 20°C, which is standard for bioavailability studies, but might affect both the activity and composition of the bacterial community (Pomeroy and Wiebe, 2001; Adams et al., 2010; Sjöstedt et al., 2012a), together with autoclaving of the media, which can cause changes in the bioavailability and composition of the DOM. However, chemostats has been suggested to be the method that most closely resembles the growth conditions bacteria encounter in natural systems (Kovárová-Kovar and Egli, 1998) and the reproducibility between the replicate chemostats provide confidence in the robustness of this method. It is therefore clear that DOM quality influences the BCC, which in turn also affects the net effect of DOM degradation. Moraine deposit type will result in the net production of CDOM and FDOM in coastal waters, while the deposits types that are formed in aquatic environments, such as FLU and LAC, will lose CDOM and FDOM as it passes through coastal waters. These findings suggest a continuum, where the presence of ancient colorless labile DOM supports a rapidly growing community and a net production of CDOM and FDOM, which in turn can be degraded by other members of the bacterial communities with the capacity to degrade CDOM and FDOM.

To achieve a better understanding of carbon turnover from coastal erosion of Cryosols in the ACZ and its effects on climate and ecology in the future, more studies including qualitative measurements on DOM, such as absorbance and fluorescence spectroscopy, coupled with both bacterial and phytoplankton community assessment should be performed. Nevertheless, it is important to note that a large proportion of bioavailable DOM in these systems may not be captured and characterized using optical measurements.

DATA AVAILABILITY STATEMENT

The datasets generated for this study can be found online using the following link: https://doi.org/10.11583/DTU.14113250.v1. The names of accession number(s) can be found below: https://www.ncbi.nlm.nih.gov/, PRJNA675030.

AUTHOR CONTRIBUTIONS

AB, CS, and JS planned and performed the experiments. AM, NS, GT, and JV led sampling site selection and coordinated and performed field sampling. AB, CS, JS, and JC analyzed samples and performed data analysis. AB, CS, and JS wrote the manuscript. All authors commented on the manuscript and contributed to the interpretation and discussion of the results.

FUNDING

This publication is part of the Nunataryuk project. The project has received funding under the European Union's Horizon 2020 Research and Innovation Programme under grant agreement no. 773421. Part of this research was supported by Japan Aerospace Exploration Agency (JAXA) Global Change Observation Mission-Climate (GCOM-C) to AM (contract #20RT000350), Independent Research Fund Denmark (9040-00266B) awarded to CS, and by the Swedish Research Council (VR, grant 2015-00188) to JS, and the Natural Sciences and Engineering Research Council of Canada (Discovery program, RGPIN-2020-06874) to JC.

ACKNOWLEDGMENTS

We acknowledge colleagues in the EU Horizon 2020 Nunataryuk project (grant no. 773421) who contributed to the sampling and logistics and colleagues at Plateforme d'Analyses Génomiques (IBIS, Université Laval, Quebec City, Canada) for performing the Illumina sequencing. H. Lantuit, M. Fritz, and G. Hugelius are thanked for providing logistical and technical support. We also thank Lea Tolstrup for assistance during the chemostat experiment. Finally we thank the editor and the three reviewers for their valuable comments.

SUPPLEMENTARY MATERIAL

The Supplementary Material for this article can be found online at: https://www.frontiersin.org/articles/10.3389/feart.2021.640580/full#supplementary-material

REFERENCES

Abbott, B. W., Larouche, J. R., Jones, J. B., Bowden, W. B., and Balser, A. W. (2014). Elevated dissolved organic carbon biodegradability from thawing and collapsing permafrost. *J. Geophys. Res. Biogeosci.* 119, 2049–2063. doi: 10.1002/2014JG002678

Adams, H. E., Crump, B. C., and Kling, G. W. (2010). Temperature controls on aquatic bacterial production and community dynamics in arctic lakes and streams. *Environ. Microbiol.* 12, 1319–1333. doi: 10.1111/j.1462-2920.2010.02176.x

Amon, R. M. W., and Meon, B. (2004). The biogeochemistry of dissolved organic matter and nutrients in two large Arctic estuaries and potential implications for our understanding of the Arctic Ocean system. *Mar. Chem.* 92, 311–330. doi: 10.1016/j.marchem.2004.06.034

Andersson, M. G. I., Catalán, N., Rahman, Z., Tranvik, L. J., and Lindström, E. S. (2018). Effects of sterilization on dissolved organic carbon (DOC) composition and bacterial utilization of DOC from lakes. *Aquat. Microb. Ecol.* 82, 199–208. doi: 10.3354/ame01890

Arrigo, K. R., and Brown, C. W. (1996). Impact of chromophoric dissolved organic matter on UV inhibition of primary productivity in the sea. *Mar. Ecol. Prog. Ser.* 140, 207–216. doi: 10.3354/meps140207

Balmonte, J. P., Buckley, A., Hoarfrost, A., Ghobrial, S., Ziervogel, K., Teske, A., et al. (2019). Community structural differences shape microbial responses to high molecular weight organic matter. *Environ. Microbiol.* 21, 557–571. doi: 10.1111/1462-2920.14485

Belicka, L. L., Macdonald, R. W., and Harvey, H. R. (2002). Sources and transport of organic carbon to shelf, slope, and basin surface sediments of the Arctic Ocean. *Deep Sea Res. Part I Oceanogr. Res. Pap.* 49, 1463–1483. doi: 10.1016/S0967-0637(02)00031-6

Berggren, M., Laudon, H., Haei, M., Ström, L., and Jansson, M. (2010). Efficient aquatic bacterial metabolism of dissolved low-molecular-weight compounds from terrestrial sources. *ISME J.* 4, 408–416. doi: 10.1038/ismej.2009.120

Berggren, M., Laudon, H., and Jansson, M. (2007). Landscape regulation of bacterial growth efficiency in boreal freshwaters. *Glob. Biogeochem. Cycles* 21:GB4002. doi: 10.1029/2006GB002844

Biskaborn, B. K., Smith, S. L., Noetzli, J., Matthes, H., Vieira, G., Streletskiy, D. A., et al. (2019). Permafrost is warming at a global scale. *Nat. Commun.* 10:264. doi: 10.1038/s41467-018-08240-4

Blanchet, M., Pringault, O., Panagiotopoulos, C., Lefèvre, D., Charrière, B., Ghiglione, J.-F., et al. (2017). When riverine dissolved organic matter (DOM) meets labile DOM in coastal waters: changes in bacterial community activity and composition. *Aquat. Sci.* 79, 27–43. doi: 10.1007/s00027-016-0477-0

Burn, C. R. (1997). Cryostratigraphy, paleogeography, and climate change during the early Holocene warm interval, western Arctic coast, Canada. *Can. J. Earth Sci.* 34, 912–925. doi: 10.1139/e17-076

Callahan, B. J., McMurdie, P. J., Rosen, M. J., Han, A. W., Johnson, A. J. A., and Holmes, S. P. (2016). DADA2: high-resolution sample inference from Illumina amplicon data. *Nat. Methods* 13, 581–583. doi: 10.1038/nmeth.3869

Canelhas, M. R., Eiler, A., and Bertilsson, S. (2016). Are freshwater bacterioplankton indifferent to variable types of amino acid substrates? *FEMS Microbiol. Ecol.* 92:fiw005. doi: 10.1093/femsec/fiw005

Cauwet, G. (1999). ""Determination of dissolved organic carbon and nitrogen by high temperature combustion," in *Methods of Seawater Analysis*, eds K. Grasshoff, K. Kremling, and M. Ehrhardt (Weinheim: Wiley-VCH Verlag GmbH), 407–420. doi: 10.1002/9783527613984.ch15

Coble, P. G. (1996). Characterization of marine and terrestrial DOM in seawater using excitation-emission matrix spectroscopy. *Mar. Chem.* 51, 325–346. doi: 10.1016/0304-4203(95)00062-3

Coble, P. G. (2007). Marine optical biogeochemistry: the chemistry of ocean color. *Chem. Rev.* 107, 402–418. doi: 10.1021/cr050350

Coch, C., Juhls, B., Lamoureux, S. F., Lafreniére, M. J., Fritz, M., Heim, B., et al. (2019). Comparisons of dissolved organic matter and its optical characteristics in small low and high Arctic catchments. *Biogeosciences* 16, 4535–4553. doi: 10.5194/bg-16-4535-2019

Colatriano, D., Tran, P. Q., Guéguen, C., Williams, W. J., Lovejoy, C., and Walsh, D. A. (2018). Genomic evidence for the degradation of terrestrial organic matter by pelagic Arctic Ocean Chloroflexi bacteria. *Commun. Biol.* 1:90. doi: 10.1038/s42003-018-0086-7

Cota, G. F., Pomeroy, L. R., Harrison, W. G., Jones, E. P., Peters, F., Sheldon, W. M., et al. (1996). Nutrients, primary production and microbial heterotrophy in the southeastern Chukchi Sea:Arctic summer nutrient depletion and heterotrophy. *Mar. Ecol. Prog. Ser.* 135, 247–258. doi: 10.3354/meps135247

Cottrell, M. T., and David, K. L. (2003). Contribution of major bacterial groups to bacterial biomass production (thymidine and leucine incorporation) in the Delaware estuary. *Limnol. Oceanogr.* 48, 168–178. doi: 10.4319/lo.2003.48.1.0168

Couture, N. J., Irrgang, A., Pollard, W., Lantuit, H., and Fritz, M. (2018). Coastal erosion of permafrost soils along the yukon coastal plain and fluxes of organic carbon to the canadian beaufort sea. *J. Geophys. Res. Biogeosci.* 123, 406–422. doi: 10.1002/2017JG004166

Crump, B. C., Amaral-Zettler, L. A., and Kling, G. W. (2012). Microbial diversity in arctic freshwaters is structured by inoculation of microbes from soils. *ISME J.* 6, 1629–1639. doi: 10.1038/ismej.2012.9

Del Giorgio, P. A., and Cole, J. J. (1998). Bacterial growth efficiency in natural aquatic systems. *Annu. Rev. Ecol. Syst.* 29, 503–541. doi: 10.1146/annurev.ecolsys.29.1.503

Dill, K. A., and Shortle, D. (1991). Denatured states of proteins. *Annu. Rev. Biochem.* 60, 795–825. doi: 10.1146/annurev.bi.60.070191.004051

Dittmar, T., and Kattner, G. (2003). The biogeochemistry of the river and shelf ecosystem of the Arctic ocean: a review. *Mar. Chem.* 83, 103–120. doi: 10.1016/S0304-4203(03)00105-1

Dou, F., Ping, C.-L., Guo, L., and Jorgenson, T. (2008). Estimating the impact of seawater on the production of soil water-extractable organic carbon during coastal erosion. *J. Environ. Qual.* 37, 2368–2374. doi: 10.2134/jeq2007.0403

Drake, T. W., Guillemette, F., Hemingway, J. D., Chanton, J. P., Podgorski, D. C., Zimov, N. S., et al. (2018). The ephemeral signature of permafrost carbon in an arctic fluvial network. *J. Geophys. Res. Biogeosci.* 123, 1475–1485. doi: 10.1029/2017JG004311

Drake, T. W., Wickland, K. P., Spencer, R. G. M., McKnight, D. M., and Striegl, R. G. (2015). Ancient low-molecular-weight organic acids in permafrost fuel rapid carbon dioxide production upon thaw. *Proc. Natl. Acad. Sci. U.S.A.* 112, 13946–13951. doi: 10.1073/pnas.1511705112

Druart, P., and De Wulf, O. (1993). Activated charcoal catalyses sucrose hydrolysis during autoclaving. *Plant Cell Tiss. Organ Cult.* 32, 97–99. doi: 10.1007/BF00040122

Dunton, K., and Crump, B. (2014). *Collaborative Research: Terrestrial Linkages to Microbial and Metazoan Communities in Coastal Ecosystems of the Beaufort Sea*. Santa Barbara, CA: Arctic Data Center.

Environment Canada (2016). *Canadian Climate Normals*. Available online at: https://climate.weather.gc.ca/climate_normals/ (accessed February 1, 2021).

Fasching, C., Behounek, B., Singer, G. A., and Battin, T. J. (2014). Microbial degradation of terrigenous dissolved organic matter and potential consequences for carbon cycling in brown-water streams. *Sci. Rep.* 4:4981. doi: 10.1038/srep04981

Fouché, J., Christiansen, C. T., Lafrenière, M. J., Grogan, P., and Lamoureux, S. F. (2020). Canadian permafrost stores large pools of ammonium and optically distinct dissolved organic matter. *Nat. Commun.* 11:4500. doi: 10.1038/s41467-020-18331-w

Fritz, M., Opel, T., Tanski, G., Herzschuh, U., Meyer, H., Eulenburg, A., et al. (2015). Dissolved organic carbon (DOC) in Arctic ground ice. *Cryosphere* 9, 737–752. doi: 10.5194/tc-9-737-2015

Fritz, M., Vonk, J. E., and Lantuit, H. (2017). Collapsing arctic coastlines. *Nat. Clim. Chang.* 7, 6–7. doi: 10.1038/nclimate3188

Fritz, M., Wetterich, S., Schirrmeister, L., Meyer, H., Lantuit, H., Preusser, F., et al. (2012). Eastern Beringia and beyond: late Wisconsinan and holocene landscape dynamics along the Yukon Coastal Plain, Canada. *Palaeogeogr. Palaeoclimatol. Palaeoecol.* 319–320, 28–45. doi: 10.1016/j.palaeo.2011.12.015

Gärtner, A., Wiese, J., and Imhoff, J. F. (2008). *Amphritea atlantica* gen. nov., sp. nov., a gammaproteobacterium from the Logatchev hydrothermal vent field. *Int. J. Syst. Evol. Microbiol.* 58, 34–39. doi: 10.1099/ijs.0.65234-0

Gasol, J. M., and Del Giorgio, P. A. (2000). Using flow cytometry for counting natural planktonic bacteria and understanding the structure of planktonic bacterial communities. *Sci. Mar.* 64, 197–224. doi: 10.3989/scimar.2000.64n2197

Gómez-Consarnau, L., Lindh, M. V., Gasol, J. M., and Pinhassi, J. (2012). Structuring of bacterioplankton communities by specific dissolved organic carbon compounds. *Environ. Microbiol.* 14, 2361–2378. doi: 10.1111/j.1462-2920.2012.02804.x

Günther, F., Overduin, P. P., Yakshina, I. A., Opel, T., Baranskaya, A. V., and Grigoriev, M. N. (2015). Observing Muostakh disappear: permafrost thaw subsidence and erosion of a ground-ice-rich island in response to arctic summer warming and sea ice reduction. *Cryosphere* 9, 151–178. doi: 10.5194/tc-9-151-2015

Guo, L., and Macdonald, R. W. (2006). Source and transport of terrigenous organic matter in the upper Yukon River: evidence from isotope (δ^{13} C, Δ^{14} C, and δ^{15} N) composition of dissolved, colloidal, and particulate phases. *Glob. Biogeochem. Cycles* 20:GB2011. doi: 10.1029/2005GB002593

Gupta, P., Chaturvedi, P., Pradhan, S., Delille, D., and Shivaji, S. (2006). *Marinomonas polaris* sp. nov., a psychrohalotolerant strain isolated from coastal sea water off the subantarctic Kerguelen islands. *Int. J. Syst. Evol. Microbiol.* 56, 361–364. doi: 10.1099/ijs.0.63921-0

Hagstrom, Å, Ammerman, J. W., Heinrichs, S., and Azam, F. (1984). Bacterioplankton growth in seawater: II. Growth kinetics and cellular characteristicsin seawater cultures. *Mar. Ecol. Prog. Ser.* 18, 41–48.

Hansen, H. P., and Koroleff, F. (1999). "Determination of nutrients," in *Methods of Seawater Analysis*, eds K. Grasshoff, K. Kremling, and M. Ehrhardt (Weinheim: Wiley-VCH Verlag GmbH), 159–228. doi: 10.1002/9783527613984.ch10

Hauptmann, A. L., Markussen, T. N., Stibal, M., Olsen, N. S., Elberling, B., Baelum, J., et al. (2016). Upstream Freshwater and Terrestrial Sources Are Differentially Reflected in the Bacterial Community Structure along a Small Arctic River and its estuary. *Front. Microbiol.* 7:1474. doi: 10.3389/fmicb.2016.01474

Helms, J. R., Stubbins, A., Ritchie, J. D., Minor, E. C., Kieber, D. J., and Mopper, K. (2008). Absorption spectral slopes and slope ratios as indicators of molecular weight, source, and photobleaching of chromophoric dissolved organic matter. *Limnol. Oceanogr.* 53, 955–969. doi: 10.4319/lo.2008.53.3.0955

Herlemann, D. P., Labrenz, M., Jürgens, K., Bertilsson, S., Waniek, J. J., and Andersson, A. F. (2011). Transitions in bacterial communities along the 2000 km salinity gradient of the Baltic Sea. *ISME J.* 5, 1571–1579. doi: 10.1038/ismej.2011.41

Herlemann, D. P. R., Manecki, M., Meeske, C., Pollehne, F., Labrenz, M., Schulz-Bull, D., et al. (2014). Uncoupling of bacterial and terrigenous dissolved organic matter dynamics in decomposition experiments. *PLoS One* 9:e93945. doi: 10.1371/journal.pone.0093945

Heslop, J. K., Winkel, M., Walter Anthony, K. M., Spencer, R. G. M., Podgorski, D. C., Zito, P., et al. (2019). Increasing organic carbon biolability with depth in yedoma permafrost: ramifications for future climate change. *J. Geophys. Res. Biogeosci.* 124, 2021–2038. doi: 10.1029/2018JG004712

Holmes, R. M., McClelland, J. W., Peterson, B. J., Tank, S. E., Bulygina, E., Eglinton, T. I., et al. (2012). Seasonal and Annual Fluxes of Nutrients and Organic Matter from large rivers to the Arctic Ocean and surrounding Seas. *Estuar. Coasts* 35, 369–382. doi: 10.1007/s12237-011-9386-6

Hoque, M. A., and Pollard, W. H. (2016). Stability of permafrost dominated coastal cliffs in the Arctic. *Polar Sci.* 10, 79–88. doi: 10.1016/j.polar.2015.10.004

Hugelius, G., Strauss, J., Zubrzycki, S., Harden, J. W., Schuur, E. A. G., Ping, C. L., et al. (2014). Estimated stocks of circumpolar permafrost carbon with quantified' ' uncertainty ranges and identified data gaps. *Biogeosciences* 11, 6573–6593. doi: 10.5194/bg-11-6573-2014

Jobbágy, E. G., and Jackson, R. B. (2000). The vertical distribution of soil organic carbon and its relation to climate and vegetation. *Ecol. Appl.* 10, 423–436.

Jones, B. M., Farquharson, L. M., Baughman, C. A., Buzard, R. M., Arp, C. D., Grosse, G., et al. (2018). A decade of remotely sensed observations highlight complex processes linked to coastal permafrost bluff erosion in the Arctic. *Environ. Rese. Lett.* 13:115001. doi: 10.1088/1748-9326/aae471

Juhls, B., Overduin, P. P., Hölemann, J., Hieronymi, M., Matsuoka, A., Heim, B., et al. (2019). Dissolved organic matter at the fluvial–marine transition in the Laptev Sea using in situ data and ocean colour remote sensing. *Biogeosciences* 16, 2693–2713. doi: 10.5194/bg-16-2693-2019

Kaiser, K., and Guggenberger, G. (2000). The role of DOM sorption to mineral surfaces in the preservation of organic matter in soils. *Org. Geochem.* 31, 711–725. doi: 10.1016/S0146-6380(00)00046-2

Kawahigashi, M., Kaiser, K., Rodionov, A., and Guggenberger, G. (2006). Sorption of dissolved organic matter by mineral soils of the Siberian forest tundra. *Glob. Chang. Biol.* 12, 1868–1877. doi: 10.1111/j.1365-2486.2006.01203.x

Kinsey, J. D., Corradino, G., Ziervogel, K., Schnetzer, A., and Osburn, C. L. (2018). Formation of chromophoric dissolved organic matter by bacterial degradation of phytoplankton-derived aggregates. *Front. Mar. Sci.* 4:430. doi: 10.3389/fmars.2017.00430

Köhler, H., Meon, B., Gordeev, V. V., Spitzy, A., and Amon, R. M. W. (2003). "Dissolved organic matter (DOM) in the estuaries of Ob and Yenisei and the adjacent Kara Sea, Russia," in *Proceedings of the Marine Science*, Vol. 6, Amsterdam.

Kovárová-Kovar, K., and Egli, T. (1998). Growth kinetics of suspended microbial cells: from single-substrate-controlled growth to mixed-substrate kinetics. *Microbiol. Mol. Biol. Rev.* 62, 646–666.

Kritzberg, E. S., Duarte, C. M., and Wassmann, P. (2010). Changes in Arctic marine bacterial carbon metabolism in response to increasing temperature. *Polar Biol.* 33, 1673–1682. doi: 10.1007/s00300-010-0799-7

Krzic, M., Watson, K., Grand, S., Bomke, A., Smith, S., Dyanatkar, S., et al. (2010). *Soil Formation and Parent Material. The University of British Columbia, Vancouver, Thompson Rivers University, Kamloops, and Agriculture and Agri-Food Canada, Summerland*. Available online at: https://landscape.soilweb.ca/about/ (accessed November 20, 2020).

Langenheder, S., Kisand, V., Wikner, J., and Tranvik, L. J. (2003). Salinity as a structuring factor for the composition and performance of bacterioplankton degrading riverine DOC. *FEMS Microbiol. Ecol.* 45, 189–202. doi: 10.1016/S0168-6496(03)00149-1

Lawaetz, A. J., and Stedmon, C. A. (2009). Fluorescence intensity calibration using the Raman scatter peak of water. *Appl. Spectrosc.* 63, 936–940. doi: 10.1366/000370209788964548

Lee, S., and Fuhrman, J. A. (1987). Relationships between biovolume and biomass of naturally derived marine bacterioplankton. *Appl. Environ. Microbiol.* 53, 1298–1303. doi: 10.1128/AEM.53.6.1298-1303.1987

Logue, J. B., Stedmon, C. A., Kellerman, A. M., Nielsen, N. J., Andersson, A. F., Laudon, H., et al. (2016). Experimental insights into the importance of aquatic bacterial community composition to the degradation of dissolved organic matter. *ISME J.* 10, 533–545. doi: 10.1038/ismej.2015.131

MacDonald, E. N., Tank, S. E., Kokelj, S. V., Froese, D. G., and Hutchins, R. H. S. (2021). Permafrost-derived dissolved organic matter composition varies across permafrost end-members in the western Canadian Arctic. *Environ. Res. Lett.* 16:024036. doi: 10.1088/1748-9326/abd971

Mann, P. J., Eglinton, T. I., McIntyre, C. P., Zimov, N., Davydova, A., Vonk, J. E., et al. (2015). Utilization of ancient permafrost carbon in headwaters of Arctic fluvial networks. *Nat. Commun.* 6:7856. doi: 10.1038/ncomms8856

Mann, P. J., Spencer, R. G. M., Hernes, P. J., Six, J., Aiken, G. R., Tank, S. E., et al. (2016). Pan-Arctic trends in terrestrial dissolved organic matter from optical measurements. *Front. Earth Sci.* 4:25. doi: 10.3389/feart.2016.00025

Martin, M. (2011). Cutadapt removes adapter sequences from high-throughput sequencing reads. *EMBnet J.* 17:10. doi: 10.14806/ej.17.1.200

Matsuoka, A., Ortega-Retuerta, E., Bricaud, A., Arrigo, K. R., and Babin, M. (2015). Characteristics of colored dissolved organic matter (CDOM) in the Western Arctic Ocean: Relationships with microbial activities. *Deep Sea Res. 2 Top. Stud. Oceanogr.* 118, 44–52. doi: 10.1016/j.dsr2.2015.02.012

McGuire, A. D., Lawrence, D. M., Koven, C., Clein, J. S., Burke, E., Chen, G., et al. (2018). Dependence of the evolution of carbon dynamics in the northern permafrost region on the trajectory of climate change. *Proc. Natl. Acad. Sci. U.S.A.* 115, 3882–3887. doi: 10.1073/pnas.1719903115

Meyers, P. A., and Ishiwatari, R. (1995). "Organic matter accumulation records in lake sediments," in *Physics and Chemistry of Lakes*, eds A. Lerman, D. M. Imboden, and J. R. Gat (Berlin: Springer), 279–328. doi: 10.1007/978-3-642-85132-2_10

Middelboe, M., Glud, R. N., and Sejr, M. K. (2012). Bacterial carbon cycling in a subarctic fjord: a seasonal study on microbial activity, growth efficiency, and virus-induced mortality in Kobbefjord. *Greenland. Limnol. Oceanogr.* 57, 1732–1742. doi: 10.4319/lo.2012.57.6.1732

Miyazaki, M., Nogi, Y., Fujiwara, Y., Kawato, M., Nagahama, T., Kubokawa, K., et al. (2008). *Amphritea japonica* sp. nov. and *Amphritea balenae* sp. nov., isolated from the sediment adjacent to sperm whale carcasses off Kagoshima. *Jpn. Int. J. Syst. Evol. Microbiol.* 58, 2815–2820. doi: 10.1099/ijs.0.65826-0

Moriarty, D. J. W. (1986). "Measurement of bacterial growth rates in aquatic systems from rates of nucleic acid synthesis," in *Advances in Microbial Ecology Advances in Microbial Ecology*, ed. K. C. Marshall (Boston, MA: Springer), 245–292. doi: 10.1007/978-1-4757-0611-6_6

Müller, O., Seuthe, L., Bratbak, G., and Paulsen, M. L. (2018). Bacterial response to permafrost derived organic matter input in an arctic fjord. *Front. Mar. Sci.* 5:263. doi: 10.3389/fmars.2018.00263

Murphy, K. R., Stedmon, C. A., Graeber, D., and Bro, R. (2013). Fluorescence spectroscopy and multi-way techniques. *PARAFAC Anal. Methods* 5:6557. doi: 10.1039/c3ay41160e

Nelson, C. E., and Carlson, C. A. (2012). Tracking differential incorporation of dissolved organic carbon types among diverse lineages of Sargasso Sea bacterioplankton. *Environ. Microbiol.* 14, 1500–1516. doi: 10.1111/j.1462-2920.2012.02738.x

Nelson, C. E., and Wear, E. K. (2014). Microbial diversity and the lability of dissolved organic carbon. *Proc. Natl. Acad. Sci. U.S.A.* 111, 7166–7167. doi: 10.1073/pnas.1405751111

Obu, J., Lantuit, H., Grosse, G., Günther, F., Sachs, T., Helm, V., et al. (2016). Coastal erosion and mass wasting along the Canadian Beaufort Sea based on annual airborne LiDAR elevation data. *Geomorphology* 293, 331–346. doi: 10.1016/j.geomorph.2016.02.014

Obu, J., Westermann, S., Bartsch, A., Berdnikov, N., Christiansen, H. H., Dashtseren, A., et al. (2019). Northern Hemisphere permafrost map based on TTOP modelling for 2000-2016 at 1 km2 scale. *Earth Sci. Rev.* 193, 299–316. doi: 10.1016/j.earscirev.2019.04.023

O'Donnell, J. A., Aiken, G. R., Swanson, D. K., Panda, S., Butler, K. D., and Baltensperger, A. P. (2016). Dissolved organic matter composition of Arctic rivers: linking permafrost and parent material to riverine carbon. *Glob. Biogeochem. Cycles* 30, 1811–1826. doi: 10.1002/2016GB005482

Oksanen, J., Guillaume Blanchet, F., Friendly, M., Kindt, R., Legendre, P., McGlinn, D., et al. (2019). *vegan: Community Ecology Package*. Available online at: https://cran.r-project.org/web/packages/vegan/index.html (accessed May 28, 2020).

Opfergelt, S. (2020). The next generation of climate model should account for the evolution of mineral-organic interactions with permafrost thaw. *Environ. Res. Lett.* 15:091003. doi: 10.1088/1748-9326/ab9a6d

Overeem, I., Anderson, R. S., Wobus, C. W., Clow, G. D., Urban, F. E., and Matell, N. (2011). Sea ice loss enhances wave action at the Arctic coast. *Geophys. Res. Lett.* 38:L17503. doi: 10.1029/2011GL048681

Palmtag, J., and Kuhry, P. (2018). Grain size controls on cryoturbation and soil organic carbon density in permafrost-affected soils. *Permafrost Periglac. Process.* 29, 112–120. doi: 10.1002/ppp.1975

Park, S., Kim, I. K., Lee, J.-S., and Yoon, J.-H. (2019). *Sulfitobacter sabulilitoris* sp. nov., isolated from marine sand. *Int. J. Syst. Evol. Microbiol.* 69, 3230–3236. doi: 10.1099/ijsem.0.003614

Paulsen, M. L., Nielsen, S. E. B., Müller, O., Møller, E. F., Stedmon, C. A., Juul-Pedersen, T., et al. (2017). Carbon bioavailability in a high arctic fjord influenced by glacial meltwater, NE Greenland. *Front. Mar. Sci.* 4:176. doi: 10.3389/fmars.2017.00176

Pollard, W. (2018). "Periglacial processes in glacial environments," in *Past Glacial Environments*, eds J. Menzies and J. J. M. van der Mee (Amsterdam: Elsevier), 537–564. doi: 10.1016/B978-0-08-100524-8.00016-6

Pomeroy, L. R., and Wiebe, W. J. (2001). Temperature and substrates as interactive limiting factors for marine heterotrophic bacteria. *Aquat. Microb. Ecol.* 23, 187–204. doi: 10.3354/ame023187

Quast, C., Pruesse, E., Yilmaz, P., Gerken, J., Schweer, T., Yarza, P., et al. (2013). The SILVA ribosomal RNA gene database project: improved data processing and web-based tools. *Nucleic Acids Res.* 41, D590–D596. doi: 10.1093/nar/gks1219

Rampton, V. N. (1982). *Quaternarygeology of the Yukon Coastal Plain*. Ottawa: Geological Survey of Canada.

Raudina, T. V., Loiko, S. V., Lim, A. G., Krickov, I. V., Shirokova, L. S., Istigechev, G. I., et al. (2017). Dissolved organic carbon and major and trace elements in peat porewater of sporadic, discontinuous, and continuous permafrost zones of western Siberia. *Biogeosciences* 14, 3561–3584. doi: 10.5194/bg-14-3561-2017

Robinson, M. D., and Smyth, G. K. (2008). Small-sample estimation of negative binomial dispersion, with applications to SAGE data. *Biostatistics* 9, 321–332. doi: 10.1093/biostatistics/kxm030

Robinson, M. D., McCarthy, D. J., and Smyth, G. K. (2010). edgeR: a Bioconductor package for differential expression analysis of digital gene expression data. *Bioinformatics* 26, 139–140. doi: 10.1093/bioinformatics/btp616

Romanenko, L. A., Tanaka, N., Svetashev, V. I., and Kalinovskaya, N. I. (2011). *Pacificibacter maritimus* gen. nov., sp. nov., isolated from shallow marine sediment. *Int. J. Syst. Evol. Microbiol.* 61, 1375–1381. doi: 10.1099/ijs.0.026047-0

Romanovsky, V. E., Smith, S. L., and Christiansen, H. H. (2010). Permafrost thermal state in the polar Northern Hemisphere during the international polar year 2007-2009: a synthesis. *Permafrost Periglac. Process.* 21, 106–116. doi: 10.1002/ppp.689

Rosenstock, B., and Simon, M. (2001). Sources and sinks of dissolved free amino acids and protein in a large and deep mesotrophic lake. *Limnol. Oceanogr.* 46, 644–654. doi: 10.4x319/lo.2001.46.3.0644

Ruiz-González, C., Niño-García, J. P., and Del Giorgio, P. A. (2015). Terrestrial origin of bacterial communities in complex boreal freshwater networks. *Ecol. Lett.* 18, 1198–1206. doi: 10.1111/ele.12499

Schirrmeister, L., Grosse, G., Wetterich, S., Overduin, P. P., Strauss, J., Schuur, E. A. G., et al. (2011). Fossil organic matter characteristics in permafrost deposits of the northeast Siberian Arctic. *J. Geophys. Res.* 116:G00M02. doi: 10.1029/2011JG001647

Schnetger, B., and Lehners, C. (2014). Determination of nitrate plus nitrite in small volume marine water samples using vanadium(III)chloride as a reduction agent. *Mar. Chem.* 160, 91–98. doi: 10.1016/j.marchem.2014.01.010

Schuur, E. A. G., McGuire, A. D., Schädel, C., Grosse, G., Harden, J. W., Hayes, D. J., et al. (2015). Climate change and the permafrost carbon feedback. *Nature* 520, 171–179. doi: 10.1038/nature14338

Semiletov, I. P., Shakhova, N. E., Pipko, I. I., Pugach, S. P., Charkin, A. N., Dudarev, O. V., et al. (2013). Space-time dynamics of carbon and environmental parameters related to carbon dioxide emissions in the Buor-Khaya Bay and adjacent part of the Laptev Sea. *Biogeosciences* 10, 5977–5996. doi: 10.5194/bg-10-5977-2013

Sipler, R. E., Kellogg, C. T. E., Connelly, T. L., Roberts, Q. N., Yager, P. L., and Bronk, D. A. (2017). Microbial community response to terrestrially derived dissolved organic matter in the coastal arctic. *Front. Microbiol.* 8:1018. doi: 10.3389/fmicb.2017.01018

Sjöstedt, J., Hagström, Å, and Zweifel, U. L. (2012a). Variation in cell volume and community composition of bacteria in response to temperature. *Aquat. Microb. Ecol.* 66, 237–246. doi: 10.3354/ame01579

Sjöstedt, J., Koch-Schmidt, P., Pontarp, M., Canbäck, B., Tunlid, A., Lundberg, P., et al. (2012b). Recruitment of members from the rare biosphere of marine bacterioplankton communities after an environmental disturbance. *Appl. Environ. Microbiol.* 78, 1361–1369. doi: 10.1128/AEM.05542-11

Smith, S. L., Romanovsky, V. E., Lewkowicz, A. G., Burn, C. R., Allard, M., Clow, G. D., et al. (2010). Thermal state of permafrost in North America: a contribution to the international polar year. *Permafrost Periglac. Process.* 21, 117–135. doi: 10.1002/ppp.690

Sorokin, D. Y. (1995). *Sulfitobacter pontiacus* gen. nov., sp. nov. — A new heterotrophic bacterium from the black sea, specialized on sulfite oxidation. *Mikrobiologiya* 64:295.

Spencer, R. G. M., Mann, P. J., Dittmar, T., Eglinton, T. I., McIntyre, C., Holmes, R. M., et al. (2015). Detecting the signature of permafrost thaw in Arctic rivers. *Geophys. Res. Lett.* 42, 2830–2835. doi: 10.1002/2015GL063498

Stapel, J. G., Schwamborn, G., Schirrmeister, L., Horsfield, B., and Mangelsdorf, K. (2017). Substrate potential of last interglacial to Holocene permafrost organic matter for future microbial greenhouse gas production. *Biogeosciences* 15, 1969–1985. doi: 10.5194/bg-15-1969-2018

Stedmon, C. A., and Nelson, N. B. (2015). "The optical properties of DOM in the ocean," in *Biogeochemistry of Marine Dissolved Organic Matter*, eds D. A. Hansell and C. A. Carlson (Amsterdam: Elsevier), 481–508. doi: 10.1016/B978-0-12-405940-5.00010-8

Strauss, J., Schirrmeister, L., Grosse, G., Fortier, D., Hugelius, G., Knoblauch, C., et al. (2017). Deep Yedoma permafrost: a synthesis of depositional characteristics and carbon vulnerability. *Earth Sci. Rev.* 172, 75–86. doi: 10.1016/j.earscirev.2017.07.007

Svoboda, P., Lindström, E. S., Ahmed Osman, O., and Langenheder, S. (2018). Dispersal timing determines the importance of priority effects in bacterial communities. *ISME J.* 12, 644–646. doi: 10.1038/ismej.2017.180

Tank, S. E., Vonk, J. E., Walvoord, M. A., McClelland, J. W., Laurion, I., and Abbott, B. W. (2020). Landscape matters: predicting the biogeochemical effects of permafrost thaw on aquatic networks with a state factor approach. *Permafrost Periglac. Process.* 31, 358–370. doi: 10.1002/ppp.2057

Tanski, G., Couture, N., Lantuit, H., Eulenburg, A., and Fritz, M. (2016). Eroding permafrost coasts release low amounts of dissolved organic carbon (DOC) from ground ice into the nearshore zone of the Arctic Ocean. *Glob. Biogeochem. Cycles* 30, 1054–1068. doi: 10.1002/2015GB005337

Tanski, G., Wagner, D., Knoblauch, C., Fritz, M., Sachs, T., and Lantuit, H. (2019). Rapid co_2 release from eroding permafrost in seawater. *Geophys. Res. Lett.* 46, 11244–11252. doi: 10.1029/2019GL084303

Textor, S. R., Guillemette, F., Zito, P. A., and Spencer, R. G. M. (2018). An assessment of dissolved organic carbon biodegradability and priming in blackwater systems. *J. Geophys. Res. Biogeosci.* 123, 2998–3015. doi: 10.1029/2018JG004470

Textor, S. R., Wickland, K. P., Podgorski, D. C., Johnston, S. E., and Spencer, R. G. M. (2019). Dissolved organic carbon turnover in permafrost-influenced watersheds of interior alaska: molecular insights and the priming effect. *Front. Earth Sci.* 7:275. doi: 10.3389/feart.2019.00275

Thingstad, T. F., Bellerby, R. G. J., Bratbak, G., Børsheim, K. Y., Egge, J. K., Heldal, M., et al. (2008). Counterintuitive carbon-to-nutrient coupling in an Arctic pelagic ecosystem. *Nature* 455, 387–390. doi: 10.1038/nature07235

Thomas, F., Hehemann, J.-H., Rebuffet, E., Czjzek, M., and Michel, G. (2011). Environmental and gut bacteroidetes: the food connection. *Front. Microbiol.* 2:93. doi: 10.3389/fmicb.2011.00093

Van der Gucht, K., Cottenie, K., Muylaert, K., Vloemans, N., Cousin, S., Declerck, S., et al. (2007). The power of species sorting: local factors drive bacterial community composition over a wide range of spatial scales. *Proc. Natl. Acad. Sci. U.S.A.* 104, 20404–20409. doi: 10.1073/pnas.0707200104

Vannote, R. L., Minshall, G. W., Cummins, K. W., Sedell, J. R., and Cushing, C. E. (1980). The river continuum concept. *Can. J. Fish. Aquat. Sci.* 37, 130–137. doi: 10.1139/f80-017

Vonk, J. E., Mann, P. J., Davydov, S., Davydova, A., Spencer, R. G. M., Schade, J., et al. (2013). High biolability of ancient permafrost carbon upon thaw. *Geophys. Res. Lett.* 40, 2689–2693. doi: 10.1002/grl.50348

Vonk, J. E., Sánchez-García, L., van Dongen, B. E., Alling, V., Kosmach, D., Charkin, A., et al. (2012). Activation of old carbon by erosion of coastal and subsea permafrost in Arctic Siberia. *Nature* 489, 137–140. doi: 10.1038/nature11392

Vonk, J. E., Tank, S. E., Bowden, W. B., Laurion, I., Vincent, W. F., Alekseychik, P., et al. (2015). Reviews and syntheses: effects of permafrost thaw on Arctic aquatic ecosystems. *Biogeosciences* 12, 7129–7167. doi: 10.5194/bg-12-7129-2015

Walker, S. A., Amon, R. M. W., and Stedmon, C. A. (2013). Variations in high-latitude riverine fluorescent dissolved organic matter: a comparison of large Arctic rivers. *J. Geophys. Res. Biogeosci.* 118, 1689–1702. doi: 10.1002/2013JG002320

Walter Anthony, K., Schneider von Deimling, T., Nitze, I., Frolking, S., Emond, A., Daanen, R., et al. (2018). 21st-century modeled permafrost carbon emissions accelerated by abrupt thaw beneath lakes. *Nat. Commun.* 9:3262. doi: 10.1038/s41467-018-05738-9

Wang, Y., Naumann, U., Wright, S. T., and Warton, D. I. (2012). mvabund - anR package for model-based analysis of multivariate abundance data. *Methods Ecol. Evol.* 3, 471–474. doi: 10.1111/j.2041-210X.2012.00190.x

Ward, C. P., and Cory, R. M. (2015). Chemical composition of dissolved organic matter draining permafrost soils. *Geochim. Cosmochim. Acta* 167, 63–79. doi: 10.1016/j.gca.2015.07.001

Weishaar, J. L., Aiken, G. R., Bergamaschi, B. A., Fram, M. S., Fujii, R., and Mopper, K. (2003). Evaluation of specific ultraviolet absorbance as an indicator of the chemical composition and reactivity of dissolved organic carbon. *Environ. Sci. Technol.* 37, 4702–4708. doi: 10.1021/es030360x

Wickland, K. P., Waldrop, M. P., Aiken, G. R., Koch, J. C., Jorgenson, M. T., and Striegl, R. G. (2018). Dissolved organic carbon and nitrogen release from boreal Holocene permafrost and seasonally frozen soils of Alaska. *Environ. Res. Lett.* 13:065011. doi: 10.1088/1748-9326/aac4ad

Wild, B., Andersson, A., Bröder, L., Vonk, J., Hugelius, G., McClelland, J. W., et al. (2019). Rivers across the Siberian Arctic unearth the patterns of carbon release from thawing permafrost. *Proc. Natl. Acad. Sci. U.S.A.* 116, 10280–10285. doi: 10.1073/pnas.1811797116

Wologo, E., Shakil, S., Zolkos, S., Textor, S., Ewing, S., Klassen, J., et al. (2020). Stream dissolved organic matter in permafrost regions shows surprising compositional similarities but negative priming and nutrient effects. *Glob. Biogeochem. Cycles* 35:e2020GB006719. doi: 10.1029/2020GB006719

Wolter, J., Lantuit, H., Herzschuh, U., Stettner, S., and Fritz, M. (2017). Tundra vegetation stability versus lake-basin variability on the Yukon Coastal Plain (NW Canada) during the past three centuries. *Holocene* 27, 1846–1858. doi: 10.1177/0959683617708441

Yamashita, Y., and Tanoue, E. (2003). Chemical characterization of protein-like fluorophores in DOM in relation to aromatic amino acids. *Mar. Chem.* 82, 255–271. doi: 10.1016/S0304-4203(03)00073-2

Yoon, J.-H., Kang, S.-J., and Oh, T.-K. (2005). *Marinomonas dokdonensis* sp. nov., isolated from sea water. *Int. J. Syst. Evol. Microbiol.* 55, 2303–2307. doi: 10.1099/ijs.0.63830-0

Zhang, D.-C., Li, H.-R., Xin, Y.-H., Liu, H.-C., Chen, B., Chi, Z.-M., et al. (2008). *Marinomonas arctica* sp. nov., a psychrotolerant bacterium isolated from the Arctic. *Int. J. Syst. Evol. Microbiol.* 58, 1715–1718. doi: 10.1099/ijs.0.65737-0

Zhang, Z., Qin, J., Sun, H., Yang, J., and Liu, Y. (2020). Spatiotemporal dynamics of dissolved organic carbon and freshwater browning in the Zoige Alpine Wetland, Northeastern Qinghai-Tibetan Plateau. *Water* 12:2453. doi: 10.3390/w12092453

Zweifel, U. L., Blackburn, N., and Hagström, Å (1996). Cycling of marine dissolved organic matter. I. An experimental system. *Aquat. Microb. Ecol.* 11, 65–77. doi: 10.3354/ame011065

Conflict of Interest: The authors declare that the research was conducted in the absence of any commercial or financial relationships that could be construed as a potential conflict of interest.

frontiers in Earth Science

ORIGINAL RESEARCH
published: 26 March 2021
doi: 10.3389/feart.2021.630493

Permafrost Carbon and CO_2 Pathways Differ at Contrasting Coastal Erosion Sites in the Canadian Arctic

George Tanski[1,2,3], Lisa Bröder[2,4], Dirk Wagner[5,6], Christian Knoblauch[7,8], Hugues Lantuit[1,6], Christian Beer[7,8], Torsten Sachs[3], Michael Fritz[1], Tommaso Tesi[9], Boris P. Koch[10,11], Negar Haghipour[4,12], Timothy I. Eglinton[4], Jens Strauss[1] and Jorien E. Vonk[2]*

[1] Permafrost Research Unit, Alfred Wegener Institute Helmholtz Centre for Polar and Marine Research, Potsdam, Germany, [2] Department of Earth Sciences, Vrije Universiteit Amsterdam, Amsterdam, Netherlands, [3] GFZ German Research Centre for Geosciences, Section Remote Sensing and Geoinformatics, Potsdam, Germany, [4] Department of Earth Sciences, Swiss Federal Institute of Technology (ETH) Zürich, Zurich, Switzerland, [5] GFZ German Research Centre for Geosciences, Section Geomicrobiology, Potsdam, Germany, [6] Institute of Geosciences, Universität Potsdam, Potsdam, Germany, [7] Institute of Soil Science, Universität Hamburg, Hamburg, Germany, [8] Center for Earth System Research and Sustainability, Universität Hamburg, Hamburg, Germany, [9] Instituto di Scienze Polari – National Research Council, Bologna, Italy, [10] Biosciences Division, Alfred Wegener Institute Helmholtz Centre for Polar and Marine Research, Bremerhaven, Germany, [11] University of Applied Sciences, Bremerhaven, Germany, [12] Laboratory of Ion Beam Physics, Swiss Federal Institute of Technology (ETH) Zürich, Zurich, Switzerland

OPEN ACCESS

Edited by:
Scott Raymond Dallimore, Geological Survey of Canada, Canada

Reviewed by:
Raymond D. Ward, University of Brighton, United Kingdom
Baptiste Dafflon, Lawrence Berkeley National Laboratory, United States

***Correspondence:**
George Tanski
george.tanski@awi.de

Specialty section:
This article was submitted to Cryospheric Sciences, a section of the journal Frontiers in Earth Science

Received: 17 November 2020
Accepted: 08 March 2021
Published: 26 March 2021

Citation:
Tanski G, Bröder L, Wagner D, Knoblauch C, Lantuit H, Beer C, Sachs T, Fritz M, Tesi T, Koch BP, Haghipour N, Eglinton TI, Strauss J and Vonk JE (2021) Permafrost Carbon and CO_2 Pathways Differ at Contrasting Coastal Erosion Sites in the Canadian Arctic. Front. Earth Sci. 9:630493. doi: 10.3389/feart.2021.630493

Warming air and sea temperatures, longer open-water seasons and sea-level rise collectively promote the erosion of permafrost coasts in the Arctic, which profoundly impacts organic matter pathways. Although estimates on organic carbon (OC) fluxes from erosion exist for some parts of the Arctic, little is known about how much OC is transformed into greenhouse gases (GHGs). In this study we investigated two different coastal erosion scenarios on Qikiqtaruk – Herschel Island (Canada) and estimate the potential for GHG formation. We distinguished between a *delayed* release represented by *mud debris* draining a coastal thermoerosional feature and a *direct* release represented by *cliff debris* at a low collapsing bluff. Carbon dioxide (CO_2) production was measured during incubations at 4°C under aerobic conditions for two months and were modeled for four months and a full year. Our incubation results show that *mud debris* and *cliff debris* lost a considerable amount of OC as CO_2 (2.5 ± 0.2 and 1.6 ± 0.3% of OC, respectively). Although relative OC losses were highest in mineral *mud debris*, higher initial OC content and fresh organic matter in *cliff debris* resulted in a ∼three times higher cumulative CO_2 release (4.0 ± 0.9 compared to 1.4 ± 0.1 mg CO_2 gdw^{-1}), which was further increased by the addition of seawater. After four months, modeled OC losses were 4.9 ± 0.1 and 3.2 ± 0.3% in set-ups without seawater and 14.3 ± 0.1 and 7.3 ± 0.8% in set-ups with seawater. The results indicate that a *delayed* release may support substantial cycling of OC at relatively low CO_2 production rates during long transit times *onshore* during the Arctic warm season. By contrast, *direct* erosion may result in a single CO_2 pulse and less substantial OC

cycling *onshore* as transfer times are short. Once eroded sediments are deposited in the *nearshore*, highest OC losses can be expected. We conclude that the release of CO_2 from eroding permafrost coasts varies considerably between erosion types and residence time *onshore*. We emphasize the importance of a more comprehensive understanding of OC degradation during the coastal erosion process to improve thawed carbon trajectories and models.

Keywords: Arctic, coastal erosion, carbon cycling, biogeochemistry, greenhouse gases, carbon dioxide, biomarkers

INTRODUCTION

The Arctic is outpacing the global warming trend, which has severe impacts on ecosystems and biogeochemical pathways (Ciais et al., 2013; AMAP, 2017). With increasing temperatures, a cascade of environmental responses is initiated. Permafrost is warming and rapidly thawing, sea ice is declining in thickness and extent, seawater temperature is rising and wave and storm intensity are increasing (Manson and Solomon, 2007; Overeem et al., 2011; Schuur et al., 2015; Biskaborn et al., 2019; Dai et al., 2019). Arctic coastlines are particularly vulnerable to thaw and erosion due to the combined effects of environmental change (Barnhart et al., 2014; Fritz et al., 2017; Nielsen et al., 2020). Along with permafrost coasts, Arctic river deltas, estuaries and wetlands are increasingly impacted by sea level rise and glacier melt (Bendixen et al., 2017; Ward, 2020). These systems provide important ecosystem services (Forbes, 2019) but are currently facing changes in their sedimentation dynamics, which impacts organic matter pathways in the coastal zone (Bendixen et al., 2017; Ward, 2020). Permafrost coasts are the dominant interface between the northern landmass and the Arctic Ocean. Therefore, coastal erosion is a key driver for carbon and sediment transport into the Arctic Ocean (Stein and Macdonald, 2004; Macdonald et al., 2015; Wegner et al., 2015). Approximately two third of the Arctic coastline is composed of ice-rich and unconsolidated permafrost sediments prone to degradation, resulting in average erosion rates of 0.57 m yr^{-1} and extremes of $>$ 25 m yr^{-1} (Are et al., 2008; Jones et al., 2009, 2018; Lantuit et al., 2012; Günther et al., 2013, 2015). With erosion, the massive reservoir of seasonally unfrozen and permafrost organic carbon (OC) in the Northern Hemisphere that stores ∼1,300 Pg (10^{15} g) OC is accessed at its coastal margins (Lantuit et al., 2012; Hugelius et al., 2014; McGuire et al., 2018). Recent studies estimate that the erosion of permafrost coasts transfers up to 430 Tg yr^{-1} of sediment and 14 Tg yr^{-1} of OC into the Arctic Ocean (Wegner et al., 2015). In the current understanding of Arctic carbon cycles, coastal erosion is considered to play a modest role in the transfer of OC from land to the Arctic Ocean (McGuire et al., 2009; Stein and Macdonald, 2004; Macdonald et al., 2015). Recent studies on abrupt permafrost erosion on land, however, suggest that OC is already fundamentally altered upon permafrost thaw, erosion and transport in aquatic systems on land, during which greenhouse gases (GHGs) can be released to the atmosphere (Abbott and Jones, 2015; Mann et al., 2015; Spencer et al., 2015; Heslop et al., 2017). During these erosional processes, the composition of OC is altered substantially with a substantial fraction potentially transformed into carbon dioxide (CO_2) and methane (CH_4), depending on oxygen availability (Vonk et al., 2012; Semiletov et al., 2016; Tanski et al., 2019). Yet, the degradation of OC from thawing permafrost coastlines has barely been considered (Vonk and Gustafsson, 2013; Fritz et al., 2017).

Coastal erosion releases large amounts of readily degradable permafrost OC, which is transported on relatively short transit times from land to sea with a high potential for GHG release (Vonk et al., 2012; Tanski et al., 2019). Once it enters the ocean, OC can be either further degraded within sediments and the water column or buried in marine sediments (Vonk et al., 2014; Bröder et al., 2018; Couture et al., 2018; Grotheer et al., 2020; Jong et al., 2020). Yet, little is known about the potential GHG formation during erosion as well as within the coastal *nearshore* corridor that receives the eroded sediments before entering the marine domain. While more comprehensive information on GHG production exist for terrestrial permafrost sites and the Arctic shelf, the coast itself remains sparsely investigated with GHG measurements only available for selected locations (Vonk et al., 2012; Shakhova et al., 2010, 2015; Karlsson et al., 2015; Overduin et al., 2015; Tanski et al., 2019). Furthermore, the biogeochemical response of permafrost OC upon erosion may depend on coastal morphology and organic matter composition. Along coastlines with thermoerosional features and high bluffs, OC may encounter long transfer times *onshore* resulting in a *delayed* release to the sea with GHG formation already taking place *onshore* (**Figures 1A,B**). In contrast, at sites with low bluffs (**Figures 1C,D**), block-failure, active layer detachment slides or cliff collapse, OC may follow a more *direct* transfer pathway to the ocean. Thus, the type of erosion is strongly related to coastal morphology and may play a substantial role for the magnitude, timing and locus of GHG release. Local bathymetry and shelf morphology further determine the fate of OC and its potential for degradation offshore with rapid burial and sequestration limiting degradation but resuspension facilitating OC turnover in the *nearshore* (Solomon, 2005; Vonk et al., 2012; Hilton et al., 2015; Spencer et al., 2015; Bröder et al., 2018; Grotheer et al., 2020; Jong et al., 2020).

Although geomorphologic studies on coastal erosion processes are manifold (e.g., Barnhart et al., 2014; Günther et al., 2015; Jones et al., 2018), these studies do not target the OC fraction or relate morphology to the understanding of OC degradation and GHG dynamics. Bridging this information void on OC transformation during land-ocean-transit and the geochemical response during coastal erosion is key to better constrain biogeochemical pathways of OC in a warming

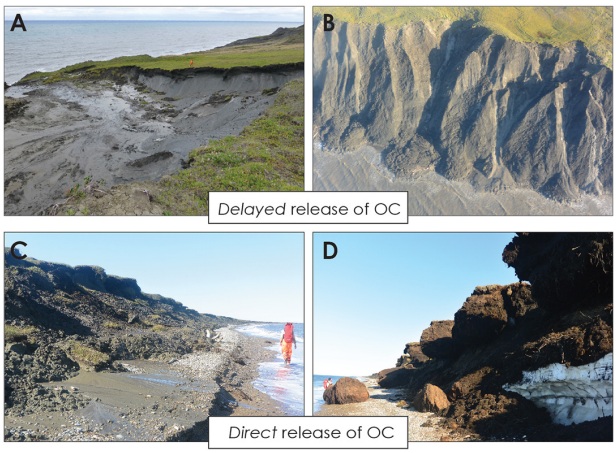

FIGURE 1 | Examples of coastal erosion types along the Yukon coast (Canadian Arctic, Beaufort Sea). Thermoerosional features and high coastal bluffs may lead to organic matter degradation *onshore* due to longer transport times and a *delayed* release into the ocean **(A,B)**. Along low bluffs, permafrost debris collapses on the beach and is removed relatively quickly by waves via a more *direct* pathway into the *nearshore* zone **(C,D)**. Photographs were taken by A. Irrgang and G. Tanski in August 2015 on Qikiqtaruk – Herschel Island **(A,B)** and the western Yukon coast **(C,D)**.

Arctic and support Earth climate modeling approaches. The objective of this study is to investigate the CO_2 production at two contrasting erosion sites along Arctic permafrost coasts to better determine the pathways and turnover of OC during transport from land to sea.

STUDY AREA

The study area Qikiqtaruk – Herschel Island is situated ∼2 km off the Yukon coast on the narrow Beaufort Sea Shelf (**Figure 2**). The local climate conditions are polar continental with mean annual air temperatures of −8.4°C (1995 to 2016) (Coch et al., 2018) and precipitation of ∼170 mm yr^{-1} (Burn, 2012). During the peak of the warm season in July temperatures are on average 7.8°C with extremes of 30°C possible (Burn, 2012). The dominant wind directions are northwest and east with storms being frequent in August and September (Dunton et al., 2006). The island is a push moraine ridge formed ∼18,000 to 23,000 years ago during the Wisconsin Glaciation with a maximum elevation of 183 m (Rampton, 1982; Pollard, 1990; Fritz et al., 2012). The sediments are composed of unconsolidated and fine-grained material of marine and glacigenic origin with glacier ice buried below the island (Blasco et al., 1990; Fritz et al., 2012). A rolling landscape incised by valleys with a lowland tundra vegetation dominated by *graminoids* and dwarf shrubs is typical for the island (Smith et al., 1989; Kennedy et al., 2001). The island is underlain with continuous permafrost with a shallow seasonal active layer of ∼40–60 cm in thickness, which has deepened by 15–25 cm since the 1980s (Kokelj et al., 2002; Burn and Zhang, 2009). The surface sediments (up to ∼1 m depth) on the island store ∼35 kg OC m^{-2} with OC storage being lower in areas of mass wasting and higher at sites of accumulation (Obu et al., 2015; Ramage et al., 2019). Permafrost sediments mainly consist of mineral soils with elevated but strongly varying OC contents when cryoturbation occurs (average 6.0 ± 4.7 wt% TOC; Tanski et al., 2017). The ground is very ice-rich with mean volumetric ground ice contents of 30–60% and maximum volumes exceeding 90%, where massive ice beds and wedge ice are present (Couture and Pollard, 2015). The open water season lasts approximately from late June to early October with landfast ice being persistent in Herschel Basin and Thetis Bay (Dunton et al., 2006). The mean tides are 0.15 m and are superimposed to a 0.66 m annual tidal cycle in late July (Huggett et al., 1975; Barnhart et al., 2014). Regional sea-level rise proceeds at rates of 1.1–3.5 mm yr^{-1} (Manson et al., 2005; James et al., 2014). The prevailing wind directions can influence water levels with northwest winds promoting a positive (higher water level) and eastern winds a negative storm surge (Hequette and Barnes, 1990; Héquette et al., 1995). The Mackenzie River plume has a strong influence on the coastal waters and transports warm water masses towards Qikiqtaruk – Herschel island, which is amplified with easterly winds (Dunton et al., 2006). Qikiqtaruk – Herschel Island is strongly impacted by thermoerosional processes and shoreline retreat. Retrogressive thaw slumps are ubiquitous and doubled in area since the 1950s (Lantuit and Pollard, 2005). On average, the island erodes at 0.68 m yr^{-1} (2000 to 2011), which is comparable to the average rates of the Yukon coast with 0.7 m yr^{-1} and the circum-Arctic with 0.57 m yr^{-1} (Lantuit et al., 2012; Obu et al., 2016; Irrgang et al., 2018). Extreme erosion rates of 14 and 22 m yr^{-1} were observed at low cliffs and active thaw slump systems, respectively (Obu et al., 2015; Cunliffe et al., 2019).

MATERIALS AND METHODS

Field Work and Sampling

Permafrost erosion debris was sampled at two active coastal erosion sites on Qikiqtaruk – Herschel Island in July and August 2017 (**Figure 2**). *Mud debris* was sampled from a mud lobe draining a retrogressive thaw slump system (**Supplementary Figure 1**) representing the *delayed* release scenario, where eroded material has relatively long residence times *onshore* before release into the ocean. We targeted a retrogressive thaw slump since these features are ubiquitous along the coastline of the western Canadian Arctic (**Figures 1A**, **2**; Pelletier and Medioli, 2014; Ramage et al., 2017). This specific thaw slump was chosen because CO_2 degradation rates of permafrost from the thaw slumps headwall are known (Tanski et al., 2019) and are used as a permafrost reference for CO_2 release *onshore*. The mud lobe draining the thaw slump is a mix of thawed permafrost, collapsed active layer and melted massive ice (e.g., buried glacier ice, wedge ice), and can be either transported directly towards the ocean or stored temporarily in mud pools on annual or decadal time scales before release into the ocean (Cray and Pollard, 2015; Tanski et al., 2017). Five samples have been taken from the mud lobe at random locations and one composite sample, *mud debris* (MUD), mixed in equal amounts from the mud lobe samples under frozen conditions in the cold lab (**Table 1**).

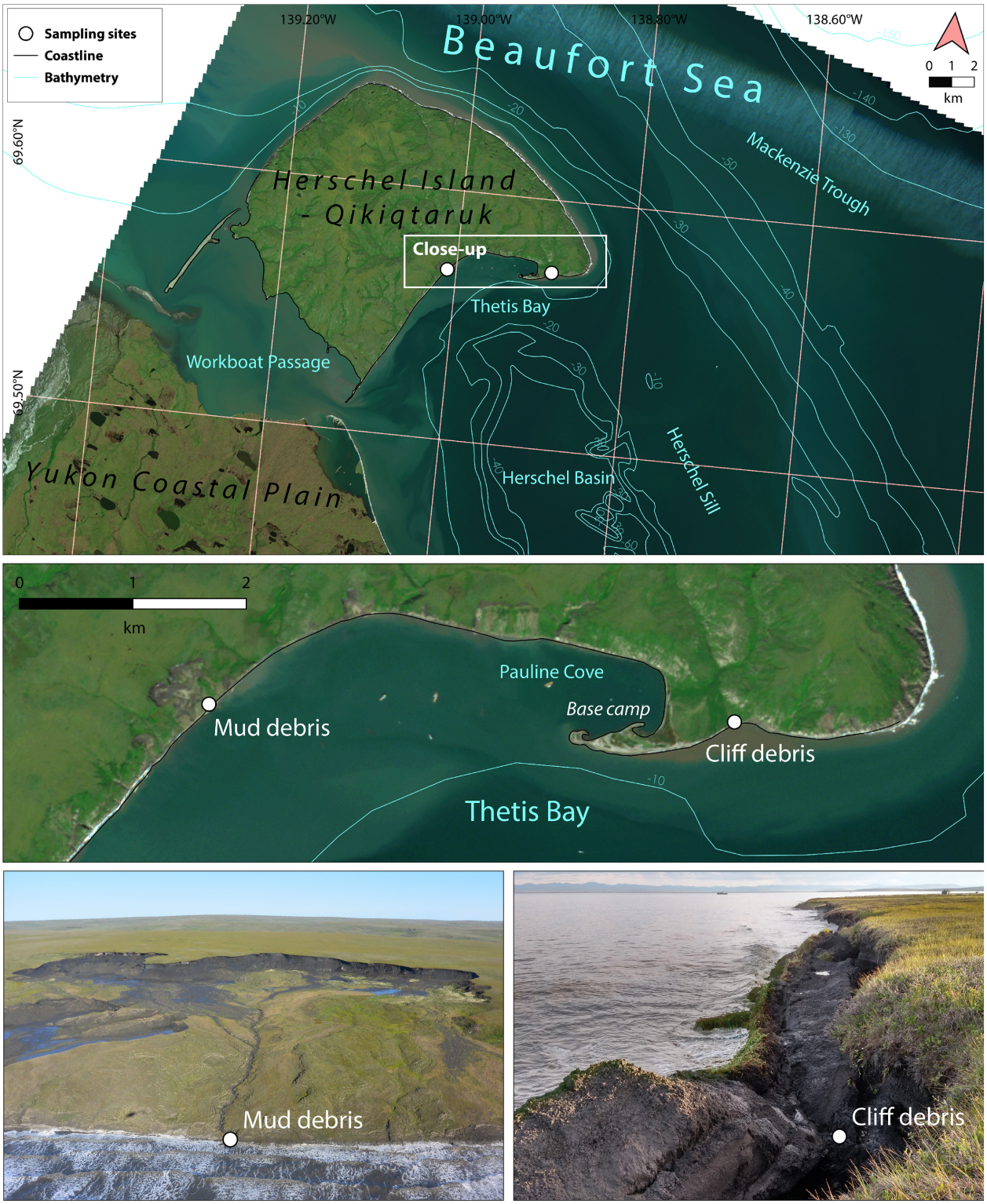

FIGURE 2 | Study area Qikiqtaruk - Herschel Island off the Yukon coast in the western Canadian Arctic. The sampling sites *mud debris* (*delayed* release) and *cliff debris* (*direct* release) are situated in the south-eastern part of the island (close-up: middle panel). The *mud debris* was taken from a mud lobe draining a retrogressive thaw slump system (lower left panel) and the *cliff debris* from an eroding cliff at the rim of an alluvial fan (lower right panel). Exact sampling locations are displayed in **Supplementary Figure 1**. Plumes and a turbid *nearshore* water column are visible and indicate substantial input and transport of eroded sediments. Satellite imagery: Sentinel 2, RGB (27 July 2017).

TABLE 1 | Summary of bulk organic matter and lipid biomarkers (*n*-alkanes) for initial (T = 0) and incubated *mud debris* (MUD) and *cliff debris* (CD) samples after two months (T = 1).

	Mud lobe	MUD (T = 0)	MUD (T = 1)	MUD* (T = 1)	Cliff	CD (T = 0)	CD (T = 1)	CD* (T = 1)
Sedimentology	n = 5	n = 1	n = 5	n = 3	n = 5	n = 1	n = 1	n = 3
Mineral SA (m^2 g^{-1})	21.5	21.5	22.2	20.7	18.0	32.4	33.6	29.2
	± 0.6	–	±1.1	± 2.9	±4.5	–	–	± 2.7
Clay (vol.%)	17.7	17.2	–	–	15.4	19.9	–	–
	± 1.5	–			± 4.5	–		
Silt (vol.%)	69.1	71.7	–	–	70.4	66.7	–	–
	± 2.1	–			± 6.9	–		
Sand (vol.%)	13.2	11.1	–	–	14.2	13.5	–	–
	± 3.3	–			± 5.4	–		
Bulk organic matter	n = 5	n = 1	n = 5	n = 5	n = 5	n = 1	n = 3	n = 3
TOC (wt%)	1.4	1.5	1.4	1.5	2.0	7.0	6.3	7.2
	± 0.03	–	±0.0	± 0.0	±0.4	–	± 0.6	±0.2
OC loading (mg m^{-2})	0.6	0.7	0.6	0.8	1.1	2.1	1.9	2.5
	± 0.02	–	±0.03	± 0.1	±0.3	–	± 0.2	±0.2
TOC/TN (atomic ratio)	10.2	10.0	9.8	11.2	11.5	14.9	13.4	14.5
	± 0.2	–	±0.3	± 0.6	±0.5	–	± 0.7	±0.9
δ^{13}C-TOC (‰)	−25.8	−25.9	−25.9	−26.1	−26.0	−26.0	−26.0	−25.9
	± 0.1	–	±0.0	± 0.5	±0.2	–	± 0.1	±0.1
Δ^{14}C-TOC (‰)	−800	−834	−836	−800	−499	−261	−253	−221
	± 75	–	±8	± 45	±100	–	± 20	±2
Age (^{14}C yr)	13,332	14,352	14,454	13,028	5679	2365	2283	1945
	± 2685	–	±418	± 1631	±1896	–	± 210	±19
***n*-alkanes**	n = 5	n = 1	n = 5	n = 4	n = 5	n = 1	n = 2	n = 3
Total[a] (µg gdw^{-1})	9.2	9.2	34.5	30.8	12.3	8.8	55.8	55.2
	± 3.4	–	±4.5	± 0.9	±5.6	–	± 6.9	±5.8
LMW[b] (µg gdw^{-1})	0.4	0.4	6.0	5.0	0.7	0.5	8.0	6.6
	± 0.2	–	±1.0	± 0.9	±0.7	–	± 2.7	±1.2
HMW[c] (µg gdw^{-1})	7.6	7.6	18.5	15.5	10.2	7.2	34.4	35.0
	± 2.9	–	±2.0	± 3.4	±4.5	–	± 4.2	±5.1
CPI[d] (C_{22-34})	4.6	4.6	2.8	2.4	6.3	5.5	3.5	4.1
	± 0.2	–	±0.3	± 0.2	±0.9	–	± 0.1	±0.5
HMW/LMW[e]	17.7	17.7	3.1	3.1	20.6	13.8	4.7	5.6
	± 5.3	–	±0.4	± 0.5	±9.3	–	± 1.1	±1.5
LMW-even/HMW-odd[f]	0.14	0.14	0.77	0.92	0.14	0.16	0.52	0.46
	± 0.04	–	±0.03	± 0.1	±0.08	–	± 0.08	±0.13

Values are given as mean with standard deviation (±) and sample size (n). The asterisk (*) indicates incubation set-ups with seawater. "Mud lobe" and "cliff" samples are in situ samples and were not incubated.

[a] $\Sigma\ C_{14-35}$.

[b] $\Sigma\ C_{14-19}$.

[c] $\Sigma\ C_{23-35}$.

[d] $CPI = 0.5\ \Sigma\ (x_i + x_{i+2} + \ldots + x_n)/\Sigma\ (x_{i-1} + x_{i+1} + \ldots + x_{n-1}) + 0.5\ \Sigma\ (x_i + x_{i+2} + \ldots + x_n)/\Sigma\ (x_{i+1} + x_{i+3} + \ldots + x_{n+1})$ with x being the concentration.

[e] $\Sigma\ C_{23-35}/\Sigma C_{14-19}$.

[f] Σ even C_{16-20}/Σ odd C_{27-31}.

The second site was a low permafrost cliff (< 5 m height) located at an alluvial fan (**Figure 2**), where *cliff debris* was collected. We chose this site to represent the *direct* release scenario with short residence time of eroded material *onshore*. This site was chosen since the erosion type is common along coasts with lower coastal bluffs (**Figures 1C,D**, **2**), where eroded material has shorter residence times *onshore* due to fast removal by wave action at high tides and storm surges (Radosavljevic et al., 2016; Cunliffe et al., 2019). We took five samples from the cliff face (Cliff, **Table 1**) and one sample from the *cliff debris* (CD) collected at the cliff toe assuming it to be an integrated signal of the *cliff* (**Table 1**). In contrast to MUD, no composite mix sample was used as we assumed that the cliff material was much more heterogeneous than the mud lobe. Thus, a mixing would have introduced an artificial bias as the mixing ratio was unclear. Surface seawater (SW) was collected approximately 2 km offshore, where water was clear and outside the range of visible erosion plumes.

All non-frozen samples from the mud debris and cliff debris (∼250–500 g wet-weight) were taken with a pre-cleaned sampling

spoon and stored in Whirl-pak bags. Samples were taken from approximately 5–10 cm below the surface, at locations where material seemed to be well-mixed during the post-erosive transport process and therefore considered representative. All (frozen) permafrost samples from the cliff face were taken with a drill hammer (Hilti, Liechtenstein) after scraping off the potentially thawed material from the cliff surface. Samples (∼500 g wet-weight) were stored in Whirl-pak bags and stored frozen in a cooler immediately to avoid thaw. Seawater was taken from the sea surface in pre-rinsed (three times) 1L Nalgene bottles. All sampled materials, including seawater, were kept frozen at −20°C until further processing in the laboratories.

Incubation Set-Ups

We simulated the erosion of *mud debris* and *cliff debris onshore* as well as in the *nearshore* in a laboratory incubation experiment at GFZ Potsdam to assess potential carbon pathways in this coastal transition zone. *Onshore* refers to incubation set-ups without seawater, mimicking erosion on land, while *nearshore* set-ups with seawater added were designed to mimic erosion into the seawater column. Frozen *mud debris* and *cliff debris* samples were homogenized and subsamples of ∼20 g placed into 120 ml glass vials (autoclaved at 125°C) at −15°C in a cold lab. The frozen seawater (SW) sample was melted slowly at 7°C in a cool (dark) room and shaken thoroughly. Just before the start of the incubation ∼30 ml of unfiltered seawater was added to the glass vials with subsamples for the *nearshore* incubation set-ups. Afterwards, the vials were sealed with a rubber septum and the headspace (ca. 90 to 100 ml) was flushed with synthetic air (Linde, Germany) consisting of 20% oxygen (O_2) and 80% nitrogen (N_2). Vials were then placed in an incubator at 4°C shielded from light. Aerobic conditions were applied by flushing the headspace with synthetic air after each CO_2 measurement to represent venting and associated oxygen supply likely occurring during the erosion process *onshore* as well as in the immediate *nearshore*. The incubation period was set to two months to capture the initial period of highest CO_2 production (Tanski et al., 2019) and conducted at 4°C as it is close to the ambient Arctic sea surface temperatures and comparable to most published permafrost incubation studies (Dutta et al., 2006; Lee et al., 2012; Schädel et al., 2014).

Hydrochemistry

Basic hydrochemical parameters pH and electrical conductivity were measured with a 3430 Digital Multiparameter meter (WTW, Germany) at room temperature at AWI Potsdam, Germany. Seawater was filtered with a 0.7 μm GF/F filter (Whatman, United Kingdom) and acidified with HCl (suprapur grade 30%) to pH 2. Dissolved organic carbon (DOC) and dissolved nitrogen (DN) concentrations were analyzed with a Shimadzu analyzer (Shimadzu, Japan) at AWI Bremerhaven, Germany.

Gas Measurements and Mass Calculation

CO_2 and CH_4 concentrations were measured with a 7890A GC (Agilent, United States) at GFZ Potsdam, Germany. Gas samples were taken on a regular basis (every other day during the first two weeks and two times a week afterwards) with a gastight syringe from the headspace of the vials and were immediately injected into the gas chromatograph. Afterwards, the headspace was flushed with synthetic air to reset aerobic conditions. After each measurement, glass vials were shaken to simulate mixing of sediments during mass movement *onshore* and by wave action and currents in the *nearshore*. The gas production was measured in parts per million (ppm) and normalized to gram dry weight (gdw^{-1}) of initial sediment. The total amount of CO_2 and CH_4 (μmol) was calculated following the methodology by Knoblauch et al. (2018) using gas concentration, headspace volume, water volume, pH, temperature and solubility including carbonate and bicarbonate concentrations for CO_2 calculations (Millero et al., 2007). All gas that remained in the glass vials after flushing was accounted for by assuming that CO_2 in the headspace was completely removed with flushing but dissolved inorganic carbon (DIC) remained in the glass vials. The derived amount of CO_2 in μmol was normalized to gdw^{-1} and recalculated into mg CO_2 gdw^{-1} using the molar mass (M) of CO_2 (44). In this study, we only report CO_2 as incubations conditions were aerobic.

Bulk Elemental and Isotopic Analyses

Sediments were weighed, freeze-dried and homogenized before chemical analysis. Elemental and stable carbon isotope analysis was conducted at AWI Potsdam, Germany, following established methodology (e.g., Schirrmeister et al., 2018). Total carbon (TC) and total nitrogen (TN) contents were measured with a VARIO EL III element analyzer (Elementar, Germany) and total organic carbon (TOC) with a VARIO MAX C analyzer (Elementar, Germany), both with a device-specific accuracy of ± 0.1wt %. For stable carbon isotope (δ^{13}C-TOC), carbonates were removed from sediments with 1.3 molar hydrochloric acid (HCl) at 95°C for three hours. Stable carbon isotopes were then measured at the Isotope Facility at AWI Potsdam with a Delta-V-Advantage mass spectrometer (MS) (Thermo Fisher Scientific, Germany) coupled with a CONFLO IV gas mixing system. Stable carbon isotope contents are given in per mil (‰) relative to the standard Vienna Pee Dee Belemnite (VPDB) with an external error better than ± 0.15‰. Radiocarbon (^{14}C-TOC) measurements were performed at the Biogeoscience laboratories and the Laboratory for Ion Beam Physics at ETH Zürich, Switzerland. Carbonates were removed by fumigation with HCl (37%, trace-metal purity) at 60°C for 72 h and samples measured on a coupled elemental analyzer-accelerator mass spectrometer (EA-AMS) system with a vario MICRO cube (Elementar, Germany) coupled to a Mini Carbon Dating System MICADAS (Ionplus, Switzerland) (e.g., Ruff et al., 2010). Radiocarbon values are reported in Δ^{14}C (‰) and ^{14}C-age as uncalibrated years (^{14}C yr).

Grain Size Analysis

Grain size of sediment particles was analyzed at AWI Potsdam following an established methodology (Schirrmeister et al., 2020). Organic material was removed by adding 100ml of 3% H_2O_2 over 3 to 6 weeks while on a shaking table. Organic-free sediments were then dispersed in 1L of water with dispersing agent (NH_4OH) in an overhead shaker to de-cluster particles.

Subsamples were then measured with a laser diffraction particle analyzer (Malvern Mastersizer 3000) with grain sizes measured between 0.375 to 1000 μm applying the Frauenhofer optical model. The cut-off value at 1000 μm was pre-set due to technical limitations of the particle analyzer.

Surface Area Analysis

Mineral surface area (SA) was measured to characterize the sediment structure of coastal debris. Approximately 1 g of subsampled sediment was combusted at 450°C for 12 h and rinsed with ultrapure water (MilliQ) to remove OC and salt, respectively. Afterwards, samples were freeze dried, degassed at 300°C with a vacuum applied for two hours and SA measured with a Nova 4200e SA analyzer (Quantachrome, United States) using the 6-point Brunauer–Emmett–Teller method (Brunauer et al., 1938).

Extraction and Analysis of Lipid Biomarkers

Lipid biomarkers (long-chain high molecular weight *n*-alkanes) were used to investigate the molecular composition of organic matter and its state of degradation (Eglinton and Hamilton, 1967). Lipid biomarkers were extracted at Vrije Universiteit Amsterdam, The Netherlands. Sediments (∼1 to 5 g) were extracted with a microwave digestion system MARS 6 (CEM, Germany) using dichloromethane (DCM) and methanol (MeOH) (9:1-volume ratio) at 100°C for 15 min. Microwave extracts were saponified with 10 ml potassium hydroxide (KOH, 0.5 M) in MeOH at 70°C for two hours. The neutral fraction was separated by wet-extraction with hexane following addition of 5 ml ultrapure water (MilliQ) with sodium chloride (NaCl). The neutral fraction was further separated into a-polar (containing the *n*-alkanes) and polar fractions by column chromatography using 5% deactivated silica (SiO_2). The *n*-alkanes were analyzed with a gas chromatograph mass spectrometer (GC-MS, Agilent, United States) at the Institute of Polar Sciences in Bologna, Italy. The GC temperature program started at 55°C followed by a ramp up of 4 to 5°C min^{-1} to a maximum temperature 300 to 310°C for 15 to 20 min. Lipid biomarker concentrations are given in μg g^{-1} TOC. In this study concentrations are reported in μg gdw^{-1} to use the same normalization as for cumulative CO_2 production.

Bulk and Molecular Degradation Proxies

We used several established proxies to assess the degradation state of organic matter. Molar TOC/TN-ratios (atomic ratio) and δ^{13}C-TOC values were used as general indicators for bulk organic matter origin, preservation and degradation state (Kuhry and Vitt, 1996; Lamb et al., 2006; Gundelwein et al., 2007).

A low TOC/TN-ratio or relative decrease indicates degradation with a preferential mineralization of TOC and immobilization of TN by microbes coupled to CO_2 release under aerobic conditions (Sollins et al., 1984; Stevenson, 1994; Strauss et al., 2015). High δ^{13}C-TOC values (enriched in ^{13}C, i.e., less negative values) indicate decomposition as organic matter degradation discriminates against the lighter carbon component (^{12}C), which results in a more negative δ^{13}C signature in the degrading fraction (Heyer et al., 1976; Strauss et al., 2015).

On a molecular level, we used the carbon preference index (CPI) for *n*-alkanes (ratio of odd over even-numbered C chain length homologues C_{22-34}) as indicator for the degree of microbial alteration of organic matter (Bray and Evans, 1961; Killops and Killops, 2004; Strauss et al., 2015). Living plants normally have CPI values greater 5 and decrease towards 1 with increasing maturity (Rielley et al., 1991; Vonk et al., 2010). High CPI values therefore indicate the presence of fresh organic matter, while mature or degraded organic matter displays lower CPI values. We further used high-molecular weight (HMW) to low-molecular weight (LMW) ratios of *n*-alkanes ($\Sigma C_{23-35}/\Sigma C_{14-19}$) as indicators for degradation since with ongoing degradation HMW compounds are broken down into LMW compounds (Killops and Killops, 2004). Additionally, we used the LMW-even to HMW-odd *n*-alkane ratio ($C_{16+18+20}/C_{27+29+31}$) with an increasing ratio indicating stronger microbial activity and degradation (Grimalt and Albaigés, 1987; Sánchez-García et al., 2014).

CO_2 Production and Model

The total CO_2 production (cum. CO_2 gdw^{-1}) over 60 days and daily production rates (μg CO_2 gdw^{-1} day^{-1}) give information on the magnitude and rates of initial aerobic TOC decomposition in a given sample and are commonly used as degradability indicators (e.g., Schädel et al., 2014). With the known total amount of CO_2 released we calculated the TOC loss in %.

CO_2 production was modeled four months and one year using an applied carbon decomposition model (Andrén and Kätterer, 1997; Knoblauch et al., 2013). The model is based on a first-order kinetic function, which reflects changes in OC content over time and considers how fast OC pools are being decomposed. Degradation rates were estimated using a non-linear least squares approach with an integrated trust-region-reflective algorithm in MATLAB (MathWorks, United States). The cumulative CO_2 production measured during the incubation was used to calibrate the model. A logarithmic transformation was applied to estimate decomposition time of OC for four months and an entire year.

RESULTS AND DISCUSSION

Organic Matter Origin and Composition

The composition of organic matter at the sampling sites was considerably different for most of the parameters considered (**Table 1**). The sediments at the investigated erosion sites mud lobe (n = 5) and cliff (n = 5) had TOC contents (1.4 ± 0.03 and 2.0 ± 0.4%), TOC/TN-ratios (10.2 ± 0.2 and 11.5 ± 0.5) and δ^{13}C concentrations (−25.8 ± 0.1 and −26.0 ± 0.2‰) typical for sediments containing terrestrial organic matter. Grain size structure was similar in both with the bulk of material (∼70 vol.%) composed of silt but was much more variable in the cliff (**Supplementary Figure 2**). The generally better sorting of mud lobe sediments may reflect hydrodynamic sorting during transport on land. The relatively high HMW/LMW *n*-alkane ratios ($\Sigma C_{23-35}/\Sigma C_{14-19}$) in mud lobe (17.7 ± 5.3) and cliff

(20.6 ± 9.3) samples indicated good preservation of wax lipids from terrestrial plant matter (Karlsson et al., 2015; Strauss et al., 2015). This is supported by a relatively high (close to 5) CPI for long-chain *n*-alkanes (C_{22-34}) in mud lobe and cliff sediments (4.6 ± 0.2 and 6.3 ± 0.9, respectively). The lower TOC/TN-ratios and $\delta^{13}C$ values in the mud lobe in combination with lower HMW/LMW ratios and CPI for *n*-alkanes indicated slightly more matured organic matter in the mud lobe and better preserved organic matter in the cliff. The ^{14}C-age of OC varied considerably between the sites with relatively old organic matter in the mud lobe (13,332 ± 2685 ^{14}C yr), most likely originating from deposition after the Wisconsin glaciation (Pollard, 1990; Fritz et al., 2012) and younger material in the cliff (5679 ± 1896 ^{14}C yr), which was potentially deposited during Holocene warm periods (Burn, 1997; Kaufman et al., 2009; Fritz et al., 2012).

The *mud debris* (MUD, $n = 1$) was a mixed sample of the mud lobe deposits and thus showed the same organic matter composition and ^{14}C-age (14,352 ^{14}C yr). Compared to the mud lobe this indicates its origin from thawed old permafrost, which was likely augmented by active layer material, melted massive ice and old slump floor deposits during transport (Lantuit and Pollard, 2005; Cray and Pollard, 2015; Tanski et al., 2017). Mineral SA of *mud debris* was 21.5 m^{-2} gdw^{-1}, reflecting the presence of fine-grained sediments in the silt and clay size fraction making up ∼72 and 17 vol.% (**Table 1**), respectively. In combination with relatively low TOC contents (1.5 wt%), the OC loading of *mud debris* was 0.7 mg OC m^{-2}. Collapsed active layer chunks from the slump headwall, which contained more modern and OC-rich sediments are usually (temporarily) deposited within the slump floor and mud lobe if not already transported offshore with the thaw stream draining the slump system (Kokelj et al., 2013; Tanski et al., 2017). During transport and mass wasting within the slump, a substantial portion of the organic matter was likely subject to degradation, resulting in the low TOC contents of the mud lobe and *mud debris* that was used in the incubation (Cray and Pollard, 2015; Tanski et al., 2017). This was supported by the much lower TOC content and TOC/TN-ratio (10.0) of the *mud debris* than the thaw slump headwall sediments (∼5 wt% and > 15, respectively; Tanski et al., 2017). These slump sediments were also characterized by the presence of fresh organic matter, reflected by CPI values for *n*-alkanes of close to 30 (Tanski et al., 2017).

The *cliff debris* (CD, $n = 1$) collected from the permafrost cliff toe was markedly different in its organic matter composition, both compared to the cliff itself and the *mud debris*. The relatively high TOC content (7.0 wt%) and TOC/TN-ratio (14.9) in combination with its younger ^{14}C-age of 2365 ^{14}C yr and higher $\delta^{13}C$ values of −26.0 ‰ indicate a strong contribution from relatively fresh and modern sources and C_3-plant material that accumulated in the *cliff debris* (Lamb et al., 2006). The mineral SA of *cliff debris* was 32.4 m^2 g^{-1} and silt and clay volumes ∼70 and 20 vol.%, respectively, indicating the presence of very fine-grained sediment fractions which in combination with high OC contents result in a high OC loading (2.1 mg OC m^{-2}). The relatively high CPI (5.5) as well as relatively high HMW/LMW ratios for *n*-alkanes (13.8) support the presence of relatively fresh organic matter in the *cliff debris* (Rielley et al., 1991; Strauss et al., 2015).

Constant vs. Rapid CO_2 Release

Considerable amounts of CO_2 were produced from *mud debris* and *cliff debris* over the two-months incubation period (**Figure 3** and **Table 2**). The total amount of CO_2 produced was significantly different (ANOVA, $p < 0.05$) between both, *mud debris* (**Figure 3A**) and *cliff debris* (**Figure 3B**), alongside with CO_2 production rates (**Supplementary Figure 3** and **Table 2**). *Mud debris* continuously released CO_2 at a relatively low rate with a maximum production of 50.6 ± 4.5 μg CO_2 gdw^{-1} day^{-1} at the beginning, which decreased to 14.0 ± 1.8 μg CO_2 gdw^{-1} day^{-1} at the end of the incubation, yielding a total of 1.4 ± 0.1 mg CO_2 gdw^{-1} over a period of two months (**Figure 3A**). Yet, when normalized to TOC content, the cumulative CO_2 production was almost three times higher from *mud debris* (93.4 ± 7.6 mg CO_2 g TOC^{-1}) compared to *cliff debris* (36.1 ± 12.7 mg CO_2 g TOC^{-1}). Outgassing of CO_2 from inorganic or petrogenic sources might have contributed to the observed CO_2 release as petrogenic OC is common in the study area and reactions of carbonates with sulphuric acid producing CO_2 were observed in thaw slump systems (Goñi et al., 2005; Drenzek et al., 2007; Zolkos et al., 2018). In contrast to the *mud debris*, *cliff debris* produced ca. three times more CO_2, adding up to a total amount of 4.0 ± 0.9 mg CO_2 gdw^{-1} over the two months of incubation, which was likely caused by the higher initial TOC content (7.0 wt%) and OC loading (2.1 mg OC m^{-2}; **Table 2** and **Figure 4**). CO_2 production rates were fairly high within the first month. Maximum rates observed were 154 ± 25.7 μg CO_2 gdw^{-1} day^{-1} and decreased to 34.2 ± 12.5 μg CO_2 gdw^{-1} day^{-1} after two months of incubation.

The total amount of CO_2 released from *mud debris* mixed with seawater was virtually the same per gram sediment (1.4 ± 0.1 mg CO_2 gdw^{-1}) and similar per g OC (96.4 ± 2.3 mg CO_2 g TOC^{-1}) as without seawater added. The CO_2 production rates were also similar with a maximum of 48.5 ± 4.9 μg CO_2 gdw^{-1} day^{-1} at the beginning (day 7) and 23.7 ± 1.4 μg CO_2 gdw^{-1} day^{-1} at the end of the incubation. The most labile OC compounds may have been mineralized and released already as CO_2 during transport *onshore* before transfer with the mud lobe to the ocean (Vonk et al., 2012; Abbott et al., 2014; Sánchez-García et al., 2014). For *cliff debris* mixed with seawater, however, the total amount of CO_2 produced was significantly higher (5.7 ± 0.4 mg CO_2 gdw^{-1}, ANOVA, $p < 0.05$), corresponding to ∼1.5 times more CO_2 released compared to without seawater added. This pattern was similar but less pronounced when normalized to g OC with 51.0 ± 6.0 mg CO_2 g TOC^{-1}. The set-ups with seawater resulted in elevated CO_2 production rates with a maximum of 328 ± 99.3 μg CO_2 gdw^{-1} day^{-1}. The production was particularly high during the first month, which likely indicates the rapid decomposition of freshly exposed and labile OC (Knoblauch et al., 2013; Schädel et al., 2014). The production rate then decreased to 29.5 ± 6.5 μg CO_2 gdw^{-1} day^{-1}, a similar value as for the set-up without seawater added. An increase in CO_2 production with addition of seawater was also observed in earlier studies for thawing permafrost from the thaw slump

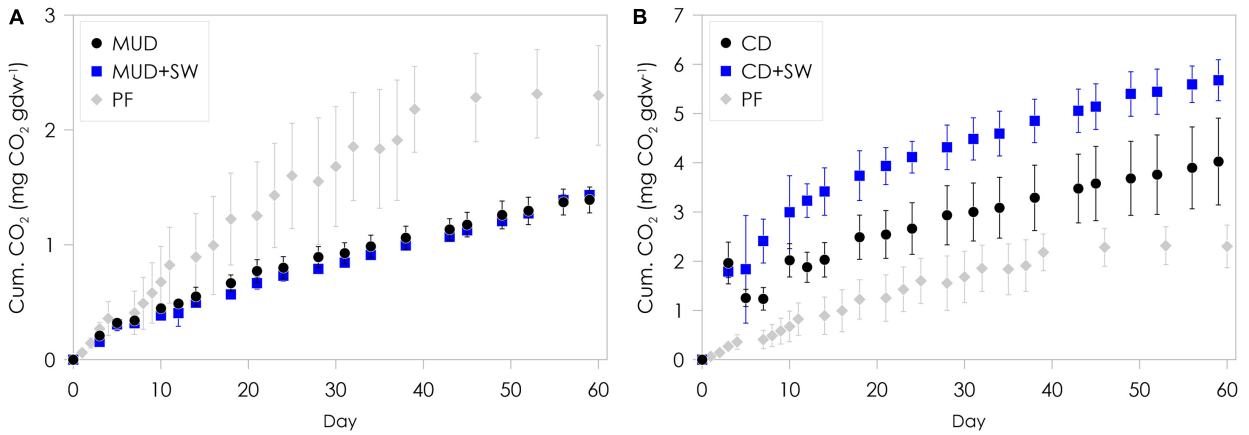

FIGURE 3 | Cumulative aerobic CO_2 production from incubated *mud debris* **(A)** and *cliff debris* **(B)**. *Mud debris* (MUD) and *cliff debris* (CD) were incubated without (black symbols) and with seawater (SW, blue symbols) for a duration of two months at 4°C under aerobic and dark conditions. Cumulative CO_2 production from permafrost (PF) is displayed as a local reference for CO_2 production from *in situ* permafrost without seawater (Tanski et al., 2019). The PF samples originate from the headwall of the thaw slump system from which the *mud debris* is released. The error bars show the standard deviation of the replicates used.

headwall, which might indicate a priming or co-metabolization effect (Bianchi, 2011; Tanski et al., 2019). Initial CO_2 production rates of *mud debris* were lower than those of *in situ* permafrost situated close to the sampling site in the thaw slump headwall (**Supplementary Figure 3**; Tanski et al., 2019). Yet, baseline production rates at the end of the two-month incubation period are slightly higher than from *in situ* permafrost. For *cliff debris,* initial as well as final CO_2 production rates were higher than for the permafrost reference site.

Following the CO_2 production in the first two months, the modeled CO_2 production and OC loss for the approximate length of the Arctic open-water season (∼four months) and an entire year, assuming that eroded sediments in the *nearshore zone* do not freeze-up anymore and that degradation is not only limited to the warm season, are substantially higher (**Table 2** and **Supplementary Figures 4, 5**). Model results explain ∼99% of the observed variations in CO_2 production for each individual sample and the residuals are usually unbiased and randomly scatter around zero. The only exceptions are residuals of cliff debris samples PI-14, PI-15 and PI-16 (**Supplementary Figure 5**), which show some pattern and hence should be dealt with cautiously. After four months, 2.7 ± 0.05 mg CO_2 gdw^{-1} would be released from mud debris *onshore*, corresponding to a TOC loss of $4.9 \pm 0.1\%$, which is slightly lower for set-ups with seawater added. The CO_2 release from *cliff debris onshore* would be 8.3 ± 0.8 mg CO_2 gdw^{-1} with TOC losses of $3.2 \pm 0.3\%$. This is also slightly lower when seawater is added. After one year upon erosion into the *nearshore*, *mud debris* would produce 6.1 ± 0.5 mg CO_2 gdw^{-1} with $11.1 \pm 0.9\%$ of the initial OC being lost. For *cliff debris* the CO_2 production would be much higher with 17.1 mg CO_2 gdw^{-1} corresponding to an OC loss of $6.9 \pm 1.7\%$. Model results based on set-ups without seawater show that the CO_2 release would be generally higher *onshore*. Yet, degradation is then limited to only ∼four months per year, making the erosion and year-round degradation of OC in the *nearshore* much more effective. On decadal timescales microbes would decompose the more refractory carbon pools and thus support further CO_2 production at low rates, adding to the cumulative release of CO_2 (Knoblauch et al., 2013; Schädel et al., 2014).

Experimental incubations that account for environmental conditions along eroding permafrost coastlines or continuous measurements of CO_2 or CH_4 from erosion sites are scarce in the Arctic, and our data are therefore challenging to put into context. GHG measurements are available from eroding permafrost cliffs at Muostakh Island (Siberian Arctic) with daily production rates ranging from 0.1 to 19.4 mg CO_2 m^{-2} day^{-1}, indicating intensive CO_2 release to the atmosphere in the warm season during erosion *onshore* (Vonk et al., 2012). For terrestrial permafrost sites elevated CO_2 concentrations of > 1000 ppm were observed at thermoerosional features such as active layer detachment slides, gullies and thaw slumps, which also released substantial amounts of CH_4 (Abbott and Jones, 2015). These features might closely resemble the biogeochemical response of permafrost and modern OC to coastal erosion *onshore* as these processes are common along eroding coastlines as well (**Figures 1A,B**). Once eroded into coastal waters, permafrost OC rapidly settles due to ballasting within mineral matrices but may further degrade during resuspension and lateral transport, thus further producing CO_2 (Vonk et al., 2012, 2014; Semiletov et al., 2016; Bröder et al., 2018; Tanski et al., 2019; Jong et al., 2020).

Organic Matter Degradation vs. CO_2 Production

The release of CO_2 during the course of only two months indicates that organic matter is quickly degraded during the coastal erosion process. The production of CO_2 was positively correlated to TOC content and was higher in the OC-rich *cliff debris* than *mud debris* (**Figure 4A**), which implies that CO_2 release is likely a function of the availability of fresh and degradable organic matter. This is supported by strong

TABLE 2 | Summary of observed and modeled cumulative CO_2 production and corresponding TOC loss in % as CO_2-C after two months (60 days), regional open-water season of four months (120 days) and a full year (365 days) for incubation set-ups with *mud debris* (MUD), MUD with seawater (SW), *cliff debris* (CD) and CD with SW.

	MUD *n* = 5	MUD + SW *n* = 5	CD *n* = 3	CD + SW *n* = 3
Incubation (60 days)				
Cum. CO_2 prod. (mg gdw^{-1})	1.4 ± 0.1	1.4 ±0.03	4.0 ± 0.9	5.7 ±0.4
Cum. CO_2 prod. (mg g TOC^{-1})	93.4 ± 7.6	96.4 ±2.3	36.1 ± 12.7	51.0 ±6.0
Cum. CO_2 prod. (μg m^{-2})	62.9 ± 7.0	76.3 ±10.3	119.8 ± 26.2	195.3 ±15.0
TOC loss (% as CO_2-C)	2.5 ± 0.2	2.6 ±0.1	1.6 ± 0.3	2.2 ±0.2
Max. CO_2 prod. rate (μg gdw^{-1} day^{-1})	50.6 ± 4.5	48.5 ±4.9	153.7 ± 25.7	328.4 ±99.3
End CO_2 prod. rate (μg gdw^{-1} day^{-1})	14.0 ± 1.8	23.7 ±1.4	34.2 ± 12.5	29.5 ±6.5
Model (120 days)				
Cum. CO_2 prod. (mg gdw^{-1})	2.7 ± 0.05	2.3 ±0.1	8.3 ± 0.8	6.8 ±1.6
TOC loss (% as CO_2-C)	4.9 ± 0.1	4.3 ±0.2	3.2 ± 0.3	2.7 ±0.6
Model (365 days)				
Cum. CO_2 prod. (mg gdw^{-1})	7.8 ± 0.1	6.1 ±0.5	18.7 ± 2.1	17.7 ±4.3
TOC loss (% as CO_2-C)	14.3 ± 0.2	11.1 ±0.9	7.3 ± 0.8	6.9 ±1.7

Maximum and end daily CO_2 production rates are reported additionally. All values are given as mean ± standard deviation with the sample size (n).

correlations between CO_2 production and initial *n*-alkane CPI values and TOC/TN-ratio (**Figure 4E**, **Supplementary Figure 6** and **Table 1**). Yet, relative TOC losses (% as CO_2-C) were significantly smaller (ANOVA, $p < 0.05$) in *cliff debris* (1.6 ± 0.3%) compared to *mud debris* (2.5 ± 0.2%) (**Figure 4B**). In general, the lower initial TOC content seems to correlate weakly with a higher (relative) TOC loss, suggesting that the old and OC-poor *mud debris* might be more prone to degradation than the relatively young and OC-rich *cliff debris* despite the lower total CO_2 release. This is expressed by the higher CO_2 production per g OC in *mud debris* (93.4 ± 7.6 mg CO_2 g TOC^{-1}) compared to *cliff debris* (31.1 ± 12.7 mg CO_2 g TOC^{-1}) (**Figures 4**, **4C**). In contrast, CO_2 production is higher from *cliff debris* when normalized to SA (119.8 ± 26.2 μg CO_2 m^{-2}) compared to *mud debris* (62.9 ± 7.0 μg CO_2 m^{-2}) (**Figure 4D**) as the mineral OC-loading for *cliff debris* is higher than for *mud debris*. The production is even higher in set-ups with seawater added, particularly for *cliff debris* (195.3 ± 15.0 μg CO_2 m^{-2}) compared to *mud debris* (119.8 ± 26.2 μg CO_2 m^{-2}). The *cliff debris* site seems to be accumulating OC-rich fine-grained sediments with high OC content, mineral SA and clay portions, which finally result in the higher CO_2 release, whereas in the coarser *mud debris* this material may already have been removed offshore with the thaw stream or redeposited within the slump. With addition of seawater, CO_2 release from *cliff debris* increased, yet not significantly (ANOVA, $p < 0.05$), alongside with TOC losses (2.2 ± 0.2%), whereas for *mud debris* CO_2 production was similar for the set-ups with and without seawater added. Although the higher relative TOC losses from *mud debris* imply that it is more prone to degradation than the relatively young and OC-enriched *cliff debris*, the addition of seawater resulted in an increase of CO_2 production and corresponding TOC loss only in *cliff debris*. This might suggest that within *mud debris* the most labile compounds were already removed, and not available for further degradation in seawater. During transport within the slump system, this removal may have occurred via melting of massive ice that promoted leaching and liberation of more labile OC compounds and mineralization to CO_2 or CH_4 *onshore* (Vonk and Gustafsson, 2013; Abbott et al., 2014; Mann et al., 2015; Tanski et al., 2017). The relatively low mineral SA and OC loading of *mud debris* compared to *cliff debris* also suggest that the finer sediment fraction hosting OC may have been removed quickly from the *mud debris* with the thaw stream to the sea (Jong et al., 2020).

Incubated *mud debris* and *cliff debris* showed no significant changes in TOC contents, TOC/TN-ratios as well as in δ^{13}C-TOC and Δ^{14}C-TOC signatures (**Supplementary Figure 6**, **Table 1**). This is not surprising given the minor TOC losses (max. 2.5% of initial OC as CO_2-C) during these short-term incubations of two months, and considering measurement uncertainties and natural heterogeneity of organic matter in individual samples. On a molecular level, however, organic matter degradation seems to be more pronounced (**Figure 4**, **Supplementary Figure 7**, and **Table 1**). The CPI for *n*-alkanes decreased in all set-ups, indicating degradation of this organic matter fraction. In *mud debris* the CPI decreased from 4.6 ± 0.2 to 2.8 ± 0.3 and 2.4 ± 0.2 without and with seawater added, respectively (**Figure 4E**). This is similar, although less distinct, in *cliff debris*, where the CPI decreased from 5.5 to 3.5 ± 0.1 and 4.1 ± 0.5. Although the marked decrease of the HMW/LMW-ratio of *n*-alkanes mainly indicates the reworking of plant wax lipids (**Figure 4F**), the increase of LMW-even to HMW-odd *n*-alkanes (**Supplementary Figure 7**) support the overall degradation of organic matter (Sánchez-García et al., 2014). Yet, LMW and HMW *n*-alkane concentrations increased in all set-ups indicating *in situ* production processes during the course of the incubation (**Table 1** and **Supplementary Figure 8**). Therefore, the used degradation proxies cannot unambiguously reflect the OC degradation process as production probably distorts the signal.

The concentration increase of LMW and HMW *n*-alkanes was highest for set-ups without seawater added. In the incubated *mud debris*, *n*-alkane concentrations increased for LMW *n*-alkanes from 0.4 to 6.0 ± 1.0 (5.0 ± 0.9 μg gdw^{-1} when mixed with seawater) and for HMW *n*-alkanes from 7.6 to 18.5 ± 2.0 (15.5 ± 3.4 μg gdw^{-1} with seawater). In *cliff debris*, this pattern was similar with LMW *n*-alkane concentrations increasing from 0.5 to 8.0 ± 2.7 μg gdw^{-1} (6.6 ± 1.2 μg gdw^{-1} with seawater). For the HMW *n*-alkane concentrations, there were virtually no differences between set-ups with or without seawater added. Concentrations increased from 7.2 to 34.4 ± 4.2

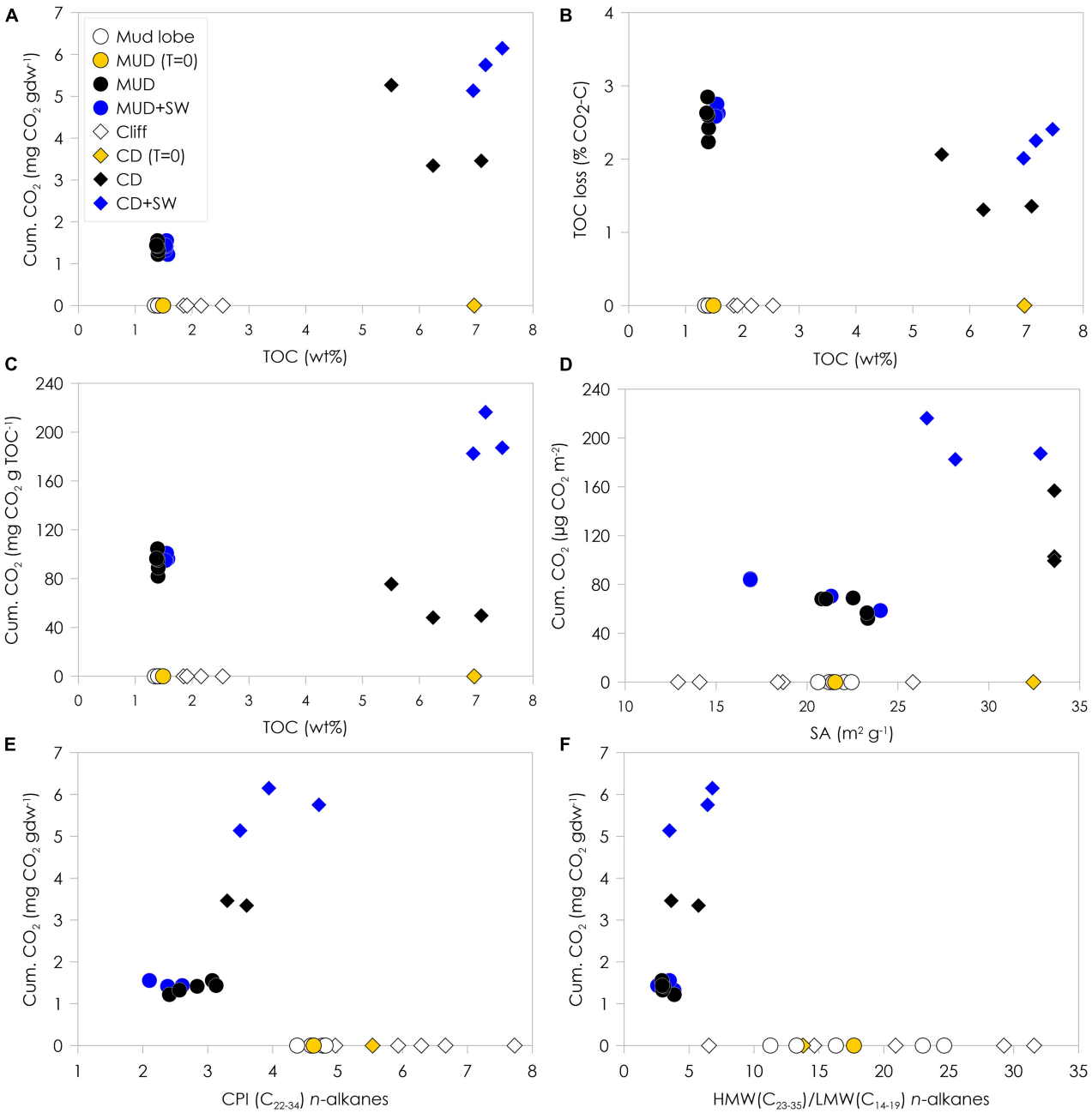

FIGURE 4 | Cumulative CO_2 production normalized to gram dry weight (gdw) and %TOC loss as CO_2-C at the end of the two month-incubation plotted against TOC content **(A,B)**, cumulative CO_2 production normalized to TOC content **(C)** and surface area **(D)** plotted against initial TOC content and surface area and cumulative CO_2 production normalized to gdw plotted against CPI *n*-alkanes **(E)** and HMW/LMW *n*-alkanes ratio **(F)**. Open symbols on the *x*-axis indicate samples from *mud lobe* and *cliff* that were not incubated to show the natural variability in the *mud lobe* and *cliff*. The *mud debris* (MUD) and *cliff debris* (CD) samples used for the incubation (T = 0) are indicated by the yellow symbols, incubated samples by the black symbols and incubated samples with seawater (SW) added by the blue symbols.

and 35.0 ± 5.1 µg gdw^{-1} with seawater added, respectively. While HMW *n*-alkane increase by up to four times during the incubation, LMW *n*-alkane concentrations increased up to 14 times compared to the initial concentrations (**Table 1**, **Supplementary Figure 9**). This substantial increase of *n*-alkanes under aerobic conditions, particularly LMW *n*-alkanes, may derive from heterotrophic microbial decomposers (Li et al., 2018; Chen et al., 2019). The predominance of even C-homologues in the LMW *n*-alkane fraction suggests a bacterial source and autochthonous production processes, which has been observed in estuarine and marine sediments (Grimalt and Albaigés, 1987). Under anoxic conditions, these LMW *n*-alkane C-homologues

can also derive from reduction of fatty acids (Debyser et al., 1977; Dastillung and Corbet, 1978). Yet, as aerobic conditions were applied during the experiment this process was probably restricted. Although no light was applied during the incubations, increases of LMW *n*-alkanes may have been also caused by algal growth as certain algae communities can thrive under extremely low radiance conditions (Suzuki et al., 1997). The lower even C-homologues in the HMW *n*-alkane fraction may point to the reduction of fatty acids or wax alcohols during degradation (Kvenvolden, 1970; Welte and Waples, 1973). Finally, contamination of lab equipment or by septa could also have been a potential source of *n*-alkanes. Yet, without further evidence the cause of the *n*-alkane increase remains speculative and biomarker from the post-incubation results should therefore be dealt with caution. However, the relatively low standard deviation of replicate analyses seems to rule out the random effect to be expected from septum leaching or contamination (**Supplementary Figure 9**).

DOC Release and Acidification

Over the course of the incubation, a minor portion of the sediment OC pool (< 0.2%) was transferred into the DOC pool of the seawater. After the incubation DOC concentrations in seawater increased from initial 1.7 ± 0.03 mg L^{-1} to 7.2 ± 0.1 mg L^{-1} and 27.8 ± 1.0 mg L^{-1} with addition of *mud debris* and *cliff debris,* respectively. The DOC increase in seawater mixed with *cliff debris* was ∼four times higher mainly due to the higher initial TOC content (**Supplementary Figure 10** and **Supplementary Table 2**). This higher DOC release probably resulted in the higher CO_2 release as OC has to be in the form of DOC to pass cell membranes before metabolization by microbes (Battin et al., 2008; Vonk and Gustafsson, 2013). Thus, when normalized to initial TOC content, DOC yields for *mud debris* and *cliff debris* after 2 month of incubation are similar with 3.1 ± 0.1 and 3.6 ± 0.1 mg g^{-1} OC, respectively. This indicates that DOC leaching and adsorption processes with mineral surfaces are of similar magnitude for both debris types during the two months of incubation (Neff and Asner, 2001; Littlefair et al., 2017). Higher DOC yields (6.6 ± 1.7 and 7.4 ± 1.4 mg g^{-1} OC, respectively) have been observed in seawater mixed with mineral and organic-rich permafrost in previous studies, where permafrost had similar initial TOC contents (1.7 ± 0.2 and 7.8 ± 0.7 wt%, respectively) to *mud debris* and *cliff debris,* yet the incubation period was twice as long (**Supplementary Figure 10**; Tanski et al., 2019). This suggests that leaching capacity and DOC yield may increase over time or that DOC components prone to leaching were already leached from *mud debris* and *cliff debris* during transport *onshore*. A dynamic balance of hydrolysis from particulate OC to DOC and subsequent mineralization into CO_2 was probably established within days (Kristensen et al., 1995). This is indicated by stabilization of CO_2 production rates after the initial CO_2 release during the first weeks stemming from rapid mineralization of the most labile compounds. Leaching of labile compounds from plant debris or mineral-bound OC is more likely for *cliff debris* since labile compounds were probably still available as transit time *onshore* until accumulation at the cliff toe was short (Dou et al., 2008; Blair and Aller, 2012; Vonk et al., 2015). In combination with the initial liberation of labile DOC compounds, priming and co-metabolization might have caused the initial increase of CO_2 production in *cliff debris* mixed with seawater (Bianchi, 2011). Input of additional nutrients with seawater might have promoted decomposition of organic matter (Mack et al., 2004). Furthermore, input of nutrients from the adjacent cliffs topsoil would have likely supported microbial metabolic efficiency in the *cliff debris* (Chen et al., 2018) and thus CO_2 production. The increase of DOC concentrations in unfiltered seawater controls from 1.7 ± 0.0 to 2.6 ± 1.0 mg L^{-1} (**Supplementary Table 2**) indicate potential production during the incubations and may support the increase of LMW *n*-alkanes observed. This could have further increased the DOC content in the seawater, which was mixed with *mud debris* and *cliff debris* and influences the CO_2 release from the seawater.

In combination with increasing DOC concentrations, a substantial acidification of the seawater mixed with *mud debris* and *cliff debris* from pH 8.2 to 7.0 ± 0.1 and 7.0 ± 0.0, respectively, was observed (**Supplementary Figure 10** and **Supplementary Table 2**). This could have been caused by a low pH of soil organic matter within eroded debris or dissolution of CO_2 produced from the debris in seawater. An even stronger pH decrease from 8.4 ± 0.1 to 5.2 ± 0.2, was observed during a longer incubation experiment with organic-rich permafrost mixed with seawater, which was likely caused by the low initial pH (6.1 ± 0.1) of the permafrost and a high DOC yield (**Supplementary Figure 10**; Tanski et al., 2019). Depending on the ratio of sediment to seawater, acidification could occur during erosion, which was shown for coastal waters in the Siberian Arctic that receive large amounts of permafrost OC. This, in turn, could result in elevated pCO_2 and outgassing to the atmosphere (Semiletov et al., 2013, 2016).

Incubations Cannot Account for Dynamic *in situ* Environmental Conditions

The measured CO_2 release rates and OC losses from eroded organic matter were obtained through experimental settings with low constant temperatures, maximum oxygen availability and dark conditions, which are classically used to study permafrost thaw through gradual active layer deepening (e.g., Lee et al., 2012; Knoblauch et al., 2013; Schädel et al., 2014). The CO_2 release observed under laboratory conditions would very likely differ from *in situ* observations. Yet, for coastal erosion processes onshore and in the nearshore coastal waters, environmental conditions are far from stable. The soil-to-water ratio under natural conditions is much lower resulting in a lower acidification as observed in the incubation vials. With a pH typical for ambient seawater (∼8.2), CO_2 production rates would probably remain similar but carbon storage in seawater would shift towards bicarbonate and carbonate (Wolf-Gladrow et al., 2007). The most important environmental parameters affecting the CO_2 production under natural conditions are most likely temperature and oxygen availability. Incubation experiments carried out at 15 or 16 °C (compared to 4 °C) showed that CO_2 production increased substantially compared to lower temperatures <4 °C

(Dutta et al., 2006; Lee et al., 2012; Knoblauch et al., 2013; Schädel et al., 2016; Tanski et al., 2019). For our study area Qikiqtaruk - Herschel Island temperatures in the coastal waters depend on wind direction and coastal orientation and range between ∼5 and 14°C during the warm season (Klein et al., 2019). This fits with observations from Cunliffe et al. (2019), which reported seawater surface temperatures between ∼6 to 10°C close to our sampling sites. During the warm season, air temperatures onshore are on average ∼8°C and soil temperatures in the active layer between 4.2 and 6.6°C with maximum values of 9.8°C (Burn, 2012; Wolter et al., 2016). The higher ambient temperatures would result in stronger OM mineralization rates onshore and in the nearshore under natural conditions compared to our incubation results. Using a Q10 value of 2 from Schädel et al. (2016), an average air temperature of ∼8°C, and a conservative seawater temperature of ∼6°C, the CO_2 production rates measured at 4°C would be ∼32% higher onshore at 8°C and ∼15% higher in the nearshore at 6°C. With warmer *in situ* seawater temperatures the solubility of CO_2 also decreases which further promotes the release of CO_2 to the atmosphere from coastal waters.

Another important driving factor for OC mineralization is the availability of oxygen. In contrast to the steady aerobic conditions during our incubation, which support efficient OC degradation and CO_2 production, less efficient anaerobic CO_2 and CH_4 production may apply onshore, where oxygen cannot penetrate deeper layers of the mud debris and cliff debris or under water-logged conditions. Under anaerobic conditions, OC mineralization is about 3 times slower than under aerobic conditions (Schädel et al., 2016; Knoblauch et al., 2018). This would result in an approximately three times lower theoretical OC loss of in mud debris and cliff debris (0.4 and 1.3%, respectively), where anaerobic conditions apply under natural condition, compared to the observed OC loss of 1.1 and 3.9%, respectively, under aerobic conditions in the experiment. In contrast to less efficient anaerobic mineralization of OM, drainage and drying of eroded material onshore could further increase oxygen penetration into eroded debris and support aerobic carbon mineralization. Inter or intra-annual refreezing cycles could further enhance macro-pore spaces and infiltration capacity of sediments (Ding et al., 2019). This could supply oxygen to pore spaces or further mechanical destruction of organo-mineral bonds, which may cause short-lived CO_2 pulses (Blair and Aller, 2012; Höfle et al., 2013; Walz et al., 2017). Additionally, drying and rewetting cycles (caused by rain, waves or high tides) could also further amplify CO_2 production by microbial mineralization of OC and weakening the physical protection of the soil matrix (Fierer and Schimel, 2003).

During transport onshore or in the nearshore water column, photo-oxidation can promote DOC degradation (by up to 40%), which is coupled to CO_2 release (Cory et al., 2013). The input of fresh nutrients, organic matter or plant litter from erosion itself, surface runoff or seawater could trigger priming effects and co-metabolism of recalcitrant organic matter combined from active layer and permafrost, thus further promoting CO_2 release (Abbott et al., 2014; Wild et al., 2014, 2016; Abbott and Jones, 2015; Walz et al., 2017; Knoblauch et al., 2018). Light conditions could further promote those priming effects in the ocean between produced algal exudates and eroded OC (Bianchi, 2011). The majority of these factors would likely lead to higher OC loss and CO_2 production under natural coastal erosion conditions compared to the experimental incubations set-ups employed in this study. Once deposited in nearshore sediments, OM degradation pathways depend on sedimentation rates and oxygen penetration depth. In our study region sedimentation rates range from 0.1 mm yr^{-1} offshore to 2 mm yr^{-1} in the vicinity of the Mackenzie River but can reach up to 0.33 cm yr^{-1} at shelf locations which promote deposition (Harper and Penland, 1982; Grotheer et al., 2020). In combination with an oxygen penetration depth of a few mm to cm in marine sediments (Glud, 2008; Arndt et al., 2013), we would assume that aerobic conditions similar as in our experiment would apply for eroded and deposited sediments within the first years of deposition and during resuspension, winnowing or longshore transport. In subsequent years, anaerobic conditions may gradually take over in the initially deposited sediments, limiting efficient OC degradation and promoting OC burial on geological time scales (Hilton et al., 2015; Bröder et al., 2018; Grotheer et al., 2020). Furthermore, due to competition with marine sulfate reduction, most likely no CH_4 would be produced in the marine surface sediments (Knoblauch et al., 2018).

CO_2 Release Dynamics Along the Yukon Coast

The erosion type and coastal morphology may strongly influence the GHG release potential along vulnerable permafrost coastlines. Our main study area, Qikiqtaruk – Herschel Island, is dominated by high cliffs (mean elevation ∼25 m) and retrogressive thaw slumps, which together affect ∼7% of the coast (**Figures 1**, **2**, Lantuit and Pollard, 2008; Ramage et al., 2017). Thermoabrasion of the cliff tops and headwall retreat in thaw slumps may result in an initial CO_2 pulse *onshore* with up to ∼4% of OC mineralized into CO_2 within one season (Tanski et al., 2019). Longer transport pathways of exposed organic matter along the sloping cliff faces or within thaw slump systems (**Figures 1A,B**) then result in a *delayed* release into the sea with further OC mineralization (∼5% OC loss as CO_2 measured during one warm season) at low rates (mimicked by *mud debris* incubations in this study) taking place in the subsequent warm seasons assuming the material discharges into the sea in the following years or even later. This adds to the initial permafrost CO_2 pulse *onshore* before release into the *nearshore* zone (**Figure 5**). Within thaw slump systems, eroded sediments can reside on long time scales *onshore* (years to decades) before release into the sea (Cray and Pollard, 2015). This long transit time can result in a substantial OC loss (up to ∼50%) with portions mineralized into CO_2 or CH_4 (Abbott et al., 2015; Tanski et al., 2017, 2019). Similarly, eroded debris can further accumulate on the beach for longer time spans (potentially exceeding one warm season) before being washed into the sea during storm surges or high tides (Obu et al., 2015; Cunliffe et al., 2019). This transition stage could further promote reworking of OC and direct CO_2 release to the atmosphere *onshore*. Photo-oxidation processes may have further increased degradation and

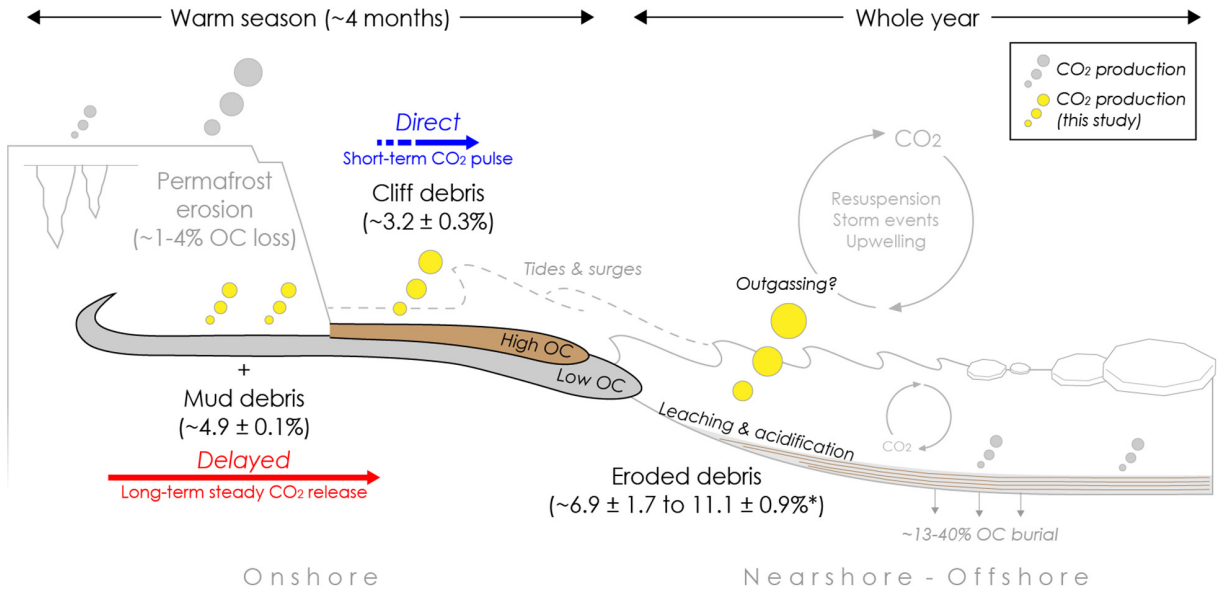

FIGURE 5 | Infographic summarizing potential organic carbon loss (%OC as CO_2) during coastal erosion processes from different erosion types in an Arctic warm season and entire year upon erosion in the sea. The magnitude of absolute carbon dioxide (mg CO_2 gdw) release is indicated by the size of yellow bubbles. Release of *mud debris* (gray flow) from thaw slumps or other thaw features into the *nearshore* is likely delayed with longer residence times *onshore,* resulting in a steady CO_2 release at low rates complementing CO_2 pulses during initial permafrost thaw and erosion. *Cliff debris* (brown flow) along low bluffs is likely to be transported more directly into the *nearshore,* resulting only in a short-term CO_2 pulse and overall low OC loss during transit (**Figure 1**). After erosion into the *nearshore* CO_2 is produced, which can be amplified by seawater, in particular for *cliff debris* and *in situ* permafrost where transport time is short. Carbon losses were modeled for the Arctic open-water season (~four months) and the entire year based on short term (~two months) incubation experiments at 4°C under dark and aerobic conditions. Carbon loss rates from permafrost erosion are taken from Tanski et al. (2019) and displayed as reference for *in situ* permafrost (~four month incubation at same conditions). The asterisk (*) indicates that once eroded into the sea OC degradation takes place during the entire year and is not limited to the warm seasons. Burial estimates are taken from Couture et al. (2018) and Grotheer et al. (2020).

CO_2 production during transit from land to sea (Cory et al., 2013; Ward and Cory, 2016).

In contrast, gully channels that intersect high bluffs, and thaw streams that drain slump systems (**Figures 1A,B**) may transport eroded permafrost OC more quickly and on a *direct* pathway towards the sea, potentially diminishing CO_2 release *onshore*. This *direct* pathway likely also applies to coastal stretches with low cliffs, which can be found especially on the southeast side of Qikiqtaruk – Herschel Island, which we tried to mimic with the *cliff debris* incubations. Along these cliffs (**Figures 2**, **5**), approximately 3% of OC can be mineralized into CO_2 within one warm season during transit *onshore*. The debris along low cliffs is likely removed quickly within one season with only larger collapsing permafrost blocks remaining for a longer period *onshore* on the beach (season to years). Correspondingly, the initial CO_2 pulse is likely complemented by continuing CO_2 production at lower rates. For this study we assumed aerated conditions during transport. Yet, when eroded material gets redeposited in mud pools or lobes *onshore*, CH_4 production may replace CO_2 production if water-logged and oxygen-depleted conditions apply (Knoblauch et al., 2013; Schädel et al., 2016).

Upon release into the *nearshore* waters, OC is likely further mineralized within erosion plumes or deposited sediments. Seawater may further promote OC mineralization (**Figure 5**), especially if transport is *direct* (in the case of collapsed permafrost or cliff debris) and if the water column is oxygen-saturated. Seawater enhances the CO_2 production from *cliff debris* with corresponding OC losses increasing from 1.6 ± 0.3 to 2.2 ± 0.2% after incubation with seawater mimicking *nearshore* conditions (**Table 2**). Enhanced OC loss was also observed for *in situ* permafrost mixed with seawater with TOC losses increasing from 1.1 ± 0.0 to 1.5 ± 0.2% in organic-rich permafrost and from 3.9 ± 0.2 to 6.2 ± 1.2% in mineral permafrost (Tanski et al., 2019). If transport to the *nearshore* is *delayed*, OC transferred to the sea probably continues to degrade at the same relatively low rates as *onshore* with OC losses of ~5% within a warm season of four months (**Figure 5**). Yet, for both scenarios organic matter degradation in *nearshore* sediments likely takes place during the entire year and is not limited only to the warm season since *nearshore* sediments do not freeze up during the cold season. Once eroded into the *nearshore*, the total OC loss as CO_2-C from *mud debris* and *cliff debris* could be ~7–11% after one year (**Figure 5**). Depending on the depositional environment, OC can be either buried on the shelf or transported towards the continental slope on up to millennial time scales (Naidu et al., 2000; Goñi et al., 2013; Bröder et al., 2018). Locally, large portions of eroded OC (~12 to 40%) are stored in *nearshore* sediments and local depressions on the shelf such as Herschel Basin (Couture et al., 2018; Grotheer et al., 2020). On the seafloor, effective aerobic degradation likely only takes place in the upper few millimeters of the sediment column and at the water-sediment boundary, where microbial communities allow

for higher respiration rates (Rasmussen and Jorgensen, 1992; Arndt et al., 2013; Brüchert et al., 2018). Bioturbation, currents and ice scouring may facilitate resuspension and therefore oxygen resupply and CO_2 production in deeper sediment columns eventually (Héquette et al., 1995; Arndt et al., 2013). Under anaerobic conditions microbial communities that can produce CH_4 can establish after years and substantial amounts of CH_4 being produced and released either directly as CH_4 or oxidized as CO_2 from the seafloor (Overduin et al., 2015; Knoblauch et al., 2018). Although further GHG production of eroded material is very likely in the *nearshore*, it is unclear if or from which water depth produced CO_2 evades to the atmosphere. Outgassing of degradation-derived CO_2 or CH_4 from oversaturated water layers, however, can occur locally and is promoted by resuspension, storms or upwelling events (Mathis et al., 2012; Vonk et al., 2012; Semiletov et al., 2016; Pipko et al., 2017).

Along the adjacent Yukon mainland coast approximately one third of the entire coastline is characterized by actively eroding cliffs (of variable elevation), with the remainder being gently sloping tundra (∼17%) and inundated coastlines (∼11%) as well as beach and gravel spits (Irrgang et al., 2018). A *delayed* release similar to the high cliffs on Qikiqtaruk – Herschel Island may apply to the actively eroding cliffs in the formerly glaciated part of the Yukon coast towards the Mackenzie Delta. Here, cliffs are high (mean elevation of up to ∼30m) and thaw slumps are ubiquitous (up to ∼16% of the coastline) promoting substantial OC turnover *onshore* before release into the ocean (Couture and Pollard, 2015; Ramage et al., 2017). In the formerly unglaciated part towards the Alaskan border (**Figures 1C,D**), cliffs are much lower (∼6.5 m mean elevation) and residence times of eroded OC *onshore* likely to be very short (weeks to years) due to the particularly high erosion rates in this region (∼1.4 m yr^{-1}), which results in a shorter time span for OC mineralization during erosion (Couture and Pollard, 2015; Irrgang et al., 2018). Along coastal parts where tundra is sloping towards the beach and thereby restricting exposure of permafrost, OC loss might be even lower and the cycling of released OC may primarily take place in the seawater column or upon deposition in *nearshore* sediments. In turn, inundation and potential permafrost degradation could promote OC mineralization *onshore* and release substantial amounts of CO_2 before transport into the ocean (Tanski et al., 2019). At present, how much OC is converted into CO_2 along the different coastal types is highly speculative. Yet, it is likely that the response of OC to erosion and the magnitude of CO_2 release varies between coastal and erosion types. Based on the annual TOC flux from land to sea of 36 Gg yr^{-1} for the Yukon coast (Couture et al., 2018), we would estimate that up to 1.8 Gg CO_2 yr^{-1} could be released as CO_2 during the erosion process onshore assuming an OC loss of up to ∼5% during the warm season and up to 3.9 Gg CO_2 yr^{-1} from *nearshore* sediments assuming an OC loss of ∼11% for an entire year since eroded sediments on the seafloor do not freeze anymore (**Figure 5**). Local dynamic environmental conditions (e.g., higher air temperatures and sunlight exposure) and processes (e.g., drying and rewetting of debris in the coastal zone) may increase OC degradation.

CONCLUSION

Coastal morphology and erosion type play a substantial role in determining the greenhouse gas release potential during erosion along permafrost coasts in the Arctic. *Mud debris* and *cliff debris* from an outflow of a thaw slump system and a low collapsing bluff, respectively, representing different coastal erosion scenarios released substantial amounts of CO_2 (1.4 ± 0.1 to 4.0 ± 0.9 mg CO_2 gdw^{-1}) over a short period (∼two months) corresponding to an initial OC loss ∼1.6–2.6%. The relatively fresh and OC-rich *cliff debris* resulted in a ∼four times higher CO_2 release than for *mud debris*. Yet, when normalized to OC content, CO_2 release was ∼three times higher from *mud debris* indicating higher biodegradability of the older and more mineral OC. CO_2 release was particularly high with addition of seawater, indicating potential priming effects in the coastal realm. Upon release into the ocean, only a small portion of OC initially enters the seawater DOC pool. Our results suggest that high bluffs or coasts with presence of thermoerosional features are characterized by a *delayed* release that consists of an initial CO_2 pulse from permafrost erosion followed by a subsequent CO_2 release at lower rates in *mud debris*, promoting OC degradation during protracted transit from land to sea in the warm season. In contrast, erosion of *cliff debris* along low bluffs that may contain proportionally more OC results only in a short-term CO_2 pulse with OC quickly removed by waves. In the *nearshore* zone, CO_2 production from eroded sediments continues provided oxygen is available, likely taking place the entire year. After the duration of an Arctic warms season (∼four month) OC losses of up ∼5% were modeled and after one year, up to ∼11% of OC could be decomposed and released as CO_2 once eroded sediments are deposited in the *nearshore*. The magnitude of CO_2 release may be underestimated when using traditional incubation experiments since coastal environmental conditions are difficult to account for yet likely enhance degradation. More sophisticated incubation set-ups that mimic changing environmental and site-specific variables, or continuous GHG measurement systems *onshore* (e.g., eddy covariance towers) and in the *nearshore* (e.g., pop-up buoys with *in situ* pCO_2 sensors), accounting for seasonal fluctuations and uptake processes from vegetation and phytoplankton, would be needed to derive the actual GHG release signal along eroding permafrost coasts in different Arctic regions.

DATA AVAILABILITY STATEMENT

The raw data supporting the conclusions of this article will be made available by the authors, without undue reservation.

AUTHOR CONTRIBUTIONS

GT, HL, DW, JV, and LB created the study design and incubation set-up. GT, DW, and TS carried out the gas concentration measurements. CK and GT recalculated gas concentration and estimated TOC losses. CB calibrated and applied the dynamic

carbon decomposition model. GT and LB carried out the extraction of lipid biomarkers. TT measured lipid biomarkers. LB, JV, GT, and TT processed and interpreted the data. HL, MF, and JS supported the bulk geochemical and stable carbon isotope analysis and data interpretation. BK measured and evaluated DOC concentrations. LB, NH, and TE carried out radiocarbon analysis and data analysis. GT wrote the manuscript with contributions from all co-authors. All authors contributed to the article and approved the submitted version.

FUNDING

We acknowledge and are grateful for the financial support from the H2020 project NUNATARYUK (grant 773421), the Helmholtz young investigators group TEAM (grant VH-NG-821 to TS) and the ERC StG project THAWSOME (grant 676982 to JV). JS was supported by the Changing Arctic Ocean program (NERC-BMBF project CACOON, grant 03F0806A) and CB by the German research foundation DFG (BE 6485/1-1).

ACKNOWLEDGMENTS

We would like to thank O. Burckhardt, J. Oury, C. Burau, D. Scheidemann, H. Meyer, M. Weiner, K. Keskitalo, and D. Jong for support during lab work. K. Klein and D. Jong are thanked for assistance during field work and J. Kahl for logistical support. We thank A. Irrgang for contributing photographs from field work. We would like to especially thank the park rangers and R. Gordon from Qikiqtaruk – Herschel Island Territorial Park for their support and guidance on their land. The Aurora Research Institute in Inuvik is thanked for the logistical support on site. Data supporting this study is available on the PANGAEA data repository (in review; data submitted on 05 January 2021).

SUPPLEMENTARY MATERIAL

The Supplementary Material for this article can be found online at: https://www.frontiersin.org/articles/10.3389/feart.2021.630493/full#supplementary-material

REFERENCES

Abbott, B. W., and Jones, J. B. (2015). Permafrost collapse alters soil carbon stocks, respiration, CH4, and N2O in upland tundra. *Glob. Change Biol.* 21, 4570–4587. doi: 10.1111/gcb.13069

Abbott, B. W., Jones, J. B., Godsey, S. E., Larouche, J. R., and Bowden, W. B. (2015). Patterns and persistence of hydrologic carbon and nutrient export from collapsing upland permafrost. *Biogeosciences* 12, 3725–3740. doi: 10.5194/bg-12-3725-2015

Abbott, B. W., Larouche, J. R., Jones, J. B., Bowden, W. B., and Balser, A. W. (2014). Elevated dissolved organic carbon biodegradability from thawing and collapsing permafrost. *J. Geophys. Res. Biogeosci.* 119, 2049–2063. doi: 10.1002/2014JG002678

AMAP (2017). *Snow, Water, Ice and Permafrost in the Arctic (SWIPA) 2017*. Oslo: Arctic Monitoring and Assessment Programme.

Andrén, O., and Kätterer, T. (1997). ICBM: the introductory carbon balance model for exploration of soil carbon balances. *Ecol. Appl.* 7, 1226–1236. doi: 10.1890/1051-07611997007[1226:ITICBM]2.0.CO;2

Are, F. E., Reimnitz, E., Grigoriev, M. N., Hubberten, H. W., and Rachold, V. (2008). The influence of cryogenic processes on the erosional arctic shoreface. *J. Coast. Res.* 241, 110–121. doi: 10.2112/05-0573.1

Arndt, S., Jørgensen, B. B., LaRowe, D. E., Middelburg, J. J., Pancost, R. D., and Regnier, P. (2013). Quantifying the degradation of organic matter in marine sediments: a review and synthesis. *Earth Sci. Rev.* 123, 53–86. doi: 10.1016/j.earscirev.2013.02.008

Barnhart, K. R., Anderson, R. S., Overeem, I., Wobus, C., Clow, G. D., and Urban, F. E. (2014). Modeling erosion of ice-rich permafrost bluffs along the Alaskan Beaufort Sea coast. *J. Geophys. Res. Earth Surf.* 119, 1155–1179. doi: 10.1002/2013JF002845

Battin, T. J., Kaplan, L. A., Findlay, S., Hopkinson, C. S., Marti, E., and Packman, A. I. (2008). Biophysical controls on organic carbon fluxes in fluvial networks. *Nat. Geosci.* 1, 95–100. doi: 10.1038/ngeo101

Bendixen, M., Iversen, L. L., Bjørk, A. A., Elberling, B., Westergaard-Nielsen, A., Overeem, I., et al. (2017). Delta progradation in Greenland driven by increasing glacial mass loss. *Nature* 550, 101–104. doi: 10.1038/nature23873

Bianchi, T. S. (2011). The role of terrestrially derived organic carbon in the coastal ocean: a changing paradigm and the priming effect. *Proc. Natl. Acad. Sci. U.S.A.* 108, 19473–19481. doi: 10.1073/pnas.1017982108

Biskaborn, B. K., Smith, S. S., Noetzli, J., Matthes, H., Vieira, G., Streletskiy, D. A., et al. (2019). Permafrost is warming at a global scale. *Nat. Commun.* 10:264. doi: 10.1038/s41467-018-08240-4

Blair, N., and Aller, R. (2012). The fate of terrestrial organic carbon in the marine environment. *Annu. Rev. Mar. Sci.* 4, 401–423. doi: 10.1146/annurev-marine-120709-142717

Blasco, S. M., Fortin, G., Hill, P. R., O'Connor, M. J., and Brigham-Grette, J. K. (1990). "The late neogene and quaternary stratigraphy of the Canadian Beaufort continental shelf," in *The Arctic Ocean Region*, eds A. Grantz, L. Johnson, and J. F. Sweeney (Boulder, CO: Geological Society of America), 491–502.

Bray, E. E., and Evans, E. D. (1961). Distribution of n-paraffins as a clue to recognition of source beds. *Geochim. Cosmochim. Acta* 22, 2–15. doi: 10.1016/0016-7037(61)90069-2

Bröder, L., Tesi, T., Andersson, A., Semiletov, I., and Gustafsson, Ö (2018). Bounding cross-shelf transport time and degradation in Siberian-Arctic land-ocean carbon transfer. *Nat. Commun.* 9:806. doi: 10.1038/s41467-018-03192-1

Brüchert, V., Bröder, L., Sawicka, J. E., Tesi, T., Joye, S. P., Sun, X., et al. (2018). Carbon mineralization in Laptev and East Siberian sea shelf and slope sediment. *Biogeosciences* 15, 471–490. doi: 10.5194/bg-15-471-2018

Brunauer, S., Emmett, P. H., and Teller, E. (1938). Adsorption of gases in multimolecular layers. *J. Am. Chem. Soc.* 60, 309–319. doi: 10.1021/ja01269a023

Burn, C. R. (1997). Cryostratigraphy, paleogeography, and climate change during the early Holocene warm interval, western Arctic coast, Canada. *Can. J. Earth Sci.* 34, 912–925. doi: 10.1139/e17-076

Burn, C. R. (2012). *Herschel Island Qikiqtaryuk - A Natural and Cultural History of Yukon's Arctic Island*. Calgary: University of Calgary Press.

Burn, C. R., and Zhang, Y. (2009). Permafrost and climate change at Herschel Island (Qikiqtaruq), Yukon Territory, Canada. *J. Geophys. Res. Earth Surf.* 114, 1–16. doi: 10.1029/2008JF001087

Chen, L., Liu, L., Mao, C., Qin, S., Wang, J., Liu, F., et al. (2018). Nitrogen availability regulates topsoil carbon dynamics after permafrost thaw by altering microbial metabolic efficiency. *Nat. Commun.* 9:3951. doi: 10.1038/s41467-018-06232-y

Chen, X., Liu, X., Wei, Y., and Huang, Y. (2019). Production of long-chain n-alkyl lipids by heterotrophic microbes: new evidence from Antarctic lakes. *Organ. Geochem.* 138:103909. doi: 10.1016/j.orggeochem.2019.103909

Ciais, P., Sabine, C., Bala, G., Bopp, L., Brovkin, V., Canadell, J., et al. (eds) (2013). "Carbon and other biogeochemical cycles," in *Climate Change 2013: The Physical Science Basis. Contribution of Working Group 1 to the Fifth Assessment Report of the Intergovernmental Panel on Climate Change*, eds T. F. Stocker, D. Qin, G. K. Plattner, M. Tignor, S. K. Allen, J. Boschung, et al. (Cambridge: Cambridge University Press).

Coch, C., Lamoureux, S. F., Knoblauch, C., Eischeid, I., Fritz, M., Obu, J., et al. (2018). Summer rainfall dissolved organic carbon, solute, and sediment fluxes in

a small Arctic coastal catchment on Herschel Island (Yukon Territory, Canada). *Arct. Sci.* 4, 750–780. doi: 10.1139/as-2018-0010

Cory, R. M., Crump, B. C., Dobkowski, J. A., and Kling, G. W. (2013). Surface exposure to sunlight stimulates CO2 release from permafrost soil carbon in the Arctic. *Proc. Natl. Acad. Sci. U.S.A.* 110, 3429–3434. doi: 10.1073/pnas.1214104110

Couture, N., and Pollard, W. H. (2015). "Ground ice determinations along the Yukon coast using a morphological model," in *Proceedings, GeoQuebec 2015, 7th Canadian Permafrost Conference*, (Québec).

Couture, N. J., Irrgang, A., Pollard, W., Lantuit, H., and Fritz, M. (2018). Coastal erosion of permafrost soils along the Yukon coastal plain and fluxes of organic carbon to the Canadian Beaufort Sea. *J. Geophys. Res. Biogeosci.* 123, 406–422. doi: 10.1002/2017JG004166

Cray, H., and Pollard, W. H. (2015). Vegetation recovery patterns following permafrost disturbance in a low arctic vegetation recovery patterns following permafrost disturbance in a low arctic setting: case study of Herschel Island, Yukon, Canada. *Arct. Antarct. Alpine Res.* 47, 99–113. doi: 10.1657/AAAR0013-076

Cunliffe, A. M., Tanski, G., Radosavljevic, B., Palmer, W. F., Sachs, T., Lantuit, H., et al. (2019). Rapid retreat of permafrost coastline observed with aerial drone photogrammetry. *Cryosphere* 13, 1513–1528.

Dai, A., Luo, D., Song, M., and Liu, J. (2019). Arctic amplification is caused by sea-ice loss under increasing CO2. *Nat. Commun.* 10:121. doi: 10.1038/s41467-018-07954-9

Dastillung, M., and Corbet, B. (1978). "La geochimie organique des sediments marins profonds. I: hydrocarbures satures et insatures des sediments," in *Geochimie Organique Des Sediments Marins Profonds*, eds A. Cabanaz and R. Pelet (Paris: CNRS), 293–323.

Debyser, Y., Pelet, R., and Dastillung, M. (1977). "Geochimie organique des sediments marins recents: Mer Noire, Baltique, Atlantique (Mauritanie)," in *Advanes in Organic Geohemistry*, eds R. Campos and J. Goni (Madrid: Empresa Nacional Adaro de Investigaciones Mineras), 289–320.

Ding, B., Rezanezhad, F., Gharedaghloo, B., Van Cappellen, P., and Passeport, E. (2019). Bioretention cells under cold climate conditions: Effects of freezing and thawing on water infiltration, soil structure, and nutrient removal. *Sci. Total Environ.* 649, 749–759. doi: 10.1016/j.scitotenv.2018.08.366

Dou, F., Ping, C.-L., Guo, L., and Jorgenson, T. (2008). Estimating the impact of seawater on the production of soil water-extractable organic carbon during coastal erosion. *J. Environ. Qual.* 37, 2368–2374. doi: 10.2134/jeq2007.0403

Drenzek, N. J., Montluçon, D. B., Yunker, M. B., Macdonald, R. W., and Eglinton, T. I. (2007). Constraints on the origin of sedimentary organic carbon in the Beaufort Sea from coupled molecular 13C and 14C measurements. *Mar. Chem.* 103, 146–162. doi: 10.1016/j.marchem.2006.06.017

Dunton, K. H., Weingartner, T., and Carmack, E. C. (2006). The nearshore western Beaufort Sea ecosystem: circulation and importance of terrestrial carbon in arctic coastal food webs. *Prog. Oceanogr.* 71, 362–378. doi: 10.1016/j.pocean.2006.09.011

Dutta, K., Schuur, E. A. G., Neff, J. C., and Zimov, S. A. (2006). Potential carbon release from permafrost soils of Northeastern Siberia. *Glob. Change Biol.* 12, 2336–2351. doi: 10.1111/j.1365-2486.2006.01259.x

Eglinton, G., and Hamilton, R. J. (1967). Leaf epicuticular waxes. *Science* 156, 1322–1334. doi: 10.2307/1721263

Fierer, N., and Schimel, J. P. (2003). A proposed mechanism for the pulse in carbon dioxide production commonly observed following the rapid rewetting of a dry soil. *Soil Sci. Soc. Am. J.* 67, 798–805. doi: 10.2136/SSSAJ2003.7980

Forbes, D. (2019). "Chapter 8 - Arctic deltas and estuaries: a canadian perspective," in *Coasts and Estuaries The Future*, eds E. Wolanski, J. W. Day, M. Ellitt, and R. Ramachadran (Amsterdam: Elsevier).

Fritz, M., Vonk, J. E., and Lantuit, H. (2017). Collapsing arctic coastlines. *Nat. Clim. Change* 7, 6–7. doi: 10.1038/nclimate3188

Fritz, M., Wetterich, S., Schirrmeister, L., Meyer, H., Lantuit, H., Preusser, F., et al. (2012). Eastern Beringia and beyond: late Wisconsinan and Holocene landscape dynamics along the Yukon Coastal Plain, Canada. *Palaeogeogr. Palaeoclimatol. Palaeoecol.* 319–320, 28–45. doi: 10.1016/j.palaeo.2011.12.015

Glud, R. (2008). Oxygen dynamics of marine sediments. *Mar. Biol. Res.* 4, 243–289. doi: 10.1080/17451000801888726

Goñi, M. A., O'Connor, A. E., Kuzyk, Z. Z., Yunker, M. B., Gobeil, C., and Macdonald, R. W. (2013). Distribution and sources of organic matter in surface marine sediments across the North American Arctic margin. *J. Geophys. Res. Oceans* 118, 4017–4035. doi: 10.1002/jgrc.20286

Goñi, M. A., Yunker, M. B., Macdonald, R. W., and Eglinton, T. I. (2005). The supply and preservation of ancient and modern components of organic carbon in the Canadian Beaufort Shelf of the Arctic Ocean. *Mar. Chem.* 93, 53–73. doi: 10.1016/j.marchem.2004.08.001

Grimalt, J., and Albaigés, J. (1987). Sources and occurrence of C12C22 n-alkane distributions with even carbon-number preference in sedimentary environments. *Geochim. Cosmochim. Acta* 51, 1379–1384. doi: 10.1016/0016-7037(87)90322-X

Grotheer, H., Meyer, V., Riedel, T., Pfalz, G., Mathieu, L., Hefter, J., et al. (2020). Burial and origin of permafrost-derived carbon in the nearshore zone of the Southern Canadian Beaufort Sea. *Geophys. Res. Lett.* 47:e2019GL085897. doi: 10.1029/2019GL085897

Gundelwein, A., Müller-Lupp, T., Sommerkorn, M., Haupt, E. T. K., Pfeiffer, E. M., and Wiechmann, H. (2007). Carbon in tundra soils in the Lake Labaz region of arctic Siberia. *Eur. J. Soil Sci.* 58, 1164–1174. doi: 10.1111/j.1365-2389.2007.00908.x

Günther, F., Overduin, P. P., Sandakov, A. V., Grosse, G., and Grigoriev, M. N. (2013). Short- and long-term thermo-erosion of ice-rich permafrost coasts in the Laptev Sea region. *Biogeosciences* 10, 4297–4318. doi: 10.5194/bg-10-4297-2013

Günther, F., Overduin, P. P., Yakshina, I. A., Opel, T., Baranskaya, A. V., and Grigoriev, M. N. (2015). Observing Muostakh disappear: permafrost thaw subsidence and erosion of a ground-ice-rich Island in response to arctic summer warming and sea ice reduction. *Cryosphere* 9, 151–178. doi: 10.5194/tc-9-151-2015

Harper, J. R., and Penland, P. S. (1982). *Beaufort Sea Sediment Dynamics. Contract Report to Atlantic Geoscience Centre*. Ottawa, ON: Geological Survey of Canada.

Hequette, A., and Barnes, P. W. (1990). Coastal retreat and shoreface profile variations in the Canadian Beaufort Sea. *Mar. Geol.* 91, 113–132. doi: 10.1016/0025-3227(90)90136-8

Héquette, A., Desrosiers, M., and Barnes, P. W. (1995). Sea ice scouring on the inner shelf of the southeastern Canadian Beaufort Sea. *Mar. Geol.* 128, 201–219. doi: 10.1016/0025-3227(95)00095-G

Heslop, J. K., Chandra, S., Sobzcak, W. V., Davydov, S. P., Davydova, A. I., Spektor, V. V., et al. (2017). Variable respiration rates of incubated permafrost soil extracts from the Kolyma River lowlands, north-east Siberia. *Polar Res.* 37:1305157. doi: 10.1080/17518369.2017.1305157

Heyer, J., Hübner, H., and Maaβ, I. (1976). Isotopenfraktionierung des Kohlenstoffs bei der mikrobiellen Methanbildung. *Isotopenpraxis Isotop. Environ. Health Stud.* 12, 202–205. doi: 10.1080/10256017608543912

Hilton, R. G., Galy, V., Gaillardet, J., Dellinger, M., Bryant, C., et al. (2015). Erosion of organic carbon in the Arctic as a geological carbon dioxide sink. *Nature* 524, 84–87. doi: 10.1038/nature14653

Höfle, S., Rethemeyer, J., Mueller, C. W., and John, S. (2013). Organic matter composition and stabilization in a polygonal tundra soil of the Lena Delta. *Biogeosciences* 10, 3145–3158. doi: 10.5194/bg-10-3145-2013

Hugelius, G., Strauss, J., Zubrzycki, S., Harden, J. W., Schuur, E. A. G., Ping, C. L., et al. (2014). Estimated stocks of circumpolar permafrost carbon with quantified uncertainty ranges and identified data gaps. *Biogeosciences* 11, 6573–6593. doi: 10.5194/bg-11-6573-2014

Huggett, W. S., Woodward, M. J., Stephenson, F., Hermiston, F. V., and Douglas, A. (1975). *Near and Bottom Currents and Offshore Tides, Ocean and Aquatic Sciences, Beaufort Sea Technical Report No. 16*. Victoria, BC: Ocean and Aquatic Sciences Department of the Environment.

Irrgang, A. M., Lantuit, H., Manson, G. K., Günther, F., Grosse, G., and Overduin, P. P. (2018). Variability in rates of coastal change along the Yukon Coast, 1951 to 2015. *J. Geophys. Res. Earth Surf.* 123, 779–800. doi: 10.1002/2017JF004326

James, T. S., Henton, J. A., Leonard, L. J., Darlington, A., Forbes, D. L., and Craymer, M. (2014). Relative sea-level projections in Canada and the adjacent mainland United States. *Geol. Surv. Canada Open File* 7737:10.4095. doi: 10.4095/295574

Jones, B. M., Arp, C. D., Jorgenson, M. T., Hinkel, K. M., Schmutz, J. A., and Flint, P. L. (2009). Increase in the rate and uniformity of coastline erosion in Arctic Alaska. *Geophys. Res. Lett.* 36, 1–5. doi: 10.1029/2008GL036205

Jones, B. M., Farquharson, L. M., Baughman, C. A., Buzard, R. M., Arp, C. D., Grosse, G., et al. (2018). A decade of remotely sensed observations highlight

complex processes linked to coastal permafrost bluff erosion in the Arctic A decade of remotely sensed observations highlight complex processes linked to coastal permafrost bluff eros. *Environ. Res. Lett.* 13:115001. doi: 10.1088/1748-9326/aae471

Jong, D., Bröder, L., Tanski, G., Fritz, M., Lantuit, H., Tesi, T., et al. (2020). Nearshore zone dynamics determine pathway of organic carbon from eroding permafrost coasts. *Geophys. Res. Lett.* 47:e2020GL088561. doi: 10.1029/2020GL088561

Karlsson, E. S., Brüchert, V., Tesi, T., Charkin, A., Dudarev, O., Semiletov, I., et al. (2015). Contrasting regimes for organic matter degradation in the East Siberian Sea and the Laptev Sea assessed through microbial incubations and molecular markers. *Mar. Chem.* 170, 11–22. doi: 10.1016/J.MARCHEM.2014.12.005

Kaufman, D. S., Schneider, D. P., McKay, N. P., Ammann, C. M., Bradley, R. S., Briffa, K. R., et al. (2009). Recent warming reverses long-term arctic cooling. *Science* 325, 1236–1239. doi: 10.1126/science.1173983

Kennedy, C. E., Smith, C. A. S., and Cooley, D. A. (2001). Observations of change in the cover of polargrass, Arctagrostis latifolia, and arctic lupine, Lupinus arcticus, in upland tundra on Herschel Island, Yukon Territory. *Can. Field Natural.* 115, 323–328.

Killops, S., and Killops, V. (2004). *Introduction to Organic Geochemistry*. Harlow: Longman Scientific & Technical.

Klein, K. P., Lantuit, H., Heim, B., Fell, F., Doxaran, D., and Irrgang, A. M. (2019). Long-term high-resolution sediment and sea surface temperature spatial patterns in arctic nearshore waters retrieved using 30-year landsat archive imagery. *Remote Sens.* 11:2791. doi: 10.3390/rs11232791

Knoblauch, C., Beer, C., Liebner, S., Grigoriev, M. N., and Pfeiffer, E. M. (2018). Methane production as key to the greenhouse gas budget of thawing permafrost. *Nat. Clim. Change* 8, 1–4. doi: 10.1038/s41558-018-0095-z

Knoblauch, C., Beer, C., Sosnin, A., Wagner, D., and Pfeiffer, E. M. (2013). Predicting long-term carbon mineralization and trace gas production from thawing permafrost of Northeast Siberia. *Glob. Change Biol.* 19, 1160–1172. doi: 10.1111/gcb.12116

Kokelj, S. V., Lacelle, D., Lantz, T. C., Tunnicliffe, J., Malone, L., Clark, I. D., et al. (2013). Thawing of massive ground ice in mega slumps drives increases in stream sediment and solute flux across a range of watershed scales. *J. Geophys. Res. Earth Surf.* 118, 681–692. doi: 10.1002/jgrf.20063

Kokelj, S. V., Smith, C. A. S., and Burn, C. R. (2002). Physical and chemical characteristics of the active layer and permafrost, Herschel Island, western Arctic Coast, Canada. *Permafrost Periglac. Process.* 13, 171–185. doi: 10.1002/ppp.417

Kristensen, E., Ahmed, S. I., and Devol, A. H. (1995). Aerobic and anaerobic decomposition of organic matter in marine sediment: which is fastest? *Limnol. Oceanogr.* 40, 1430–1437. doi: 10.4319/lo.1995.40.8.1430

Kuhry, P., and Vitt, D. H. (1996). Fossil carbon/nitrogen ratios as a measure of peat decomposition. *Ecol. Soc. Am.* 77, 271–275. doi: 10.2307/2265676

Kvenvolden, K. (1970). "Evidence for transformation of normal fatty acids in sediments," in *Advances in Organic Geochemistry*, 1966, eds G. D. Hobson and G. C. Speers (Oxford: Pergamon Press), 335–366.

Lamb, A. L., Wilson, G. P., and Leng, M. J. (2006). A review of coastal palaeoclimate and relative sea-level reconstructions using δ13C and C/N ratios in organic material. *Earth Sci. Rev.* 75, 29–57. doi: 10.1016/j.earscirev.2005.10.003

Lantuit, H., Overduin, P. P., Couture, N., Wetterich, S., Aré, F., Atkinson, D., et al. (2012). The arctic coastal dynamics database: a new classification scheme and statistics on arctic permafrost coastlines. *Estuar. Coasts* 35, 383–400. doi: 10.1007/s12237-010-9362-6

Lantuit, H., and Pollard, W. H. (2005). Temporal stereophotogrammetric analysis of retrogressive thaw slumps on Herschel Island, Yukon Territory. *Nat. Haz. Earth Syst. Sci.* 5, 413–423. doi: 10.5194/nhess-5-413-2005

Lantuit, H., and Pollard, W. H. (2008). Fifty years of coastal erosion and retrogressive thaw slump activity on Herschel Island, southern Beaufort Sea, Yukon Territory, Canada. *Geomorphology* 95, 84–102. doi: 10.1016/j.geomorph.2006.07.040

Lee, H., Schuur, E. A. G., Inglett, K. S., Lavoie, M., and Chanton, J. P. (2012). The rate of permafrost carbon release under aerobic and anaerobic conditions and its potential effects on climate. *Glob. Change Biol.* 18, 515–527. doi: 10.1111/j.1365-2486.2011.02519.x

Li, G., Li, L., Tarozo, R., Longo, W. M., Wang, K. J., Dong, H., et al. (2018). Microbial production of long-chain n-alkanes: implication for interpreting sedimentary leaf wax signals. *Organ. Geochem.* 115, 24–31. doi: 10.1016/j.orggeochem.2017.10.005

Littlefair, C. A., Tank, S. E., and Kokelj, S. V. (2017). Retrogressive thaw slumps temper dissolved organic carbon delivery to streams of the Peel Plateau, NWT, Canada. *Biogeosciences* 14, 5487–5505. doi: 10.5194/bg-14-5487-2017

Macdonald, R. W., Kuzyk, Z. Z. A., and Johanessen, S. C. (2015). The vulnerability of Arctic shelf sediments to climate change. *Environ. Rev.* 23, 461–479. doi: 10.1139/er-2015-0040

Mack, M. C., Schuur, E. A. G., Bret-Harte, M. S., Shaver, G. R., and Chapin, F. S. (2004). Ecosystem carbon storage in arctic tundra reduce by long-term nutrient fertilization. *Nature* 431, 440–443. doi: 10.1038/nature02887

Mann, P. J., Eglinton, T. I., McIntyre, C. P., Zimov, N., Davydova, A., Vonk, J. E., et al. (2015). Utilization of ancient permafrost carbon in headwaters of Arctic fluvial networks. *Nat. Commun.* 6:7856. doi: 10.1038/ncomms8856

Manson, G. K., and Solomon, S. M. (2007). Past and future forcing of Beaufort Sea coastal change. *Atmosphere Ocean* 45, 107–122. doi: 10.3137/ao.450204

Manson, G. K., Solomon, S. M., Forbes, D. L., Atkinson, D. E., and Craymer, M. (2005). Spatial variability of factors influencing coastal change in the Western Canadian Arctic. *Geo Mar. Lett.* 25, 138–145. doi: 10.1007/s00367-004-0195-9

Mathis, J. T., Pickart, R. S., Byrne, R. H., McNeil, C. L., Moore, G. W. K., Juranek, L. W., et al. (2012). Storm-induced upwelling of high p CO_2 waters onto the continental shelf of the western Arctic Ocean and implications for carbonate mineral saturation states. *Geophysical Research Letters* 39, doi: 10.1029/2012GL051574

McGuire, A., Anderson, L., Christensen, T. R., Dallimore, S., Guo, L., Hayes, D., et al. (2009). Sensitivity of the carbon cycle in the Arctic to climate change. *Ecol. Monogr.* 79, 523–555. doi: 10.1890/08-2025.1

McGuire, A. D., Lawrence, D. M., Koven, C., Clein, J. S., Burke, E., and Chen, G. (2018). Dependence of the evolution of carbon dynamics in the northern permafrost region on the trajectory of climate change. *Proc. Natl. Acad. Sci. U.S.A.* 115, 3882–3887. doi: 10.1073/pnas.1719903115

Millero, F., Huang, F., Graham, T., and Pierrot, D. (2007). The dissociation of carbonic acid in NaCl solutions as a function of concentration and temperature. *Geochim. Cosmochim. Acta* 71, 46–55. doi: 10.1016/j.gca.2006.08.041

Naidu, A. S., Cooper, L. W., Finney, B. P., Macdonald, R. W., Alexander, C., and Semiletov, I. P. (2000). Organic carbon isotope ratio ($\delta^{13}C$) of Arctic Amerasian Continental shelf sediments. *Int. J. Earth Sci.* 89, 522–532. doi: 10.1007/s005310000121

Neff, J. C., and Asner, G. P. (2001). Dissolved organic carbon in terrestrial ecosystems: synthesis and a model. *Ecosystems* 4, 29–48. doi: 10.1007/s100210000058

Nielsen, D. M., Dobrynin, M., Baehr, J., Razumov, S., and Grigoriev, M. (2020). Coastal erosion variability at the southern laptev sea linked to winter sea ice and the arctic oscillation. *Geophys. Res. Lett.* 47:e2019GL086876. doi: 10.1029/2019GL086876

Obu, J., Lantuit, H., Fritz, M., Pollard, W. H., Sachs, T., and Günther, F. (2016). Relation between planimetric and volumetric measurements of permafrost coast erosion: a case study from Herschel Island, western Canadian Arctic. *Polar Res.* 35:30313. doi: 10.3402/polar.v35.30313

Obu, J., Lantuit, H., Grosse, G., Günther, F., Sachs, T., Helm, V., et al. (2015). Coastal erosion and mass wasting along the Canadian Beaufort Sea based on annual airborne LiDAR elevation data. *Geomorphology* 293, 331–346. doi: 10.1016/j.geomorph.2016.02.014

Overduin, P. P., Liebner, S., Knoblauch, C., Günther, F., Wetterich, S., Schirrmeister, L., et al. (2015). Methane oxidation following submarine permafrost degradation: measurements from a central Laptev Sea shelf borehole. *J. Geophys. Res. G Biogeosci.* 120, 965–978. doi: 10.1002/2014JG002862

Overeem, I., Anderson, R. S., Wobus, C. W., Clow, G. D., Urban, F. E., and Matell, N. (2011). Sea ice loss enhances wave action at the Arctic coast. *Geophys. Res. Lett.* 38, 1–6. doi: 10.1029/2011GL048681

Pelletier, B. R., and Medioli, B. E. (2014). Environmental atlas of the Beaufort coastlands. *Geol. Surv. Canada Open File* 7619, 1–271. doi: 10.4095/294601

Pipko, I. I., Pugach, S. P., Semiletov, I. P., Anderson, L. G., Shakhova, N. E., Gustafsson, Ö, et al. (2017). The spatial and interannual dynamics of the surface water carbonate system and air-sea CO2 fluxes in the outer shelf and slope of the Eurasian Arctic Ocean. *Ocean Sci.* 13, 997–1016. doi: 10.5194/os-13-997-2017

Pollard, W. (1990). "The nature and origin of ground ice in the Herschel Island area, Yukon Territory," in *Proceedings of the Fifth Canadian Conference on Permafrost*, Pergélisol, 23–30.

Radosavljevic, B., Lantuit, H., Pollard, W. H., Overduin, P., Couture, N., Sachs, T., et al. (2016). Erosion and flooding — threats to coastal infrastructure in the arctic: a case study from Herschel Island, Yukon Territory, Canada. *Estuar. Coasts* 39, 900–915. doi: 10.1007/s12237-015-0046-0

Ramage, J. L., Fortier, D., Hugelius, G., Lantuit, H., and Morgenstern, A. (2019). Distribution of carbon and nitrogen along hillslopes in three valleys on Herschel Island, Yukon Territory, Canada. *Catena* 178, 132–140. doi: 10.1016/j.catena.2019.02.029

Ramage, J. L., Irrgang, A. M., Herzschuh, U., Morgenstern, A., Couture, N., and Lantuit, H. (2017). Terrain controls on the occurrence of coastal retrogressive thaw slumps along the Yukon Coast, Canada. *J. Geophys. Res. Earth Surf.* 122, 1619–1634. doi: 10.1002/2017JF004231

Rampton, V. N. (1982). Quaternary geology of the Yukon Coastal Plain. *Geol. Surv. Canada Bull.* 317:49.

Rasmussen, H., and Jorgensen, B. B. (1992). Microelectrode studies of seasonal oxygen uptake in a coastal sediment: role of molecular diffusion. *Mar. Ecol. Prog. Ser.* 81, 289–303. doi: 10.3354/meps081289

Rielley, G., Collier, R. J., Jones, D. M., and Eglinton, G. (1991). The biogeochemistry of Ellesmere Lake, U.K.-I: source correlation of leaf wax inputs to the sedimentary lipid record. *Organ. Geochem.* 17, 901–912. doi: 10.1016/0146-6380(91)90031-E

Ruff, M., Fahrni, S., Gäggeler, H. W., Hajdas, I., Suter, M., Synal, H. A., et al. (2010). On-line radiocarbon measurements of small samples using elemental analyzer and MICADAS gas ion source. *Radiocarbon* 52, 1645–1656. doi: 10.1017/S003382220005637X

Sánchez-García, L., Vonk, J. E., Charkin, A. N., Kosmach, D., Dudarev, O. V., Semiletov, I. P., et al. (2014). Characterisation of three regimes of collapsing arctic ice complex deposits on the SE Laptev sea coast using biomarkers and dual carbon isotopes. *Permafrost Periglac. Process.* 25, 172–183. doi: 10.1002/ppp.1815

Schädel, C., Bader, M. K. F., Schuur, E. A. G., Biasi, C., Bracho, R., Capek, P., et al. (2016). Potential carbon emissions dominated by carbon dioxide from thawed permafrost soils. *Nat. Clim. Change* 6, 950–953. doi: 10.1038/nclimate3054

Schädel, C., Schuur, E. A. G., Bracho, R., Elberling, B., Knoblauch, C., Lee, H., et al. (2014). Circumpolar assessment of permafrost C quality and its vulnerability over time using long-term incubation data. *Glob. Change Biol.* 20, 641–652. doi: 10.1111/gcb.12417

Schirrmeister, L., Dietze, E., Matthes, H., Grosse, G., Strauss, J., Laboor, S., et al. (2020). The genesis of Yedoma Ice complex permafrost – grain-size endmember modeling analysis from Siberia and Alaska. *Quatern. Sci. J.* 69, 33–53. doi: 10.5194/egqsj-69-33-2020

Schirrmeister, L., Grigoriev, M. N., Strauss, J., Grosse, G., Overduin, P. P., Kholodov, A., et al. (2018). Sediment characteristics of a thermokarst lagoon in the northeastern Siberian Arctic (Ivashkina Lagoon, Bykovsky Peninsula). *Arktos* 4, 1–16. doi: 10.1007/s41063-018-0049-8

Schuur, E. A. G., McGuire, A. D., Grosse, G., Harden, J. W., Hayes, D. J., Hugelius, G., et al. (2015). Climate change and the permafrost carbon feedback. *Nature* 520, 171–179. doi: 10.1038/nature14338

Semiletov, I. P., Pipko, I., Gustafsson, Ö, Anderson, L. G., Sergienko, V., Pugach, S., et al. (2016). Acidification of East Siberian Arctic Shelf waters through addition of freshwater and terrestrial carbon. *Nat. Geosci.* 9, 361–365. doi: 10.1038/NEGO2695

Semiletov, I. P., Shakhova, N. E., Pipko, I. I., Pugach, S. P., Charkin, A. N., Dudarev, O. V., et al. (2013). Space-time dynamics of carbon and environmental parameters related to carbon dioxide emissions in the Buor-Khaya Bay and adjacent part of the Laptev Sea. *Biogeosciences* 10, 5977–5996. doi: 10.5194/bg-10-5977-2013

Shakhova, N., Semiletov, I., Salyuk, A., Yusupov, V., Kosmach, D., and Gustafsson, O. (2010). Extensive methane venting to the atmosphere from sediments of the East Siberian Arctic Shelf. *Science* 327, 1246–1250. doi: 10.1126/science.1182221

Shakhova, N., Semiletov, I., Sergienko, V., Lobkovsky, L., Yusupov, V., Salyuk, A., et al. (2015). The East Siberian Arctic Shelf: towards further assessment of permafrost-related methane fluxes and role of sea ice. *Philos. Trans. R. Soc. A Math. Phys. Eng. Sci.* 373, 20140451. doi: 10.1098/rsta.2014.0451

Smith, C. A. S., Kennedy, C. E., Hargrave, A. E., and McKenna, K. M. (1989). *Soil and Vegetation of Herschel Island, Yukon Soil Survey Report*, Vol. 1. Ottawa, ON: Land Resource Research Centre, Agriculture Canada.

Sollins, P., Spycher, G., and Glassman, C. A. (1984). Net nitrogen mineralization from light- and heavy-fraction forest soil organic matter. *Soil Biol. Biochem.* 16, 31–37. doi: 10.1016/0038-0717(84)90122-6

Solomon, S. M. (2005). Spatial and temporal variability of shoreline change in the Beaufort-Mackenzie region, northwest territories, Canada. *Geo Mar. Lett.* 25, 127–137. doi: 10.1007/s00367-004-0194-x

Spencer, R. G. M., Mann, P. J., Dittmar, T., Eglinton, T. I., McIntyre, C., Holmes, R. M., et al. (2015). Detecting the signature of permafrost thaw in Arctic rivers. *Geophys. Res. Lett. Res. Lett.* 42, 2830–2835. doi: 10.1002/2015GL063498

Stein, R., and Macdonald, R. W. (2004). *The Arctic Organic Carbon Cycle: Present and Past*. Berlin: Springer.

Stevenson, F. J. (1994). *Humus Chemistry: Genesis, Composition, Reactions*. New York, NY: John Wiley & Sons.

Strauss, J., Schirrmeister, L., Mangelsdorf, K., Eichhorn, L., Wetterich, S., and Herzschuh, U. (2015). Organic-matter quality of deep permafrost carbon - A study from Arctic Siberia. *Biogeosciences* 12, 2227–2245. doi: 10.5194/bg-12-2227-2015

Suzuki, Y., Kudoh, S., and Takahashi, M. (1997). Photosynthetic and respiratory characteristics of an Arctic ice algal community living in low light and low temperature conditions. *J. Mar. Syst.* 11, 111–121. doi: 10.1016/S0924-7963(96)00032-2

Tanski, G., Lantuit, H., Ruttor, S., Knoblauch, C., Radosavljevic, B., Strauss, J., et al. (2017). Transformation of terrestrial organic matter along thermokarst-affected permafrost coasts in the Arctic. *Sci. Total Environ.* 581–582, 434–447. doi: 10.1016/j.scitotenv.2016.12.152

Tanski, G., Wagner, D., Knoblauch, C., Fritz, M., Sachs, T., and Lantuit, H. (2019). Rapid CO2 release from eroding permafrost in seawater. *Geophys. Res. Lett.* 46, 11244–11252. doi: 10.1029/2019GL084303

Vonk, J. E., and Gustafsson, O. (2013). Permafrost-carbon complexities. *Nat. Geosci.* 6, 675–676. doi: 10.1038/ngeo1937

Vonk, J. E., Sánchez-García, L., Semiletov, I., Dudarev, O., Eglinton, T., Andersson, A., et al. (2010). Molecular and radiocarbon constraints on sources and degradation of terrestrial organic carbon along the Kolyma paleoriver transect. East Siberian Sea. *Biogeosciences* 7, 3153–3166. doi: 10.5194/bg-7-3153-2010

Vonk, J. E., Sánchez-García, L., van Dongen, B. E., Alling, V., Kosmach, D., Charkin, A., et al. (2012). Activation of old carbon by erosion of coastal and subsea permafrost in Arctic Siberia. *Nature* 489, 137–140. doi: 10.1038/nature11392

Vonk, J. E., Semiletov, I. P., Dudarev, O. V., Eglinton, T. I., Andersson, A., Shakhova, N., et al. (2014). Preferential burial of permafrost-derived organic carbon in Siberian-Arctic shelf waters. *J. Geophys. Res. Oceans* 119, 8410–8421. doi: 10.1002/2014JC010261

Vonk, J. E., Tank, S. E., Mann, P. J., Spencer, R. G. M., Treat, C. C., Striegl, R. G., et al. (2015). Biodegradability of dissolved organic carbon in permafrost soils and waterways: a meta-analysis. *Biogeosci. Discuss.* 12, 8353–8393. doi: 10.5194/bgd-12-8353-2015

Walz, J., Knoblauch, C., Böhme, L., and Pfeiffer, E.-M. (2017). Regulation of soil organic matter decomposition in permafrost-affected Siberian tundra soils - Impact of oxygen availability, freezing and thawing, temperature, and labile organic matter. *Soil Biol. Biochem.* 110, 34–43. doi: 10.1016/j.soilbio.2017.03.001

Ward, C. P., and Cory, R. M. (2016). Complete and partial photo-oxidation of dissolved organic matter draining permafrost soils. *Environ. Sci. Technol.* 50, 3545–3553. doi: 10.1021/acs.est.5b05354

Ward, R. D. (2020). Sedimentary response of Arctic coastal wetlands to sea level rise. *Geomorpholgy* 370:107400. doi: 10.1016/j.geomorph.2020.107400

Wegner, C., Bennett, K. E., de Vernal, A., Forwick, M., Fritz, M., Heikkila, M., et al. (2015). Variability in transport of terrigenous material on the shelves and the deep Arctic Ocean during the Holocene. *Polar Res.* 34, 1–19. doi: 10.3402/polar.v34.24964

Welte, D. H., and Waples, D. W. (1973). Über die Bevorzugung geradzahliger n-Alkane in Sedimentgesteinen. *Naturwissenschaften* 60, 516–517.

Wild, B., Gentsch, N., Capek, P., Diáková, K., Alves, R. J. E., Bárta, J., et al. (2016). Plant-derived compounds stimulate the decomposition of organic matter in arctic permafrost soils. *Sci. Rep.* 6:25607. doi: 10.1038/srep25607

Wild, B., Schnecker, J., Alves, R. J. E., Barsukov, P., Bárta, J., Čapek, P., et al. (2014). Input of easily available organic C and N stimulates microbial decomposition of soil organic matter in arctic permafrost soil. *Soil Biol. Biochem.* 75, 143–151. doi: 10.1016/j.soilbio.2014.04.014

Wolf-Gladrow, D. A., Zeebe, R. E., Klaas, C., Körtzinger, A., and Dickson, A. G. (2007). Total alkalinity: the explicit conservative expression and its application to biogeochemical processes. *Mar. Chem.* 106, 287–300. doi: 10.1016/j.marchem.2007.01.006

Wolter, J., Lantuit, H., Fritz, M., Macias-Fauria, M., Myers-Smith, I., and Herzschuh, U. (2016). Vegetation composition and shrub extent on the Yukon coast, Canada, are strongly linked to ice-wedge polygon degradation. *Polar Res.* 35:27489. doi: 10.3402/polar.v35.27489

Zolkos, S., Tank, S. E., and Kokelj, S. V. (2018). Mineral weathering and the permafrost carbon-climate feedback. *Geophys. Res. Lett.* 45, 9623–9632. doi: 10.1029/2018GL078748

Conflict of Interest: The authors declare that the research was conducted in the absence of any commercial or financial relationships that could be construed as a potential conflict of interest.

frontiers in Earth Science

ORIGINAL RESEARCH
published: 06 July 2021
doi: 10.3389/feart.2021.689941

Serpentine (Floating) Ice Channels and their Interaction with Riverbed Permafrost in the Lena River Delta, Russia

Bennet Juhls[1], Sofia Antonova[1], Michael Angelopoulos[1], Nikita Bobrov[2], Mikhail Grigoriev[3], Moritz Langer[1,4], Georgii Maksimov[3], Frederieke Miesner[1] and Pier Paul Overduin[1]*

[1]Alfred Wegener Institute Helmholtz Centre for Polar and Marine Research (AWI), Potsdam, Germany, [2]Department of Geophysics, Institute of Earth Sciences, Saint-Petersburg State University, Saint-Petersburg, Russia, [3]Melnikov Permafrost Institute, Siberian Branch of the Russian Academy of Sciences, Yakutsk, Russia, [4]Geography Department, Humboldt Universität zu Berlin, Berlin, Germany

Arctic deltas and their river channels are characterized by three components of the cryosphere: snow, river ice, and permafrost, making them especially sensitive to ongoing climate change. Thinning river ice and rising river water temperatures may affect the thermal state of permafrost beneath the riverbed, with consequences for delta hydrology, erosion, and sediment transport. In this study, we use optical and radar remote sensing to map ice frozen to the riverbed (bedfast ice) vs. ice, resting on top of the unfrozen water layer (floating or so-called serpentine ice) within the Arctic's largest delta, the Lena River Delta. The optical data is used to differentiate elevated floating ice from bedfast ice, which is flooded ice during the spring melt, while radar data is used to differentiate floating from bedfast ice during the winter months. We use numerical modeling and geophysical field surveys to investigate the temperature field and sediment properties beneath the riverbed. Our results show that the serpentine ice identified with both types of remote sensing spatially coincides with the location of thawed riverbed sediment observed with *in situ* geoelectrical measurements and as simulated with the thermal model. Besides insight into sub-river thermal properties, our study shows the potential of remote sensing for identifying river channels with active sub-ice flow during winter vs. channels, presumably disconnected for winter water flow. Furthermore, our results provide viable information for the summer navigation for shallow-draught vessels.

Keywords: river ice, lena river delta, remote sensing, geophysics, permafrost, hydrology, navigation, cryosphere

OPEN ACCESS

Edited by:
Annett Bartsch, b.geos GmbH, Austria

Reviewed by:
Chris D Arp, University of Alaska Fairbanks, United States
Ko Van Huissteden, Vrije Universiteit Amsterdam, Netherlands

****Correspondence:***
Bennet Juhls
bjuhls@awi.de

Specialty section:
This article was submitted to Cryospheric Sciences, a section of the journal Frontiers in Earth Science

Received: *01 April 2021*
Accepted: *22 June 2021*
Published: *06 July 2021*

Citation:
Juhls B, Antonova S, Angelopoulos M, Bobrov N, Grigoriev M, Langer M, Maksimov G, Miesner F and Overduin PP (2021) Serpentine (Floating) Ice Channels and their Interaction with Riverbed Permafrost in the Lena River Delta, Russia. Front. Earth Sci. 9:689941. doi: 10.3389/feart.2021.689941

INTRODUCTION

In addition to the complex interactions between hydrological, sedimentological, and biological processes that occur in most river deltas, Arctic deltas are characterized over a long period by the cryosphere, which is strongly affected by amplified Arctic climate warming and subject to profound changes. The observed increase of solid precipitation (Prowse et al., 2011), earlier river ice break up and later freeze up (Cooley and Pavelsky, 2016; Park et al., 2016; Brown et al., 2018), thinning of the river ice (Prowse et al., 2011; Shiklomanov and Lammers, 2014; Arp et al., 2020; Yang et al., 2021), degradation of the permafrost within the river catchments (Biskaborn et al., 2019), as well as the

increase of water and heat energy discharge (Ahmed et al., 2020; Park et al., 2020) in most of the Arctic rivers induce a multitude of interacting processes controlling the physical and ecological state of these regions and the adjacent coastal and offshore waters of the Arctic Ocean. Understanding Arctic delta systems and their response to climate warming requires more detailed knowledge of the interactions between deltaic processes and the three components of the cryosphere: snow, river ice and permafrost.

Firstly, Arctic rivers are subject to a nival discharge regime, in which most of the annual discharge volume derives from snow melt during the spring freshet. For catchments draining northward to the Arctic Ocean, meltwater begins to flow in the south and accumulates from the entire river watershed northward toward the river mouth as warming moves northward in spring (e.g., Woo, 1986; Walker, 1998).

Secondly, river ice covers channels within Arctic deltas for most of the year, slowing down or even stopping the water flow within the channels. The land- and bedfast ice influence channel morphology by protecting river bars from erosion and hindering sediment transport in winter (McNamara and Kane, 2009) but also by intensifying erosion and sediment transport during the ice break-up in spring (Walker and Hudson, 2003; Piliouras and Rowland, 2020). Energetic high-water stands during ice break up encounter a delta whose channels are still frozen, which can result in ice jams and occasional flooding (Rokaya et al., 2018b; Rokaya et al., 2018a). Routing of water within a delta during this period may vary greatly from year to year and include sub- and super-ice flow.

Thirdly, permafrost interacts with Arctic rivers and their deltas in multiple ways. Ice-bonded perennially frozen river bars and beds protect channels from erosion (McNamara and Kane, 2009; Lauzon et al., 2019). Shallow channels whose river ice freezes to the bed in winter may develop or preserve permafrost beneath them, while deep channels with flowing water beneath the ice during the entire winter can form taliks (Zheng et al., 2019; O'Neill et al., 2020). Taliks can be an important source of greenhouse gases in the water and atmosphere, especially once they are connected to hydrocarbon reservoirs with geologic methane (e.g., Kohnert et al., 2017). Taliks may also become an important pathway for groundwater and groundwater exchange with river water (Charkin et al., 2017, Charkin et al., 2020). A shift from mostly surface runoff toward increased contribution from groundwater flow is expected with degrading permafrost and increasing active layer depths (Evans and Ge, 2017). The long-term stability (longer than centennial) of a deep channel's position determines the location and size of a sub-river talik. Migrating or meandering river channels can expose pre-existing taliks to the atmosphere, causing their refreezing and formation of new permafrost, and in the case of saline sediment, even cryopegs (Stephani et al., 2020). Thermal conditions beneath Arctic river channels, sandbars, intermittent channels and delta deposits and their impact on subsurface water flow have rarely been mapped. How river ice interacts with the river bottom and how important this is for sub-riverbed freeze-thaw processes, river channel morphology and delta dynamics requires study.

Ice frozen to the riverbed conducts heat effectively in winter, cooling the riverbed, whereas deeper water below floating ice insulates the bed from winter cooling. Heat exchange with the riverbed is thus affected by channel morphology and ice dynamics. Visual differences between flooded bedfast ice in shallow parts of the channel and the "dry" floating ice in the deeper part of the channels during the spring melt were first observed and described from aerial photography by Walker (1973) in the Colville River Delta, Alaska. Nalimov (1995) describes the mechanism of elevating floating ice in the channels of the Lena River Delta during the spring flood and introduces the term "serpentine ice" to describe the visually striking phenomenon during ice break-up. Reimnitz, 2002 goes on to describe serpentine ice in more detail and its influence on water flow of the Colville and Kuparuk rivers in Alaska. These studies describe the origin of the phenomenon of serpentine ice, which involves interaction with the riverbed. The questions of its effects on the riverbed, sub-channel permafrost, taliks and groundwater flow are left unexplored. Furthermore, synthetic aperture radar (SAR) remote sensing can be used to distinguish floating and bedfast ice in winter (Duguay et al., 2002; Antonova et al., 2016; Engram et al., 2018). Floating ice appears brighter on a radar image due to the rough interface between ice and water, whereas bedfast ice appears dark due to a low dielectric contrast between ice and the frozen bottom.

In this study, we hypothesize that the position of serpentine ice channels gives information on river channel bathymetry, and indirectly indicates the presence of a talik and shows its position. By comparing results from four independent techniques, we aim to better understand complex interactions between river ice and sub-river permafrost in the largest Arctic delta, the Lena River Delta. We employ synthetic aperture radar (SAR) and optical remote sensing and test their potential to distinguish the two types of river ice in order to classify deep (exceeding maximum ice thickness) and shallow (less than maximum ice thickness) channels. We complement these remote sensing observations with *in situ* electrical resistivity tomography (ERT) surveys as well as numerical modeling of the sub-river thermal regime to test our hypothesis on the spatial correspondence between the deep river channel and sub-river talik.

MATERIALS AND METHODS

Study Area

The Lena River Delta (73°N, 126°E) occupies an area of about 30,000 km^2 in the Republic of Sakha (Yakutia) in Siberia, Russia, and is the largest delta in the Arctic. About 30% of the delta area is covered by lakes and channels (Schneider et al., 2009). The total number of channels in the delta reaches 6,089 with a total length of 14,626 km (Ivanov et al., 1983). There are four major branches in the delta: Trofimovskaya, Bykovskaya, Tumatskaya, and Olenekskaya, which transport most of the total Lena River discharge (**Figure 1**). The channels that carry the most water are Trofimovskaya (62.3% of the average runoff in the summer-autumn season from 1977 to 2007) and Bykovskaya (25.1%)

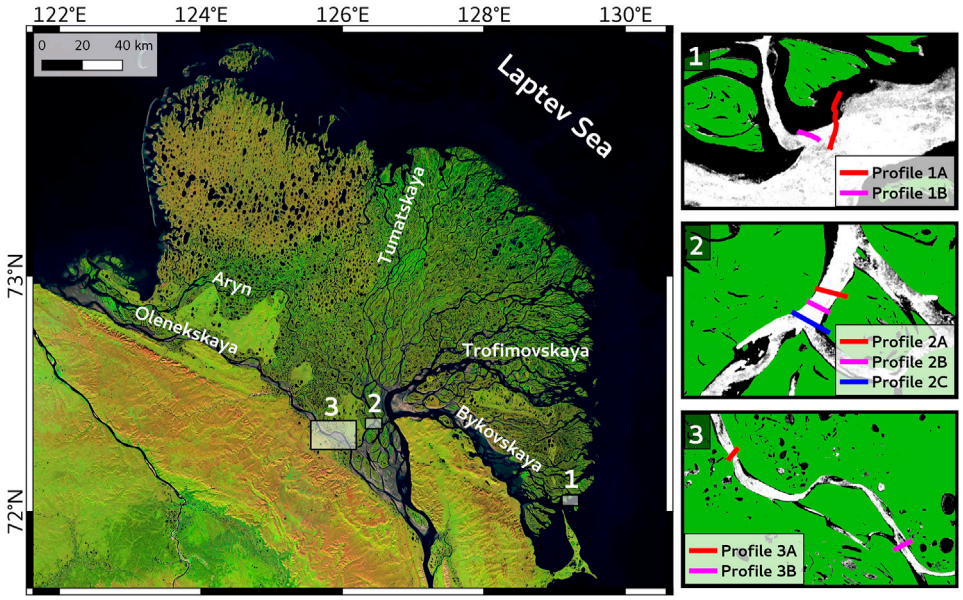

FIGURE 1 | Mosaic of Landsat 8 OLI images (generated in Google Earth Engine) of the Lena River Delta with its numerous river channels. Three sites with *in situ* electrical resistivity tomography (ERT) profiles are shown in the inset maps with the synthetic aperture radar (SAR) winter backscatter image (median of several years) in the background and a land mask (green).

TABLE 1 | List of remote sensing data used in the study.

Satellite sensor	Type	Specs	Resolution	Acquisitions/Periods	Application
Sentinel-2 MSI	Optical	Band 8	10 m	June 8, 2019 May 30, 2020	Serpentine ice mapping and profile extraction
				Sept. 1, 2016 Sept. 2, 2016	Low water level mask
Sentinel-1 SAR	Radar	GRD, IW mode	5 m × 20 m (resampled to 10 m)	Dec. 1. to April 1, 2016–2020	Serpentine ice mapping and profile extraction
				July. 1. to Oct. 1, 2016–2020	High water level mask

(Alekseevskii et al., 2014). Thus, most of the Lena River water (>85%) exits the delta eastward into the Laptev Sea.

Methods

Remote Sensing

Two types of satellite remote sensing data were used in this study: 1) optical data from the Sentinel-2 Multispectral Instrument (MSI) and 2) SAR data from Sentinel-1 mission. Although we used both instruments to detect the same river ice features, the natural processes and remote sensing principles behind the two types of observations are different.

Optical Remote Sensing

Cloud-free optical satellite data (product type S2 MSI L1C) acquired by the Multispectral Instrument (MSI) on-board the Sentinel-2 satellite (S-2) were downloaded from the Copernicus Open Access Hub (https://scihub.copernicus.eu/dhus/). The reflectance for the selected profiles (along the GPS track of the ERT profiles) was extracted from two S-2 scenes (**Table 1**) using band 8 in the near infrared (~833 nm), where the reflectance properties between ice and water differ most. For this study, we chose cloud-free S-2 scenes from late May/early June when the Lena River water level is highest and serpentine ice is present. Additionally, we used cloud-free S-2 imagery from the late summer (Sept. 1 to 2, 2016) during low water level to create a water mask for the low water in the Lena River.

Radar Remote Sensing

Radar data have the advantage of being independent of the cloud cover and polar night, and, therefore, one can explore the advantage of using multiple acquisitions over the focus area. Radar remote sensing has been employed since the 1970s to distinguish shallow and deep parts of Arctic lakes (e.g., Elachi et al., 1976), based on the distinctly different scattering properties from the bedfast ice and the ice resting on top of the unfrozen water mass. The method, however, has seldom been used for river ice.

The Sentinel-1 (S-1) mission began regular operation over the Lena Delta region in 2016, and since then, it has provided images from different overlapping orbits every 12 days. The large amount

of S-1 data acquired so far allows for their temporal aggregation, which can substantially improve the visual quality and enhance the image features. We used Google Earth Engine (GEE) to process a large amount of S-1 data. For S-1, GEE provides the level-1 Ground Range Detected (GRD) product, which gives the calibrated, multilooked, and ortho-rectified backscattering coefficient. We used the Interferometric Wide (IW) Swath Mode, which originally featured 5 m × 20 m resolution, resampled in the GRD product to a pixel size of 10 by 10 m. We used three overlapping orbits, which, when combined, covered the entire Lena Delta and the adjacent coastal areas. Data in the IW mode is dual-polarized and consists of VV and VH polarization bands for the three orbits used here. We used the VH polarization band for the analysis as it showed a higher signal-to-noise ratio than VV band (**Table 1**). We used S-1 data for two purposes: 1) to produce a mask of river channels in summer, and 2) to delineate serpentine ice within the channels.

For producing the summer channel mask, we selected S-1 images only from the period when all river channels were free of ice. According to visual inspection, the period from July 1 to October 1 was a safe choice for all studied years, i.e. no ice was observed in the channels. We used the median backscatter of five summer seasons (2016–2020). Taking the median substantially decreased the noise and facilitated the subsequent classification into land and water classes. In general, the summer images featured distinctly lower backscatter over the water and over the sandbars as a result of specular signal reflection from smooth surfaces, compared to the higher backscatter over the vegetated upland. We used this observation to perform a simple unsupervised classification on the summer median backscatter to separate land from water and sandbars. Visual comparison with optical imagery confirmed the generally good performance of the classification. Because water and sandbars were practically indistinguishable in the SAR signal, the obtained S-1 summer channel mask can also represent the high water stand during the spring flood.

For the mapping of serpentine ice in the river channels, we selected the S-1 images from the winter period when all river channels were frozen. We defined the winter period as from December 1 to April 1. We confirmed visually that break-up did not happen before April 1 for all the studied years. Both serpentine ice and land appear bright on a winter S-1 backscatter image. To avoid confusion between those classes, we used the summer channel mask and excluded the land from the analysis. We classified the two types of ice (serpentine and bedfast) within the extent of the channels.

Geoelectrical Resistivity Surveys

The application of ERT can give us a representation of the geological structure and its state at different depths along the profile of measurements. The precondition for talik detection with direct current electrical resistivity is a substantial resistivity difference between thawed and frozen sediments (Kneisel et al., 2008; Hauck, 2013). Besides temperature, bulk sediment resistivity depends on sediment composition, unfrozen water content, ice content, and the presence of dissolved salts in the pore water. We applied continuous resistivity profiling (CRP), in which a floating electrode streamer was towed behind a small boat, making discrete vertical soundings at set spatial intervals. Positioning was via a global positioning system (GPS) at one end of the cable or streamer for each measurement (site 1: Garmin GPSMAP 64s; sites 2 and 3: Garmin GPSMAP 421, see **Figure 1** for site locations). For CRP, an echo sounder measured water depth at each measurement. An IRIS Syscal Pro system was used to collect the data for all CRP measurements. The streamer was towed behind the boat and the cable floated on the water surface, with the help of regularly spaced buoys attached to the cable.

In CRP, current is injected into the water with two current electrodes and the voltage is measured with two potential electrodes. The calculated resistance is converted to an apparent resistivity using a geometric factor that depends on the configuration of the electrodes. The IRIS Syscal Pro has 10 channels to yield 10 apparent resistivities with different geometric factors at each sounding location almost simultaneously. The apparent resistivity is characteristic of a homogeneous subsurface and thus an inversion of the field data is needed to estimate the true distribution of the electrical resistivity in the ground.

The CRP at site 1 was measured on August 3, 2017 with a 120 m electrode streamer with electrodes arranged in a reciprocal Wenner-Schlumberger array. The electrodes, including the current electrodes, were spaced 10 m apart. Soundings were taken approximately every 20 m based on GPS position. A Sontek CastAway conductivity-temperature-depth (CTD) profiler was used to measure the water column electrical conductivity and temperature. CRP profiles were truncated to sections along which the cable was oriented in a straight line.

Measurements at site 2 were conducted from July 6 to July 14, 2017, at site 3 from July 6 to July 13, 2018. At sites 2 and 3, the towed streamer was 240 m long and a dipole-dipole electrode configuration was employed. The spacing of the current dipole was 20 m, the spacing of the potential dipoles varied from 10 to 40 m and the offsets varied from 25 to 200 m. At the beginning of cross-section profiles, the streamer was laid out on the beach. Despite the river current, the streamer was maintained in a roughly straight line. The CRP profiles 2A–2A', 3A–3A' and 3B–3B' were complemented by stationary ERT soundings on the banks of the river, when the instrument was placed at the water edge. One cable with electrodes was submerged to the river bottom with the far end of the cable anchored by the boat and the other cable laid on the beach, both perpendicular to the shoreline. The results of CRP and stationary ERT measurements conducted along one survey line were then combined and inverted together.

The data from site 1 was processed using Aarhus Workbench software using a 1D laterally constrained inversion. Erroneous data points (outliers) for the outermost electrode pairs were removed from the dataset and no smoothing was applied. A standard deviation of 10% was set to the apparent resistivity data upon model import. The model consisted of 16 layers. The first layer thickness was set using the water depth and the first layer resistivity was set to 100 Ωm in accordance with the measured water electrical conductivity. For profile 1B–1B', the water depths were taken from the echo-sounder. For profile 1A–1A', the water depths were extracted from digitized nautical charts because the

echo-sounder failed at many sounding locations. The CTD profile showed no stratification in the water column. We assigned a standard deviation of 10% to the water layer resistivity and left the remaining layer resistivities unconstrained in the inversion. Layer thicknesses were 1.1 m for the second layer and increased logarithmically with depth until 3.5 m at a depth of 30 m below the riverbed. Due to the wide spacing of soundings, the lateral constraint for resistivity was set to a standard deviation factor of 2.0. The vertical constraint on resistivity was set to a standard deviation factor of 4.0. The smooth inversion scheme was used to process the data, since we had no a priori information on the sediment properties for a few-layered inversion scheme. Default starting model resistivities were used and were the same everywhere in the model domain below the water layer. After the first inversion, modeled data points that fell outside the 10% error bar (forward modeled apparent resistivity outside apparent resistivity error range) were removed from the dataset if the data residual for a sounding was above 1.0. The inversion ran multiple times with reduced data points and the final result was such that each sounding had a data residual at or below 1.0 (i.e., the forward response fell within a 10% error bar on the observed data for each sounding).

Apparent resistivities at sites 2 and 3 were inverted with ZondRes2D software (http://zond-geo.com/english/zond-software/ert-and-ves/zondres2d/). A Smoothness constrained inversion with a Gauss-Newton algorithm was performed. Bathymetry data and water resistivity were included in the model as a priori information. A grid with 11 layers was used with layer thickness increasing logarithmically till a depth of about 70 m. Using a streamer twice as long as that used at site 1 increased the depth of investigation. The horizontal cell size was established in such a manner that the total number of cells was comparable to the total number of measurements to better stabilize the inversion. Joining of the cells in lower layers of the grid was also used, as the resolution of an electrical sounding decreases with depth. Then the same routine as for the data from site 1 was applied: two-stage inversion and exclusion of points for which the misfit exceeded 10% after the first run. The final root mean-squared error fell below three percent for all soundings from sites 2 and 3.

Numerical Modeling of Heat Flux

We use a 2D implementation of the permafrost model CryoGrid (Langer et al., 2016; Westermann et al., 2016) to simulate the temperature field below the Lena River. The model implementation used was defined at the upper boundary by a Dirichlet condition (surface temperature) while the lower boundary (~600 m) was defined by a constant geothermal heat flux (Neumann condition). Turbulent heat transfer through the unfrozen water column was assumed, which was emulated by setting the water column to a uniform temperature equal to the surface temperature during the ice off period (Nitzbon et al., 2019) and 0°C during the ice on period. The model framework including lateral heat transfer has been shown to work well in differently sized lake settings (Langer et al., 2016). In contrast to lakes, a well-mixed water column beneath floating ice was assumed in the model setting. The model was forced with a combination of one-year of measured Lena River water temperatures (Juhls et al., 2020) for the flowing water and 20 years of Samoylov air temperatures (Boike et al., 2019) during periods of bedfast ice. Ice growth and therefore bedfast ice periods were simulated within the model. For both temperature records, we averaged the available data to generate a 1 year forcing with daily mean temperatures. The resulting annual forcing was repeated until the model reached a steady state after a model time of 2000 years. The equilibrium at this point was independent of the assumed temperature field at the beginning of the model period. The model made use of an implicit finite difference scheme to solve the heat equation with phase change, originally established by Swaminathan and Voller (1992). The model calculated the temperature field over a transect through the river channel using a lateral grid cell spacing of 5 m and a logarithmically increasing vertical grid cell spacing with depth. The sediment properties were assumed to be homogeneous over depth and lateral distance, with a sediment porosity of 40% and a mineral thermal conductivity of 3.8 W/(mK).

RESULTS

Mapping Serpentine Ice Using Remote Sensing

Optical (spring) and radar (median winter) imagery showed very similar patterns in reflectance and SAR backscatter in the river channels (**Figure 2**). In the optical images, acquired in late May/early June, we observe high reflectance of light along serpentine ice surfaces, which is usually bordered on either side by low optical reflectance, corresponding to an ice-free water surface (**Figure 2A**). The SAR data (**Figure 2B**) features high backscatter in the deep central parts of the delta channels and low backscatter on either side where the ice is presumably frozen to the riverbed. **Figure 2** also shows that serpentine ice is not limited to the inner part of the delta, but continues offshore around the delta where it becomes wider and finally dissipates. These offshore serpentine ice features can be several tens of kilometers long and describe the continuation of the river channels in the shallow near-shore waters surrounding the Lena River Delta. Additionally, the SAR data shows wide bedfast ice areas in these near-shore zones where water depths are below ~2 m (maximum ice thickness in winter). Within the inner delta, serpentine ice covers most of the channel area. In contrast, toward the mouths of the channels, more relative bedfast ice area compared to floating ice (serpentine ice) is present where channels become wider.

Here, we present the results of the mapping of three different areas within the river channels: channel area during the high water level, channel area during the low water stand, and the deep part of the channels where ice does not freeze to the bottom (i.e., serpentine ice) for the entire Lena River Delta. The map of channels during the high water level was created using summer SAR imagery, the map of channels during the low water level using summer optical imagery, and the map of serpentine ice, i.e., the deep part of channels, using winter SAR imagery (see

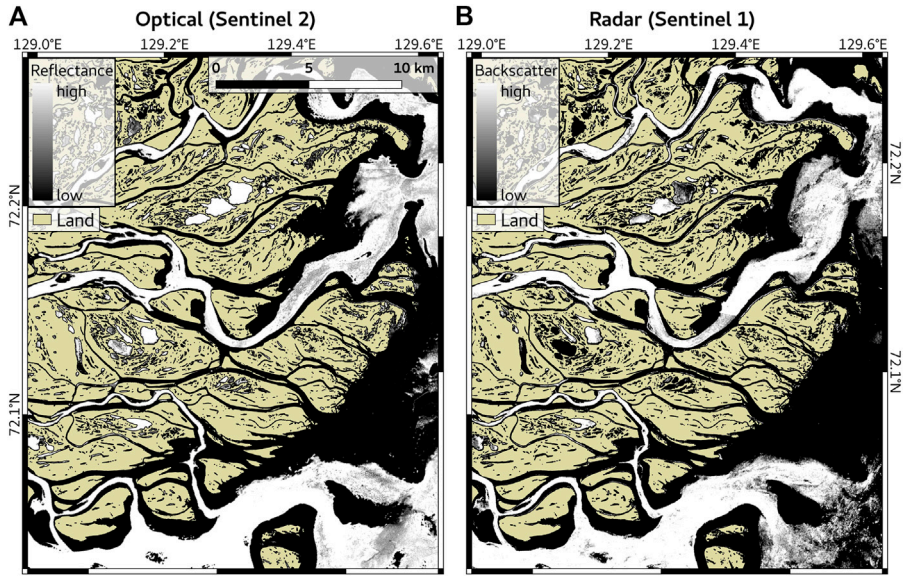

FIGURE 2 | A) Optical Sentinel-2 satellite image (band 8) from June 8, 2019 and **(B)** SAR Sentinel-1 winter median image (2016–2020, December 1 to April 1) of an area at the mouth of the Bykovskaya and Trofimovskaya Channel in the eastern Lena River Delta. Serpentine ice over the deep parts of the channels is featured by high optical reflectance **(A)** and high SAR backscatter **(B)**. Yellow filling shows the upland areas.

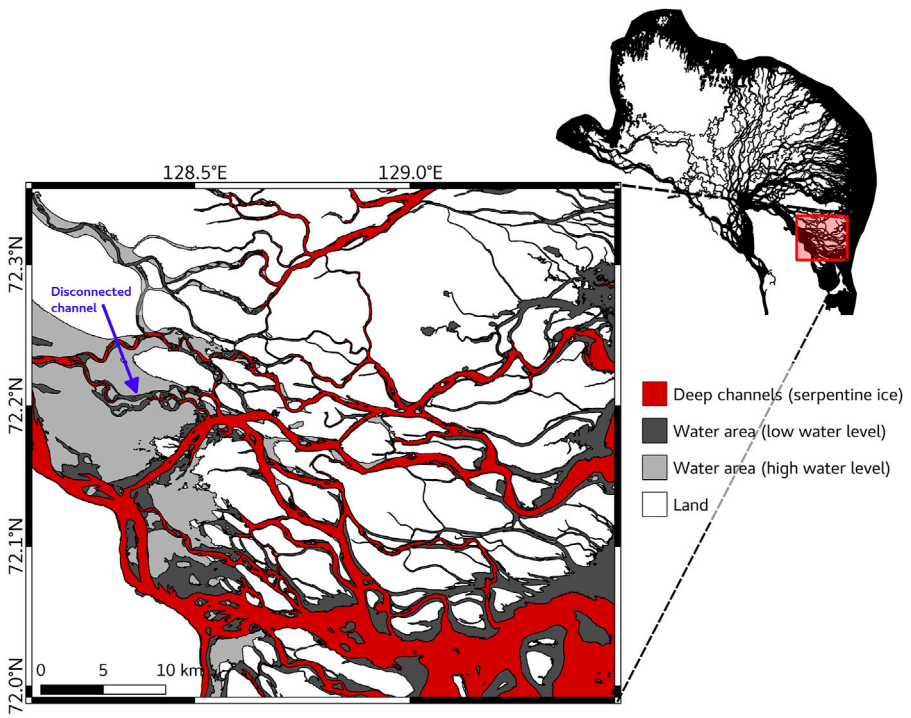

FIGURE 3 | Selected region of the Lena River Delta showing the deep parts of the river channels (red; winter SAR imagery), channel area during low water period (dark gray; optical imagery), and channel area during high water level (light gray; summer SAR imagery).

Methods). The results show the minimum and maximum area of the Lena River Delta that is covered by channels. More importantly, the serpentine ice product shows parts of many channels that are frozen completely which results in an interruption of the channel connectivity to the sea (**Figure 3**). The importance of mapping channels that are characterized by bedfast ice for hydrological routing is further described and discussed in the section *Connectivity of Lena River in Summer*

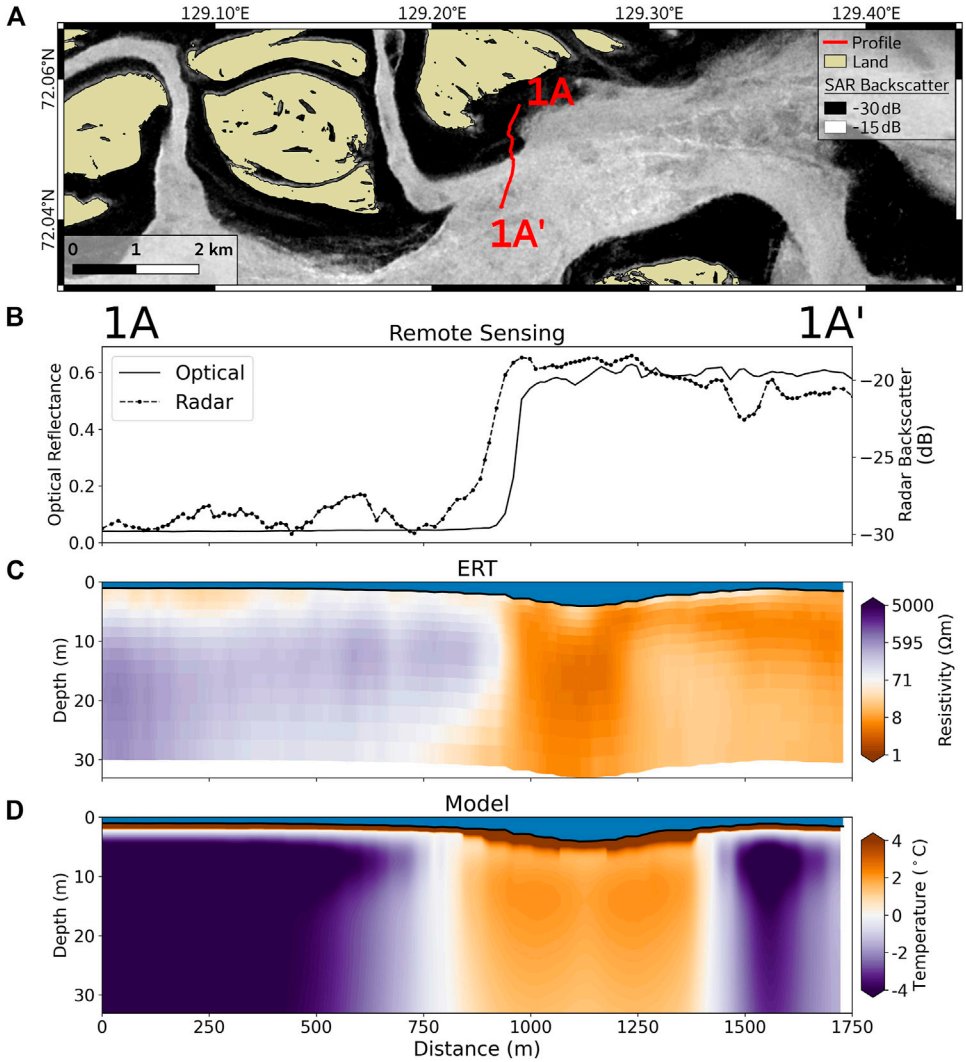

FIGURE 4 | Profile **(1A–1A')** (for the location see **Figure 1**). **(A)** GPS track of the ERT profile on top of the SAR Sentinel-1 median winter image showing the bedfast (dark) and serpentine (bright) ice. **(B)** Extracted optical reflectance and SAR backscatter along the profile. **(C)** Cross section of the inverted ERT resistivity along the profile. **(D)** Modeled sediment temperature along the profile.

vs Winter. Furthermore, the mapping of deep channels along with water extents during different water levels can provide valuable information for navigation (discussed in the section *Using Remote Sensing of the Serpentine Ice for Summer Navigation*). A portion of the dataset is shown in **Figure 3**. Shapefiles of the presented products are available online (https://github.com/bjuhls/SerpChan).

Cross-Channel Profiles of Remote Sensing, Geoelectrical and Model Data

In order to investigate the relationship between the sub-river sediment conditions and the position of the serpentine ice in the river channels, we compare remote sensing observations (reflectance and backscatter), *in situ* ERT measurements, acquired during the field campaign in summers of 2017 and 2018, and a 2D thermal numerical model along the ERT profiles at three locations (**Figures 4–6**, **Supplementary Figures S1–S4**). While site 1 is located at the mouth of the Bykovskaya Channel, site 2 and site 3 are located in the central Lena River Delta (**Figure 1**).

Along the profile 1A–1A' (**Figure 4A**), both optical reflectance and radar backscatter showed a pronounced increase at a distance of 900 m indicating a transition from bedfast ice to serpentine ice (**Figure 4B**). The ERT inversion results (**Figure 4C**) showed a lateral transition toward higher resistivity values also at a distance of 900 m. From 0 to 900 m, there was a high resistivity layer (100–1,000 Ωm) overlain by a thin mid-range resistivity layer (10–100 Ωm) below the water column. South of 900 m, the maximum resistivity in the sediment column was mostly below 10 Ωm until 1,200 m. Starting at 1,250 m, a low resistivity layer (<10 Ωm) was present from the riverbed until

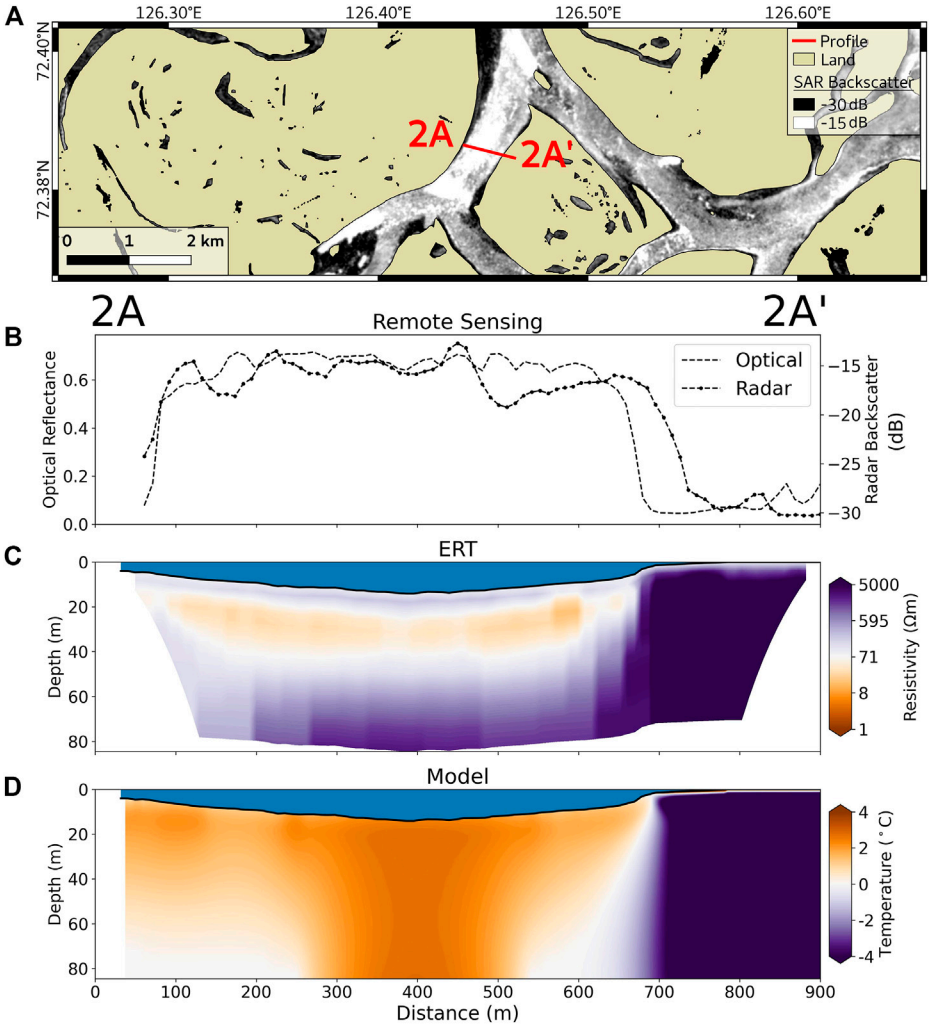

FIGURE 5 | Profile **(2A–2A')** (for the location see **Figure 1**). **(A)** GPS track of the ERT profile on top of the SAR Sentinel-1 median winter image showing the bedfast (dark) and serpentine (bright) ice. Note that bedfast ice is not present (or has minimal presence) on the profile **(2A–2A')**. **(B)** Extracted optical reflectance and SAR backscatter along the profile. **(C)** Cross section of the inverted ERT resistivity along the profile. **(D)** Modeled sediment temperature along the profile.

10 m below water level (bwl) and gradually thickened from the riverbed to 20 m bwl at the end of the profile. The low resistivity layer was overlain by a thin mid-range resistivity layer (10–50 Ωm) <2 m thick just below the water layer in some areas. Furthermore, a mid-range resistivity layer (10–30 Ωm) was also observed below the low resistivity layer after 1,200 m. Despite shallow water depths indicative of highly probable bedfast ice conditions, no resistivities exceeded 100 Ωm, like those observed in the 0–900 m segment. The resistivities exceeding 100 Ωm could reveal the thermal impacts of bedfast ice in shallow areas with water depths between 1 and 2 m from 0 to 800 m and the presence of permafrost. In deeper water (e.g., at position 1,100 m), there is a substantially lower resistivity layer beneath the riverbed, suggesting the presence of unfrozen sediment.

The modeled sediment temperature (**Figure 4D**) showed cold temperatures (<−4°C) in the areas of shallow water (<800 m and >1,400 m) and a pronounced column of warm sediment temperatures (around 0°C) in the center of the profile, largely agreeing with the resistivity results. The low-resistivity and warm-sediment column is consistent with the position of the channels that is characterized by deeper water (≥2 m) compared to the surroundings (<2 m). The modeled sediment temperature after 1,400 m also reveals a frozen permafrost body beneath shallow waters (1.1 to 1.8 m deep), but the resistivity in the sediment column did not exceed 100 Ωm. Hence, the geophysical detection of permafrost along this segment is less certain and this anomaly is addressed in the discussion.

The model is sensitive to whether there is on-ice snow (and its thickness) and to the speed of ice removal during the spring flood. We ran different scenarios to quantify the impact of these two parameters on the temperature of the sediment beneath the riverbed and the position of the permafrost table beneath the talik. Allowing snow to accumulate on the river ice (from 0 m to

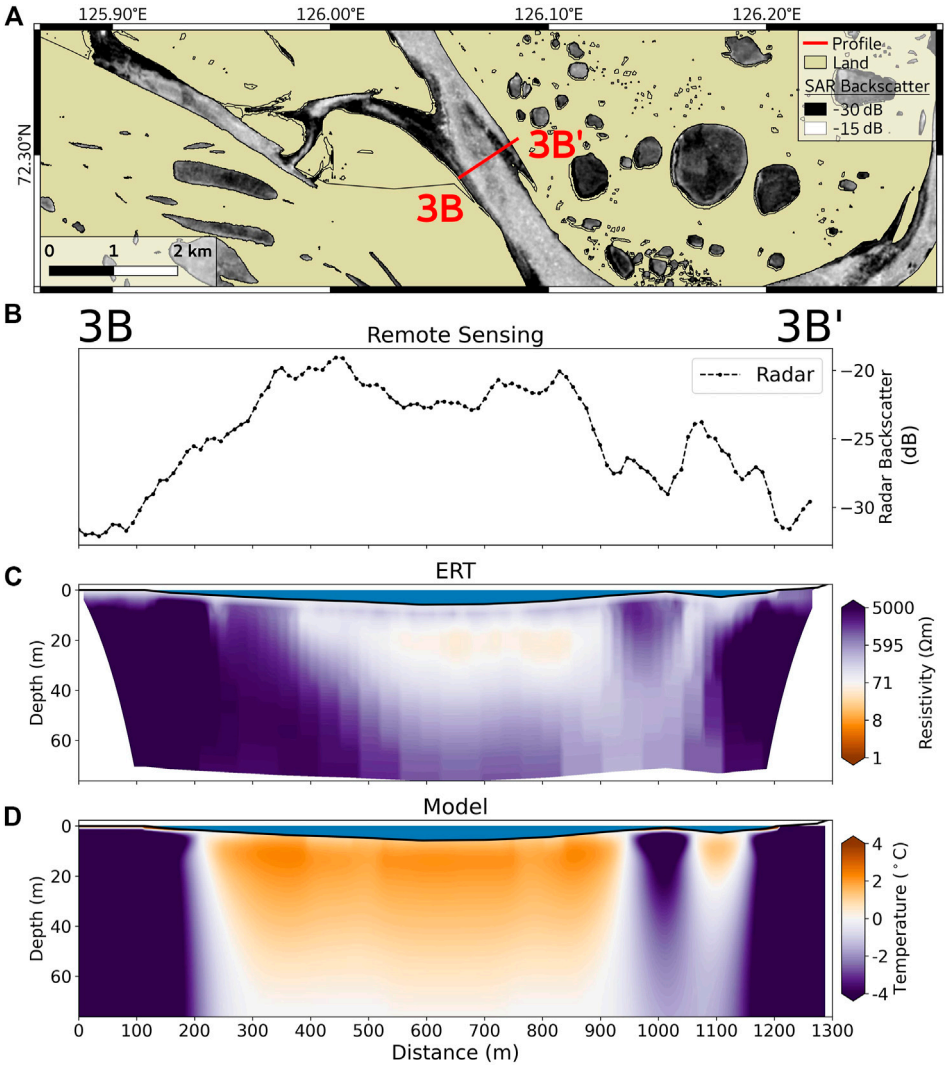

FIGURE 6 | Profile **(3B–3B')** (for the location see **Figure 1**). **(A)** GPS track of the ERT profile on top of the SAR Sentinel-1 median winter image showing the bedfast (dark) and serpentine (bright) ice. **(B)** Extracted SAR backscatter along the profile. **(C)** Cross section of the inverted ERT resistivity along the profile. **(D)** Modeled sediment temperature along the profile.

0.15 m) extended the talik size laterally (**Supplementary Figure S5**) and increased the talik temperature by up to 3°C.

The profile 2A–2A', located in the central Lena Delta, crosses a channel of the Lena River almost completely (**Figure 5**). Both optical and SAR remote sensing data showed similar development along the profile, with high optical reflectance and high SAR backscatter over the serpentine ice (**Figure 5B**). Toward both ends of the profile, the optical reflectance and SAR backscatter dropped. In contrast to site 1 (Profile 1A–1A' and 1B–1B'), this part of the channel does not have a distinctly visible area of bedfast ice but features a rather sharp transition between serpentine ice and land.

Similar to profile 1A–1A', the ERT inversion results showed a closed low-resistivity zone in the sediment beneath the deep part of the river channels for the profile 2A–2A'. The low-resistivity zone (**Figure 5C**) generally showed slightly higher resistivities compared to profile 1A–1A'. Below the low-resistivity zone, resistivities >10 Ωm were observed. The eastern side of the profile (>700 m) showed higher resistivities (1,000–10,000 Ωm).

The modeled sediment temperature for profile 2A–2A' (**Figure 5D**) showed low temperatures (<−4°C) beneath land on the eastern side. Across the whole river channel where water depth was >2 m, the sediment temperatures were positive with a zone of notably warmer sediment along the entire sediment column at the profile interval between 300 and 500 m. Toward the river shore, the lateral temperature gradient was more gradual as a function of depth. At a depth of 82 m, the sediment temperature decreased from >0°C at 500 m to −4°C at 700 m, whereas the same temperature differential spanned just several meters at the riverbed.

The profile 3B–3B', which stretched across zones of bedfast ice, serpentine ice, and land (**Figure 6A**) generally affirmed the observations from the two other profiles. SAR backscatter

(**Figure 6B**) showed generally lower backscatter (about 5 dB) over serpentine ice compared to the sites 1 and 2. Backscatter showed a gradual increase between 100 and 300 m of the profile, where presumably a transition between bedfast and serpentine ice occurs. The transition here is very smooth compared to the steep transitions from land or bedfast ice to serpentine ice in the profiles 1A–1A' and 2A–2A'. This could be related to a lower slope in bathymetry and gradual bedfast freezing in winter, as well as to the interannual variability of the transition between bedfast and serpentine ice, as the median SAR backscatter from several winters is taken. Between 950 and 1,050 m of the profile, the water was shallow (about 0.6 m) whereas another deeper part (2.7 m) was present at 1,100 m before the profile entered land. The variations in the water depth (and as a result, in the ice thickness) are also reflected in the backscatter course over the interval between 950 and 1,100 m. We could not find a suitable optical image during the spring break up for this location.

Profile 3B–3B' was characterized by a more gradually decreasing water depth with respect to the shoreline compared to Profile 2A–A'. Correspondingly, the electrical resistivities of the sediment also decreased gradually from land to increasingly deep sub-aquatic conditions. On land, the resistivities exceeded 1,000 Ωm, and such conditions were sustained in shallow water areas within approximately 100 m of the riverbank. In addition, there was a localized region of high resistivity (>1,000 Ωm) beneath a sandbar at 1,100 m. There was a horizontally oriented oval-shaped low resistivity region (10–50 Ωm) from approximately 20–30 m bwl beneath the center of the channel. Outward of the perimeter of this minimum resistivity structure, the resistivities gradually increase in all directions away from it. Beneath the center of the channel, the resistivity started to exceed 100 Ωm at a depth of approximately 40 m.

The thermal modeling results corroborate the geophysical and remote sensing results for the terrestrial and shallow water areas. More specifically, the model showed cold permafrost temperatures (<−4°C) below land, bedfast ice areas within 100 m of the riverbank, as well as below the sandbar. However, the temperature field and permafrost distribution below the narrow sandbar were strongly affected by lateral heat fluxes. That is to say, the permafrost temperature beneath the sandbar started to increase above −4°C at a depth of 40 m, whereas the sub-aerial permafrost and sediment temperatures within 100 m of the southwestern riverbank were always below −4°C. Toward the northeast, the sediment temperatures were below −4°C within 50 m of the riverbank. Similar to profile 2A–2A', the lateral temperature gradient was more gradual as a function of depth. Only between profile distances of 300–800 m was the entire sediment column just above 0°C and indicative of a talik.

DISCUSSION

Serpentine Ice Formation and its Remote Sensing

We propose two possible explanations for the visibility of serpentine ice channels in spring with optical remote sensing (**Figure 2A**): 1) In winter, the ice growth in shallow waters is limited by the channel bottom. In deeper waters, the ice continues to grow and elastically bends upward, forced by the water beneath. During the spring flood, the elevated ice stays above water level, whereas the bedfast ice becomes submerged by the flood waters. 2) During the spring flood, the strong force of water flowing beneath the ice creates vertical cracks in the zone between bedfast ice and the ice in the deeper part of a channel. It is also possible that these cracks might be already formed by winter water level variations or by the tides in the coastal zones. The bedfast ice remains anchored while the flood waters penetrate through the cracks and submerge the bedfast ice. The ice over the deep part of the channel pops up along the cracks and floats, kept in place by the submerged bedfast ice from both sides.

In either case, the optical image shows low reflectance over flooded bedfast ice and high reflectance over the elevated surface of serpentine ice (**Figure 7A**). This situation can be observed during a relatively short time during spring flood, which typically lasts only a few days before all the ice is exported to the sea or melts.

The importance and timing of processes causing the serpentine ice to elevate above the flooded bedfast ice are not well studied or documented. In this study, we propose the two hypotheses, without providing observational proofs of the described processes (e.g., bending and cracking of ice). Previous studies however, suggested similar mechanisms for serpentine ice formation (Nalimov, 1995; Walker, 1998; Reimnitz, 2002).

The visibility of serpentine ice on winter SAR backscatter images (**Figure 2A**) can be explained by mechanisms which are studied and reported for many Arctic lakes (e.g., Elachi et al., 1976; Duguay et al., 2002; Atwood et al., 2015). Areas of low backscatter generally correspond to bedfast ice, and areas of high backscatter to floating, i.e., serpentine ice. Such distinct backscatter differences result from the interface that the SAR signal encounters after it has penetrated through the fresh ice. The SAR signal either dissipates into frozen bottom sediments under the bedfast ice, resulting in low backscatter, or scatters from the rough ice-water interface, resulting in high backscatter (**Figure 7B**). Based on reported ice thicknesses of the Lena River (Yang et al., 2002, 2021), zones of serpentine ice are restricted to regions with water depths greater than ~1.5 m.

Generally, SAR remote sensing, which is independent of cloud coverage, seems to be a better tool to map serpentine ice/deep channels, compared to optical remote sensing. Considering the frequent cloud cover in the Arctic, it is well possible to miss the short-term event when relying only on optical remote sensing. Furthermore, the turbulent and chaotic processes during the river ice break-up can deform, dislocate or shatter the serpentine ice, making the use of optical imagery less reliable. An example of the disadvantage of optical reflectance compared to SAR backscatter is shown by the fact that we could not identify an optical S-2 image with a stable serpentine ice for profile 3B–3B' (**Figure 6**). For this area, the serpentine ice on the optical image was already dislocated from its original position and did not correspond to the serpentine ice on the SAR image.

On the contrary, all available S-1 data from the whole winter period can be used for mapping exactly the same ice features. While temporal aggregation seems to be a good idea for

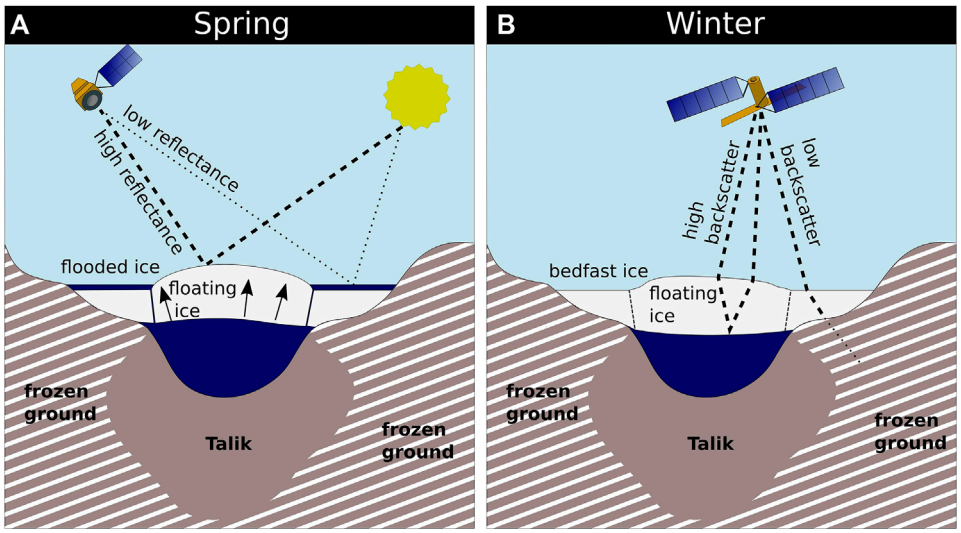

FIGURE 7 | The sharp contrast in albedo between exposed serpentine ice and flooded bedfast ice is visible in optical imagery during the spring flood **(A)**. In winter, the ice-water interface below serpentine ice is an effective reflector and produces a high radar backscatter signal **(B)**.

smoothing and improving the contrast of the S-1 imagery, it is not strictly necessary, and even a single S-1 image can provide a sound distinction between bedfast and serpentine ice. A single S-1 image can provide a better snapshot of a situation in place and time and, therefore, can be used for the time series analysis, but suffers from noise and loses in quality to the temporal average.

Bartsch et al., 2017 show that the influence of incidence angle within the range of 29–46° (range of incidence angle for the S-1 IW mode used in this study) on the C-band backscatter is less than 2 dB. This is substantially lower than the backscatter difference between bedfast and floating ice (10–15 dB, **Figures 4–6**) shown in this study. Therefore, we did not apply an incidence angle normalization on the backscatter.

Implications of Changing Ice Thickness and Deep Channels for Permafrost Presence

In this study, we show that remote sensing can be used to map channels that are suitable for the formation of sub-river taliks in freshwater Arctic deltas and estuaries. Such taliks are interpreted to exist where serpentine ice persists for most of the winter. The sharp lateral transitions from low to high of both SAR backscatter and optical reflectance are in general well co-located with the sharp lateral transitions from high to low inverted bulk electrical resistivity in the sediment. The abrupt increase in resistivity is caused by a shift in the energy balance from the ice/riverbed to the water/riverbed interface. In regions of bedfast ice, heat flux is favored by the high thermal conductivity of the river ice coupling the riverbed to cold winter air temperatures. Beneath serpentine ice, two effects combine to prevent cooling of the riverbed: water provides an insulating layer between the river ice and the bed and heat is advected by water flow from lower latitudes (de Grandpré et al., 2012). In shallow areas where bedfast ice occurs, the sediment can cool rapidly due to atmosphere-riverbed coupling through the ice mass. This coupling can preserve permafrost if the ratio of freezing-degree-day to thawing-degree-day at the riverbed is sufficiently high, as demonstrated by Roy-Leveillee and Burn (2017) for thermokarst lakes. Atmosphere-riverbed coupling can also lead to permafrost aggradation in the case of substantial sediment deposition and consequent bedfasting of the ice in winter (Solomon et al., 2008). In the case of spits and sandbars near the river mouth, permafrost development would be even faster (Vasiliev et al., 2017). In any case, ground ice formation in the sediment results in an exponential increase in electrical resistivity for diverse sediment types (Overduin et al., 2012; Wu et al., 2017; Oldenborger, 2021). Although an electrical resistivity of 1,000 Ωm is commonly attributed to frozen sands with freshwater in the pore space (Fortier et al., 1994), values between 100–1,000 Ωm are reasonable for frozen silts (Holloway and Lewkowicz, 2019). The smooth minimum structure models we applied in the inversion mimic gradual geological transitions in the subsurface rather than sharply defined bodies (Auken and Christiansen, 2004). In the absence of salts, the low resistivity zones (900–1,200 m in profile 1A–1A', **Figure 4C**, 100–700 m profile 2A–2A', **Figure 5C**, and 250–900 m in profile 3B–3B', **Figure 6C**) suggest a talik depth of at least 30 m bwl.

The formation of taliks at least 30 m bwl suggests that the location of the deep river channels in the Lena River Delta is stable. Based on visual inspection of optical remote sensing data with lower spatial resolution (MODIS) over 20 years (2000–2020, www.worldview.earthdata.nasa.gov), the serpentine ice channels occur at the same positions from year to year and vary only in their offshore extent, which can be explained by variability in the magnitude of coastal ice-flooding. While the delineation of floating and bedfast ice in thermokarst lakes using radar remote sensing (e.g., Antonova et al., 2016; Engram et al., 2018; Kohnert et al., 2018) and its potential for studying talik development (Arp et al., 2016) have been recognized, river

channels and their ice regimes are largely overlooked. Long channels with reaches of tens to hundreds of kilometers with underlying taliks can form connections to deeper methane sources (Walter Anthony et al., 2012). Due to their spatial extent, the likelihood that river channel taliks cross geological pathways for gas migration such as the fault system along the southwestern edge of the Lena Delta is perhaps higher compared to lake taliks. Open taliks beneath paleo-river valleys have also been identified as possible pathways for methane release emanating from dissociating gas hydrates in subsea permafrost (e.g., Frederick and Buffett, 2014).

As ice thickness in the Arctic rivers tends to decrease with ongoing climate warming (Vuglinsky and Valatin, 2018) and projected increasing snowfall (e.g., Callaghan et al., 2011), the proportion of serpentine ice to bedfast ice area will likely increase, resulting in increased winter water flow beneath the ice (Gurevich, 2009; Tananaev et al., 2016), positive mean annual temperatures at a greater area of the riverbed and consequent talik growth. Sensitivity analysis of the model used in our study shows that even 5 cm of snow on the river ice can reduce the ice thickness at the end of the season by up to 30 cm, affect the thermal properties of the sub-river sediment, and cause talik growth (**Supplementary Figure S5**). Our results agree with a study on terrestrial permafrost from the Mackenzie Delta region of Canada, where ground surface temperature increased from approximately −24°C in wind-swept areas to −6°C in areas with 100 cm of snow (Smith, 1975).

While the inter-annual stability of channel position is partially due to permafrost formation beneath bedfast ice, atmospheric warming may also result in more dynamic bedload sediment transport and thus increased channel mobility (McNamara and Kane, 2009). We expect that the inter-annual variations in sediment load and ice thickness as well as the long-term trends for both variables can influence the bedfast/serpentine ice regimes and the thermal properties of the riverbed sediments only for the intermittently flooded sandbars and for shallow channels. In the deeper parts of channels, the water depth is in the order of tens of meters, which prevents such channels from migration and the sub-river talik from the influence of the ice thickness changes.

The gradual shift from a bedfast to serpentine ice regime may explain the mid-range electrical resistivity anomaly at distances greater than 1,200 m in profile 1A–1A' (**Figure 4**). For this segment, the equilibrium thermal model state predicts permafrost temperatures as low as −4°C, despite the high optical reflectance and radar backscatter responses that are indicative of serpentine ice. The mid-range electrical resistivity zone (10–30 Ωm) is possibly a reflection of warming and degrading permafrost, compared to the high electrical resistivity zone (100–1,000 Ωm) north of 900 m. We interpret the latter to be colder permafrost sustained by a more stable perennially occurring bedfast ice regime. The profiles at site 1 have inverted resistivities near the riverbed of the central channel that are an order of magnitude lower (<10 Ωm) than those at sites 2 and 3 (<100 Ωm). Profile 1A–1A' also showed lower resistivities in the talik (<10 Ωm) compared to profiles 2A–2A' and 3A–3A' (approximately 10–50 Ωm). We attribute the lower resistivities of the talik at the delta's edge to possibly higher salt content in the sediment. We speculate that this is due to a number of processes including storm surges from Laptev Sea water, as well as groundwater flowing through taliks from upland areas to the nearshore zone. In fact, Fedorova et al. (2015) have suggested that infiltration of river water into taliks exerts a control on the delta's discharge. Drawing on the research of Arctic perennial springs, flowing groundwater can mobilize salts and transport them to the outlet where they are deposited (Andersen, 2002).

Connectivity of Lena River in Summer vs Winter

The Lena River discharge in winter is substantially smaller (59 km^3 for November–April) compared to summer (306 km^3 for July–October) and spring (216 km^3 for May–June) (Holmes et al., 2012). The map of serpentine ice for the whole delta (and, thus, the map of the deep channels) showed that the distribution of the water discharge through the channels also changes. **Figure 8** shows that there are many channels that are disconnected in winter due to a complete freezing of the water column, at least as determined at the spatial resolution of the imagery used here. The total area of channels in the Lena River Delta (that have a connection to the sea) in winter (1,102 km^2) is only 51% of what it is in summer (2,139 km^2). Compared to the channel connectivity in summer, substantially fewer channels connected the main Lena River channel to the sea in winter (**Figure 8**). Only four large channels (Trofimofskaya, Bykovskaya, Olenekskaya and the Aryn Channel, **Figure 1**) stay active in winter, while most of the smaller channels, many of which connect the larger channels with each other, are disconnected due to freezing of the ice to the bed. Due to the limited spatial resolution of the remote sensing data (better than at least 20 m, **Table 1**), narrower channels may remain undetected by our method.

The winter connectivity of channels and the under-ice water flow has an impact on the distribution and accumulation of the freshwater on the Laptev Sea during the ice-covered period. The interruption of flow through channels in the northern part of the Lena River Delta (Tumatskaya Channel) effectively turns off the winter under-ice freshwater supply to northern coastal waters. This may explain the observed high salinity (>20) and low turbidity of upper water beneath the landfast ice in winter compared to the outflow region east of the delta (Wegner et al., 2017; Hölemann et al., 2021). Furthermore, blocked channels probably play an important role for ice jams in the early stage of the freshet in spring (Beltaos et al., 2012; Kozlov and Kuleshov, 2019).

As climate warming drives permafrost thaw, groundwater will likely increase its contribution to the Lena River discharge (Frey and McClelland, 2009). Increasing active layer thickness and new groundwater flow pathways might be detectable by a long-term increase in winter base flow, which originates mostly from subsurface water (Juhls et al., 2020). Increasing winter discharge is observed for the Lena and other great Arctic Rivers (Yang et al., 2002; McClelland et al., 2006). The increased winter discharge is transported exclusively by the connected deep channels. Mapping

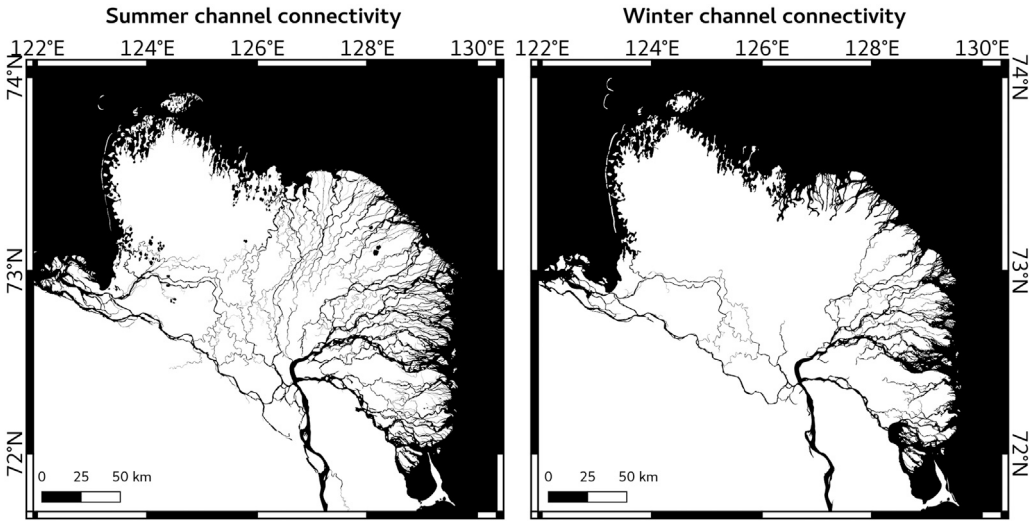

FIGURE 8 | Sea-connected Lena River channels in summer during low water level **(left)** based on optical remote sensing data (Sentinel-2) and in winter **(right)** based on SAR remote sensing data (Sentinel-1).

active delta channels becomes, therefore, increasingly important, also as a baseline for future hydrological changes to Arctic river deltas and receiving coastal waters.

Using Remote Sensing of the Serpentine Ice for Summer Navigation

Through our own field experience in the Lena River Delta, it has not escaped our notice that the delineation of serpentine ice using remote sensing provides a means of mapping navigable channels. Shipping channels in coastal zones at the mouth of Arctic deltas are characterized by extremely shallow waters and river ice dynamics make nautical markings such as buoys impractical. We tested the Sentinel-1-based map of serpentine ice to navigate along the Olenekskaya Channel in the very western part of the Lena River Delta (see **Figure 1** for the location) in summer 2016. The GPS track of the small ship (draft of 1.5 m) that was used for the travel to the western Laptev Sea followed exactly the serpentine ice course that was mapped with Sentinel-1 imagery (**Figure 9**). Whenever the ship deviated from the course defined by serpentine ice, it became grounded in the shoals. In particular, the serpentine ice map aided in navigation in the open coastal waters during the night.

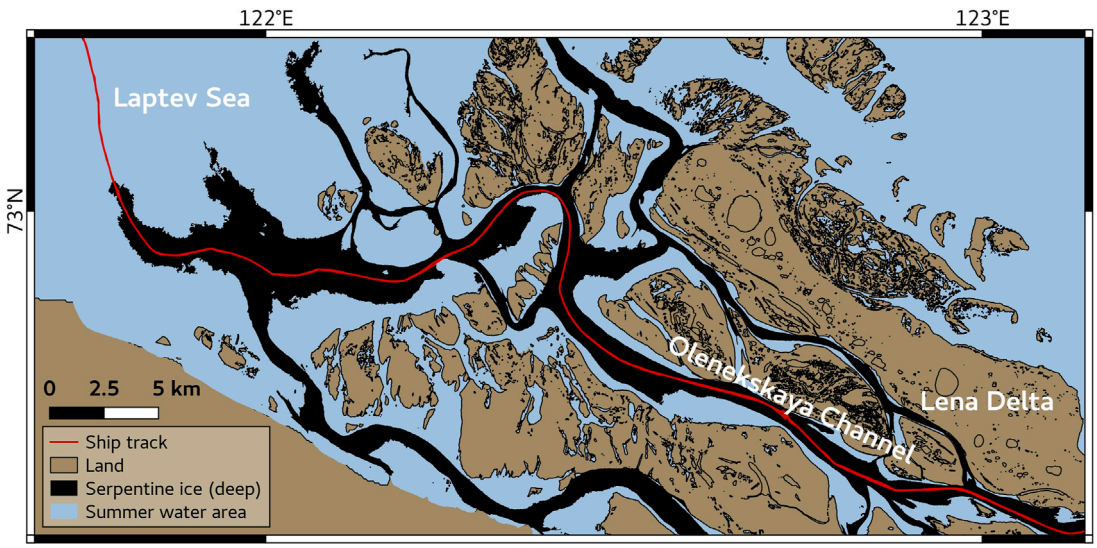

FIGURE 9 | Track of a ship (red line) navigated in summer 2016 along the Olenekskaya Channel toward the western part of the Laptev Sea. A SAR-based map of serpentine ice was used for navigating along the deep parts of the channel, surrounded by extreme shallows (<1 m).

Currently, the Bykovskaya Channel (see **Figure 1** for the location) is mostly used for regular shipping between the Laptev Sea and the upstream Lena River (www.marinetraffic.com). A direct routing from the western Laptev Sea to the main Lena River channel would save several hundreds of kilometers compared to the Bykovskaya Channel route. In consultation with local hydrographic services, the results of this study can, therefore, improve charts of traditional ship-based hydrographic surveys and ultimately the ship navigation in uncharted delta channels. Moreover, traditional hydrographic surveying techniques are costly and time consuming. In addition to mapping deeper parts of channels within the delta, we also map the prolongation of the deep channels offshore from the delta's edge to the Laptev Sea. Our results demonstrate that annual-scale monitoring of the ice regime (bedfast vs serpentine) and the deep channels position is possible. These annual maps may be used as an aid for summer navigation for shallow-draught vessels, particularly in regions where navigational charts may not be regularly updated. The proposed mapping of deep river channels can be applied to other Arctic River deltas and estuaries, such as the Mackenzie Delta and the Kolyma estuary, that are characterized by shallow water depths at the river mouth and in the coastal zones. Current and future satellite missions will ensure regular updates of the maps to account for potential channel dynamics.

CONCLUSION

The bright elongated meandering river ice structures, detected on airborne photographs over several Arctic river deltas in the beginning of the spring break-up, were given the name of "serpentine ice" in the literature. In this study, we showed that SAR and optical remote sensing can be used to map the serpentine ice, which corresponds to the parts of the river channels that are deep enough not to freeze to the bottom throughout the winter. SAR backscatter from Sentinel-1 effectively distinguished serpentine ice from bedfast (frozen to the bottom) ice based on the different dielectric properties at the ice-water (in case of serpentine ice) and ice-frozen sediments (in case of bedfast ice) interfaces in winter. Optical reflectance from Sentinel-2 distinguished the highly reflective surfaces of elevated serpentine ice from strongly absorbing water on flooded bedfast ice in spring. By extending the remote sensing data with numerical thermal modeling and shallow geophysical data (ERT) acquired at several sites within the Lena River Delta, we showed that the distribution of bedfast and serpentine ice corresponds to the zones of frozen and thawed sediments beneath the riverbed. For river channels whose position remains stable over long periods of time, the presence of serpentine ice likely suggests the presence of a deep talik. The spatial correspondence between the river ice regime (bedfast or serpentine) and the thermal state of the sub-river sediments demonstrates the great potential of remote sensing to identify not only the long existing taliks beneath deep river channels but also areas, subject to potential change of the ice regime, which can, in turn, trigger either formation of new permafrost or thaw of existing permafrost beneath the riverbed.

Our map of serpentine ice provides new information about channels open to winter sub-ice flow and reveals how bedfast ice limits hydrological routing in winter compared to summer in the Lena River Delta. Our results can improve representation of river channel shape, sediment and matter dynamics, and ice-jamming in hydrological models. Moreover, our study shows how remote sensing can complement nautical charts to locate deep channels navigable for small ships.

DATA AVAILABILITY STATEMENT

The original contributions presented in the study are included in the article/**Supplementary Materials**, further inquiries can be directed to the corresponding author. The data sets, codes and products of this study are available online (https://github.com/bjuhls/SerpChan).

AUTHOR CONTRIBUTIONS

All authors contributed to the final design of the study. BJ and SA processed remote sensing data. PO, MA, NB, GM, and MG obtained and processed the geoelectrical data. FM and ML ran the model experiments. All authors contributed to the interpretation of data and writing of the manuscript.

FUNDING

This research was supported by the EU Horizon 2020 program (Nunataryuk, grant no. 773421). ERT data at the Olenekskaya Channel were obtained in the framework of the Russian Foundations for Basic Research project №18-05-60291. Projects from the BMBF-NERC's Changing Arctic Ocean program (CACOON, NERC grant no. NE/R012806/1, BMBF grant no. 03F0806A) supported discussions within a larger group of experts.

ACKNOWLEDGMENTS

Measurements at sites 2 and 3 were performed with the use of the equipment provided by the Research Park of St. Petersburg State University, Center for Geo-Environmental Research and Modeling (GEOMODEL). We are also grateful to the comments of two reviewers. I acknowledge support by the Open Access Publication Funds of Alfred-Wegener-Institut Helmholtz-Zentrum für Polar-und Meeresforschung.

SUPPLEMENTARY MATERIAL

The Supplementary Material for this article can be found online at: https://www.frontiersin.org/articles/10.3389/feart.2021.689941/full#supplementary-material

REFERENCES

Ahmed, R., Prowse, T., Dibike, Y., Bonsal, B., and O'Neil, H. (2020). Recent Trends in Freshwater Influx to the Arctic Ocean from Four Major Arctic-Draining Rivers. *Water* 12, 1189. doi:10.3390/w12041189

Alekseevskii, N. I., Aibulatov, D. N., Kuksina, L. V., and Chetverova, A. A. (2014). The Structure of Streams in the Lena delta and its Influence on Streamflow Transformation Processes. *Geogr. Nat. Resour.* 35, 63–70. doi:10.1134/S1875372814010090

Andersen, D. T. (2002). Cold Springs in Permafrost on Earth and Mars. *J. Geophys. Res.* 107, 5015. doi:10.1029/2000JE001436

Antonova, S., Duguay, C., Kääb, A., Heim, B., Langer, M., Westermann, S., et al. (2016). Monitoring Bedfast Ice and Ice Phenology in Lakes of the Lena River Delta Using TerraSAR-X Backscatter and Coherence Time Series. *Remote Sensing* 8, 903. doi:10.3390/rs8110903

Arp, C. D., Cherry, J. E., Brown, D. R. N., Bondurant, A. C., and Endres, K. L. (2020). Observation-derived Ice Growth Curves Show Patterns and Trends in Maximum Ice Thickness and Safe Travel Duration of Alaskan Lakes and Rivers. *Cryosphere* 14, 3595–3609. doi:10.5194/tc-14-3595-2020

Arp, C. D., Jones, B. M., Grosse, G., Bondurant, A. C., Romanovsky, V. E., Hinkel, K. M., et al. (2016). Threshold Sensitivity of Shallow Arctic Lakes and Sublake Permafrost to Changing winter Climate. *Geophys. Res. Lett.* 43, 6358–6365. doi:10.1002/2016GL068506

Atwood, D. K., Gunn, G. E., Roussi, C., Wu, J., Duguay, C., and Sarabandi, K. (2015). Microwave Backscatter from Arctic Lake Ice and Polarimetric Implications. *IEEE Trans. Geosci. Remote Sensing* 53, 5972–5982. doi:10.1109/TGRS.2015.2429917

Auken, E., and Christiansen, A. V. (2004). Layered and Laterally Constrained 2D Inversion of Resistivity Data. *Geophysics* 69, 752–761. doi:10.1190/1.1759461

Bartsch, A., Pointner, G., Leibman, M. O., Dvornikov, Y. A., Khomutov, A. V., and Trofaier, A. M. (2017). Circumpolar Mapping of Ground-Fast Lake Ice. *Front. Earth Sci.* 5, 12. doi:10.3389/feart.2017.00012

Beltaos, S., Carter, T., and Rowsell, R. (2012). Measurements and Analysis of Ice Breakup and Jamming Characteristics in the Mackenzie Delta, Canada. *Cold Regions Sci. Techn.* 82, 110–123. doi:10.1016/j.coldregions.2012.05.013

Biskaborn, B. K., Smith, S. L., Noetzli, J., Matthes, H., Vieira, G., Streletskiy, D. A., et al. (2019). Permafrost Is Warming at a Global Scale. *Nat. Commun.* 10, 1–11. doi:10.1038/s41467-018-08240-4

Boike, J., Nitzbon, J., Anders, K., Grigoriev, M., Bolshiyanov, D., Langer, M., et al. (2019). A 16-year Record (2002-2017) of Permafrost, Active-Layer, and Meteorological Conditions at the Samoylov Island Arctic Permafrost Research Site, Lena River delta, Northern Siberia: An Opportunity to Validate Remote-Sensing Data and Land Surface, Snow, and Permafrost Models. *Earth Syst. Sci. Data* 11, 261–299. doi:10.5194/essd-11-261-2019

Brown, D. R. N., Brinkman, T. J., Verbyla, D. L., Brown, C. L., Cold, H. S., and Hollingsworth, T. N. (2018). Changing River Ice Seasonality and Impacts on interior Alaskan Communities. *Weather. Clim. Soc.* 10, 625–640. doi:10.1175/WCAS-D-17-0101.1

Callaghan, T. V., Johansson, M., Brown, R. D., Groisman, P. Y., Labba, N., Radionov, V., et al. (2011). The Changing Face of Arctic Snow Cover: A Synthesis of Observed and Projected Changes. *Ambio* 40, 17–31. doi:10.1007/s13280-011-0212-y

Charkin, A. N., Pipko, I. I., Yu. Pavlova, G., Dudarev, O. V., Leusov, A. E., Barabanshchikov, Y. A., et al. (2020). Hydrochemistry and Isotopic Signatures of Subpermafrost Groundwater Discharge along the Eastern Slope of the Lena River Delta in the Laptev Sea. *J. Hydrol.* 590, 125515. doi:10.1016/j.jhydrol.2020.125515

Charkin, A. N., Rutgers van der Loeff, M., Shakhova, N. E., Gustafsson, Ö., Dudarev, O. V., Cherepnev, M. S., et al. (2017). Discovery and Characterization of Submarine Groundwater Discharge in the Siberian Arctic Seas: a Case Study in the Buor-Khaya Gulf, Laptev Sea. *Cryosphere* 11, 2305–2327. doi:10.5194/tc-11-2305-2017

Cooley, S. W., and Pavelsky, T. M. (2016). Spatial and Temporal Patterns in Arctic River Ice Breakup Revealed by Automated Ice Detection from MODIS Imagery. *Remote Sensing Environ.* 175, 310–322. doi:10.1016/j.rse.2016.01.004

de Grandpré, I., Fortier, D., and Stephani, E. (2012). Degradation of Permafrost beneath a Road Embankment Enhanced by Heat Advected in groundwater 1. *Can. J. Earth Sci.* 49, 953–962. doi:10.1139/E2012-018

Duguay, C. R., Pultz, T. J., Lafleur, P. M., and Drai, D. b. (2002). RADARSAT Backscatter Characteristics of Ice Growing on Shallow Sub-Arctic Lakes, Churchill, Manitoba, Canada. *Hydrol. Process.* 16, 1631–1644. doi:10.1002/hyp.1026

Elachi, C., Bryan, M. L., and Weeks, W. F. (1976). Imaging Radar Observations of Frozen Arctic Lakes. *Remote Sensing Environ.* 5, 169–175. doi:10.1016/0034-4257(76)90047-X

Engram, M., Arp, C. D., Jones, B. M., Ajadi, O. A., and Meyer, F. J. (2018). Analyzing Floating and Bedfast lake Ice Regimes across Arctic Alaska Using 25 years of Space-Borne SAR Imagery. *Remote Sensing Environ.* 209, 660–676. doi:10.1016/j.rse.2018.02.022

Evans, S. G., and Ge, S. (2017). Contrasting Hydrogeologic Responses to Warming in Permafrost and Seasonally Frozen Ground Hillslopes. *Geophys. Res. Lett.* 44, 1803–1813. doi:10.1002/2016GL072009

Fedorova, I., Chetverova, A., Bolshiyanov, D., Makarov, A., Boike, J., Heim, B., et al. (2015). Lena Delta Hydrology and Geochemistry: Long-Term Hydrological Data and Recent Field Observations. *Biogeosciences* 12, 345–363. doi:10.5194/bg-12-345-2015

Fortier, R., Allard, M., and Seguin, M.-K. (1994). Effect of Physical Properties of Frozen Ground on Electrical Resistivity Logging. *Cold Regions Sci. Techn.* 22, 361–384. doi:10.1016/0165-232X(94)90021-3

Frederick, J. M., and Buffett, B. A. (2014). Taliks in Relict Submarine Permafrost and Methane Hydrate Deposits: Pathways for Gas Escape under Present and Future Conditions. *J. Geophys. Res. Earth Surf.* 119, 106–122. doi:10.1002/2013JF002987

Frey, K. E., and McClelland, J. W. (2009). Impacts of Permafrost Degradation on Arctic River Biogeochemistry. *Hydrol. Process.* 23, 169–182. doi:10.1002/hyp.7196

Gurevich, E. V. (2009). Influence of Air Temperature on the River Runoff in winter (The Aldan River Catchment Case Study). *Russ. Meteorol. Hydrol.* 34, 628–633. doi:10.3103/S1068373909090088

Hauck, C. (2013). New Concepts in Geophysical Surveying and Data Interpretation for Permafrost Terrain. *Permafrost Periglac. Process.* 24, 131–137. doi:10.1002/ppp.1774

Hölemann, J. A., Juhls, B., Bauch, D., Janout, M., Koch, B. P., and Heim, B. (2021). The impact of the freeze–melt cycle of land-fast ice on the distribution of dissolved organic matter in the Laptev and East Siberian seas (Siberian Arctic). *Biogeosciences* 18 (12), 3637–3655. doi:10.5194/bg-18-3637-2021

Holloway, J., and Lewkowicz, A. (2019). "Field and Laboratory Investigation of Electrical Resistivity-Temperature Relationships, Southern Northwest Territories," in 18th International Conference on Cold Regions Engineering and 8th Canadian Permafrost Conference, Quebec City, QC, Canada (American Society of Civil Engineers (ASCE)), 64–72. doi:10.1061/9780784482599.008

Holmes, R. M., McClelland, J. W., Peterson, B. J., Tank, S. E., Bulygina, E., Eglinton, T. I., et al. (2012). Seasonal and Annual Fluxes of Nutrients and Organic Matter from Large Rivers to the Arctic Ocean and Surrounding Seas. *Estuaries and Coasts* 35, 369–382. doi:10.1007/s12237-011-9386-6

Ivanov, V. V., Piskun, A. A., and Korabel, R. A. (1983). Distribution of Runoff through the Main Channels of the Lena River Delta (In Russian). *Tr. AANI (Proceedings AARI)* 378, 59–71.

Juhls, B., Stedmon, C. A., Morgenstern, A., Meyer, H., Hölemann, J., Heim, B., et al. (2020). Identifying Drivers of Seasonality in Lena River Biogeochemistry and Dissolved Organic Matter Fluxes. *Front. Environ. Sci.* 8, 53. doi:10.3389/fenvs.2020.00053

Kneisel, C., Hauck, C., Fortier, R., and Moorman, B. (2008). Advances in Geophysical Methods for Permafrost Investigations. *Permafrost Periglac. Process.* 19, 157–178. doi:10.1002/ppp.616

Kohnert, K., Juhls, B., Muster, S., Antonova, S., Serafimovich, A., Metzger, S., et al. (2018). Toward Understanding the Contribution of Waterbodies to the Methane Emissions of a Permafrost Landscape on a Regional Scale-A Case Study from the Mackenzie Delta, Canada. *Glob. Change Biol.* 24, 3976–3989. doi:10.1111/gcb.14289

Kohnert, K., Serafimovich, A., Metzger, S., Hartmann, J., and Sachs, T. (2017). Strong Geologic Methane Emissions from Discontinuous Terrestrial Permafrost in the Mackenzie Delta, Canada. *Sci. Rep.* 7, 1–6. doi:10.1038/s41598-017-05783-2

Kozlov, D. V., and Kuleshov, S. L. (2019). Multidimensional Data Analysis in the Assessment of Ice-Jam Formation in River Basins. *Water Resour.* 46, 152–159. doi:10.1134/S0097807819020088

Langer, M., Westermann, S., Boike, J., Kirillin, G., Grosse, G., Peng, S., et al. (2016). Rapid Degradation of Permafrost underneath Waterbodies in Tundra

Landscapes-Toward a Representation of Thermokarst in Land Surface Models. *J. Geophys. Res. Earth Surf.* 121, 2446–2470. doi:10.1002/2016JF003956

Lauzon, R., Piliouras, A., and Rowland, J. C. (2019). Ice and Permafrost Effects on Delta Morphology and Channel Dynamics. *Geophys. Res. Lett.* 46, 6574–6582. doi:10.1029/2019GL082792

McClelland, J. W., Déry, S. J., Peterson, B. J., Holmes, R. M., and Wood, E. F. (2006). A Pan-Arctic Evaluation of Changes in River Discharge during the Latter Half of the 20th century. *Geophys. Res. Lett.* 33, L06715. doi:10.1029/2006GL025753

McNamara, J. P., and Kane, D. L. (2009). The Impact of a Shrinking Cryosphere on the Form of Arctic Alluvial Channels. *Hydrol. Process.* 23, 159–168. doi:10.1002/hyp.7199

Nalimov, Y. V. (1995). "The Ice thermal Regime at Front Deltas of Rivers of the Laptev Sea," in *Rep Polar*. Editors H. Kassens, D. Piepenburg, J. Thiede, L. Timokhov, H.-W. Hubberten, and S. M. Priamikov (Kiel, Germany: GEOMAR Forschungszentrum für marine Geowissenschaften).

Nitzbon, J., Langer, M., Westermann, S., Martin, L., Aas, K. S., and Boike, J. (2019). Pathways of Ice-Wedge Degradation in Polygonal Tundra under Different Hydrological Conditions. *The Cryosphere* 13, 1089–1123. doi:10.5194/tc-13-1089-2019

Oldenborger, G. A. (2021). Subzero Temperature Dependence of Electrical Conductivity for Permafrost Geophysics. *Cold Regions Sci. Techn.* 182, 103214. doi:10.1016/j.coldregions.2020.103214

O'Neill, H. B., Roy-Leveillee, P., Lebedeva, L., and Ling, F. (2020). Recent Advances (2010–2019) in the Study of Taliks. *Permafr. Periglac. Process.* 31, 346–357. doi:10.1002/ppp.2050

Overduin, P. P., Westermann, S., Yoshikawa, K., Haberlau, T., Romanovsky, V., and Wetterich, S. (2012). Geoelectric Observations of the Degradation of Nearshore Submarine Permafrost at Barrow (Alaskan Beaufort Sea). *J. Geophys. Res.* 117. doi:10.1029/2011JF002088

Park, H., Watanabe, E., Kim, Y., Polyakov, I., Oshima, K., Zhang, X., et al. (2020). Increasing Riverine Heat Influx Triggers Arctic Sea Ice Decline and Oceanic and Atmospheric Warming. *Sci. Adv.* 6, eabc4699. doi:10.1126/SCIADV.ABC4699

Park, H., Yoshikawa, Y., Oshima, K., Kim, Y., Ngo-Duc, T., Kimball, J. S., et al. (2016). Quantification of Warming Climate-Induced Changes in Terrestrial Arctic River Ice Thickness and Phenology. *J. Clim.* 29, 1733–1754. doi:10.1175/JCLI-D-15-0569.1

Piliouras, A., and Rowland, J. C. (2020). Arctic River Delta Morphologic Variability and Implications for Riverine Fluxes to the Coast. *J. Geophys. Res. Earth Surf.* 125. doi:10.1029/2019JF005250

Prowse, T., Alfredsen, K., Beltaos, S., Bonsal, B., Duguay, C., Korhola, A., et al. (2011). Past and Future Changes in Arctic Lake and River Ice. *Ambio* 40, 53–62. doi:10.1007/s13280-011-0216-7

Reimnitz, E. (2002). lnteractions of River Discharge with Sea lce in Proximity of Arctic Deltas: A Review, Polarforschung 70, 123–134.

Rokaya, P., Budhathoki, S., and Lindenschmidt, K.-E. (2018a). Ice-jam Flood Research: a Scoping Review. *Nat. Hazards* 94, 1439–1457. doi:10.1007/s11069-018-3455-0

Rokaya, P., Budhathoki, S., and Lindenschmidt, K.-E. (2018b). Trends in the Timing and Magnitude of Ice-Jam Floods in Canada. *Sci. Rep.* 8, 5834. doi:10.1038/s41598-018-24057-z

Roy-Leveillee, P., and Burn, C. R. (2017). Near-shore Talik Development beneath Shallow Water in Expanding Thermokarst Lakes, Old Crow Flats, Yukon. *J. Geophys. Res. Earth Surf.* 122, 1070–1089. doi:10.1002/2016JF004022

Schneider, J., Grosse, G., and Wagner, D. (2009). Land Cover Classification of Tundra Environments in the Arctic Lena Delta Based on Landsat 7 ETM+ Data and its Application for Upscaling of Methane Emissions. *Remote Sensing Environ.* 113, 380–391. doi:10.1016/j.rse.2008.10.013

Shiklomanov, A. I., and Lammers, R. B. (2014). River Ice Responses to a Warming Arctic-Recent Evidence from Russian Rivers. *Environ. Res. Lett.* 9, 035008. doi:10.1088/1748-9326/9/3/035008

Smith, M. W. (1975). Microclimatic Influences on Ground Temperatures and Permafrost Distribution, Mackenzie Delta, Northwest Territories. *Can. J. Earth Sci.* 12, 1421–1438. doi:10.1139/e75-129

Solomon, S. M., Taylor, A. E., and Stevens, C. W. (2008). Nearshore Ground Temperatures, Seasonal Ice Bonding, and Permafrost Formation Within the Bottom-Fast Ice Zone, Mackenzie Delta, NWT. Proceedings of the Ninth International Conference on Permafrost, Fairbanks, AK, United States Fairbanks, Alaska

Stephani, E., Drage, J., Miller, D., Jones, B. M., and Kanevskiy, M. (2020). Taliks, Cryopegs, and Permafrost Dynamics Related to Channel Migration, Colville River Delta, Alaska. *Permafrost and Periglac Process* 31, 239–254. doi:10.1002/ppp.2046

Swaminathan, C. R., and Voller, V. R. (1992). A General Enthalpy Method for Modeling Solidification Processes. *Mtb* 23, 651–664. doi:10.1007/BF02649725

Tananaev, N. I., Makarieva, O. M., and Lebedeva, L. S. (2016). Trends in Annual and Extreme Flows in the Lena River basin, Northern Eurasia. *Geophys. Res. Lett.* 43 (10), 764–772. doi:10.1002/2016GL070796

Vasiliev, A. A., Melnikov, V. P., Streletskaya, I. D., and Oblogov, G. E. (2017). Permafrost Aggradation and Methane Production in Low Accumulative Laidas (Tidal Flats) of the Kara Sea. *Dokl. Earth Sc.* 476, 1069–1072. doi:10.1134/S1028334X17090203

Vuglinsky, V., and Valatin, D. (2018). Changes in Ice Cover Duration and Maximum Ice Thickness for Rivers and Lakes in the Asian Part of Russia. *Nr* 09, 73–87. doi:10.4236/nr.2018.93006

Walker, H. J., and Hudson, P. F. (2003). Hydrologic and Geomorphic Processes in the Colville River delta, Alaska. *Geomorphology* 56, 291–303. doi:10.1016/S0169-555X(03)00157-0

Walker, H. J. (1973). Spring Discharge of an Arctic River Determined from Salinity Measurements beneath Sea Ice. *Water Resour. Res.* 9, 474–480. doi:10.1029/WR009i002p00474

Walker, H. J. (1998). Arctic Deltas. *J. Coast. Res.* 14, 718–738.

Walter Anthony, K. M., Anthony, P., Grosse, G., and Chanton, J. (2012). Geologic Methane Seeps along Boundaries of Arctic Permafrost Thaw and Melting Glaciers. *Nat. Geosci* 5, 419–426. doi:10.1038/ngeo1480

Wegner, C., Wittbrodt, K., Hölemann, J. A., Janout, M. A., Krumpen, T., Selyuzhenok, V., et al. (2017). Sediment Entrainment into Sea Ice and Transport in the Transpolar Drift: A Case Study from the Laptev Sea in winter 2011/2012. *Continental Shelf Res.* 141, 1–10. doi:10.1016/j.csr.2017.04.010

Westermann, S., Langer, M., Boike, J., Heikenfeld, M., Peter, M., Etzelmüller, B., et al. (2016). Simulating the thermal Regime and Thaw Processes of Ice-Rich Permafrost Ground with the Land-Surface Model CryoGrid 3. *Geosci. Model. Dev.* 9, 523–546. doi:10.5194/gmd-9-523-2016

Woo, M. k. (1986). Permafrost Hydrology in North America1. *Atmosphere-Ocean* 24 (3), 201–234. doi:10.1080/07055900.1986.9649248

Wu, Y., Nakagawa, S., Kneafsey, T. J., Dafflon, B., and Hubbard, S. (2017). Electrical and Seismic Response of saline Permafrost Soil during Freeze - Thaw Transition. *J. Appl. Geophys.* 146, 16–26. doi:10.1016/j.jappgeo.2017.08.008

Yang, D., Kane, D. L., Hinzman, L. D., Zhang, X., Zhang, T., and Ye, H. (2002). Siberian Lena River Hydrologic Regime and Recent Change. *J.-Geophys.-Res.* 107, 14, 2002 . ACL 14-1-ACL 14-1. doi:10.1029/2002JD002542

Yang, D., Park, H., Prowse, T., Shiklomanov, A., and McLeod, E. (2021). "River Ice Processes and Changes Across the Northern Regions," in *Arctic Hydrology, Permafrost and Ecosystems*Editors D. L. Kane and K. M. Hinkel (Springer International Publishing), 379–406. doi:10.1007/978-3-030-50930-9_13

Zheng, L., Overeem, I., Wang, K., and Clow, G. D. (2019). Changing Arctic River Dynamics Cause Localized Permafrost Thaw. *J. Geophys. Res. Earth Surf.* 124, 2324–2344. doi:10.1029/2019JF005060

Conflict of Interest: The author declares that the research was conducted in the absence of any commercial or financial relationships that could be construed as a potential conflict of interest.

The handling editor declared a shared research group (HORIZON2020 Nunataryuk) with one of the authors PPO at time of review.

frontiers in Earth Science

ORIGINAL RESEARCH
published: 23 July 2021
doi: 10.3389/feart.2021.637899

Thermokarst Lagoons: A Core-Based Assessment of Depositional Characteristics and an Estimate of Carbon Pools on the Bykovsky Peninsula

Maren Jenrich[1,2], Michael Angelopoulos[1,2], Guido Grosse[1,2], Pier Paul Overduin[1], Lutz Schirrmeister[1], Ingmar Nitze[1], Boris K. Biskaborn[3], Susanne Liebner[4,5], Mikhail Grigoriev[6], Andrew Murray[7], Loeka L. Jongejans[1,2] and Jens Strauss[1]*

[1]Alfred Wegener Institute, Helmholtz Centre for Polar and Marine Research, Section of Permafrost Research, Potsdam, Germany, [2]University of Potsdam, Institute of Geosciences, Potsdam, Germany, [3]Alfred Wegener Institute, Helmholtz Centre for Polar and Marine Research, Section of Polar Terrestrial Environmental Systems, Potsdam, Germany, [4]GFZ German Research Centre for Geosciences, Section Geomicrobiology, Potsdam, Germany, [5]Institute of Biochemistry and Biology, University of Potsdam, Potsdam, Germany, [6]Melnikov Permafrost Institute, Russian Academy of Sciences, Siberian Branch, Yakutsk, Russia, [7]Nordic Laboratory for Luminescence Dating, Department of Geoscience, Aarhus University and DTU Physics, Risø Campus, Roskilde, Denmark

OPEN ACCESS

Edited by:
Alexandra V Turchyn, University of Cambridge, United Kingdom

Reviewed by:
Brendan O'Neill, Geological Survey of Canada, Canada
Edward A. Johnson, University of Calgary, Canada

***Correspondence:**
Maren Jenrich
maren.jenrich@awi.de

Specialty section:
This article was submitted to Biogeoscience, a section of the journal Frontiers in Earth Science

Received: *05 March 2021*
Accepted: *15 June 2021*
Published: *23 July 2021*

Citation:
Jenrich M, Angelopoulos M, Grosse G, Overduin PP, Schirrmeister L, Nitze I, Biskaborn BK, Liebner S, Grigoriev M, Murray A, Jongejans LL and Strauss J (2021) Thermokarst Lagoons: A Core-Based Assessment of Depositional Characteristics and an Estimate of Carbon Pools on the Bykovsky Peninsula. Front. Earth Sci. 9:637899. doi: 10.3389/feart.2021.637899

Permafrost region subsurface organic carbon (OC) pools are a major component of the terrestrial carbon cycle and vulnerable to a warming climate. Thermokarst lagoons are an important transition stage with complex depositional histories during which permafrost and lacustrine carbon pools are transformed along eroding Arctic coasts. The effects of temperature and salinity changes during thermokarst lake to lagoon transitions on thaw history and lagoon deposits are understudied. We analyzed two 30-m-long sediment cores from two thermokarst lagoons on the Bykovsky Peninsula, Northeast Siberia, using sedimentological, geochronological, hydrochemical, and biogeochemical techniques. Using remote sensing we distinguished between a semi-closed and a nearly closed lagoon. We (1) characterized the depositional history, (2) studied the impact of marine inundation on ice-bearing permafrost and taliks, and (3) quantified the OC pools for different stages of thermokarst lagoons. Fluvial and former Yedoma deposits were found at depth between 30 and 8.5 m, while lake and lagoon deposits formed the upper layers. The electrical conductivity of the pore water indicated hypersaline conditions for the semi-closed lagoon (max: 108 mS/cm), while fresh to brackish conditions were observed beneath a 5 m-thick surface saline layer at the nearly closed lagoon. The deposits had a mean OC content of 15 ± 2 kg/m^3, with higher values in the semi-closed lagoon. Based on the cores we estimated a total OC pool of 5.7 Mt-C for the first 30 m of sediment below five mapped lagoons on the Bykovsky Peninsula. Our results suggest that paleo river branches shaped the middle Pleistocene landscape followed by late Pleistocene Yedoma permafrost accumulation and early Holocene lake development. Afterward, lake drainage, marine flooding, and bedfast ice formation caused the saline enrichment of pore water, which led to cryotic talik development. We find that the OC-pool of Arctic lagoons may

comprise a substantial inventory of partially thawed and partially refrozen OC, which is available for microbial degradation processes at the Arctic terrestrial-marine interface. Climate change in the Arctic leading to sea level rise, permafrost thaw, coastal erosion, and sea ice loss may increase the rate of thermokarst lagoon formation and thus increase the importance of lagoons as biogeochemical processors of former permafrost OC.

Keywords: talik, Arctic Siberia, Yedoma, inundation, permafrost carbon, OSL (optically stimulated luminescence), coastal erosion

INTRODUCTION

Over the last 2 decades, the Arctic has been warming more than twice as fast as the global average (Johannessen et al., 2004; Berner et al., 2005; Notz and Stroeve 2016). This amplified warming has led to rapid surface warming in Siberia with modeled temperature rise of up to 4°C over the last 5 decades (Romanovsky et al., 2010; Biskaborn et al., 2019; Lenssen et al., 2019; GISTEMP Team, 2020). As a consequence, permafrost is thawing in many regions, mobilizing large amounts of sediments including organic carbon and allowing microbial decomposition of previously frozen organic matter (Strauss et al., 2013; Strauss et al. 2021; Schuur et al., 2015). Arctic coastal systems are especially affected by rapid permafrost thaw and mobilization of organic matter by erosion and marine inundation (Fritz et al., 2017). Lagoons, a frontier environment between land and ocean, are transitional and dynamic coastal landforms combining characteristics of both terrestrial and marine systems (Kjerfve, 1994; Tagliapietra et al., 2009; Harris et al., 2017). Globally, coastal lagoons are defined as shallow coastal water bodies separated from the sea by a barrier, connected at least intermittently to the ocean by one or more restricted inlets, and usually have a shore-parallel orientation (Kjerfve, 1994). As lagoons are complex and diverse systems, there are many different approaches to classify them, for example based on geomorphological and geological origin, their morphological properties such as size and water depth (Kosyan, 2016), the degree of isolation from the sea (Kjerfve, 1994), their physicochemical state (for example, salinity, ionic composition, temperature, turbidity, nutrients) (Tagliapietra et al., 2009), or the degree of influence by living organisms such as corals and humans (Brovko 1990).

Permafrost thaw results in landscape change as melting excess ground ice causes surface subsidence, eventually forming thermokarst lakes (Osterkamp et al., 2009; Jones et al., 2011; Lenz et al., 2016). Along eroding sections of Arctic coasts, lowered thermokarst terrain is affected by flooding of nearshore thermokarst lakes and basins with seawater, transforming them into thermokarst lagoons (Ruz et al., 1992; Romanovskii et al., 2000). Thermokarst lagoons are also formed by natural thermokarst lake dynamics in the course of lake drainage at coasts (Arp et al., 2010). However, rates of formation are expected to intensify as a result of ongoing climate change in the Arctic. Increasing coastal erosion (Günther et al., 2015; Jones et al., 2018), sea-level rise (Proshutinsky et al., 2001; Watson et al., 2015; Nerem et al., 2018), and higher sea water temperatures (Bindoff et al., 2007) are likely to result in an acceleration of erosion of permafrost coasts and in particular lagoon formation. Incubation experiments performed by Tanski et al. (2019) indicate that along eroding permafrost coastlines, large amounts of carbon dioxide can be produced. Therefore, thermokarst lagoon formation is an important process affecting permafrost carbon pools along rapidly changing permafrost coasts. In addition, marine inundation affects the temperature and salinity of taliks formerly beneath thermokarst lakes during their transition to the marine environment (Angelopoulos et al., 2020a). The formation of hypersaline, unfrozen ground beneath thermokarst lagoons may preserve existing thermokarst lake taliks, forming migration pathways for methane (Shakhova et al., 2019; Angelopoulos et al., 2020a). However, lagoon formation can also cause taliks to partially refreeze, provided that heat loss is faster than salt diffusion (Angelopoulos et al., 2020a). Ascending gas can get trapped below low-permeability sediment layers (Ruppel and Kessler, 2017) and be released when conditions warm up. These pathways, which may contain low-permeability ice-saturated zones, become part of the offshore environment with sufficient coastal erosion and so become potential sources of gas release in subsea permafrost areas (Frederick and Buffett, 2014; Shakhova et al., 2017).

Although thermokarst lagoons are widespread along the pan-Arctic coast (Jenrich, 2020), there is still no qualitative or quantitative assessment of their distribution or of the size of the total carbon reservoir they represent. Until now, Arctic thermokarst lagoon research has concentrated on the Mackenzie Delta region in Northwest Canada (Hill, 1990; Ruz et al., 1992; Héquette et al., 1995; Campeau et al., 2000; Solomon et al., 2000) and the Bykovsky Peninsula in Northeast Siberia. On the Bykovsky Peninsula, several lagoons have evolved from thermokarst lake basins in ice-rich Yedoma Ice Complex permafrost, and these are now actively developing in different stages (Romanovskii et al., 2000; Romanovskii et al., 2004; Ulyantsev et al., 2017; Schirrmeister et al., 2018). Still, little is known of the sedimentary history of thermokarst lagoons, the impact of marine inundation, and the amount and quality of carbon stored in greater depths.

To address these research gaps, we applied a multidisciplinary approach to characterize the sedimentological, geochronological, hydrochemical, and biogeochemical properties of two approximately 30 m deep (below lagoon ice surface level in spring) sediment cores from two typical thermokarst lagoons on the Bykovsky Peninsula (**Figure 1**). We paired this with remote sensing observations to identify, map, and characterize thermokarst lagoons in a regional context along the coast of the

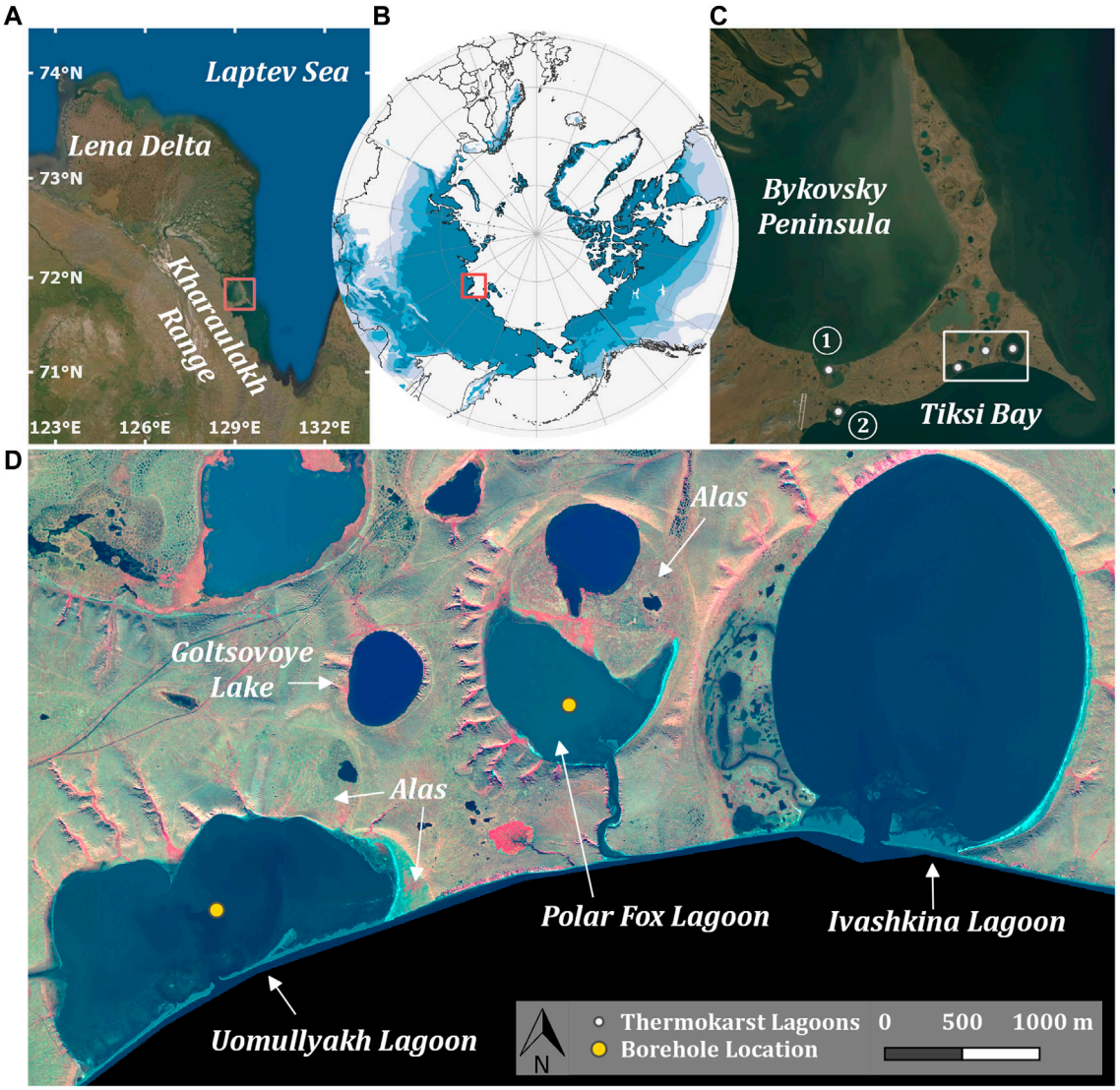

FIGURE 1 | Bykovsky Peninsula in Northeast Siberia, south of Lena Delta **(A, B)**. Both the Stepanenko ① and Safroneeva ② lagoons **(C)** as well as the Uomullyakh, Polar Fox, and Ivashkina lagoons are located at the southern coast of the Bykovsky Peninsula **(D)**. The drilling locations in the lagoon centers of Uomullyakh and Polar Fox lagoons are indicated by yellow dots **(D)**. Source imagery: **(A, C)**: ESRI Satellite World Imagery b: Permafrost extent regions based on Brown et al. (1997) **(D)** WorldView3 false colour satellite image (8-5-3), acquired 2016-09-02.

Bykovsky Peninsula. The specific aims of this paper are to characterize (1) the sediments and (2) pore water below the lagoons and (3) to quantify the regional carbon inventory based on spatially explicit lagoon areas in the region.

Study Area

The lagoons investigated here are the semi-closed Uomullyakh Lagoon (UoL) and the nearly closed Polar Fox Lagoon (PFL) (**Table 1**), located on the southern coast of the Bykovsky Peninsula (71°51′ N, 129°19′ E) (Strauss et al., 2018, **Figure 1D**). The peninsula is located in Northeast Siberia (**Figure 1B**), at the mouth of the Bykovskaya Channel, one of the main outflow channels of the Lena River Delta (**Figure 1A**). The hinterland of the Bykovsky Peninsula is the Kharaulakh Range with elevations up to 500 m above sea level (asl), which is part of the northern foothills of the Verkhoyansk Mountains. The peninsula consists of the remains of a former late Pleistocene sediment accumulation plain with elevations of up to 45 m asl (Schirrmeister et al., 2002; Schirrmeister et al., 2018). It lies within the continuous permafrost zone and is characterized by thick, ice-rich Yedoma Ice Complex deposits (Grosse et al., 2007). Postglacial sea level rise during the Lateglacial interstadial and the early Holocene inundated the shallow Laptev Sea shelf and transformed terrestrial permafrost into subsea permafrost (Romanovskii et al., 1998; Lantuit et al., 2011). Cliffs and thermokarst basins are the typical backshore coastal

TABLE 1 | Classification of lagoons into "open", "semi-closed" and "nearly closed" lagoon systems which occur along a gradient of coastal erosion.

Lagoon class	Connectivity with the sea	Impact of coastal erosion	Examples
Open	Full and broad exchange with the sea	Fully affected and far ahead in the transition to an open marine system	Stepanenko and Safroneeva lagoons (**Figure 1**), many in the northern Lena Delta, and on the Cape Halkett coast of Beaufort Sea
Semi-closed	Barrier islands or sand spits partially block exchange with the sea either temporally or spatially	Moderately to substantially affected	Uomullyakh Lagoon (**Figure 1**), many on Tuktoyaktuk Peninsula, eastern Alaskan Beaufort Sea (Harris et al., 2017)
Nearly closed	Narrow outlet/inlet channel connecting lagoon and sea, with the possibility of having lake character temporarily	Not yet affected	Polar Fox Lagoon (**Figure 1**), and other lagoons connected through small channels

landforms. Sixteen large thermokarst depressions are found on the peninsula (Grosse et al., 2005; Fuchs et al., 2018). In total, more than 50% of the Bykovsky Peninsula is strongly influenced by thermokarst and thermo-erosion landforms (Grosse et al., 2005; Lantuit et al., 2011).

According to the Köppen–Geiger world climate classification (Peel et al., 2007), the peninsula is located in the polar tundra climate zone (ET). Despite the coastal location, the climate is strongly continental with long, cold winters (September–May) and short, cool summers. In January, the mean air temperature is −30.0°C and rises to +8.5°C in July (1987–2016). The mean annual precipitation does not exceed 350 mm (Tiksi Hydrometeorological Observatory, WMO 218240). The open-water season in the southern Laptev Sea starts on average in mid-June and extends to mid-October (Lantuit et al., 2011).

During drilling campaigns within the Russian-German science cooperation Lena Expedition in 2017, deep sediment cores from two thermokarst lagoons (UoL and PFL) and one thermokarst lake (Goltsovoye Lake (GoL)) were drilled on the Bykovsky Peninsula (**Figure 1D**). Furthermore, sediment characteristics of a 6.2 m deep core from the Ivashkina Lagoon (IvL) drilled in 1999 were published by Schirrmeister et al. (2018). The results showed several stages of landscape development from the initial Yedoma Ice Complex through thaw-induced lake development and eventually lagoon formation. In this study, we report on results from the approximately 30 m deep cores from Polar Fox and Uomullyakh lagoons.

The Uomullyakh Lagoon (71°43′51″N, 129°16′21″E, **Figure 1D**) is a 2.1 km^2 large, shallow lagoon (water depth 0.8 m at the borehole location) with underlying former Yedoma and Alas permafrost (Strauss et al., 2018). The lagoon is well connected with the Tiksi Bay via a 90 m wide opening in the center of the narrow and flat sand spit, which can be flooded by storm surges. In April 2017, test hole drilling (17 locations) with a Kovacs 5 cm diameter ice auger revealed bedfast ice at all locations. However, bathymetry surveys in summer 2017 (Strauss et al., 2018) suggest that small isolated water pockets might have existed in April 2017. We recorded 40 cm of compacted snow on top of 80 cm ice, which was overlying the frozen lagoon bed at the drilling location (71°43′51″N, 129°16′29″E). In the west, the lagoon is connected to two drained thermokarst lakes basins by a former drainage channel.

The Polar Fox Lagoon (71°44′35″N, 129°20′16″E; **Figure 1D**) is a smaller sized (0.6 km^2), brackish to salty water body (water depth 3.30 m in the lagoon center) formed after partial lake drainage. This nearly closed lagoon is located in a partially drained thermokarst basin (Alas in **Figure 1D**) and is connected to the sea only during the open water season via an 800 m long and roughly 50 m wide outlet channel. The water level in the lagoon is at about sea level and water flow occurs in both directions depending on wind, wave, and tide conditions. Ice thickness measurements from April 2017 and bathymetry from July 2017 suggest that the lagoon was 75% covered with bedfast ice (Angelopoulos et al., 2020a). In the center of the lagoon, at the borehole location (71°44′58″N, 129°20′30″E), a 175 cm salty water layer was present underneath the 155 cm thick seasonal ice layer in April 2017 (Strauss et al., 2018).

Both lagoons are strongly impacted by warm freshwater discharge from the Lena River into the Buor Khaya and Tiksi bays (Juhls et al., 2019). This discharge causes large seasonal and interannual variations in temperature and salinity (**Supplementary Table S1**). For example, Polar Fox Lagoon had a salinity of 13 psu (practical salinity unit) and 44 psu below the ice cover in April 2017 and April 2019, respectively. In July 2017, the salinity dropped to less than 1 psu.

METHODS

Field Work

Fieldwork on the Bykovsky Peninsula was carried out in April 2017 (Strauss et al., 2018). Over eight days, a 33.5 m deep borehole was drilled from the ice surface on UoL (core number PG2410) and a 31 m deep borehole was drilled from the ice surface of neighboring PFL (PG2411) (**Figure 1**) using a URB2-4T drilling rig mounted on a tracked vehicle. The sediment core retrieved at UoL was 32.3 m long and at PFL 27.7 m long. Immediately after recovery, the cryolithology of the sediment cores was visually described and the cores were packed and transported frozen to AWI Potsdam. GeoPrecision temperature chains were installed in both boreholes, each with an accuracy of ± 0.1°C at 0°C and a resolution of 0.01°C. The thermistors had been calibrated in a MilliQ water-ice bath to measure their offset from 0°C prior to deployment. The chains remained in the boreholes for 5 days at Polar Fox Lagoon and 11 days at Uomullyakh Lagoon. To account for drilling heat effects, the observed temperature drift for each thermistor was analyzed following Lachenbruch et al. (1982) to estimate the

undisturbed temperature. Both sediment cores were mostly unfrozen but had some partially frozen layers. The heat generated during the drilling of the cores caused the cores to partially thaw, so that the on-site haptic observation of the frozen state included some uncertainty. The PFL raw temperature data is available from Angelopoulos et al. (2020a) and the UoL temperature data and processing are described in the supporting information (**Supplementary Figure A4**).

Laboratory Analyses

In the cold lab (−9°C), the sediment cores were opened, cleaned and split, and the cryolithology was described in more detail. Furthermore, the core halves were photographed and subsamples were taken approximately every 50 cm for laboratory analyses. For the Polar Fox core, a higher sampling resolution of about every 10 cm was used for pore water extraction.

Hydrochemical Analyses

Pore water was extracted from thawed samples using Rhizons™ with a membrane pore size of 0.15 µm and analyzed for pH, electrical conductivity (EC, mS/cm), DOC (mg/L) and stable water isotopes (δD, $\delta^{18}O$ (‰ vs. VSMOW)). The pH and EC values were measured with a WTW Multilab 540 (accuracy: ± 0.01/± 1 mV). DOC samples were acidified with 50 µL of 30% HCl supra-pure and stored at + 4°C until measured with a Shimadzu Total Organic Carbon Analyzer (TOC-VCPH) (accuracy: ± 1.5%) following Fritz et al. (2015). For analyzing the ratios of δD and $\delta^{18}O$, water and ice samples were processed following Meyer et al. (2000) and measured with a Finnigan MAT Delta-S mass spectrometer.

Sedimentology Analyses

Grain size measurements were conducted to gain information about the transportation medium and the level of sediment accumulation at the study areas. Mass specific magnetic susceptibility, describing the ability of a material to be magnetized, gives an indication of the amount of ferri- and ferromagnetic minerals in a sample. Differences in mineral composition between samples usually indicate sediment sources and changes in stratification (Liu et al., 2010). For both measurements the samples were pre-weighed and freeze-dried. The absolute ice or water content was determined based on the difference in weight before thawing and after freeze drying related to the wet weight (Phillips et al., 2015). The bulk density (BD in kg/m^3) was calculated from the ice content according to Strauss et al. (2012). The grain size distributions of 74 samples from both cores were measured with a Malvern Mastersizer 3000 laser particle size analyser with a measuring range of 0.01–1000 µm. Additional details on BD calculation and grain size measurement can be found in the supplementary material. Mass-specific magnetic susceptibility (MS in $10^{-8}\ m^3/kg$) was measured with a Magnetic Susceptibility Meter (Model MS2, Sensor Type MS 2B, Bartington Instruments) on the freeze-dried, but not homogenized samples at a frequency of 0.465 kHz (low frequency).

Bulk Biogeochemistry

To gain information about changes in the nutrient cycle during the transformation of terrestrial permafrost into sub-aquatic permafrost, the biogeochemical parameters total nitrogen (TN), total carbon (TC) and total organic carbon content (TOC), and their stable isotopes ($\delta^{13}C$ and $\delta^{15}N$) were measured and the TOC/TN ratio determined. The parameters TOC/TN and $\delta^{13}C$ are widely used as a broad indicator for the degree of decomposition and source of organic matter (OM) (e.g. Mary et al., 1992; Meyers 1994; Meyers, 1997; Gundelwein et al., 2007; Andersson et al., 2012; Strauss et al., 2015). Generally, a lower TOC/TN ratio and higher $\delta^{13}C$ indicate more decomposed organic material (Schirrmeister et al., 2011; Strauss et al., 2015). Since microorganisms prefer easily accessible carbon compounds, the organic carbon quality decreases with increasing organic matter decomposition (Schowalter, 2016). Using $\delta^{13}C$ and TOC/TN, it is possible to distinguish between land plants and marine, brackish and freshwater algae (decreasing $\delta^{13}C$ is associated with decreasingly saline environment) (Meyers et al., 1994) (**Supplementary Table S2**).

To determine TC and TN content, the homogenized, freeze dried and ground samples were measured with a carbon–nitrogen–sulfur analyzer (Vario EL III, Elementar). TOC was measured with a TOC analyser (Vario Max C, Elementar). We measured two replicates of each sample and accepted only <5% deviation for the replicates. The TOC/TN ratio is expressed as atomic TOC/TN value to ensure comparability between studies. The atomic TOC/TN value was calculated following Meyers et al. (1994) by multiplying the weight ratio with 1.167, which is the ratio of the atomic weights of nitrogen (14.007 amu, atomic mass unit) and carbon (12.001 amu). The rate of mineralization was considered high at TOC/TN < 12, moderate between 12 and 25, and low at values >25 (Walhert et al., 2004).

The volumetric TOC content (carbon density, $kg\ TOC/m^3$) was calculated following Strauss et al. (2013) according to **Eq. 1**:

$$organic\ carbon\ content = V_{ref} \cdot BD \cdot \frac{TOC_{wt\%}}{100}, \quad (1)$$

where V_{ref} is the reference volume of 1 m^3, BD in kg/m^3 and TOC in wt%.

The stable carbon and nitrogen isotopic composition was measured for all samples with TOC or TN values above the detection limit (0.1 wt%) with a ThermoFisher Scientific Delta-V-Advantage gas mass spectrometer equipped with an organic elemental analyser Carlo-Erba NC2500 (accuracy: < 0.2‰). Measured $\delta^{13}C$ and $\delta^{15}N$ was compared to the standardized Vienna Pee Dee Belemnite (VPDB) and expressed in per mille (‰ vs. VPDB). TOC and TN values below the detection limit were neglected in further calculations.

Geochronology

For radiocarbon dating, we chose samples about every 3 m ($n = 19$ for both cores). When present, macroplant remains were hand-picked under a stereomicroscope, otherwise bulk sediment was selected and dated using Accelerator Mass Spectrometry in the AWI MICADAS (MIni radioCArbon DAting System) Laboratory in Bremerhaven. Radiocarbon dates were calibrated using Calib 7.04 software after (Reimer et al., 2013) and the IntCal13 calibration curve (Stuiver et al., 2020) to calculate calibrated years before present (cal. years BP).

For optically stimulated luminescence (OSL) dating, three core segments were selected in the field from the Uomullyakh core, and two from the Polar Fox core. The core segments were frozen in their original state, wrapped in black foil, and delivered frozen to Aarhus University's Nordic Laboratory for Luminescence Dating (Roskilde, Denmark). The core segments were then thawed in a controlled-light environment and the outer ~5 mm removed to minimize the effects of smearing, and to ensure that the material used for OSL measurements had not been exposed to daylight during or after retrieval. Luminescence measurements were made using a Risø TL/OSL reader, model TLDA 20. A standard SAR protocol based on Murray and Wintle (2000; 2003) was used for quartz dose estimation, and a comparison with feldspar data was used to investigate the degree of bleaching at deposition (e.g. Möller and Murray, 2015). Radionuclide concentrations were measured using high resolution gamma spectrometry (Murray et al., 1987; Murray et al., 2018), calibrated using Certified Reference Materials produced by Natural Resources Canada (NRCAN). For detailed information see supplementary material.

Borehole Temperature Measurements and Calculation of Freezing Conditions

Ground temperature was recorded for 11 days in the Uomullyakh borehole and for 5 days in the Polar Fox borehole in April 2017. The freezing point depression ΔT_f of the sediment was calculated from the molality of dissolved ions estimated from the measured pore water electrical conductivity according to **Eq. 2** (Atkins, 2018) and then compared with the measured borehole temperatures.

$$\Delta T_f = \frac{R\left(T_{m,fw}\right)^2}{L_f} c \tag{2}$$

This equation describes the lowering of the freezing point of free water with the salt content c (mol/kg). R is the universal gas constant 8.314 J/(K mol), $T_{m,fw}$ is the freezing point of free water (273.15 K) and L_f is the latent heat of fusion of water (334,000 J/kg). For the conversion of the measured EC to molality (mol/kg) the MATLAB implementation of TEOS-10 (McDougall and Barker 2011) was used. It has been demonstrated that TEOS-10 also performs well for hypersaline solutions (Pawlowicz, 2012). Further details can be found in the supplementary material.

Lagoon Mapping

Along the coast of the Bykovsky Peninsula six lagoons exist, five of them originated from thermokarst basins (Jenrich, 2020). All of them are located in the southern part of the peninsula (**Figure 1**). We used a simple geomorphological approach to further differentiate them based on their connectivity with the ocean into open, semi-closed and nearly closed thermokarst lagoons (**Table 1**).

The extent of each of the five lagoons was determined using the Global Surface Water dataset which is based on Landsat-5, -7, and -8 satellite images from 1984 to 2018 at 30 m resolution (Pekel et al., 2016). Water bodies were defined by a water occurrence threshold of >75% over this time period. The raster dataset was vectorized and smaller geometric errors, which occurred during vectorization, were solved with the Fix Geometry function in QGIS3.6. The five Bykovsky Peninsula lagoon polygons were selected manually and these water bodies were split from the ocean by using the function "split by line". The resulting lagoon polygons were re-projected in UTM Zone 52N (EPSG:32652) to calculate the polygon area in km^2.

Upscaling Carbon Pools

The organic carbon pools of Uomullyakh and Polar Fox lagoons were estimated after Jongejans et al. (2018) using **Equation 3**, based on a deposit thickness of 30 m, the lagoon size, bulk density, and TOC content. We assume that there is no form of massive ice in the thermokarst lagoon sediments, so that the TOC pool can be calculated as:

$$TOC_{pool}\,(Mt) = \frac{thickness \cdot coverage \cdot BD \cdot \frac{TOC}{100}}{10^6} \tag{3}$$

with thickness and coverage in m, BD in kg/m^3 and TOC in wt%. For further calculations, we assumed a TOC of 0.05 wt% for the samples with TOC below the detection limit (n = 21). To compensate for data gaps caused by core loss or larger sampling distances, the BD and TOC values were first multiplied, and the depth interval given as the difference of two adjoining depths was calculated. For core loss sections, this interval was accordingly higher. The product of BD and TOC was weighted and replicated for each depth interval. To interpolate the carbon content of point measurements to greater areas, the data was resampled using the bootstrapping method after Jongejans and Strauss (2020). Assuming that the deposition of organic material in the study area did not show significant differences, the calculated C-budgets of UoL and PFL were averaged and upscaled on the three further lagoons on the peninsula. Therefore, the size of each lagoon was multiplied with the mean of the TOC pool of UoL and PFL, and divided by the mean size of UoL and PFL.

Statistics

We used the R environment to perform various statistical analyses on 10 parameters (R Core Team (2016); R version 3.6.3). In order to compare the differently scaled parameters, the data was normalized with the function "normalize". To subdivide the cores into stratigraphic zones, the stratigraphically constrained, incremental sum of squares cluster analysis (CONISS) was applied. Thereby, only stratigraphically adjacent clusters are considered for merging. The CONISS clustering was performed in R with the 'chclust' function from the package 'rioja'. The used dissimilarity index was 'bray'. In order to compare the properties at the time of sediment deposition, only sedimentological and biogeochemical parameters were included in the calculation. In total 10 parameters: mean depth, grain size (mean, volumetric proportion of clay, silt and sand), mass specific magnetic susceptibility, TOC, TN, TOC/TN and $\delta^{13}C$. Hydrochemical parameters were not used as pore water in

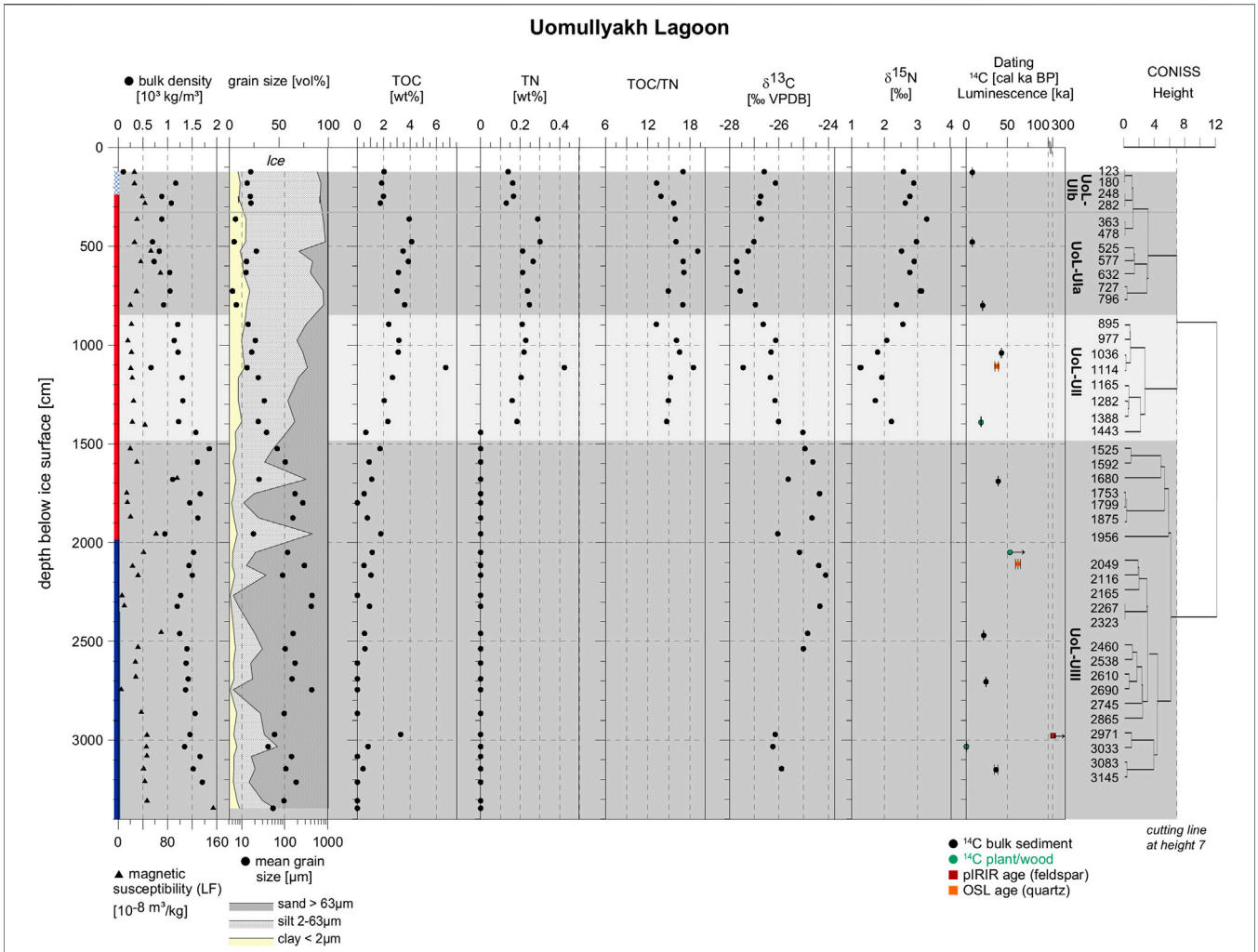

FIGURE 2 | Summary of sedimentological, geochronological and biogeochemical parameters for the Uomullyakh Lagoon core: bulk density (upper axis), mass specific magnetic susceptibility (lower axis), grain size (upper axis: volumetric proportions, lower axis: mean grain size), total organic carbon content (TOC), total nitrogen content (TN), organic carbon and nitrogen ratio (TOC/TN), stable carbon and nitrogen isotope composition ($\delta^{13}C$, $\delta^{15}N$), radiocarbon dating (^{14}C) and luminescence dating (pIRIR, OSL). The top 120 cm is the overlying ice cover. The core was divided into three stratigraphic units based on a CONISS analysis. Color bar at the *y*-axis indicates frozen (blue), unfrozen (red) and partially frozen (shaded) core segments. Note that "frozen" includes visibly frozen core sections and re-constructed frozen conditions. Arrows indicate non-finite ages.

unfrozen soil is flowing and mixing constantly and so does not represent the hydrochemical composition at the time of sediment deposition. The results were visualized in a dendrogram. The cutting point was selected based on visual validation and dating results.

A principal component analysis (PCA) was performed on the same parameters to reduce this high-dimensional data set to fewer dimensions and to detect patterns in the distribution of sedimentological and biogeochemical parameters over depth. The results were visualized in a biplot. The arrows show the loading on each variable, with the length approximating the variance and the angle between the arrows their correlation. Points close together correspond to depth that have similar scores on the PCA components. PCA was performed using the 'prcomp' function from the Package 'stats'.

RESULTS

The cores are described according to the depositional record from bottom to top. All depth specifications refer to the top of the ice cover (contains a compacted snow layer on top of lagoon ice) unless they are specifically stated as sediment depth, in which case we refer to the depth from the top of sediment. The units were separated according to a vertical cut in the dissimilarity dendrogram at height 7 for the Uomullyakh sediment core (**Figure 2**) and at height 4 for the Polar Fox sediment core (**Figure 3**). Therefore, the Uomullyakh core (PG2410, core recovery of 85%) was divided into three units, whereby Unit I was divided into two subunits: UoL-UIII ranges from 3350 to 1480 cm, UoL-UII from 1480 to 820 cm, UoL-UIa from 820 to 320 cm and UoL-UIb from 320 to 120 cm depth. The Polar Fox

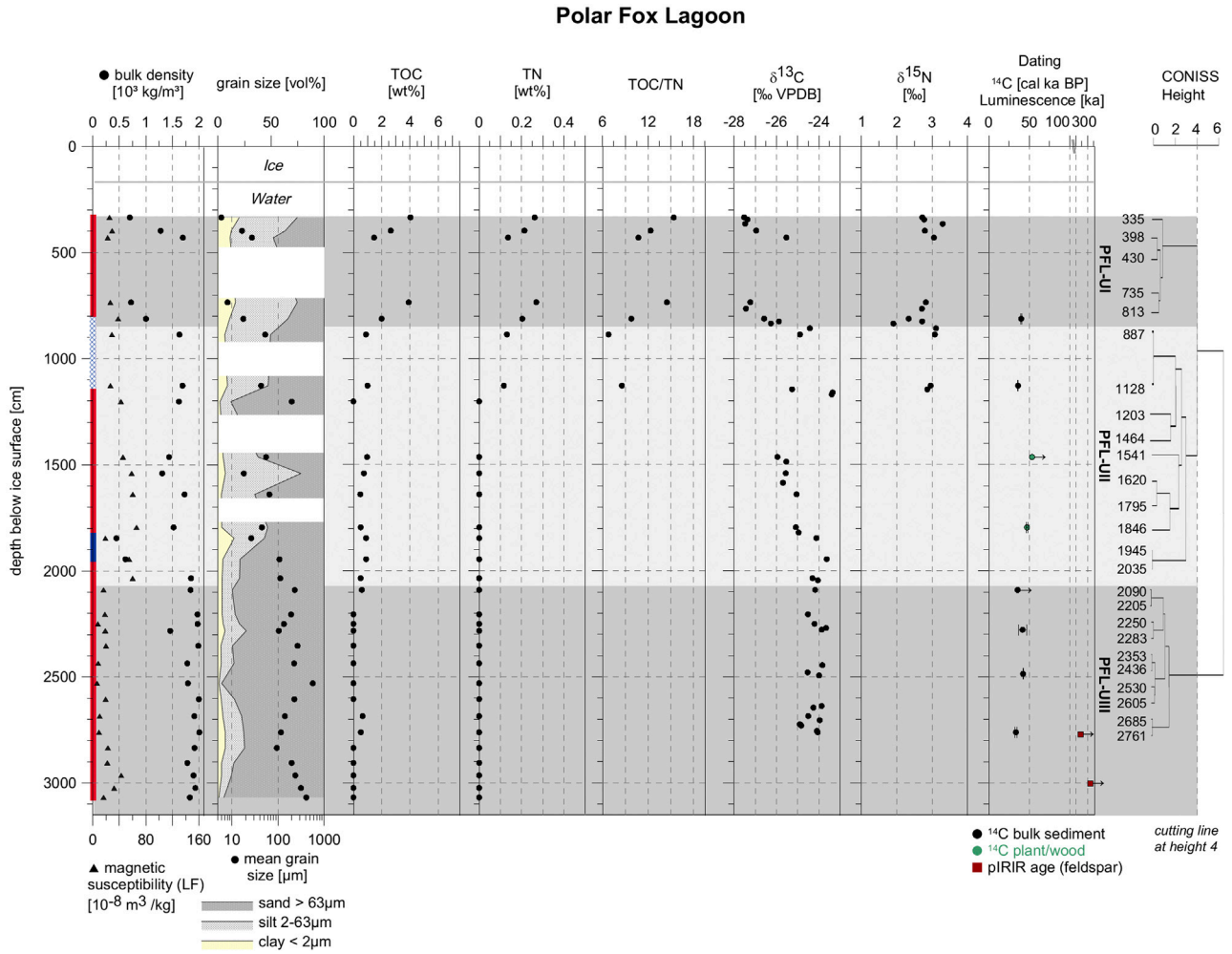

FIGURE 3 | Summary of sedimentological, geochronological and biogeochemical parameters for Polar Fox Lagoon core: bulk density (upper axis), mass specific magnetic susceptibility (lower axis), grain size (upper axis: volumetric proportions, lower axis: mean grain size), total organic carbon content (TOC), total nitrogen content (TN), organic carbon and nitrogen ratio (TOC/TN), stable carbon and nitrogen isotope composition ($\delta^{13}C$, $\delta^{15}N$), radiocarbon dating (^{14}C) and luminescence dating (pIRIR). The top 330 cm is the overlaying ice and water layer. The core is divided into three stratigraphic units based on a CONISS analysis. Color bar at the *y*-axis indicates frozen (blue), unfrozen (red) and partially frozen (shaded) core segments. Arrows indicate non-finite ages.

sediment core (PG2411, core recovery of 70%) was also divided into three units: PFL-UIII from 3070 to 2080 cm, PFL-UII from 2080 to 860 cm and PFL-UI ranges from 860 to 330 cm depth.

Core Description

At UoL, from core bottom up to 1480 cm depth (UoL-UIII), the grain-size of the sediments alternated several times from silty fine sand to coarse-grained sand. Rounded pebbles up to 2 cm in diameter were found up to 1030 cm depth. In UoL-UII, layers of silty fine sand became thicker and coarse-grained layers thinner. From 820 cm to the top (UoL-UI), the sediment consisted of black to dark grey clayish to silty fine sand with parallel sediment structures. UoL-UIb was partially frozen. From 2100 cm downwards the sediment was rich in structureless ground-ice. Between the frozen parts the core was thawed. Several organic-bearing layers were encountered along the core. At 1530 cm, a layer of large wood pieces (up to 5 cm in size) was observed.

At PFL, the sediment gradually became finer upwards in the core. From core end up to 860 cm (PFL-UIII & II), the sediment was sandy with fine, medium and coarse sand alternating frequently. Rounded pebbles up to 3 cm in diameter were found up to 1120 cm depth. Above 860 cm in PFL-Unit I, the sediment was dark grey and increasingly silty. From 630 cm onwards, shell and plant remains were encountered. Between 2245 cm and 2100 cm two 5–10 cm thick macro organic containing layers were observed. At 1810 cm, a 5 cm layer of large wood pieces (up to 8 cm in size) similar to UoL was found. The upper 1500 cm of sediment contained only sparse organic remains. The core was mostly thawed and had only small frozen sections (1815–1855 cm, 2040–2050 cm and 2970–2985 cm, and ground ice structures between 810 and 1160 cm).

Geochronology

Radiocarbon dates for the Uomullyakh Lagoon core ranged from >53.2 cal ka BP to 2.6 cal ka BP (**Figure 2**, **Supplementary Table S3**) and showed several age inversions from 1036 cm depth downwards. The upper two samples until 478 cm depth were of early Holocene age. Both the oldest sample (>53 cal ka BP) at a depth of 2049 cm, and the (even deeper) youngest sample (2.6 cal ka BP) at 3033 cm, were from plant macrofossils. Bulk organic samples also showed inversions although not so extreme, and varied between 18 and 34 cal ka BP. The luminescence ages of quartz (OSL) and feldspar (pIRIR) (**Supplementary Table S4**) were similar in range to the radiocarbon dates at 1107 cm [37 ± 2 ka (OSL), 29.9 ± 1.6 ka (pIRIR) and 43.0 ± 0.6 ka cal BP (radiocarbon)] and 2108 cm depth [63 ± 3 ka (OSL), 59 ± 4 ka (pIRIR) and >53.2 ka cal BP (radiocarbon)]. Since quartz dose recovery was satisfactory for these samples from UoL, the OSL ages are considered more reliable for these samples than the feldspar and radiocarbon ages. The lowermost luminescence age at 2978 cm was non-finite for both quartz (>100 ka) and feldspar (>300 ka). Since feldspar provided the more limiting constraint, the minimum feldspar age is shown in **Figure 2**.

Radiocarbon dates for Polar Fox Lagoon ranged from > 53.3 cal ka BP to 33.5 cal ka BP (**Figure 3**, **Supplementary Table S3**). For the uppermost sample, the radiocarbon dating failed due to insufficient organic carbon content, so that available dates started at 480 cm sediment depth (corresponding to depth of 813 cm measured from ice surface). As seen at UoL, the age dating revealed no linear trend over depth. The youngest age was found in the greatest depth (2761 cm), while the oldest sample was found at 1130 cm sediment depth. The luminescence ages included only non-finite ages for quartz and feldspar of >100 ka and >300 ka at 2771 cm and of >100 ka and >320 ka at 3002 cm depth (**Supplementary Figure S1, Table S4**). Therefore, the feldspar pIRIR ages were used for interpretation of the lowest core ages, as with UoL.

The radiocarbon ages of the lowest unit UIII of both cores were not used in the discussion because of low carbon content and high risk of contamination. The results of the luminescence dating, aiming at a depositional age of mineral grains, were considered more reliable. The two samples with quartz OSL ages from the Uomullyakh Lagoon core had ages well within the range of the method and they were in stratigraphic order.

We acknowledge the fact that shore erosion and sediment mixing in such permafrost thaw-affected aquatic environments may easily result in radiocarbon age inversions and thus challenge chronological interpretation.

Detailed dose rate results and luminescence ages are summarized in **Supplementary Table S4**. Information on radionuclide concentrations are shown in **Supplementary Table S5**.

Sediment Characteristics

Uomullyakh Lagoon

The sediments of UoL-UIII (**Figure 2**) were very poorly sorted. Up to 2000 cm depth, sand dominated with a share of up to 96 wt%, mainly fine to medium sand (measured mean grain size of the < 1 mm fraction: 161 μm) and visually observed rounded pebbles up to 2 cm in size. The upper part of UoL-UIII was also characterized by an alternation of coarser deposits (mean grain size: 193 μm) with low MS of 20 × 10^{-8} m^3/kg and fine deposits (mean grain size: 37 μm) with high MS values of 59 × 10^{-8} m^3/kg. At the lower end of UoL-UII, the TN content decreased below the detection limit of 0.1 wt%. In UoL-UII, coarse sand layers with pebbles and silty fine sand layers alternated. The sand fraction decreased (mean grain size: 24.3 μm). At 1110 cm, TOC (6.7 wt%) and TN (0.4 wt%) values were at a maximum and were associated with low $\delta^{13}C$ (−27.5‰ VPDB) and low $\delta^{15}N$ (1.3‰) values (**Supplementary Table S3**). In Unit Ia of UoL, poorly sorted clay and silt deposits were predominant with a share of 16 and 73% respectively (mean grain size: 12.5 μm) (**Figure 2**). The TOC content ranged between 3.2 and 4.5 wt% and the TN content between 0.2 and 0.3 wt%. UoL-UIb, containing the upper 200 cm, was distinguished from the lower unit UoL-UIa by coarser grain size and lower TOC and TN content (1.9 wt% and 0.15 wt%, respectively). In samples with a mean grain size below 63 μm (mainly Units I and II), the $\delta^{13}C$ values were mostly below −26‰ VPDB, whereas they were higher in coarse-grained samples. The bulk density decreased from the core bottom to the top (1600–100 kg/m^3, mean 1200 kg/m^3). For further details of the biogeochemical results see **Supplementary Table S6**. The MS ranged from 5 to 154 × 10^{-8} m^3/kg, with variations mainly in areas of abrupt changes in grain size. Fine deposits corresponded with high TOC content over the core length.

Polar Fox Lagoon

The lowermost Unit III (PFL-UIII) stretching up to 2080 cm depth was characterized by a large proportion of coarse material (sand and gravel, measured mean grain size of the <1 mm fraction: 230 μm) and a very low organic carbon content of 0.1 wt%. The sediment of this unit was mostly moderately well sorted.

In the overlying PFL-UII the sorting was poor. Silty fine sand and medium sand layers alternated (mean grain size: 72.3 μm) along with MS changes. Changes in MS correspond to rapid increases in grain size (at 630 and 530 cm depth). MS ranged between 6 and 66 × 10^{-8} m^3/kg, with particularly strong variation in the small frozen core sections. Overall, the Polar Fox Lagoon core had coarser material composition of the < 1 mm fraction than the Uomullyakh Lagoon core. The TOC content was low (0.7 wt%) and the TN content decreased to below the detection limit at 1200 cm depth.

The uppermost Unit I (PFL-UI) comprised approximately the uppermost 5 m of sediment (corresponding to a depth of 860 cm) and was characterized by clay, silt and fine sand (mean grain size: 15.1 μm). Samples of the upper and the lower half of this unit show the same pattern of decreasing grain size, associated with increasing TOC and TN contents, as well as an increase in TOC/TN ratio and a depletion in $\delta^{13}C$. In contrast to UoL-UI, TOC, maximal at 4 wt%, was highest in the uppermost sample (**Supplementary Table S7**). TN ranged between 0.14 and 0.27 wt%. Changes in MS corresponded to rapid increases

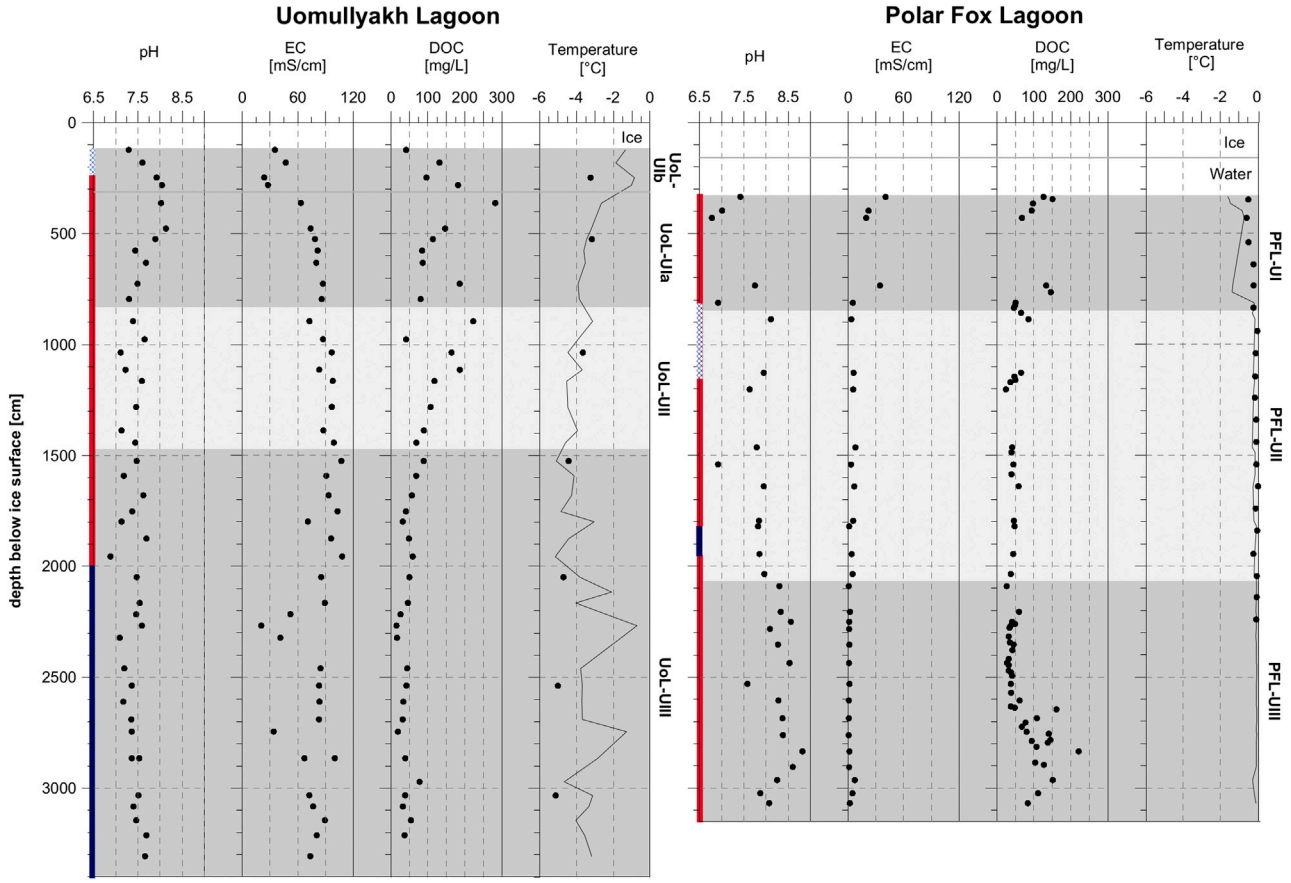

FIGURE 4 | Hydrochemical parameters of the pore water and borehole temperature of the Uomullyakh Lagoon **(left)** and the Polar Fox Lagoon cores **(right)**: pH, electrical conductivity (EC), dissolved organic carbon concentration (DOC), measured borehole temperature (point) and freezing point (line) estimated from pore water salinity. Color bar at the *y*-axis indicates frozen (blue), unfrozen (red) and partially frozen (shaded) core segments. Note that at UoL "frozen" includes visibly frozen core sections and re-constructed frozen conditions.

in grain size (at 630 and 530 cm). MS ranged between 6 and 66 × 10^{-8} m^3/kg, with particularly strong variation in the small frozen core sections.

Hydrochemistry and Reconstructed Freezing Conditions

Results of the hydrochemical analyses of pore water are shown in **Figure 4** and also in **Supplementary Table S8**. The pore water pH of both lagoons was neutral to slightly alkaline with a median of 7.5 for UoL and 8.0 for PFL. The EC was much higher in the pore water of the UoL-core with a maximum of 108 mS/cm at 1955 cm depth (median: 83.1 mS/cm) and showed higher variations over depth. Relatively low EC values at 2267 and 2745 cm depth were correlated with heavy stable water isotopes (**Supplementary Figure S2A**). The EC of the Polar Fox core pore water was highest in the upper sediment layer (max: 41 mS/cm) and showed freshwater to brackish conditions from 800 cm depth downwards (median: 3.3 mS/cm). The DOC distribution differed between the two lagoons, while the median value was similar (UoL: 58 mg/L, PFL: 50 mg/L). In UoL, the DOC concentration varied most in the uppermost unit and was highest at 360 cm depth (282 mg/L), while in PFL the greatest variation was found in the lower 5 m with the highest DOC concentration measured at 2835 cm depth (221 mg/L; **Figure 4** and **Supplementary Table S8**).

The stable water isotope composition was generally heavier in the pore water of the semi-closed Uomullyakh Lagoon (mean $\delta^{18}O/\delta D$: −20.9‰/−163.4‰) (**Supplementary Figure S2A**) than in the nearly closed Polar Fox Lagoon (mean $\delta^{18}O/\delta D$: −17.7‰/−133.7‰) (**Supplementary Figure S3A**). In the UoL core, the pore water of the upper sample had the lightest isotope composition with $\delta^{18}O$ of −19.8‰, which is comparable to the upper 5 m of PFL core pore water where its isotope composition was heaviest. There was no significant difference in isotopic composition between frozen and unfrozen samples (**Supplementary Figure S2B, S3B**). For UoL, we found a depletion of $\delta^{18}O$ with increased salinity. This was not found in the mainly freshwater to brackish dominated PFL core.

High freezing point depressions were observed for hypersaline samples (**Figure 4**) (e.g. for Uomullyakh at a depth of 1955 cm). For UoL, the borehole temperature was below the calculated

TABLE 2 | Calculated carbon pools for the upper 3 m and 30 m deposits below Uomullyakh and Polar Fox lagoons and estimated carbon pools below the three additional thermokarst lagoons of the southern Bykovsky Peninsula. Calculation is based on the bootstrapping method. The C-density of Stepanenko, Ivashkina and Safroneeva lagoons is the mean of the C-density calculated for Uomullyakh and Polar Fox lagoons.

Lagoon	Lagoon size (km^2)	C-budget (Mt)			C-density (kg/m^3)		
		3 m	30 m	Yedoma deposits	3 m	30 m	Yedoma deposits
Uomullyakh	2.10	0.15 ± 0.01	1.14 ± 0.20	0.42 ± 0.03	24.37 ± 2.09	18.03 ± 3.12	30.86 ± 1.91
Polar fox	0.64	0.05 ± 0.001	0.24 ± 0.04	0.13 ± 0.02	26.50 ± 0.57	12.55 ± 0.04	18.58 ± 2.95
Stepanenko	2.88	0.22	1.45	0.58			
Ivashkina	3.87	0.29	1.95	0.78	25.44	15.29	24.72
Safroneeva	1.89	0.14	0.95	0.38			
Total	11.39	0.85 ± 0.09	5.72 ± 0.63	2.29 ± 0.24	25.44 ± 0.75	15.29 ± 1.94	24.72 ± 4.34

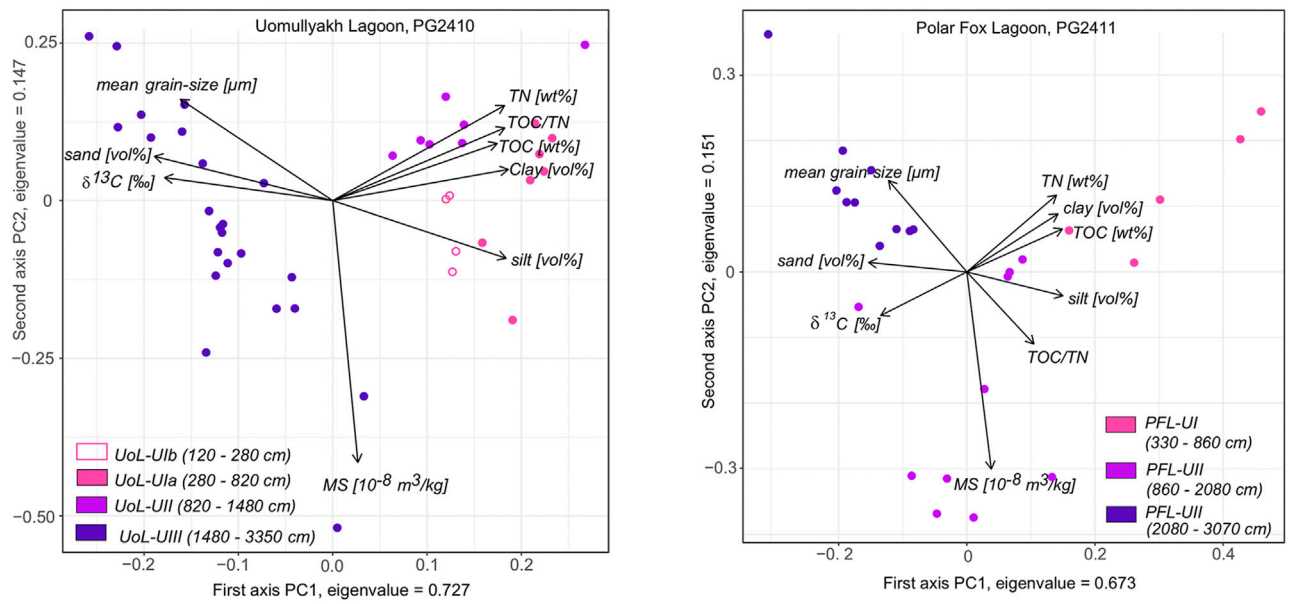

FIGURE 5 | Principal component analysis of biogeochemical parameter (TN, TOC/TN, TOC and $\delta^{13}C$) and sedimentological parameter (volumetric and mean grain size, MS) for Uomullyakh Lagoon **(left)** and Polar Fox Lagoon **(right)**. Main variance in the data is explained by differences in grain size and organic matter content and composition along the core.

freezing points in the lower core (1880 cm sediment depth and deeper) and thus the sediment could have been frozen at the time of drilling. In comparison to Uomullyakh, the Polar Fox borehole temperatures were significantly warmer (up to 5.2°C warmer) and significantly exceeded the calculated freezing point in the upper 480 cm of sediment above the partially frozen layer. Within Unit II and III of PFL, the calculated freezing point was very close to the observed temperature, suggesting that the system was close to equilibrium. This confirms the observations made in the field on the mostly thawed state of the core.

Carbon Pool Calculation

The surface areas for the Uomullyakh, Polar Fox, Ivashkina, Stepanenko, and Safroneeva lagoons were determined with remote sensing to be 2.10, 0.64, 3.87, 2.88, and 1.89 km^2, respectively. The total thermokarst lagoon area is 11.4 km^2. **Table 2** presents C-budgets and C-density calculated for the upper 3 m and 30 m of the sediment deposited in the Uomullyakh and Polar Fox lagoons. Results were extrapolated for the deposits below the other three thermokarst lagoons on the southern Bykovsky Peninsula using mean values for C-budget and C-density of Uomullyakh and Polar Fox lagoons. Below UoL, a carbon stock of 0.15 ± 0.01 Mt with a carbon density of 24.37 ± 2.09 kg/m^3 for the upper 3 m and 1.14 ± 0.2 Mt with a carbon density of 18.03 ± 3.12 kg/m^3 for 30 m thick deposits was calculated. The upper 3 m of PFL stored 0.05 ± 0.001 Mt organic carbon with a density of 26.50 ± 0.57 kg/m^3. The carbon stock amounts to 0.24 ± 0.04 Mt with a carbon density of 12.55 ± 0.04 kg/m^3 for 30 m thick deposits. The total carbon pool of the thermokarst lagoons on the southern Bykovsky Peninsula is 5.72 ± 0.63 Mt with an average carbon density of 15.29 ± 1.94 kg/m^3 for the upper 30 m (for the upper 3 m: 0.85 ± 0.09 Mt, 25.44 ± 0.75 kg/m^3).

PCA

The first two PCA axes explained 88% of the variation in the data for the Uomullyakh Lagoon core and 82% for PF Lagoon core (**Figure 5**). Though the variance is small, two groups were distinguished for both lagoon cores. Shallow depth correlated

TABLE 3 | Summary of stratigraphy, geochrononoly, sedimentology, biogeochemistry, facies, temperature, and pore water hydrochemistry deduced from multiproxy records.

Stratigraphy	Properties	UoL-core	PFL-core
Holocene lagoon deposition		**Unit Ib 320–120 cm**	
	Age	7.4 cal ka BP (radiocarbon)	
	Sediment	Dark gray clayish silt, fine sand layers → marine deposition	
	Carbon	Low OC content, moderately mineralized	
	Pore water	Lower salinity than UoL-UIa due to brine rejection from seasonal freezing, high decrease in DOC content	
	Temperature	–3.2°C, frozen due to bedfast ice	
Holocene thermokarst lake deposition		**Unit Ia 820–320 cm**	**Unit I 860–330 cm**
	Age	10.5 cal ka BP (radiocarbon)	No clear radiocarbon data
	Sediment	Mostly clayish silt (grayish-black), two sandy layers → lake deposition and external sediment input	Overall sandy silt (dark grey), plant and shell remains, slightly layered, two patterns of decreasing grain size → lake deposition, two phases of lake drainage or expansion
	Carbon	High OC content, moderately mineralized	Increasing OC content and quality with deposition of fine grained sediment
	Pore water	Hypersaline, ongoing depletion of stable water isotopes → increasingly heavy isotope signature with increasing depth suggest downward transport	Brackish to hypersaline conditions → less advanced salt intrusion than UoL
	Temperature	–3.2°C, unfrozen	0 to –0.6°C, unfrozen
Late Weichelian (MIS 2) fluvial and Yedoma deposition		**Unit II 1480–820 cm**	**Unit II 1200 cm–860 cm**
	Age	37 ± 2 ka (OSL) 43 ± 0.6–18.4 ± 0.3 ka cal BP (radiocarbon)	36.1 ka cal BP (radiocarbon)
	Sediment	Alternating, increasing thickness of silty layers (21–42% sand) → change in river discharge or orientation	Medium to coarse sand with pebbles overlaid by sandy silt (14–56% sand) → change in river orientation or dry up
	Carbon	Increasing OC content and quality	Low OC content, highly degraded
	Pore water	Hypersaline, depletion of stable water isotopes	Brackish conditions
	Temperature	–3.7 to –4.4°C, unfrozen → high freezing point depression due to high salinity	–0.1°C, partly frozen
(Middle)/Late Pleistocene fluvial deposition		**Unit III 3350–1480 cm**	**Unit III & II 3070–1200 cm**
	Age	>300 ka (pIRIR) – 63 ± 3 ka (OSL)	>360 ka – > 320 ka (pIRIR)
	Sediment	Alternating coarse and fine grained layers with pebbles (51–96% sand) → changing current conditions	More continuous and coarser grained sediment with larger pebbles (67–96% sand) → fluvial current conditions
	Carbon	Generally low OC content, highly degraded	Very low OC content, highly degraded
	Pore water	Hypersaline up to core end → was once completely thawed, isotopic composition similar to Tiksi Bay water	Fresh water conditions, light isotopic composition in comparison to UoL-UIII → different water sources of both lagoons
	Temperature	Alternating between –4.4 and –5.1°C → still partly unfrozen, refrozen talik from bottom of core up to 2000 cm depth	Uniform between –0.2 and 0.1°C → sediment completely thawed

with fine deposits and high organic matter content and quality, while in the deeper core, the variables sand content and $\delta^{13}C$ were decisive. The main variance in the data was explained by differences in grain size and organic matter contents and composition along the core.

DISCUSSION

Depositional History and Sediment Facies

At both lagoons, we identified four phases of landscape development based on sedimentological and biogeochemical parameters. These are: 1. Middle/Late Pleistocene fluvial deposition, 2. Late Weichelian (MIS 2) Yedoma deposition, 3. Holocene thermokarst lake formation and 4. Holocene lagoon formation.

The grain size distribution of sediments beneath Uomullyakh Lagoon and Polar Fox Lagoon indicates a changing depositional environment over time. In both lagoons, the sediments represent accumulation over the last glacial and interglacial cycles (**Table 3**). It is very likely that only the top few meters were accumulated since the previous interglacial. Based on stratigraphically constrained cluster analysis (CONISS) and visual observation, we distinguished four main stages of the late Quaternary history of the study area. The horizontal axis of the dendrogram (heights) represents the distance and therefore dissimilarity between clusters. The CONISS analysis of the 10 sedimentological and biogeochemical parameters at UoL showed a greater dissimilarity between clusters as for PFL. That hints to a more diverse depositional history for UoL. The cut of the dendrogram at height 7 for UoL (**Figure 2**) and height 4 for PFL (**Figure 3**), divided the cores into three main units, which is supported by the results of the PCA (**Figure 5**).

Radiocarbon ages out of stratigraphic order due to reworking of sediment as part of thawing and re-freezing processes are common for sedimentary deposits in thermokarst landscapes (Wetterich et al., 2009; Biskaborn et al., 2013; Schirrmeister et al., 2017, 2018; Jongejans et al., 2018). In the case of UoL, radiocarbon age reversals occur in Unit II (11–17 m) and Unit III (below 17 m). Possible reasons for unexpected high radiocarbon

concentrations include processes associated with the melt of large ice wedges and subsequent mixing, which transport younger material into older layers. Also, possible contamination by younger material during the drilling process and sample preparation have a larger effect when sample TOC contents are very low and available material is limited and can lead to dating bias (Oswald et al., 2005; Vyse et al., 2020). Unit II is characterized by thawed Yedoma Ice Complex deposits (see chapter 5.1.2). Existing intact Yedoma deposits, in north-east Siberian Arctic lowlands consist of massive syngenetic ice wedges several tens meters in height (Schirrmeister et al., 2002, 2011, 2013; Wetterich et al., 2014; Strauss et al., 2017; Möller et al., 2019; Fuchs et al., 2020). On the Bykovsky Peninsula only 10 km northeast of the lagoons, the Mamontovy Khayata Yedoma exposure is an example with syngenetic ice wedges up to 40 m high and 5–6 m wide (Schirrmeister et al., 2002). Likely, the same deposits were present at our drilling sites before thermokarst degradation. To estimate total thaw subsidence for the sites we measured the elevation difference of lagoon bottoms and the surrounding Yedoma upland based on height information of the ArcticDEM (Porter et al., 2018). The results suggest that Holocene permafrost degradation subsided the Yedoma surface by up to 25 m for UoL and 27 m for PFL, potentially causing mass flux of sediment and its organic carbon. At many locations across the landscape, large ice wedges thawed and the surface subsided, leaving ice wedge casts and water bodies, both of which infilled with local sediment. Where young near-surface organic matter slumped, and mixed into lower, older layers, age inversions as seen at UoL would have been created.

Though sediment mixing in such thaw-affected aquatic environments challenges chronological interpretation, comparison with deposits at other sites on the peninsula are consistent with our interpretation of the landscape development. In general, the radiocarbon age ranges of both cores correspond to previous dating from Yedoma sequences of Mamontovy Khayata (58.4–12 ka BP), about 10 km northeast (Schirrmeister et al., 2002), of Cape Razdelny (core 103/81: 40.8–21.63 ka BP) about 10 km southwest (Slagoda, 1993; Grosse et al., 2016) and of the Goltsovoye Lake (47.5–21.39 cal ka BP) less than 500 m north (Jongejans et al., 2020). Furthermore, the luminescence dating at 1107 cm and 2106 cm depth is consistent with the corresponding radiocarbon ages, showing an overall chronological succession. This sequence comprises Pleistocene ages in deep fluvial deposits, followed by late Weichelian ages in overlying Yedoma deposits. Therefore, the age range for the upper sections (UII, UI) appear reasonable. We correlate stratigraphic units between cores to assign the late Pleistocene ages of UoL-UII to the upper part of PFL-UII.

For deeper layers, especially Unit III of both cores, the results of the luminescence dating were used. The dose recovery ratios are satisfactory, and the comparison with the more-difficult-to-bleach feldspar IR_{50} and post-IRIR signals indicates that it is very likely that the quartz was well bleached at deposition (see **Supplementary Material Chapter 1.3** for a more detailed technical discussion of these issues).

Unfortunately, the quartz luminescence signals from the bottom Uomullyakh Lagoon sample, and both samples from the Polar Fox Lagoon, are saturated, and so all give minimum quartz age estimates of >100 ka. Interestingly, the feldspar pIRIR signals are also saturated, and since the dose range of the feldspar signal is considerably larger than that for the quartz OSL signal, the implied minimum age is > 300 ka. At least for the two lagoons located in a similar morphological setting and with similar sedimentology (see below) it is reasonable to assume that the bleaching history of the sediment entering the two water bodies is also similar. Luminescence dating from the adjoining Goltsovoye Lake supports this assumption (**Supplementary Table S4**). The quartz and feldspar signals of the bottom sample (fluvial deposits at 3513 cm depth) are also saturated and in the same age range as for UoL and PFL (quartz age: >90 ka, feldspar age: >280 ka). The implication of the broad agreement between the pIRIR and OSL signals in the top two Uomullyakh samples is that both were well bleached before deposition. If we extrapolate this observation to the bottom-most Uomullyakh sample and the two Polar Fox samples, we may assume that the pIRIR minimum ages should also be reliable, and since they are the most constraining, they are used in further discussion.

Middle/Late Pleistocene Fluvial Deposition – UoL-UIII (3350–1480 cm) and PFL-UIII + II (3070–1460 cm)

The first phase of landscape history at the study area is mainly characterized by fluvial deposits. Under the Polar Fox Lagoon, they range in age from >360 to >320 ka (pIRIR) and include the units PFL-UIII and the lower part of PFL-UII (in total 1590 cm). Below Uomullakh Lagoon, these deposits (Uol-UIII) have an age between >300 ka (pIRIR) to 63 ± 2 ka (OSL). This long time period is represented by only about 9 m of sediment, indicating an overall low accumulation rate under a dynamic fluvial regime with frequently alternating phases of accumulation and erosion in Unit III.

The presence of coarse sediments, rounded gravel and pebbles up to 2 cm, as well as driftwood indicates fluvial transportation and deposition (**Supplementary Figure S4**). Several studies also found fluvial sediments in similar depth underneath the neighboring Ivashkina Lagoon (Romankevich et al., 2017; Schirrmeister et al., 2018) and underlying Yedoma deposits on the Bykovsky Peninsula (Slagoda 1993; Slagoda, 2004; Siegert et al., 2002; Grosse et al., 2007; Jongejans et al., 2020). Kunitsky (1989) and Wetterich et al. (2008) assumed that the paleo-Lena River crossed the present Bykovsky Peninsula in an early Weichselian period (MIS 4 and maybe older). Our luminescence ages suggest that river transport existed over a long period from >360 ka (pIRIR) to 63 ± 2 ka (OSL).

While in UoL-UIII, discontinuous grain sizes, very poor sorting and higher organic matter content reflect frequently varying water runoff in a shallow river branch or near-shore area, PFL-UIII is distinguished by very little organic material, more continuous and coarser grain sizes, and a higher degree of sorting. Such properties reflect stable fluvial current conditions (Wetterich et al., 2008). This could suggest that UoL core was located in the near-shore area and PFL core closer to the center of a paleo river. However, the large distance between both cores

(2.5 km) and the deposition of fine grained sediment underneath the Goltsovoye Lake, located in the middle of both lagoons, makes this scenario improbable. It is more likely that two neighboring river branches, part of a braided river system or delta run through the location of today's lagoons. This assumption is encouraged by finds of fluvial deposits across the peninsula. Alternation of fine and coarse grained layers at UoL-UIII indicate ongoing changes in river morphology. In PFL-UII until 1200 cm depth, organic containing fine sand layers were interbedded with coarser sand and gravel layers similar to the upper part of UoL-UIII also indicating varying water runoff or change in river course.

A layer of large driftwood pieces of similar shape and size found in UoL-UIII (at 1530 cm), PFL-UII (at 1810 cm) as well as GoL (at 2045 cm) (Unit II in Jongejans et al., 2020) are presumably deposited at the same flood event. In comparison to PFL and GoL, UoL core showed coarser grained fluvial deposits after the flood event which go along with increased erosion of overlying sediment explaining the higher elevation of the driftwood layer at UoL. Based on biomarker analyses carried out for the Goltsovoye Lake core, Jongejans et al. (2020) concluded that the area at time of flooding was a wetland, dominated by low-centered polygons formed during the Kargin Interstadial (MIS 3).

Late Weichelian (MIS 2) Yedoma Deposition – UoL-UII (1480–820 cm) and PFL-UII (1200–860 cm)

In the second phase of the landscape development an increase in silt deposition and organic matter content, as well as a depletion of $\delta^{13}C$ point to changing environmental conditions away from high energy fluvial processes toward lower energy alluvial and other transport processes. Luminescence dating for UoL at 1107 cm to 37 ± 2 ka (OSL) revealed a late Pleistocene age (beginning of late Weichelian stadial). Radiocarbon dates from sediments of similar depth for both UoL (43 ± 0.56 cal ka BP at 1063 cm) and PFL (36.1 ± 0.39 cal ka BP at 1128 cm) are in a similar time range. Paleo-ecological data from the nearby Mamontovy Khayata Yedoma cliff (Andreev et al., 2002; Schirrmeister et al., 2002) and biomarker analyses from GoL (Jongejans et al., 2020) revealed that the climate was drier and colder, transforming the former wetland into a steppe-like tundra, which probably caused decreasing river run off and changing river morphology.

When comparing the data with those of the Yedoma Ice Complex of Mamontovy Khayata, they appear to resemble mostly the fine-grained layer of the units Uo-UII and PFL-UII. Thus, it can be deduced that ice-rich Yedoma Ice Complex deposits started accumulating when either the previously existing river fell dry or changed its course.

Holocene Thermokarst Lake Formation – UoL-UIa (820–320 cm) and PFL-UI (860–330 cm)

The third phase involves the formation of a thermokarst lake, which is a prerequisite for a thermokarst lagoon. High proportions of clay and silt as well as high TOC and TN content and shell remains (PFL at 400–440 cm) indicate that Unit I of both cores represent the lake stage. Based on the results of the CONISS analysis, we discovered ~5.5 m thick lake sediments for both lagoons, which are likely mixed with Yedoma deposits from the lake shore.

In northeast Siberia, thermokarst lake formation began with rapid warming and wetting between 14 and 11.7 ka (Kaplina and Lozhkin, 1979; Kaplina, 2009; Anthony et al., 2014; Subetto et al., 2017). Grosse et al. (2007) estimated that major lakes and basins on the Bykovsky Peninsula were formed in the early Holocene, probably starting between 12.5 and 9.4 cal ka BP when a sedimentation gap on top of local Yedoma deposits suggests widespread reorganization of the landscape. This is in agreement with a radiocarbon date of 10.5 ka cal BP at 480 cm for UoL-UIa which we interpret as lacustrine deposits.

The gravimetric ice content of Yedoma deposited at Mamontovy Khayata is between 60 and 180% (Schirrmeister et al., 2002). Assuming that the Yedoma deposits were similarly ice-rich underneath the lagoons, thawing of these ice-rich sediments explains the large surface subsidence discussed before and suggests a substantial deposit compaction during lake stage.

The size of the drained thermokarst lake basins, shown in the landform classification map of Fuchs et al. (2018) (**Supplementary Figure S5**), indicates that Uomullyakh and Polar Fox basins were once significantly larger than the current water bodies and that drainage events occurred in the past. Lake drainages are common for thermokarst landscapes and are often rapid events with formation of drainage channels cutting deep into ice-rich permafrost (Grosse et al., 2013).

In UoL-UIa, a rapid increase in grain size at 630 and 530 cm depth corresponds to erratic changes in mass specific magnetic susceptibility indicating an external input of sediment at least twice. Upstream, south-west and north-west of UoL, two drained lake basins (**Supplementary Figure S5**) are located. Drainage channels connecting the basins with UoL, still visible at satellite images, suggest that UoL has been flooded while these lakes drained. As lake drainage may cause sediment erosion and downstream deposition, it is possibly the reason for the external sediment and organic matter input found in the UoL core.

In PFL-UI, two repetitive patterns of decreasing grain size associated with increasing TOC and TN content and organic matter quality are visible and might indicate drainage events. Therefore, Polar Fox Lagoon may have drained twice during the lake phase. The first drainage could have been northwards toward the adjoining lake basin (**Supplementary Figure S5**) and the second drainage southwards to the sea leading to lagoon formation.

A wider TOC/TN ratio and lighter $\delta^{13}C$ composition of the sediment beneath UoL indicates that the organic matter was less mineralized than beneath PFL. That is likely because the UoL-UIb horizon is frozen in winter due to bedfast ice formation and subsequent lagoon bottom freezing, while PFL-UI is mostly thawed throughout the year, allowing more time for microbial degradation of organic matter. Seasonal freezing under floating ice conditions at PFL is also

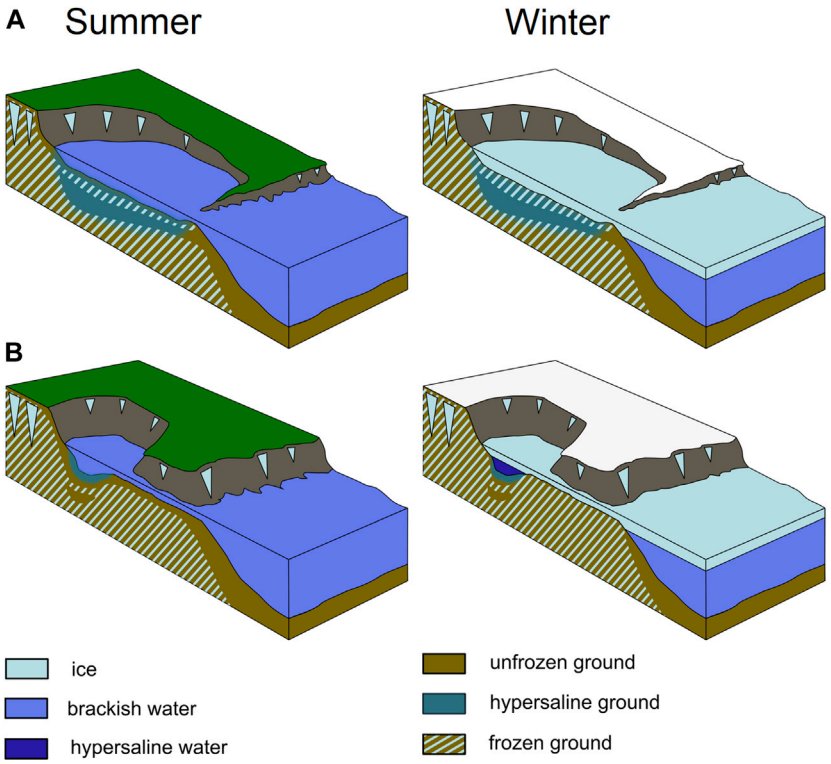

FIGURE 6 | Schematic diagram showing two types of lagoon systems in summer and winter. **(A)** semi-closed lagoon system (similar to Uomullyakh Lagoon). Bedfast ice in winter leads to salt enrichment of the pore water up to great depth. **(B)** nearly closed lagoon system (similar to Polar Fox Lagoon) which is connected during the open-water season only. The long and shallow channel mitigates sediment exchange. Floating ice that thickens in winter leads to salt enrichment of free water and upper sediment. Modified after Angelopoulos et al. (2020a).

possible but would likely only result in partial sediment freezing and a thinner seasonally frozen layer compared to UoL (Angelopoulos et al., 2020a).

Holocene Lagoon Formation – UoL-UIb (320–120 cm)

Indications for the fourth phase of landscape development, the formation of a thermokarst lagoon, were found at the boundary between UoL-UIb and UoL-UIa (between 360 and 280 cm). The increase in mass specific magnetic susceptibility and grain size, the decrease in TOC and TN content, as well as a slight decrease in TOC/TN ratio indicate a system change. In our interpretation, this shift is caused by marine inundation and marks the beginning of the third stage, the lagoon formation. Postglacial rising sea levels caused by melting of continental ice sheets led to the inundation of former terrestrial permafrost on the Laptev Sea shelf until about 5 ka (Bauch et al., 2001) when sea levels stabilized and coastal erosion of ice-rich permafrost started to dominate the coastline (Romanovskii et al., 2000; Romanovskii et al., 2004). Likely, the Uomullyakh thermokarst lake was breached by the transgressing sea and coastal erosion in the early to mid-Holocene. A similar breaching and submergence of thermokarst lakes and drained lake basins has been observed in thermokarst-affected coastal lowlands on the Alaska North Slope (Arp et al., 2010), in the Mackenzie Delta region (e.g. Ruz et al., 1992), and on Banks Island (Grasby et al., 2013).

Satellite images (e.g. **Figure 1**) indicate that the Uomullyakh Lagoon is characterized by stronger turbidity due to lack of topographical wind shadow (compared to the Yedoma upland surrounded PFL) and its connection to the sea, which enables waves to enter. High connectivity to the sea likely leads to an increased input of marine sediment (Grotheer et al., 2020). This is in agreement with sediment analyses indicating marine deposition in Uomullyakh Lagoon for the upper 2 m mixed with lacustrine deposits.

At Polar Fox Lagoon, this distinction could not be made. This is very likely caused by the different morphology of both lagoons. The Polar Fox Lagoon was formed as a result of thermokarst lake drainage, which led to the formation of a shallow and winding channel connecting lake and sea (Angelopoulos et al., 2020a). The connection to the Tiksi Bay is cut off during winter when ice formation reaches the channel bed, restricting water and sediment exchange (Spangenberg et al., 2021).

Impact of Marine Inundation

Our data suggests that deep (~20 m) hypersaline taliks (UoL) preserve organic carbon better than taliks that contain mostly

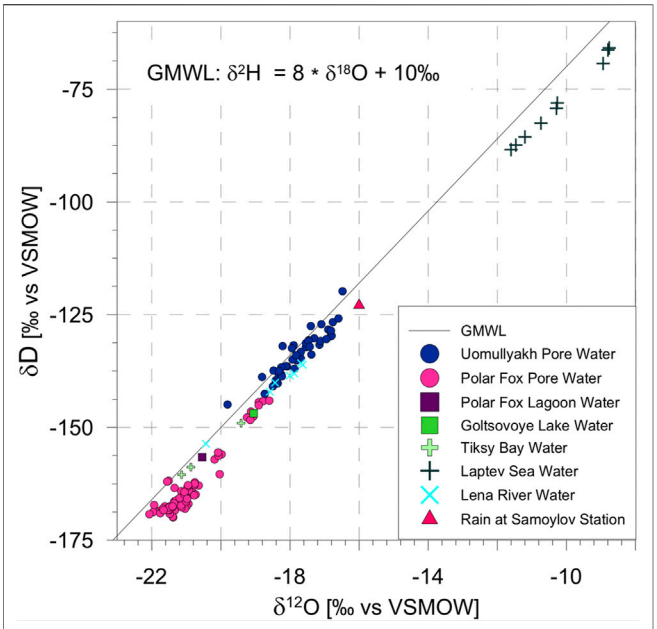

FIGURE 7 | Comparison of the stable water isotope composition of lagoon core pore water and surface water of different possible endmember; sediment pore water from April 2017 (this study); water of Polar Fox Lagoon, Goltsovoye Lake, and Tiksi Bay were sampled in July 2017 (P. Overduin, unpublished data); Laptev Sea water was sampled during expedition with the research vessel Pavel Bashmakov at the end of August 2002 (H. Meyer, unpublished data); Lena River water from summer 2005–2016 (clustered points) and one sample from April 2013 (isolated point) (H. Meyer, unpublished data). Stable water isotopes δD and $\delta^{18}O$ relative to Vienna Standard Mean Ocean Water (VSMOW).

freshwater below a thin saline layer (PFL). Drawing on microbial subsea permafrost research (Mitzscherling et al., 2017), hypersaline cryotic taliks can stress microbes and slow the decay of organic matter.

Once a connection from the lake to the sea is established, salts from seawater can diffuse into the sediment (Angelopoulos et al., 2020a) or transport into the sediment more rapidly via convection (Shakhova et al., 2017). Therefore, the frozen/thawed state of the sediment is largely a reflection of recent marine sediment deposition and salt transport. In the Uomullyakh Lagoon core, the EC of pore water generally increased with depth, from 30 mS/cm just below the seasonally frozen layer (240 cm below ice) to 108 mS/cm at 1525 cm depth below ice (mean 77 mS/cm for the entire core). The salinities were significantly higher than the Tiksi Bay water (3.8 mS/cm) (**Supplementary Table S1**) for the same time of the year. At the Polar Fox Lagoon core, the maximum EC (41 mS/cm) was measured in the uppermost sample just below the sediment surface. The relatively high EC in both lagoons suggests that brine rejection from lagoon ice formation and the seasonal isolation of the water bodies from Tiksi Bay are key processes affecting the pore water salinity.

Uomullyakh is a semi-closed lagoon, especially during the open water season when it may experience flooding and enhanced marine sediment deposition from storm surges (e.g. Nazarova et al., 2017) (**Figure 6A**). Polar Fox Lagoon, on the other hand, is a nearly closed lagoon (**Figure 6B**). It is isolated from the sea once bedfast ice forms at the shallow inlet (~0.5 m) of the connecting channel (Spangenberg et al., 2021).

At Uomullyakh Lagoon, all 17 ice-auger measurements in April 2017 revealed bedfast ice, suggesting that there was nearly no surface water exchange with Tiksi Bay. Despite a seasonally closed system for the surface water, lateral groundwater exchange in the sediment can still occur if the sub-lagoon and subsea permafrost taliks are connected. This talik connection is possible, because the sediment just offshore of the spit is also characteristic of the lagoon talik when the spit was located further south. Furthermore, permafrost aggradation beneath the spit is controlled by limited sub-aerial exposure time as the spit retreats further north with coastal erosion. The large difference in isotopic composition of the pore water between the lagoons confirms that the Uomullyakh Lagoon sediment had a larger source water contribution from Tiksi Bay (**Figure 7**). Tiksi Bay as a heavy endmember likely caused the enrichment in heavier water isotopes of the Uomullyakh Lagoon pore water. Pedrazas et al. (2020) used electrical resistivity surveys to map continuous unfrozen sediment from an onshore cryopeg to a sub-lagoon talik down to a depth of 20 m in northern Alaska, and suggested it could be a conduit for groundwater and nutrient exchange. The isotopic composition of the pore water, along with the near vertical profile of salinity with depth (5–20 m and 25–33 m; **Supplementary Figure S3**) suggests that convective processes influenced the salt distribution (Harrison and Osterkamp, 1982). In addition, there was a likely high salt content injection into the sediment following bedfast ice formation. The seasonally frozen layer can still have been permeable and susceptible to brine flow (Osterkamp et al., 1989). Although temperatures were as low as −4.4°C (at 1540 cm), the freezing point of the hypersaline sediment was calculated to have been as low as −5.1°C (at 1520 cm), resulting in a cryotic talik. At a depth of 2040 cm, the observed temperature (−4.7°C) was below the freezing point (−3.82°C), indicating the approximate depth to ice-bearing permafrost. It is unclear how the ice-bearing permafrost table evolved, but the decreasing temperature trend with depth suggests the lagoon sediment column might be warming. Therefore, it is plausible that hypersaline sediment partially froze once sufficient sediment deposition in the lagoon created a mostly bedfast ice regime with some small isolated water pockets. Now, the ice-bearing permafrost table may be degrading under warmer, but still cryotic bedfast ice conditions. This is similar to terrestrial cryopeg expansion under warming subaerial conditions (Streletskaya, 1998).

At Polar Fox Lagoon, the contemporary distribution of ice-bearing permafrost and taliks is somewhat different. Polar Fox Lagoon is presumably younger than Uomullyakh Lagoon and still contains a floating ice area with a maximum water depth of 340 cm. In the floating ice area, coupled heat and salt diffusion models suggest that the thin partially frozen permafrost layer (830 to 480 cm below the sediment surface) developed sub-aquatically after the lake to lagoon transition. The partially frozen layer depth and thickness are transient, as the top-down chemical

TABLE 4 | Comparison of biogeochemistry characteristics with different lagoons, Yedoma sites and a thermokarst lake: total organic carbon content (TOC), total nitrogen (TN), atomic carbon nitrogen ratio, stable carbon isotope composition ($\delta^{13}C$). Note that given depth are measured from the sediment surface for better comparability of the sites.

Site	Sediment	TOC range (mean) (wt%)	TN range (mean) (wt%)	Atomic TOC/TN range (mean)	$\delta^{13}C$ range (mean) (‰ VPDB)	Citation
Uomullyakh Lagoon (Bykovsky) core length: 32.3 m	Marine 0–2 m	1.7–2.0 (1.9)	0.13–0.17 (0.15)	13–17 (15)	−26.8 to −26.1 (−26.6)	This study
	Lacustrine 2–7 m	2.0–4.1 (3.4)	0.17–0.30 (0.24)	14–19 (16)	−27.7 to −26.7 (−27.3)	
	Former terrestrial Yedoma 7–15 m	0.6–6.7 (2.5)	<0.1–0.14 (0.05)	13–18 (16)	−27.5 to −25.0 (−26.0)	
	Fluvial deposits 15–32.3 m	<0.1–3.3 (0.6)	<0.1	—	−26.3 to −24.1 (−25.1)	
Polar Fox Lagoon (Bykovsky) core length: 27.7 m	Lacustrine 0–5.3 m	1.5–4.0 (2.8)	0.14–0.27 (0.22)	11–18 (15)	−27.5 to −25.5 (−26.8)	This study
	Former terrestrial Yedoma 5.3–9 m	0.5–1.0 (0.8)	<0.1–0.14 (0.05) (0.12 for upper 2 samples)	8–10 (9) $n = 2$	−25.6 to −24.1 (−25.0)	
	Fluvial deposits 12–31.5 m	<0.1–1.0 (0.2)	<0.1	—	−24.9 to −23.4 (−24.2)	
Goltsovoye Lake (Bykovsky) core length: 31.5 m	Lacustrine 0–5 m	1.0–4.3 (3.0)	0.14–0.33 (0.25)	8–16 (13)	−28.6 to −24.8 (−27.0)	Jongejans et al. (2020)
	Former Yedoma 5–28 m	<0.1–3.1 (0.7)	<0.1–0.22 (0.05)	0–36 (4)	−26.6 to −23.8 (−24.8)	
	Fluvial deposits 28–31.5 m	<0.1–17.8 (3.1)	<0.1–0.46 (0.08)	0–171 (20)	−23.6 to −24.5 (−25.7)	
Ivashkina Lagoon (Bykovsky) core length: 6.15 m	Marine 0–0.24 m	2.0–2.5 (2.2)	0.19–0.24 (0.21)	9–12 (11)	−26.4 to −26.2 (−26.3)	Schirrmeister et al. (2018)
	Lacustrine 0.24–2.51 m	1.7–2.8 (2.6)	0.14–0.26 (0.20)	10–14 (12)	−27.2 to −25.5 (−26.6)	
	Former terrestrial Yedoma 2.53–6.15 m	0.9–5.6 (2.7)	0.10–0.84 (0.26)	3–18 (13)	−27.8 to −23.9 (−26.4)	
Mamontovy Khayata (Yedoma on Bykovsky) profile length: ca. 38 m	Terrestrial 14–34 m	1.3–27.0 (4.8)	0.17–1.38 (0.40)	8–34 (20)	−28.7 to −23.9 (−26.1)	Schirrmeister et al. (2002), Schirrmeister et al. (2011)

degradation of newly formed frozen sediment lags behind the talik refreezing (Angelopoulos et al., 2020a). In bedfast ice zones (approximately 75% of Polar Fox Lagoon), electrical resistivity surveys showed that the thickness of the frozen layer and that of the overlying saline layer increased and decreased toward the shoreline, respectively.

The transient nature of frozen sediment and taliks beneath may affect CO_2 and CH_4 fluxes in the sediment column, because partially frozen sediment with an ice saturation exceeding 60% has proven to be an effective barrier to gas flow (Chuvilin et al., 2016). In the case of a shallow lagoon with bedfast ice, the frozen sediment can be saline and have a lower freezing point compared to frozen sediment without salt. Therefore, lagoons may precondition the frozen sediment for rapid thawing (compared to Yedoma permafrost) once it is exposed to warmer coastal waters in the subsea permafrost environment. This, in turn, could contribute to the development of offshore gas migration pathways for greenhouse gas released from thawing subsea permafrost (Shakhova et al., 2019). Any released gas might not reach the atmosphere, as it has to bypass numerous sinks, including anaerobic oxidation in the sediment column (Overduin et al., 2015), dissolution in the pore water and surface water, low-permeability layers, and lagoon ice. Angelopoulos et al. (2020b) provide a review of subsea permafrost within the context of global climate change, and Ruppel and Kessler (2017) provide a review specific to climate change interactions with gas hydrates.

Carbon Pool Upscaling

Permafrost thaw beneath thermokarst lakes is more rapid than gradual thaw of near-surface permafrost and could double permafrost carbon emissions this century (Walter Anthony et al., 2018; Turetsky et al., 2020). Field-based observations on carbon turnover and greenhouse gas production in thermokarst lake sediments are scarce (Heslop et al., 2015; Heslop et al., 2019a; Heslop et al., 2019b) and completely missing for thermokarst lagoons. In order to estimate potential future greenhouse gas release from emerging thermokarst lagoons, we assessed the size of the lagoon C-pool by extrapolating our TOC and BD of the two analyzed lagoons to the other three thermokarst lagoons on the Bykovsky Peninsula.

The calculations of the carbon budgets show that the carbon density differs between the neighboring lagoons, especially for greater depths (upper 3 m: 22.5 kg/m^3 (Uo) vs. 26.5 kg/m^3 (PFL); upper 30 m: 17.4 kg/m^3 (UoL) vs. 10.2 kg/m^3 (PFL), which demonstrates the small scale spatial variability of the carbon deposits. The input and output of organic matter are strongly dependent on environmental conditions and lake drainage events. Schirrmeister et al. (2018) estimated the carbon density for the upper 6 m of the thermokarst lagoons on the Bykovsky Peninsula at 25 ± 5 kg/m^3, which is in the same range as the carbon density we calculated for the upper 3 m (24.5 ± 1.4 kg/m^3), but 45% higher than the mean carbon density of the 30 m-long sediment cores (13.8 ± 3 kg/m^3). We explain this with the higher TOC values we measured in the lake influenced sediments (UoL-UIa, PFL-UI), which were the stratigraphic class dominating the Schirrmeister et al. (2018) dataset.

A similar carbon storage was estimated for thermokarst lagoons on northern Richards Island, Mackenzie Delta, Canada. Based on an average carbon content of 2.75–3% for marine and lacustrine deposits, Solomon et al. (2000) estimated

a carbon deposition of ca. 25×10^4 t in the investigated embayment area (10.3 km^2) since thermokarst lake development. This corresponds to a carbon density of 25 kg/m^3 for the upper 10 m, which is similar to the carbon density of the lacustrine sediments of the Bykovsky lagoons. Comparing the carbon stored in undisturbed, previously unthawed ice-rich Yedoma deposits of Mamotovy Khayata (Schirrmeister et al., 2011) with the TOC of Yedoma thawed under thermokarst lake and lagoon conditions (**Table 4**), we would expect to find a gradient of C loss in thawed Yedoma underneath thermokarst landforms that is linked to thaw histories. Using a simple mass balance approach, the difference in mean TOC content between the Mamotovy Khayata Yedoma and the thawed Yedoma beneath thermokarst sites (**Table 4**) can be expressed as percentage carbon loss. This approach suggests a C loss of 85% for thawed Yedoma under Goltsovoye Lake, 83% C loss for PFL, 48% C loss for UoL, and 44% C loss for IvL due to subaquatic permafrost thaw. These estimations imply that less organic carbon is lost in the more open UoL and IvL compared to the younger, nearly closed PFL and the freshwater GoL. If our assumptions are valid, this would signify that a freshwater dominated lake and the floating ice areas of nearly closed lagoon systems like PFL result in strong organic carbon loss upon thaw while seawater dominated systems seem to better preserve organic carbon. In addition, higher TOC/TN and lower $\delta^{13}C$ values for thawed Yedoma underneath UoL and IvL indicate lower organic matter degradation both more open lagoons, further supporting this hypothesis. Since approximately 75% of PFL was characterized by bedfast ice in April 2017 (Angelopoulos et al., 2020a), additional C is likely preserved in areas with thick frozen sediment. At UoL, the hypersalinity of the cryotic talik can stress microbial communities, leading to reduced population, diversity, and decay of organic matter (Mitzscherling et al., 2017). Although bacterial communities can adapt to increasingly saline conditions, past refreezing events in the upper 20 m of the sediment core (refer to "Impact of Marine Inundation" Section 5.2), can also preserve C at UoL.

The calculated average C-density of the core section referred to Yedoma deposits of the five thermokarst lagoons on Bykovsky Peninsula is 24.72 ± 4 kg/m^3 and therefore in the upper range of the C-density estimated for the 0.41×10^6 km^2 large Yedoma region (19 + 13/-11 kg/m^3) (Strauss et al., 2013) and in the lower range of terrestrial thermokarst deposits of the Yedoma region (33 + 25/-19 kg/m^3) (Schirrmeister et al., 2011; Strauss et al., 2013).

Using the lagoon C-density mean, we calculated 5.7 Mt C in the first 30 m of lagoon sediments covering an area of 11.4 km^2. This is a substantial inventory of formerly frozen C, which is now largely unfrozen and thus available for microbial degradation processes. $\delta^{13}C$ and TOC/TN values indicate that the degradation of the primarily terrestrial plant material is advanced. Highest organic matter degradation was indicated for the fluvial deposits possibly because the alluvial material was already strongly degraded at the time of deposition.

The comparison of different sites shows that the biogeochemical parameters differ between sediment types rather than between the sites (**Table 4**). For example, the lacustrine sediments at all four sites (PFL, UoL, GoL and IvL) have very similar TOC and TN contents as well as similar TOC/TN ratios and $\delta^{13}C$ signals, but they differ from the over- or underlying sediment facies (Schirrmeister et al., 2018; Jongejans et al., 2020). The lacustrine sediments in the deep sediment cores of UoL, PFL and GoL are richer in TOC and TN than the underlying former terrestrial or overlying marine sediments. High carbon accumulation in thermokarst lake sediments can be caused by shore erosion and deposition of terrestrial organic matter, high aquatic productivity, and unique preservation conditions (Anthony et al., 2014). In contrast, the biogeochemical parameters of lacustrine and underlying Yedoma deposits of the Ivashkina Lagoon differ only slightly (Schirrmeister et al., 2018). This is not surprising, as the upper part of the Yedoma deposits (IvL core reaches only to 6.15 m depth) tend to have higher carbon and nitrogen contents and lower degradation rate than the deeper deposits. An exception are the deep fluvial deposits under the GoL, where allochthonous organic material leads to very high TOC and TN contents (Jongejans et al., 2020). The TOC content of thawed talik sediments (former Yedoma deposits) is highest for the UoL, with similar values found in Taberites (2.7 ± 1.4 wt%) and late Weichelian (MIS 2) Ice Complex deposits (2.2 ± 0.9 wt %) of the Siberian permafrost region (Schirrmeister et al., 2011). The organic matter mineralization is highest for former Yedoma deposits below GoL (TOC/TN = 4) and lowest for Yedoma deposits at Mamontovy Khayata (TOC/TN = 20). The high mean TOC/TN ratio of fluvial deposits below GoL is based on five samples with very high TOC/TN ratios. The median TOC/TN ratio of 0 shows that the carbon mineralization is high for most samples of the fluvial deposits below GoL. In general, the carbon mineralization is mostly high (TOC/TN < 12) or in the lower moderate range (TOC/TN 12–25) for thermokarst affected sites. This is a common phenomenon in the warming Arctic, as rising permafrost temperatures result in increasing thermokarst development which favors the microbial decomposition of thawing organic matter (Strauss et al., 2017).

Greenhouse gas production in thermokarst lagoons connected to the marine environment is expected to differ substantially from that in thermokarst lakes: the supply of electron acceptors, specifically of sulfate, will promote sulfate reduction and anaerobic methane oxidation thus favoring the release of CO_2 relative to that of methane (Segers and Kengen, 1998). In line with this, substantial CO_2 release was recently reported for a laboratory study that incubated permafrost with seawater (Tanski et al., 2019). In addition, anaerobic methane oxidation was observed in thawing seawater-affected permafrost (Winkel et al., 2018) and thermokarst lake sediments with temperatures close to 0°C (Winkel et al., 2019). Given both our first estimate of thermokarst lagoon carbon budgets, and the expectation that the rate of formation of such lagoons will increase due to coastal erosion, thermokarst lagoons are considered important biogeochemical processors of former permafrost carbon and a critical component of the future Arctic greenhouse gas system.

CONCLUSION

This study shows that thermokarst lagoons are highly dynamic landforms at the boundary between terrestrial permafrost and marine systems. Based on two ~30 m long sediment cores from

two contrasting thermokarst lagoon systems, we examined the depositional history, the impact of marine inundation and the amount of stored organic carbon for different stages of thermokarst lagoons. We identified several different phases of sediment deposition in the semi-closed Uomullyakh Lagoon and the nearly closed Polar Fox Lagoon. The sedimentological analysis of both lagoon cores shows that fluvial deposition from a paleo-river system dominated at the sites from >360 ka to the late Pleistocene, when silty to sandy ice-rich Yedoma deposits started to accumulate in this region. These former Yedoma deposits are now present as thawed talik sediments. With the beginning of the warmer Late Glacial to Holocene period, the formation of thermokarst lakes began and resulted in lacustrine sediment deposition at both lagoons. At the more open Uomullyakh Lagoon, marine sediments overlying lacustrine deposits indicate the onset of the lagoon phase starting in the early to mid-Holocene. Inundation with seawater and formation of seasonal bedfast ice caused the saline enrichment of the pore water, which led to cryotic talik formation.

Our case study from the Bykovsky Peninsula provides a first estimate of organic carbon quantity and quality based on deep sediment cores below thermokarst lagoons. We have identified large organic carbon stocks in these special Arctic lagoon systems. We measured a mean C-density of 15.3 ± 2 kg/m^3 for the 30 m thick deposits below the lagoons, with higher values found below the semi-closed lagoon. The measured carbon density for the Yedoma deposits (24.72 ± 4 kg/m^3) is in the upper range of the estimate of terrestrial Yedoma (19 + 13/-11 kg/m^3), but lower range of terrestrial thermokarst deposits (33 + 25/-19 kg/m^3) in the Yedoma region. Based on the mean C-density and the remote sensing-based spatial extent of thermokarst lagoons, we calculate a total C storage of 5.7 Mt C in the upper 30 m of sediment in five thermokarst lagoons on the southern Bykovsky Peninsula.

Our data indicate that open thermokarst lagoons under high seawater influence seem to better preserve organic carbon more then freshwater dominated systems. This shows the potential importance of the role and contribution of thermokarst lagoons in the transformation of terrestrial permafrost carbon under increasingly marine influence.

DATA AVAILABILITY STATEMENT

The datasets presented in this study can be found in online repositories. The names of the repository/repositories and accession number(s) can be found below: https://doi.pangaea.de/10.1594/PANGAEA.922169.

AUTHOR CONTRIBUTIONS

MJ and JS designed this study. MJ led the writing of the first draft of the manuscript. JS, GG, and MG developed the overall coring plans for the Bykovsky Peninsula field campaign. JS, MG, LS, BB, PO, MA, SL, and GG conducted the field work. MA and PO did the subsampling for the Polar Fox sediment core and MJ for the Uomullyakh core. MJ and PO performed laboratory analyses. MJ led the data interpretation for both cores. MJ and IN conducted the spatial analysis and mapping of the lagoons. AM performed optical luminescence analyses and data interpretation. All co-authors contributed within their specific expertise to data interpretation.

FUNDING

This study was carried out within the NERC-BMBF project CACOON (Changing Arctic Carbon cycle in the cOastal Ocean Near-shore, grant no. 03F0806A), the ERC Project PETA-CARB (#338335), and the BMBF project KoPF (03F0764B, 03F0764F). The Alfred Wegener Institute Helmholtz Centre for Polar and Marine Research (AWI) provided baseline funding and together with the Germany Research Centre for Geosciences (GFZ) AWI provided funding for the expedition.

ACKNOWLEDGMENTS

We thank the Hydrobase Tiksi, Arctica GeoZentr, Stanislav Ostreldin, Waldemar Schneider, Dmitri Bolshiyanov, and Sergey Pravkin for their logistic contributions to the field expedition Bykovsky 2017. We thank the MICADAS Team at AWI Bremerhaven for dating the radiocarbon samples and Hanno Meyer for discussing the isotope results. Torben Windirsch is acknowledged for his support during subsampling the Uomullyakh core as well as Antje Eulenburg, Dyke Scheidemann, Jonas Sernau and Angélique Opitz for their support and assistance in the lab. We also thank Frederieke Miesner for her help on modifying **Figure 6**. We acknowledge the support by the Open Access Publication Funds of Alfred-Wegener-Institut Helmholtz Zentrum für Polar- und Meeresforschung.

SUPPLEMENTARY MATERIAL

The Supplementary Material for this article can be found online at: https://www.frontiersin.org/articles/10.3389/feart.2021.637899/full#supplementary-material

REFERENCES

Andersson, R. A., Meyers, P., Hornibrook, E., Kuhry, P., and Mörth, C.-M. (2012). Elemental and Isotopic Carbon and Nitrogen Records of Organic Matter Accumulation in a Holocene Permafrost Peat Sequence in the East European Russian Arctic. *J. Quat. Sci.* 27 (6), 545–552. doi:10.1002/jqs.2541

Andreev, A. A., Schirrmeister, L., Siegert, C., Bobrov, A. A., Demske, D., Seiffert, M., et al. (2002). Paleoenvironmental Changes in Northeastern Siberia during the Late Quaternary - Evidence from Pollen Records of the Bykovsky Peninsula'. *Polarforschung* 70, 13–25. doi:10.2312/polarforschung.70.13

Angelopoulos, M., Overduin, P. P., Miesner, F., Grigoriev, M. N., and Vasiliev, A. A. (2020b). Recent Advances in the Study of Arctic Submarine Permafrost. *Permafrost and Periglac Process* 31 (3), 442–453. doi:10.1002/ppp.2061

Angelopoulos, M., Overduin, P. P., Westermann, S., Tronicke, J., Strauss, J., Schirrmeister, L., et al. (2020a). Thermokarst lake to Lagoon Transitions in Eastern Siberia: Do Submerged Taliks Refreeze? *J. Geophys. Res. Earth Surf.* 125. doi:10.1029/2019JF005424

Anthony, K. M. W., Zimov, S. A., Grosse, G., Jones, M. C., Anthony, P. M., Iii, F. S. C., Iii, et al. (2014). A Shift of Thermokarst Lakes from Carbon Sources to Sinks during the Holocene Epoch. *Nature* 511 (7510), 452–456. doi:10.1038/nature13560

Arp, C. D., Jones, B. M., Whitman, M., Larsen, A., and Urban, F. E. (2010). Lake Temperature and Ice Cover Regimes in the Alaskan Subarctic and Arctic: Integrated Monitoring, Remote Sensing, and Modeling1. *JAWRA J. Am. Water Resour. Assoc.* 46 (4), 777–791. doi:10.1111/j.1752-1688.2010.00451.x

Bauch, H. A., Mueller-Lupp, T., Taldenkova, E., Spielhagen, R. F., Kassens, H., Grootes, P. M., et al. (2001). Chronology of the Holocene Transgression at the North Siberian Margin. *Glob. Planet. Change* 31 (1-4), 125–139. doi:10.1016/S0921-8181(01)00116-3

Berner, J., Symon, C., Arris, L., and Heal, O. W. (2005). *Arctic Climate Impact Assessment, National Science Foundation (U.S.), United States, and National Oceanic and Atmospheric Administration*. New York, N.Y.: Cambridge University Press.

Bindoff, N. L., Willebrand, J., Artale, V., Cazenave, A., Gregory, J., Gulev, S., et al. (2007). "Observations: Oceanic Climate Change and Sea Level," in *Climate Change 2007: The Physical Science Basis. Contribution of Working Group I to the Fourth Assessment Report of the Intergovernmental Panel on Climate Change*. Editors S. Solomon, D. Qin, M. Manning, Z. Chen, M. Marquis, K.B. Averyt, et al. (Cambridge, United Kingdom and New York, NY, USA: Cambridge University Press).

Biskaborn, B. K., Herzschuh, U., Bolshiyanov, D. Y., Schwamborn, G., and Diekmann, B. (2013). Thermokarst Processes and Depositional Events in a Tundra Lake, Northeastern Siberia: Thermokarst Processes in a Siberian Tundra Lake. *Permafrost Periglacial Process.* 24 (3), 160–174. doi:10.1002/ppp.1769

Biskaborn, B. K., Smith, S. L., Noetzli, J., Matthes, H., Vieira, G., Streletskiy, D. A., et al. (2019). Permafrost Is Warming at a Global Scale. *Nat. Commun.* 10 (1), 264. doi:10.1038/s41467-018-08240-4

Brovko, P. (1990). *Development of Coastal Lagoons*. Vladivostok (Russia): Publishing house of the Far East University press.

Brown, J., Ferrians, O. J., Jr, Heginbottom, J. A., and Melnikov, E. S. (1997). Circum-Arctic Map of Permafrost and Ground-Ice Conditions. *Circum-Pacific Map*. doi:10.3133/cp45

Campeau, S., Héquette, A., and Pienitz, R. (2000). Late Holocene Diatom Biostratigraphy and Sea-Level Changes in the southeastern Beaufort Sea. *Can. J. Earth Sci.* 37 (1), 63–80. doi:10.1139/e99-107

Chuvilin, E. M., Grebenkin, S. I., and Sacleux, M. (2016). Influence of Moisture Content on Permeability of Frozen and Unfrozen Soils. *Kriosfera Zemli* 20 (3), 66–72. doi:10.21782/EC2541-9994-2018-1(41-45)

Frederick, J. M., and Buffett, B. A. (2014). Taliks in Relict Submarine Permafrost and Methane Hydrate Deposits: Pathways for Gas Escape under Present and Future Conditions. *J. Geophys. Res. Earth Surf.* 119 (2), 106–122. doi:10.1002/2013JF002987

Fritz, M., Opel, T., Tanski, G., Herzschuh, U., Meyer, H., Eulenburg, A., et al. (2015). Dissolved Organic Carbon (DOC) in Arctic Ground Ice. *The Cryosphere* 9 (2), 737–752. doi:10.5194/tc-9-737-2015

Fritz, M., Vonk, J. E., and Lantuit, H. (2017). Collapsing Arctic Coastlines. *Nat. Clim. Change* 7 (1), 6–7. doi:10.1038/nclimate3188

Fuchs, M., Grosse, G., Strauss, J., Günther, F., Grigoriev, M., Maximov, G. M., et al. (2018). Carbon and Nitrogen Pools in Thermokarst-Affected Permafrost Landscapes in Arctic Siberia. *Biogeosciences* 15 (3), 953–971. doi:10.5194/bg-15-953-2018

Fuchs, M., Nitze, I., Strauss, J., Günther, F., Wetterich, S., Kizyakov, A., et al. (2020). Rapid Fluvio-Thermal Erosion of a Yedoma Permafrost Cliff in the Lena River Delta. *Front. Earth Sci.* 8. doi:10.3389/feart.2020.00336

GISTEMP Team (2020). GISS Surface Temperature Analysis (GISTEMP). version 4. NASA Goddard Institute for Space Studies. Dataset accessed 2020-22-26 at: data.giss.nasa.gov/gistemp/.

Grasby, S. E., Rod Smith, I., Bell, T., and Forbes, D. L. (2013). Cryogenic Formation of Brine and Sedimentary Mirabilite in Submergent Coastal lake Basins, Canadian Arctic. *Geochimica et Cosmochimica Acta* 110(0): 13–28. doi:10.1016/j.gca.2013.02.014

Grosse, G., Goetz, S., McGuire, A. D., Romanovsky, V. E., and Schuur, E. A. G. (2016). Changing Permafrost in a Warming World and Feedbacks to the Earth System. *Environ. Res. Lett.* 11 (4), 040201. doi:10.1088/1748-9326/11/4/040201

Grosse, G., Jones, B., and Arp, C. (2013). 8.21 Thermokarst Lakes, Drainage, and Drained Basins. *Treatise on Geomorphology*. Fairbanks: Elsevier, 325–353. doi:10.1016/B978-0-12-374739-6.00216-5

Grosse, G., Schirrmeister, L., Kunitsky, V. V., and Hubberten, H.-W. (2005). The Use of CORONA Images in Remote Sensing of Periglacial Geomorphology: An Illustration from the NE Siberian Coast. *Permafrost Periglac. Process.* 16 (2), 163–172. doi:10.1002/ppp.509

Grosse, G., Schirrmeister, L., Siegert, C., Kunitsky, V. V., Slagoda, E. A., Andreev, A. A., et al. (2007). Geological and Geomorphological Evolution of a Sedimentary Periglacial Landscape in Northeast Siberia during the Late Quaternary. *Geomorphology* 86 (1–2), 25–51. doi:10.1016/j.geomorph.2006.08.005

Grotheer, H., Meyer, V., Riedel, T., Pfalz, G., Mathieu, L., Hefter, J., et al. (2020). Burial and Origin of Permafrost-Derived Carbon in the Nearshore Zone of the Southern Canadian Beaufort Sea. *Geophys. Res. Lett.* 47 (3), e2019GL085897. doi:10.1029/2019GL085897

Gundelwein, A., Müller-Lupp, T., Sommerkorn, M., Haupt, E. T. K., Pfeiffer, E.-M., and Wiechmann, H. (2007). Carbon in Tundra Soils in the Lake Labaz Region of Arctic Siberia. *Eur. J. Soil Sci.* 58 (5), 1164–1174. doi:10.1111/j.1365-2389.2007.00908.x

Günther, F., Overduin, P. P., Yakshina, I. A., Opel, T., Baranskaya, A. V., and Grigoriev, M. N. (2015). Observing Muostakh Disappear: Permafrost Thaw Subsidence and Erosion of a Ground-Ice-Rich Island in Response to Arctic Summer Warming and Sea Ice Reduction. *The Cryosphere* 9 (1), 151–178. doi:10.5194/tc-9-151-2015

Harris, C. M., McClelland, J. W., Connelly, T. L., Crump, B. C., and Dunton, K. H. (2017). Salinity and Temperature Regimes in Eastern Alaskan Beaufort Sea Lagoons in Relation to Source Water Contributions. *Estuaries and Coasts* 40 (1), 50–62. doi:10.1007/s12237-016-0123-z

Harrison, W. D., and Osterkamp, T. E. (1982). Measurements of the Electrical Conductivity of Interstitial Water in Subsea Permafrost. Proceedings of the Fourth Canadian Permafrost Conference, Ottawa, Canada: National Research Council of Canada, 229–237.

Héquette, A., Ruz, M.-H., and Hill, P. R. (1995). The Effects of the Holocene Sea Level Rise on the Evolution of the Southeastern Coast of the Canadian Beaufort Sea. *J. Coastal Res.* 11 (2), 494–507.

Heslop, J. K., Walter Anthony, K. M., Grosse, G., Liebner, S., and Winkel, M. (2019b). Century-scale Time since Permafrost Thaw Affects Temperature Sensitivity of Net Methane Production in Thermokarst-Lake and Talik Sediments. *Sci. Total Environ.* 691 (November), 124–134. doi:10.1016/j.scitotenv.2019.06.402

Heslop, J. K., Walter Anthony, K. M., Sepulveda-Jauregui, A., Martinez-Cruz, K., Bondurant, A., Grosse, G., et al. (2015). Thermokarst Lake Methanogenesis along a Complete Talik Profile. *Biogeosciences* 12 (14), 4317–4331. doi:10.5194/bg-12-4317-2015

Heslop, J. K., Winkel, M., Walter Anthony, K. M., Spencer, R. G. M., Podgorski, D. C., Zito, P., et al. (2019a). Increasing Organic Carbon Biolability with Depth in Yedoma Permafrost: Ramifications for Future Climate Change. *J. Geophys. Res. Biogeosci.* 124 (7), 2021–2038. doi:10.1029/2018JG004712

Hill, P. R. (1990). Coastal Geology of the King Point Area, Yukon Territory, Canada. *Mar. Geology* 91 (1), 93–111. doi:10.1016/0025-3227(90)90135-7

Jenrich, M. (2020). "Thermokarst Lagoons – Carbon Pools and Panarctic Distribution," (Germany: University of Potsdam). Master Thesis. Avilable at: https://epic.awi.de/id/eprint/51597/.

Johannessen, O. M., Bengtsson, L., Miles, M. W., Kuzmina, S. I., Semenov, V. A., Alekseev, G. V., et al. (2004). Arctic Climate Change: Observed and Modelled Temperature and Sea-Ice Variability. *Tellus A: Dynamic Meteorology and Oceanography* 56 (4), 328–341. doi:10.3402/tellusa.v56i4.14418

Jones, B. M., Farquharson, L. M., Baughman, C. A., Buzard, R. M., Arp, C. D., Grosse, G., et al. (2018). A Decade of Remotely Sensed Observations Highlight Complex Processes Linked to Coastal Permafrost bluff Erosion in the Arctic. *Environ. Res. Lett.* 13 (11), 115001. doi:10.1088/1748-9326/aae471

Jones, B. M., Grosse, G., Arp, C. D., Jones, M. C., Walter Anthony, K. M., and Romanovsky, V. E. (2011). Modern Thermokarst Lake Dynamics in the Continuous Permafrost Zone, Northern Seward Peninsula, Alaska. *J. Geophys. Res.* 116 (G2). doi:10.1029/2011JG001666

Jongejans, L. L., Mangelsdorf, K., Schirrmeister, L., Grigoriev, M. N., Maksimov, G. M., Biskaborn, B. K., et al. (2020). *n*-Alkane Characteristics of Thawed Permafrost Deposits below a Thermokarst Lake on Bykovsky Peninsula, Northeastern Siberia. *Front. Environ. Sci.* 8. doi:10.3389/fenvs.2020.00118

Jongejans, L. L., and Strauss, J. (2020). Bootstrapping Approach for Permafrost Organic Carbon Pool Estimation. *Zenodo*. doi:10.5281/zenodo.3734247

Jongejans, L. L., Strauss, J., Lenz, J., Peterse, F., Mangelsdorf, K., Fuchs, M., et al. (2018). Organic Matter Characteristics in Yedoma and Thermokarst Deposits on Baldwin Peninsula, West Alaska. *Biogeosciences* 15 (20), 6033–6048. doi:10.5194/bg-15-6033-2018

Juhls, B., Overduin, P. P., Hölemann, J., Hieronymi, M., Matsuoka, A., Heim, B., et al. (2019). Dissolved Organic Matter at the Fluvial-marine Transition in the Laptev Sea Using *In Situ* Data and Ocean Colour Remote Sensing. *Biogeosciences* 16 (13), 2693–2713. doi:10.5194/bg-16-2693-2019

Kaplina, T. N. (2009). Alas Complexes of Northern Yakutia. *Earth's Cryosphere* 12, 3–17. (in Russian).

Kaplina, T. N., and Lozhkin, A. V. (1979). Age of Alas Deposits of the Coastal plain of Yakutia (Radiocarbon Substantiation). *Izv. SSSR. Ser. Geol.* 2, 69–76. (in Russian).

Kjerfve, B. (1994). Coastal Lagoons. *Coastal Lagoon Processes, 8. Elsevier Oceanography Series 60*. Elsevier Science Publisher B.V.

Kosyan, R. (2016). *The Diversity of Russian Estuaries and Lagoons Exposed to Human Influence*. New York, NY: Springer Berlin Heidelberg.

Kunitsky, V. V. (1989). *Kriolitologiya Nizo'ev Leny (Cryolithology of the Lower LENA)*. Yakutsk: Permafrost Institute Press.

Lachenbruch, A. H., Sass, J. H., Marshall, B. V., and Moses, T. H. (1982). Permafrost, Heat Flow, and the Geothermal Regime at Prudhoe Bay, Alaska. *J. Geophys. Res.* 87 (B11), 9301–9316. doi:10.1029/JB087iB11p09301

Lantuit, H., Atkinson, D., Paul Overduin, P., Grigoriev, M., Rachold, V., Grosse, G., et al. (2011). Coastal Erosion Dynamics on the Permafrost-Dominated Bykovsky Peninsula, north Siberia, 1951-2006. *Polar Res.* 30 (1), 7341. doi:10.3402/polar.v30i0.7341

Lenssen, N. J. L., Schmidt, G. A., Hansen, J. E., Menne, M. J., Persin, A., Ruedy, R., et al. (2019). Improvements in the GISTEMP Uncertainty Model. *J. Geophys. Res. Atmos.* 124 (12), 6307–6326. doi:10.1029/2018JD029522

Lenz, J., Wetterich, S., Jones, B. M., Meyer, H., Bobrov, A., and Grosse, G. (2016). Evidence of Multiple Thermokarst lake Generations from an 11 800-year-old Permafrost Core on the Northern S Eward P Eninsula, A Laska. *Boreas* 45 (4), 584–603. doi:10.1111/bor.12186

Liu, J., Chen, Z., Chen, M., Yan, W., Xiang, R., and Tang, X. (2010). Magnetic Susceptibility Variations and Provenance of Surface Sediments in the South China Sea. *Sediment. Geology* 230 (1), 77–85. doi:10.1016/j.sedgeo.2010.07.001

Mary, B., Mariotti, A., and Morel, J. L. (1992). Use Ofr 13C Variations at Natural Abundance for Studying the Biodegradation of Root Mucilage, Roots and Glucose in Soil. *Soil Biol. Biochem.* 24 (10), 1065–1072. doi:10.1016/0038-0717(92)90037-X

McDougall, T. J., and Barker, P. M. (2011). Getting Started with TEOS-10 and the Gibbs Seawater (GSW) Oceanographic Toolbox. *SCOR/IAPSO WG* 127, 1–28.

Meyer, H., Schönicke, L., Wand, U., Hubberten, H. W., and Friedrichsen, H. (2000). Isotope Studies of Hydrogen and Oxygen in Ground Ice - Experiences with the Equilibration Technique. *Isotopes Environ. Health Stud.* 36 (2), 133–149. doi:10.1080/10256010008032939

Meyers, P. A. (1997). Organic Geochemical Proxies of Paleoceanographic, Paleolimnologic, and Paleoclimatic Processes. *Org. Geochem.* 27 (5), 213–250. doi:10.1016/S0146-6380(97)00049-1

Meyers, P. A. (1994). Preservation of Elemental and Isotopic Source Identification of Sedimentary Organic Matter. *Chem. Geology* 114 (3–4), 289–302. doi:10.1016/0009-2541(94)90059-0

Mitzscherling, J., Winkel, M., Winterfeld, M., Horn, F., Yang, S., Grigoriev, M. N., et al. (2017). The Development of Permafrost Bacterial Communities under Submarine Conditions. *J. Geophys. Res. Biogeosci.* 122 (7), 1689–1704. doi:10.1002/2017JG003859

Möller, P., Benediktsson, Í. Ö., Anjar, J., Bennike, O., Bernhardson, M., Funder, S., et al. (2019). Data Set on Sedimentology, Palaeoecology and Chronology of Middle to Late Pleistocene Deposits on the Taimyr Peninsula, Arctic Russia. *Data in Brief* 25, 104267. doi:10.1016/j.dib.2019.104267

Möller, P., and Murray, A. S. (2015). Drumlinised Glaciofluvial and Glaciolacustrine Sediments on the Småland Peneplain, South Sweden - New Information on the Growth and Decay History of the Fennoscandian Ice Sheets during MIS 3. *Quat. Sci. Rev.* 122 (August), 1–29. doi:10.1016/j.quascirev.2015.04.025

Murray, A. S., Helsted, L. M., Autzen, M., Jain, M., and Buylaert, J. P. (2018). Measurement of Natural Radioactivity: Calibration and Performance of a High-Resolution Gamma Spectrometry Facility. *Radiat. Measurements* 120, 215–220. doi:10.1016/j.radmeas.2018.04.006

Murray, A. S., Marten, R., Johnston, A., and Martin, P. (1987). Analysis for Naturally Occuring Radionuclides at Environmental Concentrations by Gamma Spectrometry. *J. Radioanal. Nucl. Chem. Articles* 115, 263–288. doi:10.1007/bf02037443

Murray, A. S., and Wintle, A. G. (2000). Luminescence Dating of Quartz Using an Improved Single-Aliquot Regenerative-Dose Protocol. *Radiat. Measurements* 32, 57–73. doi:10.1016/S1350-4487(99)00253-X

Murray, A. S., and Wintle, A. G. (2003). The Single Aliquot Regenerative Dose Protocol: Potential for Improvements in Reliability. *Radiat. Measurements* 37, 377–381. doi:10.1016/S1350-4487(03)00053-2

Nazarova, L., Grebennikova, T. A., Razjigaeva, N. G., Ganzey, L. A., Belyanina, N. I., Arslanov, K. A., et al. (2017). Reconstruction of Holocene Environmental Changes in Southern Kurils (North-Western Pacific) Based on Palaeolake Sediment Proxies from Shikotan Island. *Glob. Planet. Change* 159 (December), 25–36. doi:10.1016/j.gloplacha.2017.10.005

Nerem, R. S., Beckley, B. D., Fasullo, J. T., Hamlington, B. D., Masters, D., and Mitchum, G. T. (2018). Climate-change-driven Accelerated Sea-Level Rise Detected in the Altimeter Era. *Proc. Natl. Acad. Sci. USA* 115 (9), 2022–2025. doi:10.1073/pnas.1717312115

Notz, D., and Stroeve, J. (2016). Observed Arctic Sea-Ice Loss Directly Follows Anthropogenic CO2emission. *Science* 354 (6313), 747–750. doi:10.1126/science.aag2345

Osterkamp, T. E., Baker, G. C., Harrison, W. D., and Matava, T. (1989). Characteristics of the Active Layer and Shallow Subsea Permafrost. *J. Geophys. Res.* 94 (C11), 16227–16236. doi:10.1029/JC094iC11p16227

Osterkamp, T. E., Jorgenson, M. T., Schuur, E. a. G., Shur, Y. L., Kanevskiy, M. Z., Vogel, J. G., et al. (2009). Physical and Ecological Changes Associated with Warming Permafrost and Thermokarst in Interior Alaska. *Permafrost Periglac. Process.* 20 (3), 235–256. doi:10.1002/ppp.656

Oswald, W. W., Anderson, P. M., Brown, T. A., Brubaker, L. B., Hu, F. S., Lozhkin, A. V., et al. (2005). Effects of Sample Mass and Macrofossil Type on Radiocarbon Dating of Arctic and Boreal lake Sediments. *The Holocene* 15, 758–767. doi:10.1191/0959683605hl849rr

Overduin, P. P., Liebner, S., Knoblauch, C., Günther, F., Wetterich, S., Schirrmeister, L., et al. (2015). Methane Oxidation Following Submarine Permafrost Degradation: Measurements from a Central Laptev Sea Shelf Borehole. *J. Geophys. Res. Biogeosci.* 120 (5), 965–978. doi:10.1002/2014JG002862

Pawlowicz, R. (2012). The Electrical Conductivity of Seawater at High Temperatures and Salinities. *Desalination* 300, 32–39. doi:10.1016/j.desal.2012.06.001

Pedrazas, M. N., Cardenas, M. B., Demir, C., Watson, J. A., Connolly, C. T., and McClelland, J. W. (2020). Absence of Ice-Bonded Permafrost beneath an Arctic Lagoon Revealed by Electrical Geophysics. *Sci. Adv.* 6 (43), eabb5083. doi:10.1126/sciadv.abb5083

Peel, M. C., Finlayson, B. L., and Mcmahon, T. A. (2007). Updated World Map of the Köppen-Geiger Climate Classification. *Hydrol. Earth Syst. Sci.* 11, 1633–1644. doi:10.5194/hess-11-1633-2007

Pekel, J.-F., Cottam, A., Gorelick, N., and Belward, A. S. (2016). High-Resolution Mapping of Global Surface Water and its Long-Term Changes. *Nature* 540 (7633), 418–422. doi:10.1038/nature20584

Phillips, M. R., Burn, C. R., Wolfe, S. A., Morse, P. D., Gaanderse, A. J., 'Neill, H. B. O., et al. (2015). *Improving Water Content Description of Ice-Rich Permafrost Soils*, 7th Canadian Permafrost Conference. Available at: http://works.bepress.com/dan-shugar/9/.

Porter, C., Morin, P., Howat, I., Noh, M. J., Bates, B., Peterman, B., et al. (2018). ArcticDEM. doi:10.7910/DVN/OHHUKH

Proshutinsky, A., Pavlov, V., and Bourke, R. H. (2001). Sea Level Rise in the Arctic Ocean. *Geophys. Res. Lett.* 28 (11), 2237–2240. doi:10.1029/2000GL012760

R Core Team (2016). *R: A Language and Environment for Statistical Computing*. Vienna, Austria: R Foundation for Statistical Computing.

Reimer, P. J., Bard, E., Bayliss, A., Beck, J. W., Blackwell, P. G., Ramsey, C. B., et al. (2013). IntCal13 and Marine13 Radiocarbon Age Calibration Curves 0-50,000 Years Cal BP. *Radiocarbon* 55 (4), 1869–1887. doi:10.2458/azu_js_rc.55.16947

Romankevich, E. A., Vetrov, A. A., Belyaev, N. A., Sergienko, V. I., Semiletov, I. P., Sukhoverkhov, S. V., et al. (2017). Alkanes in Quaternary Deposits of the Laptev Sea. *Dokl. Earth Sc.* 472 (1), 36–39. doi:10.1134/S1028334X17010093

Romanovskii, N., Hubberten, H.-W., Gavrilov, A. V., Tumskoy, V. E., and Kholodov, A. L. (2004). Permafrost of the East Siberian Arctic Shelf and Coastal Lowlands. *Quat. Sci. Rev.* 23 (11), 1359–1369. doi:10.1016/j.quascirev.2003.12.014

Romanovskii, N. N., Gavrilov, A. V., Kholodov, A. L., Pustovoit, G. P., Hubberten, H. W., Niessen, F., et al. (1998). Map of Predicted Offshore Permafrost Distribution on the Laptev Sea Shelf. *Nordicana*, 55. Yellowknife, Canada, 6.

Romanovskii, N. N., Hubberten, H.-W., Gavrilov, A. V., Tumskoy, V. E., Tipenko, G. S., Grigoriev, M. N., et al. (2000). Thermokarst and Land-Ocean Interactions, Laptev Sea Region, Russia. *Permafrost Periglac. Process.* 11 (2), 137–152. doi:10.1002/1099-1530(200004/06)11:2<137::aid-ppp345>3.0.co;2-l

Romanovsky, V. E., Drozdov, D. S., Oberman, N. G., Malkova, G. V., Kholodov, A. L., Marchenko, S. S., et al. (2010). Thermal State of Permafrost in Russia. *Permafrost Periglac. Process.* 21 (2), 136–155. doi:10.1002/ppp.683

Ruppel, C. D., and Kessler, J. D. (2017). The Interaction of Climate Change and Methane Hydrates. *Rev. Geophys.* 55 (1), 126–168. doi:10.1002/2016RG000534

Ruz, M.-H., Héquette, A., and Hill, P. R. (1992). A Model of Coastal Evolution in a Transgressed Thermokarst Topography, Canadian Beaufort Sea. *Mar. Geology* 106, 251–278. doi:10.1016/0025-3227(92)90133-3

Schirrmeister, L., Froese, D., Tumskoy, V., Grosse, G., and Wetterich, S. (2013). "PERMAFROST and PERIGLACIAL FEATURES | Yedoma: Late Pleistocene Ice-Rich Syngenetic Permafrost of Beringia," in *Encyclopedia of Quaternary Science*. Editors S A. Elias and C J. Mock Second Edition (Amsterdam: Elsevier), 542–552. doi:10.1016/B978-0-444-53643-3.00106-0

Schirrmeister, L., Grigoriev, M. N., Strauss, J., Grosse, G., Overduin, P. P., Kholodov, A., et al. (2018). Sediment Characteristics of a Thermokarst Lagoon in the Northeastern Siberian Arctic (Ivashkina Lagoon, Bykovsky Peninsula). *Arktos* 4 (1), 13. doi:10.1007/s41063-018-0049-8

Schirrmeister, L., Kunitsky, V., Grosse, G., Wetterich, S., Meyer, H., Schwamborn, G., et al. (2011). Sedimentary Characteristics and Origin of the Late Pleistocene Ice Complex on north-east Siberian Arctic Coastal Lowlands and Islands - A Review. *Quat. Int.* 241 (1–2), 3–25. doi:10.1016/j.quaint.2010.04.004

Schirrmeister, L., Schwamborn, G., Overduin, P. P., Strauss, J., Fuchs, M. C., Grigoriev, M., et al. (2017). Yedoma Ice Complex of the Buor Khaya Peninsula (Southern Laptev Sea). *Biogeosciences* 14, 1261–1283. doi:10.5194/bg-14-1261-2017

Schirrmeister, L., Siegert, C., Kunitzky, V. V., Grootes, P. M., and Erlenkeuser, H. (2002). Late Quaternary Ice-Rich Permafrost Sequences as a Paleoenvironmental Archive for the Laptev Sea Region in Northern Siberia. *Int. J. Earth Sci.* 91 (1), 154–167. doi:10.1007/s005310100205

Schowalter, T. D. (2016). Chapter 14 - Decomposition and Pedogenesis. *Insect Ecol.*, 4, 477–510. doi:10.1016/b978-0-12-803033-2.00014-5

Schuur, E. A. G., McGuire, A. D., Schädel, C., Grosse, G., Harden, J. W., Hayes, D. J., et al. (2015). Climate Change and the Permafrost Carbon Feedback. *Nature* 520 (7546), 171–179. doi:10.1038/nature14338

Segers, R., and Kengen, S. W. M. (1998). Methane Production as a Function of Anaerobic Carbon Mineralization: A Process Model. *Soil Biol. Biochem.* 30 (8), 1107–1117. doi:10.1016/S0038-0717(97)00198-3

Shakhova, N., Semiletov, I., and Chuvilin, E. (2019). Understanding the Permafrost-Hydrate System and Associated Methane Releases in the East Siberian Arctic Shelf. *Geosciences* 9 (6), 251. doi:10.3390/geosciences9060251

Shakhova, N., Semiletov, I., Gustafsson, O., Sergienko, V., Lobkovsky, L., Dudarev, O., et al. (2017). Current Rates and Mechanisms of Subsea Permafrost Degradation in the East Siberian Arctic Shelf. *Nat. Commun.* 8 (1), 15872. doi:10.1038/ncomms15872

Siegert, C., Schirrmeister, L., and Babiy, O. (2002). The Sedimentologieal, Mineralogieal and Geoehemieal Composition of Late Pleistoeene Deposits from the Lee Complex on the Bykovsky Peninsula, Northern Siberia. *Permafrostforschung* 70, 9., no.

Slagoda, E. A. (1993). "Genesis I Mikrostroenie Kriolitogennykh Otlozhenii Bykovskogo Polyostrova I Ostrova Muoastakh [Genesis and Microstructure of Cryolithogenic Deposits at the Bykovsky Peninsula and the Muostakh Island]," (Yakutsk: Permafrost Institute Yakutsk, 1993). Ph.D. thesis.

Slagoda, E. A. (2004). *Kriogennye otlozheniya Primorskoi ravniny morya Laptebykh: litologiya i mikromorfologiya* [Cryolithogenic Deposits of the Laptev Sea Coastal Plain: Lithology and Micromorphology]. Tyumen: Express, (in Russian).

Solomon, S., Mudie, P. J., Cranston, R., Hamilton, T., Thibaudeau, S. A., and Collins, E. S. (2000). Characterisation of marine and Lacustrine Sediments in a Drowned Thermokarst Embayment, Richards Island, Beaufort Sea, Canada. *Int. J. Earth Sci.* 89 (3), 503–521. doi:10.1007/s005310000126

Spangenberg, I., Overduin, P. P., Damm, E., Bussmann, I., Meyer, H., Liebner, S., et al. (2021). Methane Pathways in Winter Ice of a Thermokarst Lake–Lagoon–Coastal Water Transect in North Siberia. *Cryosphere* 15 (3), 1607–1625. doi:10.5194/tc-15-1607-2021

Strauss, J., Abbott, B. W., Hugelius, G., Schuur, E., Treat, C., Fuchs, M., et al. (2021). "Permafrost," in *Recarbonizing global soils: A technical manual of best management practices, Volume 2. Hot spots and bright spots of soil organic carbon* (Rome, Italy: Food and agriculture Organization of the United Nations).

Strauss, J., Boike, J., Bolshiyanov, D. Y., Grigoriev, M. N., El-Hajj, H., Morgenstern, A., et al. (2018). Russian-German Cooperation: Expeditions to Siberia in 2017, Berichte zur Polar- und Meeresforschung = Reports on polar and marine research. *Bremerhaven, Alfred Wegener Inst. Polar Mar. Res.* 725, 296, 2018 . EPIC. doi:10.2312/BzPM_0725_2018

Strauss, J., Schirrmeister, L., Grosse, G., Fortier, D., Hugelius, G., Knoblauch, C., et al. (2017). Deep Yedoma Permafrost: A Synthesis of Depositional Characteristics and Carbon Vulnerability. *Earth-Science Rev.* 172 (September), 75–86. doi:10.1016/j.earscirev.2017.07.007

Strauss, J., Schirrmeister, L., Grosse, G., Wetterich, S., Ulrich, M., Herzschuh, U., et al. (2013). The Deep Permafrost Carbon Pool of the Yedoma Region in Siberia and Alaska. *Geophys. Res. Lett.* 40 (23), 6165–6170. doi:10.1002/2013GL058088

Strauss, J., Schirrmeister, L., Mangelsdorf, K., Eichhorn, L., Wetterich, S., and Herzschuh, U. (2015). Organic-matter Quality of Deep Permafrost Carbon - a Study from Arctic Siberia. *Biogeosciences* 12, 2227–2245. doi:10.5194/bg-12-2227-2015

Strauss, J., Schirrmeister, L., Wetterich, S., Borchers, A., Davydov, S. P., and Davydov, S. P. (2012). Grain-size properties and organic-carbon stock of Yedoma Ice Complex permafrost from the Kolyma lowland, northeastern Siberia. *Global Biogeochem. Cycles* 26 (23). doi:10.1029/2011GB004104

Streletskaya, I. D. (1998). Yellowknife, Canada.Cryopeg Responses to Periodic Climate Fluctuations. Permafrost. Proceedings of the Seventh International Conference, Yellowknife, Canada, June 23–27, 1998.

Stuiver, M., Reimer, P. J., and Reimer, R. W. (2020). CALIB 7.1 [WWW Program]. http://calib.org (Accessed 02 12, 2020).

Subetto, D. A., Nazarova, L. B., Pestryakova, L. A., Syrykh, L. S., Andronikov, A. V., Biskaborn, B., et al. (2017). Paleolimnological Studies in Russian Northern Eurasia: A Review. *Contemp. Probl. Ecol.* 10 (4), 327–335. doi:10.1134/S1995425517040102

Tagliapietra, D., Sigovini, M., and Ghirardini, A. V. (2009). A Review of Terms and Definitions to Categorise Estuaries, Lagoons and Associated Environments. *Mar. Freshw. Res.* 60 (6), 497. doi:10.1071/MF08088

Tanski, G., Wagner, D., Knoblauch, C., Fritz, M., Sachs, T., and Lantuit, H. (2019). Rapid CO 2 Release from Eroding Permafrost in Seawater. *Geophys. Res. Lett.* 46 (20), 11244–11252. doi:10.1029/2019GL084303

Turetsky, M. R., Abbott, B. W., Jones, M. C., Anthony, K. W., Olefeldt, D., Schuur, E. A. G., et al. (2020). Carbon Release through Abrupt Permafrost Thaw. *Nat. Geosci.* 13 (2), 138–143. doi:10.1038/s41561-019-0526-0

Ulyantsev, A. S., Romankevich, E. A., Bratskaya, S. Y., Semiletov, I. P., and Avramenko, V. A. (2017). Organic and Carbonate Carbon in Permafrost and Thawed Deposits from Buor-Khaya Bay (Laptev Sea). *Dokl. Earth Sc.* 473 (2), 467–471. doi:10.1134/s1028334x17040237

Vyse, S. A., Herzschuh, U., Andreev, A. A., Pestryakova, L. A., Diekmann, B., Armitage, S. J., et al. (2020). Geochemical and Sedimentological Responses of Arctic Glacial Lake Ilirney, Chukotka (Far East Russia) to Palaeoenvironmental Change since ~51.8 Ka BP. *Quat. Sci. Rev.* 247, 106607. doi:10.1016/j.quascirev.2020.106607

Walhert, L., Zimmermann, S., Blaser, P., Luster, J., and Lüscher, P. (2004). Waldböden der Schweiz 1: Grundlagen und Region Jura. *(in German) [Forrest Soils of Swizerland, Chapter 1: Principles and the Jura Region]*. Bern: hep verlag.

Walter Anthony, K., Schneider von Deimling, T., Nitze, I., Frolking, S., Emond, A., Daanen, R., et al. (2018). 21st-Century Modeled Permafrost Carbon Emissions Accelerated by Abrupt Thaw beneath Lakes. *Nat. Commun.* 9 (1), 3262. doi:10.1038/s41467-018-05738-9

Watson, C. S., White, N. J., Church, J. A., King, M. A., Burgette, R. J., and Legresy, B. (2015). Unabated Global Mean Sea-Level Rise over the Satellite Altimeter Era. *Nat. Clim. Change* 5 (6), 565–568. doi:10.1038/nclimate2635

Wetterich, S., Kuzmina, S., Andreev, A. A., Kienast, F., Meyer, H., Schirrmeister, L., et al. (2008). Palaeoenvironmental Dynamics Inferred from Late Quaternary Permafrost Deposits on Kurungnakh Island, Lena Delta, Northeast Siberia, Russia. *Quat. Sci. Rev.* 27, 1523–1540. doi:10.1016/j.quascirev.2008.04.007

Wetterich, S., Schirrmeister, L., Andreev, A. A., Pudenz, M., Plessen, B., Meyer, H., et al. (2009). Eemian and Late Glacial/Holocene Palaeoenvironmental Records from Permafrost Sequences at the Dmitry Laptev Strait (NE Siberia, Russia). *Palaeogeogr. Palaeoclimatol. Palaeoecol.* 279 (1), 73–95. doi:10.1016/j.palaeo.2009.05.002

Wetterich, S., Tumskoy, V., Rudaya, N., Andreev, A. A., Opel, T., Meyer, H., et al. (2014). Ice Complex Formation in Arctic East Siberia during the MIS3 Interstadial. *Quat. Sci. Rev.* 84, 39–55. doi:10.1016/j.quascirev.2013.11.009

Winkel, M., Mitzscherling, J., Overduin, P. P., Horn, F., Winterfeld, M., Rijkers, R., et al. (2018). Anaerobic Methanotrophic Communities Thrive in Deep Submarine Permafrost. *Sci. Rep.* 8 (1), 1291. doi:10.1038/s41598-018-19505-9

Winkel, M., Sepulveda-Jauregui, A., Martinez-Cruz, K., Heslop, J. K., Rijkers, R., Horn, F., et al. (2019). First Evidence for Cold-Adapted Anaerobic Oxidation of Methane in Deep Sediments of Thermokarst Lakes. *Environ. Res. Commun.* 1 (2), 021002. doi:10.1088/2515-7620/ab1042

Conflict of Interest: The authors declare that the research was conducted in the absence of any commercial or financial relationships that could be construed as a potential conflict of interest.

Publisher's Note: All claims expressed in this article are solely those of the authors and do not necessarily represent those of their affiliated organizations, or those of the publisher, the editors and the reviewers. Any product that may be evaluated in this article, or claim that may be made by its manufacturer, is not guaranteed or endorsed by the publisher.

frontiers in Earth Science

BRIEF RESEARCH REPORT
published: 15 October 2021
doi: 10.3389/feart.2021.693824

Geologic Controls on Erosion Mechanism on the Alaska Beaufort Coast

Thomas M. Ravens[1*†] *and Sasha Peterson*[2‡]

[1]*Department of Civil Engineering, University of Alaska Anchorage, Anchorage, AK, United States,* [2]*Department of Geological Sciences, University of Alaska Anchorage, Anchorage, AK, United States*

Two prominent arctic coastal erosion mechanisms affect the coastal bluffs along the North Slope of Alaska. These include the niche erosion/block collapse mechanism and the bluff face thaw/slump mechanism. The niche erosion/block collapse erosion mechanism is dominant where there are few coarse sediments in the coastal bluffs, the elevation of the beach below the bluff is low, and there is frequent contact between the sea and the base of the bluff. In contrast, the bluff face thaw/slump mechanism is dominant where significant amounts of coarse sediment are present, the elevation of the beach is high, and contact between the sea and the bluff is infrequent. We show that a single geologic parameter, coarse sediment areal density, is predictive of the dominant erosion mechanism and is somewhat predictive of coastal erosion rates. The coarse sediment areal density is the dry mass (g) of coarse sediment (sand and gravel) per horizontal area (cm^2) in the coastal bluff. It accounts for bluff height and the density of coarse material in the bluff. When the areal density exceeds 120 g cm^{-2}, the bluff face thaw/slump mechanism is dominant. When the areal density is below 80 g cm^{-2}, niche erosion/block collapse is dominant. Coarse sediment areal density also controls the coastal erosion rate to some extent. For the sites studied and using erosion rates for the 1980–2000 period, when the sediment areal density exceeds 120 g cm^{-2}, the average erosion rate is low or 0.34 ± 0.92 m/yr. For sediment areal density values less than 80 g cm^{-2}, the average erosion rate is higher or 2.1 ± 1.5 m/yr.

Keywords: arctic, coastal erosion, mechanism, coarse sediment, areal density

OPEN ACCESS

Edited by:
Scott Raymond Dallimore, Geological Survey of Canada, Canada

Reviewed by:
Henry Patton, Arctic University of Norway, Norway
Jennifer Frederick, Sandia National Laboratories, United States

****Correspondence:***
Thomas M. Ravens
tmravens@alaska.edu

†ORCID
Thomas M. Ravens
orcid.org/0000-0002-4613-4632

‡Present address:
Sasha Peterson, Department of Environmental Science and Engineering, University of Texas at El Paso, El Paso, TX, United States

Specialty section:
This article was submitted to Cryospheric Sciences, a section of the journal Frontiers in Earth Science

Received: *12 April 2021*
Accepted: *24 September 2021*
Published: *15 October 2021*

Citation:
Ravens TM and Peterson S (2021) Geologic Controls on Erosion Mechanism on the Alaska Beaufort Coast. Front. Earth Sci. 9:693824. doi: 10.3389/feart.2021.693824

INTRODUCTION

The Arctic is experiencing high and accelerating coastal erosion rates. For example, Mars and Houseknecht (2007) used remote sensing techniques to study coastal erosion-derived land loss on a 60-km segment of the Beaufort Sea coast (between Drew Point and Cape Halkett, Alaska, **Figure 1**) and found that the amount of land loss was significantly greater in 1985–2005 (1.08 km^2 yr^{-1}) relative to the loss in 1955–1985 (0.48 $km^2 yr^{-1}$). Jones et al. (2009) working in the same area determined that the average rate of erosion increased from 6.8 m yr^{-1} (1955–1979), to 8.7 m yr^{-1} (1979–2002), and to 13.6 m yr^{-1} (2002–2007). Erosion rates are high in this location because of the high ice content of the coastal bluffs and the absence of coarse material (sand and gravel). At other locations, erosion rates are often lower but still accelerating. For example, on Barter Island, where coastal bluffs contain significant amounts of coarse material, bluff retreat rate averaged 1.8 m yr^{-1} between 1955 and 2004 and 3.8 m yr^{-1} between 2004 and 2010 (Gibbs et al., 2010). Erosion rates are generally accelerating

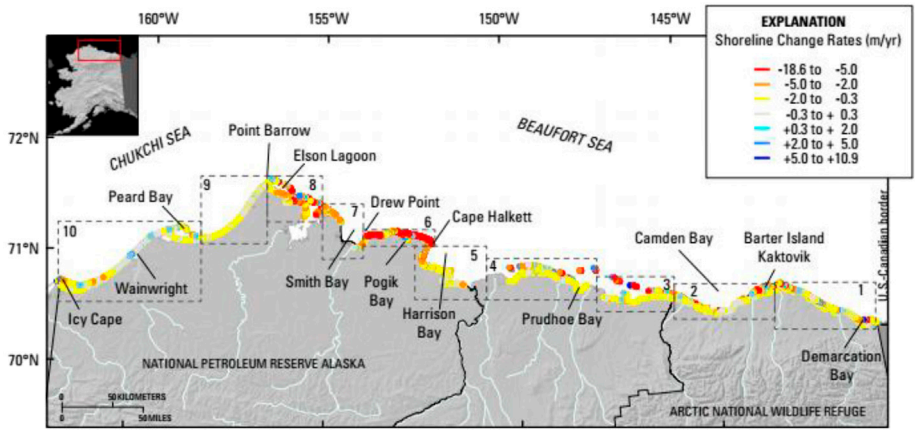

FIGURE 1 | Map of the north coast of Alaska showing color-coded shoreline change rates for the period circa-1940s (1947 and 1949) to circa-2000s (1997–2012, Gibbs and Richmond, 2015).

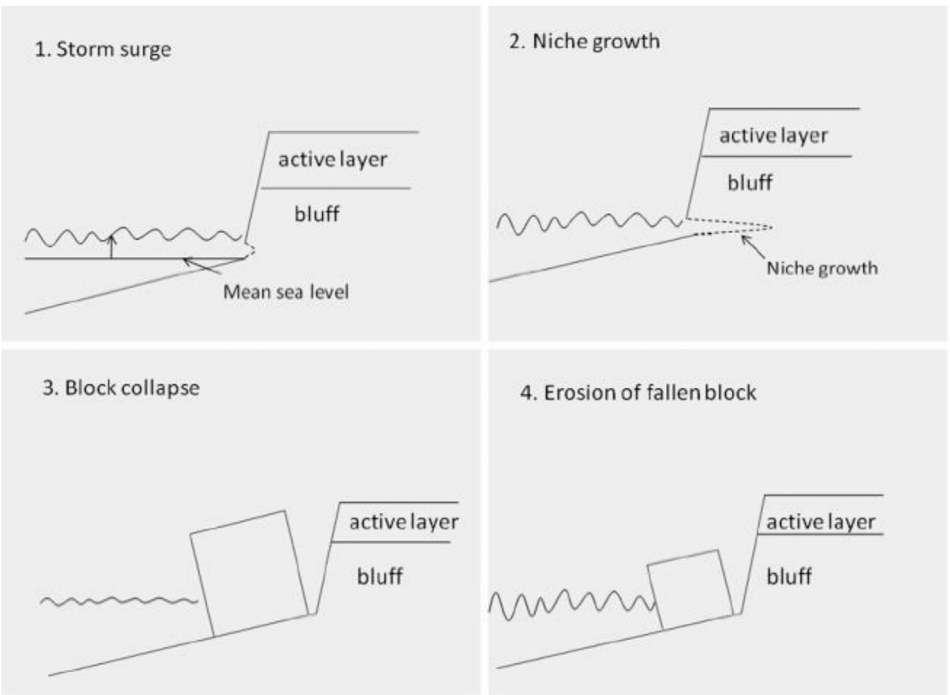

FIGURE 2 | Conceptual model of the niche erosion/block collapse erosion mechanism (from Ravens et al., 2012).

because of 1) greater spatial extent of open water, which allows for the generation of larger waves, 2) greater open water period, and 3) increased rate of coastal permafrost thaw (Barnhart et al., 2014a; Barnhart et al., 2014b; Frederick et al., 2016). Erosion threatens coastal infrastructure throughout the Arctic including governmental assets and community infrastructure. The US Army Corps of Engineers (2009) has designated 26 Alaska communities (including Barrow) "Priority Action Communities" due to the threat of erosion.

A number of arctic coastal erosion mechanisms affecting high coastal bluffs in the Arctic have been identified including niche erosion/block collapse (prevalent in the Drew Point area (Ravens et al., 2012; Barnhart et al., 2014a)) and bluff face thaw/slump (also referred to as translational-shear ice-thaw, Gibbs et al., 2013, and thermal denudation, Barankaya et al., 2021). The erosion mechanisms affecting Arctic coastal bluffs differ from the erosion of non-Arctic bluffs (e.g., Carter and Guy 1988) because of the role played by thermal processes in

FIGURE 3 | Photos of **(A)** an erosional niche from Elson Lagoon Alaska and **(B)** a fallen block by Drew Point, Alaska (image courtesy of Christopher Arp of the Alaska Science Center, U.S. Geological Survey).

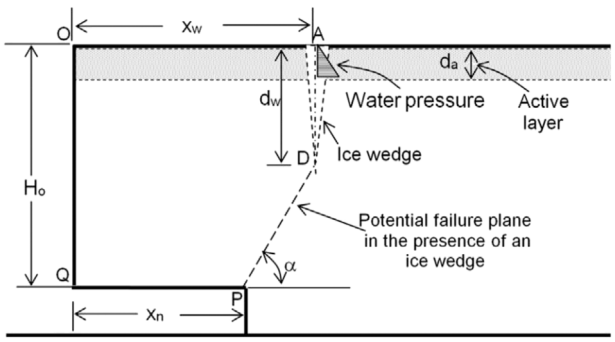

FIGURE 4 | Sketch of the bluff cross-section assumed by Hoque and Pollard (2016) in their analysis of overturning failure.

FIGURE 5 | Photo showing material that has slumped onto the beach face following bluff face thaw at Barter Island (2011 image courtesy of Li Erikson, U.S. Geological Survey). The bluff height is about 10 m and the sediment areal density is about 600 g/cm^2, based on USGS data. Interestingly, the photo was taken soon after the 2008 niche erosion/block collapse event and the niche is still in evidence.

the Arctic. With the niche erosion/block collapse erosion mechanism, typically a small beach is present before the bluff (**Figures 2**, **3**). During a storm surge event, waters rise allowing contact between sea and the base of the bluff. Waves and currents thermally and mechanically carve a niche at the base of the bluff (Kobayashi 1985). Niche growth undermines the bluffs leading to block collapse due to an overturning failure (Hoque and Pollard 2016). The lower failure plane intersects with a shore parallel ice wedge (**Figure 4**). The upper failure plane is at interface of the ice wedge and the soil. The failure is governed by the tensile strength of the frozen soil, as well as the niche depth, the ice wedge location, and the depth of the ice wedge. Niche erosion/block collapse is the predominant erosion mechanism in settings where the coastal bluffs have high ice content (~70%, Ping et al., 2011), and where the bluffs lack significant amounts of coarse material (sand and gravel). The lack of coarse material leads to a low elevation beach at the base of the bluff and frequent contact between the sea and the coastal bluffs (Ravens et al., 2011; Ravens and Peterson 2018).

Bluff face thaw/slump is the predominant erosion mechanism in settings where significant amounts of coarse sediments are common (e.g., at Barter Island, Ravens et al., 2011; Ravens and Peterson 2018). With significant amounts of coarse sediments in the coastal bluffs, the elevation of the beach before the bluff is relatively high (1–2 m above mean sea level) and contact between the sea and the base of the bluff—and niche erosion—is infrequent. For example, data provided by the USGS (Ann Gibbs, personal communication) indicates that only a single significant niche erosion/block collapse event occurred in the 1955–2010 time period at Barter Island which has significant amounts of coarse sediments (**Figure 5**). The bluff face warms due to the combined effect of a number of heat transfer processes including solar (shortwave) radiation, longwave radiation emission from the Earth's surface, absorption of downward longwave radiation from the atmosphere, sensible heat flux, and latent heat flux (Westermann et al., 2009; Ravens and Ulmgren, 2020). When the bluff face is warmed sufficiently, it thaws and material slumps to the beach face (**Figures 5**,**6**). Relatively small storms (e.g., the 1-year return period storm) are sufficient to remove the sediment that accumulates on the beach (Ravens et al., 2011).

Ravens et al. (2011) defined a parameter, the "coarse sediment areal density", and they hypothesized that this parameter

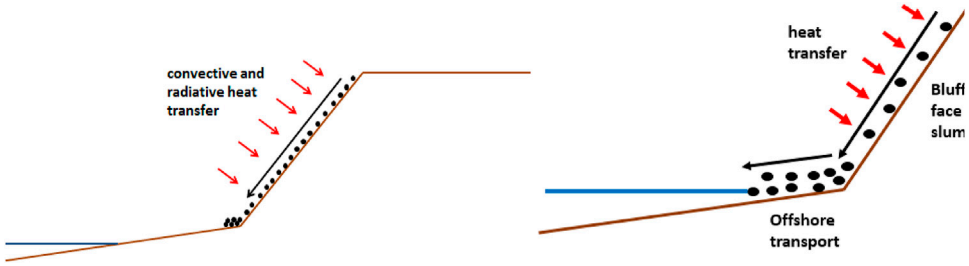

FIGURE 6 | Conceptual depiction of the bluff face thaw/slump erosion mechanism, which includes 1) the thawing of the bluff face, followed by 2) the slumping and deposition on the beach face, followed by 3) the offshore transport due to storm surge and waves.

TABLE 1 | Photographic and geologic data used in the analysis.

Photo ID	Photo location		Erosion mechanism	Barrier island present	Ping et al. (2021) site	Average sediment density	Bluff height	Coarse material (sand) content	Coarse sediment areal density	Erosion rate
—	Latitude	Longitude	—	—	—	(g cm^{-3})	(cm)	(%)	(g cm^{-2})	(m/year)
IMG_9510	70.899	−153.367	Niche/block	N	BSC17	0.69	50	21.9	7.5	3.47
IMG_8113	70.1629	−145.845	Niche/block	N	BSC39	0.64	250	54.1	86.0	0.35
IMG_0238	71.02287	−154.623	Niche/block	N	BSC15	0.37	40	48.4	7.1	2.14
IMG_9428	70.78902	−152.271	Niche/block	N	BSC20	0.61	250	30.8	46.8	2.7
IMG_8136	70.04606	−145.447	Niche/block	Y	BSC40	0.57	280	47.3	76.1	0.12
IMG_0065	71.33132	−156.566	Niche/block	Y	BSC01	1.03	40	53.2	22.0	0.31
IMG_0087	71.29122	−156.438	Niche/block	Y	BSC02	0.52	230	32.6	39.3	1.56
IMG_0124	71.21429	−156.047	Niche/block	Y	BSC03	0.38	140	34.6	18.6	4.57
IMG_0184	71.12589	−155.548	Niche/block	Y	BSC04	0.62	160	54.3	53.9	2.25
IMG_8366	70.03766	−142.72	Bluff face thaw	N	BSC46	0.60	300	88.4	158.9	0.54
IMG_8210	69.99457	−144.546	Bluff face thaw	N	BSC42	0.66	200	62.7	87.7	0.26
IMG_8385	69.98949	−142.556	Bluff face thaw	N	BSC47	0.70	320	74.4	238.0	0.96
IMG_8470	69.65694	−141.039	Bluff face thaw	N	BSC50	0.54	350	48.7	91.5	3.88
IMG_8772	70.00185	−144.828	Bluff face thaw	N	BSC41b	0.81	400	11.6	82.7	0.36
IMG_9327	70.55583	−151.709	Bluff face thaw	N	BSC24	1.53	320	90.1	441.7	0.24
IMG_7869	70.4919	−149.226	Bluff face thaw	Y	BSC31	1.12	200	90.3	202.1	-1.55
IMG_7924	70.40772	−148.778	Bluff face thaw	Y	BSC32	0.66	260	71.3	122.6	1.24
IMG_8225	70.03146	−144.319	Bluff face thaw	Y	BSC42	0.66	200	62.7	87.7	0.26
IMG_8241	70.08234	−144.002	Bluff face thaw	Y	BSC43	1.32	170	83.0	186.9	-0.24
IMG_7571	70.33116	−148.08	Bluff face thaw	Y	BSC34	1.03	300	62.5	193.2	0.33

determined whether the bluffs at a given coastal site were controlled by niche erosion/block collapse or by bluff face thaw/slumping. The sediment areal density is the dry mass of coarse sediment (sand and gravel) contained in a column of bluff sediment/soil per unit horizontal area (g cm-2). If there was a virtual column in the bluff extending from mean sea level to the bluff top, the coarse sediment areal density would be the dry mass of coarse sediment (sand and gravel) per unit horizontal area in the column. In this paper, we test this hypothesis by examining the extent to which coarse sediment areal density can predict coastal erosion mechanism. We also examine the relationship between coarse sediment areal density and coastal erosion rate.

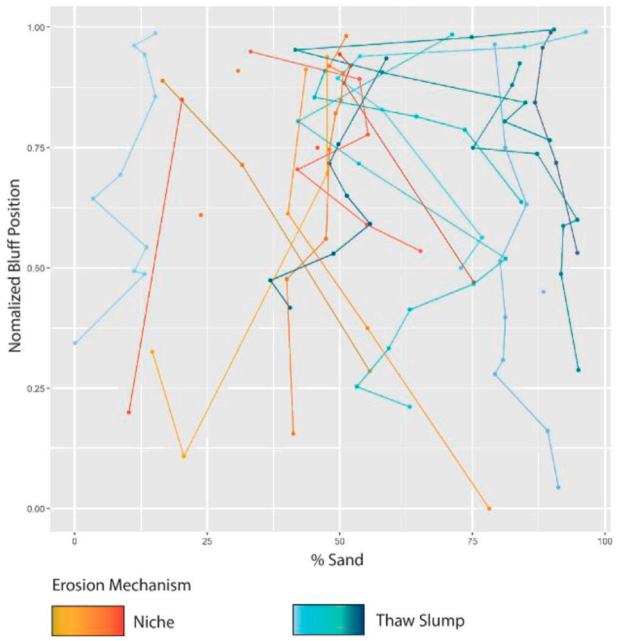

FIGURE 7 | Plot showing sand content (%) as a function of normalized bluff position (depth/bluff. height) at the various sites for which sediment data was available. The plot also identifies the erosion mechanism inferred based on aerial photo analysis. Note, in some instances, only a single bluff sample was analyzed and these data are plotted as dots. Note, the low sand content of one core (BSC41b in **Table 1**), identified as a site of bluff face thaw/slump erosion, appears to be an outlier. However, the coarse sediment areal density of this site (82.7 g/cm^2, **Table 1**) is similar to that calculated for other bluff face thaw/slump sites.

FIGURE 8 | Example photo of coastal bluffs where niche erosion/block collapse was the predominant mechanism (image courtesy of Ann Gibbs, U.S. Geological Survey).

METHODOLOGY

Coastal locations with both sediment data and aerial photo data from the north coast of Alaska between Utqiagvik (formerly Barrow) and the Canadian border were sought. Data on sediment grain size distribution (percent sand, silt, and clay) as a function of depth into the bluffs, sediment bulk density, and bluff height were obtained from 22 coastal sites according to Ping et al. (2011). Note, Ping et al. (2011) did not report on the presence of gravel so we concluded that it was negligible in their samples. However, the USGS, working at their Barter Island site, found significant gravel (Gibbs et al., 2010). The samples were collected from undisturbed areas between ice wedges after removal of slumped material. We examined oblique aerial photos from Gibbs and Richmond (2009) at locations proximal to the sites with sediment data to determine if the coastal erosion mechanism was niche erosion/block collapse or bluff face thaw/slump (**Table 1**). On average, the distance between location with sediment data and photos was about 6 km. For each photo, sand and gravel content data from one proximal core or bluff sample was used to determine the sediment areal density (**Figure 7**). Locations experiencing niche erosion/block collapse were readily determined based on the characteristic erosional blocks (**Figure 8**). Locations dominated by bluff face thaw/slump were evident based on the presence of a high elevation beach before the coastal bluff and the presence of material (e.g., vegetation) that was slumping on the bluff face (**Figure 9**). The coarse sediment areal density (g cm-2) was calculated as the product of the coarse sediment (sand and gravel) content (%), sediment bulk density (g cm-3) and the bluff height (cm), using data from Ping et al., 2011. The ice content of the bluffs was implicitly included in the sediment bulk density.

FIGURE 9 | Example photo of coastal bluffs where bluff face thaw/slumping was the predominant erosion mechanism (image courtesy of Ann Gibbs, U.S. Geological Survey).

RESULTS AND DISCUSSION

The locations of the 19 coastal sites subject to analysis, as well as the erosion mechanisms attributed to those sites based on the analysis of the aerial photos, are shown in **Figure 10**. It is noteworthy that the majority of the sites experiencing niche erosion/block collapse are on the western side of the study

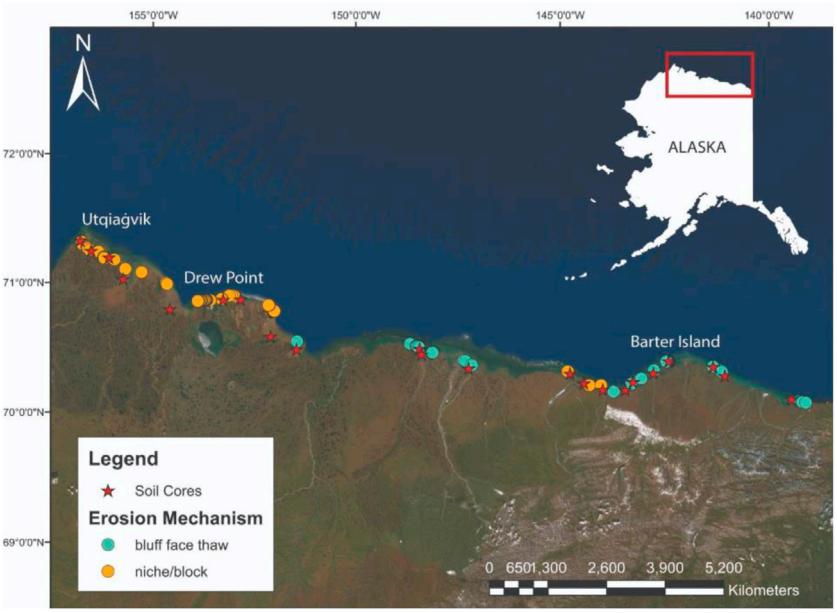

FIGURE 10 | Map of the north coast of Alaska showing the locations of the coastal sites studied as well as the erosion mechanism attributed to those sites. Base map imagery courtesy of Esri.

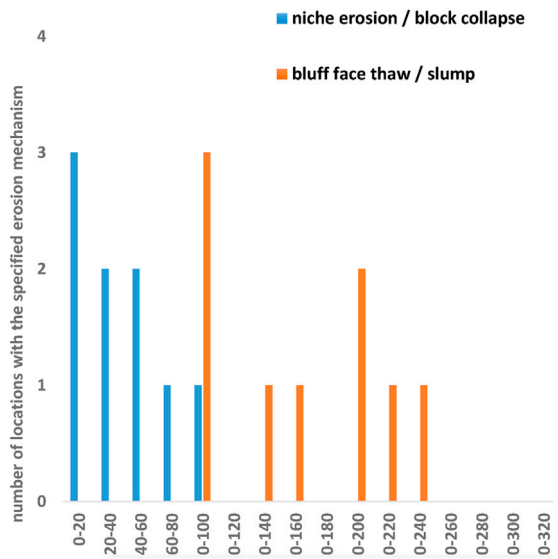

FIGURE 11 | A histogram showing the frequency of occurrence of the niche erosion/block collapse erosion mechanism and bluff face thaw/slump mechanism as a function of coarse sediment areal density.

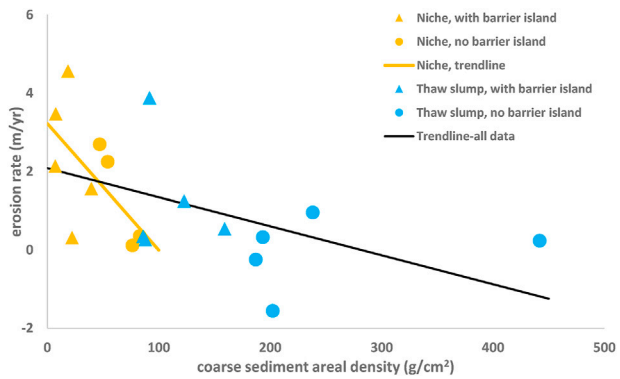

FIGURE 12 | Dependence of coastal erosion rates for the 1980–2000 time period on coarse sediment areal density, for sites experiencing niche erosion/block collapse and bluff face thaw/slump. Note, the figure provides data on coastal sites that are protected by barrier islands as well as ones without protection as indicated in the legend. Trend lines are provided for sites with niche erosion/block collapse (orange line, R^2 = 0.37) as well as considering all sites (black line, R^2 = 0.25). For bluff face thaw/slump sites, the correlation was negligible (R^2 = 0.09) and no trend line is provided.

domain, whereas the sites experiencing bluff face thaw/slump are mainly on the eastern side. Note also that there was relatively little variation of erosion mechanism with position according to our analysis. The frequency of occurrence of the niche erosion/block collapse mechanism and the bluff face thaw/slump mechanism relative to the course sediment areal density (g cm^{-2}, **Figure 11**) shows that with sediment areal density greater than 120 g cm^{-2}, the dominant erosion mechanism was bluff face thaw/slumping. With sediment areal density less than 80 g cm^{-2}, the dominant erosion mechanism was niche erosion/block collapse. One might wonder whether the erosion mechanism at specific sites, inferred based on the 2006 areal photos, might vary over time. It is noteworthy that, for example, Elson Lagoon, Drew Point, and

TABLE 2 | Average erosion rates (for 1980–2000 period) for different ranges of coarse sediment areal density.

Range of sediment areal density (g cm^{-2})	Average erosion rate (m/yr) considering all locations	Average erosion rate (m/yr) considering sites with barrier island protection
>100 g cm^{-2}	0.22±0.92	−0.06±1.17
<80 g cm^{-2}	2.1±1.5	1.8±1.8

Barter Island have been subject to numerous research papers over the past few decades, and there has been no mention of a change in erosion mechanism although there are some caveats. First, Barter Island has eroded mainly due to bluff face thaw/slump (as expected due to its high sediment areal density), but it was subject to a significant niche erosion/block collapse event during a large 2008 storm (Gibbs et al., 2010; Ravens et al., 2011). Also, Gibbs *et al.* (2019) point out the seasonality of erosion mechanism. In early to mid-summer, there tends to be more bluff face thaw/slumping because of the high levels of solar (short wave) radiation. In the second half of the summer, after the thaw of sea ice, storm surges and wave action bring aggressive mechanical forces to the coast removing previously thawed and deposited material, and potentially causing niche erosion if the beach elevation is sufficiently low.

Erosion rates for the 1980–2000 period (from Ping et al., 2011) are plotted relative to coarse sediment areal density (**Figure 12**). For sediment areal density values greater than 120 g cm^{-2} (coincident with the bluff face thaw/slump mechanism), erosion rates ranged from 1.24 m/yr to −1.55 m/yr (i.e., an accretion of 1.55 m/yr) with an average erosion rate of 0.34 ± 0.92 m/yr, **Table 2**). For sediment areal density values less than 80 g cm^{-2} (coincident with the niche erosion/block collapse mechanism), erosion rates ranged from 4.57 to 0.12 m/yr with an average of 2.1 ± 1.5 m/yr. Thus, the presence of elevated coarse sediment areal density appears to control (or reduce) the coastal erosion rate.

Analysis was also performed to determine whether the presence of barrier island protection translated to reduced erosion rates for the two ranges of sediment areal density and the associated erosion mechanisms. For locations with coarse sediment areal density above 120 g cm^{-2} (i.e., bluff face thaw/slump sites), the average erosion rate was reduced from 0.34 ± 0.92 m/yr (considering all sites) to −0.06 ± 1.17 m/yr, when only sites protected by barrier islands were considered (**Table 2**). For locations with coarse sediment areal density less than 80 g cm^{-2} (i.e., the niche erosion/block collapse sites), the average erosion rate was reduced from 2.1 ± 1.5 m/yr (considering all sites) to 1.8 ± 1.8 m/yr, when only sites protected by barrier islands were considered (**Table 1**). Thus, barrier island protection appeared to provide a small reduction in erosion rate for all levels of coarse sediment areal density (and for both erosion mechanisms) though the reduction was less than the standard deviation. When all of the data (**Figure 11**) was subject to linear regression, the erosion rate (*ER*, m/yr, 1980–2000 period) was found to be somewhat correlated with coarse sediment areal density (ρ_{areal}, g cm^{-2}) with an R^2 of 0.20: $ER = -0.0068\,\rho_{aerial} + 1.88$. This indicates that the erosion rate is negatively correlated with sediment areal density.

A significant amount of the variance in the measured erosion rate could not be explained using the coarse sediment areal density alone. Various explanations for the unexplained variance exist. First, we had to work with a significant distance (order 1 km) between the location of the erosion measurement and the borehole from which the sediment areal density was derived. Given spatial non-uniformity in the coastal stratigraphy, it is reasonable to suggest that the sediment areal density at the location of the erosion measurement differed from the density at the borehole. Second, there are many environmental variables that affect erosion but were not included in the regression including: nearshore water surface elevation, nearshore wave condition, and nearshore water and air temperature. Third, the way in which environmental variables affect arctic coastal erosion can be quite complex as indicated by process-based approaches to determine erosion rate (Ravens et al., 2012; Barnhart et al., 2014a).

The analysis presented above focuses on the predictability of Arctic coastal erosion mechanism based on sediment areal density. However, once this relationship has been established, it is noteworthy that sediment character can be inferred to some extent based on the erosion mechanism. For example, in locations where niche erosion/block collapse is dominant, we can infer that the coarse sediment in the eroding bluffs in limited. Such insights could be used in sediment transport and other studies.

CONCLUSION

The research presented here suggests that a single geologic parameter, the coarse sediment areal density, controls the dominant arctic coastal erosion mechanism of coastal bluffs on the North Slope (i.e., north coast) of Alaska. The coarse sediment areal density is the dry mass (g) of coarse sediment (sand) per horizontal area (cm2) in the coastal bluff. When the coarse sediment areal density exceeds 120 g cm^{-2}, the bluff face thaw/slump erosion mechanism is dominant. When the coarse sediment areal density is below 80 g cm^{-2}, the niche erosion/block collapse erosion mechanism is dominant. The coarse sediment areal density also has some influence on coastal erosion rates. Considering the 22 sites addressed in this study, the sediment areal density was found to have a controlling effect on erosion rate. Using erosion rates for the 1980–2000 period, when the sediment areal density exceeds 120 g cm^{-2}, the average erosion rate was of 0.34 ± 0.92 m/yr. For sediment areal density values less than 80 g cm^{-2}, the average erosion rate was as high as 2.1 ± 1.5 m/yr. Linear regression between coarse sediment areal density and erosion rate found that ~20% of the variance in erosion rate was explainable by coarse sediment areal density.

DATA AVAILABILITY STATEMENT

The original contributions presented in the study are included in the article/Supplementary Material, further inquiries can be directed to the corresponding author.

AUTHOR CONTRIBUTIONS

TR conceived the overall manuscript and did the majority of the writing. SP did the analysis of the aerial photos and sediment data.

FUNDING

Funding for this research came from the National Science Foundation (Award # 7416374) and from the Bureau of Ocean Energy Management (NSL# AK-17-01).

REFERENCES

Baranskaya, A., Novikova, A., Shabanova, N., Belova, N., MaznevJones, S. B., Ogorodov, S., et al. (2021). The Role of Thermal Denudation in Erosion of Ice-Rich Permafrost Coasts in an Enclosed Bay (Gulf of Kruzenstern, Western Yamal, Russia). *Front. Earth Sci.* 8, 2021. doi:10.3389/feart.2020.566227

Barnhart, K. R., Anderson, R. S., Overeem, I., Wobus, C., Clow, G. D., and Urban, F. E. (2014a). Modeling Erosion of Ice-Rich Permafrost bluffs along the Alaskan Beaufort Sea Coast. *J. Geophys. Res. Earth Surf.* 119, 1155–1179. doi:10.1002/2013jf002845

Barnhart, K. R., Overeem, I., and Anderson, R. S. (2014b). The Effect of Changing Sea Ice on the Physical Vulnerability of Arctic Coasts. *The Cryosphere* 8, 1777–1799. doi:10.5194/tc-8-1777-2014

Carter, C. H., and E. Guy, D., Jr. (1988). Coastal Erosion: Processes, Timing and Magnitudes at the bluff Toe. *Mar. Geology.* 84, 1–17. Available at: https://pubs.er.usgs.gov/publication/70014360. doi:10.1016/0025-3227(88)90121-1

Frederick, J. M., Thomas, M. A., BullJones, D. L. C. A., and Roberts, J. (2016). "The Arctic Coastal Erosion Problem,". SAND2016-9762. doi:10.2172/1431492

Gibbs, A. E., Erikson, L. H., Jones, B. M., and Richmond, B. M. (2010). *Characterizing Morphology and Erosional Trends of Permafrost Bluffs, Barter Island*. Alaska: AGU Fall Meeting. EP23A-0772.

Gibbs, A. E., and Richmond, B. M. (2009). Oblique Aerial Photography of the Arctic Coast of Alaska, Nulavik to Demarcation Point, August 7 -10, 2006. *U.S. Geol. Surv. Data Ser. 436* 6 (databases), 4, 2009 . Available at: http://pubs.usgs.gov/ds/436/. doi:10.3133/ds436

Gibbs, A. E., Richmond, B. M., Palaseanu-Lovejoy, M., Erikson, L. H., Jones, B. M., and Brock, J. (2013). *Remote Sensing of the Arctic Coast of Alaska Using Airborne Lidar Data.* San Francisco, CA: American Geophysical Union Fall Meeting. B51H-0406.

Gibbs, A. E., and Richmond, B. M. (2015). National Assessment of Shoreline Change: Historical Change along the north Coast of Alaska, U.S.-Canadian Border to Icy Cape. *Geol. Surv. Open-File Rep. 2015* 1048, 96. doi:10.3133/ofr20151048

Hoque, M. A., and Pollard, W. H. (2016). Stability of Permafrost Dominated Coastal Cliffs in the Arctic. *Polar Sci.* 10, 79–88. doi:10.1016/j.polar.2015.10.004

Jones, B. M., Arp, C. D., Jorgenson, M. T., Hinkel, K. M., Schmutz, J. A., and Flint, P. L. (2009). Increase in the Rate and Uniformity of Coastline Erosion in Arctic Alaska. *Geophys. Res. Lett.* 36, L03503. doi:10.1029/2008gl036205

Kobayashi, N. (1985). Formation of Thermoerosional Niches into Frozen bluffs Due to Storm Surges on the Beaufort Sea Coast. *J. Geophys. Res.* 90 (C6), 11983–11988. doi:10.1029/jc090ic06p11983

Mars, J. C., and Houseknecht, D. W. (2007). Quantitative Remote Sensing Study Indicates Doubling of Coastal Erosion Rate in Past 50 Yr along a Segment of the Arctic Coast of Alaska. *Geol* 35 (7), 583–586. doi:10.1130/g23672a.1

Ping, C.-L., Michaelson, G. J., Guo, L., Jorgenson, M. T., Kanevskiy, M., Shur, Y., et al. (2011). Soil Carbon and Material Fluxes across the Eroding Alaska Beaufort Sea Coastline. *J. Geophys. Res.* 116, G02004. doi:10.1029/2010JG001588

Ravens, T., Kartezhnikova, M., Ulmgren, M., Yager, G., Jones, B., Erikson, L., et al. (2011). *Arctic Coastal Erosion Modeling*. San Francisco, CA: Presented at the American Geophysical Union Fall Meeting.

Ravens, T. M., Jones, B. M., Zhang, J., Arp, C. D., and Schmutz, J. A. (2012). Process-based Coastal Erosion Modeling for Drew Point, North Slope, Alaska. *J. Waterway, Port, Coastal, Ocean Eng.* 138 (2), 122–130. doi:10.1061/(asce)ww.1943-5460.0000106

Ravens, T. M., and Peterson, S. (2018). "Arctic Coastal Erosion Modeling," in *A Chapter in* Advances In Coastal Hydraulics. Editors P. Vijay and K. Jim (London Singapore: World Scientific). doi:10.1142/9789813231283_0002

Ravens, T., and Ulmgren, M. (2020). *Arctic Coastal Geomorphic Change Modeling with Arctic Xbeach*. Anchorage, AK: AGU Fall Meeting.

U.S. Army Corps of Engineers. (2009). Alaska Baseline Erosion Assessment.65

Westermann, S., Lüers, J., Langer, M., Piel, K., and Boike, J. (2009). The Annual Surface Energy Budget of a High-Arctic Permafrost Site on Svalbard, Norway. *The Cryosphere* 3, 245–263. doi:10.5194/tc-3-245-2009

Conflict of Interest: The authors declare that the research was conducted in the absence of any commercial or financial relationships that could be construed as a potential conflict of interest.

Publisher's Note: All claims expressed in this article are solely those of the authors and do not necessarily represent those of their affiliated organizations, or those of the publisher, the editors and the reviewers. Any product that may be evaluated in this article, or claim that may be made by its manufacturer, is not guaranteed or endorsed by the publisher.

frontiers in Earth Science

ORIGINAL RESEARCH
published: 07 December 2021
doi: 10.3389/feart.2021.698660

Assessment of Storm Surge History as Recorded by Driftwood in the Mackenzie Delta and Tuktoyaktuk Coastlands, Arctic Canada

Roger F. MacLeod and Scott R. Dallimore*

Geological Survey of Canada–Pacific, Natural Resources Canada, Sidney, BC, Canada

The southern Beaufort coastline in Canada experiences significant storm surge events that are thought to play an important role in coastal erosion and influence permafrost dynamics. Unfortunately, many of these events have not been documented with tide gauge records. In this paper, we evaluate coastal driftwood accumulations as a proxy for estimating maximum storm surge heights and the history of these events. We use historical air photos and data derived from Unoccupied Aerial Vehicle (UAV) imagery to resurvey four coastal stranded driftwood study sites that were first appraised in 1985–86 and assess two new regional sites in the Mackenzie Delta. Maximum storm surge heights were found to be similar to observations carried out in the 1980s, however, we refine the elevations with more accuracy and reference these to a vertical datum appropriate for incorporating into sea level hazard assessments. Detailed mapping, historical air photo comparisons and the UAV acquired imagery at a site close to Tuktoyaktuk demonstrate that the highest storm surge at this site (1.98 m CGVD2013) occurred in association with a severe storm in 1970. This event shifted driftwood and floated material slightly upslope from an older event thought to occur in 1944 that reached 1.85 m (CGVD2013) elevation. The quality and accuracy of the high-resolution Digital Surface Model (DSM) and orthophoto derived from Structure from Motion (SfM) processing of the UAV photographs allowed mapping of four distinct stratigraphic units within the driftwood piles. Based on variations in anthropogenic debris composition, weathering characteristics and history of movement on aerial photographs, we conclude that no storm surge events at Tuktoyaktuk have exceeded ~1.3 m (CGVD2013) since 1970. While there has been some speculation that ongoing climate change may lead to more frequent large magnitude storm surges along the Beaufort coast, our study and available tide gauge measurements, suggest that while moderate elevation storm surges may be more frequent in the past several decades, they have not approached the magnitude of the 1970 event.

Keywords: storm surge, coastal erosion, structure from motion, coastal hazards, arctic storms, unoccupied aerial vehicle, arctic driftwood

OPEN ACCESS

Edited by:
Anna M. Irrgang,
Alfred Wegener Institute Helmholtz Centre for Polar and Marine Research (AWI), Germany

Reviewed by:
Lukas U Arenson,
BGC Engineering, Canada
Enda Murphy,
National Research Council Canada (NRC-CNRC), Canada

****Correspondence:***
Roger F. MacLeod
roger.macleod@nrcan-rncan.gc.ca

Specialty section:
This article was submitted to Cryospheric Sciences, a section of the journal Frontiers in Earth Science

Received: *21 April 2021*
Accepted: *12 November 2021*
Published: *07 December 2021*

Citation:
MacLeod RF and Dallimore SR (2021) Assessment of Storm Surge History as Recorded by Driftwood in the Mackenzie Delta and Tuktoyaktuk Coastlands, Arctic Canada. Front. Earth Sci. 9:698660. doi: 10.3389/feart.2021.698660

INTRODUCTION

As recognized in many papers in this special issue on dynamic coastal permafrost systems, the effects of storm surges and associated thermomechanical degradation of ice bonded permafrost are critical processes affecting coastal erosion in the Arctic (i.e., Lim et al., 2020; Thomas et al., 2020). Storm surges can generate elevated water levels that can reach the base of eroding coastal bluffs and they are often associated with storms which can create enhanced wave action. As a result, deep erosional niches can form in cliff sections, creating mechanical instability that can induce subsequent cliff failure and accelerate permafrost degradation (Henry and Heaps, 1976; Dallimore et al., 1996; Kobayashi et al., 1999). Wave action associated with storm surges can also cause nearshore erosion, and flooding caused by storm surges can be a geohazard as well as an environmental concern.

In the past 30 years, the Beaufort coast has experienced warming air and water temperatures (Screen and Simmonds, 2010; Cohen et al., 2014; Graham et al., 2017), and longer and more extensive ice-free conditions (Serreze et al., 2007; Comiso et al., 2008; Overeem et al., 2011; Meredith et al., 2019). These conditions result in more extensive and longer open water conditions that can enable an increased frequency and severity of storm surges (Manson and Solomon, 2007; Vermaire et al., 2013; Greenan et al., 2018). However, time series assessments of storm surges in the Arctic based on instrument records are limited. For instance, there is only one long-standing tide station along the Canadian Beaufort coast and it has significant gaps in its recording period (Shaw et al., 1998; Manson and Solomon, 2007).

The objective of this paper is to examine historical storm surge heights based on indirect estimates of stranded driftwood elevations at sites along the southern Beaufort coast in Canada. To determine elevations of the driftwood, we use modern surveying techniques based on imagery taken from an Unoccupied Aerial Vehicle (UAV) that are processed using Structure from Motion (SfM) photogrammetry techniques, complimented with high precision Real Time Kinematic Global Navigation Satellite System (RTK-GNSS) surveys. Storm surge heights are determined by mapping the uppermost elevation of wood within debris lines and driftwood piles and referencing these heights to a geodetic vertical datum. To validate that driftwood positions are a reliable indicator of water levels during storm surge events, the heights of mobilized wood are compared with tide gauge measurements before and after recent storm surge events. Given concerns that storm surges may be higher in the present climate regime than in the past, historical air photos are also appraised to investigate if the highest debris was emplaced by surge events from the past or in association with more recent events. We further investigate if these heights exceed determinations based on similar field studies done in 1985 and 1986 (Harper et al., 1988). Finally, we assess the utility of radiocarbon dating as a basis to document the age of a highly weathered driftwood line that was found partially embedded in the tundra canopy.

BACKGROUND

The coast of the Canadian Beaufort, in the vicinity of the Tuktoyaktuk Coastlands (Tuktoyaktuk Peninsula, Richards Island and the Mackenzie Delta) typically has a very shallow offshore gradient with complex coastlines with eroding headland areas, lagoons and embayments (**Figure 1**). This ice-rich lowland area has experienced rising sea-levels since glacial times (Hill et al., 1985) with current estimates of relative sea-level rise based on tide gauge measurements at Tuktoyaktuk varying from 2.5 mm per year (Greenan et al., 2018) to 2.75 mm per year [National Oceanic and Atmospheric Administration (NOAA), 2021]. Glacial isostatic adjustment makes up a portion of this change with estimates of approximately 1 mm per year of subsidence (James et al., 2014). Unfortunately, the short and intermittent instrument record does not provide for high certainty in either value. In general, the southern Beaufort coast is prone to storm surges that are typically generated from storms with wind directions from the north and northwest (Henry and Heaps, 1976; Hill et al., 1991; Manson and Solomon, 2007; Kokelj et al., 2012). Some researchers highlight that climate change is leading to an increase in sea-level, decreased seasonal sea ice extent, and allude to a possible increase in the frequency and severity of storms producing storm surges (Manson and Solomon, 2007; Vermaire et al., 2013; Greenan et al., 2018).

Coastal areas in this region are dominated by unconsolidated ice-rich permafrost that can be susceptible to periods of rapid erosion during storm surges (Dallimore et al., 1996; Kobayashi et al., 1999). Event driven erosion processes involve removal of the mantle of thawed sediment that typically forms in the early summer, exposing ice bonded permafrost in the cliff section. Wave action during storm surges can then form erosional niches that can be significantly elevated above mean sea level and reach up to 10 m back in the cliff section (Dallimore et al., 1996; Kobayashi et al., 1999). Mechanical failure of the overlying permafrost often occurs shortly after the niche formation causing rapid permafrost degradation and sediment transport to the beach area. Episodic erosional events contribute to shoreline recession, at times exceeding 10 m in a single year, or more than four orders of magnitude greater than the long-term annual average (Dallimore et al., 1996). The eroded material can result in high flux rates of organic carbon and nutrients that may result in increased greenhouse gas release to the sea and atmosphere (Fritz et al., 2017; Couture et al., 2018; Lapham et al., 2020).

Storm surges are also important as they influence a number of environmental processes. Due to the low-lying nature of the terrain along the Beaufort coast, storm surges can flood saline waters in low elevation coastal lakes and on flat lying terrestrial areas. The emplacement of saline water can result in die off of the tundra vegetation and change the aquatic and soil geochemistry (Hill et al., 2001; Emmerton et al., 2008; Pisaric et al., 2011; Lapka, 2013; Lantz et al., 2015). Storm surges have impacted large areas in the past 30 years with inundation events in the Mackenzie Delta extending up to 30 km inland (Lapka, 2013). Consequently, the terrestrial ecosystem may get significantly affected (Lantz

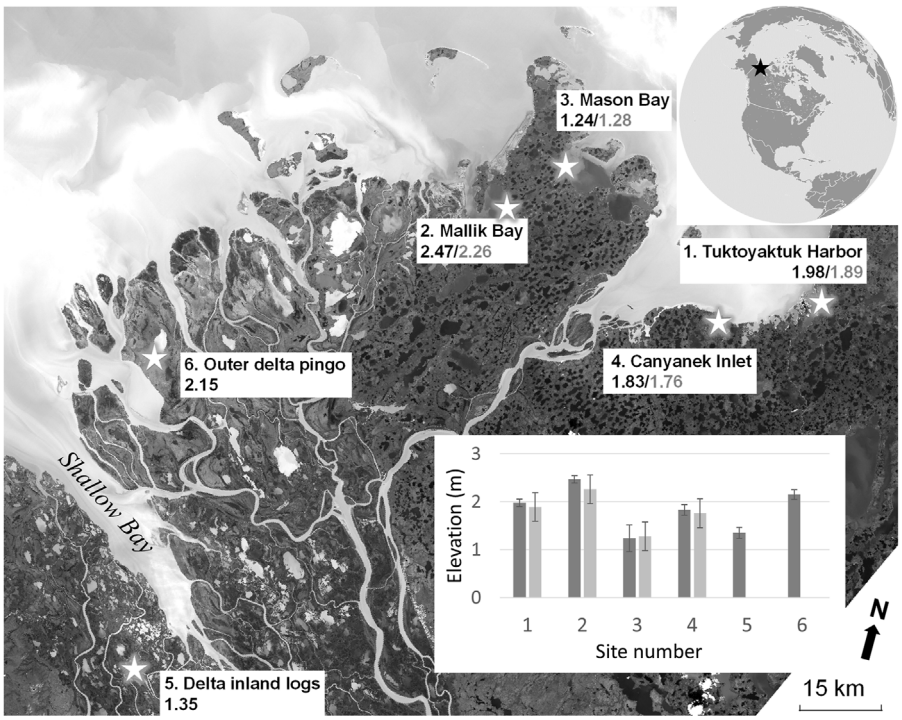

FIGURE 1 | Map showing the location of study sites. Elevations of the upper driftwood found at each site by Harper et al. (1988) are written in gray and those by this study in black. All elevations are reported in meters and in reference to the CGVD2013 vertical datum. The inset graph indicates the elevations and total accumulated error bars in measurements from this study at each site (dark boxes) alongside Harper et al. (1988) estimated total error of 0.38 m in surge elevations (lighter grey boxes).

et al., 2015). Substantial decreases in moose and waterfowl numbers have been observed by the Inuvialuit who live along the coast, impacting subsistence hunting and their traditional use of the land (Kokelj et al., 2012). However, some researchers have highlighted that in some settings, storm surges can also generate beneficial ecosystem responses (for example, Murphy et al., 2021 and references within).

Storm surges additionally pose a risk to low lying coastal settlements as they can damage infrastructure and valued cultural/archaeological sites as well as pose a hazard to residents (Reimnitz and Maurer, 1978; Kokelj et al., 2012; O'Rourke, 2017; Irrgang et al., 2019). The Hamlet of Tuktoyaktuk is particularly vulnerable (Henry, 1984; Couture et al., 2002; Forbes et al., 2005; Andrachuk and Smit, 2012), however, inland communities in the Mackenzie Delta (Akalvik, Inuvik, Tsiigehtchic) have also observed changes in water levels and saline conditions during storm surge events (Marsh and Schmidt, 1993; Kokelj et al., 2012). Storm surge hazard assessments for communities and infrastructure along the coast typically involve model simulation of the flooding extent and depth, using high resolution Digital Elevation Models (DEMs) such as those rendered by LiDAR surveys (Annis et al., 2020; Forbes et al., 2005 and, 2013; Hopkinson et al., 2011; Whalen et al., 2009). It is important to note, however, that in order to achieve reliable modeling results, accurate knowledge of past storm surge heights is needed as well as the historical frequency of these events. Strategies to protect coastal communities from flooding and enhanced erosion during storm surge events can include shore protection infrastructure as well as nature-based, non-structural countermeasures (Shah, 1982; Kavik-Axys Inc., 2010; Carter and Smith, 2011; Bridges et al., 2013; Lantuit et al., 2013; Liew et al., 2020).

Previous Field Observations of Storm Surges on the Southern Beaufort Coast

The earliest written observations of the height of a notable storm surge along the southern Beaufort coast were made in 1944 by residents living along the coast (Reimnitz and Maurer, 1978; Harper et al., 1988). Captain Larsen, of the RCMP vessel St. Roch, also arrived in Tuktoyaktuk harbor at the start of the storm on September 7, 1944 after returning from the first west to east navigation of the Northwest Passage (Larsen, 1948). Captain Larsen mentions the physical effects of storm surge erosion highlighting that "huge chunks of soil had been torn from the banks of the island, revealing old blue ice". While there was some discrepancy between observers regarding the height of the storm surge, most estimates agree with Larsen, suggesting that this event may have reached 3 m above mean sea level along the Canadian and also parts of the Alaskan Beaufort coast (Reimnitz and Maurer, 1978). Of note, the 3.0 m storm surge elevation value is used in hazard assessments for this coastal area (GNWT Department of Municipal and Community Affairs, 2014). Anecdotal accounts also confirm that another major storm surge event reaching a similar estimated height, occurred between September 13 and 16, 1970. Despite the fact that the

TABLE 1 | Highest water levels recorded at the Tuktoyaktuk tide gauge (Station 6485) between November 1, 1961 to December 31, 2020.

Rank	Date	Water Level (CD)	Water Level (CGVD2013)
1	October 4, 1963	2.23	1.43
2	September 4, 1962	2.15	1.35
3	November 4, 2017	2.03	1.23
4	August 17, 2018	1.97	1.17
4	July 21, 2019	1.97	1.17
6	September 1, 2013	1.92	1.12
7	September 1, 2018	1.90	1.10
7	August 4 to 5, 2019	1.90	1.10
9	July 30, 1963	1.89	1.09
10	August 27, 2015	1.82	1.02

Source: Fisheries and Oceans Canada, 2021.

Canadian Hydrographic Service (CHS) had established a tide station in Tuktoyaktuk in 1961, the station was not operational during this storm. As a consequence, no definitive measurement could be made of its elevation. Indeed, the intermittent operation of the tide gauge at Tuktoyaktuk is problematic in terms of assessing storm surge events in along the southern Beaufort coast. The station has not been occupied during several notable storms. For instance, no record is available of a significant storm surge that occurred between September 24–26, 1999 with widespread flooding of the outer Mackenzie Delta (Pisaric et al., 2011; Kokelj et al., 2012; Lapka, 2013; Lantz et al., 2015). **Table 1** shows the highest *recorded* storm surges at the Tuktoyaktuk tide gauge (Station 6485); the highest of which was measured at 2.23 m (Chart Datum (CD)) on October 4th, 1963. During 2018 and 2019, four separate events had observed elevations between 1.9 and 1.97 m (CD).

Recognizing the inadequacies of the instrument record, past research efforts (Forbes and Frobel, 1985; Harper et al., 1988; Reimnitz and Maurer, 1978; 1979) have assessed maximum storm events by examining indirect indicators of the surge elevation. This has included measuring the height of the driftwood debris which is common in the area. Despite an absence of trees along the coast, driftwood from the Mackenzie River drainage accumulates in coastal embayments and forms large driftwood debris piles, and at other locations continuous lines of floated debris. These driftwood piles form in different coastal settings with accumulations up to 9 ha in size (**Figure 2**). During storm surges, floating debris typically repositions itself within the piles and lines. In some instances, the lower portions of the debris are mobilized back into the water and subsequently moved to new locations.

Reimnitz and Maurer (1978 and 1979) completed the first published surveys of driftwood accumulations as an indicator of storm surge heights along the Beaufort coast in Alaska. They conducted airborne surveys of numerous driftwood lines and measured their elevations using traditional rod and level surveying techniques. As inferred for the Canadian coast, the highest debris were thought to have been deposited during the 1970 storm surge event. However, older rotting logs underneath the fresh logs at similar elevations appeared to have been emplaced by earlier events. Driftwood elevations were recorded to be 1.4–3.4 m above mean sea level (MSL) with a high variability depending on the coastal position. The maximum driftwood elevation of 3.4 m was only noted at one site.

In 1984, Forbes and Frobel (1985) examined driftwood accumulation sites along the Yukon and Northwest Territories coast with maximum wood debris height surveys conducted using rod and level surveying. The highest elevation from these surveys was recorded at Komakuk Beach (3.7 m MSL). However, it was noted that this measurement could have been influenced by possible wave run up or ice push. Near Tuktoyaktuk in a sheltered bay, a height was recorded at 2.4 m MSL (Forbes and Frobel, 1985).

More extensive work on mapping driftwood line locations and their heights was conducted in 1985 and 1986 (Harper et al., 1988). This research measured driftwood elevations at 24 locations in the Mackenzie Delta, Richards Island and the Tuktoyaktuk Peninsula. This work also used rod and level surveying to obtain measurements of heights relative to the tide height. The corresponding recorded tide heights measured at the Tuktoyaktuk tide gauge were used to adjust measured heights to MSL. The authors noted that the possible errors in their measurements could be 0.38 m, but they indicate were likely less than 0.1 m given that multiple sources of errors may be offsetting. As also observed by Forbes and Frobel (1985), a maximum storm surge elevation of 2.37 m above MSL was documented for the Tuktoyaktuk sites. This study did not ascertain if the 1970 storm was responsible for the highest driftwood elevation. The authors

FIGURE 2 | Examples of large driftwood accumulations along the southern Beaufort coast: large pile (9 ha) at Canyanek Inlet **(A)**, Two distinct driftwood lines with the highest elevation consisting of older woody debris partially buried within the soil and vegetation at Mason Bay **(B)** and an inland site in the Mackenzie Delta with wood transported over 9 km from the coast **(C)**.

TABLE 2 | Summary of driftwood research sites reported on in this paper.

Site Number	Site Name	Latitude, Longitude	Coastal setting	Relevance to past studies	Activities undertaken
1	Tuktoyaktuk Harbour	69.450, -132.948	Large driftwood accumulation in sheltered embayment on east side of Tuktoyaktuk Harbour. Thought to be the site best suited to assess local storm surge history as it affects the community just 3 km to the west. Higher fidelity historical air photos are available for comparing field observations with historical surges	Surveyed previously by Harper et al. (1988) and showed consistency with three other sites within the Tuktoyaktuk harbour. Forbes and Frobel (1985) also surveyed elevations within the Tuktoyaktuk harbour and found elevations in agreement	SfM and RTK-GNSS surveys, Radio carbon dating samples, historical air photo assessment
2	Mallik Bay	69.468, -134.111	Large driftwood accumulation located on the eastern shoreline of a large embayment on the west side of Richards Island. Over 8 km from the open ocean. The entrance of the bay is open to the dominant wind direction during storms. The shore here consists of a ~250 m long driftwood line truncated by an eroding coastal bluff on its Southern end	The maximum elevation (2.76 m MSL) found in all of Harper et al. study sites (1988)	SfM and RTK-GNSS surveys
3	Mason Bay	69.551, -134.237	Located on the leeward side of the promontory tip of Richards Island within a deep inlet and protected from wave forcing. Two clear and definitive driftwood lines are observable (**Figure 1B**)	Inlet where the second most minimum elevation (1.78 m MSL) found in all of Harper et al. (1988) research	SfM and RTK-GNSS surveys
4	Canyanek Inlet	69.377, -133.385	Very large driftwood pile 1.5 km inland of the coast. This pile consists of a large amount of wood debris of mixed weathering but rimmed with older driftwood. At just over 8 ha in size, it is the largest known driftwood debris site in the Canadian Beaufort coast	Largest debris site in the region in close proximity to the minimum elevation (1.67 m MSL) found in Harper et al. (1988) research	SfM and RTK-GNSS surveys
5	Mackenzie Delta inland driftwood	68.600, -135.559	One of several crescent shaped debris piles far inland. Shaped and oriented such that they point towards the dominant wind direction (NW) during storm surges (**Figure 1C**). Although the chosen site was 9 km from the nearest open ocean at Shallow Bay, its orientation suggests that any surge water would have travelled over 50 km of the low lying delta	Modelling Henry and Heaps (1976); Kim et al. (2021) and measured values Huggett et al. (1975) show that Shallow Bay is vulnerable to far greater water levels than the surrounding coastline due to either a possible funneling effect of water into the Bay or amplification by river outflow	SfM and RTK-GNSS surveys
6	Outer Mackenzie Delta pingo	69.089, -135.795	Located at a small open-system pingo in the outer Mackenzie Delta. The circumference of the pingo has collected driftwood of different ages	Located in an area known to have surrounded the pingo during the 1999 storm surge Lantz et al. (2015)	SfM and RTK-GNSS survey

did note, however, that the upper floated driftwood was likely older than the 1944 event as these deposits contained no anthropogenic debris (i.e., processed lumber and plastics) and thus may have predated settlement in the area.

METHODS

Field Sites

In light of the effects of ongoing climate change along the coast, a major goal of the present study was to re-assess storm surge elevations examined by Harper et al. (1988) and Forbes and Frobel (1985) to determine if any significant changes had occurred since their surveys were conducted in the 1980s. We also sought to assess UAV surveying techniques and determine maximum storm surge elevations relative to an orthometric datum. Rather than revisiting all of the sites previously surveyed, we chose four representative sites (see **Figure 1**): Tuktoyaktuk Harbour, Mallik Bay, Mason Bay, and Canyanek Inlet. Wave run up and ice push can increase the uncertainty in using driftwood as a proxy for maximum water levels, thus we focused mainly on protected embayment sites where the effects of these processes would be mitigated. Sites chosen had mixed debris of various sizes (tree stems and twigs) and care was taken to avoid areas where material seemed unevenly displaced. All sites contained driftwood that was clearly viewable from air. The tundra vegetation cover at the sites was sufficiently sparse to ensure that elevation determinations were of the ground surface next to woody debris. Two additional sites were selected in the outer Mackenzie Delta in an effort to assess spatial variability. The

locations of the study sites, one site inland and another in the outer Mackenzie Delta, are shown on **Figure 1**, with descriptions of each site provided in **Table 2**.

Unoccupied Aerial Vehicle and Structure from Motion Surveying

Recent developments in UAVs, miniaturization of sensors, photogrammetric techniques and robotic automation have allowed the collection of systematic, high resolution aerial photographs to be rendered into a single mosaiced aerial image and a Digital Surface Model (DSM). A DSM refers to data that represents the elevation of the Earth incorporating those features on it—including vegetation and/or buildings. These outputs contain finite details that make them appropriate for detailed flood mapping and assessments (Hashemi-Beni et al., 2018; Annis et al., 2020). In mostly sparsely vegetated environments, the accuracy of the DSM is similar to result obtained by LiDAR surveys, but often with greater spatial resolution (Hashemi-Beni et al., 2018; Annis et al., 2020). The Mackenzie Delta, in particular, has seen several studies that have demonstrated the application of SfM processing from UAV photographs including the monitoring of coastal erosion (Lim et al., 2020), thermokarst activity (Van der Sluijs et al., 2018) and vegetation change (Fraser et al., 2016).

UAV surveys were conducted between July 8th and 14th, 2019 with the exception of the site at the Tuktoyaktuk Harbor that was also surveyed on August 14, 2018 and July 30, 2019. At each surveyed site, a DJI Phantom 4 UAV was autonomously flown in a gridded or "lawnmower" pattern at a constant altitude. Flight planning and control was achieved using the app, Pix4D Capture. All survey sites had flights that were programed to be at 50 m altitude and with 75% overlap in photos in both the along and side track directions. Images were processed using Pix4D Mapper Pro 3.2.23 software. Additional GNSS information was incorporated into the processing to improve the absolute accuracy of the model using high contrast targets placed on the ground during the surveys. The positions of these ground control points (GCPs), were identified in the images and the recorded coordinates digitally assigned to these positions. The final SfM products were saved in GeoTIFF format in Universal Transverse Mercator (UTM) Zone 8N projection and with 3 cm spatial resolution.

Driftwood debris heights were derived by comparing the orthophotos and DSM to identify the highest floated woody debris, multiple pixels identified as the ground and not tundra vegetation were then queried to determine the ground elevation values next to the wood. At each site, the positions of five of the highest pieces of driftwood were used to derive an averaged value.

Global Navigation Satellite System Surveying

Although SfM processing produces high-resolution outputs, these surveys alone are not accurately referenced to an established datum. To tie heights to a vertical datum requires separate GNSS measurements from the UAV's GNSS system. To achieve this, the locations of the GCPs were measured using RTK-GNSS surveying. During surveys, a Spectra Precision SP80 GNSS kit was used. Base station locations were recorded for a minimum of 1 hours and more than 15 days later, post processed using the Natural Resources Canada online Canadian Spatial Reference System-Precise Point Positioning (PPP) application (Natural Resources Canada, 2020) to derive a final solution. The vertical elevations were outputted using a Canadian Geodetic Vertical Datum of 2013 (CGVD2013) vertical datum, a NAD83 CSRS reference frame and a 2010 Epoch. RTK rover measurements were all taken for a minimum of 2 minutes at a sampling rate of once every second. The recorded positions were only retained if the 2 min measurements showed a standard deviation of 3 cm or better in vertical values.

The GCPs measurements, in addition to being used to position the SfM model, were used to assess the quality of the accuracy of the models. Five to eleven GCPs were used in each survey as this number is considered robust enough to derive acceptable accuracy (Coveney and Roberts, 2017). Placement of the GCPs was focused on ensuring that at least one was placed at the minimum elevation (next to the water) and the maximum elevation of the survey area. The remaining GCPs were distributed evenly in the outer extents of the survey area but in locations that were certain to provide full varying view geometries in the photos. All UAV surveys, when in close proximity to the ocean, had a GNSS measurement at the current water level to compare with the measurement of the tide gauge in Tuktoyaktuk.

Global Navigation Satellite System and Tide Gauge Offset

Harper et al. (1988) and Forbes and Frobel (1985) measured the height of logs within driftwood accumulations relative to chart datum and they then corrected these values to MSL by applying an offset. The use of MSL is in reference to a tide gauge station's observed mean water level over several years at that location. Unfortunately, the measurements determined by the Tuktoyaktuk tide gauge are vulnerable to the possibility that the reference datum may have changed during its operation. In 1991, the station was decommissioned and remained mostly nonoperational until 2003. The holding benchmark, that helps to ensure consistency of the reference elevations, was also changed in 1996 and 2003. As a result, it is difficult to ascertain if the same datum has been used during the history of operation of the station (Permanent Service for Mean Sea Level (PSMSL), 2021). Another concern in regard to reference elevations is the realization that the sea surface elevation is affected by global variations in gravity and thereby varies spatially. This concern can be overcome by considering elevations using orthometric datum heights. Orthometric heights, are based on a geoid model, and were established to help deal with the fact that MSL is not a level surface. The orthometric and local reference of MSL, although close in height, are different depending on location. As a result, the MSL determinations by Harper et al. (1988) and Frobes and Forbel (1985) require a mathematical offset and ideally an empirical check to allow conversion to an orthometric height.

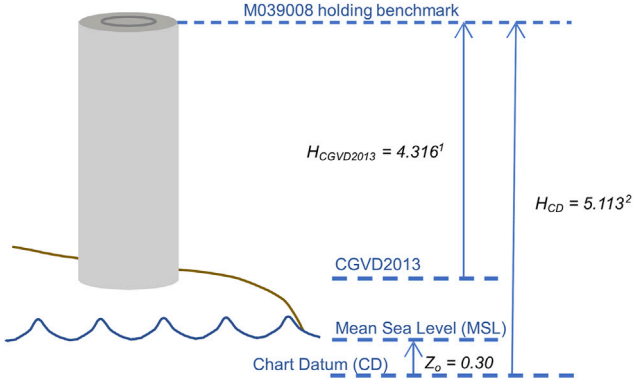

FIGURE 3 | The derivation of Mean Sea Level (MSL) found in Harper et al. (1988) referenced to CGVD2013 requires consideration of the height of the holding benchmark relative to the tide gauge chart datum and the CGVD2013 datum. Values shown are in meters and derived from the following sources: [1]Natural Resources Canada 2021 (Accessed January 22, 2021), [2]Permanent Service for Mean Sea Level (PSMSL) (Accessed January 22, 2021).

Particular attention in this study was made to determine the offset of the Tuktoyaktuk tide gauge measurement recorded in chart datum to the orthometric elevation determination—referenced as the CGVD2013 datum. This determination allows for previous research elevations to be converted to an orthometric datum and thereby avoid confusion regarding MSL. With the heights measured in reference to the CGVD2013 datum, the elevations can be used with remote sensed elevation data commonly recorded in orthometric heights to help plan and engineer coastal management activities to protect communities and infrastructure from flooding and erosion. These measurements also help to calibrate storm surge return period predictions (Kim et al., 2021).

Figure 3 displays how an offset of 0.497 m between the recorded MSL values determined in Harper et al. (1988) and Forbes and Forbel (1985) research and CGVD2013 were derived. The value for the chart datum to MSL difference (Z_o) is noted in a Harper unpublished report that states "...elevations are with respect to mean sea level (MSL), which is 0.3 m above chart datum for the Tuktoyaktuk tide gauge" (Harper, 1985) rather than the currently recognized offset of 0.35 m (Permanent Service for Mean Sea Level (PSMSL) 2021). This difference is possibly accounted for by a rising sea-level (Greenan et al., 2018; National Oceanic and Atmospheric Administration, 2020). The following equation was used to establish the offset of measured MSL values and CGVD2013:

$$H_{msltoCGVD2013} = (H_{CD} - Z_o) - H_{CGVD2013}$$

where $H_{msltoCGVD2013}$ is the height of the Mean Sea Level (MSL) found in literature in reference to CGVD2013, H_{CD} is the height of chart datum relative to the M039008 benchmark, Z_o is the height of MSL relative to chart datum, and $H_{CGVD2013}$ is the height of the benchmark relative to the CGVD2013 datum.

To assess if these calculations apply empirically, on July 9, 2019, a 17-min occupation of water level was taken directly at the CHS Tuktoyaktuk tide gauge station and within 15 m of the continuously tracking GNSS station (TUKT RACS-CHS-M039007). The GNSS receiver was setup using a tripod with its leg points supported with small sections of plywood to prevent any movement due to the gravel substrate. During the acquisition, winds were calm. The positional logging of the receiver measuring the water level was set to record at an interval of every second (1 Hz). The recordings of the water level receiver were then post-processed using the continuously tracking GNSS station as the reference station. This station ordinarily records its position in 1-hour intervals, however, during the days of the surveys, the station was arranged to record at every second (1 Hz). Results of this method showed a standard deviation of position less than 1 mm. After applying the offset equation given above, the measured CGVD2013 value yielded a GNSS measurement that was 2 cm less than the tide gauge measurement. Using these determinations at Tuktoyaktuk, rather than individual measurements at our other study sites, reduced concerns that might be caused by spatial variability in the offset between tide and GNSS datum, as well as wind, tide and geometric effects.

Verification of Structure from Motion Methodology Based on 2019 Storm Surge Event

To verify if driftwood heights are an accurate representation of water level, the Tuktoyaktuk harbor site was photographed before and after two of the four largest storm surges recorded at the Tuktoyaktuk tide station with a maximum elevation measuring 1.97 m (CD) (**Table 1**). Comparison of the SfM model surveyed on August 14, 2018 with a model surveyed on July 30, 2019 found that the highest driftwood debris that were mobilized after the surge events were displaced to an elevation approximately 4 cm lower than measured at the tide gauge. This is not unreasonable and expected as the smaller pieces of driftwood typically range in diameter from 5 to 12 cm and their draft when floated would ground them at an elevation lower than the water level. The difference in water and driftwood elevation was considered an acceptable verification of the methodology used in this study.

Evaluation of Historical Aerial Photos

Harper et al. (1988), found that high level driftwood accumulations at sheltered sites contained no man-made debris such as cut wood, or plastics. In fact, according to Harper's unpublished report (Harper, 1985) on the fieldwork conducted in 1985, the highest driftwood at two of the protected sites were speculated to be older than 50 years. Fortunately, repeat aerial photography of the Tuktoyaktuk area has been regularly undertaken. To establish if the driftwood and debris at the Tuktoyaktuk site were mobilized to their current positions during the 1970 event, we evaluated air photos available from Natural Resources Canada's National Air Photo Library (NAPL) taken before (1968: Roll A20919 Photo 0062 Scale: 1:6,000) and after the storm surge event (1972: Roll A22961 Photo 0133 Scale: 1:12,000). The images were georeferenced, to enable comparison,

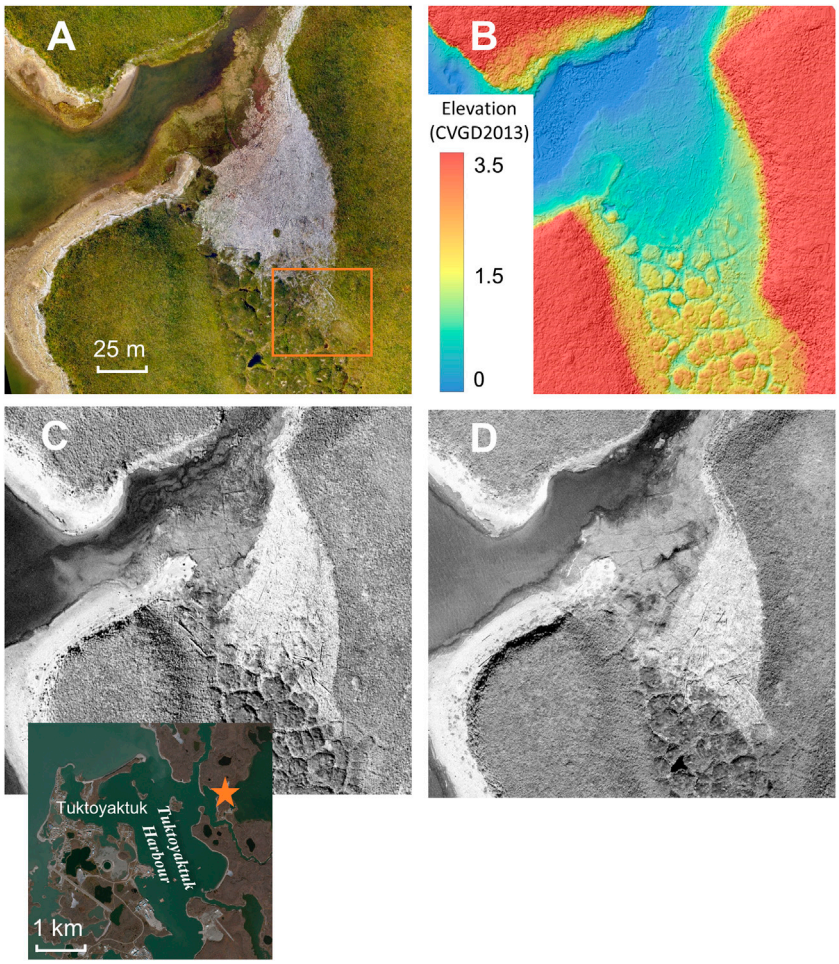

FIGURE 4 | Examples of typical datasets used for analyses at driftwood study sites. Figures **(A,B)** were derived from 2018 drone surveys and SfM processing for the Tuktoyaktuk Harbor site. Figure A is an orthophoto and B is a Digital Surface Model (DSM). The color scale in elevation values in the DSM image range from 0 m (CGVD2013) in blue to 3.0 m in red. For comparison, panchromatic air photos from 1968 to 1972 **(C,D)** respectively are shown. The orange box in A displays the extent of **Figure 5**. The inset map in the bottom left corner shows the location of this driftwood accumulation in relationship to the Tuktoyaktuk harbor.

by finding eight identifiable features found in the UAV-SfM orthophoto mosaic. Spatial resolution of the georeferenced photos was 11 and 7 cm for 1968 and 1972, respectively.

RESULTS

Digital Surface Model Construction and Surface Properties

The SfM modelling produced high resolution and accurate data that were representative of the study sites providing DSM quality sufficient to accurately measure the maximum elevations of the ground next to the driftwood debris (**Figures 4A,B**). In comparison to historical vertical aerial photographs, the SfM orthophotos were of high fidelity with excellent colour, dynamic range and radiometric resolution (**Figures 5**, **6**). This allowed assessment of colour change within the driftwood that were attributed to weathering effects of wood mobilized during different storm events. Individual tree stems, smaller branches, and floating debris could be discreetly identified, and their corresponding elevations accurately determined.

The accuracy of SfM modelled data is predominately controlled by the density of 3D points found through the process of matching identifiable features in the UAV images. **Table 3** displays point density values for the different surveyed areas. Point density for most sites was high (>500/m^2). Areas within the survey site containing ponded water and tall (~2 m) or dense vegetation produced lower densities. These are features known to be difficult for the SfM processing to resolve. However, the driftwood itself, which was the target of our study, yielded high point densities. Survey sites that contained higher point densities in turn resulted in higher reported positional accuracy.

The best modelled accuracy was found in the Mason and Mallik Bay survey sites, with greater than 1 cm vertical accuracy. Here the imagery was dominated by driftwood with short vegetation and bare ground. The Canyanek Inlet site, which had the lowest point density (234 points/m^2), contained somewhat denser and relatively taller tundra vegetation than

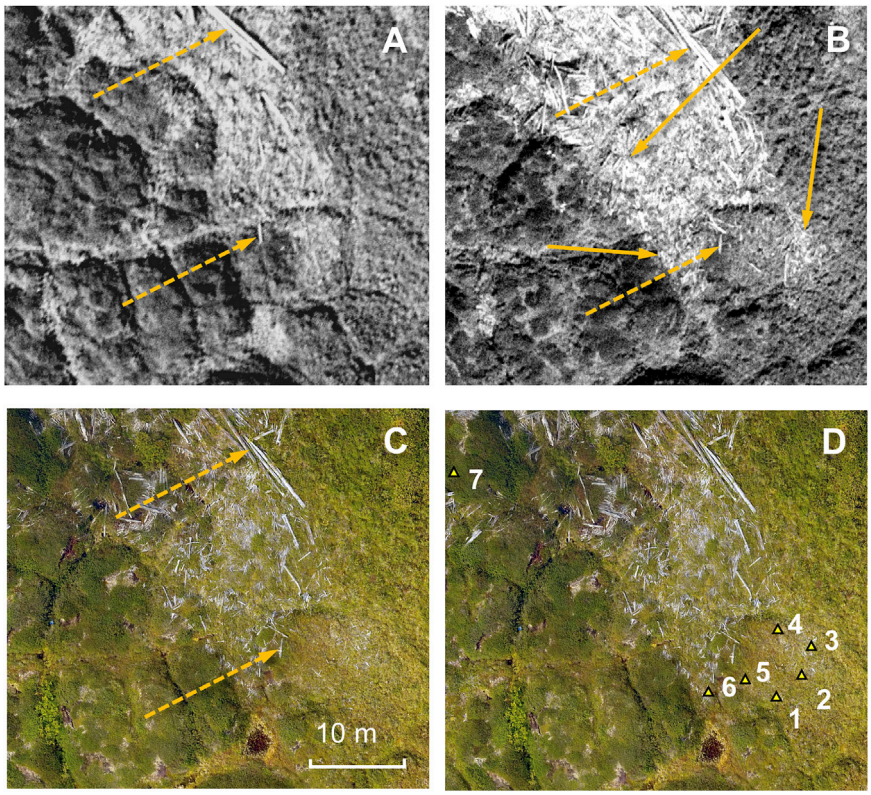

FIGURE 5 | Air photos and orthophoto from **(A)** 1968, **(B)** 1972, and **(C)** 2018 of the upper most driftwood within the Tuktoyaktuk Harbor site show the displacement of wood before and after the 1970 storm surge. The dashed arrows, highlight how individualized pieces of wood can be tracked moving upward (down and right in image) through the driftwood accumulation and have remained in place in 2018. Areas of newly deposited driftwood are shown with the solid arrows in the 1972 image. The extent of these figures are marked as an orange box in **Figure 4**. Figure D displays the location of radiocarbon dating samples taken from the upper most driftwood. Marked locations correspond to samples shown in **Table 4**.

the other sites and therefore yielded a vertical SfM model accuracy of only 4 cm.

The largest source of potential error is caused by the occupation of a GNSS base station. Because of the remoteness of sites and the reliance on using a helicopter to get to sites, the amount of available time on the ground for occupying and recording the GNSS station was limited. Consequently, the standard deviation of the vertical measurements detailed in the PPP solution reports for each of the base stations varied from 4 to 6 cm. The exception is the measurement at Mason Bay where the shortest occupation time of just over an hour and poor satellite geometries resulted in a reported precision of 24 cm within 95% of the measured values.

To further confirm the accuracy of each of the SfM models, pixels in the orthophotos that were identified as the water's edge were queried for the associated elevation from the DSM. The average of ten heights was noted. These values were then compared to the elevation recorded at the Tuktoyaktuk tide gauge during the time of the survey (corrected for the datum offset). This procedure allowed assessment of the model based on a reference to the tide gauge. The differences in these values are reported in **Table 3**. Differences do occur of up to 10 cm at Mason Bay but 3–5 cm elsewhere. These differences can be explained by the contributing errors associated with RTK-GNSS rover measurements and the base station PPP post processed recordings.

Driftwood Elevations

With the GNSS and tide gauge offset determined, the maximum driftwood elevation extracted from the SfM models at each site can be reported in orthometric CGVD2013 and compared with the MSL datum used in previous studies. These values can be seen in **Figure 1** and **Table 3**. The driftwood elevations ranged between 1.24 and 2.34 m (CGVD2013) and differed from Harper's elevations only between 4 and 10 cm. The inset graph in **Figure 1** displays the total error from the various survey components in this study as compared to Harper's estimated error of 0.38 for each site. Of importance to the Hamlet of Tuktoyaktuk, the elevation of the driftwood in the nearby sheltered harbor site was found to be 1.98 m (CGVD2013), 9 cm higher than Harper's measurements after conversion from chart datum to CGVD2013. This difference and those of the other three surveyed locations likely reflects the natural variability of driftwood elevations and the difference in survey techniques between studies. The previously published values were derived by walking through the sites, identifying

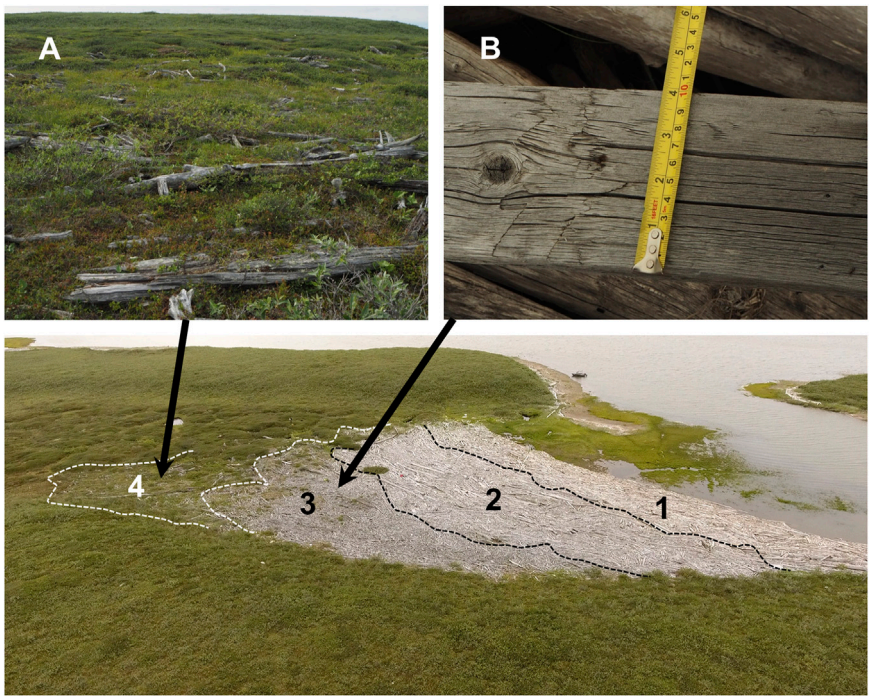

FIGURE 6 | The layers of differing ages of wood and anthropogenic debris at the Tuktoyaktuk Harbor site are visible from the air. The youngest material fronts the pile (1), whereas the second portion consists of large amounts of lumber and plywood with limited amounts of plastic items (2). Above this is the third layer with homogenously similar weathered wood and contains the rare true dimensional lumber pieces (3 and upper right photo **(B)**). The upper most location consists of only sparsely distributed heavily weathered driftwood that is embedded into the tundra surface (4 and upper left photo **(A)**).

TABLE 3 | Reported results for each surveyed site.

Site Number	Name	Size (km^2)	SfM model average point density (per m^2)	Vertical SfM accuracy (cm)	GNSS base station occupation time (hh:mm:ss)	Base station PPP precision (cm)	Elevation of highest driftwood surveyed (m)			Elevation of driftwood recorded by Harper et al. (1988) [b](m)			Difference between GNSS and Tide Gauge (cm)
							CVGD2013	MSL	CD	CVGD2013	MSL	CD	
1	Tuktoyaktuk Harbour	0.07	553	2.40	M039007 station[a]	2.3[a]	1.98	2.48	2.78	1.89	2.39	2.69	1
2	Mallik Bay	0.10	1,125	0.80	01:40:12	3.8	2.27	2.77	3.27	2.06	2.56	3.06	3
3	Mason Bay	0.13	799	0.90	01:04:17	24.1	1.28	1.78	2.08	1.28	1.78	2.08	-10
4	Canyanek Inlet	0.30	234	4.10	M039007 station[a]	4.4[a]	1.86	2.36	2.66	1.76	2.26	2.56	5
5	Mackenzie Delta inland driftwood	0.08	362	2.80	01:20:16	5.5	1.35	1.85	2.15	Not surveyed			NA
6	Outer Mackenzie Delta pingo	0.08	504	2.00	01:53:08	5.0	2.25	2.75	3.05	Not surveyed			NA

[a]*Averaged reported post-processing results after 2 min occupation times using as the Tuktoyaktuk continuously tracking GNSS, station (M039007) as the base station.*
[b]*Values shown here are sourced from unpublished survey reports by Harper which carry the elevations to the nearest cm.*

the upper limit floated debris, measuring up to seven positions, and averaging their heights. Given the low-lying nature of the area, identifying the highest driftwood is challenging, as the difference in heights is difficult to discern from the ground. The UAV derived models, on the other hand, afford desktop analysis of the entire site and the identification of woody debris that might have otherwise been missed or assumed to be lower in the field.

Comparison of the observed water level in the SfM data with the observed tide gauge value ranged from 1 to 10 cm. The largest

TABLE 4 | Radiocarbon sample dating results of the tree stem/branch "cookies" taken at the Tuktoyaktuk Harbor site. The locations of the numbered samples can be found in **Figure 5D**. Reported dates in the table are from the A.E. Lalonde AMS laboratory analysis report.

Sample Number	Lab ID	Material	^{14}C years BP (BP = AD 1950)	+/-(years)	Fraction Modern ($F^{14}C$)	+/-	calibrated AD date at the 95.4% confidence level
1	UOC-11254	Wood	104	22	0.9872	0.0028	1687–1927
2	UOC-11255	Wood	100	20	0.9876	0.0024	1691–1925
3	UOC-11256	Wood	31	19	0.9962	0.0024	1706–1915
4	UOC-11257	Wood	115	20	0.9858	0.0024	1682–1930
5	UOC-11258	Wood	125	20	0.9845	0.0024	1681–1938
6	UOC-11259	Wood	76	20	0.9906	0.0025	1695–1919
7	UOC-11260	Wood	96	19	0.9881	0.0024	1691–1923

difference occurred at Mason Bay likely due to our shorter (just over an hour) occupation and associated low reported precision of the GNSS base station. Combined accuracy from the SfM modelling and the RTK GNSS suggests that measurements derived from our data ranged (excluding Mason Bay) between 2 and 9 cm depending on site location.

Radiocarbon Dating

As observed by earlier researchers, we also found that the highest-level wood debris visibly appeared to be quite old as it was fragile from weathering processes and in some cases partly embedded into the tundra soil and vegetation. This debris, despite its condition, was intact and easily recognized to consist of tree stems and branches. No cut lumber or manufactured debris was found. To assist in the interpretation of the age of this debris, seven samples of wood material were collected from the accumulation pile at the Tuktoyaktuk Harbor survey site in 2019 and submitted for radiocarbon dating. All samples were collected from the visibly oldest driftwood selected from areas within 0.15 m vertically of the highest elevation debris line found in a DSM produced from the 2018 UAV-SfM survey. The location of each sample was recorded using the RTK-GNSS system. Samples consisted of cut sections producing tree stem/branch "cookies" of 5–10 cm diameter. Dating of the outermost portion of the driftwood was performed at the A.E. Lalonde AMS Laboratory (University of Ottawa) with calibration accomplished using the program OxCal v4.3 (Ramsey, 2009) and the IntCal13 calibration curve (Reimer et al., 2013).

The results of the radiocarbon dating of the samples taken at the locations shown in **Figure 5D** are in **Table 4**. As is typically found in organic samples dated since the Industrial Revolution, large error bars were assigned to the calibrated age determinations (ie. +/- 210–257 years). However, the minimum age determinations for the driftwood ranged from 1915 to 1938 (cal AD). It should be noted that these age determinations are for when the trees that these wood pieces were derived from died, rather than the date of a particular storm surge. It is well known that floated wood accumulating in coastal driftwood accumulations has long transit times from its source to where it is emplaced along the Beaufort coast (Eggertsson, 1994; Sander et al., 2021).

DISCUSSION

Regional Variability

Maximum driftwood elevations for the four study sites that were co-located with the Harper et al. (1988) study were all within 10 cm of their determined elevations (see **Table 2**) attesting to the rigor of their field surveying. The highest driftwood elevations were found at Mallik Bay (2.47 m CGVD2013) and Tuktoyaktuk (1.98 m CGVD2013). However, since the Mallik Bay site has a westerly fetch of ~4.5 km, it may have experienced storm wave action that somewhat elevated the wood debris positions. Conversely, the Tuktoyaktuk site is sheltered behind Tuktoyaktuk island and within an isolated bay (see inset map in **Figure 4**). Each of the resurveyed sites contained visual layering of different aged driftwood that changed in character with elevation. As shown on the oblique photo in **Figure 6**, the stratified appearance of the driftwood was evident both from the air and on the ground. The layering was mapped in detail at the Tuktoyaktuk site where the youngest layer close to the water (0–0.5 m CGVD2013) consisted mainly of tree stems, twigs, and branches, with embedded plastics, lumber and other manufactured debris throughout. The wood debris was very fresh looking and had not experienced significant weathering. The next layer (~0.5–1.1 m CGVD2013) contained weathered driftwood with significant amounts of lumber and plywood, but much less plastic debris. Wood in this layer was stacked on top of one another deeper than that of the entire accumulation. The third recognizable layer (~1.1–1.3 m CGVD2013) consisted of smaller wood debris that was notably more weathered (grey color with some decomposition on the surface of wood debris). Manufactured debris in this layer was notably sparser and consisted solely of sawn logs and cut lumber of true dimensions (see **Figure 6**) which we assume pre-date ~1969 when lumber mills in western Canada reduced their cutting dimensions. The driftwood in the uppermost layer (~1.3–1.98 m CGVD2013) was extensively weathered and contained no manufactured debris. Driftwood here was found partially buried in the tundra soil and often beginning to become overgrown with the low tundra vegetation (see **Figure 6**).

Further insights into the stratigraphy of driftwood developed by storm surges were revealed by comparing the August 2018 with the July 2019 orthophotos. Between these dates, three

significant storm surges were recorded at the Tuktoyaktuk tide gauge varying from 1.10 to 1.17 m (CGVD2013) (see **Table 1**). Mobilized wood within the accumulations changed position consistent with the layered stratigraphy. The two lowermost layers from 0 to 0.1 m were extensively modified. The lowest elevation driftwood (<~0.8 m) was completely removed and the remaining upper portion of this layer extensively reoriented. The next stratigraphic later from 1.1 to 1.3 m (CGVD2013) elevation was only partly modified with the mainly small shifts in positions laterally and upward in elevation. No change was detected in the wood debris above 1.3 m (CGVD2013) elevation nor in the positions of wood in the uppermost layer from the 1972 aerial photos to present. The larger diameter driftwood above the 1.3 m (CGVD2013) mark may be stabilized by their partial emplacement in the sediment and/or surrounding low tundra vegetation consisting largely of grasses (see **Figure 6**), however, no observations were made of either emplaced pieces of wood debris to have moved or new wood deposited above this elevation. This stratigraphic approach to evaluating the driftwood accumulations seems to be consistent with the summary of historical storm surge elevations measured on the tide gauge at Tuktoyaktuk. While the recording interval of the Tuktoyaktuk tide gauge is intermittent, the largest recorded storm events since 1970 have not exceeded 1.3 m (CGVD2013). The general conclusion from both the stratigraphic studies and the historical record is therefore that modest magnitude storm surges reaching this elevation are arguably more frequent in the present climate and sea ice regime along the southern Canadian Beaufort coast, but higher magnitude events have not occurred since 1970. This does not preclude that more frequent and severe storm surges may be more likely in the future as suggested by some authors (Manson and Solomon, 2007; Kokelj et al., 2012; Vermaire et al., 2013; Greenan et al., 2018). However, it does highlight the importance of continuing and even expanding tide gauge and weather observations as a basis to improve the instrument record. Future projections of storm frequency and intensities are based on historical observational data for which the Arctic is limited both temporarily and spatially. This lack of available data reduces the confidence in extreme high-water event occurrence predictions (Greenan et al., 2018).

The two Mackenzie Delta driftwood accumulations that had not been previously studied, had a different character than the sites described above. While recent storm surge hindcast modeling by Kim et al. (2021) suggested that a storm surge would produce water levels 1 m higher in this region as compared to surge heights in Tuktoyaktuk, we found that the driftwood elevations were lower for the inland site (1.35 m CGVD2013) and higher for the outer Delta site (2.25 m CGVD2013). While nearby Shallow Bay may experience more intense storm surges because of the orientation of the embayment relative to the storm winds from the northwest, the height of the driftwood levels inland away from the open ocean is much diminished. Given the proximity of these sites to channels of the Mackenzie River, there is potential that driftwood accumulations could have been influenced by high water levels during the freshet which can cause extensive flooding in the outer delta area (Yang et al., 2015). As the woody debris on the flanks of the inland pingo site had a discernable stratigraphy and was at a higher elevation on the northwest side versus the southeast side, this seems consistent with storm surge inundation from the northwest rather than the effects from the freshet. However, the inland driftwood site (site 5 on **Figure 1**) contained abundant manufactured debris of various ages and no discernible stratigraphy within the driftwood. While the orientation of the driftwood accumulations also suggested emplacement by storm surge influence from the northwest, the mixed debris and lack of stratigraphy may indicate some mobilization and reworking of the debris pile by flooding during the freshet. Of note however, if the accumulation resulted from a storm surge, overland flooding may have extended approximately 50 km overland.

The discussion above highlights some of the challenges of estimating storm surge elevations based upon displaced wood debris heights and concerns that secondary movement subsequent to the storm surge emplacement may have occurred. We concur with others who have noted that it is important to carefully consider the unique coastal setting of each site including the potential for wave run-up and ice push, human activity, seasonal river flooding, the abundance and character of driftwood (buoyance and draft), as well as the distance the debris has travelled (Reimnitz and Maurer, 1979; Harper et al., 1988). However, it is reassuring that Kim et al. (2021) note that there is general agreement in the driftwood elevation measurements taken by Harper et al. (1988) and their hindcast modelling of a storm surge event that occurred on August 23, 1986 in the Mackenzie Delta and Beaufort coast.

Interpretation of Extreme Storm Surge Events at Tuktoyaktuk

One important practical goal of this study was to provide accurate information on the elevation and the return period of large magnitude storm surges pertinent to assessing storm geohazards in the Hamlet of Tuktoyaktuk. This small, low-lying community has experienced prolonged coastal erosion and periodic flooding during storm surges throughout its history. As mentioned previously, many researchers have highlighted that recent climate change is likely to cause increased magnitude and frequency of these storm surges (Manson and Solomon, 2007; Kokelj et al., 2012; Vermaire et al., 2013; Greenan et al., 2018). Current estimates of sea-level rise at Tuktoyaktuk vary between 2.5 and 2.75 mm per year (Greenan et al., 2018; National Oceanic and Atmospheric Administration, 2020) which would suggest an increased risk of higher elevation storm surges over time.

We found that the highest driftwood at the Tuktoyaktuk Harbor site, and each of the sites co-located with the Harper et al. (1988) sites, was very old with weathered but intact wood, and partially embedded in the tundra. This wood, although weathered, was still identifiable as natural and having not been milled or altered with an axe or saw. Harper et al. (1988) was not able to constrain the age of the event that emplaced these pieces of wood, suggesting that the highest-level wood debris could be due to the 1970 or possibly the 1944 storm surge. We assessed aerial photographs from 1968 to

1972 to consider the timing. As shown in **Figures 4**, **5**, comparison of the geo-referenced photos and the 2018 DSM confirmed that the wood at the highest elevation 1.85 m (CGVD2013) was present in 1968 (see **Figure 4C**). At least one storm surge prior to this date had reached this elevation. However, it is apparent in the 1972 aerial photograph (**Figures 4D**; **Figure 5C**) that some of this driftwood was re-oriented and moved 8 m further upslope with an associated vertical movement up to 13 cm in elevation. We can also confirm that the age of the upper debris is not necessarily indicative of the age of the surge. The 1970 event simply floated and raised the highest-level wood that was long in place before it was mobilized to their post surge positions. We therefore attribute the reported storm surge in 1970, which reached 1.98 m (CGVD2013), as the highest elevation storm surge recorded in the driftwood debris in this area.

As no suitable aerial photographs prior to 1968 were available to document the older storm surge, we sampled seven representative driftwood pieces to attempt to constrain the ages of the high elevation driftwood using radiocarbon dating (as summarized in **Table 4**). Interpretation of the dating results is problematic because the young age of the organic carbon yields large error bars in the AMS dating method. However, it is clear that the wood is indeed old with upper bounds of the calibrated ages all being older than 1938. Using this date as the minimum age of the wood and given that the resident time of the floating driftwood before they were deposited in the driftwood accumulation could be significant (see references and discussion within Murphy et al., 2021), we conclude that it is likely, that the emplaced driftwood at 1.85 m (CGVD2013) was moved to their positions in the 1968 air photo by the 1944 storm surge reported by residents and Captain Larsen. However, the elevation was substantially less than the reported ~3 m elevation estimates made at the time. The 1970 storm surge then moved these already deposited driftwood pieces into their present locations. In summary, over the past 75 years there have been only two historical storm surges that reached ~2 m (CGVD2013) elevation and both of these occurred before 1971.

Another consideration that motivated this study was the possibility that the highest driftwood found within the accumulations along the Beaufort coast may have been emplaced by other extreme high-water events. Considering that the area is within an active seismic setting, Leonard et al. (2012) speculated that there is potential for large tsunamigenic earthquakes along the southern Beaufort coast. Empirical modelling by Leonard et al. (2014), found that a large thrust earthquake (Mw 8.4), could result in a tsunami run-up of ≥3 m along the coast of the Tuktoyaktuk Peninsula. In addition, recent marine geology and multibeam studies have also shown that the upper slope of the Beaufort Sea, ~120 km north of Tuktoyaktuk, is a site where numerous large submarine mass failures have occurred in the past (Mosher, 2009; Cameron and King, 2019; Paull et al., 2021; Riedel et al., 2021). Some of these events appear to be within the last 1,000 years (Cameron and King, 2019; Paull et al., 2021) and potentially of sufficient size to trigger a tsunami.

As discussed above, the air photos before and after the 1970 storm surge allow definitive determination that the highest driftwood occurrences at the Tuktoyaktuk harbor site were deposited by a 1970 storm surge and that the older driftwood at a similar elevation most likely was emplaced from a storm surge in 1944. Both the 1970 and 1944 events were coincident with storms, with no observed ground shaking from an earthquake. However, given the observed wood decomposition and incorporation within the tundra cover (see difference between **Figures 5B,C**), it is plausible that earlier events could be recorded with woody debris that are now buried. An observation along the Beaufort coast in Alaska (Reimnitz and Maurer, 1979) of woody debris estimated to be 70–200 years old found at an elevation 1–2 m above the 1970 storm surge driftwood debris support this possibility.

CONCLUSION

In this study, we use UAV and SfM methods to revisit four coastal driftwood accumulation study sites that were first appraised in 1985–86 by Harper et al. (1988) and add two new sites in the Mackenzie Delta to consider if extreme storm surge magnitudes along the southern Beaufort coast are more substantive in today's climate setting than in the past. This assessment provides a basis for the determination of the height and return period for maximum storm surge events and also assessment of the stratigraphic record preserved from more recent moderate elevation storm surges. We establish the elevations in a vertical datum (CGVD2013) that is relevant for modern hazard assessment in the Tuktoyaktuk and Mackenzie Delta area.

Maximum driftwood elevations showed spatial variability across surveyed sites. The site nearest the community of Tuktoyaktuk measured a maximum elevation of 1.98 m (CGVD2013). At this same site, UAV/SfM observations before and after recent storm events (between August 2018 to July 2019) discern four distinct stratigraphic units of different debris composition and weathering characteristics within the driftwood (0–0.5 m; 0.5–1.1 m; 1.1–1.3 m; 1.3–1.98 m CGVD2013). Air photos, taken shortly before and after the storm surge in 1970, confirm that the existing upper driftwood was mobilized and set in its current positions by this event. However, this event mobilized driftwood that was already in place at 1.85 m. Based on a 1938 minimum radiocarbon age determined on wood sampled from this elevation, we conclude that this previous event may have been associated with a 1944 storm surge, which was previously reported on from anecdotal observations.

No storm surges of a magnitude approaching that of the 1944 and 1970 events have occurred to 2021. Tide gauge records and our stratigraphic studies of driftwood debris indicate that more frequent, moderate elevation storm surges that reach elevations of ~1.3 m (CGVD2013) have prevailed in the last decade as compared to those recorded in past decades.

This research demonstrates the utility of the SfM/UAV method for high resolution and accurate determinations of ground surface elevations associated with debris grounded by historical storm surges. While our study was in the local Mackenzie Delta area, the widespread occurrence of ground debris along the Yukon and Alaskan coast offers the opportunity to extend this technique to the surrounding

region or to document the regional variability in storm surge elevations after a future event. While the SfM/UAV technique is gaining widespread use in the geosciences, our experience suggests that this technique may be appropriate for wide range of periglacial process studies. We presently are assessing the utility of the SfM/UAV method for permafrost subsidence, uplift, and creep studies. In terms of coastal risk assessment, our work demonstrates the importance of continuous long-term tide gauge and GNSS monitoring as a basis for understanding the frequency and magnitude of future storm surge events. Given the importance of these events and their regional variability, a distributed monitoring network along the Canadian and Alaskan Beaufort coast would be highly valued.

DATA AVAILABILITY STATEMENT

The raw data supporting the conclusions of this article will be made available by the authors upon request, without undue reservation.

AUTHOR CONTRIBUTIONS

RM and SD designed the study, organized the field operations, and conducted the collection and interpretation of the data. Aside from the radiocarbon dating, RM performed all data analysis. RM wrote the initial manuscript with contributions to the writing and revision from SD. Both authors gave their approval to the final version of the manuscript.

FUNDING

The research described in this paper was supported by the Geological Survey of Canada through its Public Safety Geoscience Program and the Program for Energy Research and Development. The Polar Continental Shelf Program also provided logistical support.

ACKNOWLEDGMENTS

We thank Dustin Whalen from the GSC for his efforts to advance coastal research at Tuktoyaktuk and the residents of the Hamlet of Tuktoyaktuk who have encouraged our work. Michelle Côté assisted with permitting and community consultation. Mathew Dare of the Aurora Research Institute collected a series of aerial photographs that were used to interpret the 2019 driftwood positions at Tuktoyaktuk. Andrew Schaeffer provided field assistance, valued critical comments on the manuscript and acted as an internal reviewer of the paper. Finally, this study has benefited from the comments and suggestions made by three critical reviewers and the guidance provided by the coordinating editor. NRCan contribution number / Numéro de contribution de RNCan: 20210424.

REFERENCES

Andrachuk, M., and Smit, B. (2012). Community-Based Vulnerability Assessment of Tuktoyaktuk, NWT, Canada to Environmental and Socio-Economic Changes. *Reg. Environ. Change* 12 (4), 867–885. doi:10.1007/s10113-012-0299-0

Annis, A., Nardi, F., Petroselli, A., Apollonio, C., Arcangeletti, E., Tauro, F., et al. (2020). UAV-DEMs for Small-Scale Flood Hazard Mapping. *Water* 12 (6), 1717. doi:10.3390/w12061717

Bridges, T., Henn, R., Komlos, S., Scerno, D., Wamsley, T., and White, K. (2013). Coastal Risk Reduction and Resilience: Using the Full Array of Measures. Available at: https://usace.contentdm.oclc.org/digital/collection/p266001coll1/id/5275/(accessed October, 2021).

Cameron, G. D. M., and King, E. L. (2019). Mass-Failure Complexes on the Central Beaufort Slope, Offshore Northwest Territories. *Geol. Surv. Can. Open File.* 8356, 40. doi:10.4095/314644

Carter, R. A., and Smith, H. N. (2011). "Challenges of Coastal Engineering in Alaska," in Proc. 2011 Solutions to Coastal Disasters Conf, Anchorage, Alaska, 286–297. doi:10.1061/41185(417)26

Cohen, J., Screen, J. A., Furtado, J. C., Barlow, M., Whittleston, D., Coumou, D., et al. (2014). Recent Arctic Amplification and Extreme Mid-Latitude Weather. *Nat. Geosci* 7 (9), 627–637. doi:10.1038/ngeo2234

Comiso, J. C., Parkinson, C. L., Gersten, R., and Stock, L. (2008). Accelerated Decline in the Arctic Sea Ice Cover. *Geophys. Res. Lett.* 35 (1), 1–6. doi:10.1029/2007GL031972

Couture, N. J., Irrgang, A., Pollard, W., Lantuit, H., and Fritz, M. (2018). Coastal Erosion of Permafrost Soils Along the Yukon Coastal Plain and Fluxes of Organic Carbon to the Canadian Beaufort Sea. *J. Geophys. Res. Biogeosci.* 123 (2), 406–422. doi:10.1002/2017JG004166

Couture, R., Robinson, S., Burgess, M., and Solomon, S. (2002). Climate Change, Permafrost, and Community Infrastructure: A Compilation of Background Material from a Pilot Study of Tuktoyaktuk, Northwest Territories. *Geol. Surv. Can. Open File.* 3867, 83. doi:10.4095/213753

Coveney, S., and Roberts, K. (2017). Lightweight UAV Digital Elevation Models and Orthoimagery for Environmental Applications: Data Accuracy Evaluation and Potential for River Flood Risk Modelling. *Int. J. Remote Sensing* 38 (8-10), 3159–3180. doi:10.1080/01431161.2017.1292074

Dallimore, S. R., Wolfe, S. A., and Solomon, S. M. (1996). Influence of Ground Ice and Permafrost on Coastal Evolution, Richards Island, Beaufort Sea Coast, N.W.T. *Can. J. Earth Sci.* 33, 664–675. doi:10.1139/e96-050

Eggertsson, O. (1994). Mackenzie River Driftwood—A Dendrochronological Study. *Arctic* 47, 128–136. Available at: http://www.jstor.org/stable/40511551 (accessed January, 2021).

Emmerton, C. A., Lesack, L. F. W., and Vincent, W. F. (2008). Mackenzie River Nutrient Delivery to the Arctic Ocean and Effects of the Mackenzie Delta during Open Water Conditions. *Glob. Biogeochem. Cycles* 22 (1), a–n. doi:10.1029/2006GB002856

Fisheries and Oceans Canada (2021). Data from: Station Inventory Data. Station 6485. Available at: https://www.isdm-gdsi.gc.ca/isdm-gdsi/twl-mne/inventory-inventaire/interval-intervalle-eng.asp?user=isdm-gdsi&region=CA&tst=1&no=6485&ref=maps-cartes (Accessed April 10, 2021).

Forbes, D. L., and Frobel, D. (1985). Coastal Erosion and Sedimentation in the Canadian Beaufort Sea. *Geol. Surv. Can.* 85-1B, 69–80. doi:10.4095/120230

Forbes, D. L., Whalen, D. J. R., Jacobson, B., Fraser, P., Manson, G. K., Couture, N. J., et al. (2013). "Co-design of Coastal Risk Assessment for Subsistence Infrastructure in the Inuvialuit Settlement Region, Western Arctic Canada [Conference Poster]," in ArcticNet Annual Science Meeting 2013, Halifax, NS, Canada. Available at: https://arcticnetmeetings.ca//asm2013/docs/full_program.pdf (Accessed December 8, 2020).

Forbes, D. L., Whalen, D., Solomon, S. M., and Manson, G. K. (2005). "First Applications of Airborne Lidar for Arctic Coastal Mapping: Potential Contributions to Building Community Resilience under Climate Change [Conference Poster]," in ArcticNet Annual Science Meeting 2005, Banff, AB, Canada. Available at: http://www.arcticnet.ulaval.ca/pdf/posters_2005/forbes_et_al.pdf (Accessed January 30, 2020).

Fraser, R. H., Olthof, I., Lantz, T. C., and Schmitt, C. (2016). UAV Photogrammetry for Mapping Vegetation in the Low-Arctic. *Arctic Sci.* 2 (3), 79–102. doi:10.1139/as-2016-0008

Fritz, M., Vonk, J. E., and Lantuit, H. (2017). Collapsing Arctic Coastlines. *Nat. Clim Change* 7 (1), 6–7. doi:10.1038/nclimate3188

GNWT Department of Municipal and Community Affairs (2014). Northwest Territories Hazard Identification Risk Assessment. Available at: http://www.maca.gov.nt.ca/wp-content/uploads/2014/04/Northwest-Territories-Hazard-Identification-Risk-Assessment.pdf (accessed September, 2020).

Graham, R. M., Cohen, L., Petty, A. A., Boisvert, L. N., Rinke, A., Hudson, S. R., et al. (2017). Increasing Frequency and Duration of Arctic Winter Warming Events. *Geophys. Res. Lett.* 44 (13), 6974–6983. doi:10.1002/2017GL073395

Greenan, B. J. W., James, T. S., Loder, J. W., Pepin, P., Azetsu-Scott, K., Ianson, D., et al. (2018). "Changes in Oceans Surrounding Canada: Chapter 7," in *Canada's Changing Climate Report*. Editors E. Bush and D. S. Lemmen (Ottawa, ON: Government of Canada), 343–423. Available at: https://www.nrcan.gc.ca/sites/www.nrcan.gc.ca/files/energy/Climate-change/pdf/CCCR-Chapter7-ChangesInOceansSurroundingCanada.pdf (accessed January, 2021).

Harper, J. R. (1985). *Final Report Field Surveys of Log Debris Lines in the Tuktoyaktuk Vicinity Implications to Storm Surge Evaluation*. Unpublished report. Sidney, Britsh Columbia: Dobrocky Seatech Ltd.

Harper, J. R., Henry, R. F., and Stewart, G. G. (1988). Maximum Storm Surge Elevations in the Tuktoyaktuk Region of the Canadian Beaufort Sea. *Arctic* 41, 48–52. doi:10.14430/arctic1691

Hashemi-Beni, L., Jones, J., Thompson, G., Johnson, C., and Gebrehiwot, A. (2018). Challenges and Opportunities for UAV-Based Digital Elevation Model Generation for Flood-Risk Management: A Case of Princeville, North Carolina. *Sensors* 18 (11), 3843. doi:10.3390/s18113843

Henry, R. F. (1984). Flood Hazard Delineation at Tuktoyaktuk. Institute of Ocean Sciences, Department of Fisheries and Oceans. Available at: http://publications.gc.ca/collections/collection_2012/mpo-dfo/Fs97-17-19-eng.pdf (accessed January, 2021).

Henry, R. F., and Heaps, N. S. (1976). Storm Surges in the Southern Beaufort Sea. *J. Fish. Res. Bd. Can.* 33 (10), 2362–2376. doi:10.1139/f76-283

Hill, P. R., Hequette, A., Ruz, M. H., and Jenner, K. A. (1991). Geological Investigations of the Canadian Beaufort Sea Coast. *Geol. Surv. Can. Open File* 2387, 348. doi:10.4095/132386

Hill, P. R., Lewis, C. P., Desmarais, S., Kauppaymuthoo, V., and Rais, H. (2001). The Mackenzie Delta: Sedimentary Processes and Facies of a High-Latitude, Fine-Grained Delta. *Sedimentology* 48 (5), 1047–1078. doi:10.1046/j.1365-3091.2001.00408.x

Hill, P. R., Mudie, P. J., Moran, K., and Blasco, S. M. (1985). A Sea-Level Curve for the Canadian Beaufort Shelf. *Can. J. Earth Sci.* 22 (10), 1383–1393. doi:10.1139/e85-146

Hopkinson, C., Crasto, N., Marsh, P., Forbes, D., and Lesack, L. (2011). Investigating the Spatial Distribution of Water Levels in the Mackenzie Delta Using Airborne LiDAR. *Hydrol. Process.* 25 (19), 2995–3011. doi:10.1002/hyp.8167

Huggett, W. S., Woodward, M. J., Stephenson, F., Hermiston, F. V., and Douglas, A. (1975). Near Bottom Currents and Offshore Tides. Beaufort Sea Project, Department of the Environment. Available at: www.publications.gc.ca/pub?id=9.877636&sl=0 (accessed June, 2021).

Irrgang, A. M., Lantuit, H., Gordon, R. R., Piskor, A., and Manson, G. K. (2019). Impacts of Past and Future Coastal Changes on the Yukon Coast - Threats for Cultural Sites, Infrastructure, and Travel Routes. *Arctic Sci.* 5 (2), 107–126. doi:10.1139/as-2017-0041

James, T. S., Henton, J. A., Leonard, L. J., Darlington, A., Forbes, D. L., and Craymer, M. (2014). Relative Sea-Level Projections in Canada and the Adjacent mainland United States. *Geol. Surv. Can. Open File.* 7737, 72. doi:10.4095/295574

Kavik-Axys Inc (2010). Review of Tuktoyaktuk Habour as a Base for Offshore Oil & Gas Exploration and Development. Environmental Studies Research Funds Report No. 179. Alberta & Northwest Territories. Available at: https://publications.gc.ca/site/eng/9.811369/publication.html (accessed July, 2021).

Kim, J., Murphy, E., Nistor, I., Ferguson, S., and Provan, M. (2021). Numerical Analysis of Storm Surges on Canada's Western Arctic Coastline. *J. Mar. Sci. Eng.* 9 (3), 326. doi:10.3390/jmse9030326

Kobayashi, N., Vidrine, J. C., Nairn, R. B., and Soloman, S. M. (1999). Erosion of Frozen Cliffs Due to Storm Surge on Beaufort Sea Coast. *J. Coast. Res.* 15, 332–344. Available at: www.jstor.org/stable/4298946 (accessed July, 2021).

Kokelj, S. V., Lantz, T. C., Solomon, S., Pisaric, M. F. J., Keith, D., Morse, P., et al. (2012). Using Multiple Sources of Knowledge to Investigate Northern Environmental Change: Regional Ecological Impacts of a Storm Surge in the Outer Mackenzie Delta, N.W.T. *Arctic* 65, 257–272. doi:10.14430/arctic4214

Lantuit, H., Overduin, P. P., and Wetterich, S. (2013). Recent Progress Regarding Permafrost Coasts. *Permafrost Periglac. Process.* 24 (2), 120–130. doi:10.1002/ppp.1777

Lantz, T. C., Kokelj, S. V., and Fraser, R. H. (2015). Ecological Recovery in an Arctic delta Following Widespread saline Incursion. *Ecol. Appl.* 25 (1), 172–185. doi:10.1890/14-0239.1

Lapham, L. L., Dallimore, S. R., Magen, C., Henderson, L. C., Powers, L. C., Gonsior, M., et al. (2020). Microbial Greenhouse Gas Dynamics Associated with Warming Coastal Permafrost, Western Canadian Arctic. *Front. Earth Sci.* 8, 576. doi:10.3389/feart.2020.582103

Lapka, S. (2013). Oceanic Storm Surges in the Outer Mackenzie Delta, NWT Canada: Remote Sensing of Tundra Disturbance and Restoration from saline Intrusion. [master's thesis]. Calgary (AB): University of Calgary.

Larsen, H. A. (1948). *The North-West Passage 1940-1942 and 1944- the Famous Voyages of the Royal Canadian Mounted Police Schooner "St. Roch'*. City Archives, Vancouver Canada: Open Library of the University of British Columbia. Available at: https://open.library.ubc.ca/collections/bcbooks/items/1.0391835#p1z-4r1440f:Tuktoyaktuk%20 (accessed July, 2021).

Leonard, L. J., Rogers, G. C., and Mazzotti, S. (2012). A Preliminary Tsunami hazard Assessment of the Canadian Coastline. *Geol. Surv. Can. Open File.* 7201, 119. doi:10.4095/292067

Leonard, L. J., Rogers, G. C., and Mazzotti, S. (2014). Tsunami Hazard Assessment of Canada. *Nat. Hazards* 70 (1), 237–274. doi:10.1007/s11069-013-0809-5

Liew, M., Xiao, M., Jones, B. M., Farquharson, L. M., and Romanovsky, V. E. (2020). Prevention and Control Measures for Coastal Erosion in Northern High-Latitude Communities: A Systematic Review Based on Alaskan Case Studies. *Environ. Res. Lett.* 15 (9), 093002. doi:10.1088/1748-9326/ab9387

Lim, M., Whalen, D., Martin, J., Mann, P. J., Hayes, S., Fraser, P., et al. (2020). Massive Ice Control on Permafrost Coast Erosion and Sensitivity. *Geophys. Res. Lett.* 47 (17), e2020GL087917. doi:10.1029/2020gl087917

Manson, G. K., and Solomon, S. M. (2007). Past and Future Forcing of Beaufort Sea Coastal Change. *Atmosphere-Ocean* 45 (2), 107–122. doi:10.3137/ao.450204

Marsh, P., and Schmidt, T. (1993). Influence of a Beaufort Sea Storm Surge on Channel Levels in the Mackenzie Delta. *Arctic* 46, 35–41. doi:10.14430/arctic1319

M. Meredith, M. Sommerkorn, S. Cassotta, C. Derksen, A. Ekaykin, and A. Hollowed (Editors) (2019). *IPCC Special Report on the Oceans and Cryosphere in a Changing Climate* (Geneva: Intergovernmental Panel on Climate Change). Available at: https://repository.library.noaa.gov/view/noaa/27411/noaa_27411_DS1.pdf (accessed March, 2021).

Mosher, D. (2009). International Year of Planet Earth 7. Oceans: Submarine Landslides and Consequent Tsunamis in Canada. *Geosci. Can.* 36 (4), 179–190. Available at: https://www.erudit.org/en/journals/geocan/2014-v41-n2-geocan36_4/geocan36_4ser04/(accessed January, 2021).

Murphy, E., Nistor, I., Cornett, A., Wilson, J., and Pilechi, A. (2021). Fate and Transport of Coastal Driftwood: A Critical Review. *Mar. Pollut. Bull.* 170, 112649. doi:10.1016/j.marpolbul.2021.112649

National Oceanic and Atmospheric Administration (NOAA) (2020). Sea Level Trends. Relative Sea Level Trend 970-211 Tuktoyaktuk, Canada. Available at: https://tidesandcurrents.noaa.gov/sltrends/sltrends_station.shtml?id=970-211 (Accessed March 14, 2020).

Natural Resources Canada (2020). Canadian Spatial Reference System-Precise Point Positioning. Available at: https://webapp.geod.nrcan.gc.ca/geod/tools-outils/ppp.php (Accessed October 15, 2020).

Natural Resources Canada (2021). Station Report. Available at: https://webapp.geod.nrcan.gc.ca/geod/data-donnees/station/report-rapport.php?id=M039008 (Accessed January 22, 2021).

O'Rourke, M. J. E. (2017). Archaeological Site Vulnerability Modelling: The Influence of High Impact Storm Events on Models of Shoreline Erosion in the Western Canadian Arctic. *Open Archaeol* 3 (1), 1–16. doi:10.1515/opar-2017-0001

Overeem, I., Anderson, R. S., Wobus, C. W., Clow, G. D., Urban, F. E., and Matell, N. (2011). Sea Ice Loss Enhances Wave Action at the Arctic Coast. *Geophys. Res. Lett.* 38 (17), a–n. doi:10.1029/2011GL048681

Paull, C. K., Dallimore, S. R., Caress, D. W., Gwiazda, R., Lundsten, E., Anderson, K., et al. (2021). A 100-km Wide Slump along the Upper Slope of the Canadian Arctic Was Likely Preconditioned for Failure by Brackish Pore Water flushing. *Mar. Geology.* 435, 106453. doi:10.1016/j.margeo.2021.106453

Permanent Service for Mean Sea Level (PSMSL) (2021). Tuktoyaktuk. Available online at: https://www.psmsl.org/data/obtaining/stations/1000.php (Accessed January 22, 2021).

Pisaric, M. F. J., Thienpont, J. R., Kokelj, S. V., Nesbitt, H., Lantz, T. C., Solomon, S., et al. (2011). Impacts of a Recent Storm Surge on an Arctic Delta Ecosystem Examined in the Context of the Last Millennium. *Proc. Natl. Acad. Sci.* 108 (22), 8960–8965. doi:10.1073/pnas.1018527108

Ramsey, C. B. (2009). Dealing with Outliers and Offsets in Radiocarbon Dating. *Radiocarbon* 51 (3), 1023–1045. doi:10.1017/S0033822200034093

Reimer, P. J., Bard, E., Bayliss, A., Beck, J. W., Blackwell, P. G., Ramsey, C. B., et al. (2013). IntCal13 and Marine13 Radiocarbon Age Calibration Curves 0-50,000 Years Cal BP. *Radiocarbon* 55 (4), 1869–1887. doi:10.2458/azu_js_rc.55.16947

Reimnitz, E., and Maurer, D. K. (1979). Effects of Storm Surges on the Beaufort Sea Coast, Northern Alaska. *Arctic* 32 (4), 329–344. Available at: https://www.jstor.org/stable/40509007 (accessed November, 2020). doi:10.14430/arctic2631

Reimnitz, E., and Maurer, D. K. (1978). Storm Surges in the Alaskan Beaufort Sea. US Geol. Survey Open File, 78–593. Available at: http://dggs.alaska.gov/webpubs/usgs/of/text/of78-0593.pdf (accessed June 11, 2019).

Riedel, M., King, E. L., Cameron, G. D. M., Blasco, S., Conway, K. W., Dallimore, S. R., et al. (2021). A Chronology of Post-Glacial Mass-Transport Deposits on the Canadian Beaufort Slope. *Mar. Geology.* 433, 106407. doi:10.1016/j.margeo.2020.106407

Sander, L., Kirdyanov, A., Crivellaro, A., and Büntgen, U. (2021). Short Communication: Driftwood Provides Reliable Chronological Markers in Arctic Coastal Deposits. *Geochronology* 3 (1), 171–180. doi:10.5194/gchron-3-171-2021

Screen, J. A., and Simmonds, I. (2010). The Central Role of Diminishing Sea Ice in Recent Arctic Temperature Amplification. *Nature* 464, 1334–1337. doi:10.1038/nature09051

Serreze, M. C., Holland, M. M., and Stroeve, J. (2007). Perspectives on the Arctic's Shrinking Sea-Ice Cover. *Science* 315 (5818), 1533–1536. doi:10.1126/science.1139426

Shah, V. K. (1982). Performance of Sand-Filled Tube Shore Protection Tuktoyaktuk, North West Territories, Canada. *Coastal Eng.* 1982, 1901–1913. doi:10.1061/9780872623736.114

Shaw, J., Taylor, R. B., Solomon, S., Christian, H. A., and Forbes, D. L. (1998). Potential Impacts of Global Sea-Level Rise on Canadian Coasts. *Can. Geographer* 42 (4), 365–379. doi:10.1111/j.1541-0064.1998.tb01352.x

Thomas, M. A., Mota, A., Jones, B. M., Choens, R. C., Frederick, J. M., and Bull, D. L. (2020). Geometric and Material Variability Influences Stress States Relevant to Coastal Permafrost bluff Failure. *Front. Earth Sci.* 8, 143. doi:10.3389/feart.2020.00143

Van der Sluijs, J., Kokelj, S., Fraser, R., Tunnicliffe, J., and Lacelle, D. (2018). Permafrost Terrain Dynamics and Infrastructure Impacts Revealed by UAV Photogrammetry and thermal Imaging. *Remote Sensing* 10 (11), 1734. doi:10.3390/rs10111734

Vermaire, J. C., Pisaric, M. F. J., Thienpont, J. R., Courtney Mustaphi, C. J., Kokelj, S. V., and Smol, J. P. (2013). Arctic Climate Warming and Sea Ice Declines Lead to Increased Storm Surge Activity. *Geophys. Res. Lett.* 40 (7), 1386–1390. doi:10.1002/grl.50191

Whalen, D., Forbes, D. L., Hopkinson, C., Lavergne, J. C., Manson, G. K., Marsh, P., et al. (2009). "Topographic LiDAR-Providing a New Perspective in the Mackenzie Delta," in Proc. 30th Canadian Symposium on Remote Sensing, Lethbridge, Alberta. Available at: http://scholar.ulethbridge.ca/sites/default/files/hopkinson/files/whalen_etal_csrs_lethbridge2009.pdf?m=1458144712 (accessed June, 2020).

Yang, D., Shi, X., and Marsh, P. (2015). Variability and Extreme of Mackenzie River Daily Discharge during 1973-2011. *Quat. Int.* 380-381, 159–168. doi:10.1016/j.quaint.2014.09.023

Conflict of Interest: The authors declare that the research was conducted in the absence of any commercial or financial relationships that could be construed as a potential conflict of interest.

The handling editor is currently organizing a Research Topic with one of the authors SD.

Publisher's Note: All claims expressed in this article are solely those of the authors and do not necessarily represent those of their affiliated organizations, or those of the publisher, the editors, and the reviewers. Any product that may be evaluated in this article, or claim that may be made by its manufacturer, is not guaranteed or endorsed by the publisher.

frontiers in Earth Science

ORIGINAL RESEARCH
published: 21 February 2022
doi: 10.3389/feart.2022.694062

Merging Satellite and *in situ* Data to Assess the Flux of Terrestrial Dissolved Organic Carbon From the Mackenzie River to the Coastal Beaufort Sea

Clément Bertin[1]*, *Atsushi Matsuoka*[2,3], *Antoine Mangin*[4], *Marcel Babin*[2] and *Vincent Le Fouest*[1]

[1]LIttoral ENvironnement et Sociétés (LIENSs)—UMR 7266, La Rochelle, France, [2]Takuvik Joint International Laboratory, CNRS, Québec, QC, Canada, [3]Institute for the Study of Earth, Oceans, and Space, University of New Hampshire, Durham, NH, United States, [4]ACRI-ST, Sophia Antipolis, France

In response to global warming, the Arctic is undergoing rapid and unprecedented changes that alter the land-to-sea forcing in large Arctic rivers. Improving our knowledge of terrestrial dissolved organic carbon (tDOC) flux to the coastal Arctic Ocean (AO) is thus critical and timely as these changes strongly alter the biogeochemical cycles on AO shelves. In this study, we merged riverine *in situ* tDOC concentrations with satellite ocean-color estimates retrieved at the land-marine interface of the Mackenzie Delta to make a first assessment of the tDOC export from its main outlets to the shelf. We combined tDOC and river discharge data to develop a regression model that simulated tDOC concentrations and fluxes from daily to interannual (2003–2017) time scales. We then compared the simulated satellite-derived estimates to those simulated by the model constrained by *in situ* tDOC data only. As the satellite tDOC estimates reflect the delta effect in terms of tDOC enrichment and removal, our results inform us of how much tDOC can potentially leave the delta to reach the ocean (1.44 ± 0.14 $TgC.yr^{-1}$). The chemodynamic relationships and the model suggest contrasting patterns between Shallow Bay and the two easternmost delta outlets, which can be explained by the variability in their geomorphological settings. At the seasonal scale and for all outlets, the satellite-derived tDOC export departs from the estimate based on *in situ* tDOC data only. During the river freshet in May, the satellite-derived tDOC export is, on average, ~15% (Shallow Bay) to ~20% (Beluga Bay) lower than the in situ-derived estimate. This difference was the highest (–60%) in 2005 and exceeds 30% over most of the last decade, and can be explained by qualitative and quantitative differences between the $tDOC_{in\ situ}$ and $tDOC_{sat}$ datasets in a period when the freshet is highly variable. In contrast, in summer and fall, the satellite-derived tDOC export is higher than the in situ-derived estimate. The temporal difference between the satellite and in situ-derived export estimates suggests that predicting seasonal tDOC concentrations and fluxes from remote Arctic deltas to the coastal AO remains a challenge for assessing their impact on already changing carbon fluxes.

Keywords: terrestrial DOC, land-to-sea interface, permafrost, Mackenzie delta, space remote sensing

OPEN ACCESS

Edited by:
Louise Farquharson, University of Alaska Fairbanks, United States

Reviewed by:
Eurico D'Sa, Louisiana State University, United States
Benjamin M. Jones, University of Alaska Fairbanks, United States

***Correspondence:**
Clément Bertin
clement.bertin1@univ-lr.fr

Specialty section:
This article was submitted to Biogeoscience, a section of the journal Frontiers in Earth Science

Received: *12 April 2021*
Accepted: *12 January 2022*
Published: *21 February 2022*

Citation:
Bertin C, Matsuoka A, Mangin A, Babin M and Le Fouest V (2022) Merging Satellite and in situ Data to Assess the Flux of Terrestrial Dissolved Organic Carbon From the Mackenzie River to the Coastal Beaufort Sea. Front. Earth Sci. 10:694062. doi: 10.3389/feart.2022.694062

1 INTRODUCTION

In response to climate change, the Arctic is undergoing unprecedented changes in both its watersheds and coastal ocean. Since the 1970s in the Arctic, the surface air temperature has increased by 2.7°C (Box et al., 2019) resulting into an increase of the sea surface temperature in summer (Timmermans and Labe, 2021). These changes alter the land-to-sea forcing with important regional and basin-wide implications for sea ice formation, ocean stratification and heat flux, underwater light regime, nutrients delivery, and marine ecosystems (Searcy et al., 1996; Mulligan et al., 2010; Brown et al., 2020; Juhls et al., 2020). Arctic rivers' discharge and permafrost are key components of this coupling. Northern permafrost contains 1,460–1,600 Gt of organic carbon in the form of frozen organic matter, nearly twice as much as carbon than is currently in the atmosphere (Tarnocai et al., 2009; Schuur et al., 2015). Most of this carbon is stored in the Arctic, where permafrost covers 65% of Russian (Tumel, 2002) and 50% of Canadian lands (Vincent et al., 2017). This carbon pool represents about half the world's soil carbon (Hugelius et al., 2014).

Riverine freshwater inputs to the Arctic Ocean (AO) are the largest of any ocean per basin volume (Opsahl et al., 1999). The Arctic hydrological cycle has intensified resulting in a steady increase in the liquid flow of pan-Arctic rivers over the past 30 years (Box et al., 2019). Because of rapid permafrost thaw, the export flux of terrigenous dissolved organic carbon (tDOC) to the coastal AO tends to increase (Fritz et al., 2017) and reaches rates of change as high as 39% in the Mackenzie River system during the 1978–2012 period (Tank et al., 2016). In addition, the land-to-sea flux of terrestrial organic carbon mobilized through coastline erosion has nearly doubled between 1955 and 2018 (Bristol et al., 2021). Once in the coastal AO, a fraction of this riverine and eroded tDOC pool can be degraded and further mineralized into inorganic carbon (Lønborg, 2020, and reference therein) that in turn likely unbalances the delicate air-sea gas exchanges on shelves (Manizza et al., 2013; Spencer et al., 2016; Tanski et al., 2016; Tanski et al., 2021).

In this context, there is a growing need to quantify land-to-sea fluxes of tDOC and to investigate the coastal ecosystem response at the seasonal scale, where the physical-biogeochemical interactions play a role on AO shelves. Such an effort has been considerably reinforced since the 2000s with the PARTNERS/ArcticGRO (AGRO) pan-Arctic monitoring program (Holmes et al., 2020; Shiklomanov et al., 2020), which provides high-quality *in situ* measurements of tDOC concentrations. Watershed models also improved considerably to become high-value predictive tools (McGuire et al., 2016) but still require improvements in their ability to resolve the complex mechanistic processes behind tDOC mobilization and transformation within Arctic watersheds (Kicklighter et al., 2013; Liao et al., 2019). Field observations thus remain essential to further understand the coastal ecosystem responses.

The remoteness of Arctic rivers imposes that *in situ*-based tDOC fluxes are estimated up to hundreds of kilometers upstream from their main outlets and based on only a few measurements per year (~4 on average; Holmes et al., 2020). This strongly hampers a robust assessment of the estimated tDOC export from the land-marine transition to the coastal AO waters and, most importantly, precludes any effect of the delta on concentrations (enrichment/removal) (see Kipp et al., 2020). Using radiometric satellite data, Griffin et al. (2018) more than doubled the number of available data during the open water season and highlighted the strong variability of tDOC estimates that can be observed within Arctic rivers systems. Juhls et al. (2020) highlighted the synoptic (~ 4 days) variability of tDOC concentrations within the Lena Delta and point out the growing need to assess tDOC concentrations within the land-ocean interface. The high-frequency sampling improved the yearly assessment of tDOC export to Laptev Sea and highlighted the strong seasonality of tDOC quality (Juhls et al., 2020).

In the present study, we investigate the value of merging *in situ* tDOC concentrations with radiometric satellite tDOC estimates retrieved within nearshore waters at the three main outlets of the Mackenzie Delta in the assessment of the seasonal to interannual flux of tDOC to the shelf. The paper is organized as follows. First, we provide an overview of the Mackenzie watershed and delta. Second, we describe the approach used to simulate tDOC concentrations and fluxes within the Mackenzie Shelf. Then, we compare the simulated tDOC concentrations and fluxes with and without the inclusion of satellite tDOC concentration estimates. Finally, we discuss the potential of coastal satellite tDOC data in assessing the seasonal to interannual flux of tDOC to the AO with perspectives for future developments.

2 MATERIALS AND METHODS

We estimated daily tDOC concentrations ($tDOC_{est}$) and fluxes from the Mackenzie River to the shelf (**Figure 1**) using the USGS load estimator (LOADEST) model (Runkel et al., 2004). This modeling approach was successfully applied in Arctic rivers to simulate tDOC fluxes from sparse *in situ* data (Holmes et al., 2012; Tank et al., 2016; Shrestha et al., 2019). The tDOC data nomenclature further used in the paper and the data treatment and procedure to simulate the daily tDOC fluxes and concentrations are given in **Figure 2**.

2.1 Study Area

The Mackenzie Delta is located in the westernmost Canadian Arctic in the southeastern Beaufort Sea (**Figure 1**). It is the second largest delta in the AO (Burn and Kokelj, 2009), whose waters spread into the most riverine of all pan-Arctic shelves with respect to its size and residence time (Macdonald et al., 1988). The Mackenzie River drains a 1.68 million km^2 wide area and brings, on average, 306 km^3 of fresh water into the AO each year (Mulligan and Perrie, 2019). Permafrost underlies 82% of this massive watershed (Holmes et al., 2013) and the soil organic carbon content of Mackenzie deltaic alluvium is estimated to 34–41 PgC (Tarnocai et al., 2009; Hugelius et al., 2014). Riverine freshwater reaches the coastal ocean through a complex river network made of channels of different sizes of which the main ones end up into three major outlets: Shallow Bay, Beluga Bay and Kugmallit Bay (Morley, 2012). The three coastal bays are shallow but differ by their geology upstream and their ocean geomorphological settings downstream on the shelf. On the West, a flat topography and numerous lakes and

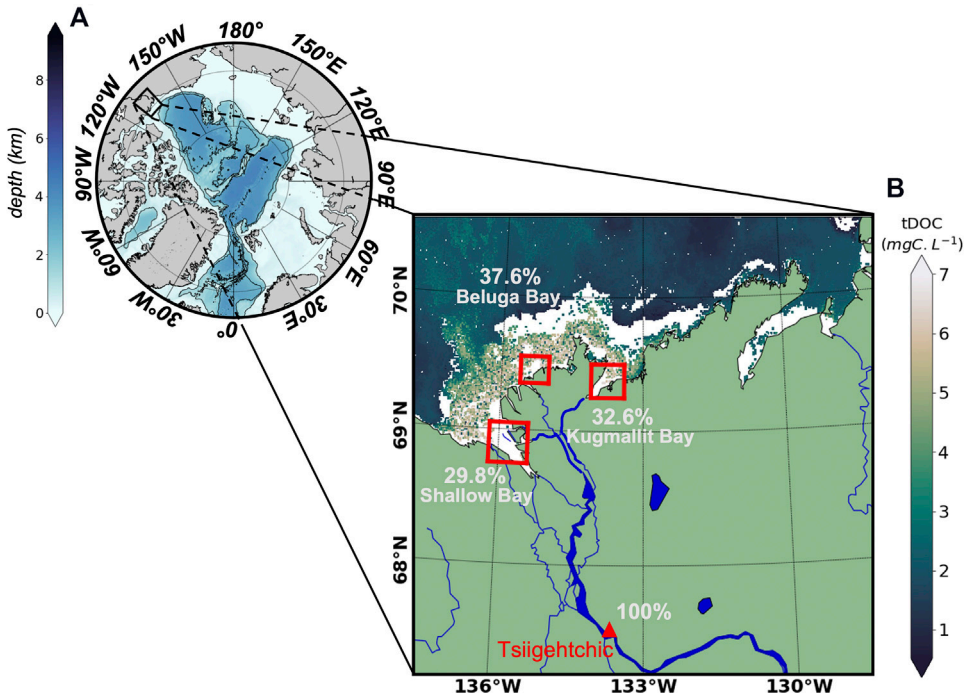

FIGURE 1 | Polar stereographic map of **(A)** the Arctic Ocean bathymetry with the northeastern Beaufort Sea delimited in black and **(B)** the Mackenzie Delta area with the *in situ* (ArcticGRO/PARTNERS, red triangle) and satellite (red squares) sampling locations overlaid. For each outlet of the Mackenzie Delta, the weights applied to the total river discharge measured at the Tsiigehtchic station are given. An AMODIS satellite scene of tDOC concentration (28 August 2007) is overlaid.

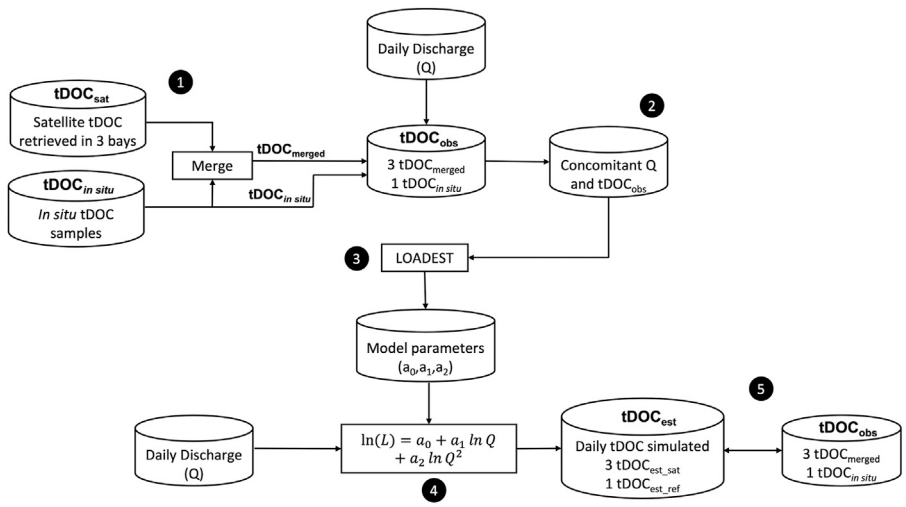

FIGURE 2 | Schematic representation of the procedure used to generate the simulated tDOC flux and concentrations with the LOADEST model. Numbers 1–5 refer to the main steps fully detailed in the Materials and Methods section.

channels surround Shallow Bay (Nill et al., 2019). The bay is supplied by three main river channels and its plateau rapidly ends up as a deep canyon. By contrast, Beluga Bay extends far into the coastal ocean. The low-lying grounds of this northernmost part of the delta are mainly inundated tundra composed of sedge and lakes grading into marshes (Harper, 1990; Burn and Kokelj, 2009). The easternmost part of the delta, Kugmallit Bay, which is characterized by rolling hills and termorkarst lakes is highly subject to environmental changes (Nill et al., 2019). The Mackenzie River outflow into the ocean is modulated by the presence of a persistent ice barrier (stamukha; Carmack et al., 2004) close to the shelf,

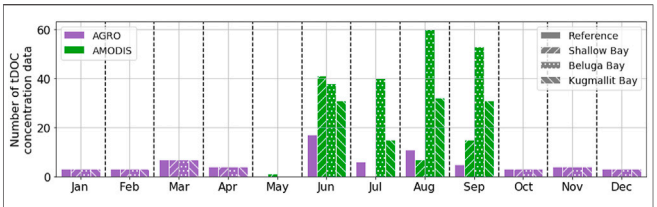

FIGURE 3 | Monthly distribution of available *in situ* (AGRO) and satellite (AMODIS) tDOC concentrations over the 2003–2017 period. The solid patterns refer to the "Reference" dataset, whereas the dotted and hatched patterns refer to the "Satellite" datasets.

whose break-up results into pulses of freshwater discharge (Doxaran et al., 2015; Matsuoka et al., 2016).

2.2 The *in situ* and Satellite-Derived Data: tDOC Concentration and River Discharge

We used *in situ* tDOC ($tDOC_{in\ situ}$) concentrations and freshwater discharge data (2003–2017) from the water quality dataset provided by the Arctic Great River Observatory (ArcticGRO; Holmes et al., 2020; Shiklomanov et al., 2020). Data encompassed the PARTNERS (2003–2007), ArcticGRO I (2009–2012), II (2012–2016) and III (2017–2020) campaigns. Data were sampled at the Tsiigehtchic station (67.45°N, 133.74°W) about 200 km upstream of the Mackenzie Delta (**Figure 1**). River discharge was measured daily over the whole period (2003–2017), whereas the sampling frequency of tDOC concentrations was year-dependent (0–7 measurements per year).

Satellite-derived tDOC ($tDOC_{sat}$) concentration estimates were determined for the same time period as *in situ* data (2003–2017) from radiometric spectral reflectance data retrieved with a 1 km horizontal resolution at nadir by the Moderate-Resolution Imaging Spectro-radiometer (MODIS) aboard the Aqua satellite (AMODIS). 1,051 scenes constituted the satellite dataset for the entire period (2003–2017). Colored dissolved organic matter (CDOM) absorbance at 443 nm ($a_{CDOM(\lambda=443)}$) was derived from spectral reflectance data using the semi-analytical algorithm of Matsuoka et al. (2013). $tDOC_{sat}$ concentrations were estimated by applying satellite-derived $a_{CDOM(\lambda=443)}$ data to an empirical relationship between *in situ* tDOC concentration and $a_{CDOM(\lambda=443)}$. This relationship ($DOC = 10^{2.532}.a_{CDOM}(443)^{0.448}$) was established using data across different seasons and areas, allowing its application to the whole AO (Matsuoka et al., 2017). The mean uncertainty of the satellite estimates of DOC concentrations was 28% (Matsuoka et al., 2017). The seasonal contribution to both *in situ* and satellite-derived tDOC data used in this study is given in **Figure 3**.

2.3 Merging the *in situ*/Satellite tDOC Data

We generated one *in situ*/satellite merged dataset for Shallow Bay, Beluga Bay and Kugmallit Bay. Between May and September (open water season), we substituted the $tDOC_{in\ situ}$ concentrations by the $tDOC_{sat}$ concentrations available. We then merged the satellite data with the $tDOC_{in\ situ}$ concentrations available between October and april to generate a merged tDOC ($tDOC_{merged}$) dataset for each outlet (step 1, **Figure 2**). For each satellite scene, we subsampled $tDOC_{sat}$ concentrations within a 600 km^2, 306 and 441 km^2 surface area for Shallow Bay, Beluga Bay and Kugmallit Bay, respectively (**Figure 1**). We calculated the median of all valid pixels only when 50% had non-missing $tDOC_{sat}$ values to limit biases due to sea ice or cloud cover. To compute the $tDOC_{sat}$ flux, we weighted the freshwater discharge at the three delta outlets based on the channels contributions reported by Morley (2012). We estimated the percentage of the total river discharge measured at the Tsiigehtchic station that was delivered to Shallow Bay, Beluga Bay and Kugmallit Bay to 29.8, 37.6 and 32.6%, respectively (Morley, 2012; Blackburn et al., 2015) (**Figure 1**). To account for the water transport between the Tsiigehtchic station located 250 km upstream on the river path and the delta outlets, we applied a +1 day offset on the river discharge data. We estimated this value by multiplying the daily river discharge with the mean distance between the Tsiigehtchic station and the delta outlets (250 km), the mean width of the Mackenzie River at Tsiigehtchic (1 km) and the water level measured by the Water Survey of Canada at Tsiigehtchic station. We obtained four $tDOC_{obs}$ datasets: three based on $tDOC_{merged}$ data for each delta outlet (hereafter "Satellite") and 1 based on $tDOC_{in\ situ}$ data only (hereafter "Reference").

2.4 The LOADEST Modeling Approach

2.4.1 The Model Selection

We constrained the LOADEST model with time coincident observations of tDOC concentration ($tDOC_{obs}$) and freshwater discharge (Q) data to build up a logarithmic relationship between the tDOC load (equivalent to daily flux) and river discharge based on the following general **Equation 1**:

$$\ln(L) = a_0 + a_1 \ln Q + a_2 \ln Q^2 + a_3 \sin(2\pi dtime) + a_4 \cos(2\pi dtime) + a_5 dtime + a_6 dtime^2 \quad (1)$$

where L is tDOC load ($kg.day^{-1}$), Q the river discharge ($m^3.s^{-1}$), $dtime$ the decimal time (YYYYMMDD) and $a_n\,(n\epsilon[0;6])$ the n regression coefficients. The multicollinearity between the explanatory variables ln Q and $dtime$ was handled by a centering procedure as follow:

$$X_{LOADEST} = X - \bar{X} + \frac{\sum (X - \bar{X})^3}{2.\sum (X - \bar{X})^2} \quad (2)$$

where X was either $dtime$ or $\ln Q$.

Based on the Akaike Information Criterion (AIC) (Akaike, 1974), the LOADEST approach allowed to select the best fitting model through nine different combination of the terms included in **Equation (1)** (**Supplementary Table S1**).

We chose the model by calculating a first estimate of both $\ln(L)$ and $tDOC_{est}$ concentrations based on time coincident ArcticGRO $tDOC_{in\ situ}$ and discharge data through the automated regression model selection set in LOADEST (model 0). According to the AIC, LOADEST selected two different models as best fitting models (models 2 and 7, **Supplementary Table S1**). By referring to the Schwarz Posterior Probability Criterion (SPPC) also computed as an AIC comparative parameter, model 2 (**Eq. (3)**) was identified as the most accurate:

$$\ln(L) = a_0 + a_1 \ln Q + a_2 \ln Q^2 \quad (3)$$

Furthermore, model 2 precluded any spurious numerical trend induced by the *dtime* explanatory variable present in model 7. We thus assumed model 2 (**Eq. (3)**) as the best regression model to assess daily tDOC fluxes and concentrations entering the Mackenzie shelf.

2.4.2 Simulated Daily tDOC Concentration and Flux

We applied model 2 to all $tDOC_{obs}$ datasets to highlight the effect of satellite data on the tDOC flux assessment. For each $tDOC_{obs}$ dataset, we first extracted river discharge data concomitant with available $tDOC_{obs}$ data from the entire daily river discharge dataset (step 2, **Figure 2**). In LOADEST, these data were then used to constrain model 2 to retrieve the regression coefficients (a_0, a_1 and a_2) of the model (step 3, **Figure 2**). Finally, we ran model 2 using the regression coefficients thus obtained and forced it with the entire daily river discharge data to simulate the tDOC flux at the daily scale (step 4, **Figure 2**). From the simulated flux, we calculated back the $tDOC_{est}$ concentrations at daily scale by dividing the daily flux by the river discharge. We thus obtained a "Reference" estimate of tDOC concentration ($tDOC_{est\_ref}$) from model 2 ran with the regression coefficients derived from the $tDOC_{in\ situ}$/Q relationship (see step 3, **Figure 2**). Similarly, we obtained three "Satellite" estimates of tDOC concentration ($tDOC_{est\_sat}$) derived from each outlet-specific $tDOC_{merged}$/Q relationship (step 3, **Figure 2**) for Shallow Bay, Beluga Bay and Kugmallit Bay. We give the constants obtained for each regression model in **Supplementary Table S2**.

2.5 Comparison of Simulated *Versus* Observed tDOC Concentrations

We used four comparison metrics to compare the tDOC concentrations simulated by model 2 ($tDOC_{est}$) based on the *in situ* data (hereafter $tDOC_{est\_ref}$) and merged *in situ*/satellite data (hereafter $tDOC_{est\_sat}$) with the time coincident observed ($tDOC_{obs}$) (step 5, **Figure 2**). We calculated the correlation coefficient (*r*), the Nash-Sutcliffe model efficiency index (NSE), the unbiased Root Mean Square Error (URMSE), and the Median Percent Error (MPE) as follows:

$$r = \sqrt{1 - \frac{\sum_{n=1}^{N} (tDOC_{obs} - tDOC_{est})^2}{\sum_{n=1}^{N} (tDOC_{est} - \langle tDOC_{est} \rangle_n)^2}} \quad (4)$$

$$NSE = \frac{\sum_{n=1}^{N} (tDOC_{obs} - \langle tDOC_{obs} \rangle_n)^2 - \sum_{n=1}^{N} (tDOC_{obs} - tDOC_{est})^2}{\sum_{n=1}^{N} (tDOC_{obs} - \langle tDOC_{obs} \rangle_n)^2} \quad (5)$$

$$URMSE = \sqrt{\frac{\sum_{n=1}^{N} ((tDOC_{est} - tDOC_{obs}) - (\langle tDOC_{est} \rangle_n - \langle tDOC_{obs} \rangle_n))^2}{N}} \quad (6)$$

$$MPE = Median\left(100. \left| \frac{tDOC_{est} - tDOC_{obs}}{tDOC_{obs}} \right| \right) \quad (7)$$

The NSE (unitless) relates the residual variance (i.e. the "noise") between the $tDOC_{est}$ and $tDOC_{obs}$ values to the variance within the $tDOC_{obs}$ values (i.e. the "information") (see Nash and Sutcliffe, 1970). A NSE value of 1 indicates that the noise is null. A NSE value near 0 means the noise is comparable to the observed variance suggesting that the simulated values are as accurate as the observed mean. A negative NSE value suggests that the mean value of observations is a better predictor than the model. The URMSE measures the size of the discrepancies between the simulated and observed values. The MPE is the median of the absolute percentage error and provides insights on the regression model accuracy.

We also calculated the relative error between the "Reference" and "Satellite" daily tDOC flux estimates as follows:

$$\delta\alpha_r = 100 * \frac{\sum \phi_{Sat} - \phi_{Ref}}{\phi_{Ref}} \quad (8)$$

where ϕ_{Sat} and ϕ_{Ref} are the "Satellite" and "Reference" daily tDOC flux, respectively.

3 RESULTS

3.1 Chemodynamic Q-tDOCobs Relationships

The relationships between the $tDOC_{obs}$ concentrations and associated freshwater river discharge suggested the presence of two distinct clusters, which distinguished by the river discharge intensity and the source of available tDOC data (**Figure 4**). A first cluster corresponded to the sea-ice covered season (October to april) characterized by a low river discharge and $tDOC_{in\ situ}$ concentrations only. A second cluster reflected open water (May to September) conditions with a higher river discharge and mostly $tDOC_{sat}$ concentrations. We used the Spearman correlation coefficient (*r*) to assess the strength of the relationships between the coincident river discharge Q and the $tDOC_{obs}$ concentrations (i.e. $tDOC_{in\ situ}$ or $tDOC_{merged}$) in the full dataset (January to December) and the same dataset but restricted to the open water season (May to September) (**Table 1**). The $tDOC_{obs}$ concentrations did not follow a Normal distribution (Shapiro test, $p < 0.05$), except for $tDOC_{in\ situ}$ during the open water season (Shapiro test, $p > 0.05$) for which a Pearson correlation coefficient was used. In all datasets, *r* was positive when accounting for the full ($0.48 < r < 0.79$) and open water ($0.39 < r < 0.79$) data. Compared to Q-$tDOC_{in\ situ}$ relationships, the strength of the correlation in the merged datasets varied amongst the delta outlets. The merging of satellite-derived and *in situ* tDOC concentrations increased the Q-$tDOC_{obs}$ correlation in Shallow Bay in both datasets (r = 0.79) compared to Q-$tDOC_{in\ situ}$ ($0.59 < r < 0.68$). In Kugmallit Bay, *r* was similar in the full dataset (r = 0.58 *versus* r = 0.59) but decreased in the open water season (r = 0.43 *versus* r = 0.68). In Beluga Bay, *r* decreased in both the full (r = 0.48 *versus* r = 0.59) and open water (r = 0.43 *versus* r = 0.68) datasets. This suggests that the strength of the Q-$tDOC_{merged}$ relationship was sensitive to the $tDOC_{sat}$ concentration retrieved nearby each outlet of the delta, with Beluga Bay differing markedly from the other two bays.

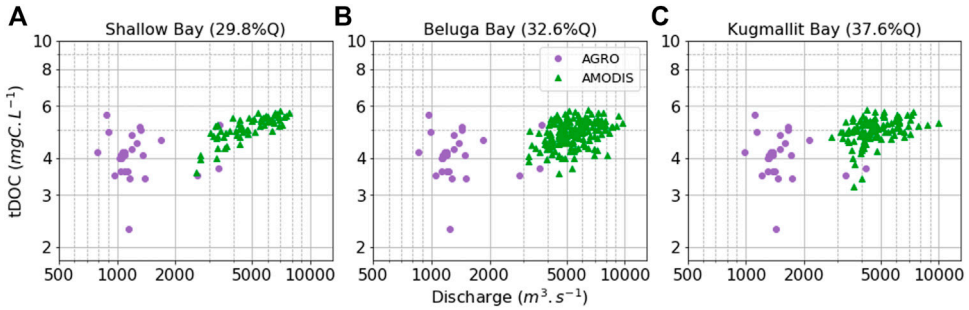

FIGURE 4 | Q-tDOC relationships for the merged in situ-satellite dataset ($tDOC_{merged}$) on **(A)** Shallow Bay, **(B)** Beluga Bay and **(C)** Kugmallit Bay. Green triangles indicate the satellite tDOC concentration estimates (AMODIS). Purple dots indicate the *in situ* tDOC measurements (AGRO). Note the logarithmic scales on both axes.

TABLE 1 | Correlation coefficients between the river discharge and the $tDOC_{in\ situ}$ ("Reference" dataset) or $tDOC_{merged}$ ("Satellite" datasets) concentrations for all data and the open water season data (May-September). Bold values indicate a Person correlation coefficient; the Spearman correlation coefficient is used otherwise (*** p-value < 0.001).

Dataset	All data	Open water data
Reference	0.59***	**0.68*** **
Satellite—Shallow Bay	0.79***	0.79***
Satellite—Beluga Bay	0.48***	0.39***
Satellite—Kugmallit Bay	0.58***	0.43***

TABLE 2 | Comparison metrics between the simulated $tDOC_{est\_ref}$ and $tDOC_{in\ situ}$ concentrations ("Reference") and between the simulated $tDOC_{est\_sat}$ and the $tDOC_{merged}$ concentrations ("Satellite").

Metrics	Reference	Satellite		
		Shallow bay	Beluga bay	Kugmallit bay
N	66	91	218	136
R	0.66	0.76	0.52	0.60
NSE	0.44	0.58	0.27	0.35
URMSE	0.82	0.46	0.45	0.50
MPE	12.74	4.37	5.68	6.01

n, Number of data available; r, correlation coefficient; NSE, Nash-Sutcliffe efficient index; URMSE, Unbiased Root Mean Square Error ($mgC.L^{-1}$); MPE, median percent error.

3.2 Simulated tDOC Concentrations: Merged vs. *in situ* Datasets

We used quantitative metrics to compare the simulated $tDOC_{est\_ref}$ and $tDOC_{est\_sat}$ concentrations with the observed $tDOC_{in\ situ}$ and $tDOC_{merged}$ concentrations, respectively (**Table 2**). The number of $tDOC_{obs}$ data increased with the inclusion of the remotely sensed $tDOC_{sat}$ estimates. In Shallow Bay, the increase reached 38% while it was 2-fold and 3-fold in Kugmallit and Beluga Bay, respectively. The data dispersion (URMSE) between $tDOC_{in\ situ}$ and $tDOC_{est\_ref}$ concentrations was 0.82 mgC L^{-1}. When using $tDOC_{est\_sat}$ estimates, URMSE decreased by 39–45%. The median percent error (MPE) between the $tDOC_{in\ situ}$ and the $tDOC_{est\_ref}$ concentrations was 12.7%. The MPE decreased by 2-fold (Kugmallit and Beluga bays) to 3-fold (Shallow Bay) with the $tDOC_{est\_sat}$ estimates. The correlation coefficient (r) varied little among the Reference and Satellite datasets and was relatively high (0.52–0.76), which suggested a high goodness-of-fit. With respect to the "Reference" estimates (r = 0.66), *r* increased in Shallow Bay but decreased in Beluga Bay. The Nash-Sutcliffe model efficiency index (NSE) showed a pattern similar to that depicted by *r*. The NSE between the $tDOC_{in\ situ}$ and $tDOC_{est\_ref}$ concentrations was 0.44 suggesting that the regression model was a fairly good predictor of the observed concentrations. Using $tDOC_{est\_sat}$, the NSE remained positive increasing in Shallow Bay (NSE = 0.58) but decreasing in Beluga Bay (NSE = 0.27). Overall, $tDOC_{est\_sat}$ estimates simulated in Beluga Bay departed the most from the observed $tDOC_{merged}$ concentrations (**Table 2**). These results mirrored with the lowest Q-$tDOC_{merged}$ correlation coefficients estimated in Beluga Bay (**Table 1**).

TABLE 3 | Comparison metrics between the simulated $tDOC_{est\_sat}$ and the $tDOC_{merged}$ concentrations ("Satellite"). in Beluga Bay according to the C50 (50% valid pixels), C40 (40% valid pixels), C60 (60% valid pixels) and 2C50 (2-fold larger surface area +50% valid pixels) subsampling conditions.

Metrics	C50	C40	C60	2C50
N	218	303	120	258
R	0.52	0.50	0.50	0.42
NSE	0.27	0.25	0.25	0.18
URMSE	0.45	0.47	0.47	0.45
MPE	5.68	5.83	5.01	5.66

n, Number of data available; r, correlation coefficient; NSE, Nash-Sutcliffe efficient index; URMSE, Unbiased Root Mean Square Error ($mgC.L^{-1}$); MPE, median percent error.

3.3 Sensitivity Analysis on the Remotely-Sensed Data Subsampling

We tested the hypothesis that the predictive ability of the regression model applied to Beluga Bay was sensitive to the AMODIS data subsampling conditions. We then calculated the median of $tDOC_{sat}$ concentration estimates for each of the three new conditions: 40% of valid pixels (C40), 60% of valid pixels (C60), and a 2-fold subsampling surface area along with 50% of valid pixels (2C50). From these conditions, we simulated three

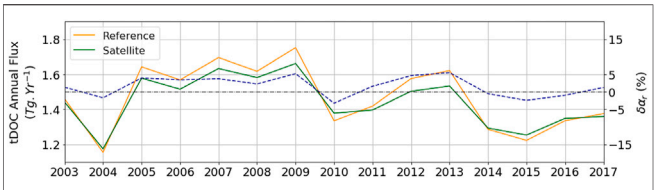

FIGURE 5 | Simulated annual tDOC flux ($TgC.yr^{-1}$) estimated from the "Reference" dataset (orange line) and the "Satellite" dataset (green line). The dashed blue line represents the error of the "Satellite" estimate relative to the "Reference" estimate ($\delta\alpha_r$, %).

new $tDOC_{est\_sat}$ concentration estimates based on the three new $tDOC_{merged}$ datasets obtained according to the same method described in **Section 2**. For each subsampling condition, we used the metrics to compare with the subsampling condition of 50% of valid pixel (C50) we previously applied (**Table 3**). Between the C50 and C60 conditions, the data quantity dropped by 45%. The correlation coefficient, the NSE and the URMSE were similar, whereas the MPE was slightly improved. Between the C50 and C40 conditions, the data quantity increased by 39% and all metrics showed limited variations. Overall, the amplitude of change of the comparison metrics between C40, C50 and C60 (**Table 3**) was much lower than between the "Reference" and "Satellite" estimates (**Table 2**, **3**). By contrast, a doubling of the sampled surface area (2C50, +18% of $tDOC_{sat}$ data) led to a decrease of r and the NSE compared to C40, C50, C60 and "Reference" estimate. However, no marked changes in the URMSE and MPE were observed. Increasing the number of $tDOC_{sat}$ data by widening the subsampled area decreased the strength of the correlation and increased the noise between the simulated $tDOC_{est\_sat}$ and the observed $tDOC_{merged}$ concentrations. Overall, the simulated $tDOC_{est\_sat}$ concentrations obtained in 2C50 departed the most from the simulated $tDOC_{est\_ref}$ estimates (**Table 2**, **3**).

3.4 Annual and Seasonal Patterns of the Simulated tDOC Flux

Over 2003–2017, we simulated the yearly flux of tDOC based on the simulated $tDOC_{est\_ref}$ and the $tDOC_{est\_sat}$ concentrations obtained for the three delta outlets. We estimated the total "Satellite" flux by summing the flux simulated at each outlet. The total yearly flux was 1.47 ± 0.18 (*min* 1.15 – *max* 1.75) and 1.44 ± 0.14 (*min* 1.17 – *max* 1.66) $TgC.yr^{-1}$ for the "Reference" and "Satellite" datasets, respectively. Both flux estimates showed comparable interannual patterns. The relative error between the "Satellite" and the "Reference" estimates did not exceed 5% (**Figure 5**). The yearly flux increased between 2004 and 2009 (1.17–1.66 $TgC.yr^{-1}$) and tended to decrease between 2010 and 2017. However, the yearly flux did not show any significant interannual trend over the 15 years ($r = -0.3$, $p > 0.05$).

Although we reported no substantial differences between the simulated "Reference" and "Satellite" $tDOC_{est}$ flux estimates at the annual scale, both departed at the seasonal scale (**Figure 6**). During the seasonal peak of river discharge in May, the "Satellite" flux estimate was lower than the "Reference" flux estimate by 15% (Shallow Bay) to 20% (Beluga Bay) on average. Such a difference in the tDOC flux estimates coincides with unevenly distributed tDOC concentrations amongst the datasets in June (**Figure 7**). By contrast, between mid-July and November the "Satellite" flux estimate was on average higher than the "Reference" flux estimate. In November, the mean difference reached 12 and 17% in Shallow Bay and Kugmallit Bay, respectively. At the interannual scale, the relative error on the total simulated tDOC flux reported at the spring river freshet exhibited a high variability (**Figure 8**). From 2011 to 2017, the "Satellite" flux estimate was generally more than 30% lower than the "Reference" flux estimate. The highest interannual difference was reached in 2005, when the "Satellite" flux estimate was ~60% lower than the "Reference" flux estimate.

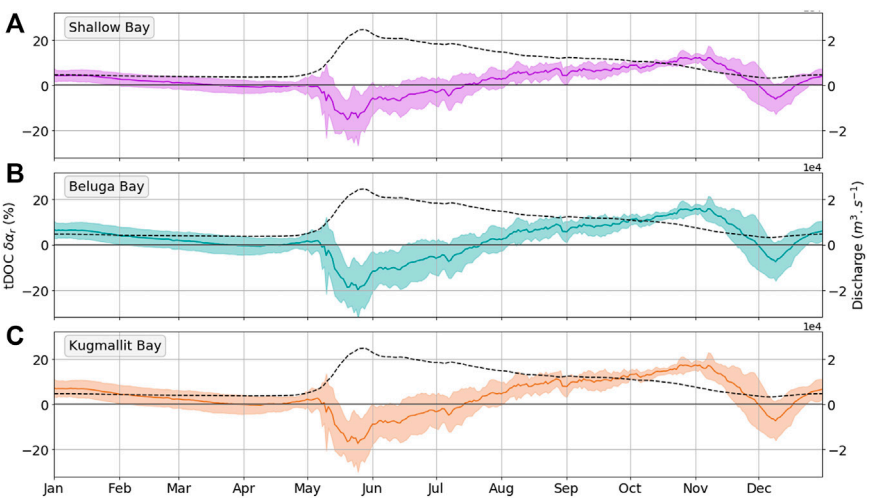

FIGURE 6 | Error of the simulated daily tDOC flux estimated from the "Satellite" dataset relative to the "Reference" estimate ($\delta\alpha_r$, %) averaged over the 2003–2017 period for **(A)** Shallow Bay, **(B)** Beluga Bay and **(C)** Kugmallit Bay. The shaded area represents the mean ± SD. The black dashed line corresponds to the daily freshwater river discharge averaged over the 2003–2017 period.

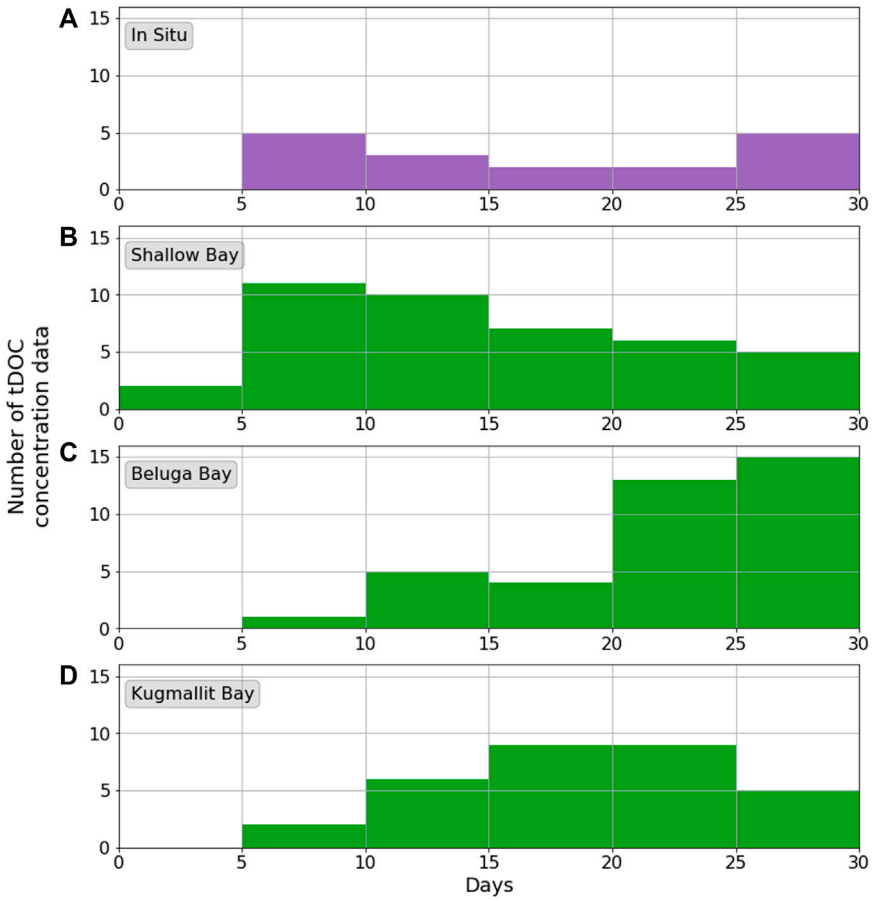

FIGURE 7 | Temporal distribution in June (2003–2017) of the **(A)** $tDOC_{in\ situ}$ concentrations, and **(B)** $tDOC_{sat}$ concentrations for Shallow Bay, **(C)** Beluga Bay and **(D)** Kugmallit Bay.

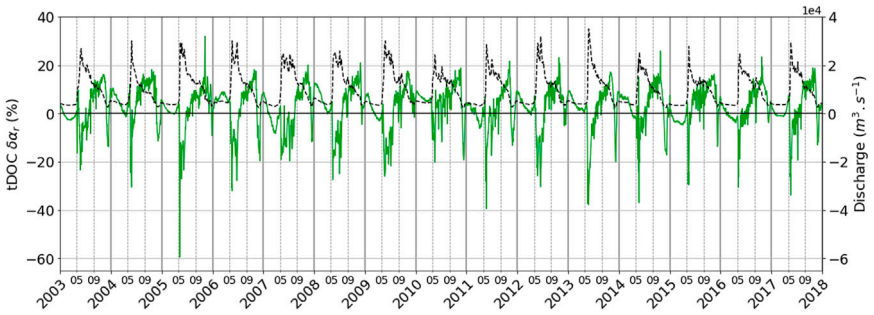

FIGURE 8 | Error of the simulated daily tDOC flux estimated from the "Satellite" dataset relative to the "Reference" estimate ($\delta\alpha_r$, %) (green line) and daily freshwater river discharge (black dashed line).

4 DISCUSSION

4.1 A Complex Land-To-Sea Interface

The presence of a chemodynamic Q-tDOC relationship, i.e. the higher the river discharge the higher the tDOC concentration, reported upstream in the Mackenzie River path is widely accepted (Raymond et al., 2007; Holmes et al., 2012; Shrestha et al., 2019). In the Peel River catchment, Shrestha et al. (2019) suggested a significant Q-tDOC correlation (r = 0.52), which is in the range of the values we report in this study ($0.48 < r < 0.79$). This result

suggests that the positive Q-tDOC chemodynamic relationship estimated more than 200 km upstream from the delta also applies to the fluvial-marine interface farther downstream. Our results show that the chemodynamic Q-$tDOC_{merged}$ relationship varies amongst the three delta outlets and is the weakest in Beluga Bay (r = 0.48). Such a decrease in the Q-$tDOC_{merged}$ relationship for Beluga Bay suggests a less conservative behavior of the tDOC concentrations. After the spring freshet, the river water is stored in deltaic lakes and floods the vegetated floodplain (Normandin et al., 2018), which can modify its chemistry before draining to the delta channels and ultimately to the Mackenzie Shelf (Emmerton et al., 2008a). Processes like autotrophic production and leaching can enhance tDOC levels in river water over a wide range of variability (15–350%) as tDOC is transported through the delta (Emmerton et al., 2008a; Kipp et al., 2020). In the upper part of the delta, tDOC removal through the flocculation process (up to 45%; Kipp et al., 2020) can occur at low salinities in the more estuarine waters and can outbalance the delta enrichment effect. All these processes likely play a role in explaining the distinct Q-$tDOC_{merged}$ relationship we observe for Beluga Bay. In this part of the delta, the alluvial plain is low-lying (<2 m) and intersected by an important network of lakes and channels. In spring, the delta is flooded with freshwater during the freshet (Mackay, 1974). In summer and fall, it is very exposed to the ocean influence and occasionally flooded when strong North-Northwestern winds trigger storm surges and marine intrusions into the delta (Mackay, 1974; Marsh and Schmidt, 1993; Manson and Solomon, 2007). Storm surges can be severe and flood the delta with saline waters over tens of kilometers inland from the coast leading to substantial changes in vegetation (Pisaric et al., 2011; Kokelj et al., 2012; Lantz et al., 2015). High surface area flooding in Beluga Bay compared to the east and west of the upper delta area (Kuenzer et al., 2015) may lead to differences in the mobilization and biogeochemistry of tDOC at the fluvial-marine transition. As satellite tDOC estimates retrieved at the fluvial-marine transition reflect the delta effect in terms of tDOC enrichment and removal, our results inform on how much tDOC can potentially leave the delta to reach the coastal ocean.

The weaker Q-$tDOC_{merged}$ relationship reported in Beluga Bay (r = 0.48), and to a lesser extent in Kugmallit Bay (r = 0.58), likely explains the difference in the model performance between the three delta outlets. Overall, the use of $tDOC_{sat}$ data in the model improves the match between the simulated ($tDOC_{est\_sat}$) and observed ($tDOC_{obs}$) concentrations. This is particularly true for Shallow Bay for which the Q-$tDOC_{merged}$ relationship is the strongest (r = 0.79) even compared to the Q-$tDOC_{in\ situ}$ relationship (r = 0.59). There is growing evidence that tDOC concentrations and quality vary in the course of the main channels of the Mackenzie Delta (Emmerton et al., 2008b; Griffin et al., 2018; Kipp et al., 2020; Schwab et al., 2020). The use of satellite tDOC retrieved in nearshore waters in the very close vicinity of the delta outlets allows for the effect of regional biogeochemical signatures to be considered in the estimated land-to-sea fluxes of tDOC. The satellite tDOC concentrations are most likely due to bio- and photo-degradation processes (Gonçalves-Araujo et al., 2015; Matsuoka et al., 2015) that occur upstream along the river path and that watersheds model are not yet able to represent (Rawlins et al., 2021). Our approach implicitly accounts for these processes without explicitly describing them as their weight on the downstream fate of tDOC is not yet well understood. Nevertheless, caution should be addressed to local non-deltaic sources of tDOC to the ocean. Offshore the delta, strong winds erode the shoreline permafrost of the Beluga Bay Islands, which may deliver extra carbon to the coastal waters (Lim et al., 2020). These inputs, however, may be limited compared to those originating from the delta (Tanski et al., 2016). Assuming a shoreline of 2,077 km for our study area (Harper, 1990) and a tDOC flux of 1.37 $kgC.m^{-1}.yr^{-1}$ (Bristol et al., 2021), coastal erosion would translate into a tDOC flux of ~3.10^{-6} $TgC.yr^{-1}$ into the shelf. This flux is several order of magnitude lower than the riverine flux estimated between 1.04–1.76 $TgC.yr^{-1}$ (Macdonald et al., 1988; Dittmar and Kattner, 2003; Raymond et al., 2007; Holmes et al., 2012; Le Fouest et al., 2013).

4.2 The Seasonal Shift of tDOC Flux

The mean annual flux of tDOC we estimated using satellite-derived tDOC data ($tDOC_{est\_sat}$ = 1.44 ± 0.14 TgC) fits within the reported range, which was estimated from different methodologies using punctual field measurements, climatologies and/or regression model (1.04–1.76; Macdonald et al., 1988; Dittmar and Kattner, 2003; Raymond et al., 2007; Holmes et al., 2012; Le Fouest et al., 2013). The use of satellite data has no marked impact on the interannual variability but on the seasonality of the simulated tDOC concentrations and fluxes. From May to June, when the river freshet occurs, the $tDOC_{est\_sat}$ export flux represents up to ~40% of the total annual flux. Compared to the simulated tDOC export flux estimated from *in situ* data only, we report a decrease in the $tDOC_{est\_sat}$ flux in May at the onset of the seasonal peak of river discharge. According to the delta outlet, this decrease reaches 15–20%, on average, but can reach up to 60%. This decrease occurs between winter and the beginning of the open water season, when the data quantity and temporal distribution of $tDOC_{in\ situ}$ and $tDOC_{sat}$ start to differ (April-June, **Figure 3**). In June, the $tDOC_{sat}$ data quantity is higher ($31 < n < 41$) than in the $tDOC_{in\ situ}$ dataset (n = 17). While the medians of the tDOC concentration compare among the datasets ($tDOC_{in\ situ}$ = 5.3 $mgC.L^{-1}$, 5.0 < $tDOC_{merged}$<5.4 $mgC.L^{-1}$), the amplitude of variation is lower in the $tDOC_{merged}$ dataset (4.1–5.8 $mgC.L^{-1}$) than in the $tDOC_{in\ situ}$ dataset (4.2–8.1 $mgC.L^{-1}$). The $tDOC_{in\ situ}$ data quantity is mostly evenly distributed throughout June, whereas it increases in Beluga Bay, and to a lesser extent in Kugmallit Bay, to reach a maximum at the end of June (**Figure 7**). Such differences between the $tDOC_{in\ situ}$ and $tDOC_{sat}$ datasets likely constrain the constants obtained for each regression model (**Supplementary Figure S1**), which in turn translate into different tDOC flux estimates in this period of the year when the freshet occurs (**Figures 6**, **7**). Ocean color data are usually not available in May due to the presence of landfast ice in the Mackenzie Delta. Some data could be available between the landfast and pack ice but could be unreliable due to the high snow/ice albedo. New space sensors such as Sentinel-2/MSI or Landsat-8/OLI could

help overcome this drawback by significantly improving the spatial resolution of imagery (~30 m). Nevertheless, caution should be addressed to the pixel contamination due to the adjacency effect or sub-pixel-contamination, especially for landfast ice problematics. For now, uncertainties related to the lack of data during the freshet period hamper the model capacity to simulate the land-to-sea flux of tDOC in this critical period of the year.

The temporal shift in the seasonal distribution of the land-to-sea flux of tDOC induced by the use of satellite tDOC data, i.e. a decrease in May-June and an increase in July-November, may have implications on both the physical and biogeochemical settings of the coastal Beaufort Sea. In the Mackenzie Delta, tDOC has a high potential for biological degradation at the spring freshet (Gareis and Lesack, 2020; Behnke et al., 2021). A decrease of the riverine flux in May-June would imply that a lesser fraction of bioavailable tDOC would be delivered and potentially processed by heterotrophic bacteria within the marine ecosystem (Colatriano et al., 2018; Vaqué et al., 2019). In turn, as most of the tDOC is colored (~94%; Matsuoka et al., 2017) and then absorbs light, phytoplankton might leverage more favorable light conditions in this period because less tDOC would be delivered by the Mackenzie Delta to the coastal waters. Whether such a decrease of the tDOC flux at the spring freshet will have a substantial impact on the heterotrophic-autotrophic balance remains to be determined. In contrast, tDOC is rather refractory in summer, because the biological removal is enhanced and the enrichment limited along the river path (Holmes et al., 2008). A steady increase of the tDOC flux between July and November as we report in our study could then translate into a greater proportion of tDOC that escapes remineralization and accumulates in the oceanic waters. Because the interannual variability of this seasonal shift is high, such biogeochemical responses might be exacerbated in the future. This is particularly true in a context of Arctic warming, which is expected to alter both the river discharge seasonality and the quality of the tDOC exported (see Behnke et al., 2021).

4.3 Future Developments

Using satellite tDOC data, we increased the size of the dataset available during the ice-free period by more than 39%, which is comparable to the study of Griffin et al. (2018) focused on inland waters within the Mackenzie River. The chemodynamic relationships and metrics we estimated for Beluga Bay suggest that the median of the satellite-derived tDOC concentration was sensitive to the subsampling procedure of the remote sensing scenes. The sensitivity analysis suggests that the model is not highly sensitive to the number of valid pixels in satellite scenes but rather to the size of the subsampled surface area. As a larger subsampled area may reflect more contrasted environmental conditions, it may alter the value of the tDOC concentration median. Compared to the other two delta outlets, the differences between the simulated and observed tDOC concentrations reported for Beluga Bay could then indicate a different tDOC dynamics within the land-to-sea interface. For all bays, the robustness of the model to the number of data within a subsampled area allows for some flexibility in the methodology, because it may offset potential issues related to cloud and/or sea ice cover. In addition, we will leverage newer space sensors such as Sentinel-2/MSI or Landsat-8/OLI to improve the spatial and temporal resolution (i.e. high-resolution ocean color data are available every 3–5 days when all available sensors are used) of radiometric records in nearshore Arctic environments. If the pixel contamination due to sea ice could be overcome, such remotely sensed data would provide tDOC concentrations estimates at the immediate vicinity of the streams' mouth, hence limiting the effect of tDOC degradation/enrichment occurring upstream on the delta estimate. With respect to river discharge, we used daily time-series measured ~100 km upstream the delta to constrain the regression model within the upper part of the delta at the land-ocean transition. The forthcoming Surface Water and Ocean Topography (SWOT) space mission that aims to measure river water surface elevation, top width, and free-surface slope might allow periodic estimation of freshwater discharge for Arctic rivers wider than 50 m (Biancamaria et al., 2016; Durand et al., 2016). As tDOC concentrations are also related to the watershed slope (Connolly et al., 2020), these new promising data combined with satellite tDOC retrievals in nearshore waters might help refine the land-to-sea flux of tDOC in the upper Mackenzie Delta.

Since the past 17 years, the ArcticGRO/PARTNERS program led to a large and very highly valuable dataset of water quality for the Mackenzie River. The sampling frequency is on a monthly basis spanning from January to December with a mean sampling frequency of about 4 days each year. In the Arctic, the retrieval of tDOC from space is limited to the open water season (mostly from June to September). *In situ* measurements of freshwater discharge and tDOC concentrations at the sea ice break-up and spring freshet are hence essential to constrain a regression model as we used in our study and to generate a realistic seasonal cycle of tDOC concentration and flux. In a context of Arctic warming, it is important to maintain and eventually extend such a water quality monitoring to gain robustness in model predictions. Besides, new datasets such as for the Mackenzie river temperature (Tokuda et al., 2019) could further be used to improve the regression models and then to better predict the seasonal to interannual tDOC dynamics (see Shrestha et al., 2019) in response to climate change.

5 CONCLUSION

This study investigated the value of merging riverine *in situ* tDOC concentrations with satellite ocean-color estimates retrieved at the three main outlets of the second largest Arctic Delta to assess the seasonal to interannual flux of tDOC to the coastal AO. By using satellite observations, we show that we can substantially increase the quantity of data available during the open water season to constrain predictive

regression models. We also identified a spatial variability in the tDOC concentrations and flux amongst the three main delta outlets likely reflecting distinct biogeochemical patterns within the land-to-sea interface. The robustness of the approach suggests it could be applied to other Arctic deltas/estuaries to assess the pan-Arctic flux of tDOC if reliable remotely sensed tDOC data are available in such complex land-to-sea interfaces (see Juhls et al., 2019). However, our results also highlight that such predictive models would require more *in situ* and satellite-derived tDOC data especially in fall-winter and at the sea ice breakup to improve their ability to resolve the strong seasonal variability that prevails in such critical and remote environments. There is evidence now that the Arctic permafrost thaw alters both quantitatively and qualitatively the coastal waters biogeochemistry. It then motivates the need to quantify the land-to-sea fluxes of terrestrial organic matter at high spatial and temporal resolution to further investigate the coastal ecosystem response at the synoptic and seasonal time scales at which operates the physical-biogeochemical coupling in the ocean. In addition, the fraction of terrestrial organic matter outgassed into CO_2 through marine physicochemical and microbial processes remains very uncertain although it might unbalance the delicate air-sea gas exchanges. Assessing in a robust way the terrestrial fluxes of organic matter to the coastal ocean is thus paramount to better understand and predict how changes in the land-sea linkages might alter the coastal carbon budget and air-sea CO_2 fluxes at regional scale in the AO.

DATA AVAILABILITY STATEMENT

The raw data supporting the conclusions of this article will be made available by the authors, without undue reservation.

AUTHOR CONTRIBUTIONS

AtM and MB created and shared the original satellite dataset. CB organized the database and performed simulations and data processing. CB, AtM, AnM and VF analysed simulations and data processing results. CB wrote the first draft of the manuscript. All authors contributed to manuscript revision, read, and approved the submitted version.

FUNDING

CB was supported by a PhD fellowship from the French Ministry of Higher Education, Research and Innovation. This work is part of the Nunataryuk project. The project has received funding under the European Union's Horizon 2020 Research and Innovation Programme under grant agreement no. 773421. This work was also funded by the Centre National de la Recherche Scientifique (CNRS, LEFE program). Part of this research was supported by Japan Aerospace Exploration Agency (JAXA) Global Change Observation Mission-Climate (GCOM-C) to AM (contract #19RT000542). This work was supported by the NASA Earth Science Division's Interdisciplinary Science (IDS) program through an award to the Jet Propulsion Laboratory, California Institute of Technology, under contract with National Aeronautics and Space Administration (80NM0018D0004).

SUPPLEMENTARY MATERIAL

The Supplementary Material for this article can be found online at: https://www.frontiersin.org/articles/10.3389/feart.2022.694062/full#supplementary-material

REFERENCES

Akaike, H. (1974). A New Look at the Statistical Model Identification. *IEEE Trans. Automat. Contr.* 19, 716–723. doi:10.1109/TAC.1974.1100705

Behnke, M. I., McClelland, J. W., Tank, S. E., Kellerman, A. M., Holmes, R. M., Haghipour, N., et al. (2021). Pan-Arctic Riverine Dissolved Organic Matter: Synchronous Molecular Stability, Shifting Sources and Subsidies. *Glob. Biogeochem Cycles* 35, e2020GB006871. doi:10.1029/2020GB006871

Biancamaria, S., Lettenmaier, D. P., and Pavelsky, T. M. (2016). The SWOT Mission and its Capabilities for Land Hydrology. *Surv. Geophys.* 37, 307–337. doi:10.1007/s10712-015-9346-y

Blackburn, J., She, Y., Hicks, F., and Nafziger, J. (2015). "Ice Effects on Flow Distributions in the Mackenzie Delta," in 18 th Workshop on the Hydraulics of Ice Covered River, Québec City, Canada, 15.

Box, J. E., Colgan, W. T., Christensen, T. R., Schmidt, N. M., Lund, M., Parmentier, F.-J. W., et al. (2019). Key Indicators of Arctic Climate Change: 1971-2017. *Environ. Res. Lett.* 14, 045010. doi:10.1088/1748-9326/aafc1b

Bristol, E. M., Connolly, C. T., Lorenson, T. D., Richmond, B. M., Ilgen, A. G., Choens, R. C., et al. (2021). Geochemistry of Coastal Permafrost and Erosion-Driven Organic Matter Fluxes to the Beaufort Sea Near Drew Point, Alaska. *Front. Earth Sci.* 8, 598933. doi:10.3389/feart.2020.598933

Brown, K. A., Holding, J. M., and Carmack, E. C. (2020). Understanding Regional and Seasonal Variability Is Key to Gaining a Pan-Arctic Perspective on Arctic Ocean Freshening. *Front. Mar. Sci.* 7, 606. doi:10.3389/fmars.2020.00606

Burn, C. R., and Kokelj, S. V. (2009). The Environment and Permafrost of the Mackenzie Delta Area. *Permafrost Periglac. Process.* 20, 83–105. doi:10.1002/ppp.655

Carmack, E., Macdonald, R., and Jasper, S. (2004). Phytoplankton Productivity on the Canadian Shelf of the Beaufort Sea. *Mar. Ecol. Prog. Ser.* 277, 37–50. doi:10.3354/meps277037

Colatriano, D., Tran, P. Q., Guéguen, C., Williams, W. J., Lovejoy, C., and Walsh, D. A. (2018). Genomic Evidence for the Degradation of Terrestrial Organic Matter by Pelagic Arctic Ocean Chloroflexi Bacteria. *Commun. Biol.* 1, 90. doi:10.1038/s42003-018-0086-7

Connolly, C. T., Cardenas, M. B., Burkart, G. A., Spencer, R. G. M., and McClelland, J. W. (2020). Groundwater as a Major Source of Dissolved Organic Matter to Arctic Coastal Waters. *Nat. Commun.* 11, 1479. doi:10.1038/s41467-020-15250-8

Dittmar, T., and Kattner, G. (2003). The Biogeochemistry of the River and Shelf Ecosystem of the Arctic Ocean: a Review. *Mar. Chem.* 83, 103–120. doi:10.1016/S0304-4203(03)00105-1

Doxaran, D., Devred, E., and Babin, M. (2015). A 50 % Increase in the Mass of Terrestrial Particles Delivered by the Mackenzie River into the Beaufort Sea (Canadian Arctic Ocean) over the Last 10 Years. *Biogeosciences* 12, 3551–3565. doi:10.5194/bg-12-3551-2015

Durand, M., Gleason, C. J., Garambois, P. A., Bjerklie, D., Smith, L. C., Roux, H., et al. (2016). An Intercomparison of Remote Sensing River Discharge Estimation Algorithms from Measurements of River Height, Width, and Slope. *Water Resour. Res.* 52, 4527–4549. doi:10.1002/2015WR018434

Emmerton, C. A., Lesack, L. F. W., and Vincent, W. F. (2008a). Mackenzie River Nutrient Delivery to the Arctic Ocean and Effects of the Mackenzie Delta during Open Water Conditions. *Glob. Biogeochem. Cycles* 22. doi:10.1029/2006gb002856

Emmerton, C. A., Lesack, L. F. W., and Vincent, W. F. (2008b). Nutrient and Organic Matter Patterns across the Mackenzie River, Estuary and Shelf during the Seasonal Recession of Sea-Ice. *J. Mar. Syst.* 74, 741–755. doi:10.1016/j.jmarsys.2007.10.001

Fritz, M., Vonk, J. E., and Lantuit, H. (2017). Collapsing Arctic Coastlines. *Nat. Clim Change* 7, 6–7. doi:10.1038/nclimate3188

Gareis, J. A. L., and Lesack, L. F. W. (2020). Ice-out and Freshet Fluxes of CO2 and CH4 across the Air-Water Interface of the Channel Network of a Great Arctic delta, the Mackenzie. *Polar Res.* 39. doi:10.33265/polar.v39.3528

Gonçalves-Araujo, R., Stedmon, C. A., Heim, B., Dubinenkov, I., Kraberg, A., Moiseev, D., et al. (2015). From Fresh to Marine Waters: Characterization and Fate of Dissolved Organic Matter in the Lena River Delta Region, Siberia. *Front. Mar. Sci.* 2, 108. doi:10.3389/fmars.2015.00108

Griffin, C. G., McClelland, J. W., Frey, K. E., Fiske, G., and Holmes, R. M. (2018). Quantifying CDOM and DOC in Major Arctic Rivers during Ice-free Conditions Using Landsat TM and ETM+ Data. *Remote Sensing Environ.* 209, 395–409. doi:10.1016/j.rse.2018.02.060

Harper, J. R. (1990). Morphology of the Canadian Beaufort Sea Coast. *Mar. Geology.* 91, 75–91. doi:10.1016/0025-3227(90)90134-6

Holmes, R. M., Coe, M. T., Fiske, G. J., Gurtovaya, T. Y., McClelland, J. W., Shiklomanov, A. I., et al. (2013). Climate Change Impacts on the Hydrology and Biogeochemistry of Arctic Rivers. *Glob. Impacts Clim. Change Inland Waters* 51, 3–20.

Holmes, R. M., McClelland, J. W., Peterson, B. J., Tank, S. E., Bulygina, E., Eglinton, T. I., et al. (2012). Seasonal and Annual Fluxes of Nutrients and Organic Matter from Large Rivers to the Arctic Ocean and Surrounding Seas. *Estuaries and Coasts* 35, 369–382. doi:10.1007/s12237-011-9386-6

Holmes, R. M., McClelland, J. W., Raymond, P. A., Frazer, B. B., Peterson, B. J., and Stieglitz, M. (2008). Lability of DOC Transported by Alaskan Rivers to the Arctic Ocean. *Geophys. Res. Lett.* 35, L03402. doi:10.1029/2007GL032837

Holmes, R. M., McClelland, J. W., Tank, S. E., Spencer, R. G. M., and Shiklomanov, A. I. (2020). Water Quality Dataset, Version YYYYMMDD. Arctic Great Rivers Observatory. Available at: https://www.arcticgreatrivers.org/data.

Hugelius, G., Strauss, J., Zubrzycki, S., Harden, J. W., Schuur, E. a. G., Ping, C.-L., et al. (2014). Estimated Stocks of Circumpolar Permafrost Carbon with Quantified Uncertainty Ranges and Identified Data Gaps. *Biogeosciences* 11, 6573–6593. doi:10.5194/bg-11-6573-2014

Juhls, B., Overduin, P. P., Hölemann, J., Hieronymi, M., Matsuoka, A., Heim, B., et al. (2019). Dissolved Organic Matter at the Fluvial-marine Transition in the Laptev Sea Using *In Situ* Data and Ocean Colour Remote Sensing. *Biogeosciences* 16, 2693–2713. doi:10.5194/bg-16-2693-2019

Juhls, B., Stedmon, C. A., Morgenstern, A., Meyer, H., Hölemann, J., Heim, B., et al. (2020). Identifying Drivers of Seasonality in Lena River Biogeochemistry and Dissolved Organic Matter Fluxes. *Front. Environ. Sci.* 8, 53. doi:10.3389/fenvs.2020.00053

Kicklighter, D. W., Hayes, D. J., McClelland, J. W., Peterson, B. J., McGuire, A. D., and Melillo, J. M. (2013). Insights and Issues with Simulating Terrestrial DOC Loading of Arctic River Networks. *Ecol. Appl.* 23, 1817–1836. doi:10.1890/11-1050.1

Kipp, L. E., Henderson, P. B., Wang, Z. A., and Charette, M. A. (2020). Deltaic and Estuarine Controls on Mackenzie River Solute Fluxes to the Arctic Ocean. *Estuaries and Coasts* 43, 1992–2014. doi:10.1007/s12237-020-00739-8

Kokelj, S. V., Lantz, T. C., Solomon, S., Pisaric, M. F. J., Keith, D., Morse, P., et al. (2012). Using Multiple Sources of Knowledge to Investigate Northern Environmental Change: Regional Ecological Impacts of a Storm Surge in the Outer Mackenzie Delta, N.W.T. *ARCTIC* 65, 257–272. doi:10.14430/arctic4214

Kuenzer, C., Klein, I., Ullmann, T., Georgiou, E., Baumhauer, R., and Dech, S. (2015). Remote Sensing of River Delta Inundation: Exploiting the Potential of Coarse Spatial Resolution, Temporally-Dense MODIS Time Series. *Remote Sensing* 7, 8516–8542. doi:10.3390/rs70708516

Lantz, T. C., Kokelj, S. V., and Fraser, R. H. (2015). Ecological Recovery in an Arctic delta Following Widespread saline Incursion. *Ecol. Appl.* 25, 172–185. doi:10.1890/14-0239.1

Le Fouest, V., Babin, M., and Tremblay, J.-É. (2013). The Fate of Riverine Nutrients on Arctic Shelves. *Biogeosciences* 10, 3661–3677. doi:10.5194/bg-10-3661-2013

Liao, C., Zhuang, Q., Leung, L. R., and Guo, L. (2019). Quantifying Dissolved Organic Carbon Dynamics Using a Three-Dimensional Terrestrial Ecosystem Model at High Spatial-Temporal Resolutions. *J. Adv. Model. Earth Syst.* 11, 4489–4512. doi:10.1029/2019MS001792

Lim, M., Whalen, D., J. Mann, P. P., Fraser, P., Berry, H. B., Irish, C., et al. (2020). Effective Monitoring of Permafrost Coast Erosion: Wide-Scale Storm Impacts on Outer Islands in the Mackenzie Delta Area. *Front. Earth Sci.* 8, 454. doi:10.3389/feart.2020.561322

Lønborg, C., Carreira, C., Jickells, T., and Álvarez-Salgado, X. A. (2020). Impacts of Global Change on Ocean Dissolved Organic Carbon (DOC) Cycling. *Front. Mar. Sci.* 7, 24. doi:10.3389/fmars.2020.00466

Macdonald, R. W., Iseki, K., O'Brien, M. C., McLaughlin, F. A., McCullough, D., Macdonald, D. M., et al. (1988). *NOGAP B-6. Volume 5, Chemical Data Collected in the Beaufort Sea and Mackenzie River Delta, March-July 1987*. Canada: Fisheries and Oceans.

Mackay, J. R. (1974). *The Mackenzie Delta Area, N.W.T (Miscellaneous Report/ Geological Survey of Canada)*. Ottawa: Geological Survey of Canada.

Manizza, M., Follows, M. J., Dutkiewicz, S., Menemenlis, D., Hill, C. N., and Key, R. M. (2013). Changes in the Arctic Ocean CO2sink (1996-2007): A Regional Model Analysis. *Glob. Biogeochem. Cycles* 27, 1108–1118. doi:10.1002/2012GB004491

Manson, G. K., and Solomon, S. M. (2007). Past and Future Forcing of Beaufort Sea Coastal Change. *Atmosphere-Ocean* 45, 107–122. doi:10.3137/ao.450204

Marsh, P., and Schmidt, T. (1993). Influence of a Beaufort Sea Storm Surge on Channel Levels in the Mackenzie Delta. *ARCTIC* 46, 35–41. doi:10.14430/arctic1319

Matsuoka, A., Babin, M., and Devred, E. C. (2016). A New Algorithm for Discriminating Water Sources from Space: A Case Study for the Southern Beaufort Sea Using MODIS Ocean Color and SMOS Salinity Data. *Remote Sensing Environ.* 184, 124–138. doi:10.1016/j.rse.2016.05.006

Matsuoka, A., Boss, E., Babin, M., Karp-Boss, L., Hafez, M., Chekalyuk, A., et al. (2017). Pan-Arctic Optical Characteristics of Colored Dissolved Organic Matter: Tracing Dissolved Organic Carbon in Changing Arctic Waters Using Satellite Ocean Color Data. *Remote Sensing Environ.* 200, 89–101. doi:10.1016/j.rse.2017.08.009

Matsuoka, A., Hooker, S. B., Bricaud, A., Gentili, B., and Babin, M. (2013). Estimating Absorption Coefficients of Colored Dissolved Organic Matter (CDOM) Using a Semi-analytical Algorithm for Southern Beaufort Sea Waters: Application to Deriving Concentrations of Dissolved Organic Carbon from Space. *Biogeosciences* 10, 917–927. doi:10.5194/bg-10-917-2013

Matsuoka, A., Ortega-Retuerta, E., Bricaud, A., Arrigo, K. R., and Babin, M. (2015). Characteristics of Colored Dissolved Organic Matter (CDOM) in the Western Arctic Ocean: Relationships with Microbial Activities. *Deep Sea Res. Part Topical Stud. Oceanography* 118, 44–52. doi:10.1016/j.dsr2.2015.02.012

McGuire, A. D., Koven, C., Lawrence, D. M., Clein, J. S., Xia, J., Beer, C., et al. (2016). Variability in the Sensitivity Among Model Simulations of Permafrost and Carbon Dynamics in the Permafrost Region between 1960 and 2009. *Glob. Biogeochem. Cycles* 30, 1015–1037. doi:10.1002/2016GB005405

Morley, J. K. (2012). Observations of Flow Distributions and River Breakup in the Mackenzie Delta, NWT. Master's thesis. Edmonton (Canada): University of Alberta.

Mulligan, R. P., and Perrie, W. (2019). Circulation and Structure of the Mackenzie River Plume in the Coastal Arctic Ocean. *Continental Shelf Res.* 177, 59–68. doi:10.1016/j.csr.2019.03.006

Mulligan, R. P., Perrie, W., and Solomon, S. (2010). Dynamics of the Mackenzie River Plume on the Inner Beaufort Shelf during an Open Water Period in Summer. *Estuarine, Coastal Shelf Sci.* 89, 214–220. doi:10.1016/j.ecss.2010.06.010

Nash, J. E., and Sutcliffe, J. V. (1970). River Flow Forecasting through Conceptual Models Part I - A Discussion of Principles. *J. Hydrol.* 10, 282–290. doi:10.1016/0022-1694(70)90255-6

Nill, L., Ullmann, T., Kneisel, C., Sobiech-Wolf, J., and Baumhauer, R. (2019). Assessing Spatiotemporal Variations of Landsat Land Surface Temperature and Multispectral Indices in the Arctic Mackenzie Delta Region between 1985 and 2018. *Remote Sensing* 11, 2329. doi:10.3390/rs11192329

Normandin, C., Frappart, F., Lubac, B., Bélanger, S., Marieu, V., Blarel, F., et al. (2018). Quantification of Surface Water Volume Changes in the Mackenzie Delta Using Satellite Multi-mission Data. *Hydrol. Earth Syst. Sci.* 22, 1543–1561. doi:10.5194/hess-22-1543-2018

Opsahl, S., Benner, R., and Amon, R. M. W. (1999). Major Flux of Terrigenous Dissolved Organic Matter through the Arctic Ocean. *Limnol. Oceanogr.* 44, 2017–2023. doi:10.4319/lo.1999.44.8.2017

Pisaric, M. F. J., Thienpont, J. R., Kokelj, S. V., Nesbitt, H., Lantz, T. C., Solomon, S., et al. (2011). Impacts of a Recent Storm Surge on an Arctic delta Ecosystem Examined in the Context of the Last Millennium. *Proc. Natl. Acad. Sci.* 108, 8960–8965. doi:10.1073/pnas.1018527108

Rawlins, M. A., Connolly, C. T., and McClelland, J. W. (2021). Modeling Terrestrial Dissolved Organic Carbon Loading to Western Arctic Rivers. *J. Geophys. Res. Biogeosci* 126, e2021JG006420. doi:10.1029/2021JG006420

Raymond, P. A., McClelland, J. W., Holmes, R. M., Zhulidov, A. V., Mull, K., Peterson, B. J., et al. (2007). Flux and Age of Dissolved Organic Carbon Exported to the Arctic Ocean: A Carbon Isotopic Study of the Five Largest Arctic Rivers. *Glob. Biogeochem. Cycles* 21. doi:10.1029/2007GB002934

Runkel, R. L., Crawford, C. G., and Cohn, T. A. (2004). Load Estimator (LOADEST): A FORTRAN Program for Estimating Constituent Loads in Streams and Rivers. *Tech. Methods* 4, A5. doi:10.3133/tm4a5

Schuur, E. A. G., McGuire, A. D., Schädel, C., Grosse, G., Harden, J. W., Hayes, D. J., et al. (2015). Climate Change and the Permafrost Carbon Feedback. *Nature* 520, 171–179. doi:10.1038/nature14338

Schwab, M. S., Hilton, R. G., Raymond, P. A., Haghipour, N., Amos, E., Tank, S. E., et al. (2020). An Abrupt Aging of Dissolved Organic Carbon in Large Arctic Rivers. *Geophys. Res. Lett.* 47, e2020GL088823. doi:10.1029/2020GL088823

Searcy, C., Dean, K., and Stringer, W. (1996). A River-Coastal Sea Ice Interaction Model: Mackenzie River Delta. *J. Geophys. Res.* 101, 8885–8894. doi:10.1029/96JC00120

Shiklomanov, A. I., Holmes, R. M., McClelland, J. W., Tank, S. E., and Spencer, R. G. M. (2020). Arctic Great Rivers Observatory. Discharge Dataset, Version 20201122. Available at: https://www.arcticrivers.org/data.

Shrestha, R. R., Prowse, T. D., and Tso, L. (2019). Modelling Historical Variability of Phosphorus and Organic Carbon Fluxes to the Mackenzie River, Canada. *Hydrol. Res.* 50, 1424–1439. doi:10.2166/nh.2019.161

Spencer, R. G. M., Mann, P. J., Dittmar, T., Eglinton, T. I., McIntyre, C., Holmes, R. M., et al. (2015). Detecting the Signature of Permafrost Thaw in Arctic Rivers. *Geophys. Res. Lett.* 42, 2830–2835. doi:10.1002/2015GL063498

Tank, S. E., Striegl, R. G., McClelland, J. W., and Kokelj, S. V. (2016). Multi-decadal Increases in Dissolved Organic Carbon and Alkalinity Flux from the Mackenzie Drainage basin to the Arctic Ocean. *Environ. Res. Lett.* 11, 054015. doi:10.1088/1748-9326/11/5/054015

Tanski, G., Bröder, L., Wagner, D., Knoblauch, C., Lantuit, H., Beer, C., et al. (2021). Permafrost Carbon and CO2 Pathways Differ at Contrasting Coastal Erosion Sites in the Canadian Arctic. *Front. Earth Sci.* 9, 630493. doi:10.3389/feart.2021.630493

Tanski, G., Couture, N., Lantuit, H., Eulenburg, A., and Fritz, M. (2016). Eroding Permafrost Coasts Release Low Amounts of Dissolved Organic Carbon (DOC) from Ground Ice into the Nearshore Zone of the Arctic Ocean: Permafrost Coasts Release Low Amounts of Doc. *Glob. Biogeochem. Cycles* 30, 1054–1068. doi:10.1002/2015GB005337

Tarnocai, C., Canadell, J. G., Schuur, E. A. G., Kuhry, P., Mazhitova, G., and Zimov, S. (2009). Soil Organic Carbon Pools in the Northern Circumpolar Permafrost Region. *Glob. Biogeochem. Cycles* 23. doi:10.1029/2008gb003327

Timmermans, M.-L., and Labe, Z. (2021). "Sea Surface Temperature," in *ArcticReport Card*. Editors M. T. Druckenmille, and M. Thoman R L (Washington, D.C, USA: National Oceanic and Atmospheric Administration), 41–45. doi:10.25923/2y8r-0e49

Tokuda, D., Kim, H., Yamazaki, D., and Oki, T. (2019). Development of a Global River Water Temperature Model Considering Fluvial Dynamics and Seasonal Freeze-Thaw Cycle. *Water Resour. Res.* 55, 1366–1383. doi:10.1029/2018WR023083

Tumel, N. (2002). in *Permafrost. The Physical Geography of Northern Eurasia*. Editor M. Shahgedanova (Oxford: Oxford Univ. Press).

Vaqué, D., Lara, E., Arrieta, J. M., Holding, J., Sà, E. L., Hendriks, I. E., et al. (2019). Warming and CO2 Enhance Arctic Heterotrophic Microbial Activity. *Front. Microbiol.* 10, 494. doi:10.3389/fmicb.2019.00494

Vincent, W. F., Lemay, M., and Allard, M. (2017). Arctic Permafrost Landscapes in Transition: towards an Integrated Earth System Approach. *Arctic Sci.* 3, 39–64. doi:10.1139/as-2016-0027

Conflict of Interest: The authors declare that the research was conducted in the absence of any commercial or financial relationships that could be construed as a potential conflict of interest.

Publisher's Note: All claims expressed in this article are solely those of the authors and do not necessarily represent those of their affiliated organizations, or those of the publisher, the editors and the reviewers. Any product that may be evaluated in this article, or claim that may be made by its manufacturer, is not guaranteed or endorsed by the publisher.

Advantages of publishing in Frontiers

OPEN ACCESS
Articles are free to read for greatest visibility and readership

FAST PUBLICATION
Around 90 days from submission to decision

HIGH QUALITY PEER-REVIEW
Rigorous, collaborative, and constructive peer-review

TRANSPARENT PEER-REVIEW
Editors and reviewers acknowledged by name on published articles

Frontiers
Avenue du Tribunal-Fédéral 34
1005 Lausanne | Switzerland

Visit us: www.frontiersin.org
Contact us: frontiersin.org/about/contact

REPRODUCIBILITY OF RESEARCH
Support open data and methods to enhance research reproducibility

DIGITAL PUBLISHING
Articles designed for optimal readership across devices

FOLLOW US
@frontiersin

IMPACT METRICS
Advanced article metrics track visibility across digital media

EXTENSIVE PROMOTION
Marketing and promotion of impactful research

LOOP RESEARCH NETWORK
Our network increases your article's readership